AN EXPERIMENTAL INVESTIGATION OF DUAL-POLARIZED ATMOSPHERIC PROPAGATION AT 73 GHz

by

JOHN BASIL PETERS

B.A.Sc., The University of British Columbia, 1977

A THESIS SUBMITTED IN PARTIAL FULFILMENT OF

THE REQUIREMENTS FOR THE DEGREE OF

DOCTOR OF PHILOSOPHY

in

THE FACULTY OF GRADUATE STUDIES

(Department of Electrical Engineering)

We accept this thesis as conforming

to the required standard

THE UNIVERSITY OF BRITISH COLUMBIA

February 1982

In presenting this thesis in partial fulfilment of the requirements for an advanced degree at the University of British Columbia, I agree that the Library shall make it freely available for reference and study. I further agree that permission for extensive copying of this thesis for scholarly purposes may be granted by the head of my department or by his or her representatives. It is understood that copying or publication of this thesis for financial gain shall not be allowed without my written permission.

Department of Elec. Eng.

The University of British Columbia
1956 Main Mall
Vancouver, Canada
V6T 1Y3

Date April 7, 1982

ABSTRACT

This thesis describes the design, construction and results of an accurate, 73 GHz, dual-polarized atmospheric propagation experiment conducted over a 1.8 km total length radar path. The millimetre-wave equipment consisted of a switched-polarization transmitter and a two-channel receiving system which included a phase-compensated crosspolar cancellation network and a novel, high-performance microstrip IF/LO diplexer. Meteorological instrumentation consisted of an improved electrostatic disdrometer, a raingauge network with high temporal and spatial resolution and a three-vector anemometer.

A comprehensive experimental model was developed to predict the system crosspolar discrimination (XPD) response during a wide variety of conditions. This model was used to analyze, for what is believed to be the first time, the effects of: orthomode transducer port mismatches, the frequency response and error sensitivity of crosspolar cancellation systems and the range of possible cancelled system XPD responses during rain. This model also led to the development of a phase compensation technique used to improve the stability of the crosspolar cancellation network. The application of the experimental model resulted in far more accurate determinations of path XPD than would have been otherwise possible.

The cancelled XPD results showed a reasonable correlation to horizontal wind velocities and agreed with model predictions for effective

mean canting angles ranging between 0 and 6°. The frequent observation of negative differential attenuations and erratic uncancelled XPDs led to the conclusion that drops along the path often did not have consistent shapes and canting angles. This is believed to be due to extremely variable wind conditions. Copolar attenuations considerably lower and higher than expected from the standard predictions were observed. The higher attenuations are satisfactorily explained as resulting from vertical wind conditions and are correlated to the predictions from a proposed model which includes the effects of constant vertical wind velocities.

TABLE OF CONTENTS

Page

Page

Page

Page

LIST OF FIGURES

Page

Page

Page

Page

Page

Page

LIST OF TABLES

Page

ACKNOWLEDGEMENTS

I would like foremost, to acknowledge the contribution, encouragement and moral support of Dr. M.M.Z. Kharadly whose wealth of knowledge about practical and theoretical microwave techniques and critical insight helped make this project successful.

I am also very grateful to Dr. Peter Watson, of the University of Bradford, U.K. for providing the forward scattering amplitudes on which the calculations in Chapter 4 are based.

Mr. Jack Stuber, formerly of the Electrical Engineering machine shop, made several contributions to this work, including the construction of: the antenna and reflector mounts and shields, raingauges, disdrometer and numerous waveguide sections.

Mr. James Johnston, who was a technician in our lab was also very helpful in: the final disdrometer calibration, microcomputer software and preparation of this report.

I would also like to specially thank Gail Schmidt for typing this report.

Mr. Tony Leugner, of the Electrical Engineering Department was extremely helpful by servicing the data acquisition minicomputer system and by constructing the disdrometer preamplifier and mixer bias circuits.

Many members of the departmental technical staff, including: Al MacKenzie, Chris Sheffield, Derek Daines, Dave Fletcher, and Wally Walters, provided invaluable assistance at one time or another during the course of this work.

Assistance in the development of the first version of the disdrometer was provided by: Mike Koombes, Vince Loney and William Wong.

The software for data handling and presentation was developed by: Ian Vogelesang, Brian Thompson, Peter Chun, Lisbeth Seeley, Eric Minch, Andrew Milne, Ramon Valerda, Ho Jun Lee and Len Smart.

The Postgraduate Scholarship I received from the Natural Sciences and Engineering Research Council is also greatfully acknowledged.

Funds for this project were provided by the Communications Research Center, Ottawa, under the following DSS contracts: OSU77-00056, OSU77-000261, OSU78-00012, OSU79-00009, OSU80-00129, OSU81-00057, and by the Natural Science and Engineering Research Council under grant A-3344.

1. INTRODUCTION

Increasing utilization of the microwave spectrum has created an active interest in the application of the millimetre-wave bands [1.1]-[1.12] and orthogonal polarization frequency reuse [1.6], [1.13]-[1.15]. Many new systems employing atmospheric propagation of the higher microwave and millimetre frequencies are now being developed. The main uses planned for these higher frequencies are wideband terrestrial and satellite communication links, (both analog and digital) and a variety of radar applications. Millimetre-wave systems are also rapidly becoming practical because of advances in higher frequency solid-state components and integrated circuit technologies.

To be able to effectively apply the millimetre frequencies and the techniques of polarization frequency reuse, accurate information about the effects of atmospheric propagation, especially during rain, must be available to system designers. The mathematical methods for predicting the important atmospheric propagation parameters during rain are fairly well developed and litte controversy persists about the basic theory. However, the usefulness of these mathematical models is limited because very little is known about some of the meteorological parameters necessary for accurate predictive calculations. There have also been a significant number of reported experimental measurements which do not appear to agree with the basic theoretical predictions based on simultaneous meteorological observations. In most instances, this is probably due to inaccurate or incomplete meteorological instrumentation or inadequacies in the meteorological or experimental models. These factors create a definite need for accurate millimetre-wave and dual-polarized propagation data with comprehensive meterological observations to verify the basic theory and to learn more about the meteorological conditions important to these areas of atmospheric propagation.

1.1 Spectrum Demand

Increasing demand for terrestrial microwave systems and the phenomenal growth in satellite communications has significantly reduced the availability of licensable channels in the lower microwave spectrum. In Canada, the recent rate of growth of licenced assignments has been 10-20% per year in this frequency range [1.16]. The main areas of increasing application are multi-channel entertainment video, high-speed business data and telephony. Spectrum congestion problems have been compounded by the rapid increase in satellite communications systems, which in the past, have shared frequency bands with terrestrial services. As more satellite systems are planned for urban areas, frequency coordination with terrestrial services has become increasingly difficult [1.17], [1.18]. Frequency coordination problems will spread to higher frequencies and become even more severe for lower frequencies, due to the large number of new satellite systems planned for the next few years, as shown in Fig. 1.1 [1.19]. Since it is unusual for channel allocations to be relinquished once they have been assigned, the radio spectrum is, in some ways, similar to a nonrenewable resource.

In response to the need for more licensable spectrum, the 1979 World Administrative Radio Conference (WARC-79) significantly revised the

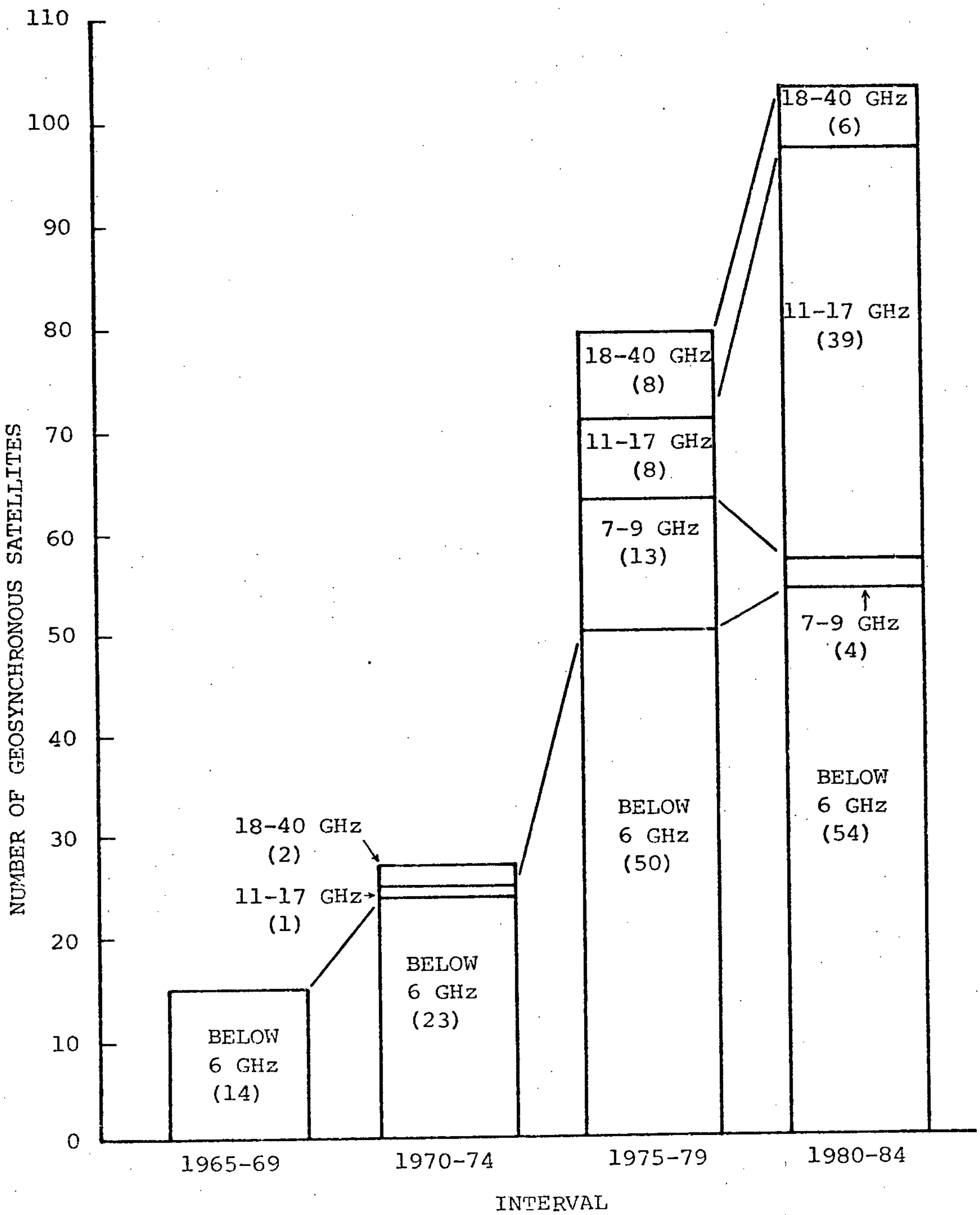

Fig. 1.1. Geosynchronous satellites in orbit and planned.

International Table of Frequency Allocations above 40 GHz. These new allocations are considered to "reflect a high level of interest and activity in this portion of the spectrum" and were "created with the objective of stimulating development of this spectrum resource" [1.20]. The millimetre-wave spectrum, referred to here as 30-300 GHz (i.e. the EHF band) can be roughly characterized by bands defined by regions of high clear-weather attenuation caused by molecular-resonance absorption. Fig. 1.2, shows the atmospheric attenuation bands caused by oxygen and water vapour [1.21]. Table 1(a) from [1.20], gives the frequency limits and band designations for the absorption bands and windows in the frequency range 40-275 GHz. A summary of the WARC-79 allocations, from [1.20] is shown in Table 1(b) to 1(e). Complete spectrum allocations resulting from WARC-79 are included in [1.22].

1.2 Millimetre Applications

Even though all types of services are allocated in the frequency range above 40 GHz, the specific characteristics of these frequencies make certain applications more advantageous than others. Applications employing atmospheric propagation where millimetre-wave systems have some benefit over microwave or optical systems include:

- short haul point-to-point or local distribution terrestrial links [1.23], [1.26], [1.29], [1.30], [1.31], [1.36].
- small, lightweight, portable communication systems [1.5], [1.24], [1.30], [1.31], [1.32], [1.33].

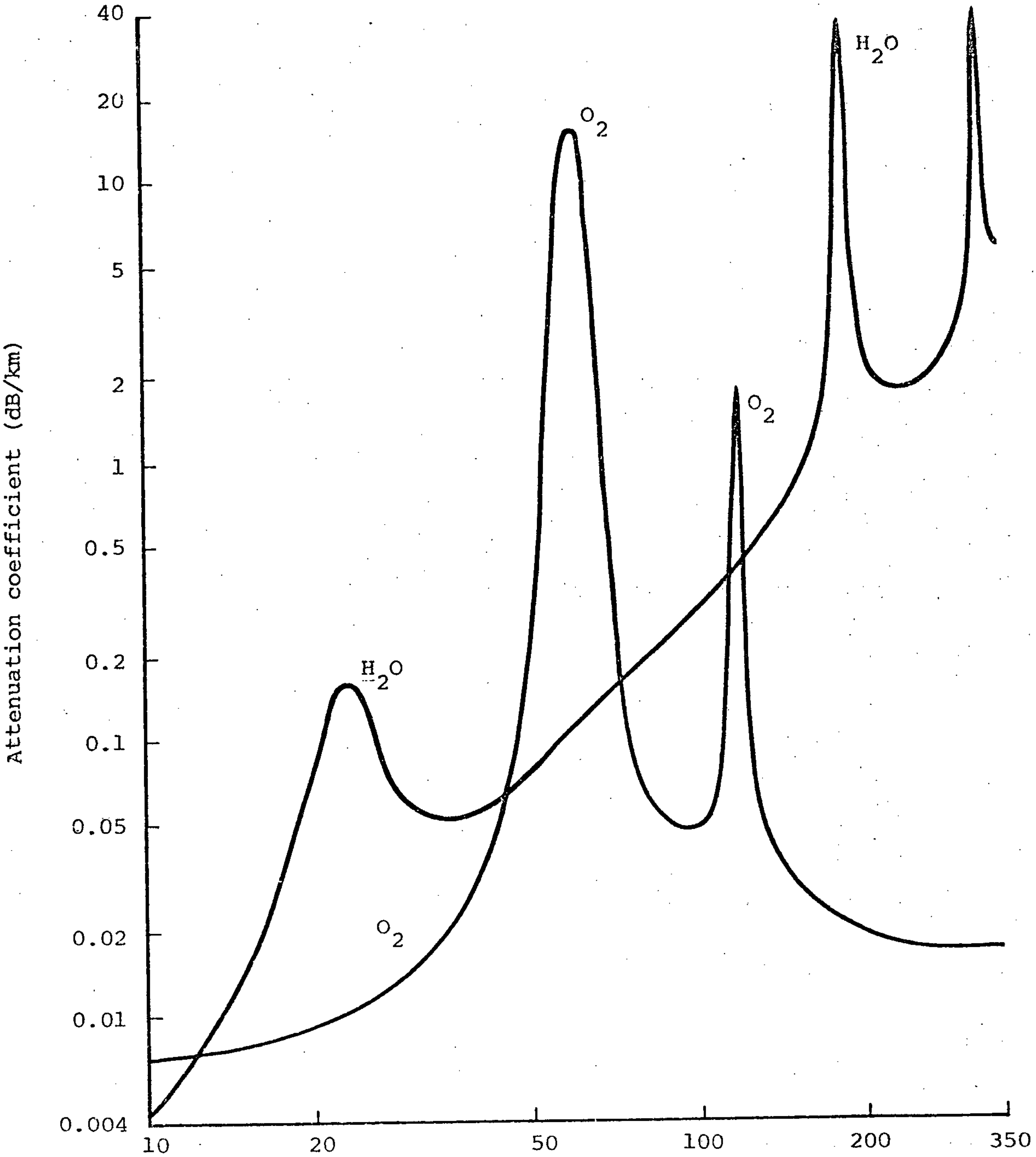

Fig. 1.2. Atmospheric attenuation due to molecular absorption.

TABLE 1(a) SUMMARY OF ALLOCATIONS ABOVE 40 GHz

Total Width of Spectrum Allocated	235 GHz
Number of Services	21
Bands Allocated Exclusively	0
Average Spectrum/Band:	
<100 GHz	2.5 GHz
>100 GHz	5.8 GHz
Average Services/Band	3.5

TABLE 1(b) ATMOSPHERIC WINDOW AND ABSORPTION BAND LIMITS

Window	Absorption Band	Limits (GHz)
W_1		39.5-51.4
	A_1	51.4-66
W_2		66-105
	A_2	105-134
W_3		134-170
	A_3	170-190
W_4		190-275

TABLE 1(c) ALLOCATIONS TO SATELLITE SERVICES

Service	W_1	A_1	W_2	A_2	W_3	A_3	W_4	Total	Total Bandwdith, GHz
Amateur-Satellite	1		2		2		2	7	21.7
Fixed	4		5		3		5	17	69.5
Inter		2		2		4		8	44.0
Mobile	3		4		1		2	10	52.5
Broadcasting	1		1					2	4
Radionavigation	1		2		1		2	6	44.5

TABLE 1(d) ALLOCATIONS TO SCIENTIFIC SERVICES

Service	W_1	A_1	W_2	A_2	W_3	A_3	W_4	Total	Total Bandwidth, GHz
Earth Exploration-Satellite	1	5	2	2	2	2	4	18	69.8
Radio Astronomy	1		1	1	1	1	2	7	49
Space Research	1	5	2	2	2	2	4	18	69.8

TABLE 1(e) ALLOCATIONS TO TERRESTRIAL SERVICES

Service	W_1	A_1	W_2	A_2	W_3	A_3	W_4	Total	Total Bandwidth, GHz
Amateur	1		2		2		2	7	21.7
Fixed	6	3	7	2	4	4	6	32	124.7
Mobile	8	3	9	2	5	4	7	38	169
Broadcasting	1		1					2	4
Radiolocation		1	3	1	2		3	10	53
Radionavigation	1		2		1		2	6	44.5

- a wide variety of high resolution radar applications [1.23], [1.24], [1.26], [1.28].
- secure communication links operating in absorption bands (especially at 60 GHz) [1.5], [1.23], [1.24], [1.26], [1.32], [1.33].
- very wideband digital links [1.25], [1.31], [1.35].
- multichannel video systems [1.30].
- satellite communication systems [1.2], [1.4], [1.23], [1.24], [1.26], [1.27].

and

- radiometer, remote sensing and imaging systems, [1.23], [1.24], [1.25], [1.26], [1.27], [1.28], [1.34].

1.3 Advantages and Disadvantages of Millimetre Frequencies

The major factors which make millimetre frequencies advantageous in these applications arise from the short wavelength, large operating bandwidths and availability of spectrum. Shorter wavelengths result in physically smaller components, higher antenna gains and lower antenna beamwidths (for a specified antenna aperture). Narrow antenna beamwidths are desirable because they ease frequency coordination problems, reduce multipath fading, lower the probability of unauthorized reception or jamming, and yield higher resolutions in radar and radiometer systems. Bandwidths of several gigahertz are more easily obtainable in millimetre systems because they represent a smaller percentage of the operating frequency. The availability of spectrum in the millimetre range will mean that more systems, with higher bandwidths, can be licensed in any geographical area. Another advantage of millimetre-wave systems in high resolution radar applications is their ability to penetrate fog, smoke and dust [1.23], [1.24]. In communication systems requiring a high degree of security, the absorption bands in the millimetre range, especially at 60 GHz, are an advantage because they can further reduce the probability of unauthorized reception. [1.23], [1.32], [1.33].

The disadvantages of millimetre-wave systems are higher copolar attenuation (CPA) due to rain and molecular absorption and lower component performance/cost ratios. Attenuation due to rain and other hydrometeors increases with frequency up to approximately 100 GHz. This factor will ultimately limit the reliability of millimetre systems employing atmospheric propagation. Millimetre components are currently more expensive than microwave components of comparable performance because higher mechanical precision is required, semiconductors are more difficult to fabricate and production volumes are low. Even though nothing can be done about higher rain attenuation, great advances are being made in millimetre components.

1.4 Millimetre Semiconductors and Integrated Circuits

In the past few years, developments in millimetre semiconductors have led to dramatic improvements in device performance. For the past few years, the power output levels of solid-state millimetre sources has been increasing at the rate of 3 dB per year [1.37]. It is now possible to obtain 17 W peak at 94 GHz in low-duty-cycle pulses from a single IMPATT diode [1.38] and 63 W peak at 92 GHz from combined IMPATTS [1.39]. Recently, a 61 GHz IMPATT amplifier with 50 dB gain and a 2.5 W power output was demonstrated [1.40].

At the TRG division of Alpha Industries, signficant advances have been made in the millimetre application of beam lead diodes. This technology has improved the performance of mixers at frequencies up to 140 GHz and allows mass production techniques to be used to reduce costs [1.41], [1.42]. These beam lead diodes were used in a suspended stripline mixer which yielded a total double sideband receiver noise figure of 5.8 dB at 110 GHz [1.33].

Recent advances in millimetre frequency integrated circuit technologies also promise to reduce the cost of components. Several types of transmission line structures have been demonstrated to be advantageous for millimetre-wave IC fabrication. These include:

- dielectric waveguide [1.43], [1.44], [1.46].
- image waveguide [1.45], [1.46].
- fin line [1.47], [1.48].
- microstrip line [1.49], [1.50], [1.51].
- suspended stripline [1.41], [1.42], [1.52].

and

- E-plane waveguide [1.53].

These techniques will yield large reductions in component costs when volumes can justify the use of modern integrated circuit production methods [1.38].

1.5 Orthogonal Polarization Frequency Reuse

Orthogonal polarization frequency reuse can double spectrum utilization and result in significant system cost reductions. During normal clear-weather conditions it is possible to transmit two orthogonal (linear or circular) polarizations through one pair of antennas with insignificant atmospheric coupling between polarizations. This can allow separate communications channels to occupy the same frequency or can be used to alleviate frequency coordination problems in congested areas.

Polarization frequency reuse can offer tremendous cost advantages in both terrestrial and satellite system because both polarizations can share a common antenna system. In terrestrial systems, topographical conditions often necessitate the use of large towers to support antennas. These towers can often cost more than the systems' electronic components. By using a common antenna for two polarizations, the total cost of purchasing, shipping, installing and maintaining the antenna and tower can be greatly reduced. In satellite systems, these economic advantages are even greater because antennas are a larger portion of total system costs and because mounting additional antennas on the actual satellite would be extremely expensive.

Unfortunately, some atmospheric conditions can cause coupling between polarizations and a reduction in the path crosspolar discrimination (XPD) and therefore system reliability. A reduction in path XPD can occur as signals propagate through rain (or other hydrometeors) or during multipath propagation. Multipath XPD reduction is very important in the lower microwave region but because this report is concerned only with millimetre propagation, multipath XPD will not be discussed in detail. Rain can cause a reduction in XPD because raindrops are not spherical and in the presence of vertical wind gradients can have a preferred axis orientation, or canting angle. Depolarization occurs because the two polarizations experience a differential attenuation and differential phase shift propagating through the anisotropic rain medium.

1.6 Propagation Theory and Experiment

To be able to design economical systems with predictable reliability using millimetre-waves or polarization frequency reuse, accurate knowledge of atmospheric propagation phenomena is required. At the present time, sufficient, reliable information is not available on propagation at higher frequencies and in different geographical regions. The advancement of practical atmospheric propagation knowledge requires a combination of theoretical and experimental investigations.

The basic mathematical methods for predicting atmospheric propagation through rain are fairly well developed. In the case of the calculation of rain attenuation for a set of assumed rain conditions, the earlier uncertainties and controversies appear to have been resolved in the past few years. Theoretical methods for predicting dual-polarization propagation parameters during rain are less mature but there appears to be agreement on the basic techniques. Several investigators are continuing to refine the calculation of XPD, mainly by including more comprehensive meteorological models.

The main inadequacy in the theoretical prediction of atmospheric propagation during rain is a lack of knowledge about the meteorological inputs to the calculations. To calculate rain attenuation, the number and sizes of raindrops at all points within the propagation path must be known. This is extremely difficult to predict because very limited actual drop size data are available and it is known that the drop size distribution depends on rainrate – which also has large temporal, spatial and geographical variations – the type of rainstorm, vertical wind velocities, position within a raincell and other meteorological conditions. For dual-polarization propagation calculations, in addition to the previous information, it is necessary to know the drop shape and canting angle statistics. Because of the extreme difficulty of accurately measuring these parameters in natural rain, almost no information about canting angles presently exists.

Radio system designers in Canada are very fortunate to have a recently published, detailed study of rainrate statistics across Canada [1.54]. Similar data, with less geographical resolution, have also recently been published by Crane, showing rainrate regions for all areas of the earth [1.55], [1.56].

While these data bases greatly improve the accuracy of system reliability predictions, much more data are needed to be able to make accurate millimetre or dual-polarization propagation predictions. For millimetre propagation predictions, drop size information is important because the calculations are very much more sensitive to drop distribution than in the microwave range due to the larger drop size-to-wavelength ratio. For accurate XPD predictions, the canting angle statistics are essential. The difficulty of measuring these parameters means that system designers will not be able to accurately predict millimetre or dual-polarized propagation parameters, in a given geographical location, by using available meteorological statistics and propagation calculations. Because it is not feasible to measure all the required meteorological parameters accurately, there is considerable interest in attempting to determine effective rain conditions by comparing simultaneous propagation and measurable rain conditions.

Experimental data on atmospheric propagation with simultaneous meterological observations are needed to: validate the theoretical methods, provide practical and directly applicable propagation data and to gain knowledge of the effective meteorological parameters required for propagation predictions during natural rain. Many investigators have mentioned the need for experimental data for comparison to theoretical calculations, including: Neves and Watson [1.57], Zavody and Harden]1.59], Llewellyn Jones [1.60], Bulter [1.61], Evans, Uzunoglu and Holt [1.62], Dintelmann and Rucher [1.13] and Ippolito [1.19].

Data obtained on propagation in one frequency range and location can be useful in a variety of applications. If adequate meteorological information is included with the propagation data, it is possible to improve predictions in other geographical areas if similar, comparable meterological statistics are available. Propagation information obtained on terrestrial links can also be useful in predicting link performance on satellite paths [1.8], [1.64], [1.65]. Specific propagation results can also be useful at other frequencies by the use of frequency scaling [1.55], [1.66].

The need for accurate experimental data is especially great above about 40 GHz because very limited data have been published [1.9], [1.58], [1.59], [1.60], [1.63]. Experimental work is also important in the millimetre range because the larger drop size-to-wavelength ratio and freedom from multipath give most importance to different propagation problems than those which are fairly well understood in the microwave region. In addition, there have been a number of cases where data from experiments, especially dual-polarized or millimetre frequency investigations, did not agree with theoretical calculations, probably because of inadequate meterological observations [1.61], [1.62], [1.64], [1.67]-[1.73]. More, specific examples of this lack of agreement are included in the next two sections which survey previous propagation experiments.

1.7 Previous Dual-Polarized Propagation Experiments

The experiments reviewed in this section are described here by the general term dual-polarized because they use two polarizations to study the anisotropic nature of atmospheric propagation during rain. This short survey of higher frequency, dual-polarized experiments is included to outline the different experimental techniques, survey the experimental system performances, and review the results obtained. At frequencies below about 18 GHz, there have been several excellent investigations of dual-polarized propagation. These studies are not mentioned here for the sake of brevity and because the important meterological conditions and propagation effects are, to some extent, different in the microwave and millimetre wave frequency ranges. There have also been several comprehensive dual-polarized satellite propagation experiments at frequencies up to 30 GHz which are not dicussed here.

DeLange, Dietrich and Hogg have reported a 60 GHz dual-polarized experiment on a 1.03 km. link at Bell Labs, Holmdel, New Jersey [1.74]. A switched transmitted polarization and a switched polarization single-channel receiver were used. Approximate isolations of 30 dB and 34 dB were achieved.

Fig. 4 in this reference shows a sharp, deep null in one polarization discrimination characteristic of the operating system. (These nulls are believed to be similar to those described in Section 2.5 of this report.)

In the discussion of the experimental results, the authors describe the results for one storm behaving "the way one might expect from simple theory: i.e. differential attenuation always positive (fade in horizontal polarization was greater than in vertical). The crosstalk [XPD] variations were pretty much the same for both polarizations, with the ratio [XPD] becoming poorer during the deeper fade". However, a different storm "did not produce results expected from the simple theory. For a considerable portion of the time, the differential attenuation was negative, indicating that the attenuation of the vertical component was greater than that of the horizontal component. The fact that the crosstalk ratio in both channels (Fig. 9) improved slightly in this case may be explained by referring to (Fig. 4) [the system isolation] which shows the clear weather operating point near +0.5 degree; a negative rotation (caused by the rain) of the vertical component from this value would reduce the cross-coupled energy and thereby improve the ratio". This report concludes that the 60 GHz differential attenuation "is seldom greater than 2 dB and the average differential is only 1.25 dB, even for fades greater than 30 dB".

Hogg and Chu [1.75] have presented data from this experiment in the form of a graph relating horizontal CPA to XPD. These results show a lower value of XPD than expected. This is attributed to the low clear-weather, crosspolar-discrimination level of their measuring system. No attempt was made to separate this clear weather XPD level from the atmospheric measurements.

Thomas [1.76] has compared some of the 60 GHz XPD data from this experiment to his calculated values. The effect of the finite experimental system isolation on the measured data seems to have been considered as a simple scalar addition. Using this technique, good agreement with calculated values was obtained for the two data points compared.

Neves and Watson have described a dual-polarized 36.5 GHz experimental investigation conducted over a 13.6 km link near the University of Bradford, U.K. [1.77]. In this study, the CW transmitted signal was polarized at 45°. Separate antennas continously monitored the vertical and horizontal components of the received signal. This experimental method was chosen to facilitate accurate measurements of differential attenuation, differential phase shift and 45° crosspolarization. With this set up, the received signals will have similar levels and high S.N.R. thus improving the accuracy of differential measurements. This polarization will also yield the highest levels of depolarized signals, but will result in a low sensitivity to canting angle measurements. Also included in this reference are earlier results for XPD over the same path for vertical transmitted polarization.

The rain instrumentation for this experiment consisted of a rapid response rain gauge and disdrometer at the receiving site. This data, along with wind information was used to construct a "synthetic storm model" to describe the meterological conditions along the path.

The authors conclude that their crosspolarization, differential phase and differential attenuation measurements were in good agreement with a theoretical rain model with 3° to 4° canting angle, 20° mean modulus and 20° to 25° standard deviation. They also report a greater number of larger drops in medium-heavy rainfall than given by the Laws-Parson drop size distribution.

Semplak conducted an experiment to measure 30.9 GHz polarization rotation over a 2.6 km path at Bell Labs, Holmdel, New Jersey [1.78]. In this experiment, the transmitted wave was oriented vertically and the receiver polarization was rapidly switched between plus and minus 45° with respect to vertical. The sum and difference powers for both received signals was used to calculate the polarization rotation. The XPD was then calculated using:

$$\text{XPD (dB)} = 20 \log_{10} (\tan \alpha) \tag{1.1}$$

where α is the measured polarization rotation. Results from this experiment showed that the minimum value of XPD was about 10 dB lower than its average value over a wide range of copolar attenuations. Semplak also showed a dependence of polarization rotation on cross-path wind velocity.

An earlier experiment by Semplak, also at 30.9 GHz, but over a 1.89 km path in the same location, used a similar experimental system to measure differential attenuation [1.79]. In this case, the transmitted wave was polarized at 45° and the receiver was switched between vertical and horizontal polarizations. The average relationship between the observed copolar and differential attenuations agreed well with the theoretical predictions. Rainrate does not appear to have been measured in either of these two experiments.

Turner described a dual polarization experiment at 22 GHz conducted over a 4 km link in Suffolk, England [1.80]. Two different modulation frequencies were used, but it was also necessary to switch the transmitted polarization to prevent interaction between channels within the IF amplifiers. Isolations of 29 dB and 30 dB were achieved. Variations in crosspolar signal levels observed during high wind velocities were attributed to inadequate antenna mount stability. Thirteen rainstorms were observed with copolar attenuations up to 8 dB and rainrates in excess of 15 mm/hr and on "no occasion [was] significant crosspolarization due to rain observed". However, on occasions when multipath was observed on other links in the area, "considerable variation in crosspolar signal was seen". Slow variations in crosspolar signal levels were also reported during apparently stable conditions with some indication that these effects were related to sunrise and sunset. Suggestions as to the cause of this effect included: moisture on radomes, multipath and variations in refractive index.

Shimba and Morita conducted a crosspolarization measurement experiment on 2.9 km and 4.3 km paths in Japan [1.81]. A single, 19 GHz, horizontally polarized signal was transmitted and both received polarizations were monitored. The receiving system crosspolar discrimination was approximately 35 dB. It is interesting to note that the data presented in this paper shows two periods during rainstorms where the measured XPD increased by appoximately 10 dB. This effect was not commented on by the authors.

Morita, Hosoya and Akeyama [1.82] reported another 19 GHz dual-polarization experiment at a second location in Japan over a 4 km path. In this experiment two different transmitted frequencies (19.3 and 19.4 GHz) and switched frequency receivers were employed. This method resulted in very high system isolations of 46 and 56 dB. The results for this location showed lower values of depolarization than for the similar experiment [1.81] described previously. Data presented in this paper also shows values of XPD more than 10 dB higher than clear weather values. The authors conclude that "the correlation between rain attenuation and depolarization was not necessarily high".

In a later paper describing both of the previous experiments, Shimba, Morita and Akeyama [1.83] conclude that there was a high correlation between attenuation and XPD for the combined data from both experiments. The large scatter of XPD data points at low attenuations, including values higher than the clear weather isolation, were thought to result from raindrop adherence to the radomes. No explanation as to why the wet radomes would cause this effect was offered. This paper also concludes that the copolar attenuation was about 30% greater than predicted.

1.8 Previous Single-Polarized Propagation Experiments

This section includes a short review of single-polarization millimetre propagation experiments designed to measure rain attenuation. Most of the experiments surveyed are the higher frequency investigations with good meteorological instrumentation.

Sander reported a millimetre wave attenuation investigation using vertically polarized waves at 52, 90.8 and 150 GHz simultaneously [1.84]. The experiment was conducted over a 1008 m total length radar path using a corner reflector at the Massachusetts Institute of Technology. Raingauges and Lammers type electrostatic disdrometers were used at three locations along the path. The disdrometers used in the experiment had a 25 cm^2 sampling area and six size classes. The author mentions that the instrument was subsequently redesigned to have a 100 cm^2 sample area and sixteen categories, but no details or results from the improved instrument were included in this reference. The results from this experiment show a wide scatter in the attenuation vs rainrate plots. Sander concludes that "Mainly because of the imperfections of the meteorological equipment used, but also because of the inhomogeneity of rain, only the statistical averages of our results verify the theoretical assumptions."

Humpleman and Watson conducted a 60 GHz attenuation experiment on a 680 m vertically polarized link at the University of Bradford, England [1.85]. Fast-response raingauges were located at each end of the path. An electrostatic disdrometer, developed by Sander [1.84], with a sampling time of 1 min. was used to measure the dropsize distribution. Synthetic storm models using the 700 mb or 850 mb pressure level effective wind velocities from radiosonde information were used to calculate path rainrates from the raingauge and disdrometer data. The calculated path rainrate gave a dramatic improvement in the correlation with measured attenuation for individual storms compared to using either of the rainrates measured at the ends of the path. Disdrometer evidence is presented which indicates that the variations in the attenuation-calculated path rainrate relation are due to dropsize distributions.

The attenuation calculated using the disdrometer data also shows much better agreement with the observed attenuation than the calculations using the Laws and Parsons distribution. In certain periods of heavy rain, attenuations were measured which were considerably lower than predicted for the Laws and Parsons dropsize distributions. An example is also included which shows a transistion from larger to smaller drops as a storm traverses the path.

Keizer, Snieder and de Haan have reported a 94 GHz, vertically polarized attenuation experiment over a 935 m path near The Hague, Netherlands [1.86], [1.87]. Path rainrate was measured with the raingauges spaced about 500 m apart. An electromechanical disdrometer with a 50 cm^2 sample area and 83 second sample period was used to monitor the drop size distribution. Horizontal windspeed, wind direction, pressure and humidity were also recorded. The agreement between the measured attenuation and the attenuation calculated from the disdrometer data was considered to be "very satisfactory." For low rainrates the measured attenuations were, in most cases, slightly higher than calculated. This was attributed to an increase in water vapour concentration of 1-2 g/m^3 resulting in a predicted 0.1 to 0.2 dB/km increase in attenuation.

Llewellyn Jones and Zavody conducted a 110 GHz attenuation experiment over a 2.65 km path in the Windsor-Slough area, England [1.88], [1.89], [1.90]. No meteorological data appears to have been recorded in this experiment. In this investigation, the objective was to record data for a one year period and determine link reliability statistics for this location.

Zavody and Harden have simultaneously measured vertical attenuation at 36 GHz and 110 GHz on a 220 m path in Slough, England [1.59]. Four rapid response raingauges, spaced about 40 m apart were used to measure the path rainrate. An electromechanical disdrometer with a 50 cm^2 sample area and 30 second sample period was also used. At 36 GHz, good agreement between measured attenuation and predicted attenuation for spheroidal drops was obtained. The 110 GHz results show a much larger scatter in the attenuation vs. rainrate plots. The authors state that a "significant number of the measured values lie outside the limiting curves for this range." An example is also included in this paper showing a reduction in drop sizes as a storm travels across the path. During another event, drops were much smaller than predicted by Laws and Parsons. In this storm no drops larger than 2.1 mm diameter were observed in rainrates over 15 mm/hr.

1.9 Thesis Objectives

The principal objective of this work is to develop an experimental system to study dual-polarized atmospheric propagation near 73 GHz. This investigation is part of an ongoing research program into millimetre-wave propagation which is being supported by the Communications Research Centre, Department of Communications, Ottawa. As an earlier part of this research program, a preliminary study of single-polarization 74 GHz copolar attenuation was conducted over the same path at the University of British Columbia [2.1]. During this investigation, attenuation and rainrate data were recorded for rainrates up to 10 mm/hr. The data were compared with the theory of Ryde and Ryde. Some of the equipment developed for this previous study was retained for this project, including: most of the data acquisition computer interface and software, parts of the raingauge network and the basic reflector.

More specifically, the first objective of this work is to record simultaneous meteorological and dual-polarized 73 GHz propagation data which are as accurate and as complete as possible. These propagation data include copolar attenuation and crosspolar discrimination for vertical and horizontal polarizations. The second objective is to construct and test a model capable of describing the XPD response of the experimental system. The final objective is to attempt to interpret some of the propagation observations in terms of various meteorological parameters including: horizontal and vertical wind velocities, dropsize distribution and type of rainstorm. The achievement of these objectives required the design and construction of a dual-polarized millimetre-wave transmitter, receiver and antenna system and meteorological instrumentation for measuring rain and wind parameters.

A dual-polarized millimetre wave link was established over a path on the University of British Columbia campus. Different dual-polarized experimental methods were compared to determine which was most suitable for this investigation. After a basic method had been chosen, applicable 73 GHz transmitting and receiving antenna systems were designed and constructed with the maximum possible performance compatible with the budget available. Comprehensive testing of components, subassemblies and the entire system was carried out to characterize, as thoroughly as possible, the millimetre-wave systems and thus reduce the uncertainty in the data arising from the nonideal behaviour of the experimental system.

The previous sections illustrated the importance of accurate, comprehensive meteorological instrumentation in this type of investigation. To measure path rainrate, a network of raingauges with high temporal and spatial resolution was installed along the propagation path. After a study of measurement methods, an accurate instrument to measure raindrops sizes, referred to here as a disdrometer, was developed. An anemometer was included to measure three components of the wind velocity vector.

An experimental model was developed to separate, as far as possible, the effects of the experimental system from the dual-polarized atmospheric propagation measurements. This model significantly improves the accuracy of the comparisons between the observed and theoretically predicted crosspolar discrimination (XPD). The theoretical calculations used the well established, basic mathematical techniques and meteorological observations to predict the atmospheric propagation conditions. The model incorporates actual measurements made of the experimental system dual-polarized performance, and reduces the uncertainty in the results due to the nonideal behaviour of the system components.

The experiment was designed to ensure the millimetre wave propagation data was as accurate and complete as possible within the available time and budget. These data should be useful to improve the basic understanding of the effects of the millimetre components and atmosphere (especially during rain) on millimetre-wave systems employing atmospheric propagation. These results should also be helpful in the verification of the basic theoretical prediction methods. In summary, this experiment should add to what is already known about dual-polarized and millimetre wave systems and improve the accuracy of the predicted performances of a variety of systems employing atmospheric propagation.

2. MILLIMETRE-WAVE EXPERIMENTAL SYSTEM

The dual-polarized millimetre-wave system used for investigating atmospheric propagation characteristics at 73.5 GHz used switched-polarization sampling and basically consisted of a CW transmitter, radar path and two channel receiver. A radar path was chosen because of the operational advantages of locating the transmitter and receiver in the same laboratory. Identical parabolic antennas with dual-polarity feeds were used for transmitting and receiving. Dual-polarization propagation measurements were made by periodically switching the transmitted signal between vertical and horizontal polarizations. The two-channel receiver continually monitored both linear polarizations. This resulted in each received channel representing a time multiplexed sample of one copolar and one crosspolar signal level. The basic system is shown in Fig. 2.1.

2.1 Comparison of Dual-Polarization Measurement Methods

The basic measurement methods which can be used to study linear dual-polarization propagation employ either a two-frequency dual-polarized transmitted signal or a switched-polarization transmitted signal. In the dual-frequency method, either two slightly different frequencies - which are close enough to be considered as propagating identically - or two different modulation frequencies on a common carrier frequency are transmitted with perpendicular polarizations. In the receiving subsystem, frequency selective circuits in both polarization channels separate the frequencies corresponding to each originally transmitted polarization. This method yields four

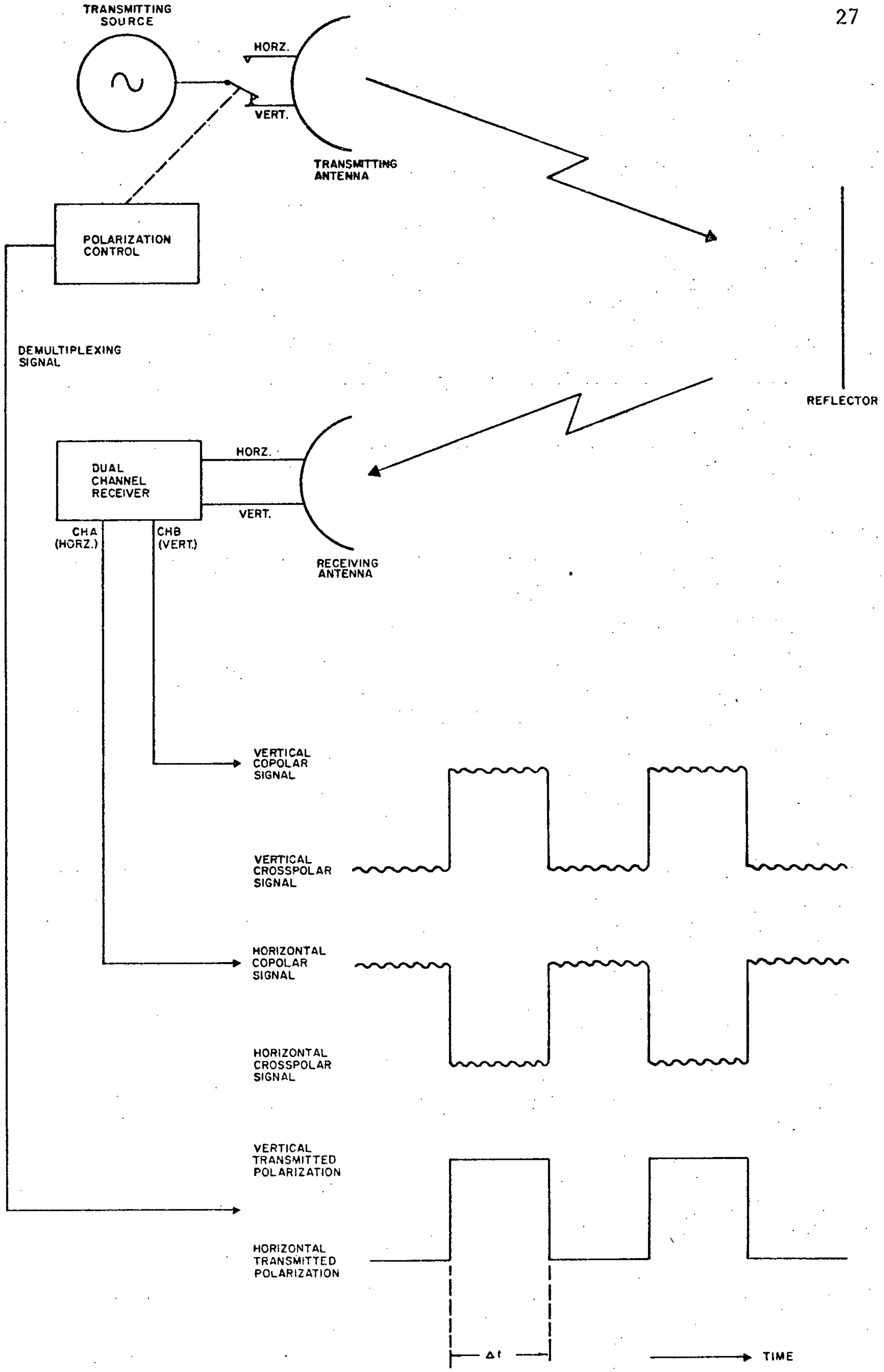

Fig. 2.1. Basic millimetre-wave experimental system.

simultaneous signals each corresponding to one element of the dual-polarization transmission matrix. In the switched-polarization method, the transmitted signal is sequentially switched between vertical and horizontal polarization and a two-channel receiver continually monitors both received polarizations. The switching rate is designed to be higher than the temporal resolution of the meteorological measuring equipment. With this system, the received signals must be demultiplexed to determine the four transmission matrix elements.

The switched polarization scheme was chosen for this experiment because of its implementation advantages. The dual-frequency schemes require either two separate transmitting signal sources, or high-level modulation circuits. If the two-source method is used, either the sources have to be phase-locked to each other or the receiver must include two phase-locked local oscillators, one for each transmitting source. If a single source with high level modulators is used, two frequency selective circuits for each received channel are needed.

It is very difficult to realize frequency selective circuits and amplifiers with the high isolation and dynamic range required for this type of experiment. Because complex filters are not feasible at millimetre frequencies, filtering would have to be done at an intermediate frequency (IF) or baseband. Filtering at IF is possible but sophisticated filters must be employed to achieve the necessary signal isolation. Baseband filters are easier to build but the large dynamic range of the signals puts tight constraints on the entire receiving system linearity, (nonlinearities before the baseband filters would produce intermodulation distortion which would reduce the isolation between channels and degrade the system accuracy). Dual-frequency schemes also require four signal level measuring subsystems to filter, average, detect and digitize the received amplitudes. The switched polarization method requires a polarization switching circuit but uses only a single transmitting source and one local oscillator. In this case, only two received signal level measuring subsystems are necessary. The advantages of reduced complexity and cost made the switched polarization method far more desirable in this experiment.

2.2 Transmitting System

The transmitting system block diagram is shown in Fig. 2.2. The system consists of a klystron oscillator, klystron power supply, isolators, frequency reference coupler, power level monitor, calibrated attenuator, feedline, pressurization system and polarization switch.

2.2.1 Klystron and Supply

The transmitting signal is generated by a Varian model 2101B reflex klystron oscillator. The klystron power supply circuits, cooling system and load isolator were designed to minimize incidental frequency modulation and transients in the tube output. This is important to ensure that the system sensitivity is not impaired and that the reliability of the phase lock system is not reduced.

The klystron is extremely susceptible to frequency modulation of its output by induced voltages on its power leads, stray magnetic fields or changes in load impedance. For example, the modulation sensitivity of the

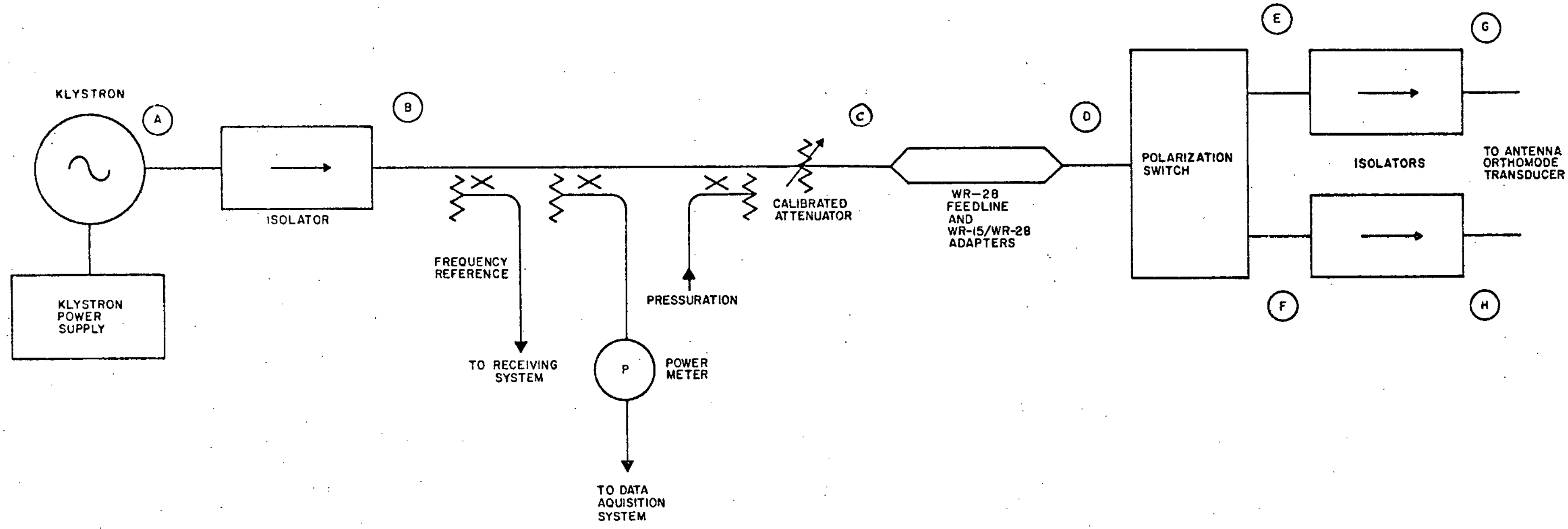

Fig. 2.2. Transmitting system block diagram.

tube reflector voltage is approximately 3 MHz/V. Incidental power line frequency modulation on the klystron output will reduce the received signal-to-noise level because the 60 Hz modulation sidebands will be rejected by the 30 Hz bandwidth of the receiver second IF filters (see Section 2.3.2).

Klystron frequency purity and stability also affect the reliability of the receiver phase lock circuits (see Section 2.3.1). If the receiver loses phase lock, reacquisition must be done manually. Because the experiment is often operated unattended, loss of phase lock can result in long periods of lost data. Loss of lock occurs when the change in the klystron frequency exceeds the receiver phase locked loop hold-in range or tracking rate. This usually occurs on a transient condition caused by a power line transient, thermal transient or "micro-arc" within the klystron tube. Micro-arcs unavoidably occur within tubes of this type because the extremely small cavities required for millimetre frequencies result in high field potentials between tube elements. If frequency modulation is also present on the klystron signal, the receiver's available lock range and ability to track transient frequency changes is reduced because the phase locked loop must also track the periodic frequency modulation.

The klystron power supply circuit is shown in Fig. 2.3. The Weinschel Z815C klystron supply was chosen because it has a heavily filtered dc filament supply. Low ripple on klystron filament supplies is necessary to prevent direct 60 Hz modulation via the tube cathode. A transient suppression network is included between the supply and klystron to limit currents during periods of micro-arcing. This circuit will reduce the transient frequency excursion and help prevent internal pitting of the tube

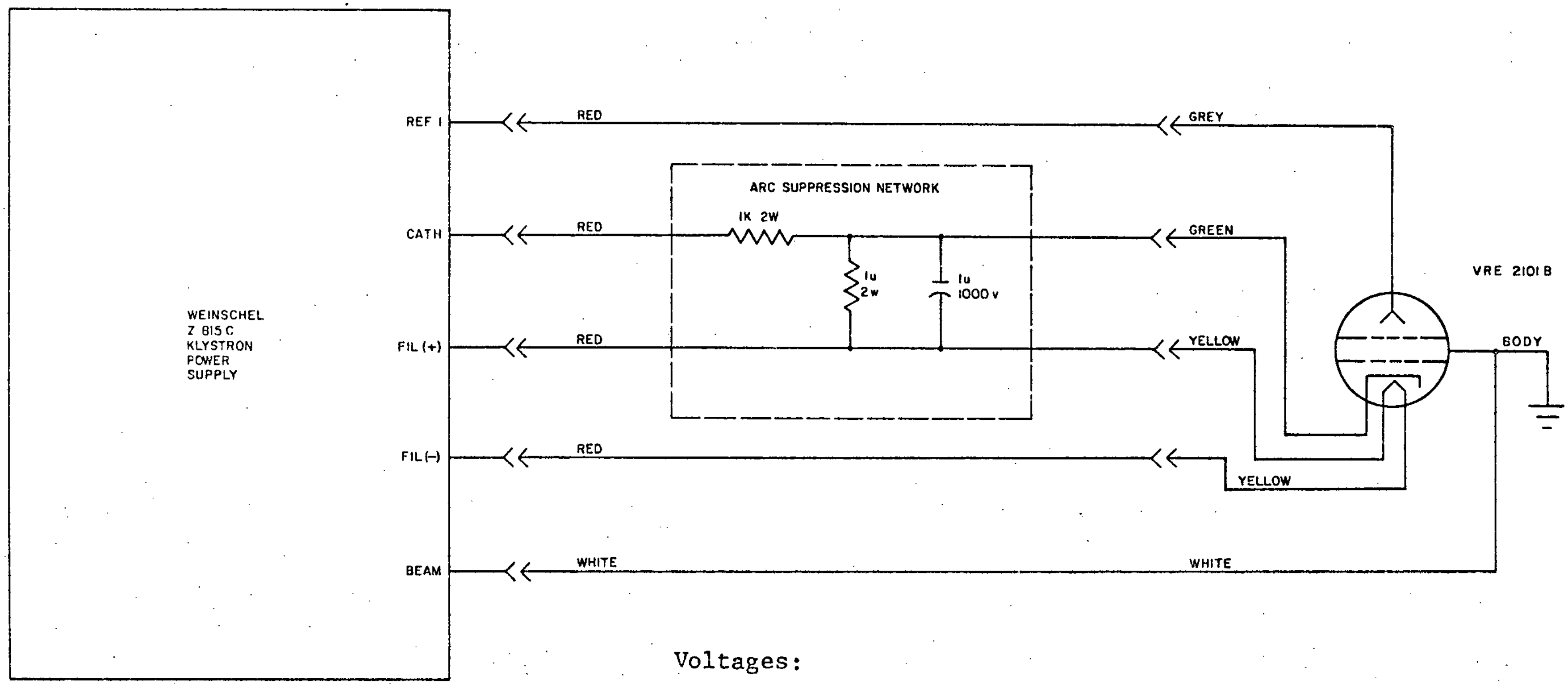

Voltages:

Reflector 1	640 V
Beam	2500 V
Filament	6.3 V

Fig. 2.3. Klystron power supply circuit.

elements during arcing. If the tube elements become pitted it will be more susceptible to arcing because of the higher field gradients around the discontinuities in the damaged area. With the voltages shown in Fig. 2.3 the measured klystron output was 470 mW.

The klystron is mounted on a large aluminum heat sink (Varian model VAE-2000C/2) which is cooled by a 100 cfm blower. The blower is mounted approximately one metre from the klystron and the air flow is directed to the tube via a section of 10 cm diameter flexible plastic tubing. This was necessary to prevent modulation of the klystron output by induced 60 Hz currents and fields from the blower motor.

An isolator is included after the klystron because it was observed that even with the isolation provided by the feedline loss and with a measured feedline VSWR of less than 1.2:1, the klystron frequency shifted approximately 200 kHz when the polarization was switched. This was due to frequency pulling as a result of small changes in the load impedance presented to the klystron in the different polarization switch states. This step change in frequency occasionally caused the receiver phase-lock system to lose lock. With the isolator in the circuit no frequency pulling could be measured.

2.2.2 Reference Signals and Calibrated Attenuator

The power level and operating frequency of the klystron were continually recorded to ascertain that these quantities did not drift during data acquisition. The frequency reference signal is derived from a 20 dB directional coupler and is used to phase lock the receiving system to the transmitted signal. Frequency monitoring of the klystron is accomplished indirectly by recording the receiver local oscillator frequency, a multiple of which was phase locked to the klystron frequency. This is explained in detail in Section 2.3.4. The level reference signal was sampled through another 20 dB coupler and measured by a Hughes model 44894H temperature compensated thermistor mount connected to an HP-432A power meter. The output signal from the power meter is connected to one of the analog inputs of the data acquisition system.

A calibrated rotary vane attenuator is permanently mounted in the path of the transmitting signal to facilitate checks of receiver linearity and noise level.

2.2.3 Feedline and Pressurization

A waveguide feedline is used to carry the klystron signal from the laboratory up one floor to the roof where the polarization switch was located. The polarization switch was mounted adjacent to the transmitting antenna to avoid having to run two feedlines to the transmitting antenna. WR-28 waveguide was used for the feedline because the theoretical and measured attenuation of this oversize waveguide was lower than for the WR-15 waveguide used elsewhere in this experiment [2.1], [2.2], [2.3]. The measured attenuation of the 6.5 meter WR-28 feedline and WR-15/WR-28 adapters at 73.5 GHz was 9.5 dB, approximately 1.5 dB higher than specified in [2.1]. This discrepancy is likely due to increased corrosion on the interior waveguide walls. The frequency response of the oversize feedline was measured to be better than ± 0.5 dB over a 400 MHz band centered at 73.5 GHz.

The feedline was lightly pressurized to prevent an accumulation of condensation. Dry air was connected to the waveguide through a directional coupler installed so that the incident wave was coupled to the internal coupler termination, as shown in Fig. 2.2.

2.2.4 Polarization Switching

2.2.4.1 Comparison of Polarization Switching Methods

Accurate measurement of crosspolarization propagation parameters in this frequency range requires very high polarization isolation and measuring system sensitivity. The polarization switch isolation and insertion loss directly degrade total system isolation and sensitivity. Switching methods were evaluated by trading-off switch isolation and insertion loss against cost and delivery time. Three basic switching schemes were compared: Faraday rotation, waveguide junction with absorptive single-pole single-throw (SPST) switches and single pole double-throw (SPDT) switches. These methods are shown schematically in Fig. 2.4.

Faraday rotation in a section of cylindrical waveguide provides the most direct method of polarization switching. Linear polarization rotation is controlled by varying the dc current through a coil which changes the magnetization of the ferrite element in the waveguide. A device of this type is the TRG-V145. Unfortunately, this type of polarization switch is not applicable to this experiment because it has only 20 dB crosspolarization isolation. Additional isolation cannot be obtained by cascading because each section would result in a further ninety degree polarization rotation.

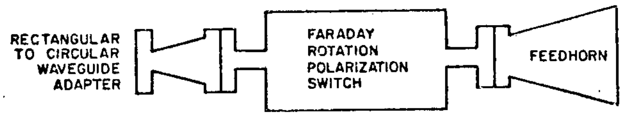

(a) Faraday rotation

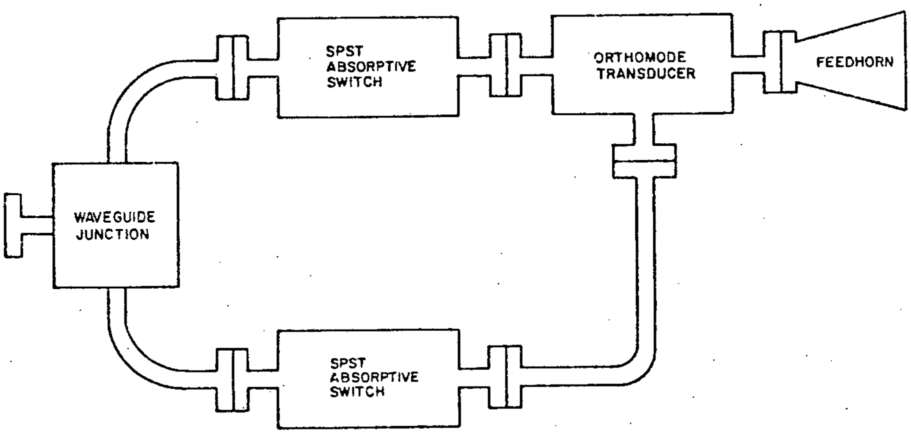

(b) Junction with absorptive SPST switches

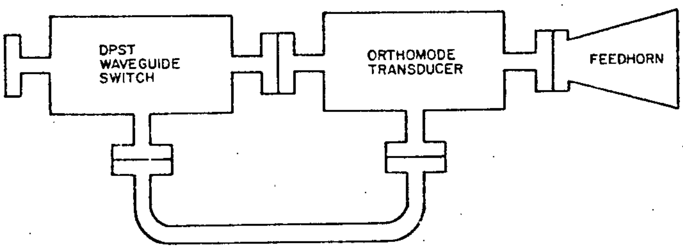

(c) DPDT switch

Fig. 2.4. Polarization swiching methods.

The other two basic methods, shown in Fig. 2.4(b) and 2.4(c), utilize an orthomode transducer. An orthomode transducer is a passive reciprocal waveguide junction with one circular and two rectangular waveguide ports. A signal with arbitrary polarization entering the circular waveguide will be resolved into two orthogonal polarization components which will leave the junction through the rectangular ports. Because the junction is reciprocal, if signals are applied to the rectangular ports they will leave the junction via the circular port but with orthogonal linear polarizations. Standard orthomode transducers in this frequency range will have losses below 1 dB and isolations of 30-35 dB.

Both of these schemes achieve polarization switching by sequentially applying the transmitting signal to either the vertical or horizontal port on the orthomode transducer. SPST switches are used in the method shown in Fig. 2.4(b) because, in this frequency range, these switches are much easier to implement than SPDT switches. When using SPST switches the transmitting signal is divided in a waveguide splitter (either a "T" junction or a 3 dB hybrid) resulting in only half the available signal being applied to the antenna. The switches must be absorptive to avoid reflections at one port of the waveguide junction when the switch is in the off state.

PIN diode switches with isolators and Faraday rotation attenuators were considered for the absorptive SPST switches. Isolators are required with the diode switches because they are unmatched in the off state. A typical PIN diode switch is the Hughes 47974VA-1000. This single diode switch has a 2.5 dB insertion loss and only 15 dB isolation. Cascading three similar switch sections would provide adequate isolations but would also yield an unacceptably high insertion loss. Faraday attenuators achieve on-off attenuation by rotation of the waveguide polarization either parallel, or perpendicular to, a resistive attenator card. A device of this type, the TRG-V120 has a 10 μs switching time, 1.4 dB insertion loss and 40 dB isolation.

The only available type of SPDT switch in this frequency range is an electromechanical waveguide switch. These switches use a solenoid to physically connect an input waveguide port to either of two output waveguide ports. Several manufacturers supply switches of this type. The Systron-Donner DBB-614-LE2 SPDT waveguide switch is specified at 50 dB isolation and 0.7 dB insertion loss.

The most suitable schemes for polarization switching in this experiment used either the Faraday rotation attenuators and waveguide splitter or the SPDT electromechanical waveguide switch. Insertion loss in the first method would be at least 4.4 dB compared to only 0.7 dB for the SPDT switch. The isolation of the Faraday attenuators was also only 40 dB compared to 50 dB for the second method. A finite lifespan resulting from mechanical wear appeared to be the only disadvantage of the electromechanical switch. The SPDT electromechanical waveguide switch was chosen for this experiment because of its superior specifications, considerably lower cost and shorter quoted delivery time.

2.2.4.2 Polarization Switch Specifications and Testing

A summary of the electrical specifications of the Systron-Donner model DBB-614-LE2 waveguide switch used in this experiment are given in Table 2.1.

TABLE 2.1 DBB-614-LE2 Electromechanical DPST Waveguide Switch Specifications.

Insertion loss	0.7 dB
VSWR	1.15
Isolation	50 dB min
Switching time	30 ms
Operating lifespan	100 000 cycles min. 250 000 cycles typ.
Solenoid power	28 VDC @ 50 W

Measurements were made on the waveguide switch at 73.5 GHz to verify its specifications. The measured insertion loss of the switch was below 0.7 dB in either state. Isolation between output ports was measured to be between 75 and 80 dB.

2.2.4.3 Polarization Switch Subsystem

The waveguide switch, integral power supply, and switching circuit were assembled in a waterproof steel enclosure and mounted adjacent to the transmitting antenna. The schematic diagram of the polarization switch subsystem is shown in Fig. 2.5. A photograph showing the internal layout and construction is included as Fig. 2.6. Referring to Fig. 2.5, the purpose of the power transistor switch is to reduce the current which must be remotely switched to control the switch solenoid. A non-resetable electromechanical counter is included to record the number of switching cycles for the purpose of monitoring switch condition and lifetime.

The switch assembly is controlled by a control unit located near the data acquisition electronics. The schematic of the control unit is shown in

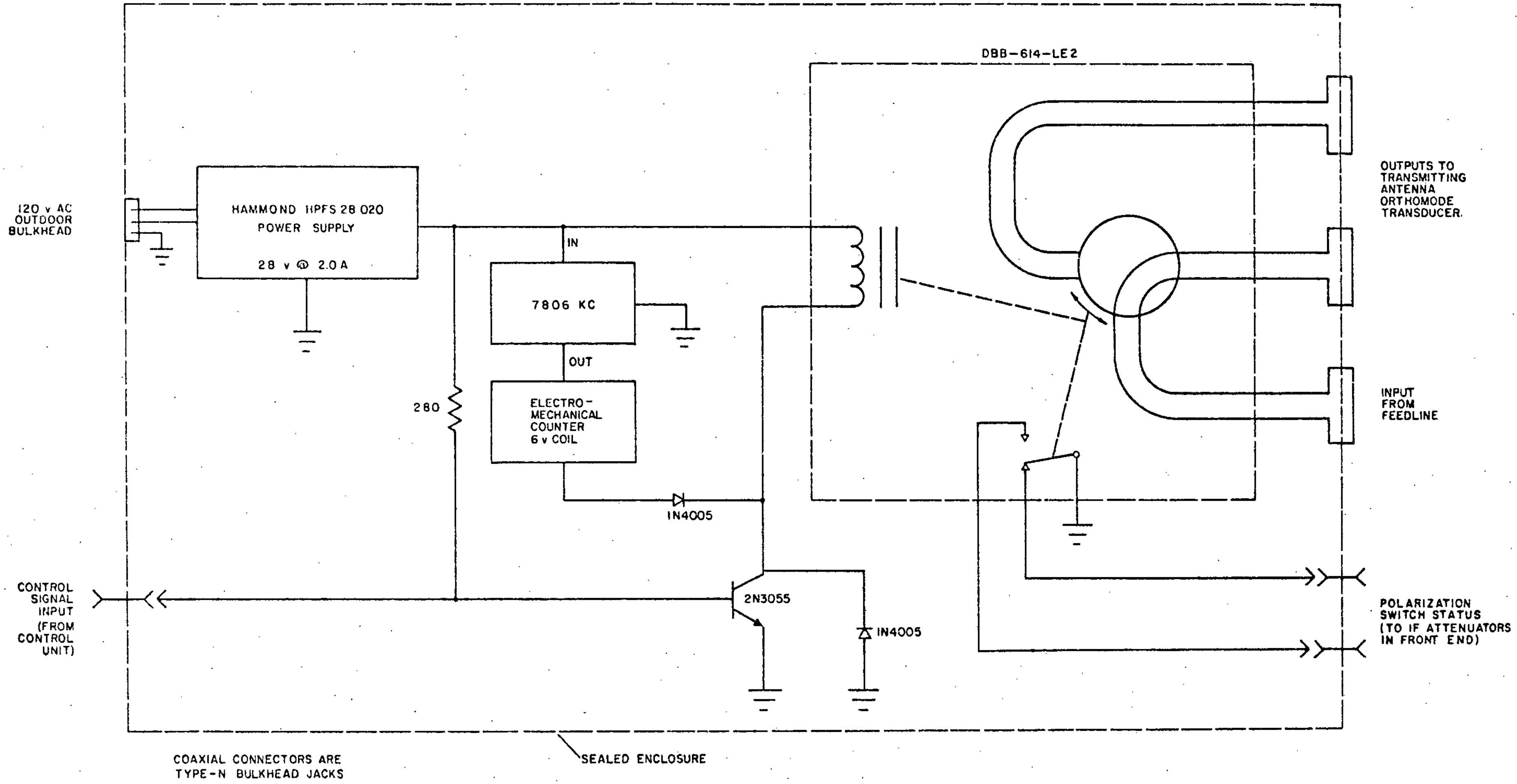

Fig. 2.5. Polarization switch subsystem schematic.

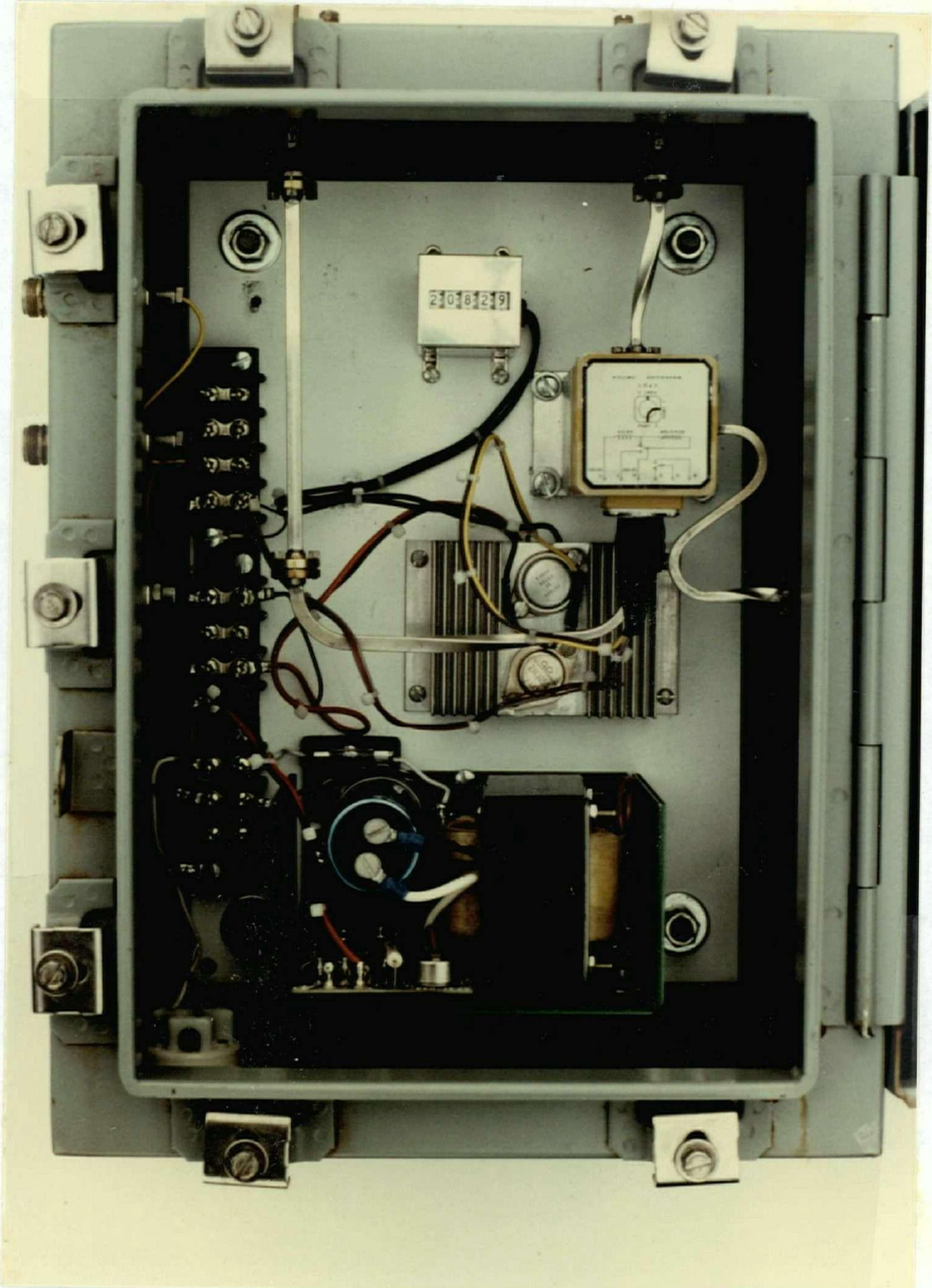

Fig. 2.6. Polarization switch subsystem photograph.

Fig. 2.7. The control unit has the provision for automatic, manual and remote switching. Automatic switching times derived from the 60 Hz line frequency are front panel switching selectable for periods of 1 s, 2 s, 5 s, 10 s, 15 s, 20 s, 30 s, 1 min. 1 min. and 4 min. An LED is provided to give a visual indication of the switch status in any mode. A status signal is supplied for input to the data acquisition system so the status of the polarization switch can be recorded and subsequently used as a data demultiplexing signal.

Isolators are installed between the outputs of the polarization switch and the inputs to the transmitting antenna. These are necessary because the waveguide switch presents a short circuit to the output port which is not connected to the input port. Without the isolator, a reactive immittance would be presented to the unused port on the transmitting antenna orthomode transducer. This was found to seriously degrade the polarization provided by the orthomode transducer. Initial measurements made without the isolators indicated that the total system polarization isolation was extremely frequency sensitive and was degraded by as much as 5 to 15 dB, depending on the angle of the reflection coefficient presented to the orthomode transducers. This effect is discussed further in Sections 2.5 and 5.5.2.

2.2.5 Signal Levels in the Transmitting System

The measured signal levels at certain points throughout the transmitting system are given in Table 2.2. The reference points are identified by letters A-H on the transmitting system block diagram, Fig. 2.2.

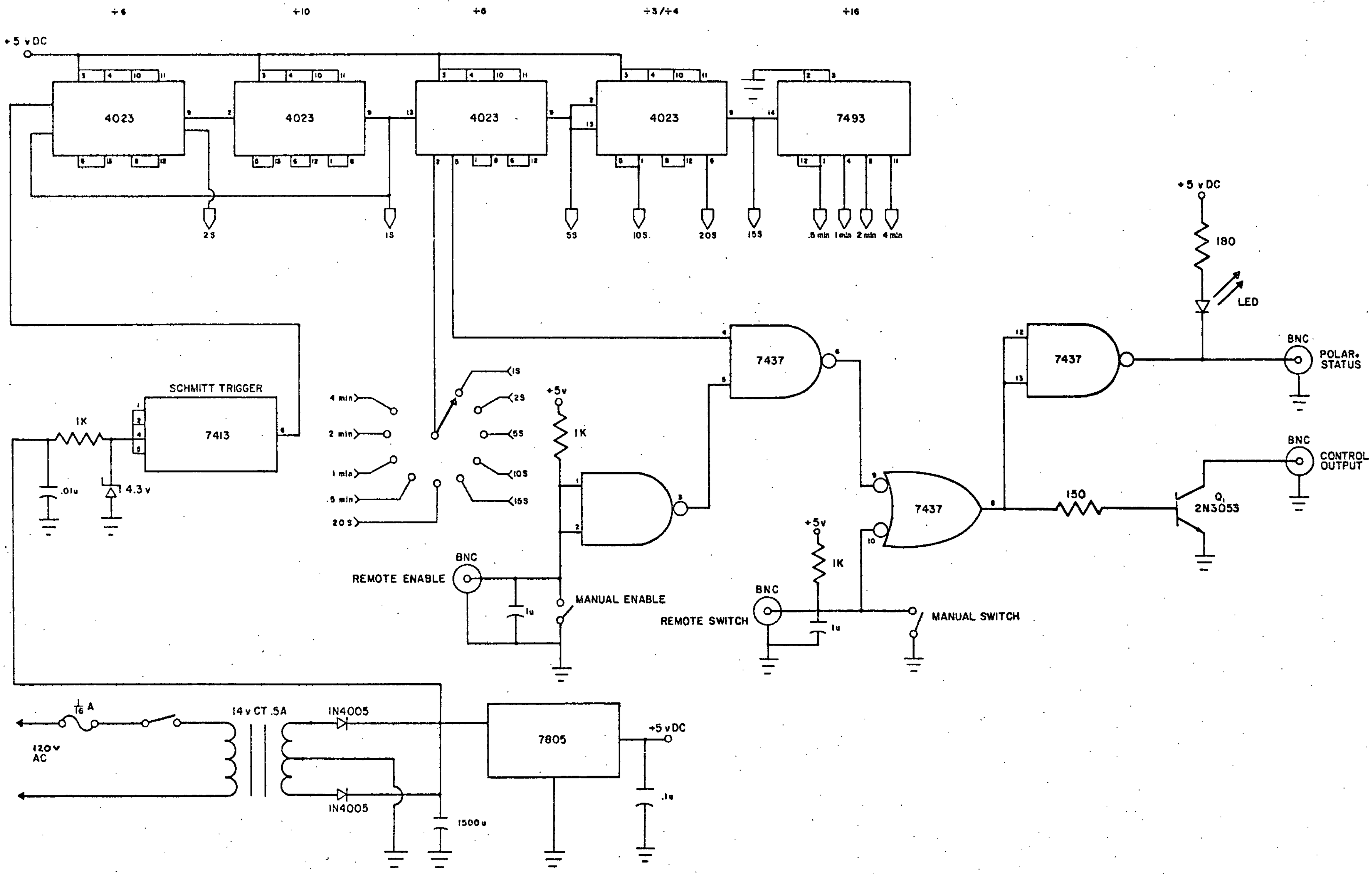

Fig. 2.7. Polarization switch control unit schematic.

TABLE 2.2 Transmitting System Signal Levels

LOCATION	REF Fig. 2.2	P_{out} (dBm)
Klystron Output	A	26.7
After Klystron Isolator	B	25.3
Input to Feedline	C	23.0
Input to Polarization Switch	D	13.5
Horizontal Output of Polarization Switch	E	10.1
Vertical Output of Polarization Switch	F	8.4
Input to Horizontal Ant. Port	G	8.5
Input to Vertical Ant. Port	H	6.5

From Table 2.2 it should be noted that the signal transmitted with horizontal polarization is 2 dB higher than for vertical polarization. This is due to the difference in lengths and number of bends of the waveguide needed to connect the waveguide switch and antenna ports. This difference was corrected for during data analysis.

The signal loss from the klystron to the antenna ports is approximately 18 dB and 20 dB for horizontal and vertial transmitted polarizations, respectively. This is mainly due to unavoidable component insertion loss, feed-line loss and the typical 2 dB/m insertion loss of straight WR-15 waveguide. Up to 8 dB could be gained if the klystron and power supply were mounted on the roof in proximity to the transmitting antenna. This was not done because of the difficulties of providing adequate shelter for these components.

2.3 Receiving System

The basic components of the two-channel dual-conversion receiving system are the millimetre-wave front-end, phase locked receiver and digital signal level measurement units. A block diagram is shown in Fig. 2.8. Down-conversion of the 73.5 GHz signal to the first IF frequency is accomplished in the millimetre-wave front-end. To reduce signal loss, the front-end is mounted adjacent to the receiving antenna. The receiver generates the fundamental phase-locked local oscillator signal and linearly converts the first IF signal to the second IF frequency. Local oscillator signals and first IF signals are carried between each channel of the front end and receiver on a common coaxial cable. The second IF signal output from the receiver is processed and converted to a digital value by the digital amplitude measurement units. This digital data is then interfaced to the data acquisition system.

2.3.1 Receiver

The receiver used in this experiment is a Scientific Atlanta model 1751 which was available in the Electrical Engineering Department. This receiver is not ideally suited for the millimetre frequency range because of its low local oscillator and IF frequencies. However, these disadvantages

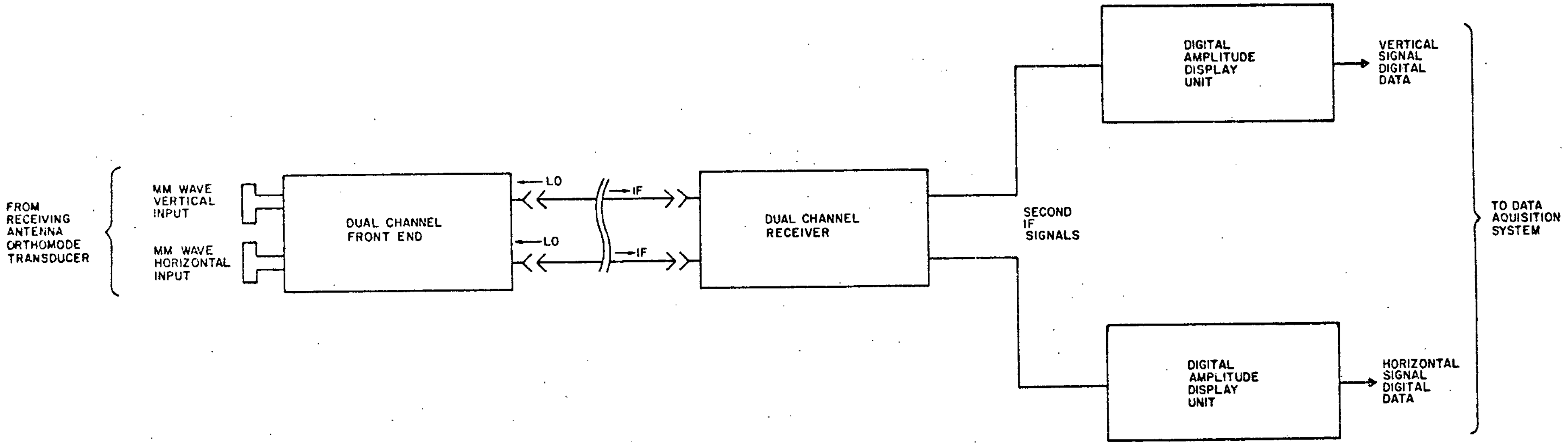

Fig. 2.8. Receiving system block diagram.

were not serious enough to justify the purchase or construction of alternative equipment.

Fig. 2.9 is a simplified block diagram of the model 1751 receiver adapted from the receiver manual. The diagram is included to help explain the aspects of the receiver operation relevant to the front-end design and system operation. The receiver was designed with a very small effective predetection bandwidth in order to improve sensitivity. For this reason the local oscillator has to be phase locked to the transmitted signal to correct for frequency drift in both the local oscillator and transmitted signal. The millimetre-wave reference signal is a sample of the klystron output as described in Section 2.2.2. This 73 GHz signal is the RF input to the automatic phase control (APC) channel external mixer. The first local oscillator is a 2-4 GHz backward wave oscillator (BWO) which supplies an LO signal to the APC harmonic mixer and external two channel-front end. The phase of the IF signal from the APC channel is compared to the 45 MHz reference oscillator to generate the error signal applied to the BWO. By this method the first IF in both signal channels is maintained exactly at the frequency of the 45 MHz reference oscillator.

To acquire phase lock, the receiver LO must be manually tuned to within a few kilohertz of the locked frequency. This lack of automatic search and acquisition means that if the receiver loses lock due to a transient frequency change or loss of power, no data will be recorded until the receiver is manually relocked. To help reduce data loss due to this and

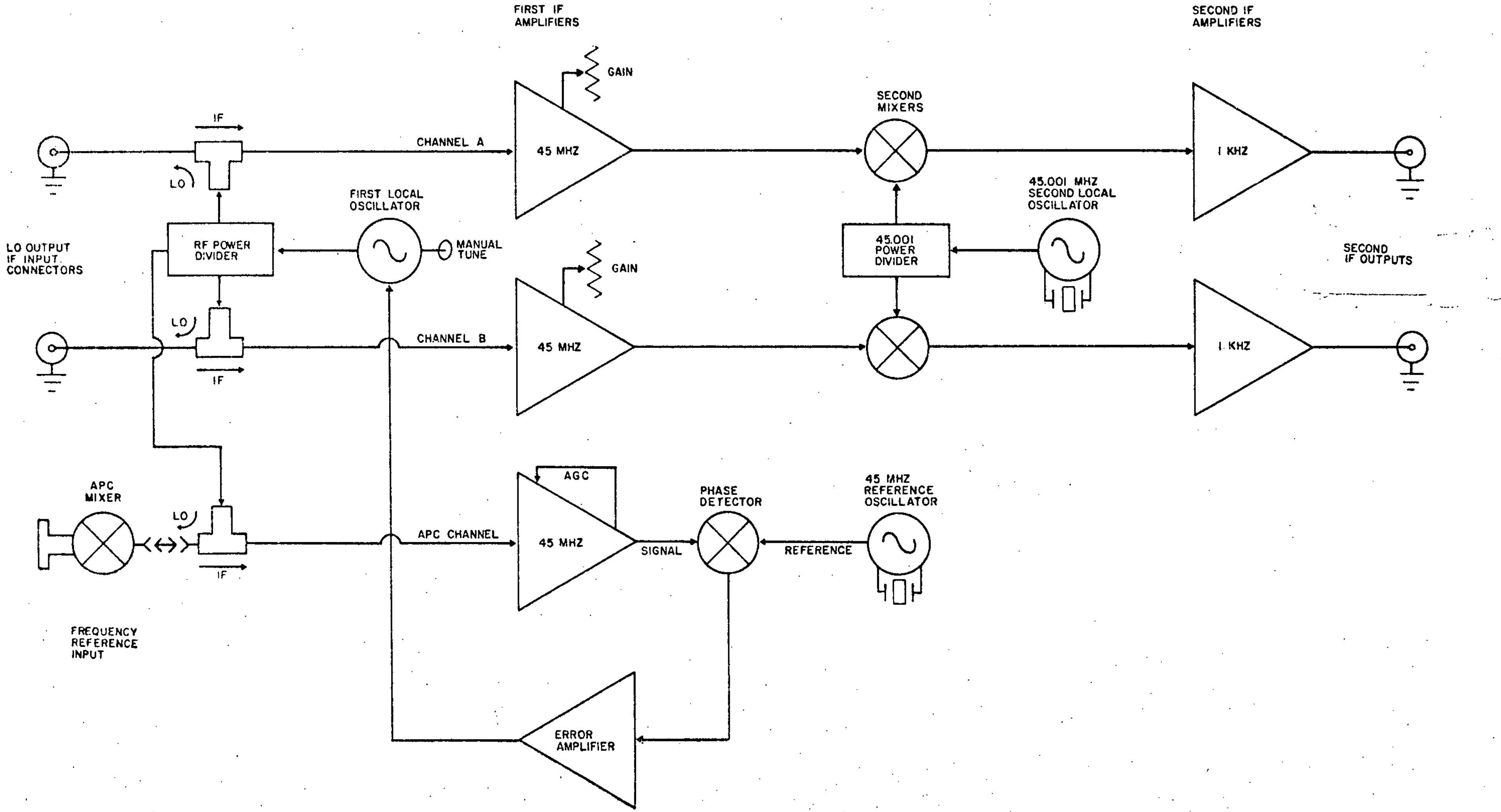

Fig. 2.9. Receiver block diagram.

other resettable electronic failures during unattended operation, an alarm system is connected to the telephone lines.

After amplification in the 45 MHz first IF amplifier, the signal is converted by the internal second mixer and crystal-controlled second LO to the 1 kHz second IF frequency. After further amplification in the second IF amplifer, the 1 kHz signal is applied to an internal analog amplitude metering system and receiver output jacks. The 1 kHz second IF output is the input to the digital amplitude measuring units.

This receiver was designed to be used with harmonic mixers similar to the Scientific Atlanta model 13 series. These mixers have a waveguide RF input port and a single coaxial connection to the mixer diode to supply the LO signal and remove the IF signal. This single coaxial connection to the mixer reduces the coaxial cable requirements and is a definite advantage when the mixers are located some distance from the receiver.

2.3.1.1 Receiver Specifications

A summary of the relevant specifications of the Scientific Atlanta model 1751 receiver are given in Table 2.3.

TABLE 2.3 Scientific Atlanta Model 1751 Receiver Specifications

Local oscillator frequency	2 - 4 GHz
Local oscillator power output	16 dBm
First IF frequency	45 MHz
Second IF frequency	1 kHz
Dynamic range*	60 dB
Linearity*	±0.25 dB for 60 dB 45 MHz IF signal range greater than -110 dBm.

* With Scientific Atlanta Model 13 series mixers.

No specifications are given for the receiver IF bandwidths. The first IF stages have a measured 3 dB bandwidth of approximately 7 MHz and therefore do not reduce the predetection bandwidth of the receiver. When used alone, the receiver effective predetection bandwidth is essentially limited by the 1 kHz second IF frequency. However, when the receiver is used in conjunction with its companion digital amplitude measurement units, second IF filters in these units determine the overall receiver predetection bandwidth.

2.3.2 Digital Amplitude Measurement Units

The Scientific Atlanta model 1832 digital amplitude measurement units amplify, filter, detect, average and digitize the second IF signals from the receiver. Active filters in this unit limit the entire receiver predetection bandwidth to 30 Hz. For this experiment the signal averaging time was selected to be 1 second. The amplitude of the signal is converted to a digital number with 0.1 dB resolution and ± 0.1 dB accuracy. This digital data is interfaced to the data acquisition system in binary coded decimal (BCD) format.

2.3.3 Two-Channel Front-End

2.3.3.1 Basic Mixer Considerations

Measurement of dual polarization propagation phenomena near 73 GHz required a more sophisticated front-end than could be supplied by the receiver manufacturer. Single polarization measurements at this frequency over the same radar path with larger antennas and using the Scientific Atlanta model 13A-50 mixers yielded a fade margin which was reported as 40 dB [2.1]. This was considered as being the indicated signal level above the indicated noise level. Due to a reduction in receiver linearity at low signal levels the useful measurement range may have been closer to 35 dB for that system. For this dual-polarization propagation experiment, economic constraints dictated the use of smaller diameter antennas. The clear weather crosspolar signal level was also estimated to be about 40 dB below the copolar signal level using these antennas. For these reasons considerably more front-end sensitivity was required to provide an acceptable dual-polarization measurement range.

Scientific Atlanta had produced a superior V-band mixer called the model 17-50-45. This mixer had a diode frequency tripler to increase the LO frequency and hence reduce mixer conversion loss. Early attempts to use this mixer were not successful because of inadequate receiver LO output [2.1].

This mixer was modified to incorporate a local oscillator power amplifier. The modified model 17-50-45 mixer has a 7-8 dB increase in sensitivity over the model 13A-50. Modifications and test results of this mixer are documented in [2.4]. Preliminary dual-polarization measurements with this mixer showed that its sensitivity was not adequate. For these reasons the decision was made to design a completely new two-channel front-end.

The front-end circuit configuration evolved from design constraints imposed by cost and the available receiver. In the frequency range of interest, low noise signal amplification requires prohibitively expensive maser or parametric amplifiers. For this reason the incoming RF signal from the antenna is directly converted down to the 45 MHz IF frequency. The feasibility of employing fundamental mixers in the front-end was investigated because conversion losses of under 10 dB are achievable. Three possible schemes for generating the fundamental local oscillator were considered:

- a free running klystron LO and triple conversion receiving system. This method would use a free running klystron to downconvert the incoming signal to an IF in the low GHz range. After amplification, this IF signal would be mixed with the receiver phase-locked LO to produce a second IF signal compatible with the receiver. (With this scheme the receiver phase locked loop would have to track frequency changes in both klystrons, resulting in lower lock reliability.)
- a klystron LO phase locked to a harmonic of the receiver BWO.
- a millimetre LO generated by frequency multiplication of the receiver BWO.

Unfortunately, none of these alternatives came close to being possible within the budgetary constraints of this project. As a result, the two-channel front-end was designed around harmonic mixers.

2.3.3.2 Front-End Circuit Description

The two-channel 73.5 GHz receiver front-end was designed to be as sensitive as economically possible, provide identical signal transfer characteristics on each channel, have high channel-to-channel isolation and operate in conjunction with the Scientific Atlanta 1751 receiver. Each of the identical front-end channels consists basically of a harmonic mixer, isolator, mixer bias circuit, local oscillator chain, IF preamplifier, IF diplexer and digitally programmable IF attenuator.

A block diagram of the complete two-channel front-end is shown in Fig. 2.10. A more detailed drawing of one channel which shows part numbers, port impedances and signal levels is shown in Fig. 2.11. A local oscillator amplifier and frequency tripler is incorporated to reduce the mixing harmonic-number and hence conversion loss. An IF diplexer interfaces the IF and LO signals to their common coaxial cable. To improve sensitivity, a low-noise IF preamplifier is included. The mixer bias current required for optimum mixer performance is supplied by the mixer bias circuits. The entire two-channel front-end and power supply is enclosed in a waterproof housing and is mounted in close proximity to the receiving antenna to minimize the RF signal attenuation. A photograph of the IF/LO diplexers, LO amplifiers and frequency multipliers is shown in Fig. 2.12. A photograph of the two-channel

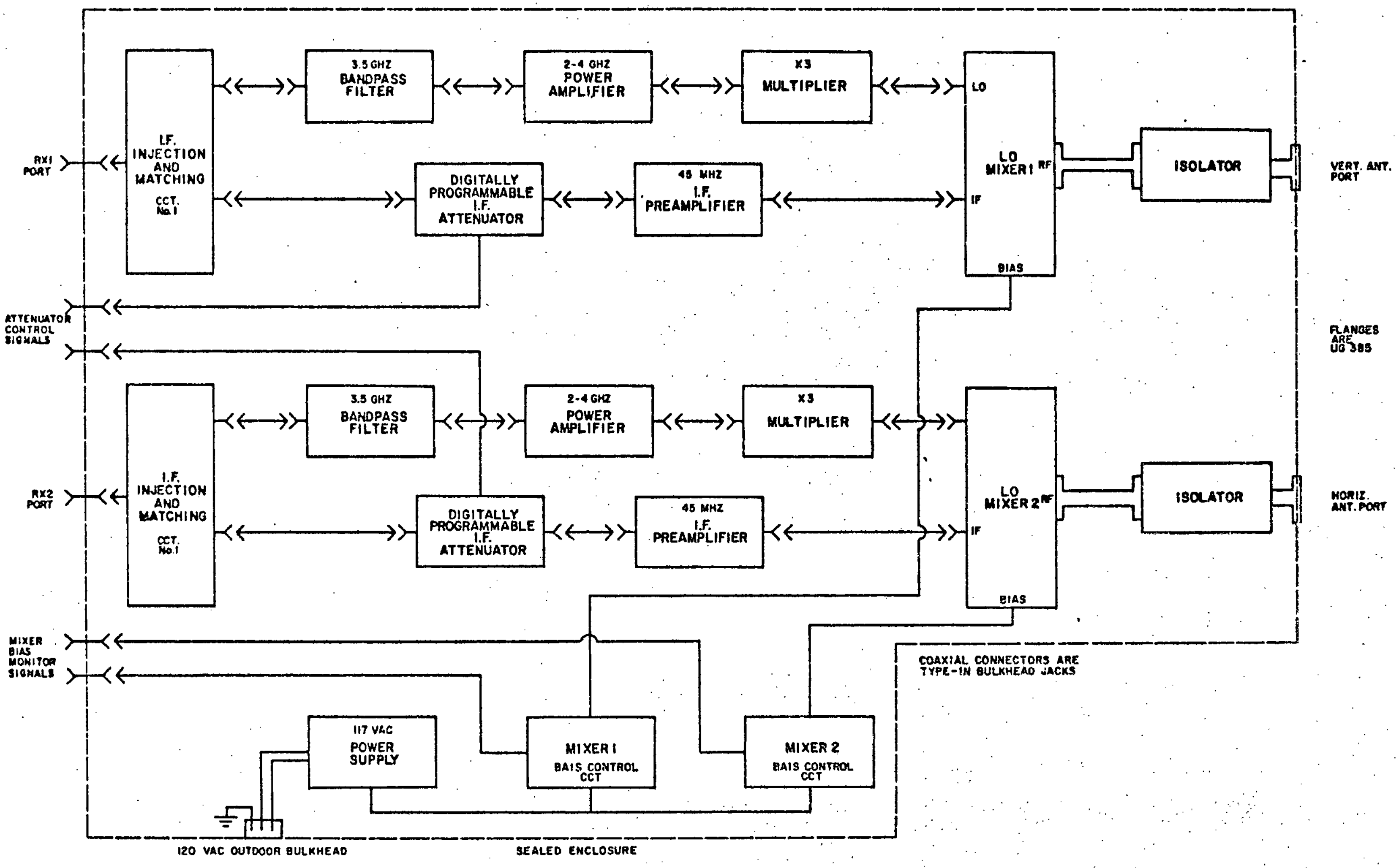

Fig. 2.10. Complete front-end diagram.

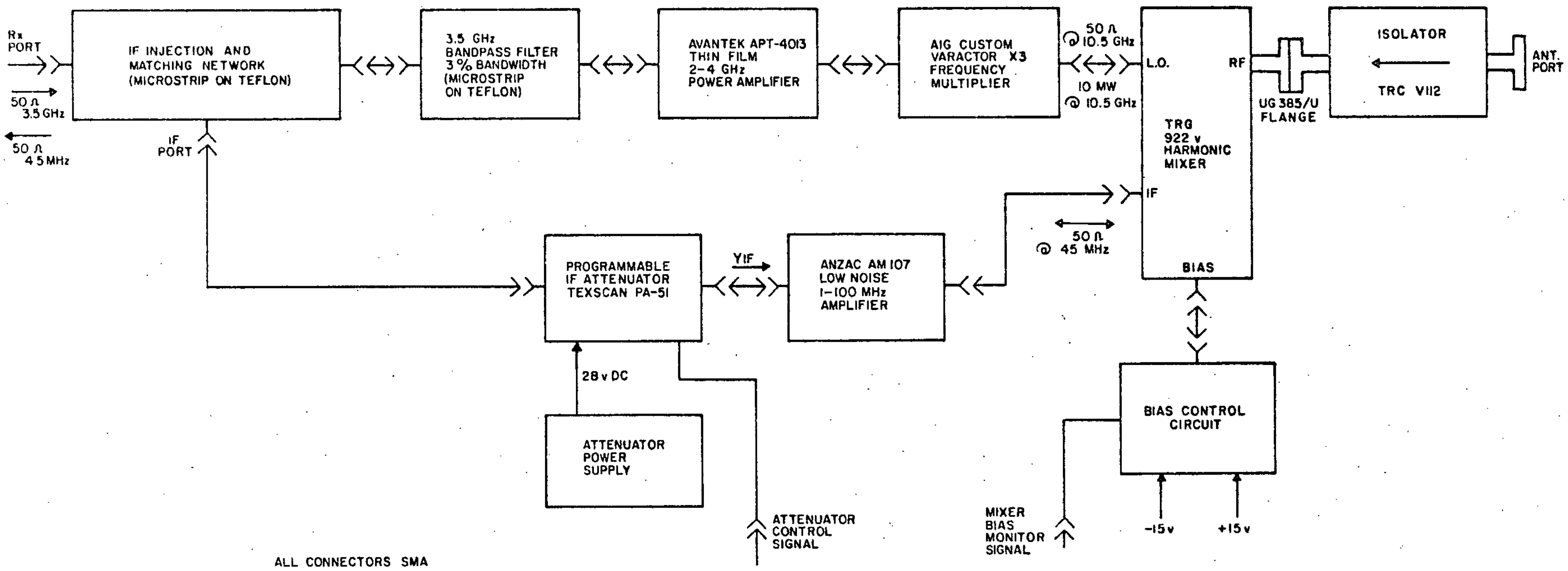

Fig. 2.11. Detailed block diagram of one channel.

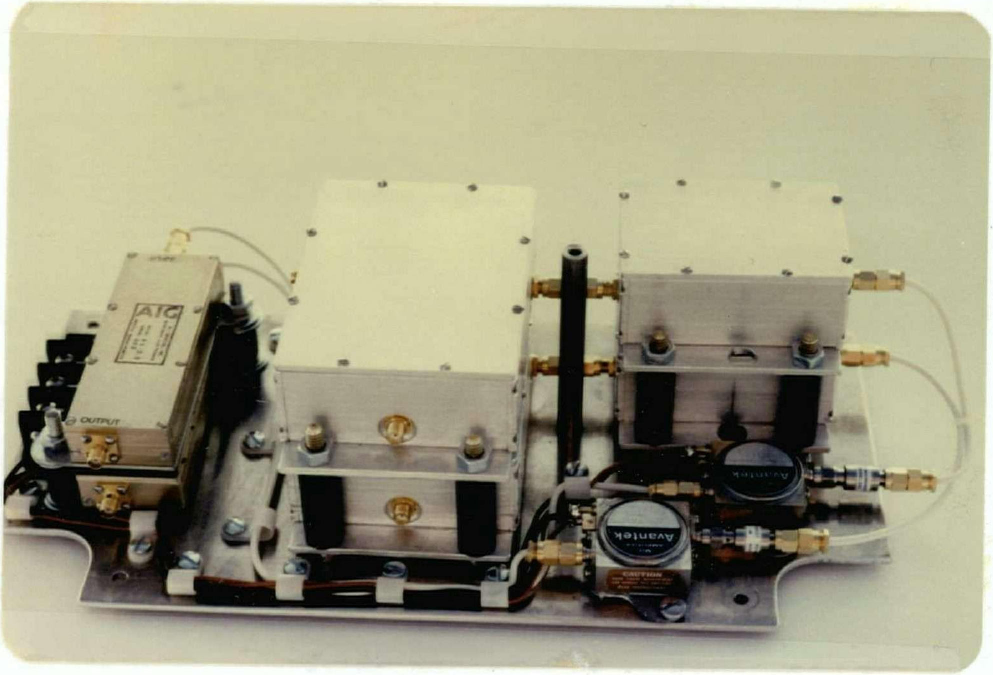

Fig. 2.12. IF/LO diplexers, LO amplifiers and frequency multipliers.

receiver front end with the IF preamplifier and attenuator assembly removed is shown in Fig. 2.13. The complete front end is shown in Fig. 2.14.

2.3.3.3 Harmonic Mixers

The most important components in the front-end are the harmonic mixers and accordingly these were selected first. The required characteristics of the mixers were: V-band RF signal range, 45 MHz IF frequency and harmonic mixing. The two mixers which were seriously considered for this system were the TRG 922-V and the Hughes 47434H-1000. These two mixers have very similar conversion loss specifications. The Hughes mixer, however, requires significantly higher LO power for lowest conversion loss. The Hughes mixer incorporates a silicon Schottky barrier diode which is not normally replaceable in the field. The TRG mixer uses a gallium-arsenide diode mounted in a field-replaceable Sharpless wafer mount. Both mixers have satisfactory IF frequency ranges. The TRG mixer was chosen because of its lower LO power requirement, field replaceable diode and because the TRG mixer was slightly less expensive.

2.3.3.4 Mixer Specifications

The specifications of the TRG 922-V harmonic mixers relevant to the front-end circuit description and receiving system operation are given in Table 2.4.

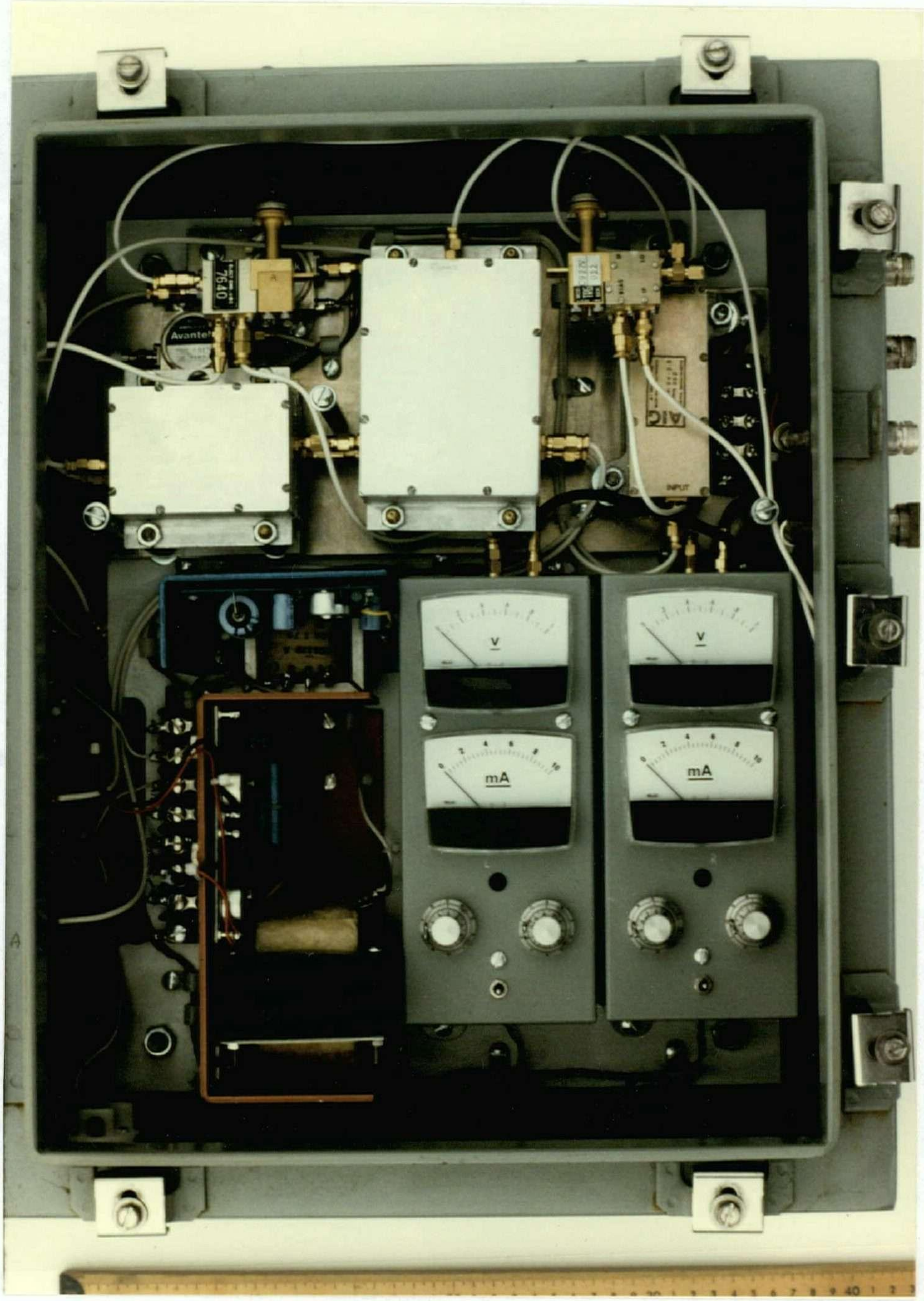

Fig. 2.13. Front-end without IF preamplifiers and attenuators.

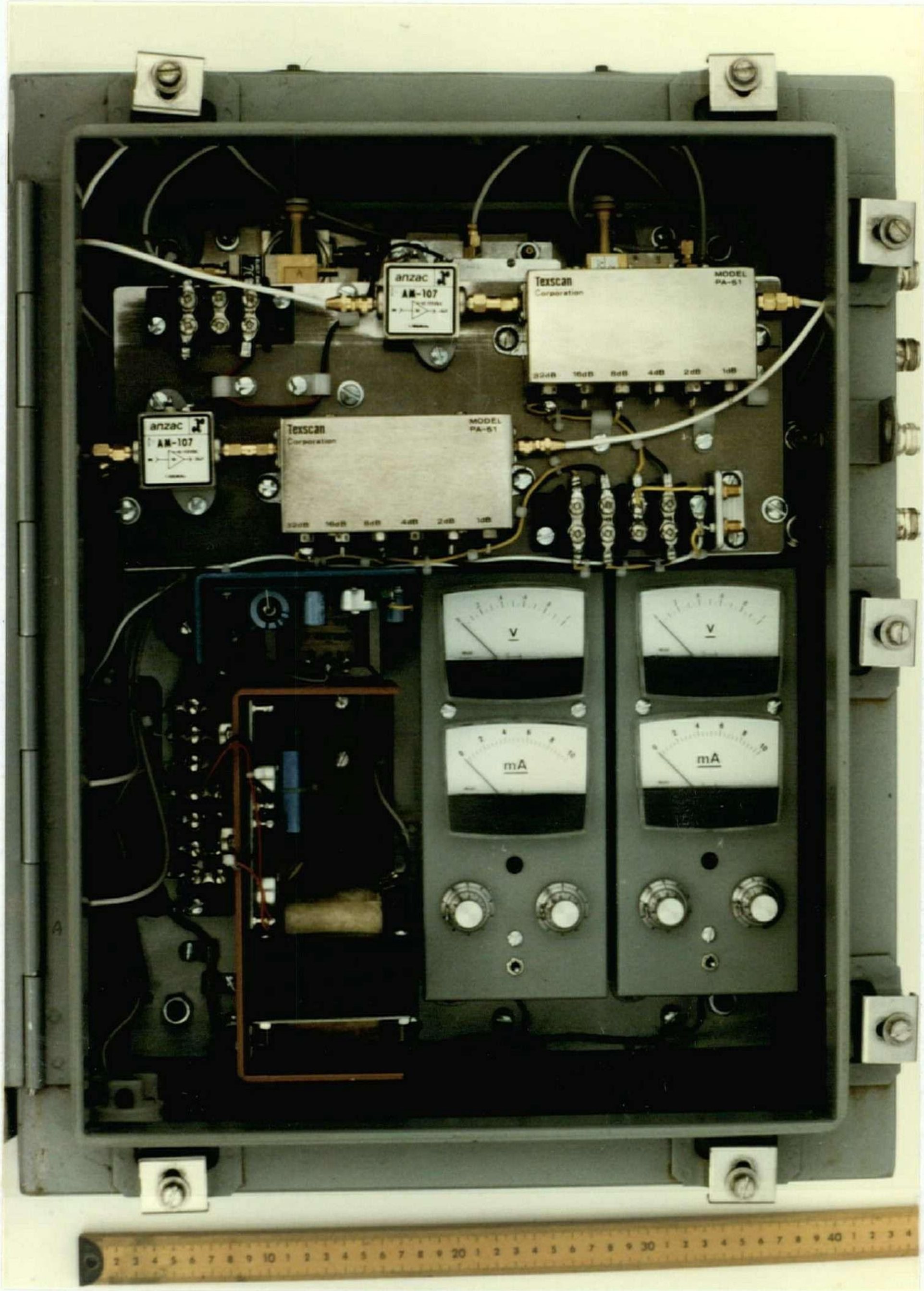

Fig. 2.14. Complete front-end.

TABLE 2.4 TRG-922-V Harmonic Mixer Specifications:

Conversion loss Harmonic number	Conversion loss
21	39-42 dB
10	28 dB
9	26 dB
8	24 dB
7	22-23 dB
6	18 dB
LO frequency	8.2-12.4 GHz
LO power	10 mw Typ.
LO port impedance	50 Ω
LO/IF Isolation	25 dB Min.
IF Bandwidth	10 MHz to 500 MHz
IF Port Impedance	50 Ω
RF VSWR	2:1 Typ.
Bias Requirements	-0.7 V @ 2 mA Typ.
Max. diode current	4 mA

2.3.3.5 IF/LO Diplexer

IF/LO diplexers are required to interface the Scientific Atlanta model 1750 receiver to the TRG 922V harmonic mixers. The receiver was intended to be used with mixers employing a single coaxial connection to the mixing diode to provide the LO injection and to remove the IF signal. The TRG 922V mixers are constructed in the more common configuration employing separate LO and IF ports. The design of the IF/LO diplexer circuit is documented here because this type of receiving system and mixer configuration is very useful and this type of diplexer has low insertion loss, is easily realizable in microstrip and has not, to our knowledge, been described elsewhere.

The design objective for the diplexer was a well-matched, low-loss connection between corresponding ports at the IF and LO frequencies. It is important to have a well-matched, low-loss connection between the IF preamplifier output port and the receiver LO/IF cable because a mismatch or loss associated with this connection will reduce the receiving system sensitivity. A well-matched connection at the LO frequency is also required to ensure reliable operation of the receiver local oscillator source and to minimize LO loss through the coaxial connection from the receiver.

The local oscillator in the receiver is operated at approximately the V-band signal frequency divided by twenty-one, which, in this case, is 3.5 GHz. Other components of the system do not allow operation except in a narrow two or three percent bandwidth around the center frequency of 73.5 GHz. Therefore, the IF/LO diplexer circuit for this system is required to operate only over a similar percentage bandwidth. Referring to Fig. 2.11, the specific requirements of the IF/LO diplexer are:

(a) to provide a matched connection with minimum loss from the receiver port to the LO multiplier chain input over a bandwidth of a few percent centered at 3.5 GHz.

and

(b) to provide a minimum-loss, matched connection from the IF signal port to the receiver port at 45 MHz.

The requirement for minimum-loss connections precludes the possibility of a directional coupler type network for LO injection or IF removal, as is often employed in IF/LO diplexers. Fortunately, since the frequency difference between the LO and IF is large and because narrowband operation is acceptable, a simple microstrip transmission line circuit could be designed to meet the network requirements. This circuit was designed heuristically and its operation verified analytically.

The IF/LO diplexer consists of an IF injection and matching circuit and a local oscillator bandpass filter both realized in microstrip. The connection of these components is shown in Fig. 2.11. The IF injection and matching circuit was designed to provide a low-loss, matched connection for the IF signal to the receiver without significant loss or mismatch to the LO signal. The LO bandpass filter prevents loss to the IF signal and ensures that only the desired 3.5 GHz LO signal is applied to the power amplifier.

The operation of the IF injection and matching circuit, shown in Fig. 2.15 can be explained using conventional transmission line analysis. The input admittance at planes A-A of the 25 Ω open circuit shunt stubs is given by:

$$Y_A = \frac{1}{Z_A} = \frac{1}{-jZ_1 \cot \beta\ell} = jY_1 \tan \beta\ell \quad \text{where } Z_1 = 25\ \Omega\ , \tag{2.1}$$

assuming negligible transmission line attenuation and negligible radiation from the open-circuit terminations. At each node there are two shunt stubs, effectively in parallel. The combined admittance at each node is therefore given by

$$Y_B = 2Y_A = j2Y_1 \tan \beta\ell \tag{2.2}$$

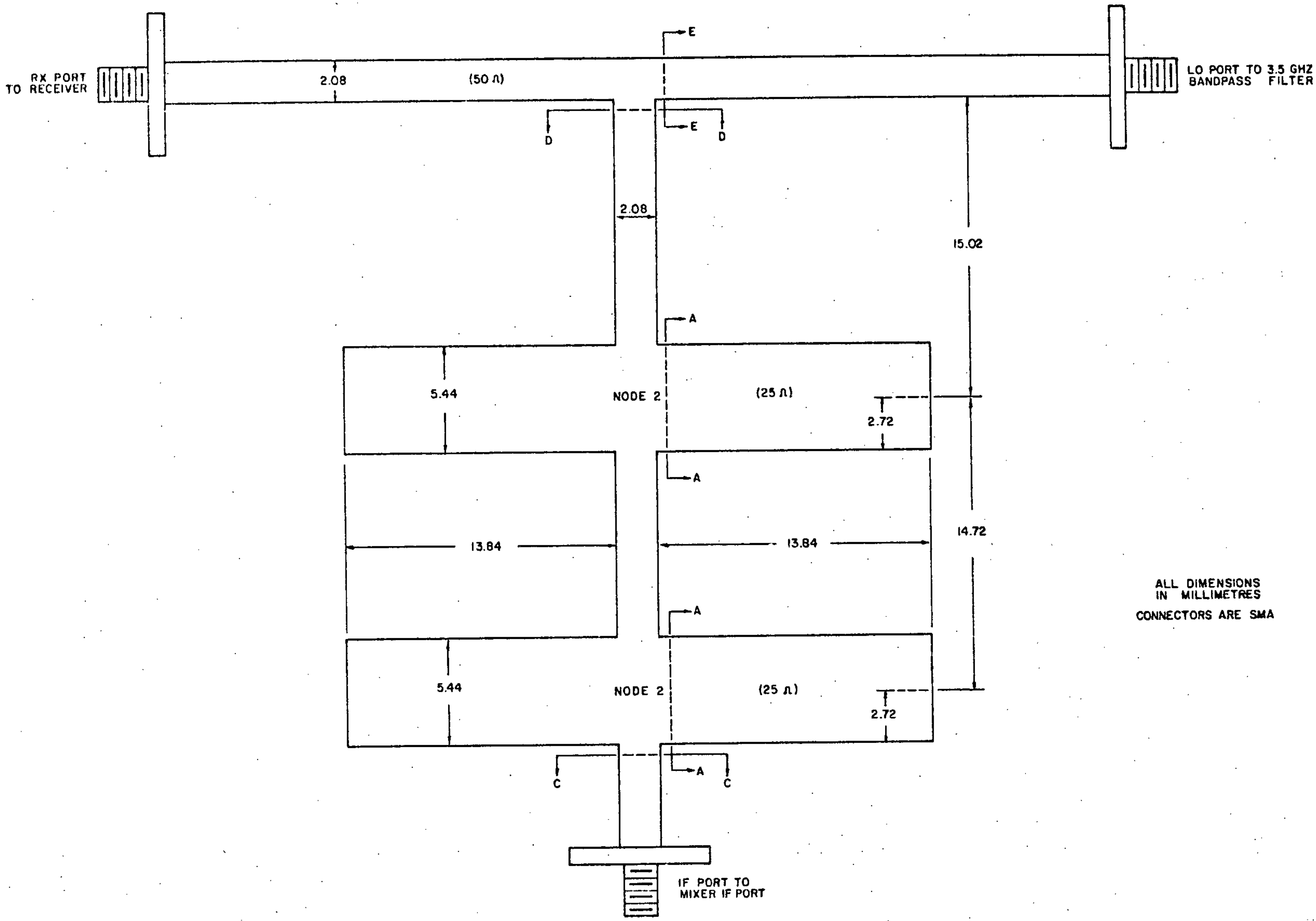

Fig. 2.15. IF injection and matching circuit.

Each stub is a quarter wavelength long at the LO frequency. If the transmission line wavelength at 3.5 GHz is designated λg_{LO}, the admittance Y_B at a frequency, f, or wavelength, λg, can be rewritten as:

$$Y_B = 2j\ Y_1 \tan\left(\frac{2\pi}{\lambda g} \cdot \frac{\lambda g_{LO}}{4}\right) \tag{2.3}$$

$$= j.08 \tan\left(\frac{\pi}{2} \cdot \frac{f}{f_{LO}}\right)$$

This admittance appears in parallel with the admittance looking into plane C-C, which will be referred to as Y_C. The total admittance at node 1 is therefore:

$$Y_3 = Y_C + Y_B \tag{2.4}$$

This admittance, Y_3, will be transformed by the section of 50 Ω line between node 1 and node 2 which is also one quarter wavelength long at f_{LO}. The admittance at node 2 now becomes:

$$Y_4 = Y_B + .02\ \frac{Y_3 + j.02 \tan\left(\frac{\pi}{2} \frac{f}{f_{LO}}\right)}{.02 + j\ Y_3 \tan\left(\frac{\pi}{2} \frac{f}{f_{LO}}\right)} \tag{2.5}$$

Finally, looking into plane D-D the admittance is:

$$Y_D = .02\ \frac{Y_4 + j.02 \tan\left(\frac{\pi}{2} \frac{f}{f_{LO}}\right)}{.02 + j\ Y_4 \tan\left(\frac{\pi}{2} \frac{f}{f_{LO}}\right)} \tag{2.6}$$

One of the problems in designing the matching network is that Y_{IF}, the admittance looking into the output port of the IF attenuator, is unknown in the vicinity of f_{LO}. Even if the admittance Y_{IF} were known, the admittance at plane C-C, i.e. Y_C, would not be known unless the exact length of the coaxial connection between the mixer preamplifier and the IF port is also determined. For this reason, the IF injection and matching network must have a very low sensitivity to the value of Y_C. This is accomplished in part by using low impedance lines for the shunt quarter-wave stubs. At frequencies around f_{LO}, the admittance Y_B will be very large and thus will reduce the effect of Y_C which appears in parallel. The quarter-wave section between nodes 1 and 2 will further reduce the unknown effect of Y_C by transforming the admittance at node 1 to a low admittance at node 2, which will be small compared to Y_B. The result is that, regardless of Y_C, the admittance at node 2 is large, ensuring the admittance at plane D-D is small. The very low admittance at plane D-D will cause almost no reflection on the LO line to the LO port at 3.5 GHz.

To verify the operation of the IF injection and matching circuit theoretically, a computer program was written in the BASIC language. The program was used to predict the VSWR on the local oscillator line over the local oscillator frequency range of the receiver. The results are shown graphically in Fig. 2.16. Different values of Y_C between $+j10^{25}$ and $-j10^{25}$ mhos produced no significant change in the VSWR over the frequency range 2 to 4 GHz. The predicted response of this network shows a more than adequate bandwidth.

The effect of the IF injection and matching circuit on the 45 MHz IF signal can be analyzed in the same manner up to plane D-D. In this case Y_{IF} is known to be approximately 50 Ω at 45 MHz. The difference in the

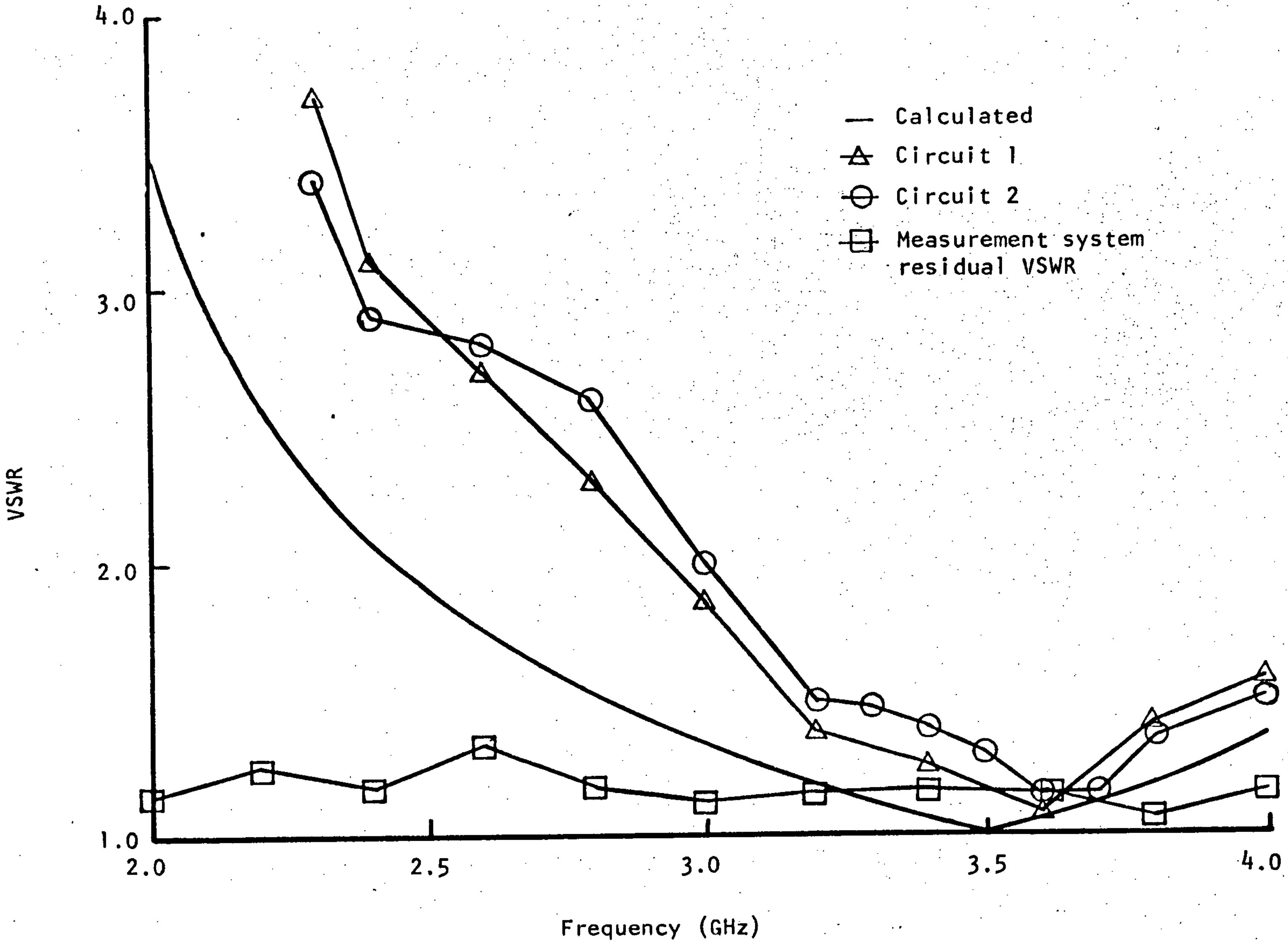

Fig. 2.16. IF injection and matching circuit performance.

analysis arises when the effect of the impedance looking to plane E-E at 45 MHz is considered. This admittance, Y_E, must be very low at 45 MHz to prevent IF signal mismatch. To ensure that Y_E is small, the 3.5 GHz bandpass filter is placed at the output of the LO port. The bandpass filter topology described by Cohn [2.11] chosen because it was a transfer function zero at dc, and presents almost an open circuit at 45 MHz. This small admittance is transformed by the length of 50 Ω line from the bandpass filter to plane E-E resulting in a small capacitive susceptance at plane E-E. Thus the effect of the IF injection and matching network at 45 MHz is just to add a small capacitive susceptance at nodes 1 and 2 and at plane E-E.

The predicted effect of these shunt susceptances is to produce a small VSWR on the IF line. The resultant VSWR on the IF line will be 1.4 if the distance from the filter to plane E-E is approximately 15 cm. This value increases only to VSWR = 1.6 if the distance increases to 25 cm.

The microstrip substrate chosen for the fabrication of the IF injection and matching circuit and LO bandpass filter is a copper-clad teflon fibreglass material. This material was chosen because it is easily machinable and has a comparatively low dielectric constant ($\epsilon_r = 2.55$). A low dielectric constant makes circuit elements physically larger (resulting in less stringent fabrication tolerances), and reduces the effects of dispersion caused by the dielectric inhomogeneity. Unfortunately, the lower dielectric constant also results in decreased open circuit resonator Q due to relatively large radiation losses.

The choice of the substrate thickness was determined by the open-circuit resonator Q. Both circuits include open-circuit quarter wave or half wave microstrip lines - which are referred to as open circuit resonators. Microstrip resonator Q is determined by conductor loss, dielectric loss and radiation loss. These losses have been calculated for the copper and teflon-fibreglass laminate over the frequency range of interest using equations in [2.5] and [2.6]. The results show that the radiation losses are dominant and that the conductor losses are much larger than the dielectric losses. The open-circuit resonator Qs were found to be comparable for the available substrate thicknesses of 10 and 30 mils in the frequency and impedance ranges required. The 30 mil substrate thickness was chosen because it would result in larger circuit dimension and correspondingly lower fabrication tolerances. The laminate used was GX-6098-22-030-55 by 3M Company.

Single microstrip characteristic impedances were calculated using Hammerstad's synthesis equations [2.7]. The line geometries were corrected for conductor thickness in the IF injection and matching circuit using Wheeler's method [2.8]. Corrections for dispersion using Getzinger's equations [2.9] at the LO frequency yielded increases in effective dielectric constant of approximately 1% for 25 Ω lines and 0.5% for 50 Ω lines.

A correction for the T-junction discontinuity using Hammerstad's method [2.7] resulted in only a 300 μm increase in the T-shunt arm length. The stub-length correction due to the open circuit discontinuity capacitance was determined from [2.10] and [2.5]. The final dimensions for the IF injection and matching circuit on the specified laminate are given in Fig. 2.15.

Cohn's bandpass filter topology was chosen for the LO filter to satisfy the requirement of high input impedance at the IF frequency. The bandpass filter was designed to have a 5% bandwidth, second order, Butterworth response. The coupled microstrip even and odd mode impedances were calculated from Cohn [2.11]. The microstrip widths and spacings were derived from Garg and Bahl's coupled microstrip analysis equations [2.12]. A BASIC language computer program was written to determine the strip widths and spacings iteratively from the mode impedances. To correct for the unequal phase velocities of the two modes the procedure described by Kojfez and Govind [2.13] was employed. Open circuit end-correction was calculated from [2.10].

The final dimensions for the 3.5 GHz bandpass filter are shown in Fig. 2.17. The microstrip substrate which was available was clad in 2 ounce copper (thickness = 71 microns). This thickness of copper would normally require that a correction be applied to the dimensions in Fig. 2.17 to account for the capacitance between the vertical edges of adjacent conductors. In addition, under-etching problems were also anticipated with this conductor thickness in the region of the first gap which has a spacing of only 0.2896 mm. To circumvent these problems the copper thickness on the upper side of the laminate was pre-etched to approximately 12 microns before the photoresist was applied.

The etched microstrip circuits were mounted in custom fabricated aluminum boxes. Several small machine screws and a silver loaded adhesive were used to mount the substrates and ensure a low-inductance ground connection. Coaxial connections were made to the 50 Ω microstrip transmission lines by threading SMA bulkhead jacks into the boxes so the center conductors of the connectors aligned exactly with the copper

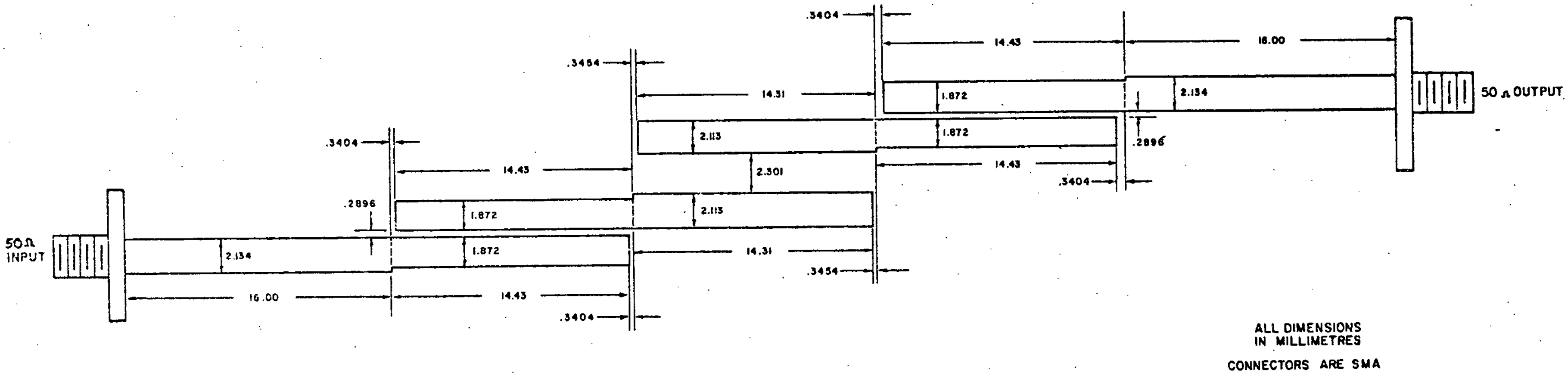

Fig. 2.17. 3.5 GHz microstrip bandpass filter.

conductors. The dimensions of the boxes were chosen by using the rule-of-thumb that the case walls should be more than three times the conductor width and more than five times the substrate thickness from the microstrip conductors [2.14], [2.5]. The completed IF injection and matching unit is shown in Fig. 2.18 and the LO bandpass filter is shown in Fig. 2.19.

The IF injection and matching circuit assemblies were tested by measuring the VSWR looking to the receiver port. Measurements were made with the LO port terminated with 50 Ω and the IF port open-circuited, short-circuited and terminated in 50 Ω. A 50 Ω slotted coaxial line was used to measure the VSWR over the range 2 - 4 GHz. The effect of the impedance presented to the IF port could only be noticed at the lowest frequencies (i.e. close to 2 GHz) and even then it had a very small effect on the receiver port VSWR. Fig. 2.16 shows the measured VSWR for each of the two IF injection and matching units together with the calculated VSWR. The measured values are slightly higher than those calculated. This is attributed to the effects of the coaxial-to-microstrip discontinuities and to the residual VSWR of the measurement system. This residual VSWR is also shown in Fig. 2.16. The measured values were obtained without resorting to any tuning of the etched circuit and show that the IF injection and matching circuit performed very well and had much greater than the required bandwidth. The insertion loss of the IF injection and matching circuit was measured to be 0.5 dB.

Testing of the two 3.5 GHz bandpass filters was accomplished by measuring the filter insertion loss between 3.2 and 3.8 GHz. The results, which again did not require post-fabrication tuning, are shown in Fig. 2.20

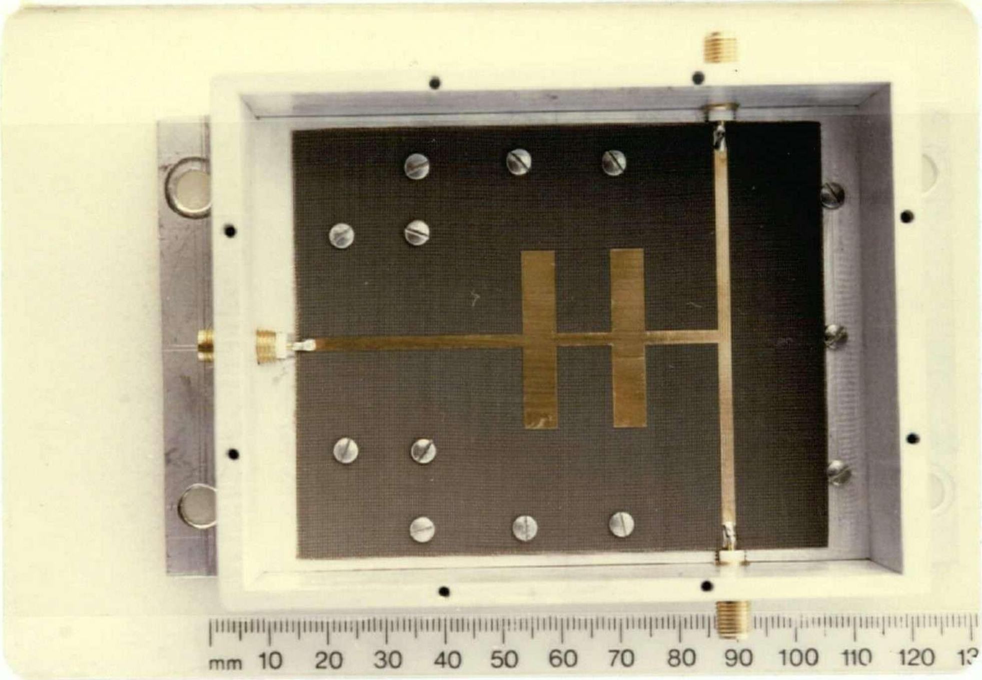

Fig. 2.18. IF injection and matching circuit photograph.

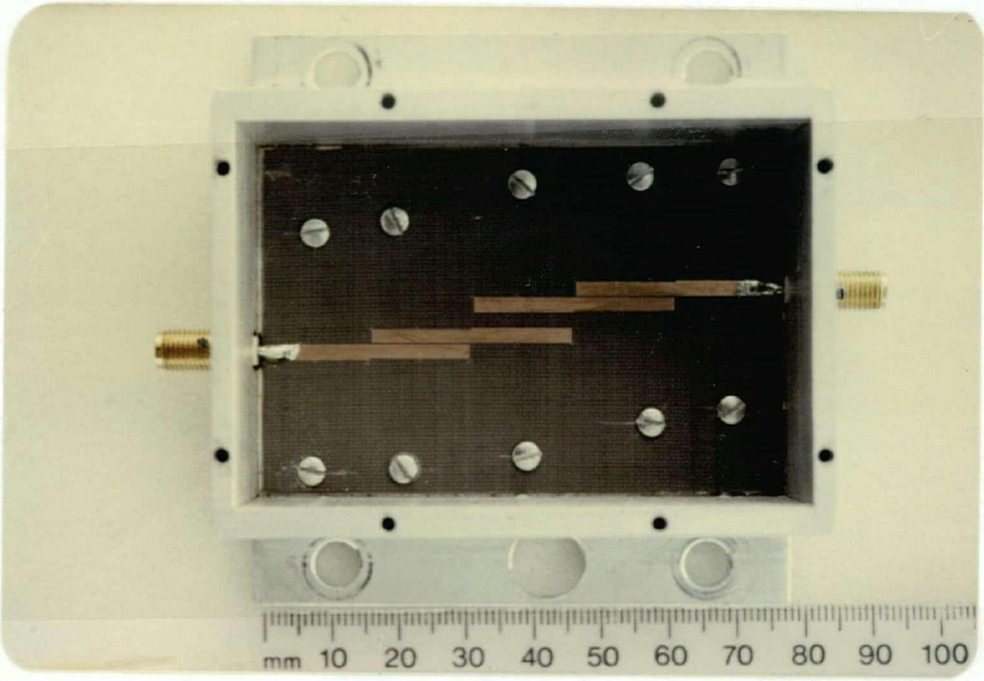

Fig. 2.19. 3.5 GHz bandpass filter photograph.

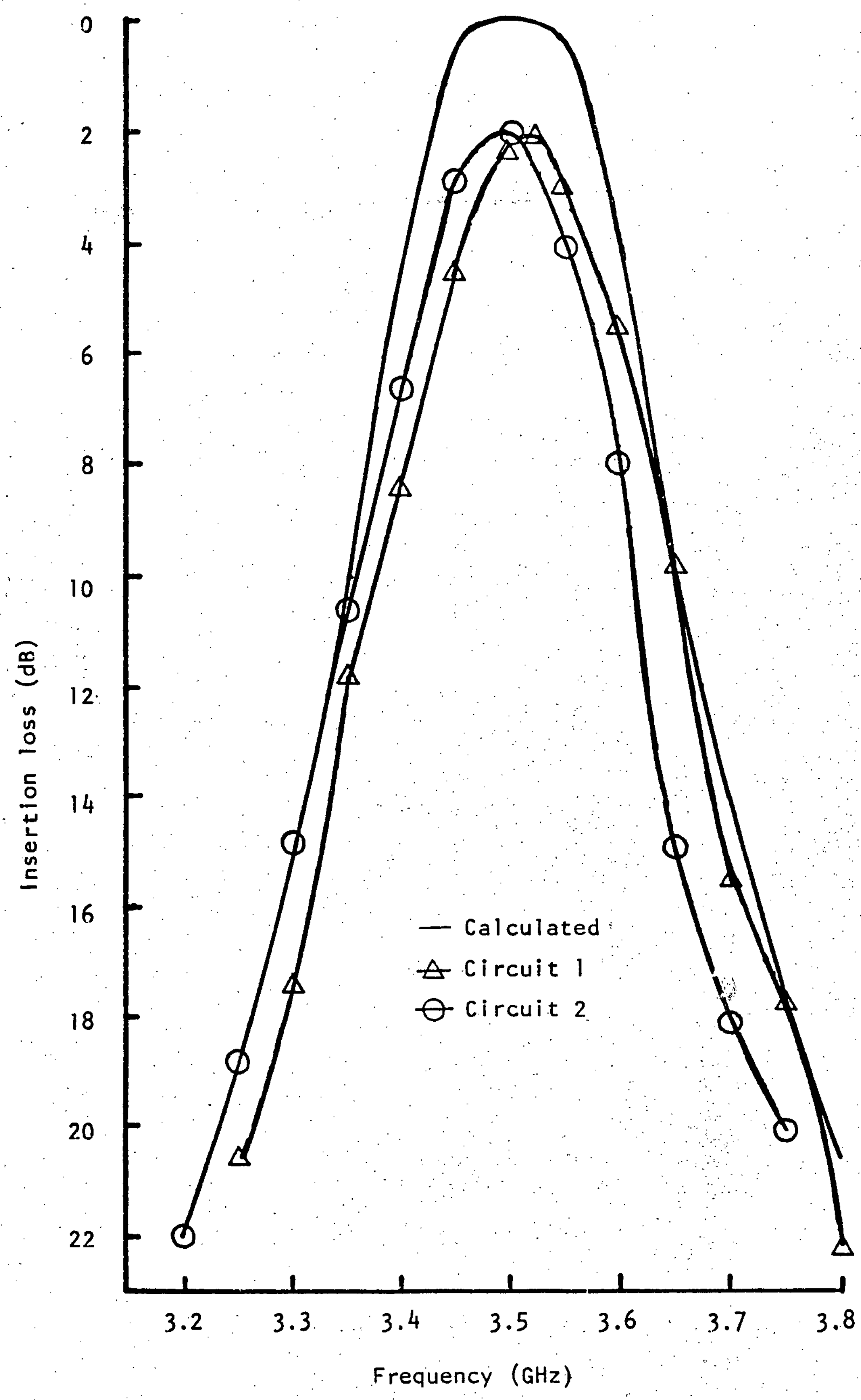

Fig. 2.20. 3.5 GHz bandpass filter performance.

along with the theoretical, lossless response. Microstrip losses, which produce finite resonator Q's, account for the 2 dB filter insertion loss. Agreement between calculated and measured results is considered to be extremely good. Some difference between the two units was observed and can be attributred to fabrication tolerances (i.e. underetching, copper thickness) and dielectric permittivity variation.

It was noticed that when the bandpass filter enclosure lid was in place a notch in the filter response occurred at about 3.52 GHz. Because of the "sharpness" of the notch and the adequate distance from the circuit to the lid, resonances of the enclosure were investigated. The inner dimensions of the aluminum enclosure are d = 51.1 mm, b = 76.2 mm and a = 24.5 mm, (Fig. 2.19). Resonances occur in rectangular enclosures at frequencies given by:

$$f_{\substack{nm\ell \\ \text{resonant}}} = c \sqrt{\left(\frac{\ell}{2d}\right)^2 + \left(\frac{m}{2b}\right)^2 + \left(\frac{n}{2a}\right)^2} \tag{2.7}$$

for either TE or TM modes. By exhaustive search, the $nm\ell$ = 110 resonant frequency was found to be 3.53 GHz which is within measurement error of the observed notch. The effect of this resonance was eliminated by placing a small piece of microwave absorbing foam on the inner side of the enclosure lid.

2.3.3.6 Local Oscillator Frequency Multiplier

The receiver front-end incorporates local oscillator frequency multiplier circuits to reduce harmonic mixing conversion loss. The harmonic mixing process relies on the nonlinear mixer diode junction to produce harmonics of the local oscillator signal. The local oscillator frequency is chosen so that one of its harmonics mixes with the signal frequency to produce a signal at the IF frequency. The harmonic generation efficiency of the mixer diode decreases monotonically as the harmonic number increases. This results in increasing mixer conversion loss with increasing local oscillator harmonic number (ref. Section 2.3.3.4). A preliminary investigation into the operation of the TRG mixers at high harmonic numbers showed unacceptably high conversion loss. The TRG mixers were modified slightly at the factory by increasing the size of the local oscillator coupling capacitors to test the feasibility of mixing using the twenty-first harmonic of a 3.5 GHz local oscillator. The resulting conversion loss was between 39 and 42 dB. This conversion loss was unacceptable because of the high sensitivity required to accurately measure crosspolar signal levels.

A tradeoff between conversion loss and circuit realizability resulted in the selection of a times three frequency multiplier. Referring to the mixer specifications, Section 2.3.3.4, a conversion loss of 18-26 dB can be achieved using a local oscillator in X-band, and mixing with the 6th to 9th harmonic. An investigation of these harmonic numbers showed that the most feasible mixer harmonic number was the 7th, requiring a times three frequency multiplier, and resulting in a predicted 22-23 dB conversion loss. It also may have been possible to select a times four multiplier and mix with the fifth harmonic. This would have resulted in a further 5 dB reduction in conversion loss, but was decided against because the resultant 14.7 GHz signal would have been above the recommended local oscillator range of the mixer. The sixth harmonic was not usable because it would have required operating the receiver local oscillator at 4.08 GHz, near the absolute upper limit of its range (4.1 GHz), where reliable phase-locking is not possible. Circuits to utilize the eighth or ninth harmonic were realizable but these harmonics would result in higher conversion losses than the seventh.

The frequency multiplier circuits accept a 3.5 GHz input and produce a 10.5 GHz output at a level of 13 dBm for each mixer. The 13 dBm output includes a maximum 3 dB budget for cable loss and mismatch to result in 10 dBm minimum at each mixer LO port. A frequency multiplier in this frequency range uses the nonlinear junction capacitance of a silicon varactor or step recovery diode to produce the harmonic signal. The multiplier input, output and bias circuits have to be carefully matched to the diode characteritics to result in stable, efficient operation. Fabrication and testing of efficient and stable harmonic multipliers in this frequency range requires test equipment which was not available in the Electrical Engineering Department. For this reason commerically built multiplier circuits were purchased.

Due to the many possible combinations of multiplier frequencies and power levels and their inherent narrow bandwidths, multiplier circuits have to be custom fabricated. The specific requirements and small quantities involved in this order made it very difficult to find a supplier. The A.I. Grayzel, Inc. Company which specializes in frequency multipliers was able to supply a device to our specifications at a good price and with an acceptable delivery time. Design tradeoffs involving efficiency and bandwidth were negotiated directly with the company's circuit designers.

2.3.3.7 Frequency Multiplier Specifications and Testing

The manufacturer's specifications for the A.I. Grayzel model OX-3.5 frequency multipliers are given in Table 2.5.

TABLE 2.5 A.I. Grayzel OX-3.5 Frequency Multiplier Specifications

Input frequency	3.5 GHz
Output frequency	10.5 GHz
Input power required for 20 mW output	135 mW
Bandwidth	2 %

The three frequency multipliers (one is a spare) were tested by supplying an input power of 150 mW at frequencies between 3.45 and 3.55 GHz and measuring the X-band power output. Results of this test are plotted in Fig. 2.21. The results of a second test with different 3.5 GHz input powers is shown in Fig. 2.22. These tests showed that none of the three multipliers met the manufacturers specified power output. The manufacturer suggested that the cause of the reduced output might be either that the generator or load impedance presented to the circuits was not matched or that the generator produced an unexpected output waveform. Subsequent tests including attenuator pads (to ensure matched impedances) and different signal sources did not improve the multiplier performance.

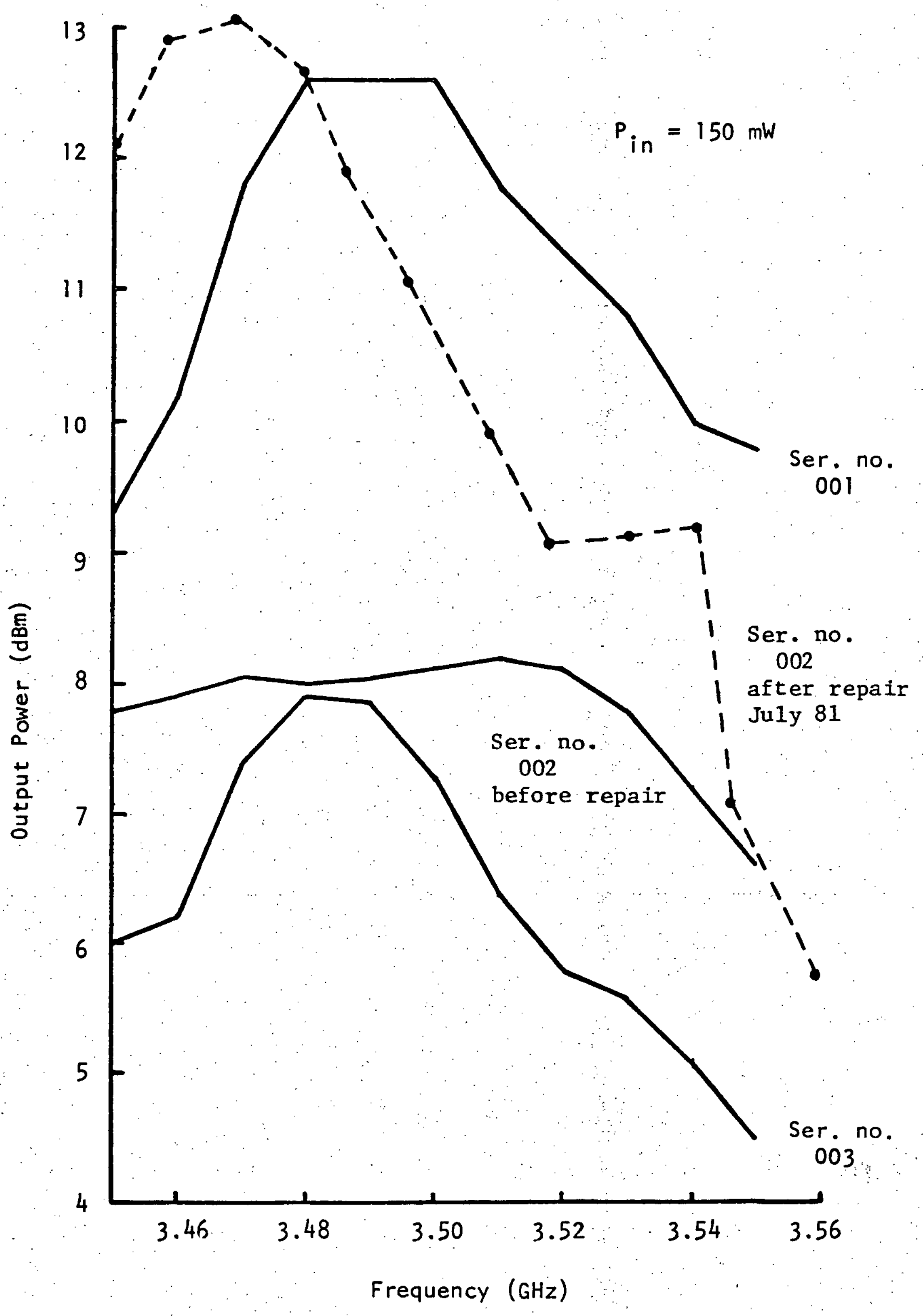

Fig. 2.21. Frequency multiplier frequency response.

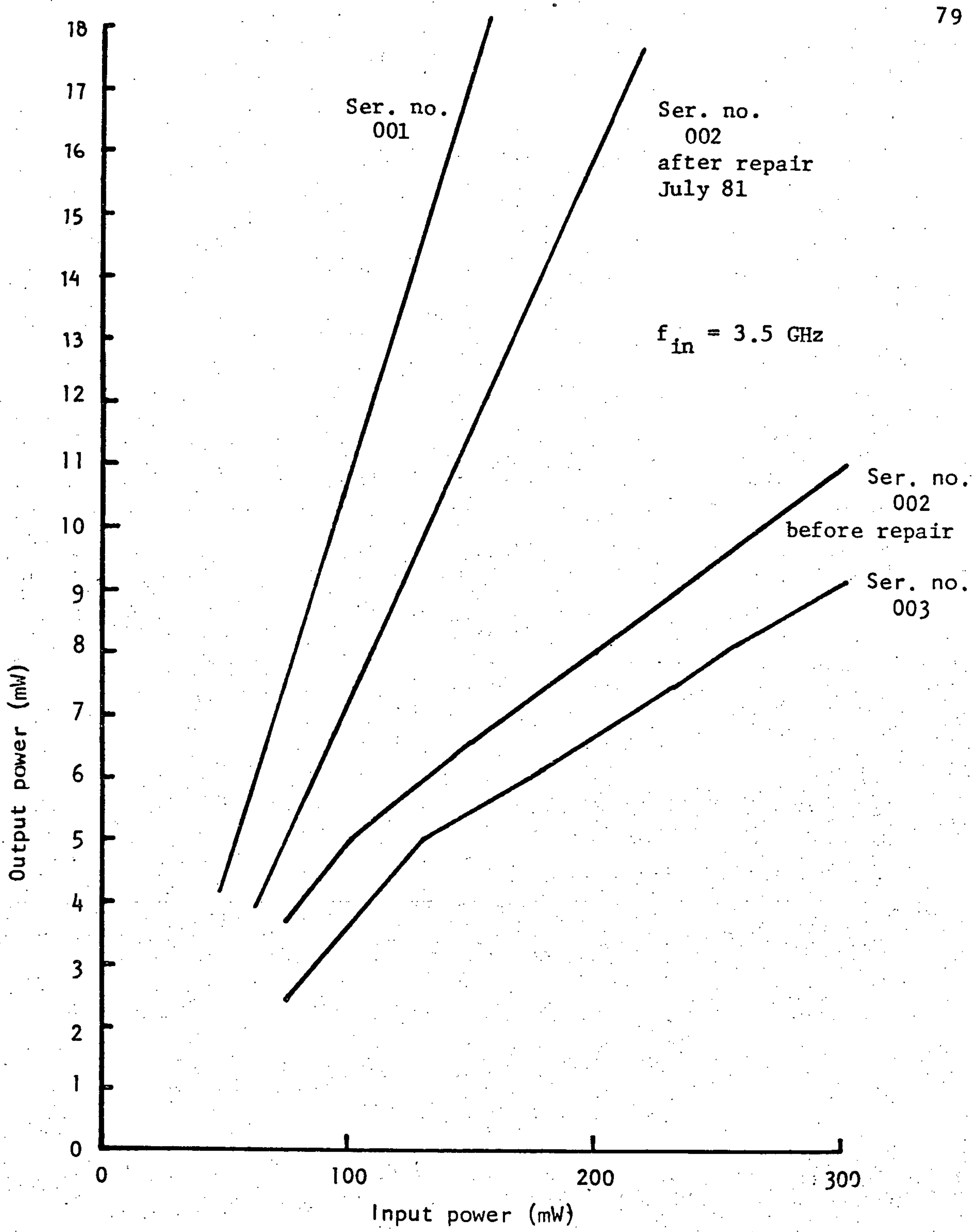

Fig. 2.22. Frequency multiplier conversion loss.

Because the multipliers were sealed and time constraints did not initially permit returning them to the manufacturer, the possibility of supplying a higher input power to the multipliers was investigated.

Power inputs of up to 500 mW were considered safe by the manufacturer. Fortunately, the amplifiers chosen during the design phase to provide the 3.5 GHz input to the multipliers, did have enough extra gain and power output capability to make this solution possible.

Multiplier, serial no. 002, was eventually returned to the manufacturer for repair and realignment in mid 1981. Its subsequent performance is also shown in Figs. 2.21 and 2.22.

2.3.3.8 Local Oscillator Power Amplifier

Power amplifiers are included in the front-end to supply the 3.5 GHz drive level for the frequency multipliers. The two-channel front-end is mounted adjacent to the receiving antenna and is connected to the receiver via two 35 metre long coaxial cables. Low-loss 7/8 inch, air-dielectric cable is used to minimize signal attenuation. These cables have a measured attenuation of 4 dB at the LO frequency. With the maximum LO output from the receiver, 16 mW of LO drive is available at the input to the front-end. The expected insertion loss of the IF injection and matching circuit and LO band-pass filter is about 1 dB and 3 dB respectively. This results in an 8 dBm maximum input to the LO power amplifier. To provide the design 135 mW multiplier input level, the power amplifier required a minimum gain of 14 dB. The Avantek APT-4013 thin-film power amplifier met these specifications with best economy. These devices have a minimum gain of 18 dB and a power output at saturation of 25 dBm over a frequency range of 2-4 GHz. This extra gain and output capacity made it possible to use the frequency multipliers, which did not perform according to their design specifications, in one of the possible LO chain configurations which are discussed in the next section.

2.3.3.9 LO Frequency Multiplier Circuit Configurations

Three circuit configurations, shown in Fig. 2.23, were investigated for the LO frequency multiplier chain. The receiver provides two LO output connectors as shown in Fig. 2.9. A front panel adjustable attenuator is included to set the output level at each connector. In circuits (a) and (b) of Fig. 2.23 only one LO connection is used with the multipliers, amplifiers and a two-way power divider to provide LO signals for both mixers. These configurations have the advantage of requiring fewer amplifier and multiplier modules.

Circuit (a) which uses a 10.5 GHz power divider, requires only one amplifier and multiplier but when this circuit was tested, however, there was only 35 dB isolation between channels. The low IF/LO isolation specification of the mixers (Section 2.3.3.4) prompted an investigation into whether the first IF signal was being coupled between mixers through the LO connections even though no 45 MHz signal could be observed on the LO cables. A test was performed by adding sections of X-band waveguide between the power divider and mixer LO ports. This waveguide would not allow any 45 MHz signals to propagate out from the mixer LO ports. The isolation between channels did not improve. As a result the presence of 45 MHz sidebands on the 10.5 GHz LO signal was suspected. No spectrum analyzer was available to verify this

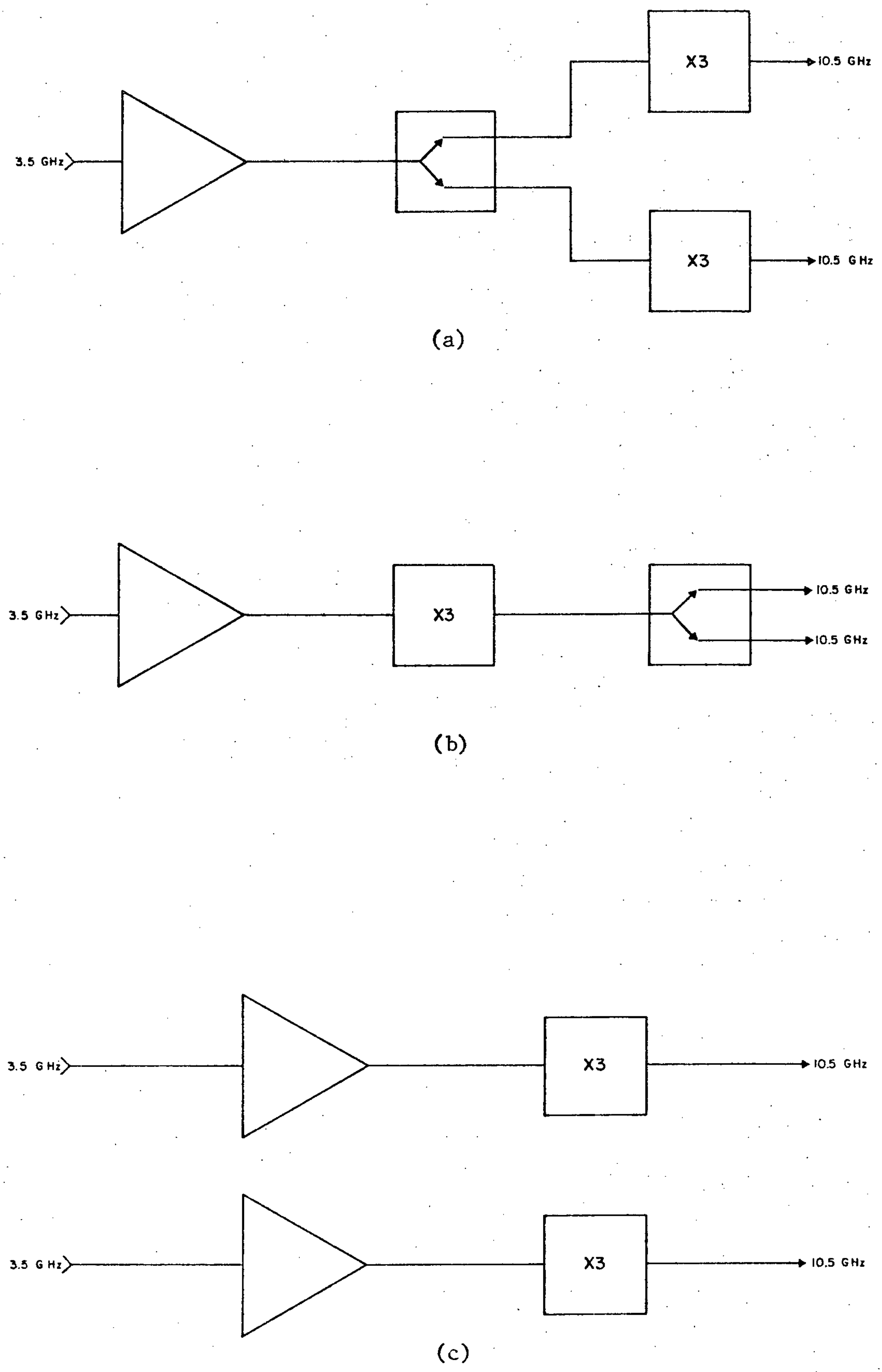

Fig. 2.23. LO frequency multiplier chain circuit configurations.

suspicion. To test this theory one of the outputs from the 10.5 GHz power divider was used as the input to a single ended X-band waveguide mixer with a coaxial IF connection. The mixer IF port was connected to the second IF channel of the receiver. This resulted in an indicated signal level in the second channel which was 40 dB below that in the channel with the harmonic mixer and V-band input, thus verifying the presence of 45 MHz sidebands on the LO signal. This indirect modulation of the LO signal was probably due to the changing impedance of the mixer diode over a cycle of the IF waveform. This problem could likely have been alleviated by including isolators after the power divider, but this would not have been cost effective.

Circuit (b) uses a 3.5 GHz power divider, one amplifier and two frequency multipliers. This circuit would be less susceptable to 45 MHz modulation of the LO signal because of the reverse isolation of the multipliers. It was not usable however, because the unexpectedly high conversion loss of the multipliers meant there was insufficient amplifier output to drive two multipliers. (The previous circuit had a similar disadvantage.) The increased cost of an amplifier with sufficient gain and output negated any advantage of this circuit over circuit (c).

In comparison with circuits (a) and (b), circuit (c), which employs two amplifiers and two multipliers, has extremely high channel-to-channel isolation and the added advantage of being able to use the front panel attenuators to set the individual mixer LO levels (and thus easily compensate for the differences in multiplier efficiency.) To provide 10 mW at the mixer LO port in this configuration, the amplifier driving multiplier 002 (before repair) must supply close to 25 dBm (multiplier 003 was not used). For these reasons circuit (c) was chosen for the final front-end design.

2.3.3.10 Mixer Bias Circuits

The front-end includes a mixer bias circuit to bias each mixer diode at the optimum point on its V-I characteristic for minimum conversion loss. These circuits supply a dc output voltage which is adjustable from zero to approximately -1V. To protect the mixer diodes (which are extremely expensive) against operator errors and circuit failure, an overcurrent shutdown is provided. The current shutdown threshold is adjustable from 0 to 4 mA. Most of the active components in this circuit are duplicated to reduce the probability of diode damage even if a component in the mixer bias circuit fails. Reverse voltage protection diodes are included to protect the mixer diodes against reverse voltage damage in the event of a failure of the positive power supply. Voltage and current meters are included in each bias current as an aid in mixer bias adjustment. The mixer diode voltage is coupled through an isolation resistor to an external jack on the bias circuit enclosure. These signals are applied to analog input ports on the data acquisition system. By monitoring the mixer diode voltage, any changes in either the bias or LO signal applied to the mixer can easily be detected. A schematic of one mixer bias circuit is shown in Fig. 2.24.

2.3.3.11 Digitally Programmable IF Attenuators

In order to increase the receiving systems dynamic range, a digitally programmable attenuator, Texscan model PA-51, is included in each IF signal

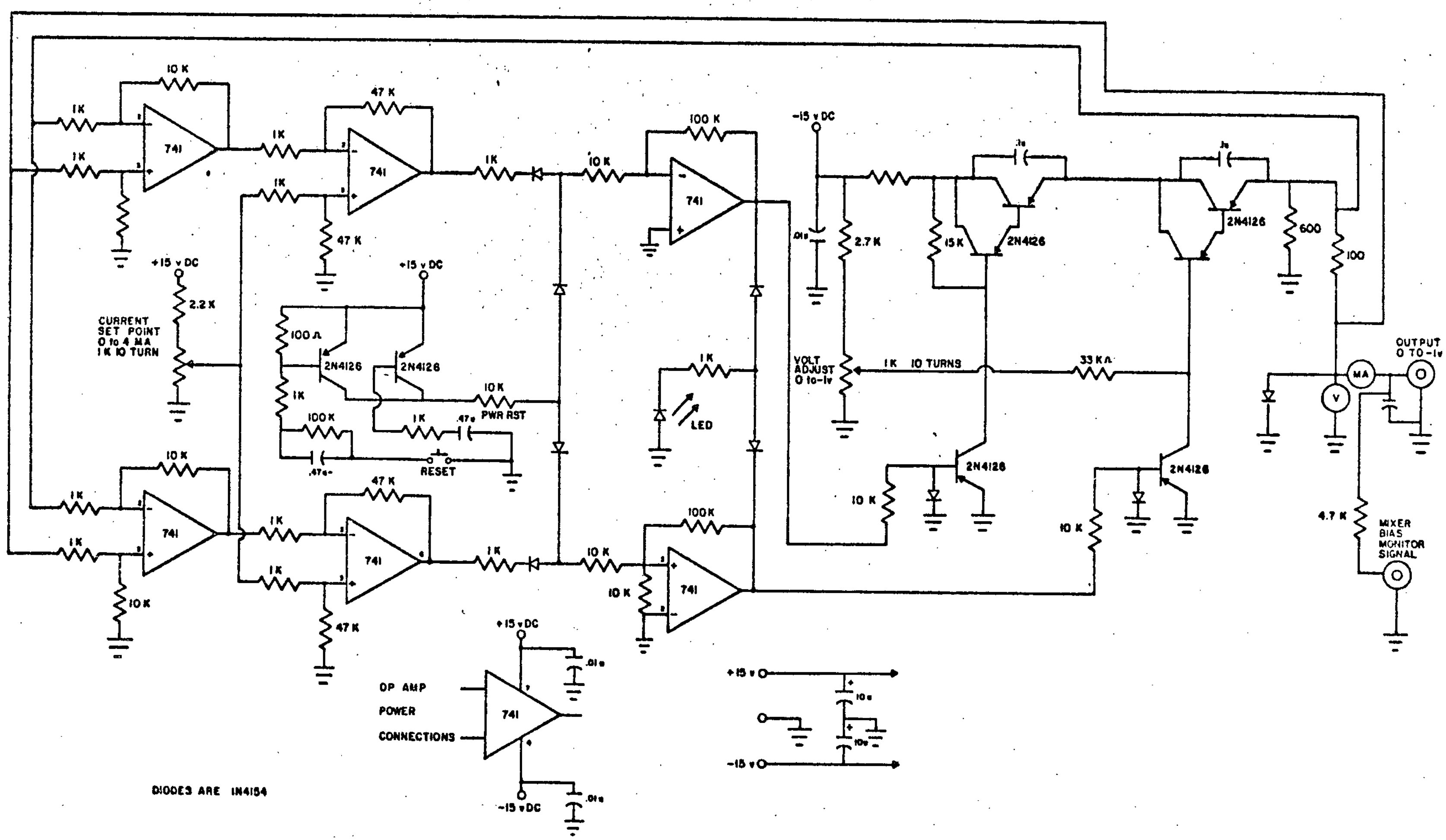

Fig. 2.24. Mixer bias circuit schematic.

path. In any receiving system, dynamic range is limited at high signal levels by saturation or non-linearity and at low signal levels by the noise level. In this system, each receiver channel must sequentially monitor a copolar and a crosspolar signal level. The gain of each receiver channel was adjusted for maximum sensitivity (with the programmable attenuator set at minimum) for best crosspolar measurement sensitivity. During copolar signal measurement the programmable attenuator reduces the IF signal level to prevent receiver saturation.

The model PA-51 attenuator is programmable from 0 to 63 dB in 1 dB steps and switches in 6 ms. Switch contacts in the polarization switch were used to control the attenuator (refer to Fig. 2.5 and 2.11). When the data was analyzed, software was used to correct for the reduced receiver copolar gain.

2.3.3.12 IF Preamplifier

Low noise IF preamplifiers are included in the front end to improve sensitivity and thus increase signal-to-noise ratio during crosspolar signal measurements. The front end single-sideband noise figure is given by [2.15]:

$$F_{F.E.} = L_C(F_{IF} + t_m - 1) \tag{2.8}$$

where:

L_C = mixer conversion loss (power ratio)

F_{IF} = total IF noise figure (power ratio)

t_m = mixer noise temperature ratio

The total IF noise figure is that of the IF amplifier cascade and can be approximated by

$$F_{IF} \cong F_{1st_{AMP}IF} + \frac{F_{2nd_{AMP}IF} - 1}{G_{1st_{AMP}IF}} \tag{2.9}$$

The mixer noise temperature ratio is related to the mixer noise figure by:

$$F_M = L_C \cdot t_m \tag{2.10}$$

The expression for the front end noise figure cannot be evaluated directly because manufacturers do not quote mixer noise figures for harmonic mixers in this frequency range. An estimate of the mixer noise temperature ratio can be derived from equations appearing in [2.16] and [2.17]. The single sideband mixer noise figure for the case of a resistivity terminated image is given by [2.16]:

$$\begin{aligned} F_M &= \frac{1}{L_C}\left[\frac{T_D}{T_0}(L_C - 2) + 2\right] L_C \\ &= t_m \cdot L_C \end{aligned} \tag{2.11}$$

where

T_D = diode noise temperature (°K)

T_0 = ambient temperature (°K)

This expression is derived from the equations in [2.16] and does not agree with the equation for mixer noise figure in [2.17]. The authors of both references discuss the discrepancies in these mixer noise figure equations and it is not obvious which is precisely correct. However, the differences in the two expressions will not produce a significant error in the following analysis.

Solving for t_m yields:

$$t_m = \frac{1}{L_C}\left[\frac{T_D}{T_0}(L_C - 2) + 2\right] \qquad (2.12)$$

References [2.16], [2.17] and [2.18] state that for an ideal Schottky diode:

$$T_D \cong \frac{T_0}{2} \ (°K) \qquad (2.13)$$

This value is probably very optimistic for this type of application [2.19]. [2.20] but will be used in an attempt to ascertain the relative contribution of the IF preamplifier to the front-end noise figure. Using this expression for T_D, t_m can be rewritten as:

$$t_m = 0.5 + \frac{1}{L_C} \qquad (2.14)$$

This expression for t_m can now be substituted into the expression for the front-end noise figure, (2.8), to yield,

$$F_{FE} = 1 + L_C(F_{IF} - 0.5) \qquad (2.15)$$

The equation illustrates the relative effect of the IF preamplifier noise figure.

The first stage of IF gain in the Scientific Atlanta receiver uses a 40235 transistor. This device is not characterized for noise figure at the IF frequency but extrapolation of its specifications indicates its noise figure is in the vicinity of 3.3.dB at 45 MHz. Lower noise figures are now possible at 45 MHz. The low noise amplifier selected to be used as an IF preamplifier is the Anzac Electronics AM-107-8408. This amplifier has 10 dB gain and a 1.5 dB maximum noise figure over a frequency range of 1-100 MHz. The 10 dB gain will reduce the noise contribution of the first IF stage in the receiver to approximately 0.3 dB. The total IF noise figure is then 1.8 dB, an approximate improvement of 1.5 dB. This improvement in IF noise figure results in a 2.0 dB improvement in front-end noise figure at a very low cost.

2.3.4 Frequency Counter

An EIP model 351C microwave frequency counter was used to continuously measure the 3.5 GHz receiver LO frequency. This was done to monitor the millimetre-wave klystron frequency, which is exactly twenty-one times the receiver LO frequency plus or minus the 45 MHz IF frequency. Because the klystron was free-running, changes in its supply voltages, case temperature and cavity tuning all affect its operating frequency. Changes in the millimetre frequency can result in changes in the received signal levels due to the frequency sensitive behaviour of many components in the experimental system. To ensure that frequency changes did not corrupt data during an event and to be able to compare data and system behaviour over longer periods, seven BCD digits of frequency data from the counter were continuously recorded along with the other experimental data.

2.3.5 Receiving System Performance

2.3.5.1 Calculated Sensitivity

The noise figure of the receiving system front-end is given by:

$$F_{FE} = 1 + L_C(F_{IF} - 0.5) \tag{2.15}$$

From Section 2.3.3.12 the total IF noise figure is:

$$F_{IF} = 1.5 = 1.8 \text{ dB} \tag{2.16}$$

The mixer conversion loss with the local oscillator chain described in Section 2.3.3.6 was estimated from the manufacturer's catalogue, to be 22-23 dB. However, the measured mixer conversion loss in the front-end with a 10 mW LO level, was 26 dB with a measurement accuracy of ±1 dB. Using these values, the front-end single-sideband noise figure is calculated to be also 26 dB.

This value of noise figure would be applicable to the calculation of a receiving system sensitivity if this front-end were used in a single-conversion non-radiometer type receiver with no image band noise rejection [2.15]. However, with the Scientific Atlanta model 1751 receiver, an additional sensitivity degradation results because there is also no second-conversion image-noise rejection. This problem will be illustrated using the frequency domain representation in Fig. 2.25. In the single conversion case, the RF and IF signal spectrum are shown in Fig. 2.25(a) and 2.25(b) respectively. If the IF signal in Fig. 2.25(b) were to be detected, the desired signal would be corrupted by noise from frequencies within the IF passband downconverted from both the signal and image channels. Because

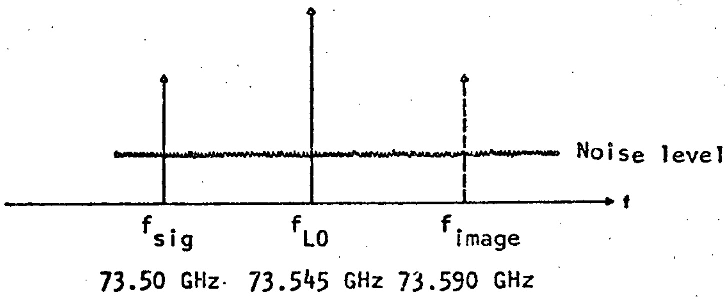

(a) RF signal spectrum

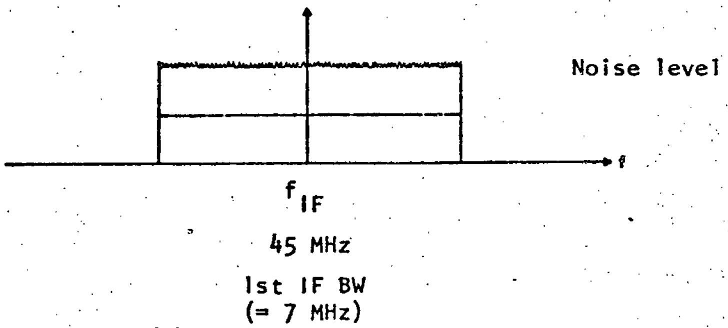

(b) First IF spectrum

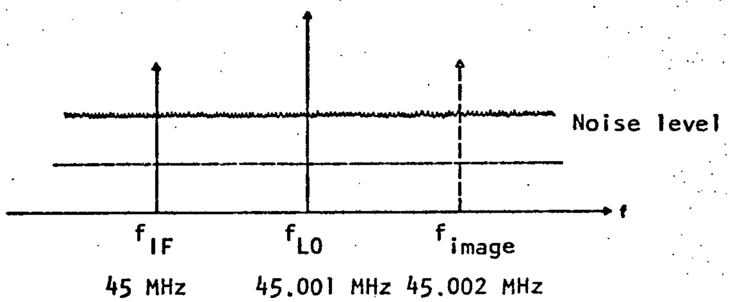

(c) Second conversion spectrum

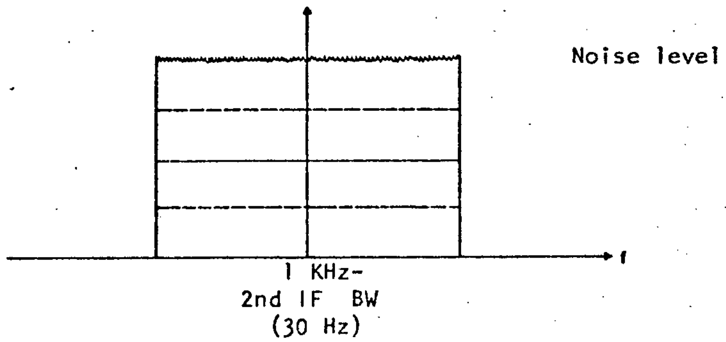

(d) Second IF spectrum

Fig. 2.25. Receiver: signal, IF, LO and noise in the frequency domain.

nothing is done to reject the image band noise the IF signal-to-noise ratio is reduced by 3 dB. This is the reason single sideband mixer noise figures are approximately 3 dB higher than double sideband mixer noise figures [2.15], [2.17], [2.21].

In a typical double-conversion receiving system, the noise figure would be unchanged because a first IF bandpass filter would be provided to attenuate the second-conversion image noise. In the model 1751 receiver no such filter is included because the 1 kHz second IF frequency is too low to make such filtering practical. (This second IF frequency was chosen because 1 kHz is a widely used standard frequency and thus makes the receiver compatible with different detection systems.) The first and second IF spectrum diagrams in Figs. 2.25(c) and 2.25(d) show how in this case an additional doubling of noise power occurs before signal detection. To be able to use standard equations to convert the noise figure to sensitivity this extra noise component will be accounted for by using an "effective" receiving system noise figure of 29 dB.

The noise contribution of the receiver, referred to its input, can also be expressed as an effective input noise temperature, T_e using [2.15]:

$$T_e = T_o(F-1) \tag{2.17}$$

where T_o = 290°K. From (2.17) this receiver has a noise temperature of T_e = $2.3 \cdot 10^5$°K.

The equivalent input noise power of the receiver can be calculated using this noise temperature and the receiver predetection noise bandwidth. The predetection bandwidth is determined by the second order filters in the digital amplitude measurement units. The 30 Hz - 3 dB bandwidth of these filters corresponds to a noise equivalent bandwidth of approximately: $B_n = 44$ Hz [2.22]. Equation 2.18 relates the equivalent input noise power, P_n, to these quantities:

$$P_n = kT_eB_n \tag{2.18}$$

where k = Boltzman's constant = $1.38 \cdot 10^{-23}$ J/°K. Thus, for this receiver $P_n = 1.4 \cdot 10^{-16}$ W = -129 dBm.

2.3.5.2 <u>Measured Receiving System Sensitivity</u>

An attempt was made to measure the equivalent input noise power of the receiving system by using a spectrum analyzer to observe the first IF signal after the receiver IF amplifier. Because of the high gain of the receiver IF amplifier, there is no sensitivity reduction due to noise contributions of the following stages. A resolution bandwidth of 30 Hz was used for the measurements to approximate the receiver predetection bandwidth. However, the noise band-width of the Gaussian filters in the analyzer are approximately 1.2 times their 3 dB bandwidths [2.23], necessitating a noise level measurement correction of -0.7 dB.

An additional correction of +2.5 dB is required when observing random noise to correct for the spectrum analyzers average level indication and logarithmic compression [2.23]. Thus the "indicated" signal-to-noise ratio on the spectrum analyzer was 1.8 dB higher than that for the complete receiving system with the same input signal.

Figure 2.26 is a photograph of the spectrum analyzer display for a -100 dBm input signal at 73.5 GHz. When measuring noise levels on a spectrum analyzer, the average noise level is usually displayed by adjusting the video filter bandwidth to be one-hundredth or less of the resolution bandwidth [2.23]. This procedure could not be followed for this measurement because the minimum video filter bandwidth was 10 Hz. As a result, the average noise level can only be estimated. From several observations similar to Fig. 2.26, the approximate signal-to-noise ratio is 24 dB ± 3 dB. After including the correction factors, this corresponds to an equivalent input noise power for the receiving system of -122 dBm. With the uncertainty in the measured conversion loss and noise level and the estimates in the calculated noise figure, and because of the numerous possible impedance mismatches, this value was considered to be in reasonable agreement.

Another possible cause for the discrepancy between the calculated and measured receiving system sensitivities is local oscillator noise. Because the mixers used in the front-end are single-ended, they will have very low LO noise rejection. Any LO noise sidebands at frequencies plus or minus 45 MHz from the center of the LO spectrum will combine with the LO center frequency and produce an IF output. This will result in an unexpectedly higher noise level in the previously described test. Due to the very high sensitivity of this receiver, even if a spectrum analyzer could be used to monitor the 73.545 GHz multiplied LO signal at the mixer diode, these noise sidebands would probably not be observable. The potential for this type of sensitivity degradation could be eliminated by using a much higher first IF frequency.

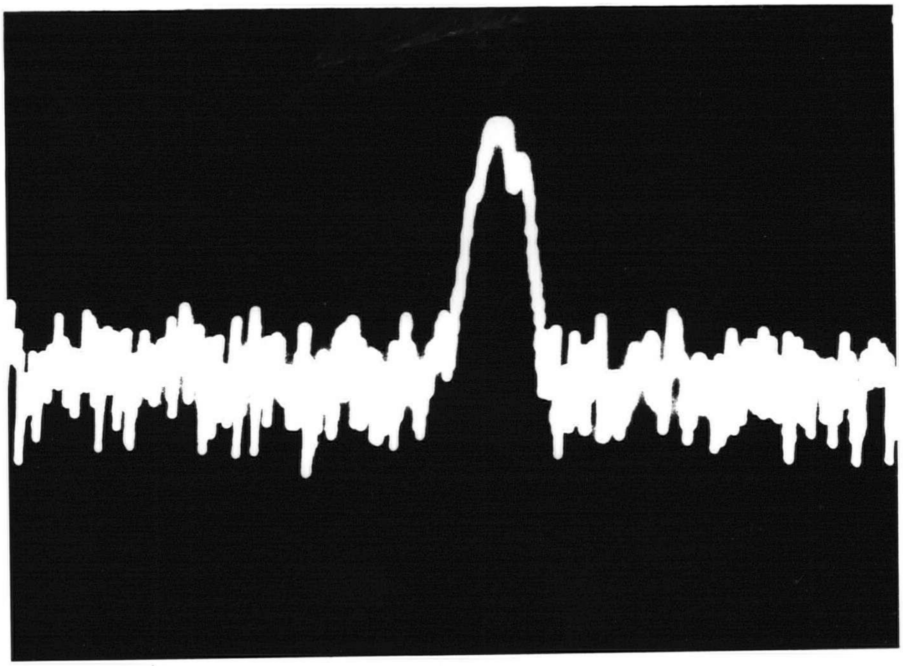

f CENTER = 45 MHz

Scan width = 100 Hz/div.

Resolution bandwidth = 30 Hz

Video filter = 10 KHz

Scan time = 10 s

Vertical scale = 10 dB/div.

Signal into receiver is 73.5 GHz @ -100 dBm.

Fig. 2.26 Spectrum analyzer display of 1st IF signal.

2.3.5.3 Receiving-System Small-Signal Performance

At low input-signal levels, the measurement accuracy of the receiving system is corrupted by noise. The complete receiving system was tested by applying a known signal level to the mixer inputs. Fig. 2.27 shows the indicated digital signal levels for each channel with 0 dB corresponding to a -40 dBm input level. The average value, and minimum and maximum indicated values for a 1.0 sec. sampling period are shown.

During these tests it was extremely difficult to prevent signal leakage into the front-end. This problem was also observed during similar tests in [2.24]. Radiation from the klystron and waveguide flanges resulted in a significant ambient signal level. Signal ingress into the front-end resulted in a higher indicated noise level, greater nonlinearity and larger peak-to-peak fluctuations. To reduce the ambient level and front-end ingress, the front-end was shielded and moved as far away from the klystron as practical. In addition, all waveguide junctions were visually inspected after connection and then wrapped in metal foil. These measures reduced the undesired signal level by more than 20 dB but the indicated noise levels were still 5 to 6 dB higher than when the front end was mounted on the roof. For this reason the actual receiving system performance is actually 5 to 6 dB better than indicated in Fig. 2.27.

The results from tests performed on the bench (Fig. 2.27) indicate that average indicated levels of the receiving system are linear to with ± 0.3 dB for input levels down to -95 dBm. At this input level, peak-to-peak noise fluctuations are 1.0 dB or less. (When the system was installed on the roof, similar performance was obtained for -100 dBm.) The effect of these

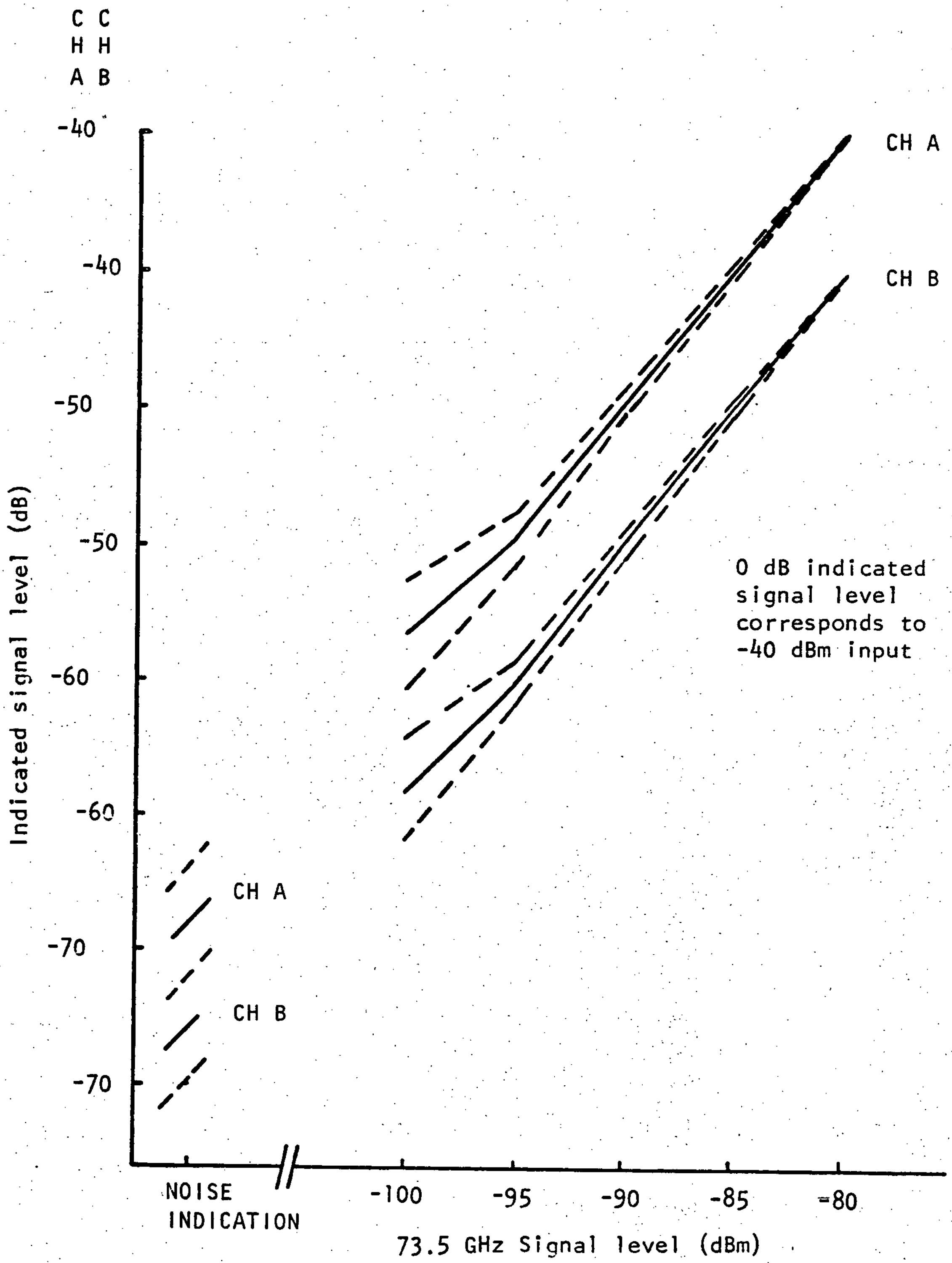

Fig. 2.27. Receiving system small signal performance on the bench.

fluctuations in indicated signal level can be reduced by averaging during data analysis. The nonlinearity at low signal levels was likely due to signal ingrees.

This front end is approximately 30 dB more sensitive than the Scientific Atlanta model 13-50A mixer, but an exact comparison has not been made.

2.3.5.4 Receiving System Isolation and Frequency Response

The measured channel-to-channel isolation of the complete receiving system was greater than 75 dB. This is the measurement limit imposed by saturation in the channel with the signal applied (without IF attenuation) and noise level in the other channel.

Fig. 2.28 shows a typical response of the complete receiving system to input frequencies between 73.0 and 73.5 GHz. The frequency response of the receiving system is mainly determined by the frequency multipliers and mixers. Changing the position of the mixer backshort tuning adjustment will significantly alter the receiving system frequency response.

2.3.5.5 Front-end Alignment

The following procedure is followed to align the front end for a new receiver frequency.

1. Adjust the LO level for 10 mW at the mixer LO port. CAUTION: Do not exceed 20 mW LO level or the mixer diode may be damaged. LO level is adjusted by the receiver front panel LO attenuator or by placing a fixed pad with SMA connectors on the LO amplifier input. Fig. 2.29 shows a typical variation in mixer conversion loss for various LO levels.

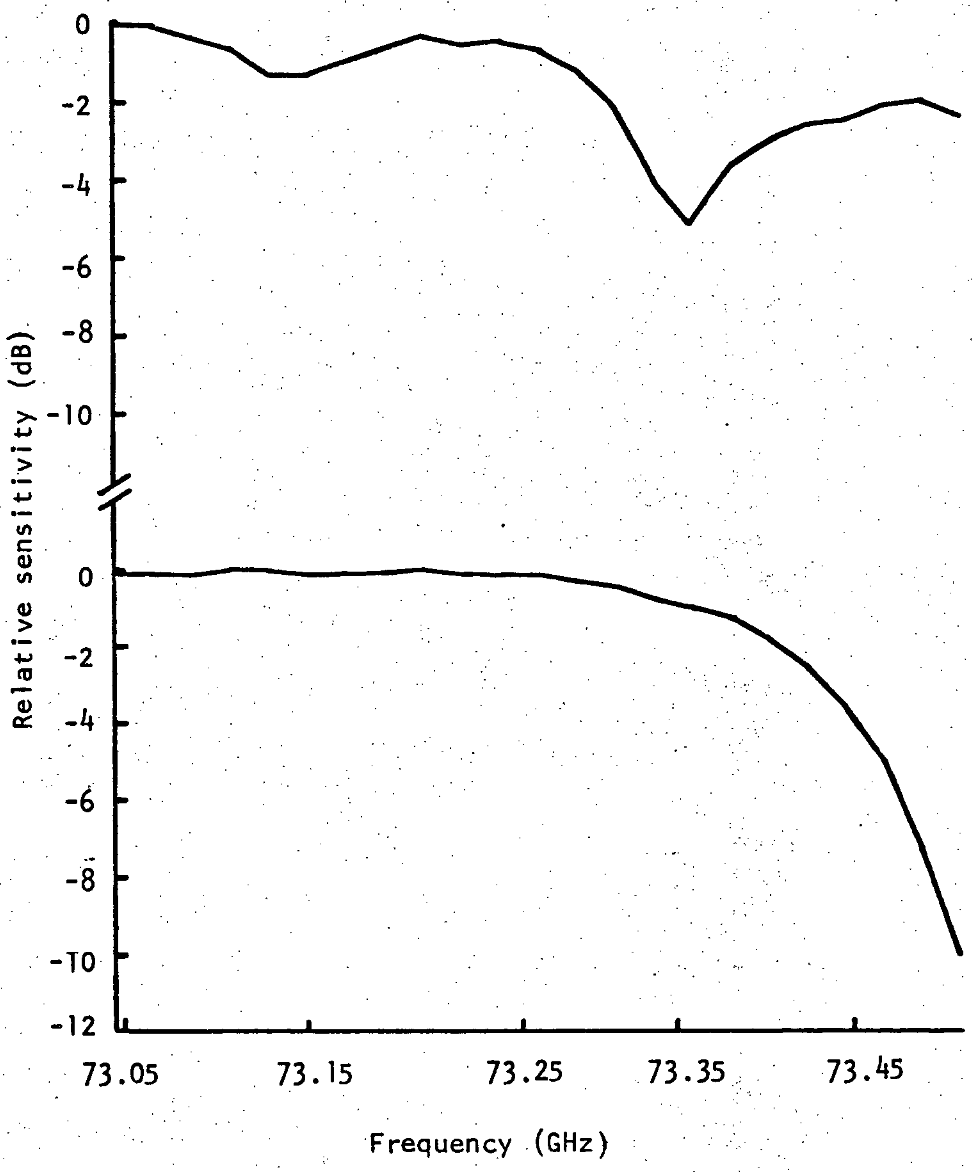

Fig. 2.28. Receiving system frequency response.

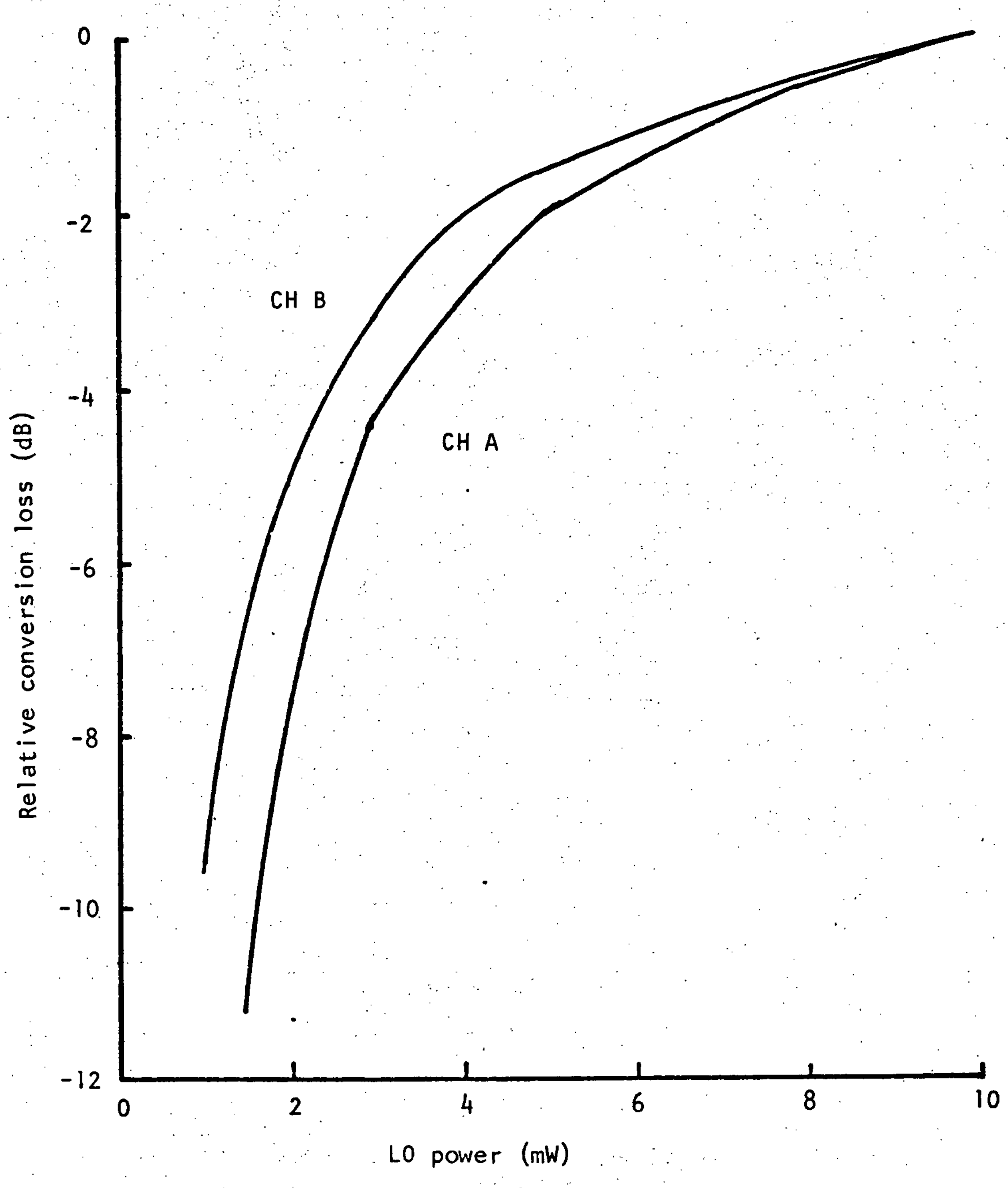

Fig. 2.29. Effect of LO level on conversion loss.

2. Adjust the mixer bias level for maximum signal indication. CAUTION: Do not exceed 4 mA diode current. Fig. 2.30 shows a typical variation in signal and noise level for various mixer bias conditions. (These results would be changed for different LO levels and tuning positions.) Because the noise level is relatively constant, it is permissible to adjust for maximum signal level only. The optimum bias setting is very dependent on LO drive level.
3. Adjust the mixer waveguide backshort for maximum signal indication. The maxima for the backshort closest to the diode will give the widest frequency response.
4. Repeat steps 2 and 3.

2.4 Propagation Path

The radar propagation path for this experiment is located on the campus of the University of British Columbia. Antennas for both transmitting and receiving are mounted on the roof of the Electrical Engineering building. The antennas are separated by a horizontal distance of 20 metres to prevent any stray coupling. The reflector is mounted on the roof of the Gage Towers building 880 metres away. This provides a total path length of 1.76 km. Fig 2.31, from [2.1], shows the path details. Fig. 2.32 is a photograph showing the path looking from the reflector toward the antennas.

2.5 Antennas and Orthomode Transducers

TRG model V822 Cassegrain parabolic antennas are used for both transmitting and receiving. These antennas are 61 cm in diameter and have

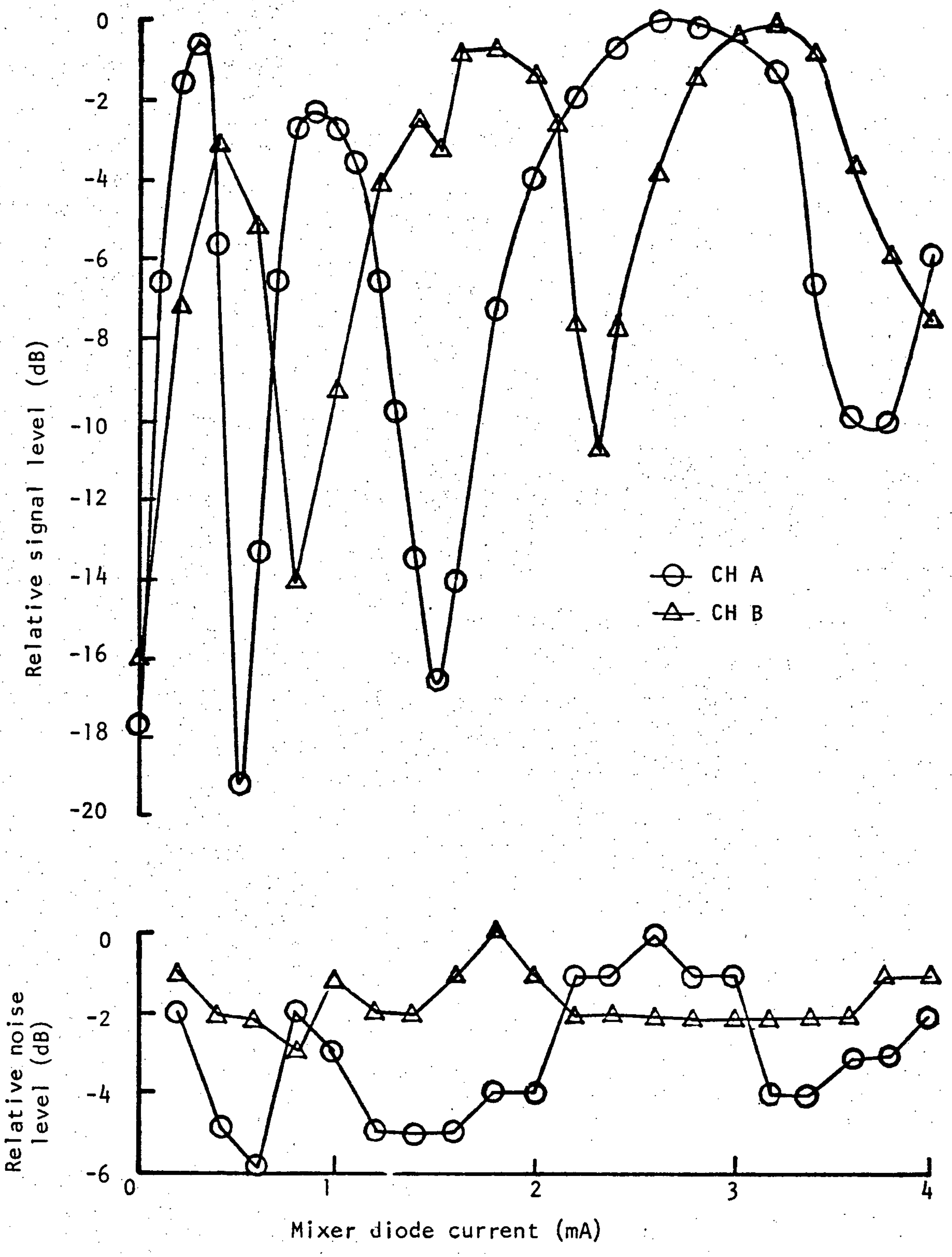

Fig. 2.30. Effect of mixer bias current on front-end performance.

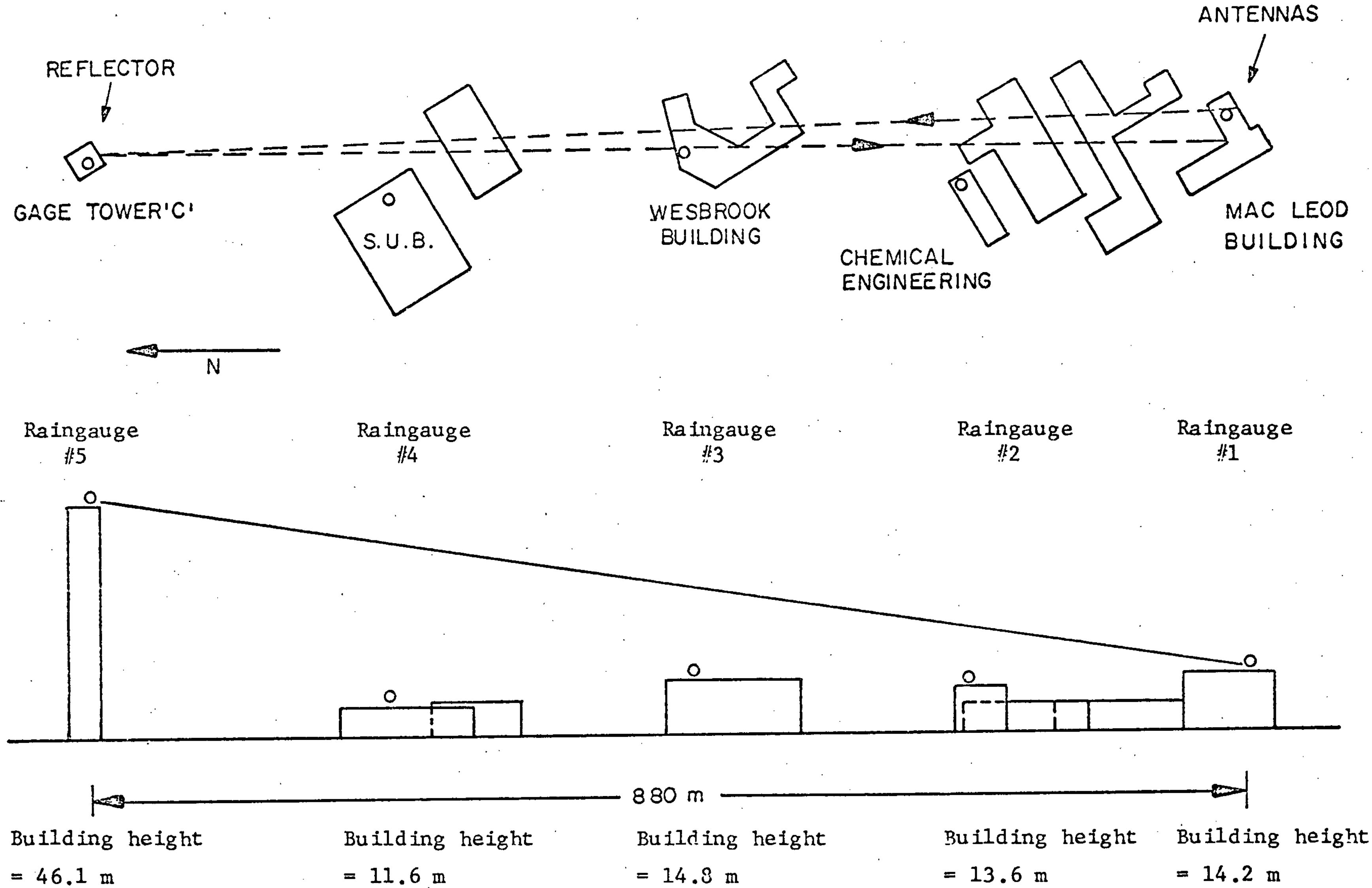

Fig. 2.31. Propagation path details.

Fig. 2.32. Propagation path photograph.

machined aluminum reflectors. Corrugated, conical, scalar feed horns are incorporated for polarization insensitive characteristics, high aperture efficiency and low sidelobe levels [2.25]. Dual-linear polarization capability is realized by including orthomode transducers which interface to the circular waveguide ports on the feedhorns. The orthomode transducers for these antennas were specially manufactured to yield the highest possible polarization isolation. The manufacturers specifications for the two antennas assemblies are included in Table 2.6. Crosspolar isolation performance, measured by the manufacturer, for the complete antennas is shown in Fig. 2.33.

TABLE 2.6 TRG V822 Antenna Specifications at 73.5 GHz.

	Serial no. 22	Serial no. 23
On axis gain		
through port	50.6 dB	50.9 dB
cross port	50.6 dB	50.9 dB
VSWR		
through port	1.07	1.12
cross port	1.09	1.11
3 dB Beam Width		
through port	0.45°	0.45°
cross port	0.46°	0.45°
Sidelobe levels (max.)		
through port	-23 dB	21 dB
cross port	-22 dB	21 dB

Additional tests were made on the orthomode transducers to supplement the manufacturer's polarization isolation data. This was accomplished by

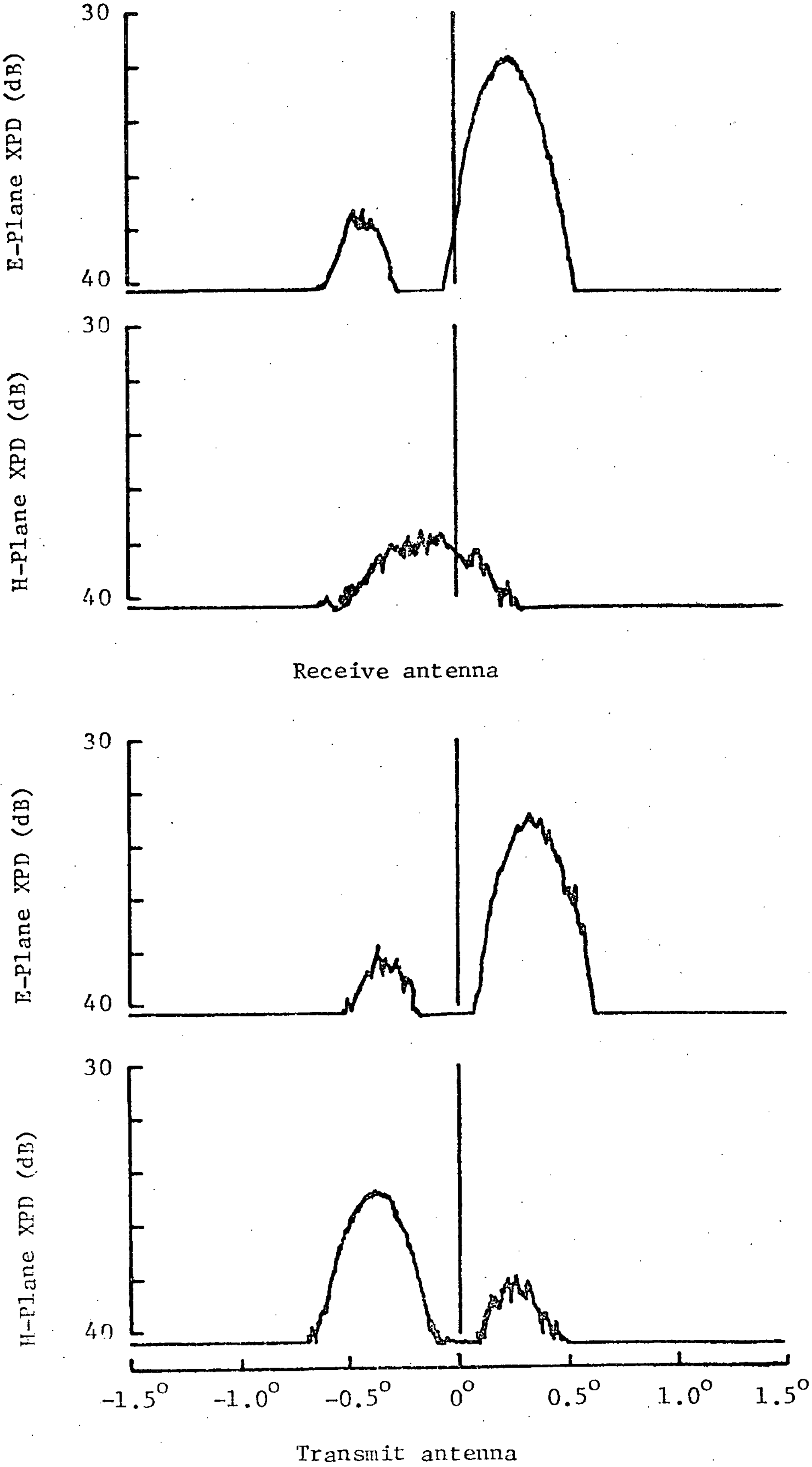

Fig. 2.33. Antenna crosspolar isolation performance.

connecting the two orthomode transducers "back-to-back" through their circular waveguide ports as shown in Fig. 2.34. Isolation between the two perpendicular pairs of rectangular waveguide ports were measured using a power meter with the unused ports of the transducers terminated with matched loads. The test results, (which are corrected for the source and power meter frequency response) for frequencies between 73.0 and 73.6 GHz, are shown in Fig. 2.35.

The copolar insertion losses of the two orthomode transducers were found to be slightly different. The average insertion loss for the straight arm - straight arm connection was 0.8 dB less than for the cross arm - cross arm connection. This fact introduced some uncertainty into the manufacturers antenna gain specifications, which are identical for each arm - an unlikely result in view of the different insertion losses.

The crosspolar isolation between ports was also found to be different. This is likely due to the different ways the polarization isolation was realized in the cross and through arms. It is also possible that the differences between the two isolations is partly due to a slight polariztion orientation mismatch between the transducers for one of the polarizations, i.e. the output polarizations may not be exactly perpendicular. This could not be investigated because the circular flanges had locating pins which prevented the polarization orientations between the transducers from being varied in this test configuration.

When a similar test of crosspolar isolation for the two back-to-back orthomode transducers was made using the receiving system instead of the power meter, a very different frequency response was observed. This

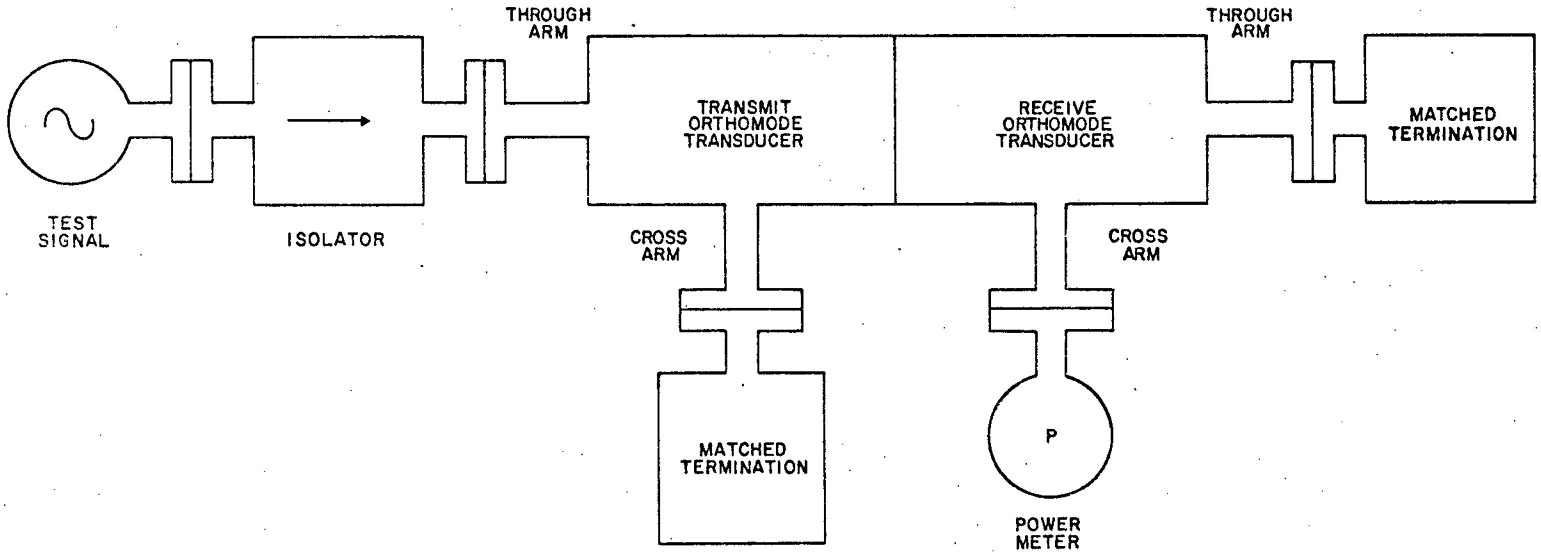

Fig. 2.34. Orthomode transducer test configuration.

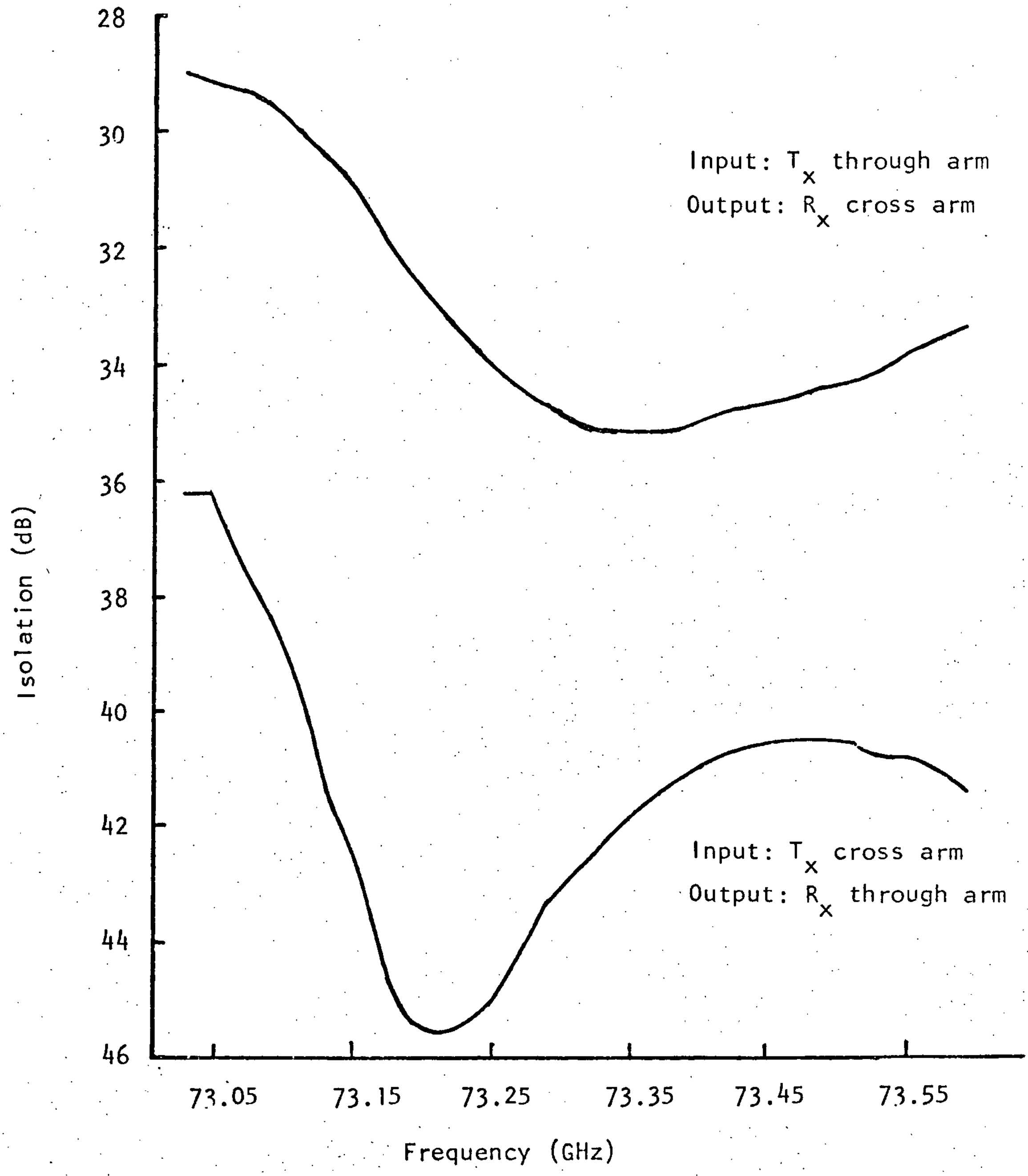

Fig. 2.35. Orthomode transducer test results with matched terminations.

difference prompted several new isolation-frequency response tests under slightly different conditions. It was discovered that even very small mismatches occurring on the rectangular ports of the orthomode transducers produced large changes in the measured isolation.

As an example, Fig. 2.36 shows the response which was obtained by deliberately mismatching the unused cross arm of the transmit orthomode transducers and repeating the test shown in Fig. 2.34. The mismatch was produced by placing a waveguide E-H tuner between the matched termination and the transmit transducer cross arm port. A second test was performed using the receiving system with a variable attenuator before one mixer and an isolator ahead of the second mixer as shown in Fig. 2.37. The crosspolar isolation without the isolator and with no attenuation shows a similar result to Fig. 2.36. The improvements which result with the addition of the isolator and with 10 dB and 20 dB attenuation are shown in Fig. 2.38. This observed degradation of performance due to even slight mismatches is the reason all ports of both orthomode transducers are connected through isolators. The theoretical explanation of the mechanism believed to be responsible for this impedance sensitive behaviour of the OMT is presented in Section 5.5.2.

2.5.1 Crosspolar Cancellation Network

The impetus for the investigation of methods to improve the crosspolar measurement range at 73 GHz resulted from several factors:

1. Theoretically predicted levels of XPD near 73 GHz are very high. Published calculations predict XPD values around 40 - 50 dB for 20 dB

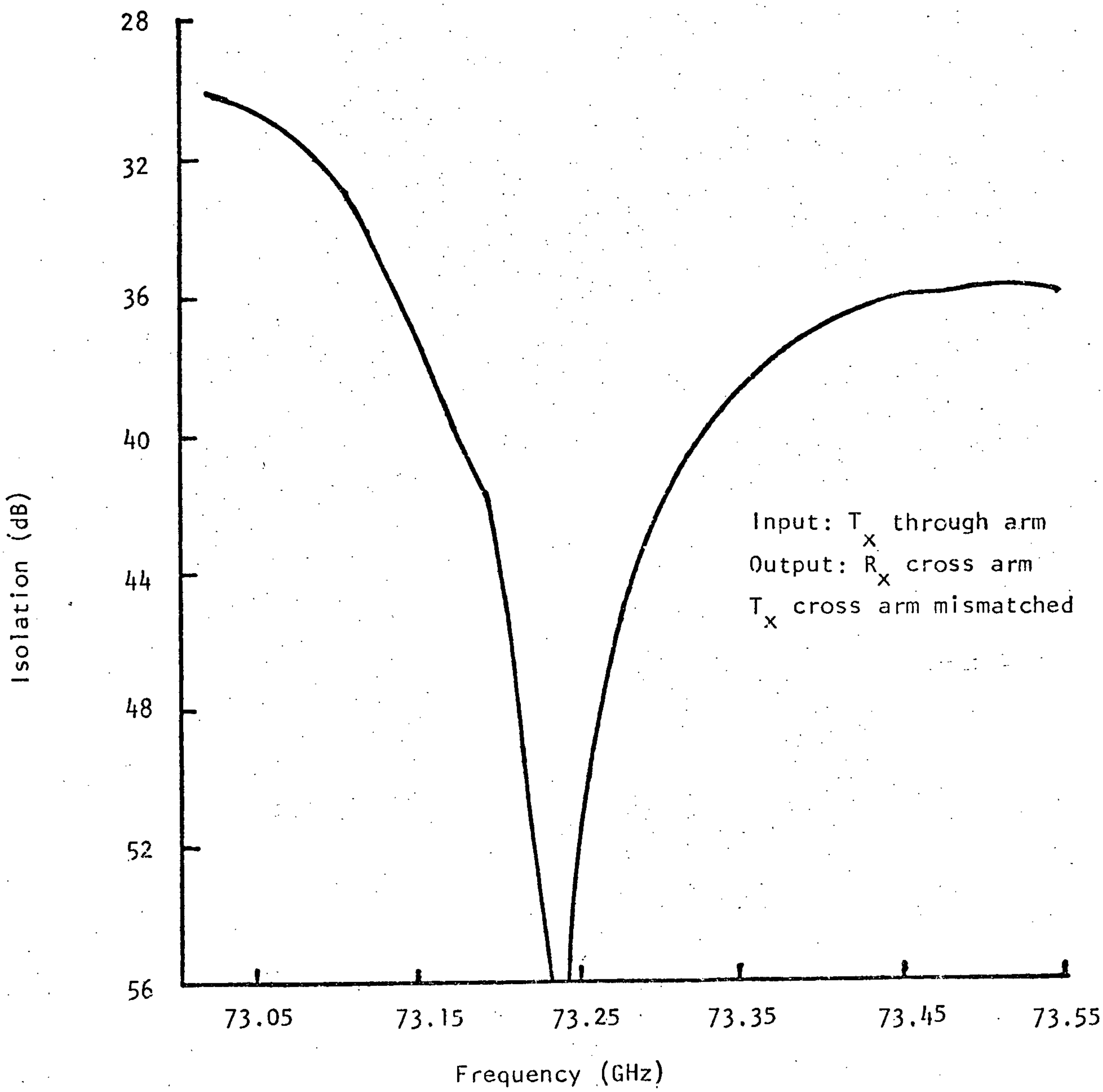

Fig. 2.36. Orthomode transducer test results with one port mismatched.

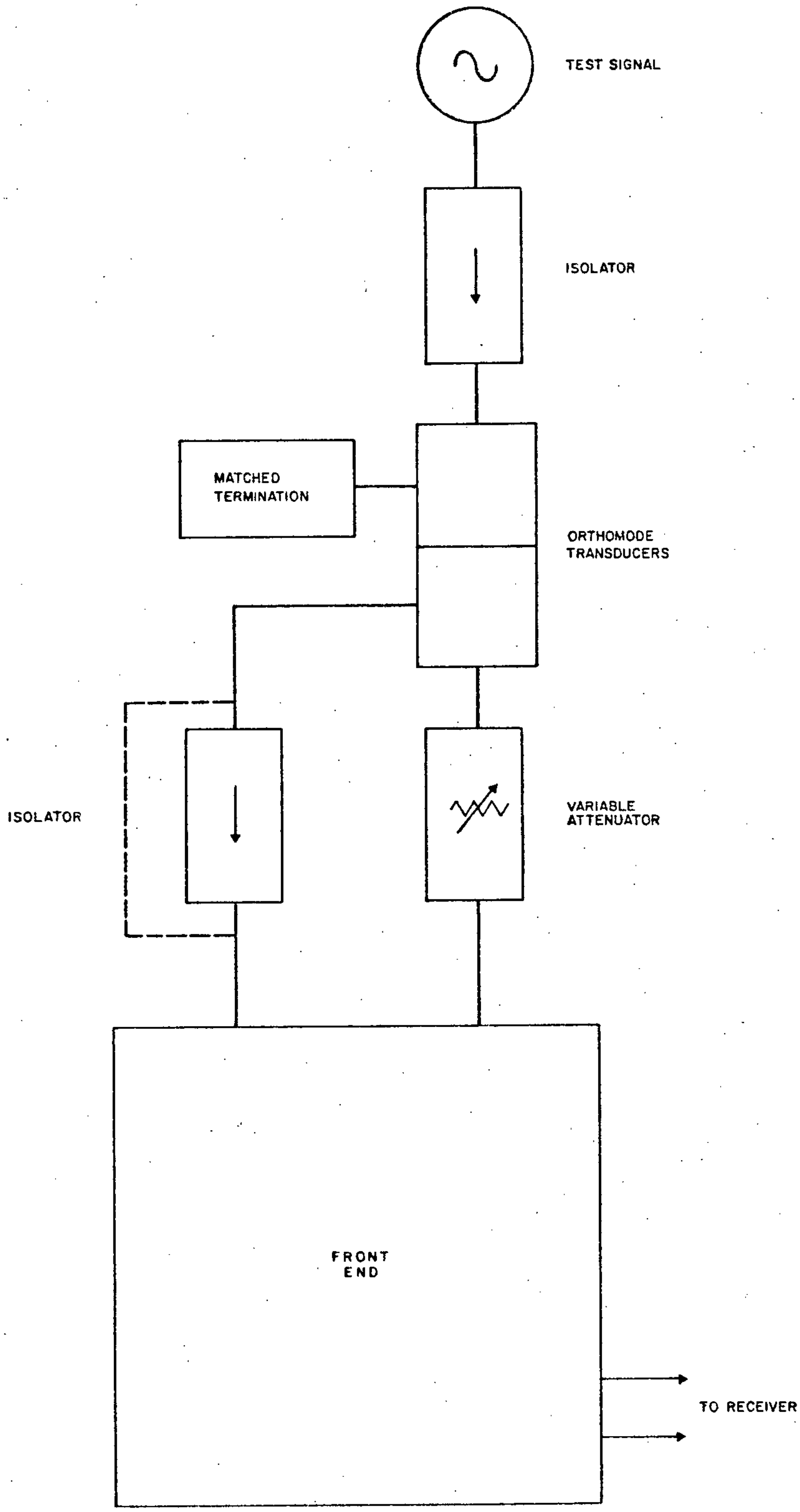

Fig. 2.37. Orthomode transducer test with the receiving system front-end.

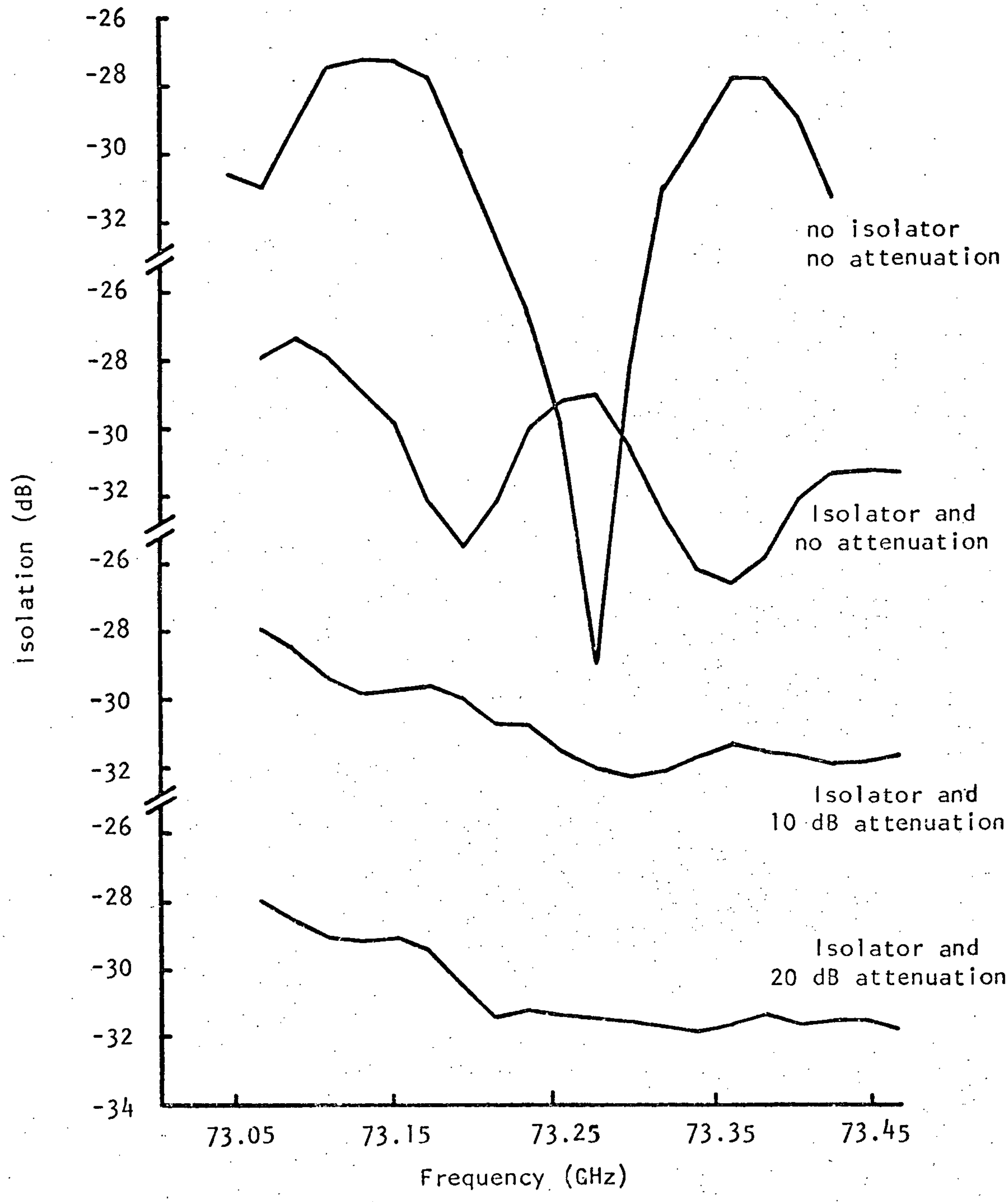

Fig. 2.38. Test results for Fig. 2.37.

copolar fades. The probability of a 20 dB or greater copolar fade on the UBC path is very low (approximately 10 min/year).

2. Even with the excellent performance of the specially fabricated orthomode transducers (OMT), careful alignment could not yield simultaneous isolations on both channels of greater than approximately 34 dB and 36 dB. These isolations in this frequency range are extremely high but still do not result in easily interpreted XPD data for most rainfall events. Measurements taken without the crosspolar cancellation network have confirmed that system XPD's will only be a few dB different that the clear weather values, (refer to Chapter 6).

3. It is possible with certain combinations of OMT port terminations and antenna and feed alignments to have clear weather, system isolations higher than 34-36 dB for one polarization over narrow frequency ranges. Unfortunately this appears to be accompanied by very poor isolation in the other channel. Simultaneous improvement is not possible because adjusting port terminations and alignments does not provide sufficient degrees of freedom. A complete explanation of the effects of OMT port terminations and alignment are found in Section 5.5.2 and 2.5.3 respectively.

2.5.1.1 <u>XPD Improvement Methods</u>

There are two basic methods which have been used to improve the XPD of microwave or millimetre-wave systems. These techniques are most commonly referred to in the literature as orthogonalization and cancellation. (Other terms which have been used to describe cancellation methods are cross coupling [2.26], [2.27] and the matrix method [2.28]). Both techniques require four independently variable parameters to completely correct a dual-polarized link. Orthogonalization uses a rotatable differential phase shifter and a rotatable differential attenuator in a circular waveguide. XPD improvement is accomplished in essentially the same way in which a depolarizing medium, (i.e. rain) decreases XPD. Cancellation techniques incorporate two directional couplers, an attenuator and a phase shifter for each channel to be corrected. The undesired depolarized signal is cancelled by vector subtraction of a sample of the perpendicularly polarized copolar signal.

Both basic methods may be applied statically or adaptively. Static XPD improvement is used to increase clear-weather XPD by compensating for the crosspolar signals due to the finite isolation of the system's orthomode transducers and antennas and is usually employed to improve the XPD measurement range in propagation experiments. In an adaptive application, an electronic control system - usually including a microprocessor - varies the four XPD - improvement - network parameters to continually correct for depolarization resulting from anomalous propagation conditions. All of the available references on adaptive systems applied these techniques to satellite links.

The orthogonalization method for XPD improvement was first proposed by T.S. Chu [2.29], [2.30]. This method requires a differential phase shifter and differential attenuator which can be oriented at any desired angle between horizontal and vertical. The rotatable differential phase shifter transforms the general dual-polarized signal - which is comprosed of two non-orthogonal, elliptically-polarized components - into linearly polarized non-orthogonal waves. These linearly polarized waves can then be made orthogonal by a suitable differential attenuation applied at the correct angle between horizontal and vertical. A network to literally fulfill these requirements can only be constructed in circular waveguide and, therefore, must be installed immediately after the feedhorn on the receiving antenna. The major disadvantage of this technique is the difficulty of fabricating and adjusting the network and the fact that the network must precede the receiver front-end and therefore will reduce sensitivity [2.31], [2.26]. The advantage of this method, however, is that it will probably produce the widest operating bandwidth because the entire circuit is fabricated within a single, short section of waveguide [2.27].

Kannowade [2.32] has further analyzed the Chu type orthogonalization network for adaptive correction on satellite links. He has also proposed a method of realizing a Chu type orthogonalization in a rectangular waveguide network installed after the orthomode transducer. This is accomplished by incorporating two networks for coordinate rotation each of which is constructed from two 3-dB couplers and a phase shifter. Differential phase shift and attenuation are accomplished by applying different amounts of phase shift and attenuation to signals in each separate signal path.

No example of an actual application of the Chu method could be found in the literature. This is because at lower microwave frequencies - where almost all existing systems operate - a simplification of this technique is practical. Depolarization at lower frequencies is mainly due to differential phase shift [2.31]. If differential attenuation can be ignored, Williams [2.33] has shown that a suboptimal orthogonalization circuit can be realized with only two controllable parameters. This theory was used to fabricate a 4/6 GHz orthogonalization circuit from two polarizers (which act as a differential phase corrective network), three rotary joints and an orthomode transducer [2.33]. The circuit was electronically controlled via two motors. Actual operation on a satellite link [2.34] showed that this adaptive system was capable of maintaining a system XPD of better than 25 dB for rainrates as high as 130 mm/hr. Uncorrected, the link XPD was as low as 10 dB for the same maximum rainrate.

A similar simplfication of the Chu orthogonalization method may be practical near 35 GHz, where depolarization is almost entirely due to differential attenuation [2.26]. In this case, the suboptimal network would only require a rotatable differential attenuation. No examples of this type of XPD improvement could be found in the literature.

Evans and Thompson [2.35] were probably the first to publish a description of a cancellation network to improve XPD in a microwave system. The basic cancellation technique, which has been used in various applications, is accomplished by the vector subtraction of a suitably attenuated and phase-shifted sample of the undesired signal from the channel previously containing both the desired and undesired signals. In microwave cancellation networks, directional couplers are usually used to sample the undesired signal and to inject the cancellation signal vector. This technique can be applied at RF, IF and in some systems, even at baseband.

The advantages of cancellation over orthogonalization are that cancellation: is easier to implement, uses readily available components, is easier to adjust manually or electronically and can be implemented after amplification in systems where the coupler insertion loss would be objectionable [2.26]. Cancellation techniques can also be readily applied to single or dual-polarization systems.

Evans and Thompson [2.35] installed a single-channel cancellation network on an 11.6 GHz, 1.6 km experimental link at the University of Essex, England. The network was used to improve the clear weather system isolation from around 40 dB to 55-60 dB. No details of the circuit realization were given. Results were shown for an "artificial" precipitation event and the authors note that "the variation of the crosspolar signal for the cancelled link are consistent, whereas, for the uncancelled link, the addition of the system and atmospheric phasors yields a signal which fluctuates around the clear weather value." The published results also seem to show some drift in the clear-weather crosspolar signal levels, especially on the cancelled link.

Sobieski [2.36] has described a switched polarization experiment at 12 GHz over a 2 km link at the Universite Catholique de Leuvain, Belgium. The construction of this experiment was not complete when [2.36] was written, but the authors intended to incorporate a two-channel cancellation network to improve the XPD measurement range. An alternative circuit realization for use at IF frequencies was proposed. This cancellation network used four 3 dB hybrid junctions and four attenuators but no phase shifter.

Dilworth [2.26] has reported a single-channel adaptive cancellation network installed on the 11.6 GHz link at the University of Essex, England. The network included two 10 dB couplers, a PIN diode attenuator and a varactor phase-shifter, all fabricated in microstrip. This circuit increased the clear weather linear XPD from 40 dB to 60 dB, which was the system noise floor. Dilworth and Evans [2.37] have recently published results where this cancellation network was used adaptively to correct circular polarization on the same experimental link. A microcomputer was used to control the cancellation network by searching for the minimum crosspolar signal level. This system was able to maintain an XPD of better than 40 dB even during a rain-induced, 10 dB copolar fade.

O'Neill [2.38] has described a receiving system including a single channel cancellation network designed for propagation measurements using the European Orbital Test Satellite. This 11.7 GHz circuit used the standard configuration of two directional couplers, an attenuator and a phase shifter, to statically improve the clear weather XPD. The only results presented in this paper were those originally presented by Evans and Thompson [2.35].

Dintelmann [2.39] has published a description of a 12 GHz cancellation network in an Orbital Test Satellite propagation experiment underway at the Research Institute of the Deutsche Bundesport, Darmstadt, F.R.G. Single channel cancellation networks for linear and circular cancellation networks are described. In this experiment cancellation is used statically to improve the XPD measurement range.

Murphy, in this thesis, [2.40] has reported a single channel cancellation network in a fixed polarization 30 GHz propagation experiment on a 1.02 km link at University College, Cork, Ireland. This reference does not include any discussion of the construction, operation or performance of the cancellation network. The XPD results indicate that a clear weather average XPD of 52-56 dB was obtained. Some results seem to indicate that the crosspolar signal level drifted over a considerable range.

2.5.1.2 XPD Improvement in this Experiment

A single channel crosspolar cancellation network was chosen for XPD improvement in this experiment. Cancellation was selected instead of orthogonalization because rotatable differential attenuators and phase shifters with the necessary degree of control would have been exceedingly difficult to fabricate. Only one channel was equiped with a cancellation network because it was hoped that OMT port termination impedance and antenna and feed alignment could be used to improve the XPD level on the other channel. This would allow comparison to be made between the XPD response of cancelled and uncancelled systems. No information is lost by not cancelling both channels because the off diagonal elements in the dual-polarized transmission matrix are equal (See Chapter 4). In addition, if only one cancellation network was installed, it would be possible to significantly reduce the length of waveguide required to interconnect the directional couplers, attenuator and phase shifter. Short interconnections are desirable to increase the operating bandwidth, as discussed in Section 5.6.2.

2.5.1.3 RF vs. IF Cancellation

In all of the previously discussed experiments, where cancellation networks were actually installed in working systems, cancellation was performed at the propagating-signal frequency. Theoretically, cancellation could also be applied in the IF sections of a receiver which had two separate IF channels.

The advantages of IF cancellation are that:

- there would be no reduction in receiving system sensitivity.

- necessary components such as couplers, attenuators and phase shifters would be far less expensive at the lower frequency.
- flexible - coaxial rather than waveguide interconnections can be used, and
- the electrical length of interconnections in terms of the cancellation frequency would be much shorter, resulting in a larger operating bandwidth, as discussed in Section 5.6.2.

The only disadvantage of IF cancellation is that phase or gain drift in either channel of the receiving system preceding the cancellation network will translate directly to a cancellation network error [2.27]. An analysis of the cancellation error due to phase and gain errors or drifts is given in Section 5.6.1.

The advantages of IF cancellation prompted an investigation into the gain and phase stability of the receiving system front-end. Considerable operating experience with the front-end, both installed in the experimental system and on the bench, has shown that the gain stability was very good. Typical gain variations on the bench, after a warm up period, are one or two tenths of a dB for periods over an hour. Gain variations when the front-end is installed in the system are slightly larger, presumably due to scintillations (for short term variations) and temperature changes (for long term variations). The gain variations are negligible for propagation measurements and may even have been tolerable in an IF cancellation system.

However, it was discovered that the front-end had an unacceptable AM-PM conversion factor. A 0.1 dB change in the front-end gain induced by a small adjustment in the receiver LO output was found to result in an approximate 10 to 15 degree phase shift in that channel. This phase shift appeared to be due to the local oscillator frequency multipliers, but the harmonic mixers may also have been partially responsible. The phase shift is believed to be due to a change in the multiplier or mixer diode impedance resulting from the small amplitude variation. This is not entirely unexpected, however, because both devices are designed to operate under maximally non-linear conditions. From Section 5.1.6 it is obvious that this degree of AM-PM conversion would result in unacceptable crosspolar signal level drift in an IF cancelled system. For this reason it was decided to perform the crosspolar cancellation at 73 GHz.

2.5.1.4 Crosspolar Cancellation Circuit Description

The single-channel millimetre-wave crosspolar cancellation circuit was designed to provide the greatest possible degree of tunability and the largest obtainable operating bandwidth. These design constraints were imposed by the desire for maximum measurement range and the unavoidable frequency drift of the free running millimetre-wave source. A high degree of tunability is necessary to be able to adjust the circuit for almost total clear weather crosspolar signal cancellation. Large cancellation circuit bandwidth is desirable to reduce the changes in the clear-weather crosspolar-signal baseline due to source frequency drift and ambient temperature changes. Cancellation network tunability is determined by the adjustability of the attenuator and phase shifter. (The effects of small adjustment errors on crosspolar cancellation is discussed in Section 5.6.1). Bandwidth is limited by the total phase variation with frequency between the undersired-crosspolar and cancellation signals at the junction of the combining coupler.

The most significant source of this phase variation is the electrical length of the signal path between the sampling and combining directional coupler ports. (This is described in detail in Section 5.6.2).

The directional couplers incorporated in the crosspolar cancellation circuit were specified on the basis of the uncorrected clear weather crosspolar isolation. If the entire experimental system was aligned for best crosspolar isolation for only one polarization, the isolation for the other polarization was typically in the range between 25 and 30 dB. Using 25 dB as a worst case estimate and considering the insertion loss of the attenuator, phase shifter and the waveguide interconnections, resulted in the selection of 10 dB couplers for both the sampling and combining directional couplers. "Identical" couplers are used to equalize the vertical and horizontal insertion loss of the cancellation network. The couplers used are Microwave Associates MA-655. These couplers have an insertion loss of approximately 0.8 dB, which will result in a corresponding reduction in receiving system sensitivity.

Adjustability was the major criterion applied in the selection of the attenuator and phase shifter. Devices chosen were the Demornay Bonardi DBB-410 and DBB-910, respectively. These components are almost identical mechanically and incorporate micrometer drive tuning which will provide the maximum degree of adjustability. The attenuator is adjustable from 0 to 40 dB with a 0.5 dB insertion loss. The phase shifter is adjustable over a range greater than 360° and has a maximum insertion loss of 1.25 dB at 360° phase shift. The physical length between the waveguide flanges on each of these components is 14.6 cm.

The mechanical layout of the crosspolar cancellation network was designed to minimize the length of the waveguide connections between the circuit elements and thus maximize the bandwidth. This was accomplished by attaching the couplers directly to the front-end input ports and by mounting the attenuator and phase shifter as physically close to the couplers as possible.[1] The total physical length of the waveguide circuit between the two coupler junctions, including the length of the attenuator, phase shifter, coupler arms and interconnections, is approximately 93 cm.

Fig. 2.39 is a schematic of the crosspolar cancellation network.

2.5.2 Antenna Mounting and Rain Shields

Fig. 2.40 is a photograph of the transmitting antenna showing its rain shield and mounting method, the receiving antenna is identical. The antenna mounts are fabricated from heavy gauge mild steel and angle iron stock. The mounts are attached to the concrete railing around the building roof. The extreme rigidity of these mounts insures there will be no antenna deflection even during severe wind conditions.

---

1 The shortest possible coin-silver WR-15 waveguide interconnections were fabricated by filling the waveguide sections with a low melting temperature metal alloy before bending. Filling the waveguide with solid metal before bending significantly reduces the minimum practical bend radius and therefore the total length of the interconnection. The metal alloy is removed after bending by heating the waveguide section and then flushing it with very hot water.

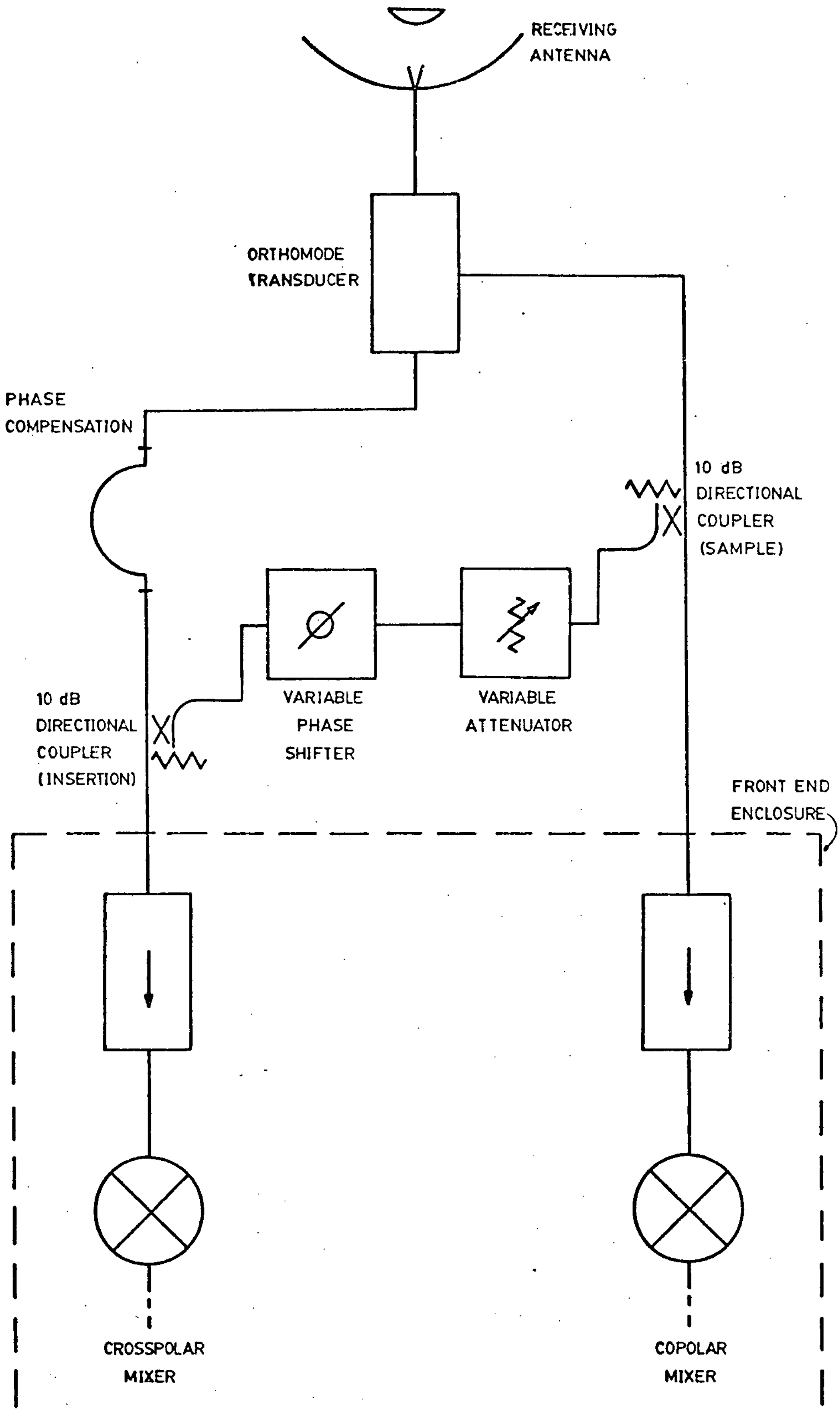

Fig. 2.39. Crosspolar cancellation network.

Fig. 2.40. Transmitting antenna photograph.

Fig. 2.42. Reflector photograph.

A poly-vinyl-chloride (PVC) rain shield covers the top half of each antenna to prevent rain accumulation on the antenna components. The mounting stress of the PVC shield is distributed by connecting it to an aluminum ring with numerous small fasteners. PVC was chosen for its toughness and durability. With this mounting method, these shields have survived several large wind storms without damage. The shields did not cause any measurable change in the antenna gain or introduce any observable pointing error.

It is important not to allow rain to accumulate on the antenna reflector, subreflector or feedhorn to prevent a reduction in crosspolar isolation. Several experimentors have reported crosspolar isolation reduction due to rain accumulation [2.41], [2.42], [1.80], [1.85].

2.5.3 Antenna Alignment

The antennas are first aligned for maximum copolar signal level and then for minimum crosspolar signal level. After a coarse alignment of both antennas and the reflector, the copolar signal was maximized by iteratively adjusting the antenna azimuth and elevation. The polarization angle of the antennas is most easily adjusted by loosening the set screws in the collar which secures the feedhorn and then rotating the entire feedhorn and orthomode transducer assembly. The transmitted polarizations were first adjusted to be exactly vertical and horizontal by using a small bubble level. Then the receiving antenna feed assembly was rotated to the angle which gave the minimum crosspolar signal level.

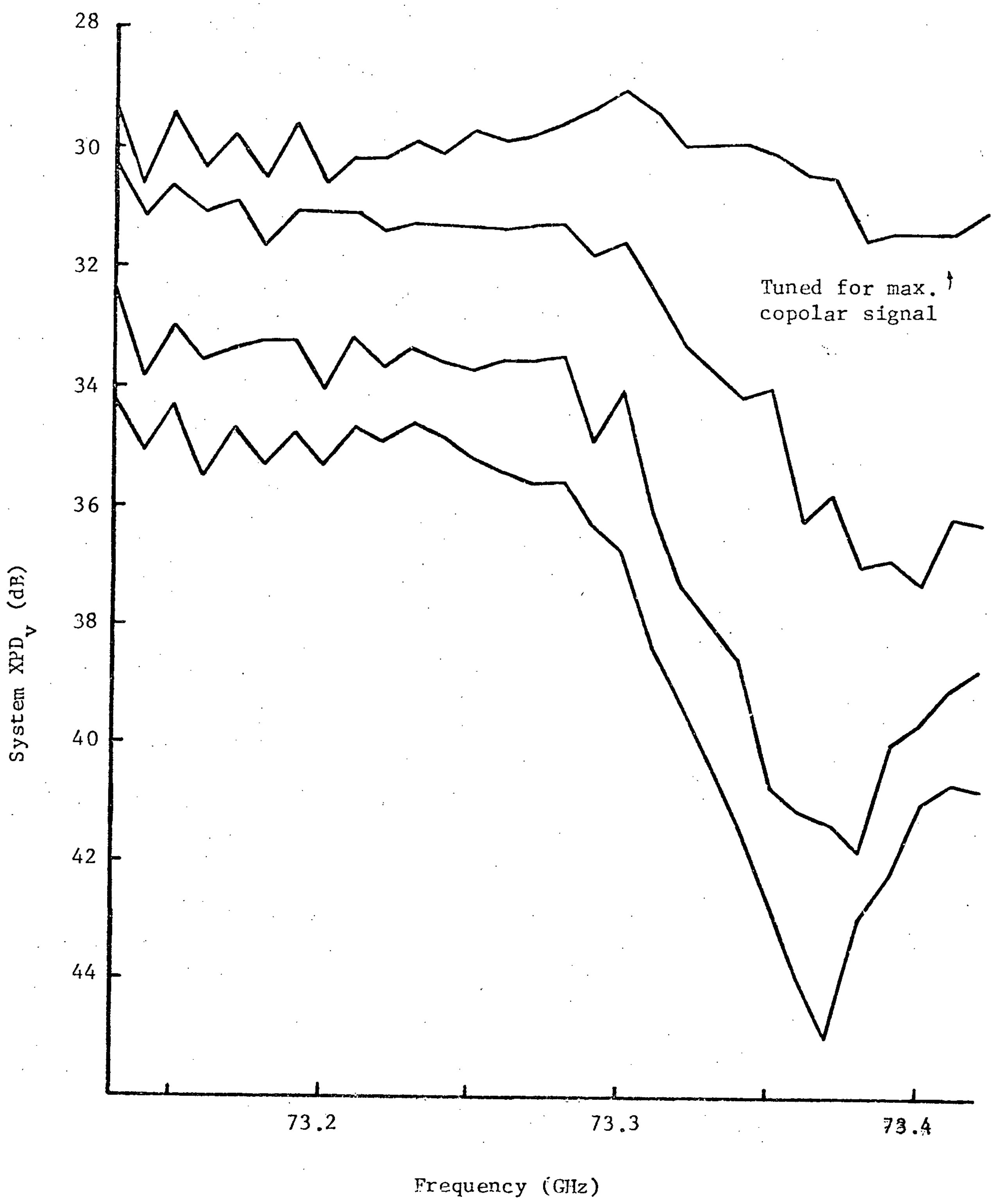

Fig. 2.41. System XPD for different antenna alignments.

At this point, the antenna azimuth and elevations were readjusted. The purpose of this second adjustment was to ensure that the antennas were pointed with the crosspolar null aligned exactly with the reflector. The maximum gain of the copolar lobe nominally corresponds to the null in the crosspolar lobe and crosspolar levels typically increase at pointing angles deviating from this null [2.43], [2.44], [1.80]. It is not unusual however, for the pointing angle corresponding to the crosspolar null to be slightly different from the pointing angle for maximum copolar gain [2.45]. [2.46], [2.47], [2.48]. In this case, the most desirable alignment is for minimum crosspolar level. Fig. 2.33 shows that the best isolation does occur for angles slightly off axis for the antennas used in this experiment. To determine the precise antenna alignment for best system XPD, it is necessary to examine the XPD through a range of frequencies. The theoretical explanation for the reason why it is not sufficient to examine system XPD at one frequency is given in Chapter 5. Fig. 2.41 shows the system XPD's measured for three slightly different transmit-antenna azimuth adjustments. The final antenna alignment involved a tradeoff between copolar and crosspolar signal levels to yield the maximum system XPD.

2.6 Reflector

The one metre square, flat reflector used as the radar path target is shown in Fig. 2.42. It is constructed from a sheet of 9.5 mm thick plate glass supported by an angle-iron frame. A coating of "Scotchtint", a plastic loaded with metallic particles, was used to make the surface reflective [2.1]. A PVC rain shield with an aluminum frame was installed on the reflector to prevent water accumulation which may cause depolarization (as discussed in Section 2.5.2).

The calculated 3 dB beamwidth of the reflector radiation pattern is approximately 0.21° [2.50]. This angular displacement corresponds to an approximate deflection of only 3.7 mm at the top of the reflector. To prevent wind deflection of the reflector, two stabilizing struts were installed on the upper reflector corners. These tubular struts are adjustable to allow proper strut tensioning after reflector alignment.

A test was performed to verify that the received signal levels were from the reflector and not due to reflections from the building on which the reflector was mounted or antenna coupling. This was accomplished by comparing received signal levels for the reflector aligned and misaligned. The copolar levels were 34-38 dB lower for various misaligned reflector positions. Cross-polar levels were observed to be at least 30 dB lower for reflector misalignment. A more accurate measurement could not be made for the crosspolar levels because of limitations imposed by the receiver sensitivity. Some of the measured signal when the reflector was misaligned may have been from a minor lobe on the reflector radiation pattern. This is likely because the reflector mount only allowed reflector misalignments of a few degrees. This was not investigated further because the minimum 30 dB change in level was sufficient to ensure accurate results even during deep fades.

2.7 Transmission Loss

After the antennas and reflectors were aligned, a comparison was made between the calculated and measured transmission loss between the transmitting and receiving antenna ports. This was done to verify the antenna and reflector alignments and to be sure that there were no significant antenna-feedline mismatches.

A prerequisite for the calculation of the transmission loss is the verification of operation in the far field of the antennas and reflector. The boundary between the near field region and the far field region for a radiating aperture is commonly estimated to occur at a distance $R = \frac{2D^2}{\lambda}$ where D = aperture diameter or square side-dimension [2.49]. At the operating frequency, the far field of the antennas begins at a distance of approximately 180 m and the far field of the reflector begins at about 500 m.

When considering the antenna and reflector together it is not necessary to have them separated by the sum of their near field distances. Instead, to ensure the two aperture systems can be described by far field approximations. Jasik [2.50] suggests the approximation:

$$d > \frac{0.9}{\lambda} \sqrt{A_1^{\,2} + 6A_1 \cdot A_2 + A_2^{\,2}} \tag{2.19}$$

where Ai = aperture area.

For one antenna ($A_1 = 0.292\ m^2$) and the reflector ($A_2 = 1\ m^2$) the required separation is d = 370 meters. Therefore, far field approximations can safely be used for this system.

The angle between the normal to the reflector and either of the antennas is only 0.651°. For this angle, the projected area of the reflector along the antenna axis is insignificantly smaller than the reflector physical area. Therefore the antenna will be assumed to occupy the same location perpendicular to the reflector.

The two way path loss or "basic transmission loss" [2.51] at 73.5 GHz is given by:

$$L_{\substack{PATH\\TWO\\WAY}} = 10 \log_{10}\left[\frac{4\pi(2r)}{\lambda}\right]^2 \tag{2.20}$$

The entire reflector surface is well within the first Fresnel zone at this distance because the variation in path length from the center of the reflector to one of its corners is approximately one sixteenth of a wavelength [2.52]. Therefore, the reflector gain can be calculated from [2.50]:

$$G_{REF} = 10 \log_{10} \left[\frac{2\ A_{REF}}{\lambda r}\right]^2 \tag{2.21}$$

$$= -5.1 \text{ dB}$$

The atmospheric loss due to molecular absorption is nominally 0.3 dB/km at this frequency (see Fig. 1.2 and [2.53]) or about 0.5 dB for the total path, but this value will depend on the atomospheric water vapour content, which is quite variable.

The specified antenna port VSWR are less than 1.12. This produces a transmission loss of 0.014 dB which is neglible.

Thus the total transmission loss is:

$$L_{TOT} = L_{\substack{PATH\\TWO\\WAY}} - G_{RX} - G_{TX} - G_{REF} + L_{ATMOS} \tag{2.22}$$

$$= 134.7 - 50.6 - 50.9 - (-5.1) + 0.5$$

$$= 38.8 \text{ dB}$$

The transmission loss was measured by connecting a calibrated attenuator between the model 13-50A mixer and the feedline port normally connected to the transmitting antenna. This is possible because this mixer was connected to the receiver via a long flexible coaxial cable. This method has the advantage that the loss and mismatch in the transmitting antenna feedline and mixer coaxial cable are automatically included in the measurement.

When 43 dB of attenuation was inserted, the receiver indicated the same signal level as when this mixer was connected directly to the receiving antenna. There is an estimated ± 2 dB uncertainty in this measurement due to attenuator accuracy and possible impedance mismatch.

The calculated transmission loss is 4.2 dB less than the measured value. Experimental uncertainty cannot account for the total difference. The extra loss is probably due to a combination of reflector imperfections, reflector misalignment, waveguide flange mismatch, mixer mismatch, error in the specified antenna gains, and uncertainty in the atmospheric water vapour content.

2.8 Fade Margin

Using the measured path loss and a usable receiver sensitivity of – -100 dBm, the copolar signal fade margin is approximately 65 dB. This can be extended to approximately 70 dB if averaging times of ten seconds or over are used during data analysis. It is more difficult to estimate a crosspolar measurement fade margin because of the uncertainty in the crosspolar baseline and because the crosspolar level increases with respect to the copolar level during deep fades. If a crosspolar baseline 40 dB below the copolar baseline is assumed and depolarization is ignored (i.e. worst case) there would still be at least a 25 dB fade margin.

2.9 Data acqusition system

In this experiment a minicomputer based data acqusition system samples, preprocesses and records the experimental data. This system is an extension of the one described in [2.1]. The original data acqusition system ran on the department's NOVA 840 minicomputer under the RDOS disk operating system. The software for this system was modified to be able to operate using the core resident RTOS (Real Time Operating System). Using RTOS, the data acquisition system can be operated on either the NOVA 840 or a smaller, more available, SUPERNOVA system. After preprocessing, the data is recorded on one half inch, 9-track magnetic tape. Data analysis is then performed on the main university computing facilities.

The following data is recorded from peripheral instruments in digital form once per second:

- channel A and B received signal levels
- local oscillator frequency

- real time

A sixteen channel A/D converter is used to sample the following parameters once per second:

- three wind velocity vectors
- temperature
- polarization state
- mixer diode voltages
- klystron power output

The status of the five raingauges are sampled 16 times per second.

Hardware and software provisions also exist to record sixteen drop size categories once per second.

3. METEOROLOGICAL INSTRUMENTATION

3.1 Raingauge Network

3.1.1 Path - Rainrate Measurement

To be able to make accurate comparisons between observed propagation phenomena and meteorological conditions it is imperative that the path rainrate be sampled with sufficient spatial and temporal resolution. In two reviews by Crane [3.1], [3.2] he concludes that the lack of agreement between measured propagation and meteorological conditions was, up to that time, primarily due to inadequate rainfall observations. Fedi [3.3] and Fedi and Mandarini [3.4] have analyzed the errors due to raingauge spacing and integration time for a similar experiment. Watson [3.5], Hogg [3.6], Barsis and Samson [3.7], and Bodtmann and Ruthroff [3.8] have also discussed the importance of raingauge spacing and integration time in propagation experiments.

High spatial and temporal resolution is required for path rainrate measurements because rainfall is not uniform, but instead, occurs in "cells" of finite horizontal extent. Rain cells vary in extent from a few kilometers up to approximately twenty kilometres. Within a rain cell, rainrates may only be uniform over distances of a few hundreds of metres. Rain cells can also change morphologically over periods of a few seconds and travel horizontally at speeds approaching the wind velocity. Fig. 3.1 from [3.6], gives two examples of rain cell structure and temporal change. Small rain cells and rapidly changing point rainfall rates are characteristic of heavy rainfall or thundershower activity. Medium and light rainfall is typically much more

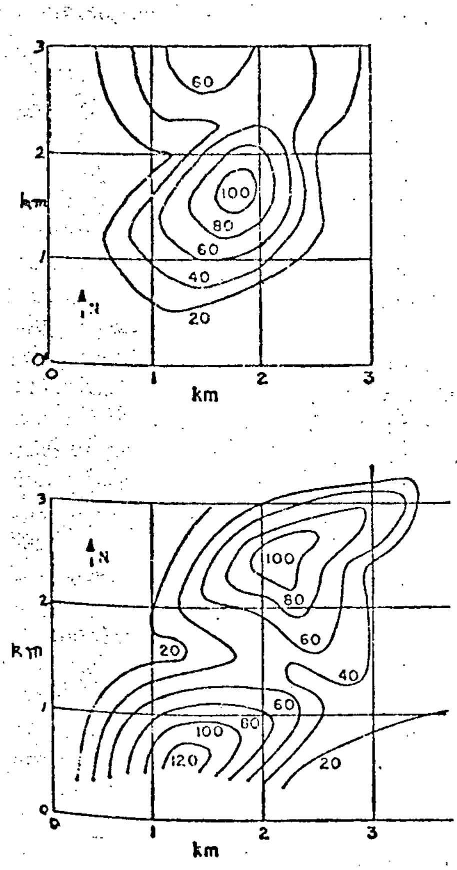

(Top) Plot of rainfall-rate contours (in millimeters per hour), showing two rain cells on the Bedfordshire rain-gauge network; (bottom) contours 2 minutes later.

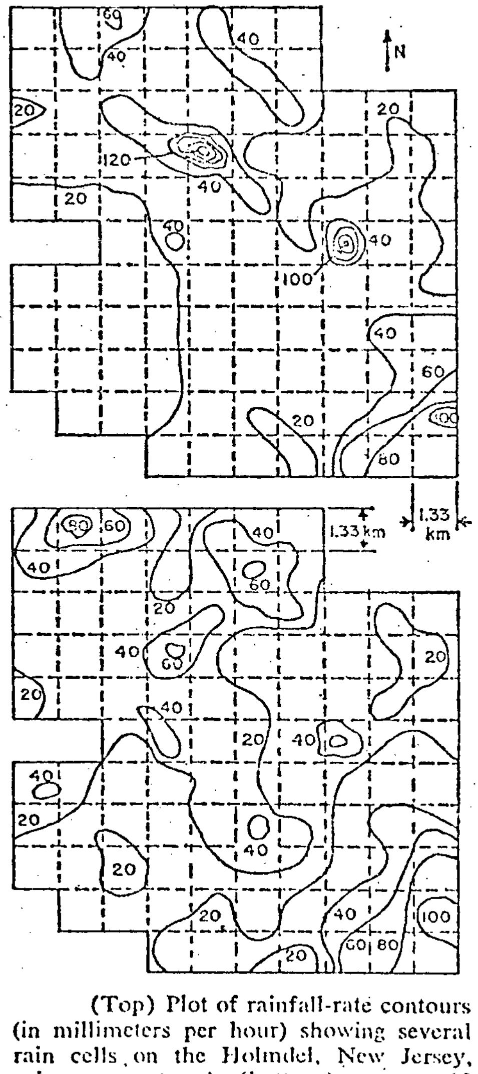

(Top) Plot of rainfall-rate contours (in millimeters per hour) showing several rain cells on the Holmdel, New Jersey, rain-gauge network; (bottom) contours 10 seconds later.

Fig. 3.1. Rain cell examples, from [3.6].

uniform horizontally and changes much more slowly. Further data on rain cells is available in [3.9].

To be able to characterize the rainrate along a path with reasonable accuracy it is necessary to have rainguage spacings of a few hundred metres and integration times of a few tens of seconds. Crane [3.1] suggests spacings of "several hundred metres". Fedi and Mandarini [3.4] have estimated the spread of attenuation values which they expected for a propagation experiment at 30 GHz using raingauges with a 730 sq.cm. collecting area spaced at 100 m and 1 km and with integration times of 10 sec and 60 sec. Their results are shown in Fig. 3.2.

3.1.2 Rain Gauge Types

The two basic types of non-disdrometer rain gauges which have been used in propagation experiments are the tipping-bucket and capacitive. A tipping-bucket rain gauge collects water in a funnel and directs it to a small two chambered bucket. When a quantity of water equal to the gauge "tip-size" has accumulated the weight of the water causes the bucket to tip and empty, allowing the second chamber to start filling. An electrical signal is generated as the bucket tips. A capacitive rain gauge works by directing the water from a collecting funnel between two parallel plates which form the electrodes of a capacitor. The resulting change in capacitance is usually monitored as a shift in the frequency of an oscillator circuit incorporating the capacitor.

Capacitive rain gauges have been used by several investigators at Bell Laboratories [3.10], [3.11], [3.12] and by Fedi and his coworkers [3.13],

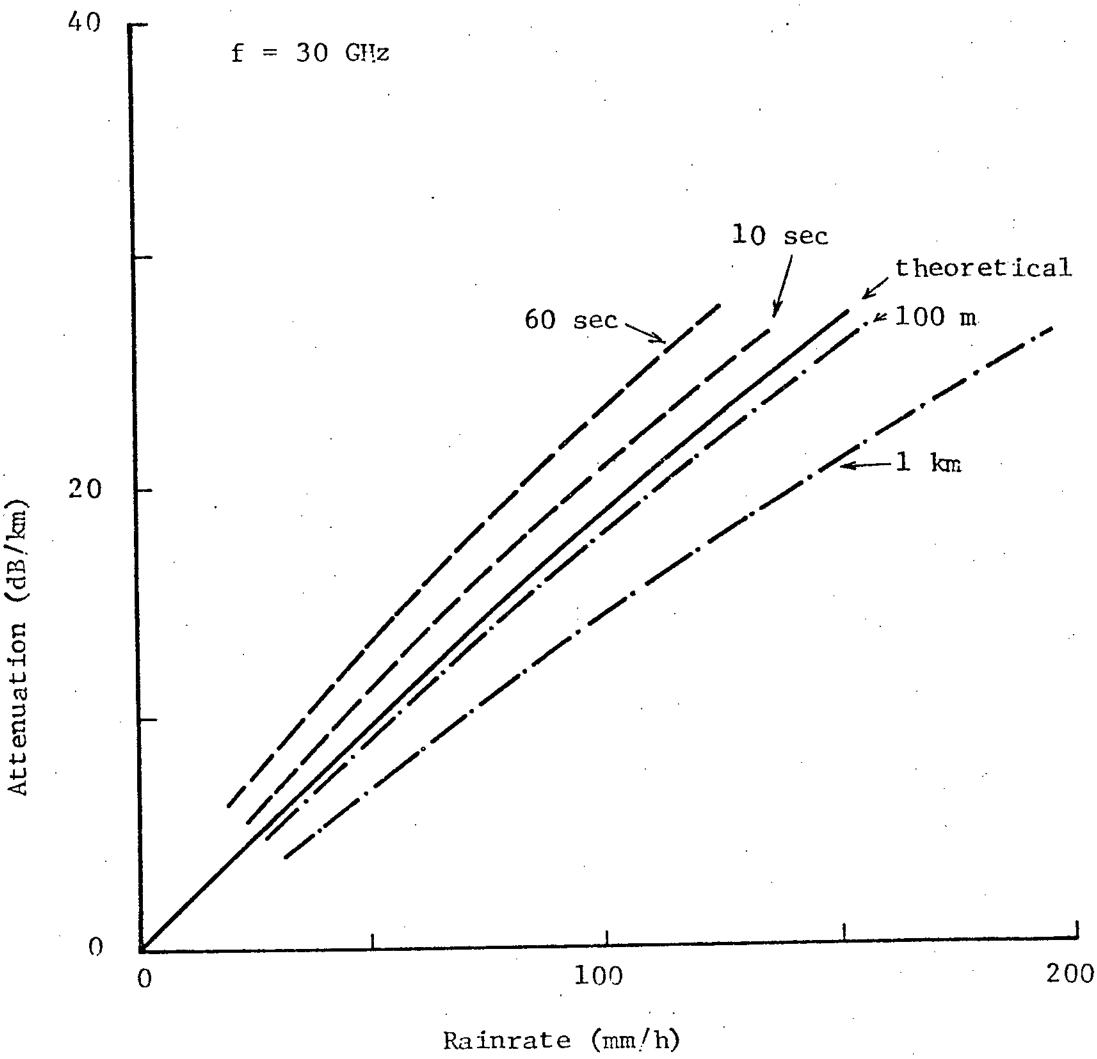

Fig. 3.2. Attenuation spread for different raingauge spacing and integration times.

[3.3]. The basic advantage of these rain gauges is their quasi-instantaneous response and their ability to measure extremely high rain rates. Fedi and Merlo [3.13] have shown the superior response of capacitance gauges compared to tipping-bucket rain gauges for rainrates between 100 and 400 mm/hr. The disadvantages of the capacitive type gauges are their periodic maintenance requirements [3.10] and inability to measure low rainrates. Freeny and Gabbe [3.11] report satisfactory readings only above 10 mm/hr. Fedi [3.3] using a slightly improved version, has obtained results down to 5 mm/hr with only small reductions in accuracy. Capacitive rain gauges were tried in an earlier study at UBC but were abandoned because of their poor performance at low rain rates [2.1].

The tipping-bucket rain gauge is "simple, reliable and requires a minimum of maintenance" [3.3] but has the disadvantage of averaging the rainrate over the period between tips. Tipping-bucket gauges have been used in propagation experiments by Goldhirsh [3.14], Blevis, Dohoo and McCormick [3.15], Fedi [3.3], Skerjanec and Samson [3.16] and Ippolito [3.17]. The tip size of the gauges used in these experiments were: 0.25 mm [3.15], [3.16], [3.17] and 0.2 mm [3.3]. This results in an integration time at 50 mm/hr of 18 and 14.4 seconds respectively. These periods are compatible with the limits described in Section 3.1.1, but unfortunately lower rainrates have correspondingly longer integration times.

Fedi [3.3] has analyzed the expected error of capacitive and tipping-bucket raingauges at various rainrates. The analysis showed that the gauges he used had very similar accuracies for higher rainrates and that the tipping bucket gauges were more accurate for lower rainrates. Segal [3.9] also includes a discussion of raingauge accuracy. Fig. 3.3 from [3.9] shows the effect of horizontal windspeed on gauge catch efficiency. The reduction in collection efficiency is due to wind turbulence around the gauge carrying drops away from the collecting aperture.

3.1.3 Rain Gauges

The previous considerations in conjunction with the extremely low probability of intense rainfall in Vancouver (see Fig. 3.4 from [3.9]) led to the selection of tipping bucket rain gauges for this experiment. To reduce the problems of integration-time averaging, rain gauges with a very small tip size (0.05 mm of rain) were constructed. The first version of these 920 cm^2 collecting area rain gauges is described in [2.1]. These rain gauges had a tip size which was adjustable to a minimum of 0.05 mm. However, at this tip size these gauges suffered some inaccuracy due to water retention in the bucket. This problem was alleviated by incorporating a new bucket geometry and by the inclusion of several small ball bearings in a cavity in the lower portion of the bucket. These ball bearings roll from one end of the bucket to the other as the bucket tips. This results in a rapid and forceful tip, greatly reducing the water retained in the bucket. This extremely small tip size results in an integration time of only 3.6 seconds at 50 mm/hr. and acceptable integration times down to a few mm/hr. (It is not possible to put an exact lower limit on the acceptable integration time because at low rain-rates the rate-of-change of point rainrate is also greatly reduced.)

A small permanent magnet attached to the bucket opens and closes a glass encapsulated reed switch as the bucket tips. The circuit which

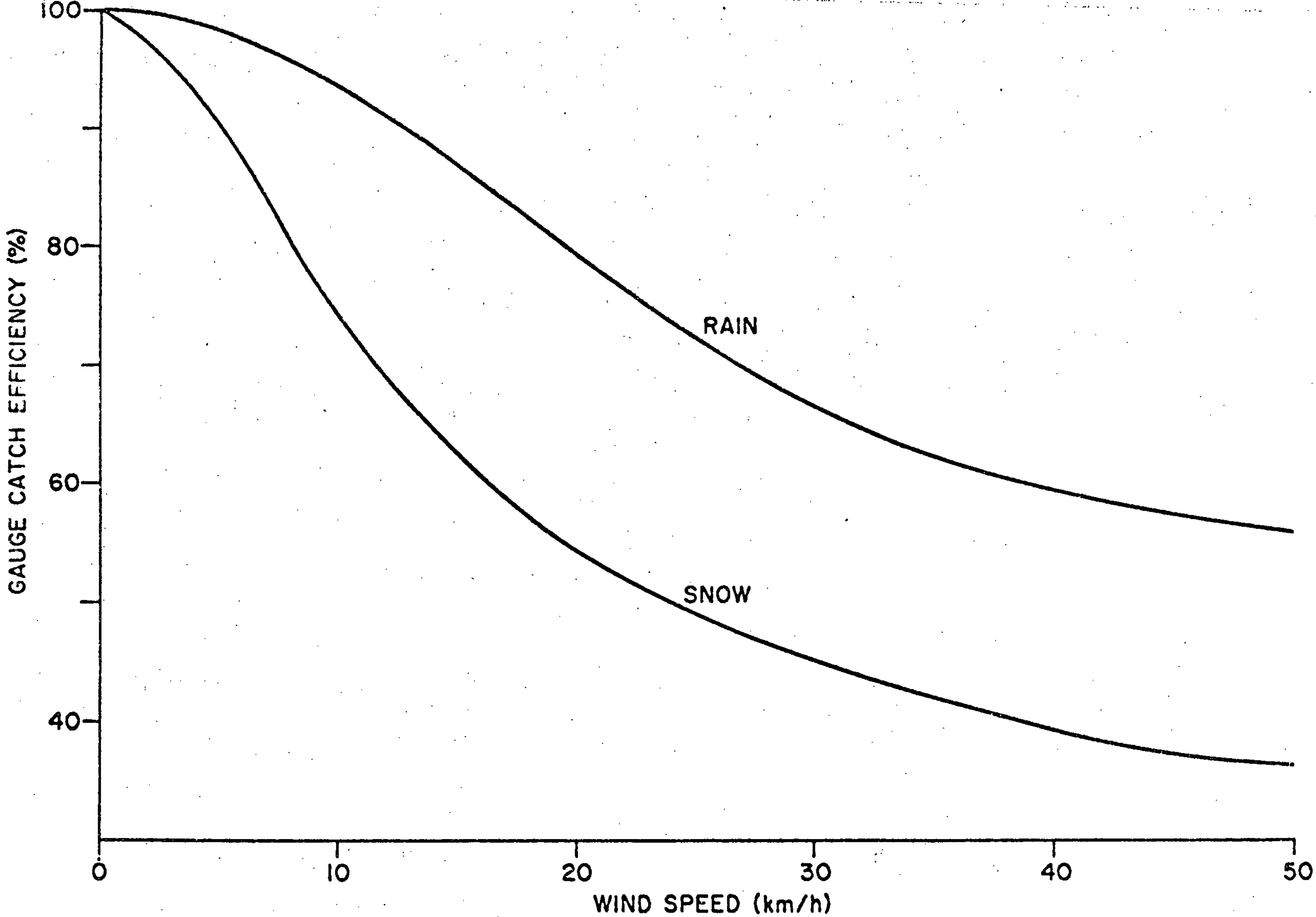

Fig. 3.3. Precipitation gauge catch efficiency as a function of horizontal windspeed, from [3.9.]

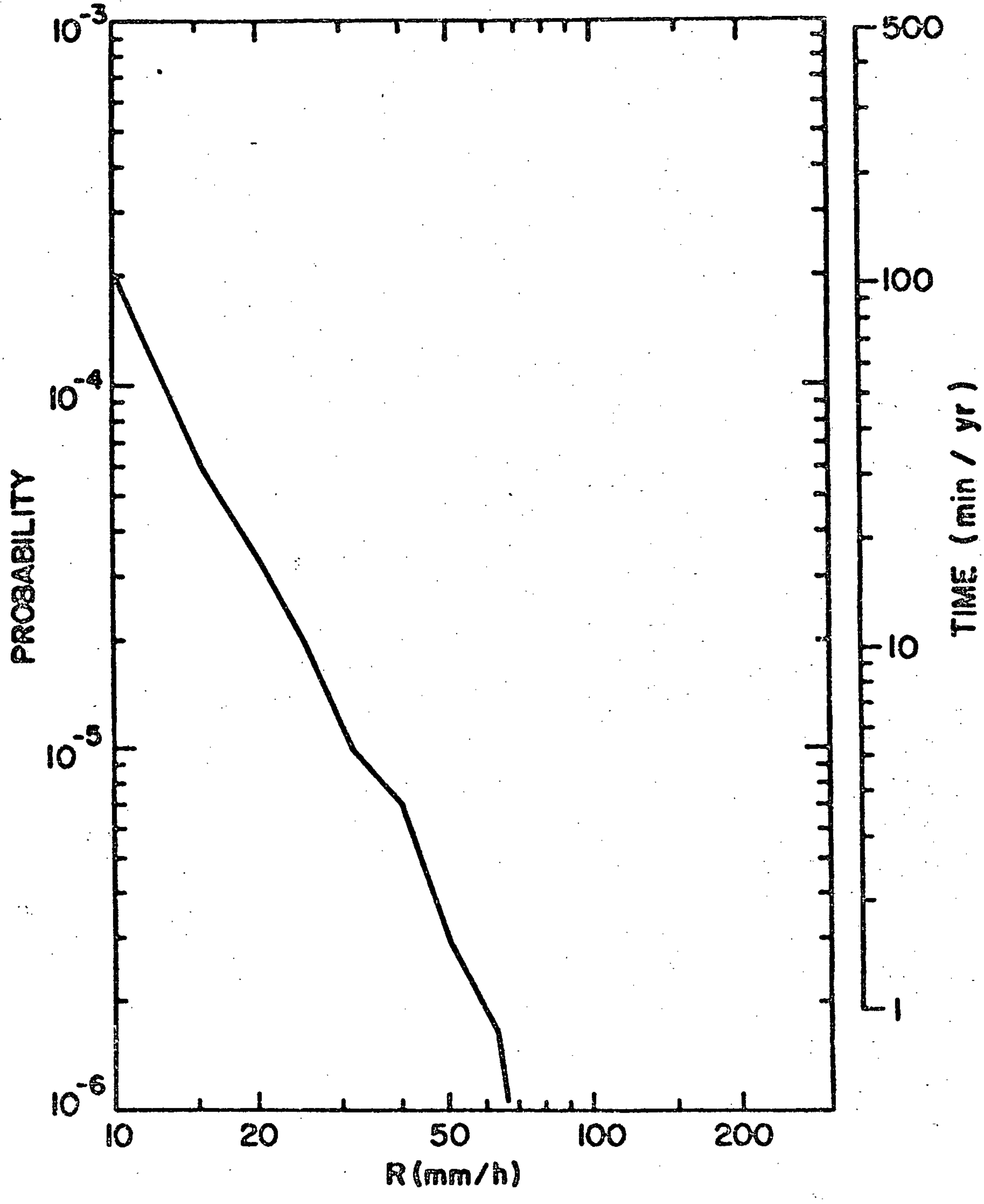

Fig. 3.4. Probability of exceeding a specified rainrate in Vancouver, from [3.9.]

interfaces the rain gauges to the data acquisition system is described in [2.1].

The accuracy of the rain gauges is determined by the tip size accuracy and the tip interval sampling period. The average tip size accuracy - measured by allowing a large, known volume of water to pass through the gauge and recording the number of tips - is better than ± 1% for all gauges. Sampling of the rain gauge tip interval is done sixteen times a second by the data acquisition system. At low rain rates the total measurement error is almost entirely due to the tip size accuracy. At higher rain rates the sampling interval is the larger source of error. At 50 mm/hr rainrate the total error is below ± 2.7%. A photograph of one rain gauge with its cover removed is included as Fig. 3.5.

3.1.4 Raingauge Locations

Rainrate in this experiment is measured by a network of five rain gauges spaced along the propagation path. These rain gauges are located on building rooftops at the locations shown in Fig. 2.31. This spacing (approximately 220 metres) should give adequate spatial resolution for virtually all rainstorms in this climatic region. The rain gauge signals are transmitted to the data acquisition system on dedicated half-duplex telephone lines.

3.2 Raindrop Size Measurement

To be able to accurately correlate observed 73 GHz attenuation and meteorological conditions, the rain drop size distribution must also be measured. Most propagation studies have compared attenuation observations to

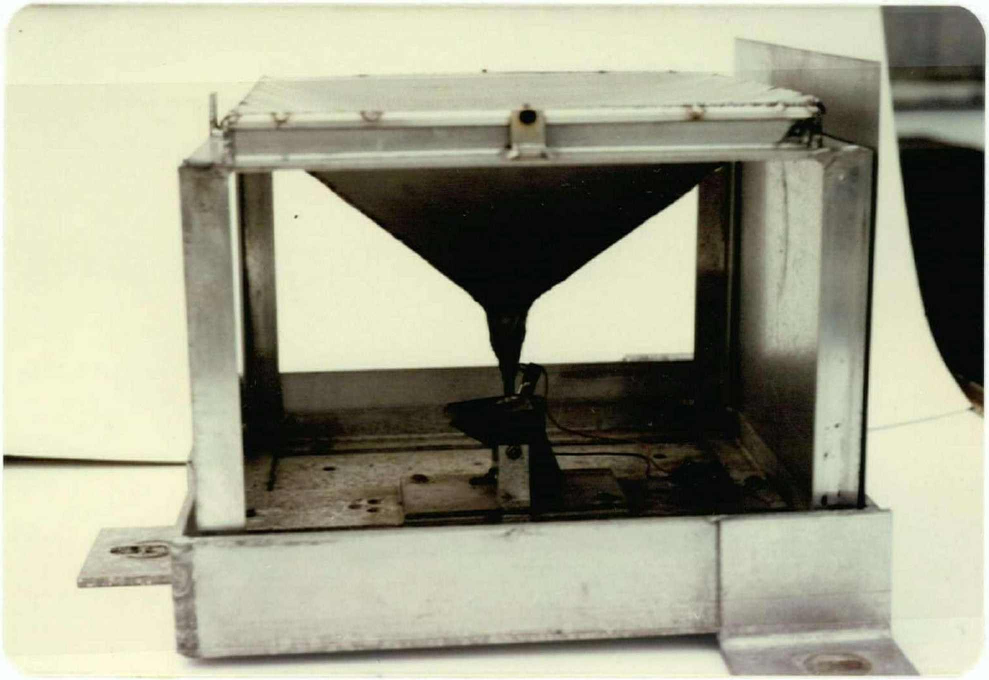

Fig. 3.5. Raingauge with cover removed.

calculated values based on the "standard" rain-drop size distributions referred to as the Laws and Parsons, Marshall and Palmer and Joss et al distributions. These distributions seem to provide reasonable agreement for most observations on an average basis, especially at the lower frequencies. However, some experimenters have made attenuation observations, especially in the millimetre frequency range, which do not appear to fall within the limits calculated from these distributions [3.18], [3.19], [3.20], [3.4].

Some of the discrepancies between measured and calculated attenuation are undoubtably due to the natural, wide variation in rain drop size distribution. Crane [3.2], Keizer et al. [3.21], Goldhirsh [3.22], Watson [3.5], Emery and Zavody [3.23] and others have commented on the large variability of drop size distributions.

Simultaneous measurement of the drop size distribution, especially including the smaller drops, is far more important in the upper millimetre range than at the lower millimetre and microwave frequencies. For shorter wavelengths, the effect of the smaller drops is more important because of the increased diameter-to-wavelength ratio. In the lower millimetre range, near 35 GHz, the drop size distribution has only a small effect on the attenuation [3.24], [3.25], [3.4]. However, in the range between 50 and 100 GHz the sensitivity of attenuation to drop size distribution is very high [3.21], [3.24], [3.2], [1.58], [1.85]. For these reasons, the measurement of drop size distribution has been given careful consideration in the design of this experiment.

3.3 Raindrop size transducer methods

The three basic transducer mechanisms considered for real-time measurement of raindrop sizes were: optical, electromechanical and electrostatic. A careful search of the literature uncovered references to two modern electromechanical methods, a wide variety of optical schemes and two english language references to electrostatic methods. No comprehensive comparison of the different methods has been published. A review of the disdrometer transducer methods is included here to show why the electrostatic method was chosen for further investigation.

3.3.1 Optical Methods

Optical methods rely on either: scanning, arrays of sensors, laser scintillation correlation, beam extinction or scattering. Optical methods, with the exception of the laser correlation method, have the advantage that the drop size is measured directly, without relying on simultaneous knowledge or assumptions about the drop velocity or direction of travel. However, the scanning and array methods may require correction for drop geometry and orientation (i.e. canting angle). An additional advantage of the optical methods, with the exception of the laser method, is that wind will not degrade the operation of the transducer. All optical methods suffer some operating problems due to the large variations in ambient light level. The scanning, array and laser methods also have high electronic hardware overheads associated with signal processing.

3.3.1.1 Optical Scanning Methods

Optical scanning methods would utilize either television-type cameras or flying-spot scanners. Conventional television cameras were considered not suitable because scanning rates were not adequate to record a drop falling at its terminal velocity. Even if an imaging tube could be scanned fast enough (even in one dimension), the hardware requirements for ultra-high speed, real-time digitization and image processing would be prohibitive for this experiment. Flying-spot scanner type equipment could probably be constructed with adequate scan rates but the practical problems associated with high levels of ambient light seem to preclude their use. No examples of disdrometers using either of these approaches were found in the literature.

3.3.1.2 Optical Array Methods

Methods using arrays of photodetectors are the most promising of the feasible optical methods. The basic operation depends on the drop partially occluding the light from a source which would normally have fallen unobstructed on the elements of a photodetector array. The difficulty with this method is fabricating the array of detectors. To have the required resolution, the effective spacing between array elements would need to be less than the minimum measurable drop diameter (i.e. preferrably less than 250 microns). This precludes the possibility of an array fabricated from discrete photodetectors unless a lens or fibre optic system was also incorporated. A preliminary investigation showed the lens system would be quite large and probably require special fabrication. The disadvantages of the fibre optic system are the difficulty of construction for large arrays and large individual fibre beamwidths.

Excellent monolithic photodetector arrays with good resolution are available. The major problem is that the linear size of the arrays is limited. This will mean that the collecting area using a single array will usually be too small to obtain a statistically valid sample of the raindrop distribution [3.26]. The arrays cannot be linearly concatenated to form a larger array because of the integrated circuit packages used. Conceivably, several arrays could be staggered to form a larger array, but this would only be acceptable if the drops fell vertically. It is however, probably still feasible to use a large number of arrays in reasonably close proximity and combine their measured raindrop histograms to improve the reliability of the statistical sample.

A small integrated optical array has been used by Cunningham [3.27] to make measurements on a variety of hydrometeors. The problem of the small sample size was alleviated in this case by orienting the array vertically, and affixing it to the exterior of a jet aircraft, thus considerably increasing the number of drops sampled per unit time.

Knollenberg [3.28] has constructed an optical array for hydrometeor size measurement using optical fibers and discrete photodetectors. In this method, one end of each optical fiber is placed in a linear array and the other end is connected to a photomultiplier tube. There are obvious problems associated with the fabrication of large arrays using this method, even if smaller photodetectors could be employed. This type of array was used for sampling from aircraft where the small linear array extent is not a disadvantage.

3.3.1.3 Laser Scintillation Correlation Method

Raindrop size measuring apparatus employing an expanded laser source and vertically separated sensors has recently been developed by Wang et al [3.29] [3.30]. This technique has the unique property of measuring the average raindrop size distribution over a path of up to 200 meters in length. A medium power cw laser is optically expanded to a 20 cm beam diameter and oriented horizontally along the path. The receiver consists of two horizontal linear photodetectors separated vertically by a few centimetres. The scintillation in the outputs of the two sensors, due to the passage of drops through the beam, are correlated in an analog circuit. The correlator output for different correlation delays is then proportional to the number of drops which travelled the vertical distance between the sensors in the correlation delay time.

Unfortunately this technique relies on the assumption of a time-invariant monotonic relationship between drop-size and vertical velocity. As a result, changes in drop vertical velocity due either to vertical wind velocities or turbulence will produce a distorted raindrop size histogram. The error in calculated drop size due to a change in drop vertical velocity can be determined from the known drop size terminal velocity relationships [3.31]. As an example a 1 m/s updraft would produce an approximate error in diameter of 23% for a 3 mm drop and 40% for a 5 mm drop.

Vertical wind velocities will also produce vertically correlated optical scintillation which will result in a correlator noise output. The other disadvantage of this method is the high cost of the laser source and expander.

3.3.1.4 Optical Scattering and Extinction Methods

One of the first real-time raindrop measurement systems was a photoelectric raindrop spectrometer constructed by Mason and Ramanadham [3.32]. This disdrometer measured the light scattered by a drop as it fell near an intense source. The scattered light at an angle of 20 degrees off-axis was collected in a telescope-type lens system and directed to a photomultiplier tube. The drops were then electronically sorted into eight size categories. Dingle and Shulte [3.33] constructed a disdrometer similar to the one described by Mason and Ramanadham. In this reference the theory for an optimum scattering type instrument is presented. The instrument was calibrated with drops from 0.72 mm to 3.13 mm in diameter. The resulting calibration curve shows that the output pulse height is proportional to the drop diameter squared.

Very recently, Klaus [3.34] has reported a similar photoelectric disdrometer. In this case the degree of extinction of a beam is used to determine the drop size. This system uses solid-state diode sources and detectors and a microprocessor to sort the drops into eight categories.

A serious limitation of both these analog optical systems is the change in the small-signal sensitivity of the photodetectors with changes in ambient light level. This is particularly troublesome during periods of rain when the ambient light level can be quite variable [3.31]. This type of system could conceivably be improved by using narrow bandwidth optical filters and higher intensity light sources. Dingle and Shulte [3.33] have also designed a "light shield" which improved the operation of their scattered light disdrometer to some extent.

3.3.2 Electromechanical Methods

The disdrometers most commonly used in propagation studies are the electromechanical types which convert the impact from a drop as it falls on the sensor to an electronic signal. The mechanical to electric energy conversion is accomplished using either a moving coil in a static magnetic field, piezoelectic transducers or a conventional audio microphone.

3.3.2.1 Moving Coil in Magnetic Field Method

The disdrometer using a moving coil in a magnetic field was described by Joss and Waldvogel [3.35], Georgii and Jung [3.36], and Rowland [3.37]. It has been used in studies by Waldvogel [3.38], Joss, Thams and Waldvogel [3.39], Brewer and Kreuels [3.40] and Keizer, Snieder, and Haan [3.41].

The construction of the coil-magnet transducer is very similar to a conventional acoustic loudspeaker. A collecting surface, usually 50 cm^2, is connected to the moving coil. The collecting surface is designed to have a low mass for maximum signal output. The coil is situated in the air gap of a permanent magnet. The momentum of the drop causes a displacement of the coil thus producing an electric signal at the coil terminals.

In some models, a second coil-magnet assembly is also included. In this case, the coil is energized with an amplified, filtered form of the signal from the first coil. This produces negative feedback which can then be used to modify the sensor response time.

3.3.2.2 Piezoelectric Method

The piezoelectric disdrometer was probably first described by Flach [3.42]. It was subsequently adapted and expanded upon by Rowland [3.37]. The Flach type piezoelectric disdrometer uses a solid acrylic clyinder with a beveled top. The cylinder and a piezoelectric transducer are then bonded to a brass block. The impact of the drop on the top of the cylinder causes an acoustic wave to travel through the cylinder to the transducer. Rowland instead cast the transducer in a solid block of epoxy and thus eliminated the brass block. The piezoelectric disdrometer has been used by Goldhirsh [3.22], [3.43] and Rowland, Bennett and Miller [3.44].

3.3.2.3 Other electromechanical Disdrometers

Other electromechanical disdrometers have been constructed using conventional audio microphones. Kinnell [3.45] used a dynamic microphone, Katz [3.46] a condenser microphone and Cunningham [3.47] a carbon microphone. These instruments couple the displacement of a larger membrane to the microphone using air or a fluid. None of these instruments were satisfactory but they did lead to the design of the other electromechanical transducers described previously.

3.3.2.4 Factors Affecting the Accuracy of Electromechanical Methods

Rowland [3.37] has compared the two basic types of electromechanical disdrometer transducers. The coil-magnet transducer gave an output peak voltage proportional to $D^{3.7}$ and the piezoelectric proportional to $D^{3.5}$. The range of measurable drop sizes is ultimately limited on the upper end by amplifier saturation and on the lower end by various noise sources. This large value of diameter exponent will mean the smallest measurable drop size will be larger for electromechanical transducers than for transducers with a pulse proportional to a lower power of the drop diameter (assuming similar noise levels).

The major disadvantage of electromechanical transducers is their sensitivity to drop vertical velocity. Rowland also investigated the response of these sensors to drops falling below terminal velocity. He found the response of the transducers was reasonably well predicted by the quantity: mv^2/D, where m = drop mass, v = velocity and D = drop diameter. This, is to a first approximation, the average force applied to the sensor during the period of drop collision [3.37]. Rowland used this function to produce a correction factor for drops falling at vertical speeds other than their still air terminal velocity. However, to be able to use this correction, actual drop vertical velocity must be known. This requires simultaneous knowledge of the vertical wind speed and the drop direction of travel with respect to the sensor.

Kinnell [3.48] has examined the effects of drop shape, drop velocity and impact location on the Joss-Waldvogel disdrometer. This investigation found a discontinuity in the response of the transducer associated with drop velocity. No definite conclusions regarding the cause or effect of this discontinuity were given. Variations in the position of the drop impact on the target were observed to cause a change in transducer output which was described as "quite large". The drop shape was also found to introduce a significant uncertainty in transducer reponse. Kinnell concludes that "variations in factors such as rain drop velocity and raindrop shape generated by air movements might produce unacceptable errors in the measurement of raindrop size by the disdrometer under some rainfall conditions".

A further disadvantage of the coil-magnet transducers is their susceptability to wind-produced acoustic noise. This problem is accentuated by the requirement of a low mass, large area collecting surface. Wind shielding is only partially effective in reducing this problem and can itself introduce errors when drops are not falling almost vertically.

3.3.3 Electrostatic Methods

Electrostatic methods work by first arranging for a drop to artificially accumulate a charge which is related to the drop size and then measuring this charge as the drop impacts on a conductor at ground potential. The only detailed english language reference to electrostatic measurement of rain-drop sizes which could be located was a paper by Lammers [3.49]. An earlier paper by Keiley and Millen [3.50] described a similar electrostatic technique to measure cloud-drop sizes. A Lammers-type disdrometer was built and used by Sander [1.84], [3.51]. A unit developed by Sander was also used by Humpleman and Watson [1.85].

The instrument described by Lammers basically consisted of two fine horizontal wire grids separated horizontally by a small distance. The top grid was connected to a 300 V positive dc supply. A high impedance amplifier was connected between the bottom grid and ground. The grids were constructed from parallel strands of 0.05 mm tungsten wire spaced 0.75 mm apart. This instrument had a 25 cm^2 collecting area.

Lammers found that this instrument produced a pulse amplitude proportional to $D^{2.32}$ and yielded high signal-to-noise ratios even for drops as small as 1 mm diameter. Experiments with this transducer did show that the drops had time to completely discharge as they passed through the lower grid. This is important to ensure that the pulse amplitude is not dependent on how many grid wires the drop contacts. High-speed photographic observations of drops as they passed through the grids showed some drop breakup, but this did not cause "much variation" in the output signal.

The explanation given by Lammers as to how the transducer functioned was basically that the drop acquired a charge by conduction as it passed through the upper grid and deposited this charge in the lower grid, resulting in a pulse from the amplifier.

The electrostatic instrument described by Keiley and Miller [3.50] was designed for measurements of cloud-drop size distributions. Drops sampled by this instrument were directed through a small conducting orifice by a high velocity air stream. They then impacted on a solid conducting target which was connected to an amplifier. A potential difference of 400 V was maintained between the orifice and target plate. The 200 micron diameter sampling orifice of this instrument was not a disadvantage because it was used on the exterior of an aircraft.

The voltage pulse produced by this instrument was approximately proportional to the drop diameter squared. In this instrument the sampled drop does not contact the conducting orifice. Keiley and Miller believed that the pulse was due to a hemispherical induced charge acquired by the drop as it crossed the air gap. The actual pulse was believed to result from the cancellation of the charge on one side of the drop as it struck the target. This instrument was sensitive enough to measure drop sizes down to 4 microns.

3.3.4 Comparison of Methods

An exact quantitative comparison between drop size measurement methods is not possible because comparable data are not available for different methods. A summary of the major advantages and disadvantages are given below:

- Optical scanning methods are either too slow or prohibitively expensive and suffer from ambient light problems.
- Optical array methods have the advantage of direct size measurement but have inadequate sampling sizes and require correction for drop orientation and canting angle.
- Laser correlation has the advantage of measuring the path average distribution but suffers from the disadvantage that drop velocity is actually being observed. This method is also very expensive.

- Linear optical methods (i.e. scattering and extinction) are simple and inexpensive but have sensitivity and ambient light level problems.
- The two electromechanical methods are very well documented and are easy to implement but have the disadvantage that the transducer pulse is proportional to $D^{3.5}$ to $D^{3.7}$ and drop velocity squared. This results in a low sensitivity to small drops. These instruments also have errors due to drop shape, angle of incidence and impact location.
- The electrostatic method is simple and relatively easy to construct but is not well documented. It produces a pulse approximately proportional to drop diameter squared and seems to offer excellent sensitivity to small drops. No data was available on the errors due to drop velocity, shape, angle of incidence or impact location. Intuitively, these sources of error should be less serious than for the electromechanical methods.

These considerations led to the selection of the electrostatic method for further investigation in this experiment. The potential for improved sensitivity was particularly attractive because of the short wavelength being studied and the recent speculations in the literature that higher than predicted attenuations in the higher millimetre range (i.e. above 40 GHz) were partly due to under-estimating the number of small drops, as discussed in Section 3.2. It was also hoped that the electrostatic method would be less prone to the types of errors which degrade the accuracy of the electromechanical transducers.

3.4 Disdrometer Transducer

The electrostatic disdrometer transducers constructed for this experiment are based on the instrument described by Lammers [3.49]. The first disdrometer built was very similar to the one reported in [3.49]. This instrument and its associated electronics are described in [3.52], [3.53]. Experience accruing from the construction and operation of this first instrument resulted in several improvements to the basic design. These improvements were incorporated in a second generation transducer.

The first transducer built had a 25 cm^2 sampling area and grids formed from double layers of horizontal wires with 0.45 mm horizontal spacing. This double layer grid system was also used by Lammers and results from the method used to form the grids. Because of the small spacing between the wires, the most feasible way to construct the grids is by winding the wire on a frame similar to the one shown in Fig. 3.6, producing a double layer structure. The grid spacing was reduced from the 0.75 mm used by Lammers to 0.45 mm to improve the minimum measurable drop size. The diameter of the individual grid wires was reduced from the 0.05 mm used by Lammers to 0.038 mm to reduce drop breakup. Nichrome wire was used because it was readily available and corrosion resistant.

The basic operating limitations of this transducer were found to result from movement of the grid wires and the double grid structure. Movement or oscillation of the grid wires resulted in a time varying change in the capacitance of the grids which in turn produced an output from the transducer preamplifier. Significant motion of the grid wires resulted from: the passage of the drop through the grids, high wind velocities and building

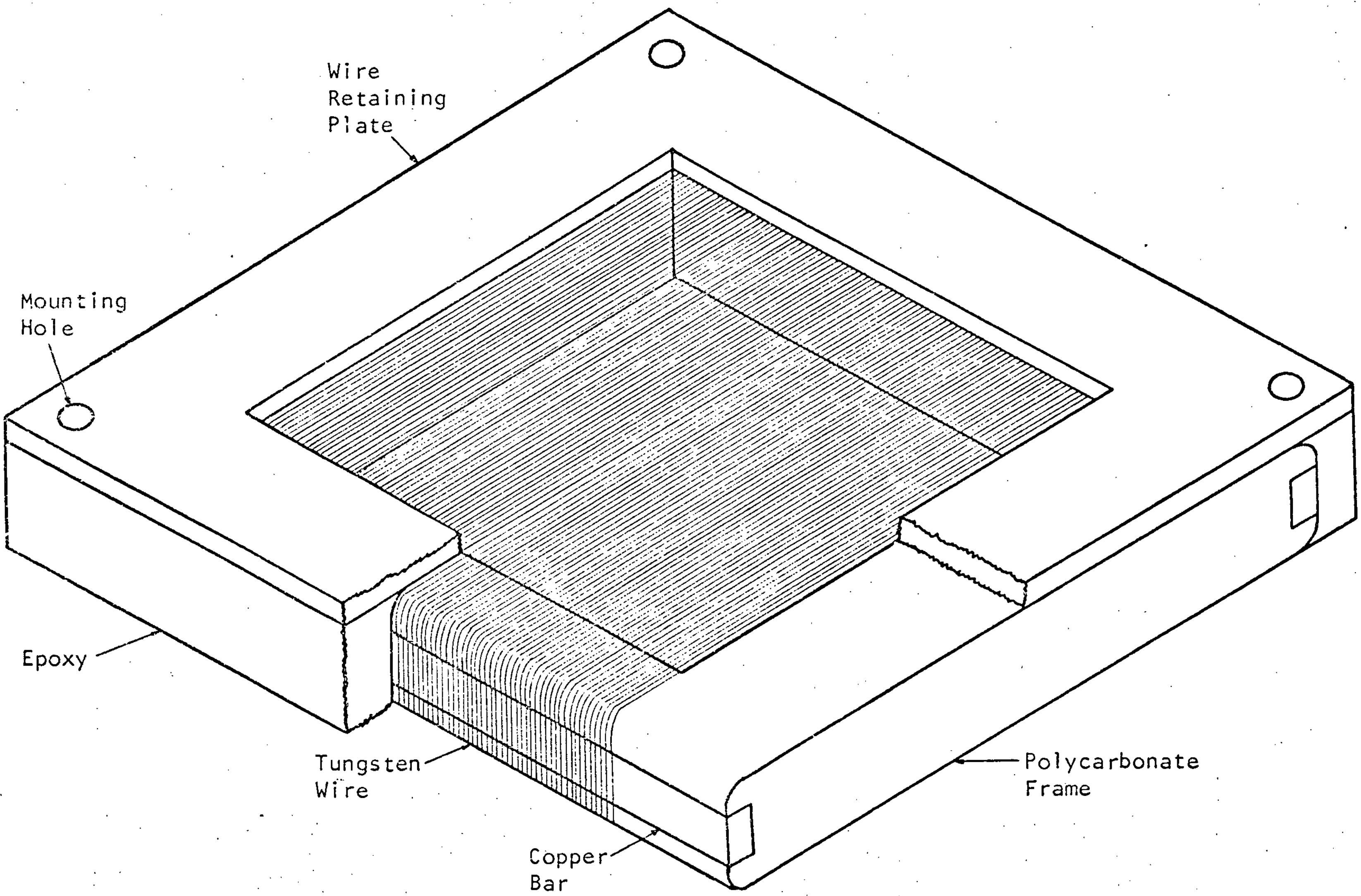

Fig. 3.6. Disdrometer transducer grid.

vibration. Passage of the drop through the grids resulted in a decaying sinusoidal output from the transducer after the main pulse. This did not seem to seriously affect the main pulse accurcy but did significantly increase the total period of the pulse due to a single drop and hence the minimum period between drops for accurate results. Grid motion due to wind was not usually as detrimental as grid motion due to building vibration. The building vibration was apparently caused by the movement of large numbers of students between classes and a large ventilation fan motor on the roof. These undesired signals could not be reduced by filtering because they were relatively broadband and occupied frequencies similar to the major spectral components of the desired pulse.

The double grid structure was a disadvantage because it resulted in greater drop breakup and increased water retention. It was observed that after a period of operation in actual rain there were small droplets of water attached to the grid wires. The amount of water was considerably larger on the lower grids layers. This was believed to be due to the increasing drop breakup and splatter resulting from the drop passage through each successive grid layer. Retained water on the upper grid results in reduced disdrometer accuracy because a part of the drop captured by the upper grid will not discharge on the lower grid, resulting in a reduced output for that drop. In addition, if this water is dislodged by a subsequent drop, the indication for that drop will be larger. Water retained on the lower grid is not thought to be detrimental.

Another problem with the first disdrometer was leakage currents between the upper and lower grids. After long periods of operation, the baseline or dc output level of the transducer preamplifier often drifted. When the transducer was cleaned in alcohol and dried, this problem disappeared. This seemed to indicate that a high resistance leakage path had been established along the surface of the grid frame, and was probably due to contaminants entering the transducer with the rain and a buildup of moisture.

The design of the second disdrometer transducer alleviated the problems discussed previously, increased the sampling size and further reduced the grid conductor spacing. The sampling area of the transducer was increased to 50 cm^2 in order to reduce the period of time required for a statistically valid drop distribution sample. (A 50 cm^2 sampling area is also used on almost all electromechanical disdrometers.)

The major improvement incorporated in the second disdrometer was an improved grid structure. These grids used a single layer of more closely spaced wire with far greater wire tension. Grid wire spacing was further reduced to 0.234 mm to facilitate the measurement of smaller drops. This grid spacing is believed to be very close to the minimum practical spacing for grids of this area. A single grid layer was used to reduce breakup, splatter and water retention. The maximum possible wire tension was used to minimize the grid movement and to increase the natural oscillating frequency of the grid vibrations. Maximum wire tension is also necessary for best wire spacing uniformity.

The wire chosen for the grid was 0.038 mm tungsten. This choice involved a tradeoff between the smallest possible diameter-to reduce breakup-and the highest possible tensile strength-to allow maximum wire tension.

Tungsten was chosen over other metals because it is corrosion resistant, has very high tensile strength and was available in the diameter range required.

Fig. 3.6 shows the grid frame and the method of winding the wire. Polycarbonate was chosen for the frame because it is insulating, extremely strong and easily machinable. Frame rigidity was found to be extremely important because the combined forces of the approximately four hundred wires - each of which is under a tension close to the breaking point of the wire - tends to deform the grid near the center. This deformation would then result in a reduction in the wire tension and spacing uniformity in the middle of the grid. A copper bar is bonded into a slot on each side of the frame to provide an electrical contact between the wires and a connection to the grid. Slots for each wire were machined into the polycarbinate and copper bar using the thread cutting facilities on a lathe. After the threads were cut, a 9.4 cm x 9.4 cm area was milled through the frame. The grid area is larger than the sampling aperture to ensure that drops entering the aperture at an angle pass through both grids. The distances from the grid wires to the grid mounting holes were increased to reduce the probability of surface leakage between grids. In addition, nylon, rather than metal, supports were used between grids.

The most difficult process in the grid fabrication was actually winding the wire onto the frames. Initial attempts to wind the wire onto the frames by hand were not satisfactory because of the extreme difficulty of maintaining uniform wire tension. If the winding were to be done by hand it was estimated that each grid would probably require two men for approximately one day. The method finally devised to wind the grids used a lathe to slowly rotate the frame and an automatic wire tensioning mechanism. This reduces the time for fabricating one grid to less than one man-day.

After the grid was wound, the wires were bonded with epoxy to the frame along the entire outside edge. Then another piece of polycarbonate sheet, cut to the same dimensions as the frame, was bonded to the top of the frame to further secure the wires. One set of the two layers of wires were then cut away to leave a single layer of wires on the frame. This elaborate method of securing the wires was found to be necessary to prevent the high wire tension from causing bond failure after the wires were cut.

The two grid assemblies and supporting structure are mounted in the aluminum housing shown in Fig. 3.7 and Fig. 3.8. The grids are located near the top opening to ensure that drops passing through the aperture pass through both grids and that water does not splash back up to the grids from the drain grating on the bottom of the housing. To prevent water accumulation on the housing top, the top slopes towards the sides of the unit. Splashing into the aperture is reduced by a lip around the opening and an expanded metal grid slightly above the housing top. (The effectiveness of these splash reduction methods has not been experimentally verified.) A removable lid is provided to protect the grid sides from dust and hail when the disdrometer is not in use. Connections to the grids are via type-N jacks mounted on the side of the housing. Fig. 3.9 shows the complete disdrometer transducer.

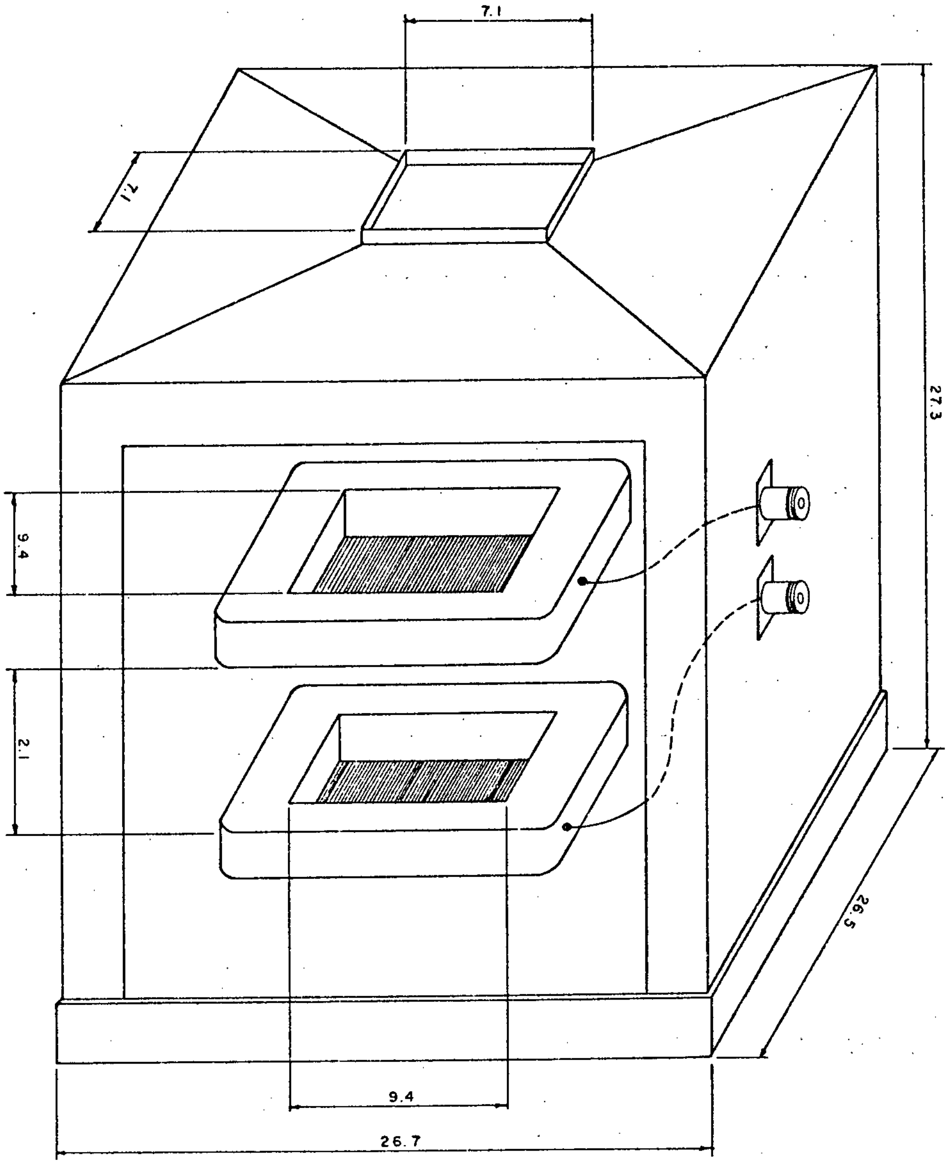

All measurements in centimetres

Fig. 3.7. Disdrometer transducer dimensions.

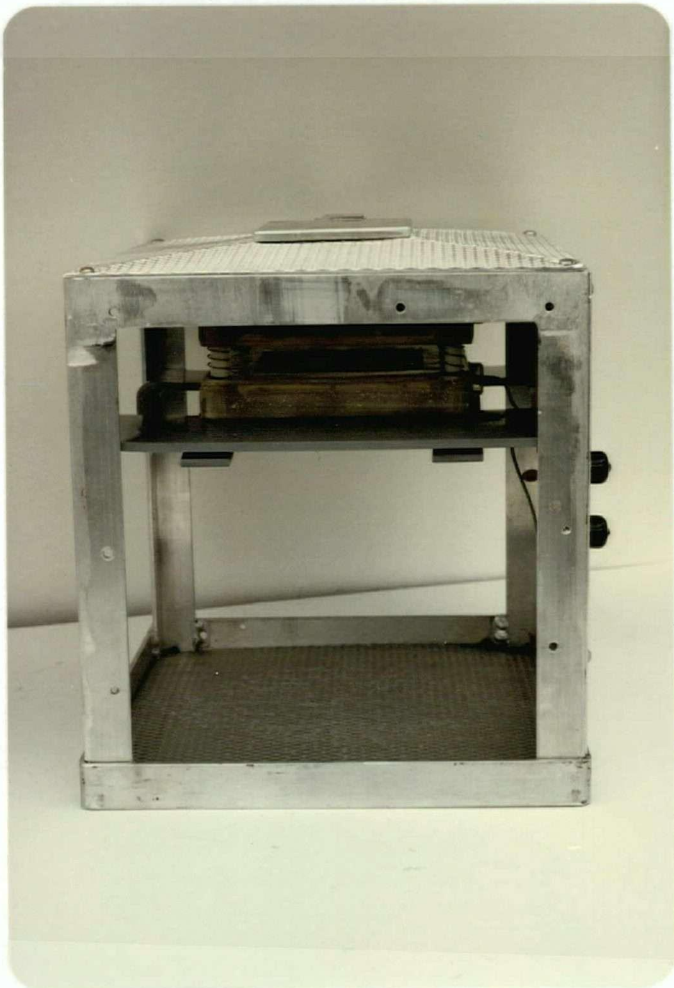

Fig. 3.8. Disdrometer transducer with cover removed.

Fig. 3.9. Complete disdrometer transducer.

3.5 Disdrometer Electronics

The interconnection of the disdrometer transducer, preamplifier, peak detector and microprocessor is shown in Fig. 3.10. A 300 V primary battery, Eveready 493 or Mallory M722 supplies the dc voltage to the upper grid. Batteries are used for the grid and preamplifier supplies because power supplies are neither as convenient nor as safe for operating this type of device in wet conditions. Power supplies in the vicinity of the transducer also tend to induce 60 Hz noise onto the lower transducer grid. The 0.005 μF capacitor connected from the upper grid to ground was found to reduce the susceptability of the transducer to 60 Hz electrostatic interference.

The transducer preamplifier, shown in Fig. 3.11, converts the flow of charge from the lower grid to ground into a buffered voltage pulse. This charge produces a voltage across the amplifier input resistance shown as R_{in} in Fig. 3.10. R_{in} is essentially equal to R_1 in Fig. 3.11. A discrete JFET is used as the first stage in the preamplifier because this device results in better low frequency noise performance than can be obtained with monolithic operational amplifiers. Metal film resistors are used in the first stages of the preamplifier to reduce thermal noise contributions. Capacitor C_1 is provided for testing the preamplifier using a signal generator. In normal operation this capacitor is shorted. When driven by a signal generator, the voltage gain of the preamplifier is adjustable from approximately 0.5 to 15. At a gain setting of 2.4 the amplifier has a 3 dB frequency response from 0.1 Hz to 1.8 MHz. The preamplifier is mounted in a gasketed die cast box and mounted directly on the transducer housing using a type N plug-plug adapter.

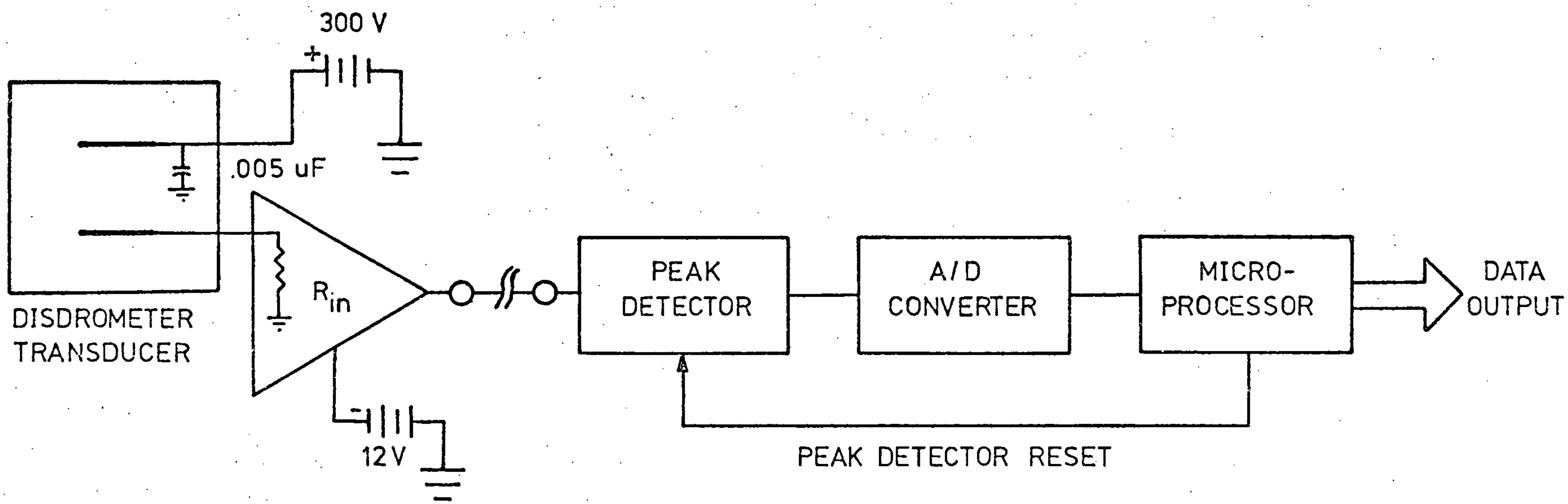

Fig. 3.10. Disdrometer system block diagram.

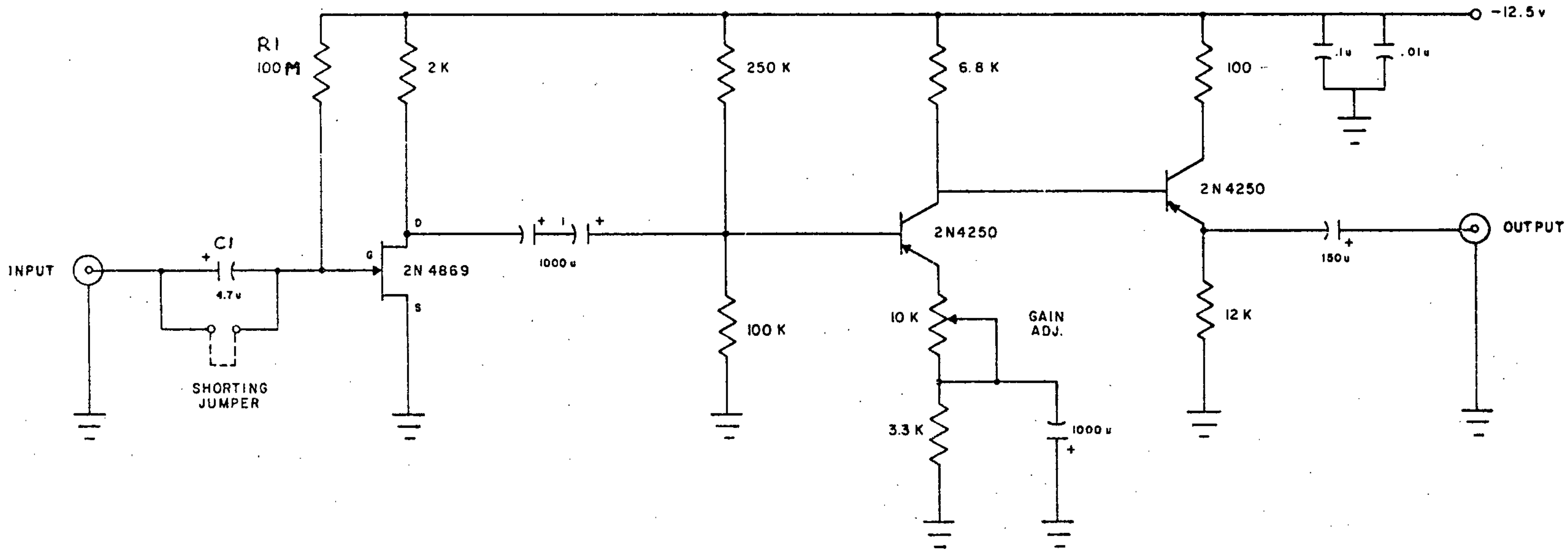

Fig. 3.11. Transducer preamplifier.

The peak detector, shown in Fig. 3.12, stores the peak value of the preamplifier output pulse. This circuit was designed to have a fast response, low overshoot and high dynamic range. More than adequate holding time is provided for the A/D conversion of the stored pulse. The microprocessor resets the peak detector after A/D conversion. The 12 bit A/D converter converts the pulse amplitude to a digital quantity for input to the microprocessor. Pulses are then sorted into up to sixteen size categories. The microprocessor outputs the number of drops in each category which were detected during the sample intervals.

Two different schemes were used to record the microcomputer data output. At first, the microcomputer was interfaced to the data acquisition minicomputer. The number of drops was transferred each second and recorded on the magnetic tape along with all the other experimental data. This method worked well and was used to produce the data reported in [3.53]. The disadvantage of this method was the high software and computing costs associated with processing the large amounts of data recorded. Because only short periods of disdrometer data were actually analyzed and because integration times of up to one minute (depending on rainrate) are required for a statistically valid sample, a semimanual method was adopted to handle the disdrometer data. The microcomputer is now interfaced directly to a hardcopy printer. A hardware timer, which is manually synchronized to the data acquisition system, is used to define sample and print periods. At the end of the sample period, the microcomputer prints out the number of drops in each size category. Drop size data is then analyzed with the aid of a programmable calculator.

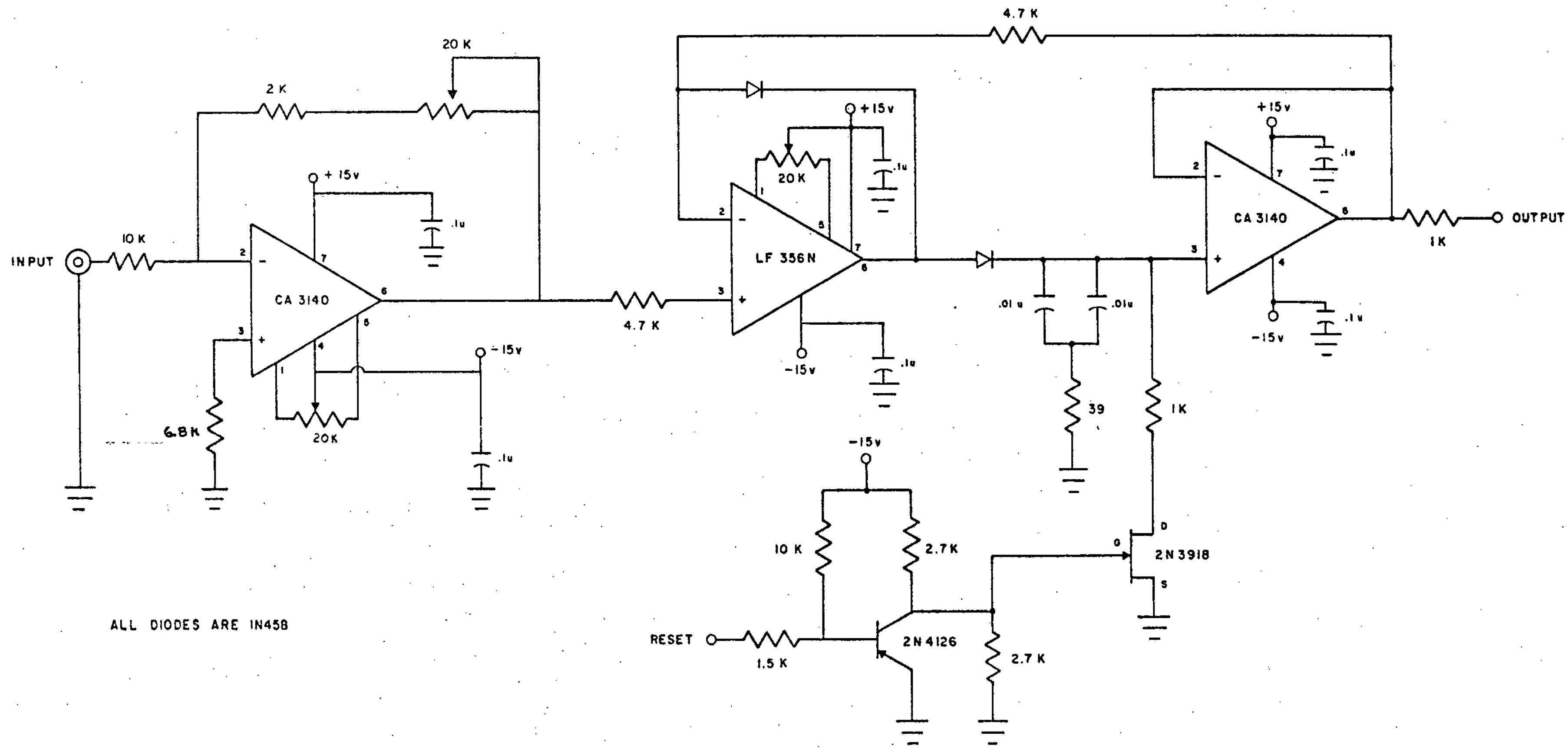

Fig. 3.12. Peak detector.

3.6 Disdrometer System Test Results

The effects of various disdrometer circuit parameters were investigated in an attempt to experimentally optimize the disdrometer system. Fig. 3.13 shows the peak pulse amplitudes for various drop sizes with different grid voltages. With preamplifier voltage gains of only 1 to 2 the preamplifier saturated on the largest drops when using a 600 V battery. Because the sensitivity of the transducer is limited by the time varying capacitance produced by grid movement, a larger grid voltage did not improve the transducer signal to noise ratio. For these reasons no advantage could be realized by using more than one 300 V battery to power the upper grid.

The selection of the preamplifier input resistance, R_{in}, involves a tradeoff between the pulse amplitude and pulse period. Fig. 3.14 shows that larger values of R_{in} are desirable because they produce large pulse amplitudes. However, larger values of R_{in} also result in longer pulse periods as shown in Fig. 3.15. The pulse period is defined here as the time from the start of the pulse to when the preamplifier output settles to the noise level. The pulse period is linearly related to the value of R_{in}. This is mainly due to the time constant of the transducer capacitance-amplifier input resistance product. In a rainfall of 50 mm/hr the average interval between drop arrivals in a 50 cm^2 area is approximately 35 msec. As a result the value of R_{in} was chosen to be 100 MΩ, which provides an acceptable pulse amplitude and a pulse period of approximately 16 msec.

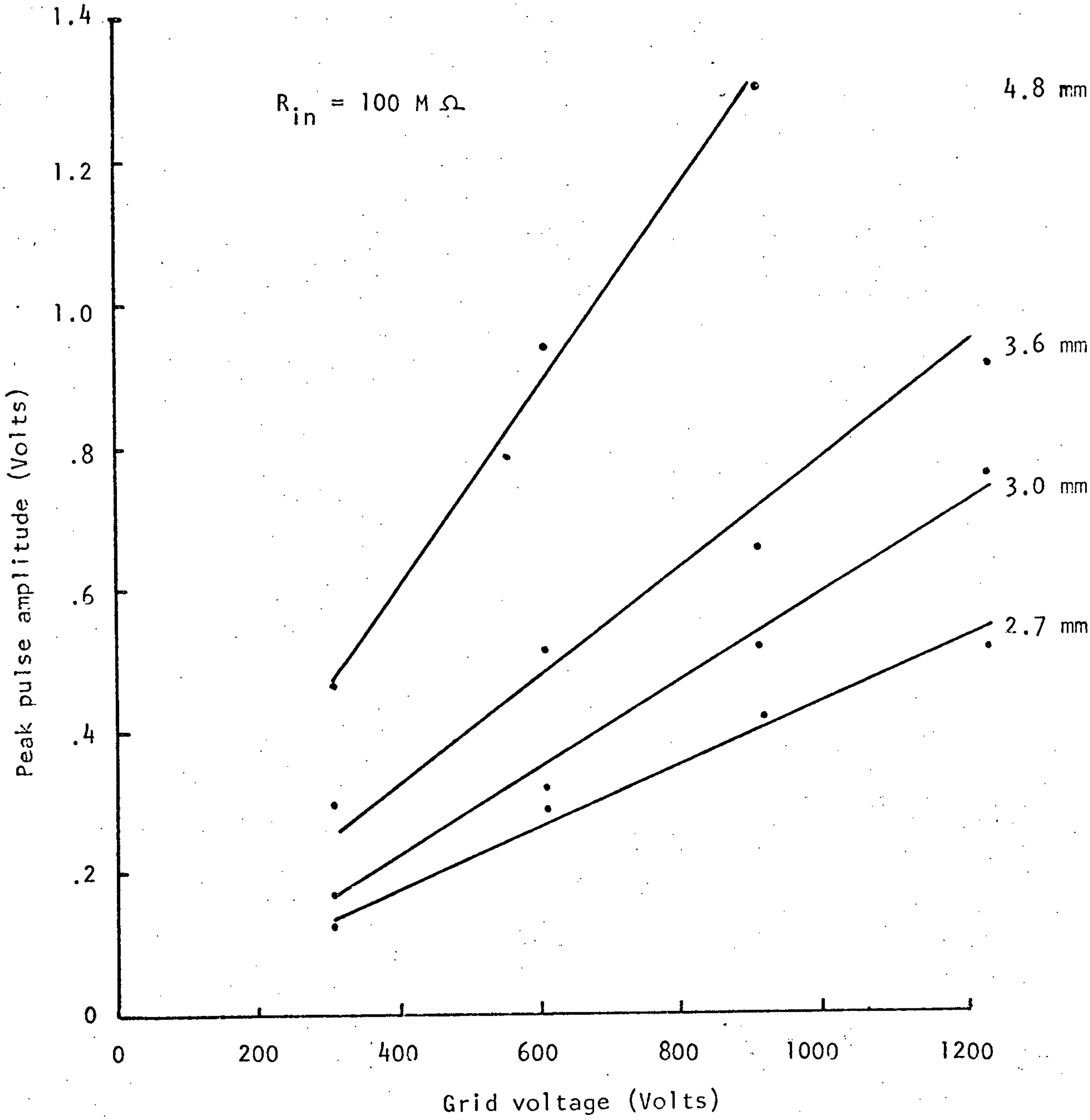

Fig. 3.13. Peak pulse amplitude vs grid voltage for different drop diameters.

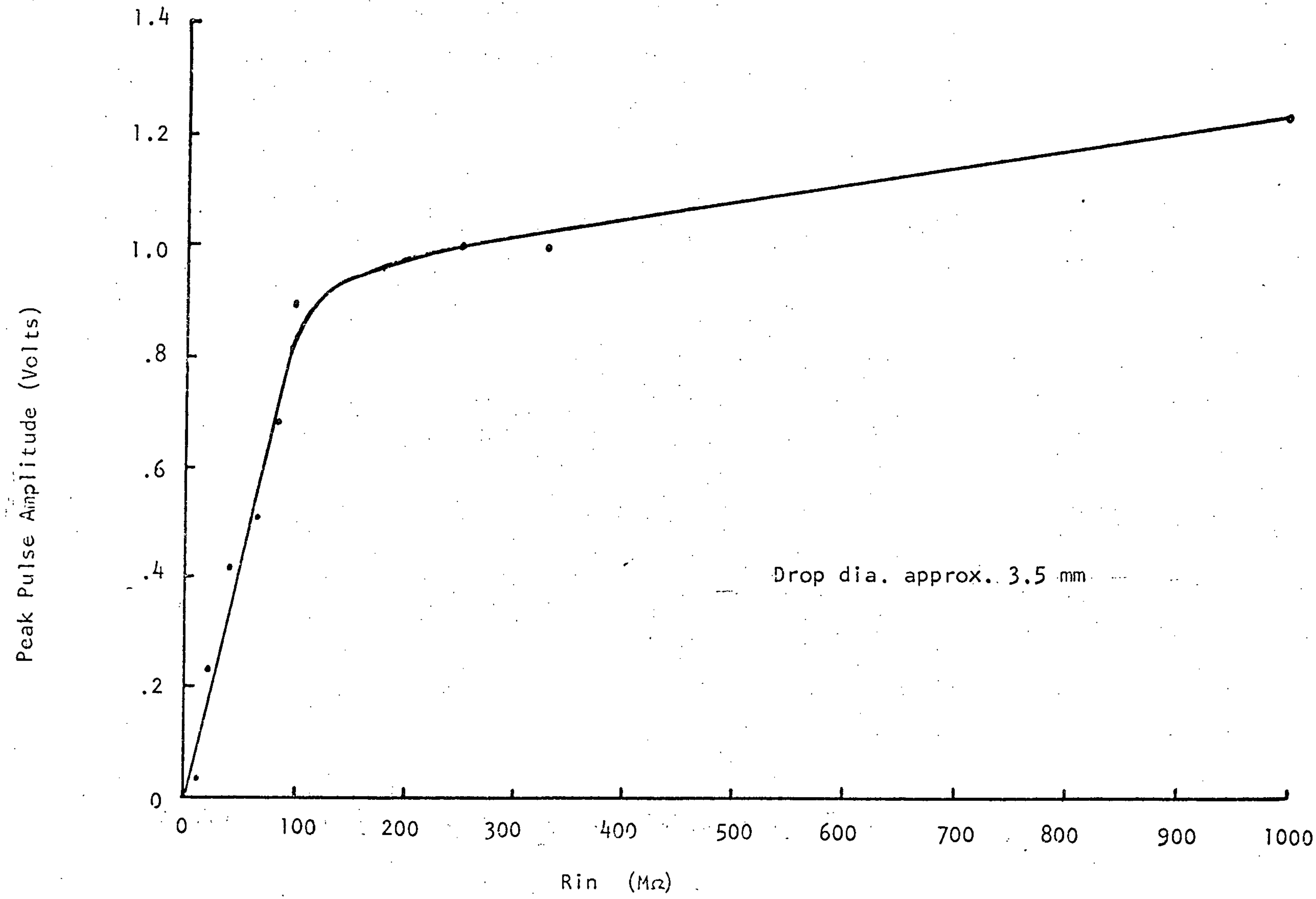

Fig. 3.14. Peak pulse amplitude vs R_{in}.

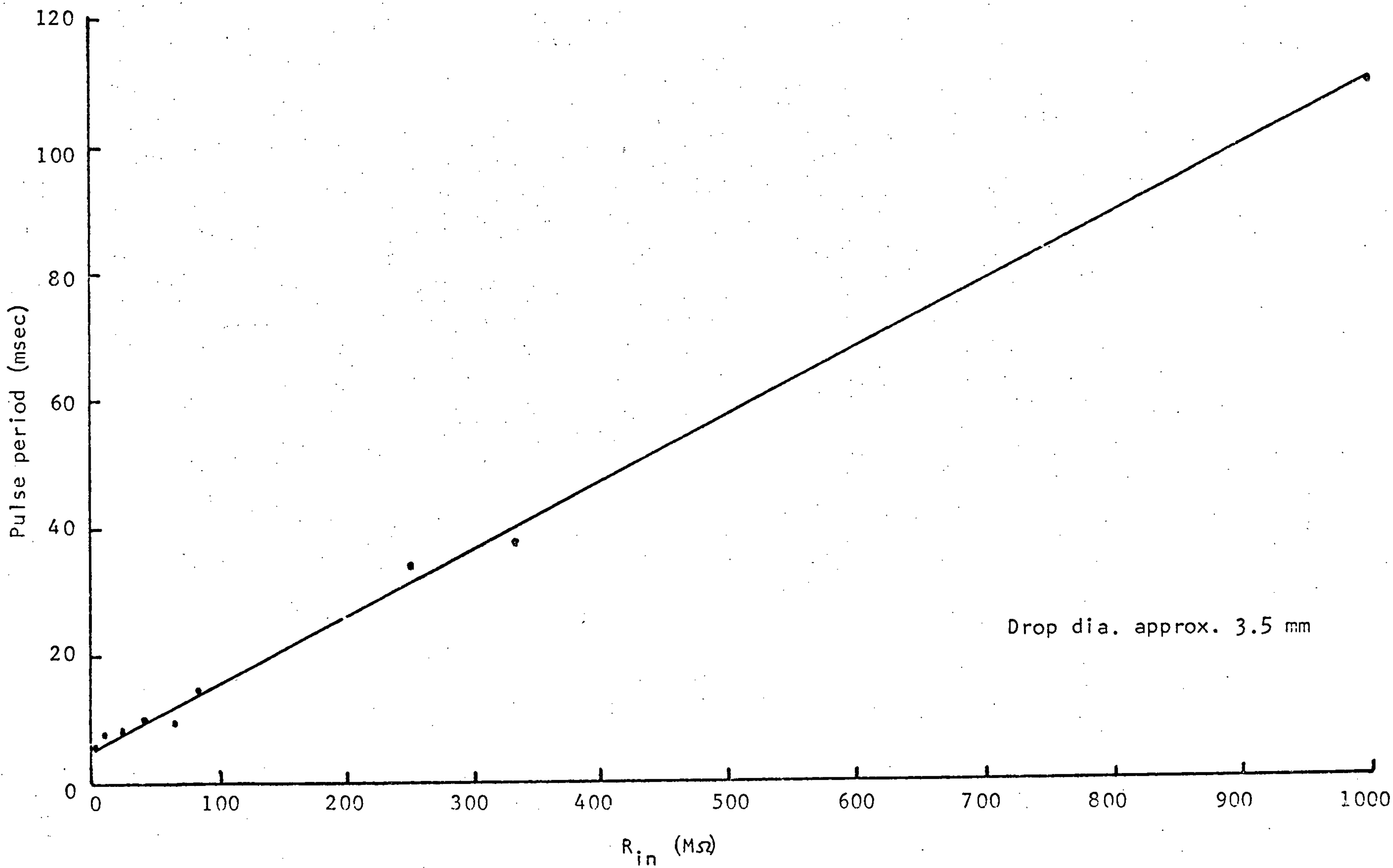

Fig. 3.15. Pulse period vs R_{in}.

3.7 Disdrometer Calibration

The disdrometer was calibrated by measuring the peak pulse amplitude of drops of known size and velocity. Large drops were formed by dripping water through nozzles of various cross sections. Small drops were formed with a specially constructed apparatus, shown in Fig. 3.16, which directed a variable air flow around a vibrating hypodermic needle. By using different combinations of needle diameter, air flows, vibration frequency and vibration amplitude, drops as small as 0.5 mm could be formed. The drop sizes were determined by weighing a number of drops collected in a very small container. Drop velocities were controlled by varying the distance each drop fell.

The calibration results for drops at terminal velocity are shown in Fig. 3.17. This same data is shown in Fig. 3.18 but here the square root of the pulse amplitude is plotted against drop size, resulting in an almost linear curve. A least squares exponential curve fit to this data results in the relationship:

$$V_{PEAK} = 0.027\, D^{2.62} \tag{3.1}$$

where V is in volts and D is in mm. From the results gathered from several similar calibrations, it has been found that the exact relationship between the peak pulse amplitude and drop size depends on the preamplifier bandwidth and time constant.

The effects of drop velocity on the peak pulse amplitude for various size drops is shown in Fig. 3.19. This graph shows that the peak response was linearly related to the drop velocity.

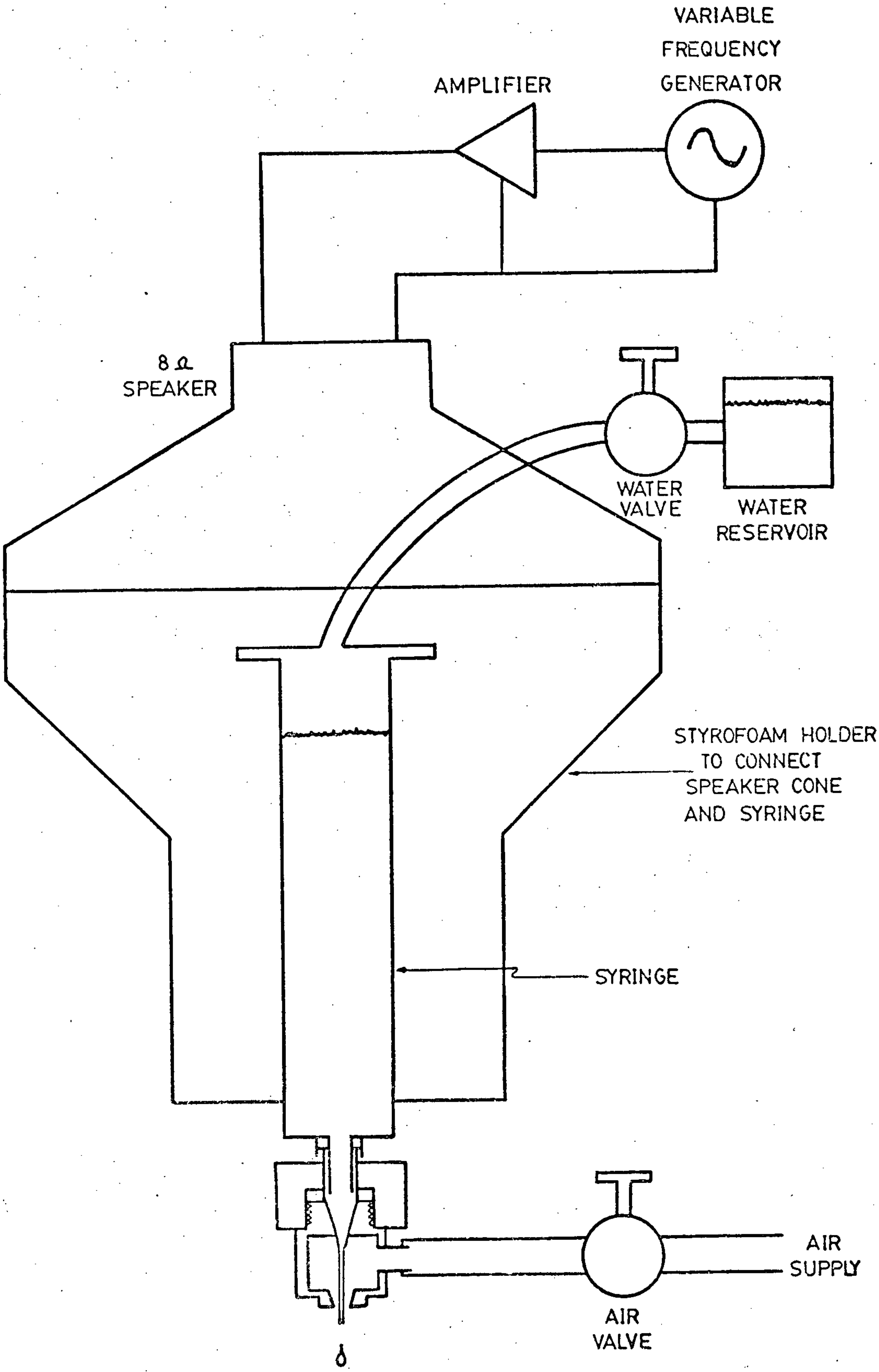

Fig. 3.16. Apparatus for creating small drops.

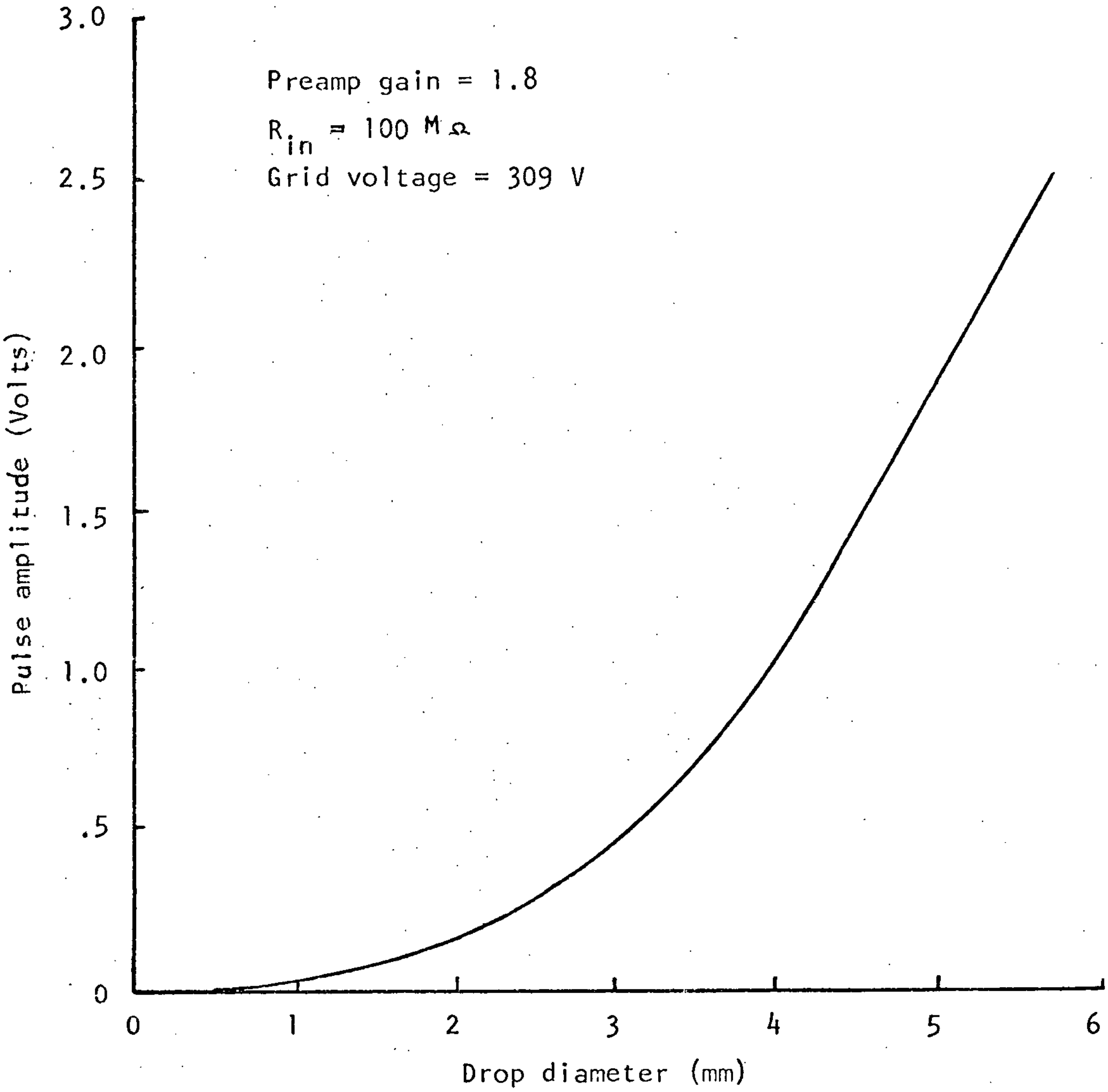

Fig. 3.17. Disdrometer calibration for drops at terminal velocity.

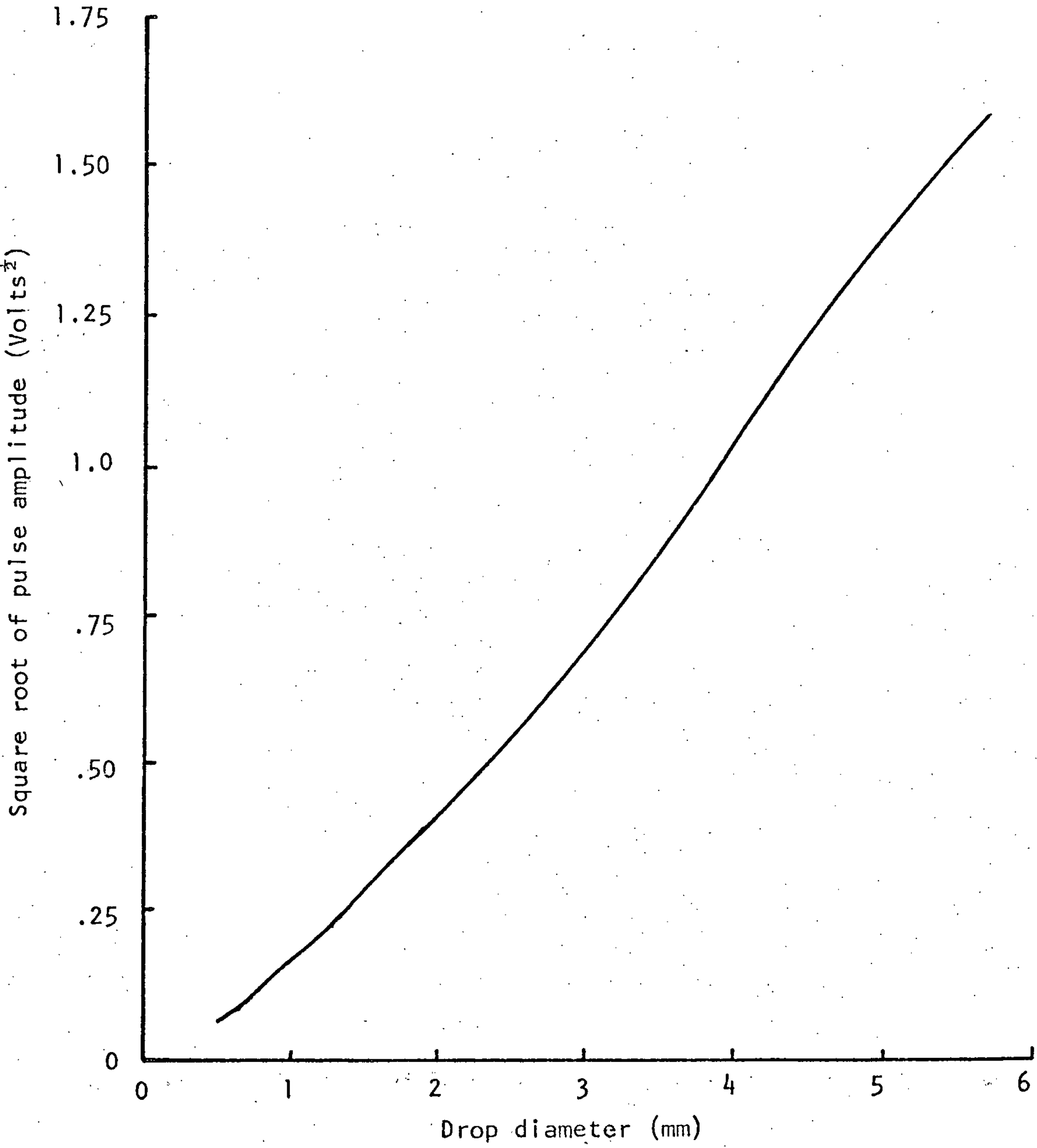

Fig. 3.18. Square root of pulse amplitude vs drop diameter.

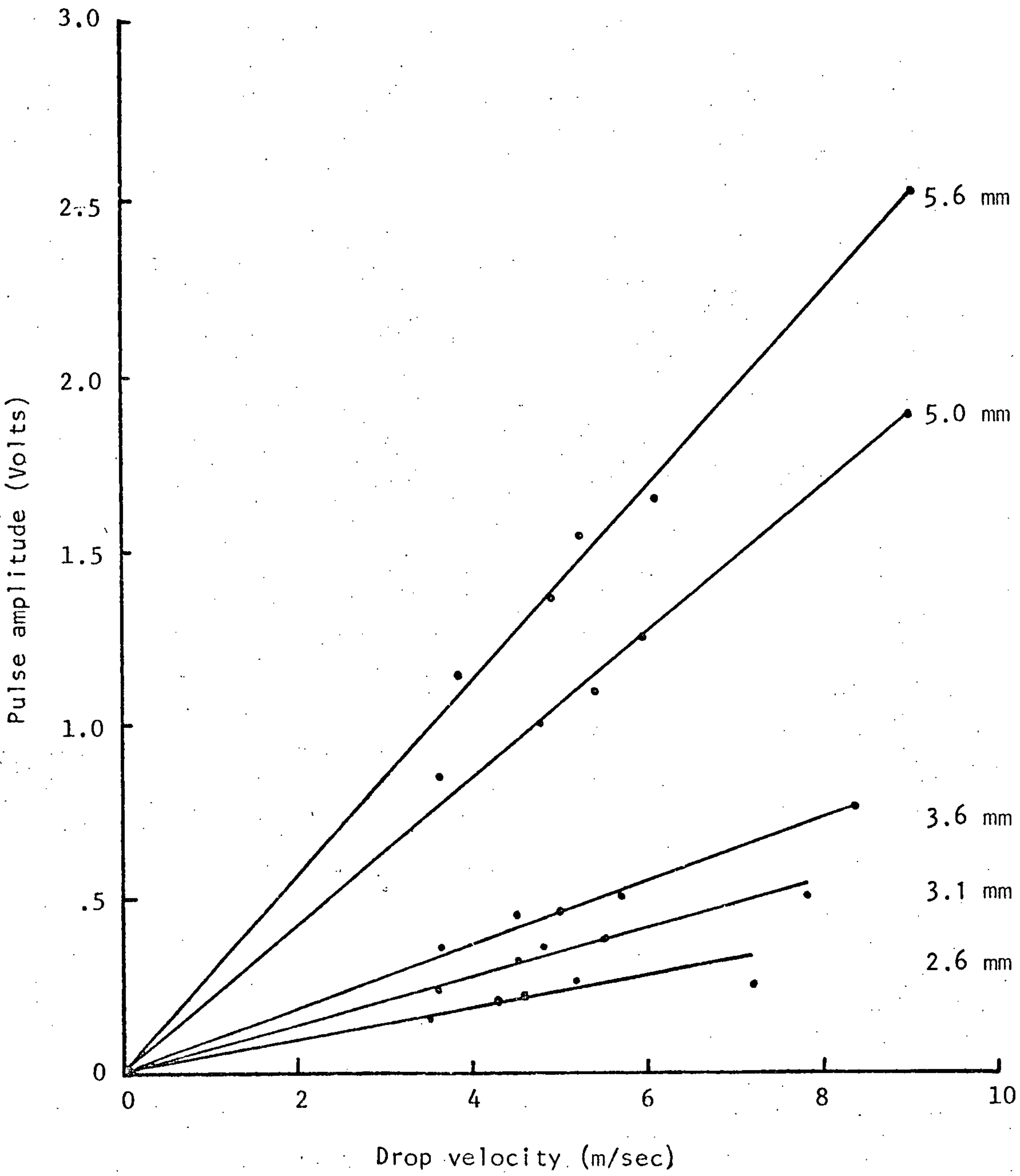

Fig. 3.19. Effect of drop velocity on pulse amplitude.

This electrostatic disdrometer system has an output pulse proportional to $D^{2.62}$ and linearly related to drop velocity. In comparison, the electromechanical disdrometers produce pulses proportional to $D^{3.5}$ to $D^{3.7}$ and velocity squared. These differences make the electrostatic disdrometer advantageous for measuring small drops and less susceptible to wind velocity errors. An additional advantage over electromechanical devices is the fact that the output pulse is independent of impact location on the transducer.

The disadvantages of this disdrometer arise from the deleterious effects of residual water retention. After a period of operation in actual rain, the upper grid often accumulates small water droplets. These are the result of extremely small drops which have inadequate velocities to escape the hydrostatic attraction of the grid wires and from larger drops striking the edge of the transducer housing and splashing onto the grid. When these water droplets are dislodged, there will be an erroneous transducer output. In this experiment, this problem was overcome by periodically blowing the upper grid dry. This could easily be accomplished automatically with a series of small air jets inside the transducer housing. A second problem with this transducer arises when the entire grid frame structure is saturated with small water droplets. This only occurs after several hours of operation but when a leakage path is established between the grids, the entire system saturates and the disdrometer must be completely dried. If the disdrometer was fitted with air jets, this problem would probably be overcome also.

The disdrometer system actually used in this experiment would measure drops down to 0.3 to 0.35 mm in diameter. Drops were sorted into the thirteen "standard" drop categories used in most experiments.

3.8 Anemometer

Three components of the wind velocity vector were continually measured on the roof of the Electrical Engineering building. The anemometer assembly is mounted on top of a 8 m tower as shown in Fig. 3.20, to reduce reading inaccuracies due to turbulence near the building. Wind direction is converted to an analog signal using a three-phase syncro circuit described in [2.1]. Horizontal and 60° elevation wind velocity are measured using propellers and dc generators manufactured by the R.M. Young Co. The model 8078 generators used have a 2.40 V output at 1800 rmp. Model 21281 propellers were selected because of their low threshold and large low speed response. These four-blade propellers are made from expanded polystyrene beads, are 23 cm in diameter and have a 30.6 cm effective pitch. Their threshold is between 0.1 and 0.2 m/s and they are calibrated at 9.18 m/s horizontal for 1800 rpm.

The horizontal and 60° elevation wind speed are used to calculate the vertical wind speed during data analysis. This method alleviates the low speed problems which would arise due to propeller threshold and generator bearing friction if the propeller was mounted vertically.

If the anemometer propeller angular response was ideal, the vertical wind velocity would be given by:

$$V_{VERT} = \frac{V_{60°} - V_{HORIZ} \cos 60°}{\sin 60°} \qquad (3.2)$$

The measured angular response of the propellers from the manufacturers specifications, is shown in Fig. 3.21. Using the data from this graph, the actual vertical wind is calculated from:

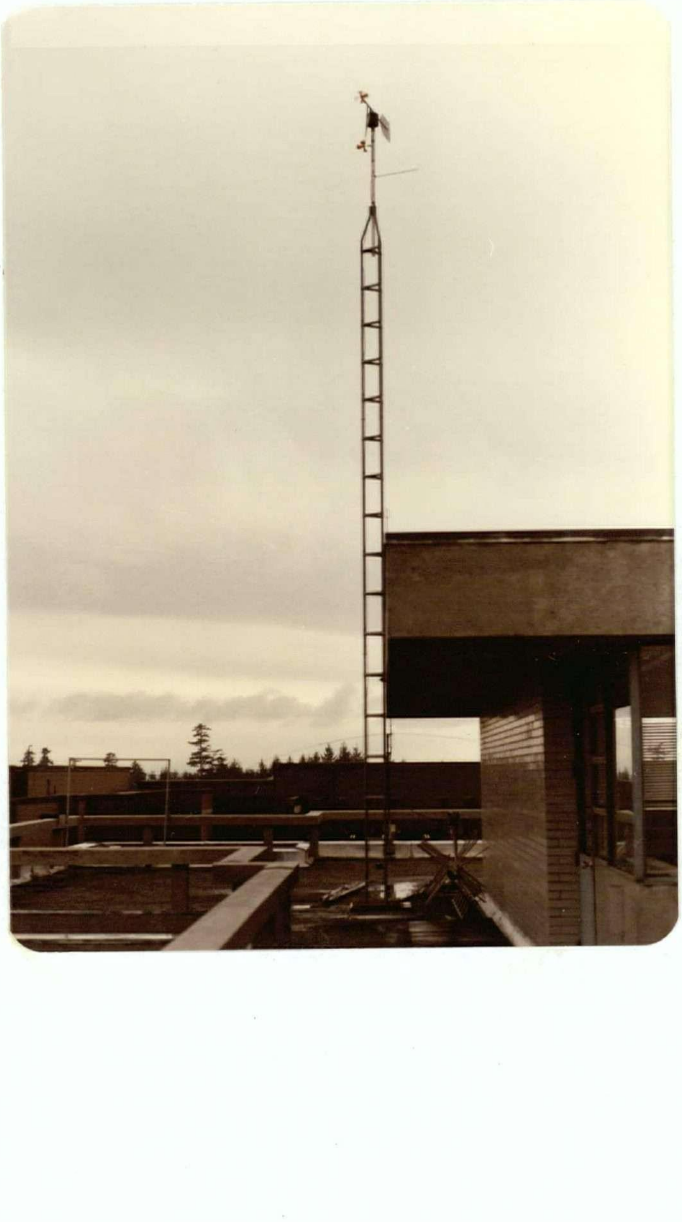

Fig. 3.20. Anemometer photograph.

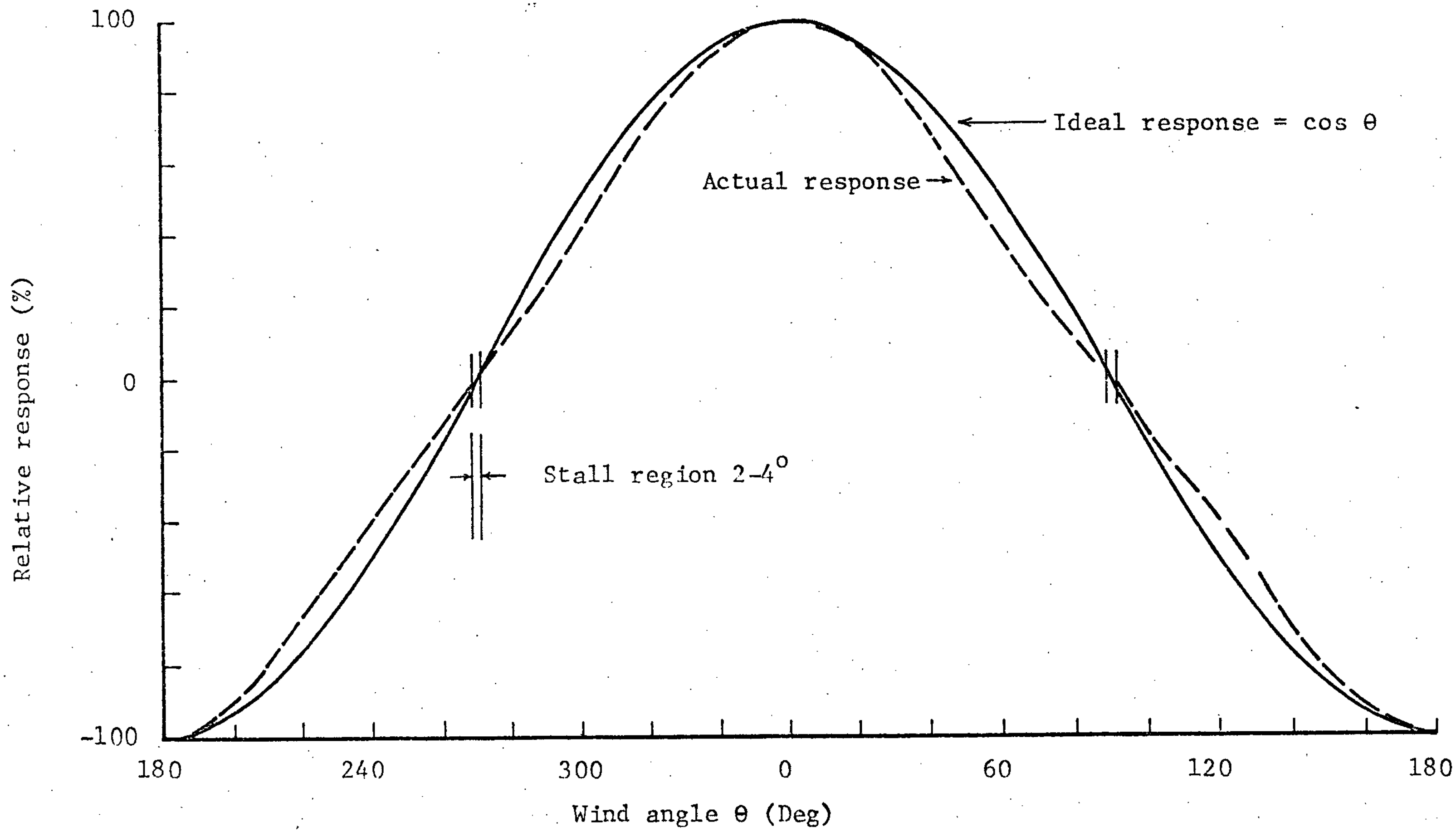

Fig. 3.21. Anemometer propeller angular response.

$$V_{VERT} = \frac{V_{60°} - 0.40\ V_{HORIZ}}{0.82} \tag{3.3}$$

3.9 Temperature Measurement

A commercial temperature probe, B & K Precision TP-28, was used to monitor the ambient air temperature. This unit provides an output of 10 mV per °C or °F. Boiling water and ice were used to calibrate the device before use. The temperature transducer output was connected to one of the analog channels on the data acquisition system for continuous recording.

4. THEORETICALLY PREDICTED PROPAGATION PARAMETERS

The purpose of this chapter is to use existing theoretical methods to predict the propagation parameters for different rain conditions. Results of these calculations will be used as inputs to the experimental model described in the next chapter and compared to the measured propagation data. The predictive procedures require that the parameters of the rain medium, including rainrate, rain drop size distribution, rain temperature, canting angle and drop shape, be specified. From the drop shape and temperature, the complex scattering amplitude for each drop size can be calculated. For a specific drop size distribution, the scattering amplitudes are then used to calculate the attenuation and phase shift at different rainrates for waves linearly polarized along the drop major and minor axes (or principal planes). From these intermediate results and an assumed canting angle, it is then possible to calculate the vertical and horizontal copolar attenuation and phase shift, differential attenuation, differential phase shift and XPD s for both polarizations.

It was necessary to calculate these propagation parameters because crude approximations and interpolations would have been needed to compare the dual-polarized results of this experiment to published propagation data. The following is a brief survey of the previously published theoretical results. Chu [4.1], in one of the earlier papers in this area, did include graphical results applicable in this frequency range. The problem is that practical constraints mean that data can only be presented for a few different rain conditions. For example, this reference includes a graph showing differential phase shift, but only at rainrates of 5, 25 and 100 mm/h and for one drop size distribution. Data are also presented for XPD_H at the same rainrate but only for a simultaneous 20 dB copolar fade and one canting angle. Recently, Evans [4.2] and Holt and Evans [4.3] have published results showing XPD for both polarizations vs. CPA for 57, 94 and 137 GHz but, unfortunately, data are only presented for a constant canting angle of 2° and one drop distribution. In another recent paper, Neves and Watson [4.4] have published comprehensive calculated results including scattering amplitudes, XPD at different canting angles, differential attenuation and differential phase at 36.5 GHz. Oguchi [4.5] has also published tables of scattering amplitudes, principal-plane complex propagation constants and XPD for different canting angles at 34.8 GHz.

The development of this chapter will follow the natural sequence of the predictive calculations. Accordingly, the meterological inputs to the calculations will be discussed first. Then, the scattering amplitude data will be presented. These two sets of information will then be used to compute the propagation parameters at the frequency of interest for a variety of rain conditions.

4.1 Meterological Inputs

To predict the macroscopic propagation properties of a transmission path, assumed to contain spatially uniform rain, it is necessary to sum the effects of each individual drop along the path. This requires a knowledge of the microscopic rain properties including the number of drops of each size per unit volume (drop size distribution) the drop shape, the drop orientation (canting angle) and rain temperature. Lack of information about these microscopic rain properties is the largest source of uncertainty in predicting propagation parameters. Because it is so difficult to accurately measure some of these microscopic rain parameters in natural rain, it is often necessary to resort to models or estimates. This usually means that the predictive calculations must be performed for a range of assumed rain conditions. The resulting range of values can then be compared to the measured propagation conditions with the hope of being able to match the observations to a consistent set of rain parameters.

4.1.1 Rainrate

Rainrate is the most readily measured rain parameter and therefore is convenient to use as the prime indicator of the rain medium condition when comparing predictions and observations. Because rainrate is extremely variable, the predictive calculations must be performed for a wide range of values. The upper limit on the rainrate used in these calculations was determined by the highest expected rainrate in this location. Propagation parameters were calculated for the following rainrates: 1.25, 2.5, 3.75, 5.0, 6.25, 7.5, 10, 12.5, 15, 17.5, 20, 25, 30, 40 and 50 mm/h. Since all of the propagation parameters are smoothly varying functions of rainrate, interpolation can be used between these values if necessary.

4.1.2 Drop Size Distribution

Even though a variety of methods have been used to study raindrop size distributions, their wide variability in natural rain means that a selection of distrubtions must be used in predictive calculations. The "standard" distributions which are widely used for propagation predictions are the: Joss et al. Thunderstorm, Widespread and Drizzle [4.6], Marshall and Palmer [4.7] and Laws and Parsons [4.8]. A negative exponential distribution is usually used to characterize all of these distributions except the Laws and Parsons (where a negative exponential does not accurately fit the tabulated data). The basic form of these distributions is given by:

$$N_D(D,R) = N_0 e^{-\Lambda D} \tag{4.1}$$

where:

$$\Lambda = \alpha R^{-\beta}$$

and:

- $N(D,R)$ is the number of drops per m^3 in the size category between D-0.5 mm and D + 0.5 mm at a given rainrate, R.
- R is the rainrate in mm/h.
- D is the equivolumetric drop size diameter in mm.
- α, β are constants

N_o was originally considered a constant [4.6], [4.7], but Harden, Norbury and White [4.9] have pointed out that the original Joss et al distributions did not satisfy the rainrate integral equation. In other words, if the drops described by the distribution at a certain rainrate were considered to be falling at their terminal velocity in still air, the rainrate calculated from the sum of the drops of all sizes did not agree with the rainrate used in the distribution. Olsen [4.10] proposed that N_o be renormalized as a function of R so that the distributions did satisfy the rainrate integral equation over a certain range of rainrates.

Olsen indicated that the largest discrepancy with the rainrate equation was for the Joss Thunderstorm distribution. Neves and Watson [4.4] and Shkarofsky [4.11] have recently used the renormalized Joss Thunderstorm distribution. Shkarofsky, however, does not use the renormalized versions for the other distributions, presumably because Olsen has indicated that the greatest rainrate discrepancy is for the Joss Thunderstorm distribution. To test whether it was necessary to use the renormalized distributions in this work, sample calculations of 74 GHz copolar attenuation were performed using both normalized and unnormalized distributions. The test calculations showed that the largest attenuation differences were for the thunderstorm distribution but that the two drizzle distribution attenuations were also significantly different. For this reason, it was decided to use the renormalized distributions exclusively for the following calculations. To avoid confusion with the unnormalized distributions, these distributions will be referred to as the Joss/Olsen Thunderstorm, etc.

The renormalized distributions and their range of greatest validity for the new values of N_o are given below [4.10]:

1. Joss/Olsen Thunderstorm:

$$N_D(D,R) = 1.31\ 10^3\ R^{0.084}\ \exp\ (-3.0\ DR^{-0.21}) \tag{4.2}$$

rainrate: 25-150 mm/hr

2. Marshall and Palmer or Joss/Olsen Widespread:

$$N_D(D,R) = 6.62\ 10^3 R^{0.021}\ \exp(-4.1\ DR^{-0.21}) \tag{4.3}$$

rainrate: 1-50 mm/hr

3. Joss/Olsen Drizzle:

$$N_D(D,R) = 3.38\ 10^4 R^{-0.03}\ \exp(-5.7 DR^{-0.21}) \tag{4.4}$$

rainrate: 0.25-5 mm/hr

The Laws and Parsons distribution was not used because it cannot be accurately described by a negative exponential distribution. This means that calculations can only be performed at the relatively few rainrates where the tabulated drop distributions are given [4.8]. The Marshall and Palmer distribution closely fits the Laws and Parsons data except for the small drop sizes [4.11]. Calculated 74 GHz attenuation values for the Laws and Parsons distributions would be between the values for the Joss Thunderstorm and Marshall and Palmer distributions [4.10].

The drop size diameter categories used in these calculations are 0.5 mm intervals centered on 0.5, 1, 1.5, ... 6.5 mm. These categories were used by Laws and Parsons and appear to have been adopted as a standard by the majority of investigators since. Because these intervals are separated by only 0.5 mm, it is important to remember that the number of drops per unit volume in these categories is one half the value of N_D, as conventionally defined, which is the number in a 1 mm width size category.

Implicit in the relationship between the standard drop size distributions and their corresponding rainrates, is the assumption of zero vertical wind velocity. Nonzero vertical wind velocities can significantly alter the raindrop size distribution above the ground. The effects of vertical wind velocities on copolar attenuation are analyzed in Section 4.4.

4.1.3 Drop Shape

The most accurate description of the shape of falling water drops appears to be the one developed by Pruppacher and Pitter [4.12]. A water drop falling in air assumes a shape so that the internal and external forces at the surface of the drop are in equilibrium. The aerodynamic forces are symmetrical about a vertical axis through the center of drop mass for a drop falling in still air. As a result, the drop shape is symmetrical around this axis. Pruppacher and Pitter accurately determined the drop's asymmetric oblate spheroidal shape by solving a pressure balance equation at the surface of the drop. Oguchi [4.5] used the techniques described by Pruppacher and Pitter to calculate the deformation (or eccentricities) for the Laws and Parsons drop sizes. Oguchi concluded that the propagation parameters calculated at frequencies up to 34.8 GHz using Pruppacher-Pitter drop shapes did "not differ too much" from those calculated earlier for oblate spheroids. The scattering amplitudes used in the following calculations are for the Pruppacher-Pitter drop eccentricities.

The largest uncertainties in the applicability of the Pruppacher-Pitter drop shape arise from the assumption that the air surrounding the drop is not in a state of turbulence and the fact that drop collisions are ignored. Warner [4.13] has calculated that drops collide every few seconds in heavy rain. He also states that drop oscillations can persist for several seconds. Warner concludes that "raindrops are likely to take on a variety of shapes and orientations" and that "they are unlikely to follow closely a mean orientation or canting angle". Haworth and McEwen [4.14] have recently used a 20 GHz bistatic scatter link to study the Doppler spectrum of the incoherent forward scattered signal from rain, hoping to detect drop vibrations. They conclude that "suggestive but not conclusive evidence for the detection of drop vibrations has been presented...".

4.1.4 Canting Angle

As a raindrop falls, vertical wind gradients cause the orientation of the drops axis of symmetry (or minor axis) to shift from vertical. The angle between the axis of symmetry and vertical is called the canting angle. Brussaard [4.15], explained that this wind gradient is caused by friction with the ground and results in a decreasing wind speed with decreasing height in the region below 1 km in height. The vertical wind gradient is influenced by the height above ground, wind speed and type of terrain. Brussard's model for canting angle also showed a theoretical relationship between drop size and canting angle. Fig. 4.1, from [4.15] shows Brussaard's predictions for canting angle as a function of drop size and height above ground for a horizontal wind speed of 15 m/s.

Maher, Murphy and Sexton [4.16] later developed a theoretical model to explain the distribution of canting angles based on the effects of wind

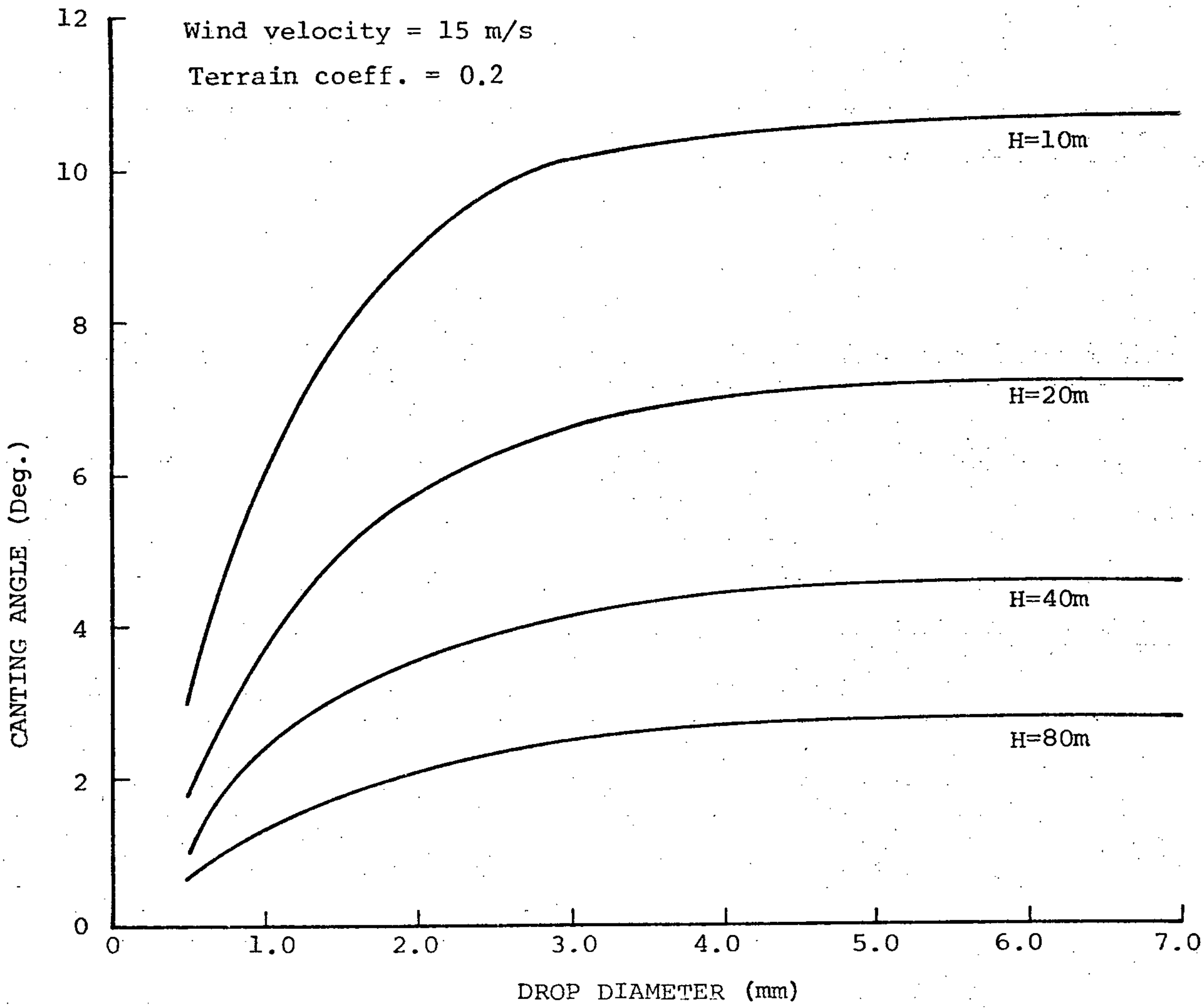

Fig. 4.1. Canting angle as a function of size and height.

gusting. Their model provided an explanation of the simultaneous observation of drops with positive and negative canting angles.

Very little data exist from the direct measurement of canting angles. The most notable investigation of canting angle was carried out by Sanders [4.23] using a "raindrop camera". In this study 463 photographs from two storms were collected and the canting angles were measured using a protractor. Results for the two storms showed that about 40% of the drops had a canting angle in excess of 15° and about 25% had negative canting angles in excess of −15°.

These theoretical models and limited experimental observations indicate that drops have a distribution of canting angles in natural rain. The theoretical models to predict canting angles include many variables, some of which are almost as difficult to measure as the canting angle itself. For these reasons it is not, at present, possible to make meaningfully accurate estimates of canting angle distributions for use in propagation predictions. As a result, most experimental investigators have simply used a variety of constant or "effective" canting angles in calculations for comparisons with experimental data, even though theoretical models have now been developed which can use more complicated canting angle models. Watson [4.17] discusses this problem of relating measurements to canting angle statistics. As a solution, Watson has defined an "equivalent mean canting angle as that value of canting angle in a constant-canting-angle rainfall model required to give an equivalent crosspolarization to that measured in the rainstorm." This definition will be used in this experiment. In this study, propagation parameters were calculated for constant or equivalent mean canting angles of 1, 2, 3, 4, 6, 8, 10, 15, 20, 30 and 45° (which is equivalent to the circular polarization case for any canting angle.)

Some qualititive improvement on the assumption of a constant canting angle can be made by considering the results of Oguchi [4.5] and Kobayashi [4.18]. These two papers show graphs of crosspolar isolation [XPI] (which, for practical purposes is equal to XPD [4.19], [4.18]) as a function of the canting angle standard deviation. Both graphs use the principal plane attenuations calculated by Oguchi [4.5], but for some reason, which is not readily apparent, the two sets of results differ by a small amount. The results show that XPI (or XPD) will improve for increasing standard deviation. Oguchi states that "when the standard deviation exceeds 30°, cross-polarization factors tend to improve as compared with those calculated for equioriented raindrops." He also concludes that "the results show that the canting angle of the equioriented model is replaced by the effective canting angle and the differential propagation constant is reduced by a multiplying factor. An example of the calculations based on the measured canting-angle distribution by Sauders [1971], shows that the correction to the differential propagation constant is 48%, and the cross-polarization factor for circular polarization, calculated at 34.8 GHz for a rainrate of 50 mm/h and for a propagation path of 1 km, improves about 7.5 dB as compared with that for equioriented model." Chu [4.1] also used a constant multiplying factor to correct results calculated for a constant canting angle model. A recent review by Olsen [4.20] includes a survey of methods used in predictive calculations to account for canting angle distributions. These results indicate that the calculations for a constant canting angle will be a worst-case condition compared to a distribution with the same mean but they could probably be corrected if adequate canting angle information were available.

4.1.5 Rain Temperature

Kinzer and Gunn [4.21] have published a comprehensive study which showed that raindrops can be much cooler than the surrounding air due to evaporation. They conclude that the drop temperature is within a few tenths of a degree Celcius of the temperature indicated by a ventillated wet bulb thermometer, regardless of drop size. It turns out, however, that in the higher millimetric range, the effect of drop temperature does not significantly effect the calculated attenuations. Olsen [4.10] has published results which indicate that the difference in attenuation for rain temperatures between 0 and 20°C are negligible in the frequency range above approximately 50 GHz. He concludes that "it is only for frequencies below about 15 GHz where temperature variations have a significant effect on the calculated value of A [attenuation], and even then the effect is not large".

Rogers and Olsen [4.22] have published a graph showing the variation in 70 GHz attenuation for rain temperatures between −5°C and 40°C. these results indicate that attenuation over the approximate range of 3°C to 23°C is, for all practical purposes, identical to the attenuation at the 20°C reference temperature. For this reason it appears to be possible to use any reasonable value for drop temperature in the frequency range used in this experiment. The scattering parameters used in the following calculations are for a drop temperature of 20°C.

4.1.6 Spatial Uniformity

It was shown in Section 3.1.1 that the rainrate during natural rain is not uniform horizontally. This will also mean that the drop distribution and canting angle will vary along a long propagation path. To include the effects of this horizontal meterological variability on long paths, investigators have used synthetic storm models and distributions of rain parameters within individual rain cells when predicting propagation effects, e.g. [1.85], [4.4], [4.24].

Fortunately, in this experiment, the physical length of the radar path is only 900 m. It is therefore reasonably accurate to assume, for calculation purposes, that the meteorological conditions along this path are uniform and can be characterized by the path average rainrate calculated from the five raingauges. When making comparisons to individual rain events, the validity of this assumption can easily be checked by comparing the results from the individual raingauges along the path.

4.2 Scattering Amplitudes

The forward scattering amplitudes presented in this section[2] were calculated using a field point-matching program developed by Dissanayake and Watson [4.25] using the following conditions:

1. Frequency = 74 GHz.
2. Pruppacher-Pitter drop shape eccentricities.

---

[2]Provided by Dr. P.A. Watson, University of Bradford, U.K.

3. Drop temperature = 20°C.

4. Refractive index = 3.6994 + j2.1824.

5. Angle of incidence = 90° (i.e. terrestrial path).

6. Laws and Parsons drop sizes.

The scattering complex amplitudes under these conditions for the drop principle planes are shown in Table 4.1.

Table 4.1 Forward Scattering Amplitudes at 74 GHz

Drop Diameter (mm)	$S_I(o)$		$S_{II}(o)$	
0.5	$1.67648 \cdot 10^{-2}$	$-j5.81169 \cdot 10^{-2}$	$1.69305 \cdot 10^{-2}$	$-j5.84513 \cdot 10^{-2}$
1.0	$3.70110 \cdot 10^{-1}$	$-j3.43414 \cdot 10^{-1}$	$3.81541 \cdot 10^{-1}$	$-j3.46684 \cdot 10^{-1}$
1.5	1.03925	$-j2.98682 \cdot 10^{-1}$	1.07658	$-j2.74903 \cdot 10^{-1}$
2.0	1.68310	$-j3.79032 \cdot 10^{-1}$	1.77801	$-j3.14879 \cdot 10^{-1}$
2.5	2.60981	$-j4.39117 \cdot 10^{-1}$	2.80529	$-j2.26872 \cdot 10^{-1}$
3.0	3.56138	$-j4.89027 \cdot 15^{-1}$	3.88261	$-j1.05223 \cdot 10^{-1}$
3.5	4.71177	$-j6.19467 \cdot 10^{-1}$	5.21626	$+j9.11839 \cdot 10^{-2}$
4.0	5.9625	$-j7.0845 \cdot 10^{-1}$	6.6288	$+j3.5173 \cdot 10^{-1}$
4.5	7.3685	$-j8.49 \cdot 10^{-1}$	8.240	$+j6.571 \cdot 10^{-1}$
5.0	8.932	$-j9.65 \cdot 10^{-1}$	9.953	$+j1.013$
5.5	10.6	$-j1.06$	11.8	$+j1.39$
6.0	12.4	$-j1.1$	13.8	$+j1.8$
6.5	14.0	$-j1.2$	15.9	$+j2.4$

4.3 Calculated Propagation Parameters

In this section, the scattering amplitudes will be used to calculate the copolar attenuation and phase shift, differential attenuation, differential phase shift, and XPD's for all of the meteorological conditions discussed in Section 4.1. The first step in the procedure is to calculate the principal plane attenuations and phase shifts. Principal plane complex attenuations (i.e. magnitude and phase) would be equal to the copolar attenuations for vertical and horizontal linear polarizations if all drops had zero canting angle. In this case, when all the drops are aligned and the transmitted polarizations are in the drop principal planes, there will also be no signal depolarization.

For nonzero canting angles, the transmitted polarization is linearly transformed to be parallel with the drop principal planes. After propagation through the anisotropic medium, the vectors are retransformed to yield the received vertical and horizontal signals. This procedure results in the elements of the medium transmission matrix (i.e. the propagation parameters assuming ideal antennas). From these results the differential attenuation and phase shift and the XPDs for both polarizations can be directly calculated.

4.3.1 Principal Plane Attenuations and Phase Shifts

The basic method for calculating the attenuation and phase shift for linear polarization parallel to the drop major and minor axes is attributed to Van de Hulst [4.26]. From [4.1], the equations are:

$$A_{I,II} = 0.434 \frac{\lambda^2}{\pi} \sum_{\substack{\text{Drop}\\\text{sizes}}} \operatorname{Re}\{S_{I,II}(0)\} N_D \cdot \Delta D \;..\; (\text{dB/km}) \tag{4.5}$$

$$\Theta_{I,II} = -36 \frac{\lambda^2}{4\pi^2} \sum_{\substack{\text{Drop}\\\text{sizes}}} \operatorname{Im}\{S_{I,II}(0)\} N_D \cdot \Delta D \;..\; (\text{deg/km}) \tag{4.6}$$

where:

- $S_{I,II}$ are from Table 4.1

- N_D are from (4.2) - (4.4)

- $\Delta D = 0.5$ as discussed in Section 4.1.2

- the summation is over the Laws and Parsons drop sizes (Section 4.1.2) For a zero canting angle the subscripts I and II are applicable for vertical and horizontal polarizations, respectively.

Hogg and Chu [4.27] note that the relationship between (4.5) and the traditional Medhurst [4.28] method for calculating copolar attenuation can be shown by the following relationship between the extinction cross section, Q, and the forward scattering function:

$$Q = \frac{\lambda^2}{\pi} \operatorname{Re} \{S(0)\} \tag{4.7}$$

Figs. 4.2 and 4.3 show the magnitudes and angles of the principal plane attenuations vs rainrate for the three drop size distributions discussed in Section 4.1.2.

The values calculated from (4.5) were compared to the results from Olsen's [4.9] $A = \alpha R^{\beta}$ equation. Values for α and β for 74 GHz were obtained by linear interpolation of Olsen's published values at 70 and 80 GHz. Comparisons were made for the rainrates in Section 4.1.1 which were in the range of the rainrates used in the regressions by Olsen for each of the drop size distributions in Section 4.1.2. The average value of A_I and A_{II} agreed with Olsen's results to within 3.7%, 6%, and 4.3% (percent of dB difference) for the Joss/Olsen Drizzle, M & P or Joss/Olsen Widespread and Joss/Olsen Thunderstorm distributions, respectively. The largest differences were all at the largest valid value of rainrate for each distribution, indicating that some of the difference is likely due to increasing error in the regression

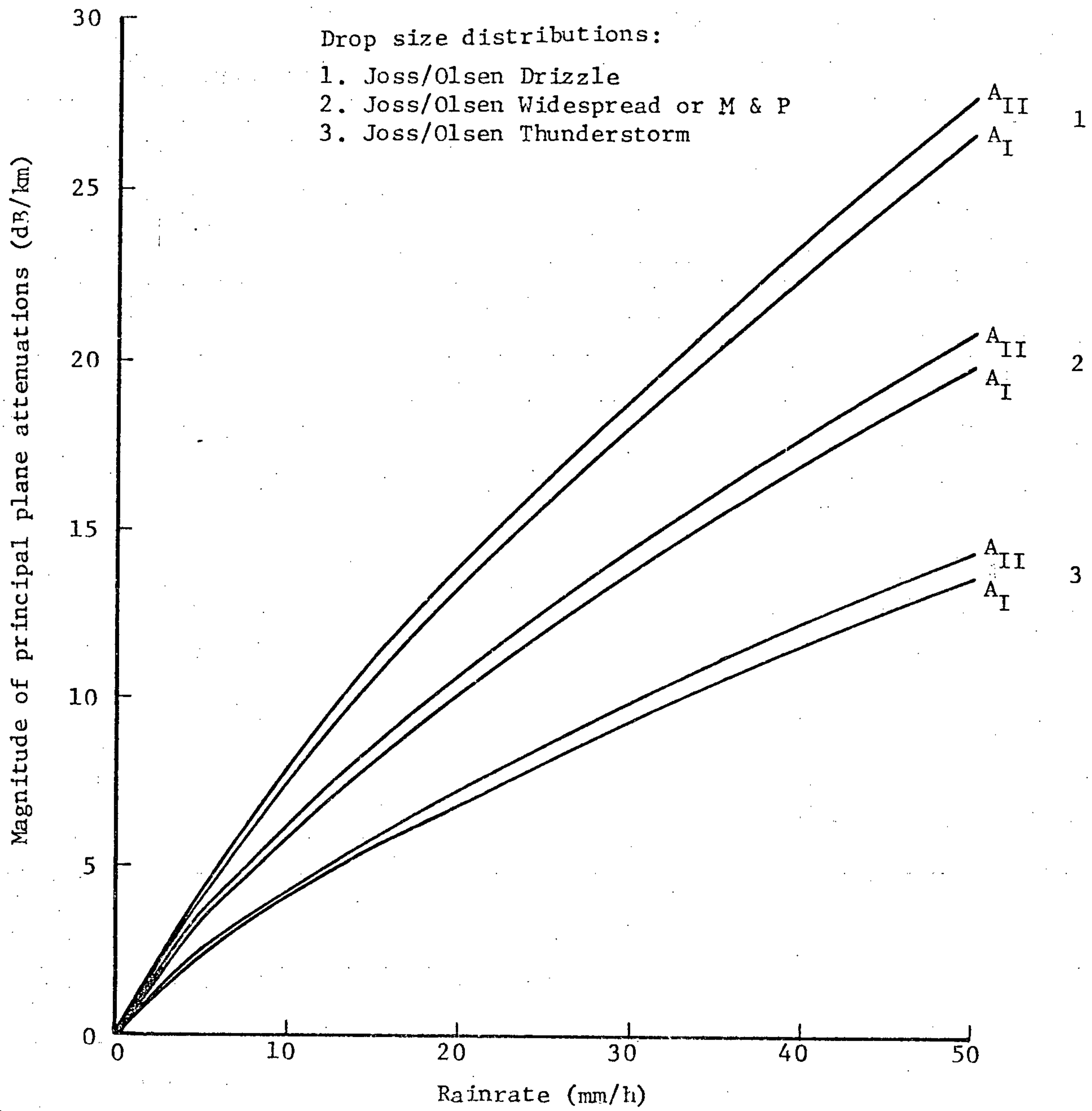

Fig. 4.2. Magnitude of principal plane attenuation vs. rainrate.

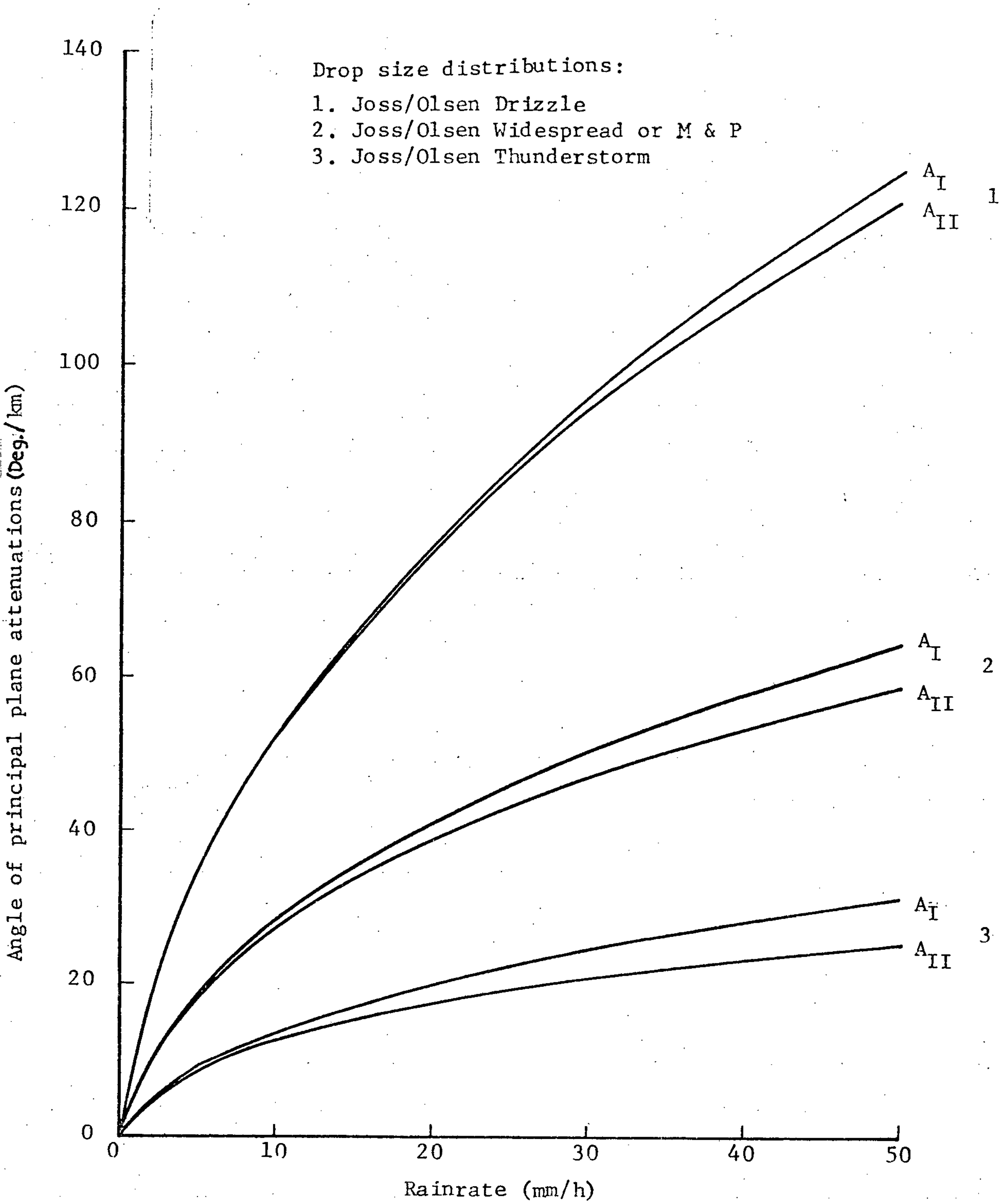

Fig. 4.3. Angle of principal plane attenuations vs. rainrate.

performed by Olsen. The agreement between the two sets of calculations is considered to be very good.

4.3.2 Propagation Parameters for Canted Raindrops

The propagation parameters for a rain medium composed of drops with a constant canting angle are calculated by transforming the transmitted polarization into the drop principal planes, applying the principal plane complex attenuations and then retransforming the polarizations back into vertical and horizontal components.

The geometry for this calculation is shown in Fig. 4.4.

The transformation from vertical and horizontal polarization to the principal plane directions (I and II) is given by:

$$\begin{bmatrix} E_I \\ E_{II} \end{bmatrix} = \begin{bmatrix} \cos\phi & -\sin\phi \\ \sin\phi & \cos\phi \end{bmatrix} \begin{bmatrix} E_V \\ E_H \end{bmatrix} \tag{4.8}$$

The reverse transformation, from the principal planes to vertical and horizontal is:

$$\begin{bmatrix} E_V \\ E_H \end{bmatrix} = \begin{bmatrix} \cos\phi & \sin\phi \\ -\sin\phi & \cos\phi \end{bmatrix} \begin{bmatrix} E_I \\ E_{II} \end{bmatrix} \tag{4.9}$$

If the subscripts TX and RX are used to designate the transmitted and received signals respectively and T_1 and T_2 are used to describe the complex attenuations over the transmission path, then the effect of the rain medium on waves linearly polarized in the I and II directions can be described by:

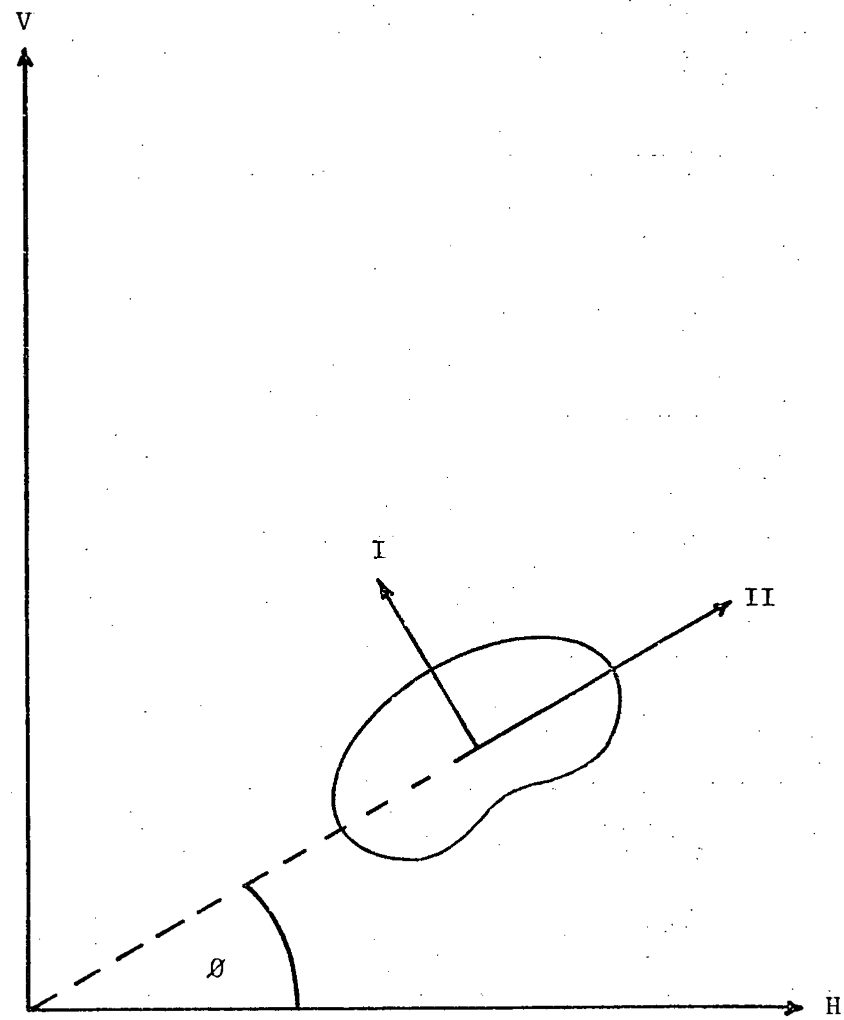

Fig. 4.4. Geometry for canted drop calculations.

$$\begin{bmatrix} E_{I_{RX}} \\ E_{II_{RX}} \end{bmatrix} = \begin{bmatrix} T_1 & 0 \\ 0 & T_2 \end{bmatrix} \begin{bmatrix} E_{I_{TX}} \\ E_{II_{TX}} \end{bmatrix} \tag{4.10}$$

The off-diagonal elements of this matrix are zero because no depolarization occurs for signals linearly polarized in the principal planes. Similarly, the path transmission matrix for vertical and horizontal polarizations can be written:

$$\begin{bmatrix} E_{V_{RX}} \\ E_{H_{RX}} \end{bmatrix} = \begin{bmatrix} T_{11} & T_{12} \\ T_{21} & T_{22} \end{bmatrix} \begin{bmatrix} E_{V_{TX}} \\ E_{H_{TX}} \end{bmatrix} \tag{4.11}$$

Using (4.8)-(4.10) to describe equation (4.11)

$$\begin{bmatrix} E_{V_{RX}} \\ E_{H_{RX}} \end{bmatrix} = \begin{bmatrix} \cos\phi & \sin\phi \\ -\sin\phi & \cos\phi \end{bmatrix} \begin{bmatrix} T_1 & 0 \\ 0 & T_2 \end{bmatrix} \begin{bmatrix} \cos\phi & -\sin\phi \\ \sin\phi & \cos\phi \end{bmatrix} \begin{bmatrix} E_{V_{TX}} \\ E_{H_{TX}} \end{bmatrix} \tag{4.12}$$

Solving for T_{ij} yields:

$$T_{11} = T_1 \cos^2\phi + T_2 \sin^2\phi \tag{4.13}$$

$$T_{22} = T_1 \sin^2\phi + T_2 \cos^2\phi \tag{4.14}$$

$$T_{12} = T_{21} = (T_2 - T_1)\,\frac{\sin 2\phi}{2} \tag{4.15}$$

These equations for T_{ij} are equivalent to those given by Neves and Watson [4.4] except that they formally use the ensemble average along the path of the canting angle. The differences are the substitution of $\cos^2\langle|\phi|\rangle$, $\sin^2\langle|\phi|\rangle$ and $\langle\sin 2\phi\rangle$ for the corresponding terms present in

(4.13)-(4.15). The formal use of the ensemble average is rigorously correct but is not used here to simplify notation and because only constant canting angles are actually used in the following calculations.

From (4.15) it can be seen that the depolarizing contribution of drops with positive and negative canting angles tend to cancel. This is the basic mechanism which explains the results of Oguchi [4.5] and Kobayashi [4.18] which show XPI improvements for large canting angle standard deviations (ref. Section 4.1.4). It is also important to note that if the sign of mean canting angle changes, the angles of T_{12} will change by 180°.

It should be pointed out that even though depolarization contributions from positive and negative canting angles cancel, the depolarized signals resulting from the two way propagation of a radar path will not cancel. This can be readily shown by resolving the signal transmitted into the anisotropic rain medium into components parallel to the drop axes, which lie in the principal planes of the medium. The two way propagation of the path, in the +Z and -Z directions, will yield results identical to (4.13)-(4.15) for the same total path length, assuming a homogeneous rain medium along the path.

Using (4.13)-(4.15), the following, directly measurable, propagation parameters can be defined:

$$\text{Differential attenuation} = 20 \log(|T_2|-|T_1|) \tag{4.16}$$

$$\text{Differential phase} = \arg(T_2)-\arg(T_1) \tag{4.17}$$

$$XPD_V = 20 \log \left| \frac{T_{12}}{T_{11}} \right| \tag{4.18}$$

$$XPD_H = 20 \log \left| \frac{T_{12}}{T_{22}} \right| \quad (4.19)$$

It is important to note that the copolar attenuations (T_{11} and T_{22}) are linearly related to the propagation path length, assuming uniform rain. It is, therefore, also possible to express differential attenuation and differential phase on a per kilometer basis. However, because T_{12} is a vector, rather than scalar, difference, it is not possible to precisely express T_{12}, and therefore XPDs, on a per unit length basis. (It should be mentioned that there is an approximation for XPD which uses a "small argument approximation" that results in an expression for XPD that is linearly related to path length [4.20].) For this reason, the following results for T_{12} and XPDs are given for the 1.8 km path length used in this experiment.

The following graphs show a representative sampling of the propagation parameters calculated at 74 GHz for the meteorological conditions described in Section 4.1. Differential attenuation, differential phase, magnitude of T_{12}, angle of T_{12}, and XPD_H vs rainrate are shown in Figs. 4.5, 4.6, 4.7, 4.8 and 4.9 respectively. XPD_H vs CPA_H is shown in Fig. 4.10.

It is very interesting to note that the XPD vs rainrate relation, shown in Fig. 4.9 is almost totally independent of drop size distribution. This occurs because the higher CPA for the distributions with smaller drops is almost perfectly compensated by a lower value of T_{12} as shown in Figs. 4.2 and 4.7.

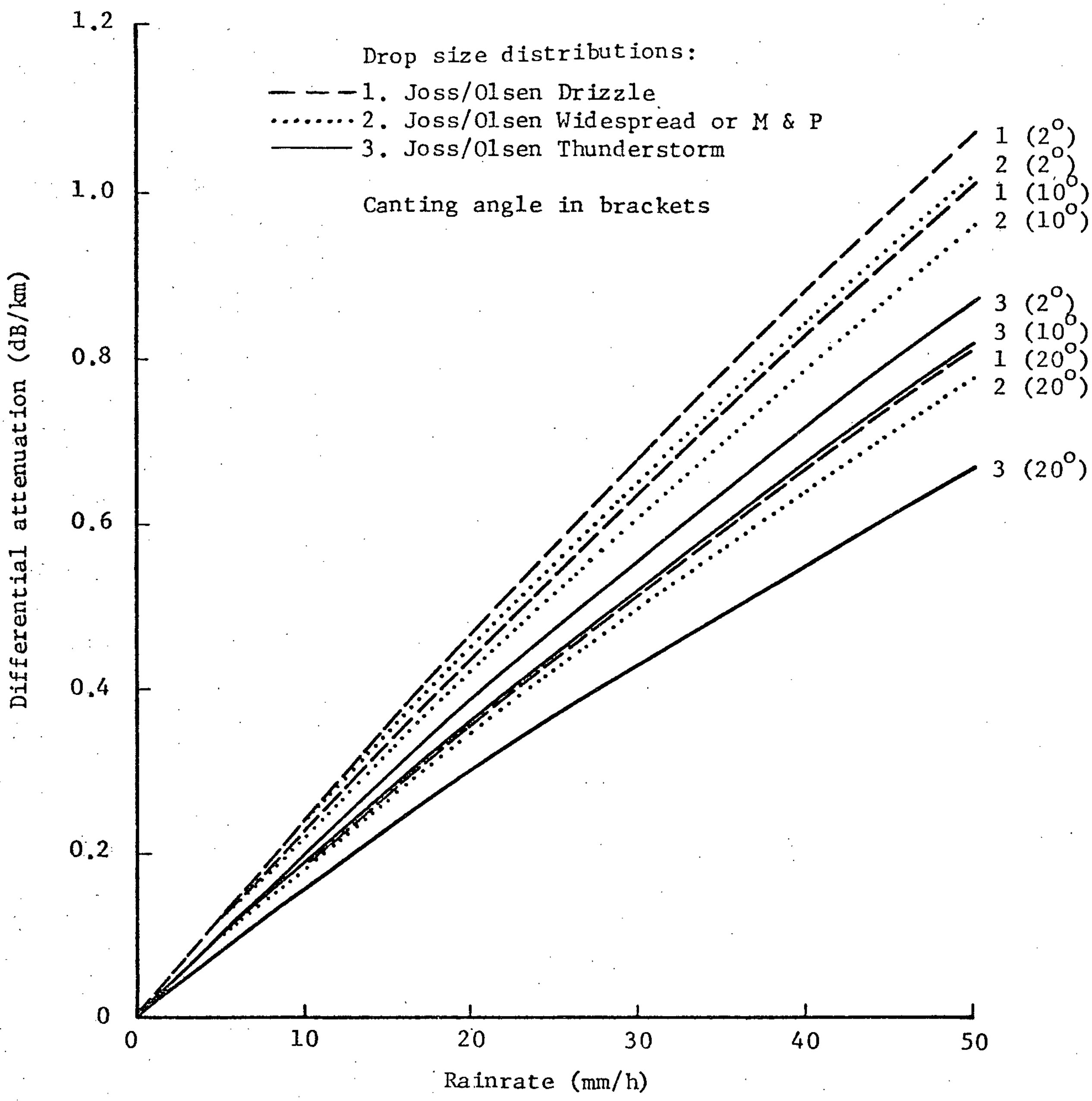

Fig. 4.5. Differential attenuation vs. rainrate and canting angle.

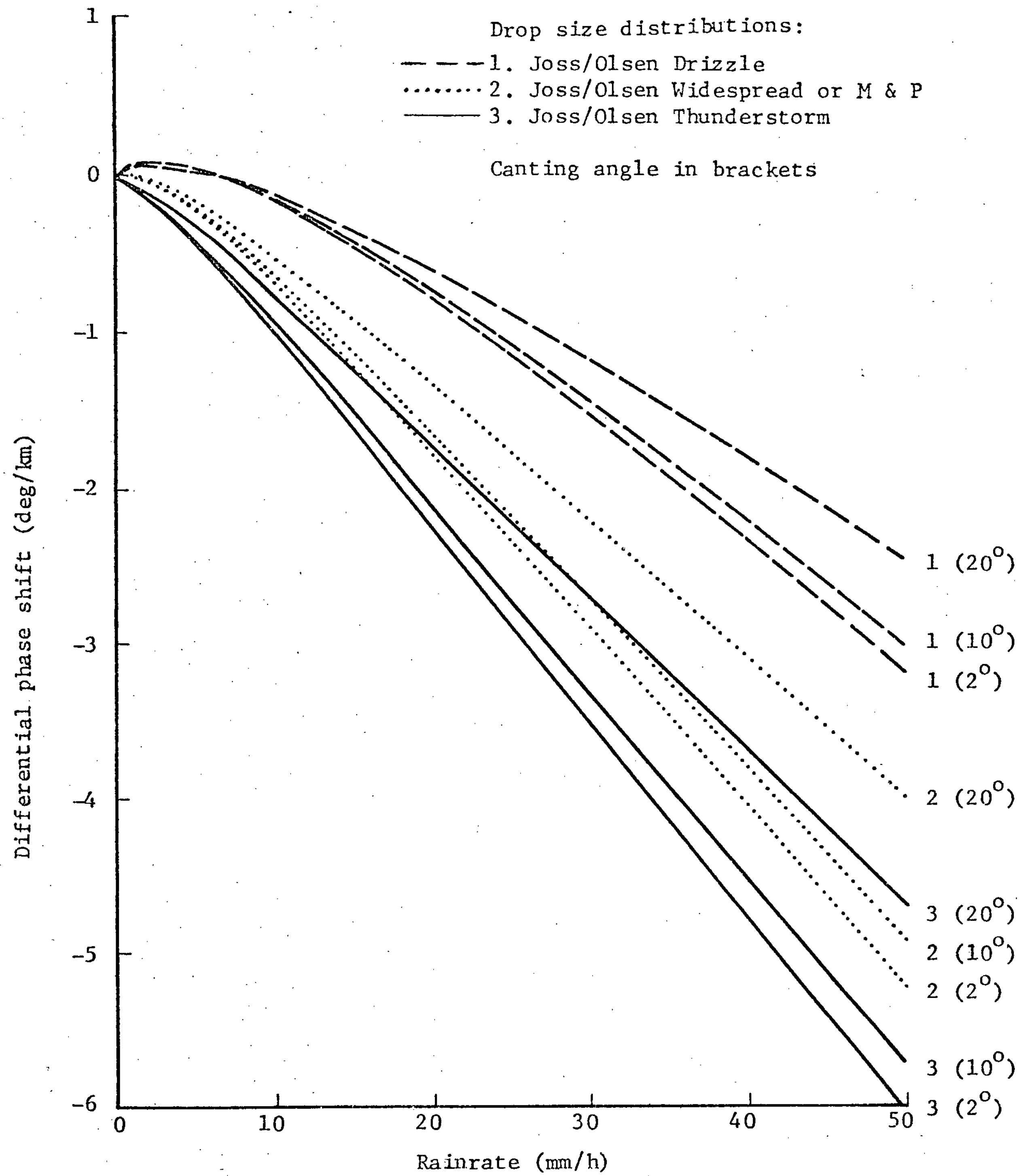

Fig. 4.6. Differential phase shift vs. rainrate and canting angle.

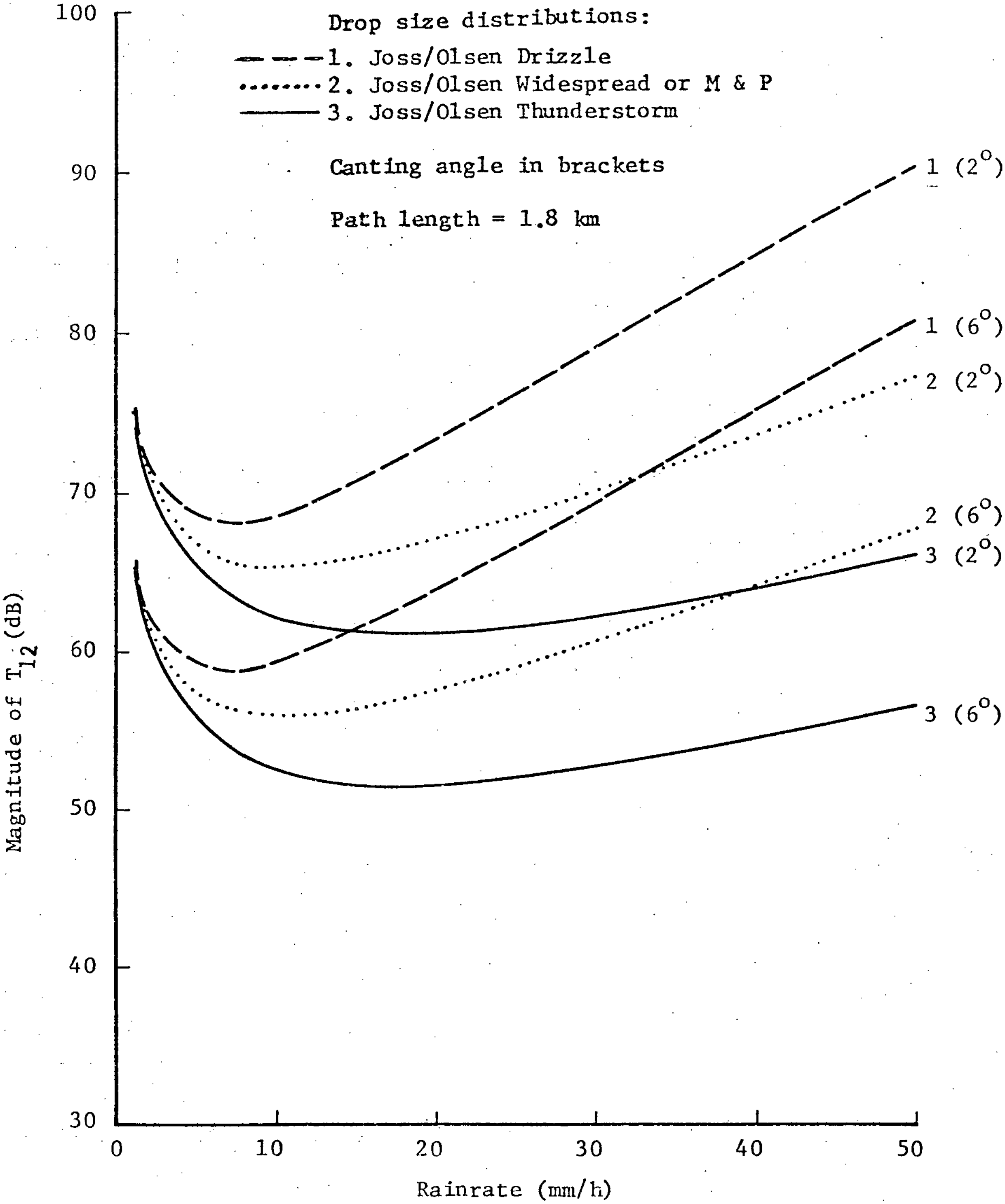

Fig. 4.7. Magnitude of T_{12} vs. rainrate.

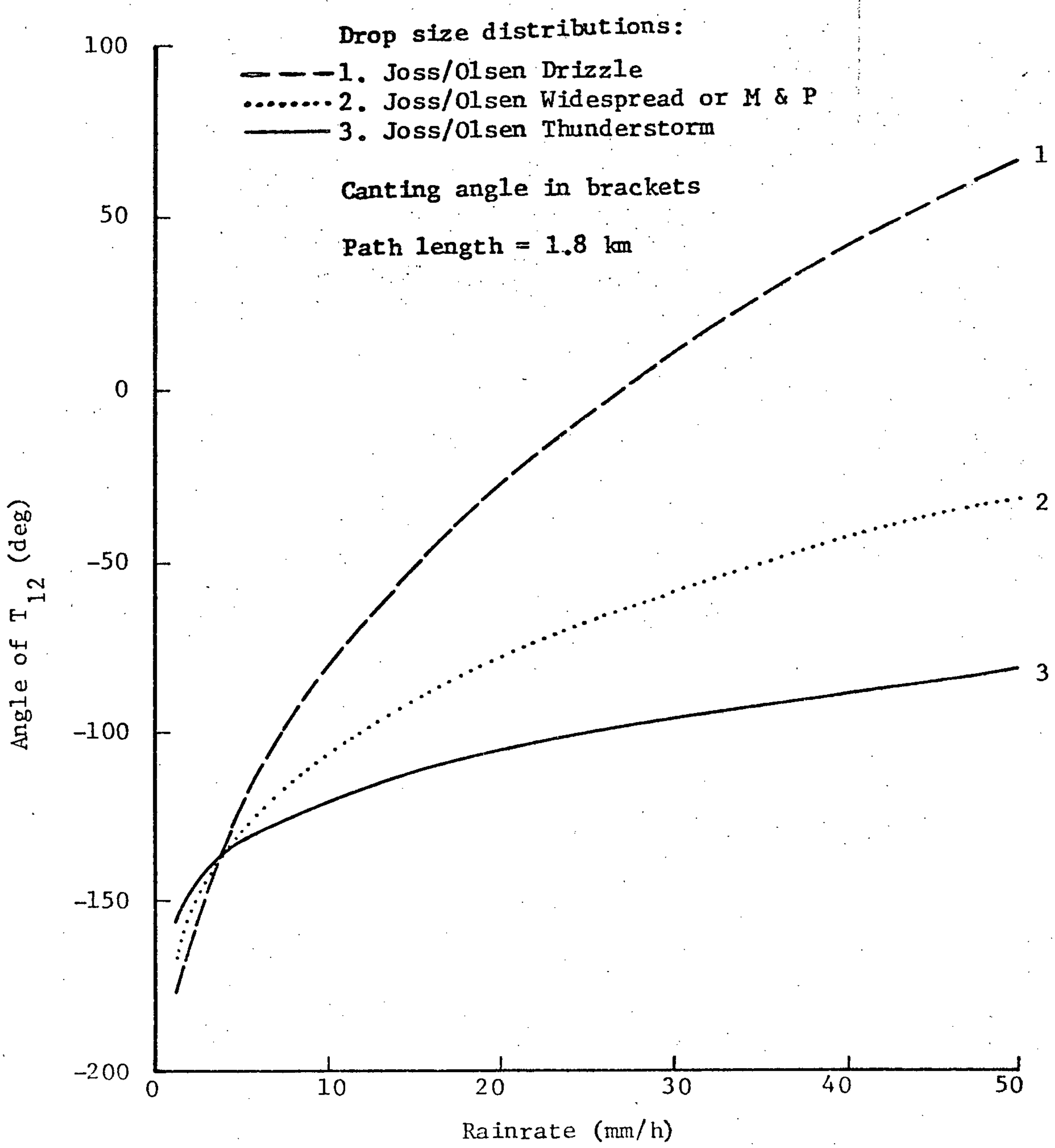

Fig. 4.8. Angle of T_{12} vs. rainrate.

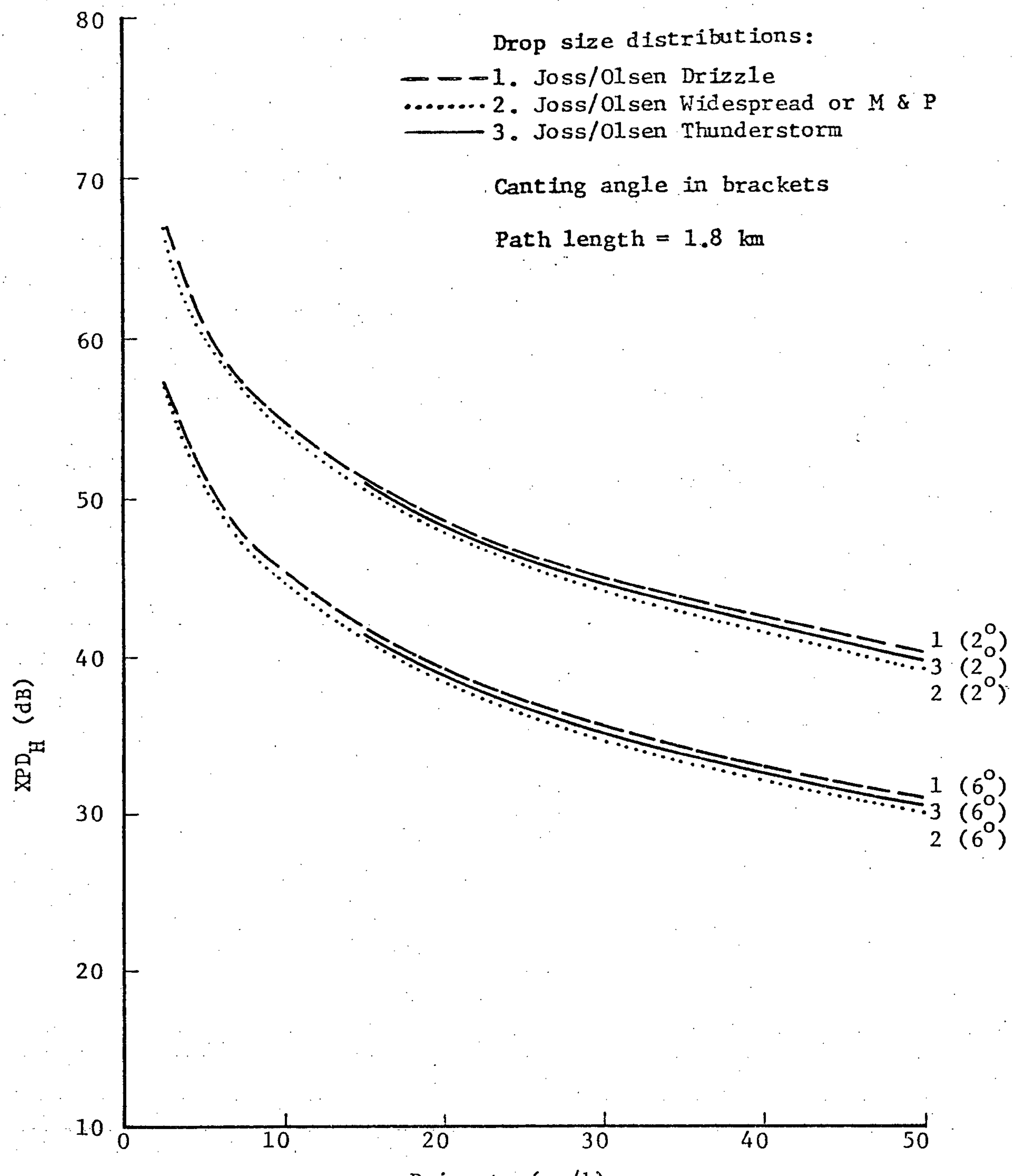

Fig. 4.9. XPD vs. rainrate for horizontal polarizations.

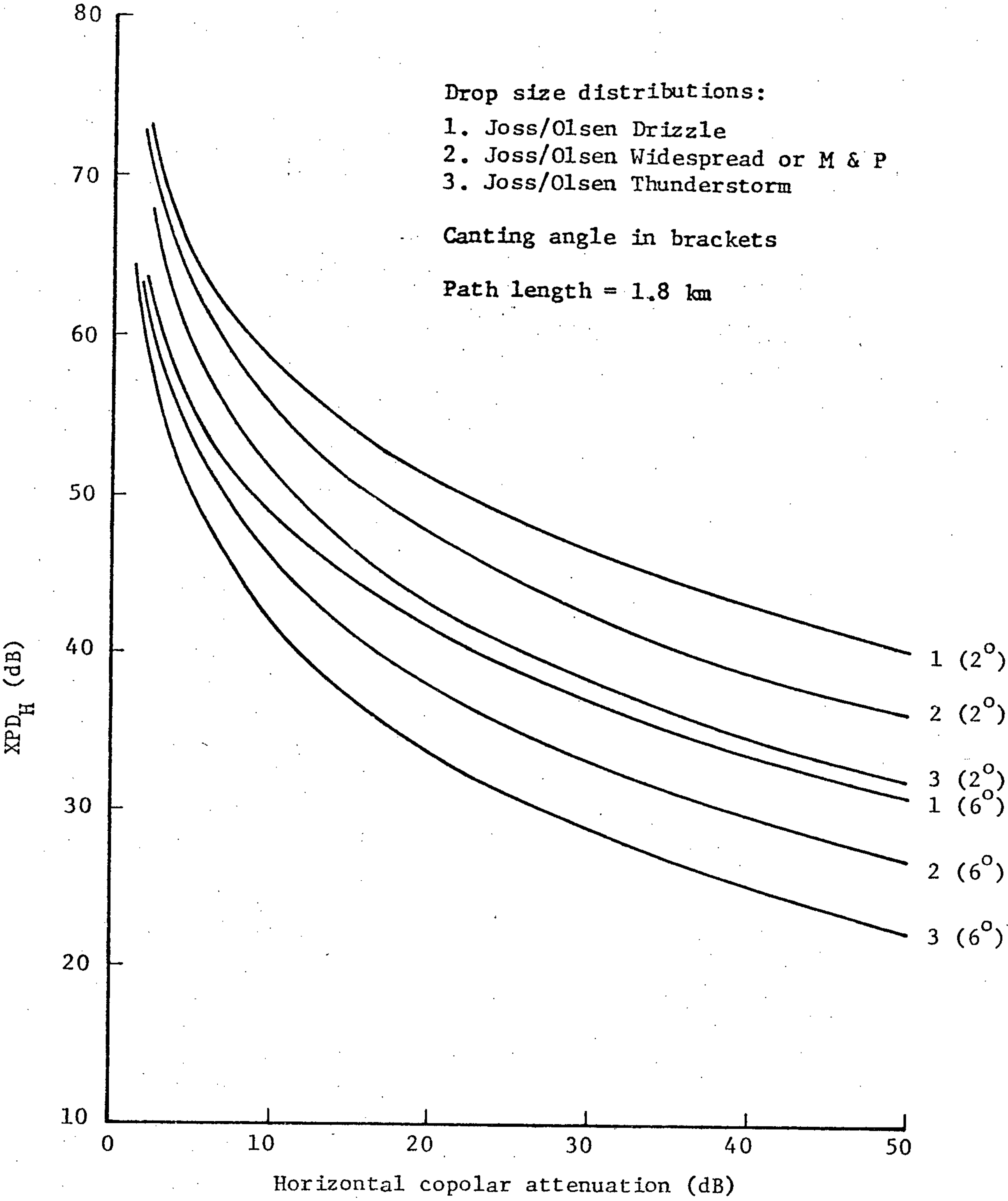

Fig. 4.10 . XPD vs. CPA for horizontal polarization.

4.4 Effects of Vertical Wind on Copolar Attenuation

Vertical components of wind velocity can significantly affect attenuation by changing the drop size distribution above the ground [4.28]. The distribution is altered because the vertical wind equally affects the different fall velocities of drops of different sizes. In this section, the effects of a constant vertical wind velocity component on CPA will be estimated in terms of the change in the attenuation/measured-rainrate relation. All other propagation parameters will, of course, also be similarly affected by a change in the drop size distribution.

There are at least two known causes for vertical wind velocities. Semplak and Turrin [4.29] state that "the classical picture for vertical wind movement at the interface of the cold front is updrafts associated with the retreating warm system and downdrafts in the advancing cold front". The second cause of vertical wind is changes in topography. From Caton [4.30], "... lee-wave vertical velocities of order 1 m sec^{-1} may occur over a substantial azimuth sector to at least 20 km downstream of even small hills 100 m high. The wavelength of such waves is typically 5-16 km..."

In still air, drops fall at a terminal velocity at which the forces of gravity and aerodynamic drag are in equilibrium. Terminal velocities for the standard drop sizes are given in Table 4.2 from [4.31]:

Table 4.2 Drop Terminal Velocities in Still Air

Drop Diameter (mm)	Terminal Velocities (m/s)
0.5	2.06
1.0	4.03
1.5	5.40
2.0	6.49
2.5	7.41
3.0	8.06
3.5	8.53
4.0	8.83
4.5	9.00
5.0	9.09
5.5	9.13
6.0	9.14
6.5	9.14

For cases where there is a constant vertical wind velocity, the steady-state vertical fall velocity is given by:

$$V_{\substack{DROP\\VERT}} = V_{\substack{DROP\\STILL\\AIR}} - V_{\substack{VERT\\WIND}} \tag{4.20}$$

where positive vertical wind velocities are defined to be upward.

To estimate the effects of a vertical wind velocity, it will be assumed that the vertical wind only occurs at heights below the rain cell and that the vertical wind has a constant velocity to heights well above the microwave path. These are reasonable assumptions when the vertical wind is created by topographical changes but are of course not strictly valid for vertical winds associated with weather fronts. For this vertical wind model, the drop size distribution leaving the raincell is the same as would be measured on the ground in the absence of vertical wind. It will also be assumed that the depth of the vertical wind region is sufficient for the drops to reach their steady state velocities. Under these assumptions, the actual rainrate measured at the ground will not be altered but the drop size distribution in the vertical wind region will be changed.

It should be mentioned that some other investigators [3.4], [4.32] appear to have approached this problem from the opposite point of view and assumed that the effect of vertical wind is to change the rainrate measured on the ground. This approach is not believed to be as realistic as the one described here because of the equal change in the vertical velocities for drops of different sizes.

Because the drop size distribution is inversely proportional to the drop velocity, the value of N_D for each drop size in the presence of vertical wind is now given by:

$$N_{D_{\substack{VERT\\WIND}}}(D) = N_{D_{\substack{STILL\\AIR}}}(D) \cdot \frac{V_{DROP_{STILL\ AIR}}(D)}{V_{DROP_{\substack{VERT\\WIND}}}(D)} \tag{4.21}$$

This calculation may only be valid for vertical wind velocities up to the smallest still air drop velocity considered (i.e. 2.06 m/s). At higher upward wind velocities, the drop motion would also be upward and then this simple model would predict a constantly increasing number of drops near the top of the vertical wind region.

Horizontal CPAs for distributions calculated from (4.21) at several wind velocities are shown in Fig. 4.11. For this analysis, it has been assumed that the drop size distribution above the vertical wind region is described by the Joss/Olsen Widespread or Marshall and Palmer distribution. Even though the vertical wind model used here is probably a simplification of

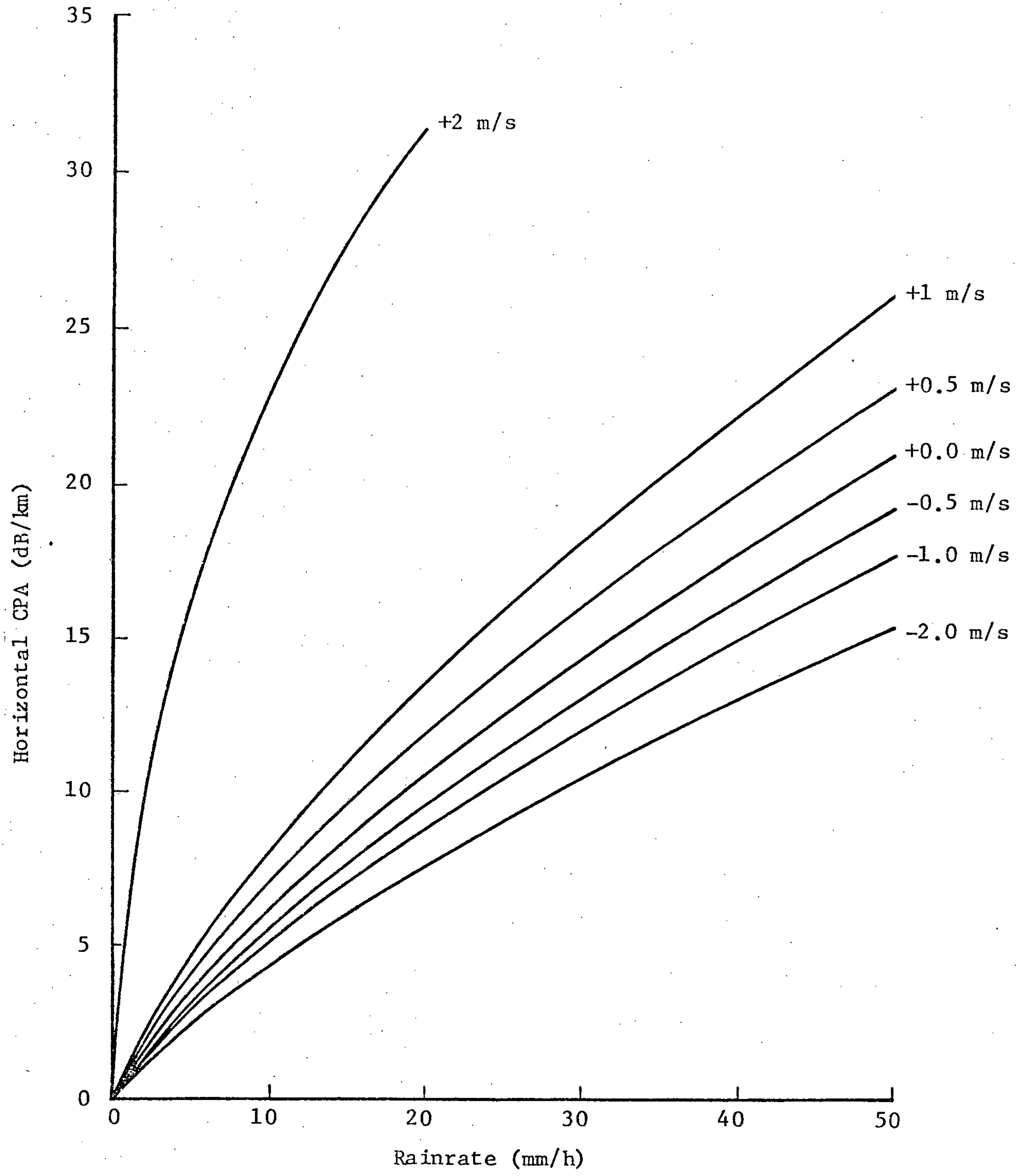

Fig. 4.11. Horizontal CPA vs. rainrate for different vertical wind velocities.

the actual conditions during natural rain, the results in Fig. 4.11 are considered to be sufficiently accurate for vertical velocities below 2 m/s for comparison to experimental results. These results illustrate the importance of measuring vertical wind velocities in propagation experiments.

4.5 Backscatter Calculation

Because a radar path is used in this experiment, a component of the received signal will result from backward scattering from the rain volume common to both antenna beams. The rain backscattered copolar signal, referred to as rain clutter, is a limiting factor in radar systems and accordingly has been studied theoretically and experimentally by several investigators. A calculation of the rain backscatter for this path will be made to estimate the relative level of this undesired signal compared to the signal returned from the reflector at the end of the path.

The type of radar configuration used in this experiment is referred to as a bistatic radar because the transmitting and receiving antennas are not collocated. Rain backscatter for a bistatic radar can be calculated from [4.33]:

$$P_R = P_T \frac{A_R A_T}{4\pi\lambda^2 R_1^2 R_2^2} \beta V \sigma(\theta) e^{-\alpha R_1 - \alpha R_2} \qquad (4.22)$$

where: P_R, P_T are the received and transmitted powers.

A_R, A_T are the antennas' effective areas

R_1, R_2 are the ranges to the rain volume common to the antenna beams

β is the scattering cross section per unit volume

V is the scattering volume

$\sigma(\theta)$ gives the angular properties of the scattering process

and $e^{-\alpha R}$ is the atmospheric attenuation

In this experiment, the ranges and antenna effective areas are equal. The scattering direction in this case is negligibly different from directly backward, so $\sigma(\theta)$ can be ignored if the backscatter cross section is used for β. Therefore, ignoring attenuation, this equation can be rewritten for this experiment as:

$$\frac{P_R}{P_T} = \frac{A^2}{4\pi\lambda^2 R^4}\,\beta\,V \tag{4.23}$$

The volume common to the 3 dB beamwidths of the two antennas is difficult to calculate exactly because of the complicated geometry of the volume and because small errors in the assumed pointing angles will result in large changes in this volume. An additional complication arises in this experiment because of the proximity of the building on which the reflector is mounted. On top of this building, a penthouse shields the rain volume behind and above the reflector from both antenna beams. The rain volume behind and below the reflector is shielded by the top floor of the building. Therefore, only the common rain volume in front of the reflector can backscatter a signal. The first point common to both antenna 3 dB beamwidths is approximately 660 m from the antennas. (If the building were not there, the farther common point would be about 1300 m from the antennas). The antenna 3 dB beamwidths are about 6.8 m in diameter at the reflector. This results in a common volume in front of the reflector or approximately 3000 m^3. (Without the building this would have been approximately 11000 m^3).

Calculated backscatter cross sections for frequencies between 20 and 100 GHz have recently been published by Crane [4.34]. These calculated results appear to agree well with the experimental results published by Currie, Dyer and Hayes [4.35] and Dyer and Currie [4.36]. Crane's calculated backscatter cross sections per unit volume at 73 GHz are appoximately $1.0 \cdot 10^{-3}\ m^{-1}$ and $1.1 \cdot 10^{-3}\ m^{-1}$ for the Laws and Parsons and Marshall and Palmer drop size distributions, respectively, at a rainrate of 50 mm/hr.

Using these results the linearly polarized, copolar backscatter can be calculated using (4.23). The results for this calculation, which ignores attenuation, predicts a received, rain backscattered signal approximately 92 dB below the transmitted signal at the antenna ports for a rainrate of 50 mm/h.

Attenuation was ignored in this calculation to allow a simplified comparison to be made between the received rain backscatter and reflector signals. Because of the geometry of the antenna beams' common volume, the major portion of the rain backscatter will originate within a short distance of the reflector. As a result the rain backscatter and reflector signal will experience very similar attenuations. This allows a direct comparison to be made between the calculated rain backscatter and the transmission loss calculation in Section 2.7. The calculated transmission loss including the reflector was approximately 39 dB, or 53 dB higher than the rain backscattered signal at a rainrate of 50 mm/h.

Another way to compare the signals from the rain and reflector is to compare the two scattering cross sections. For the rain volume, the scattering cross section is about 3 m^2 at 50 mm/h. The scattering cross section for a square flat plate with an edge dimension of "a" can be calculated from [2.50]:

$$\sigma = \frac{4\pi a^4}{\lambda^2} \tag{4.24}$$

Equation (4.24) gives a scattering cross section for the reflector of $7.5 \cdot 10^5$ m^2, or about 54 dB larger than the 50 mm/h rain cross section.

It is not possible to accurately estimate the magnitude of the depolarized backscatter at this frequency because very little is known about this phenomena. Shimabukuro [4.33] states that "The scattered wave is nearly completely polarized over the entire range of scattering angles. There is a slight depolarization at angles away from the forward and backscatter directions, with the maximum depolarization occuring near $\theta = 90°$." The only references which could be located containing quantitive information on depolarized backscatter were by Tsang and Kong [4.37], Oguchi [4.38] and Shupyatsky [4.39]. The first two of these references discuss aspects of the theory and do not contain any results which are directly applicable to this problem. However, the results in Tsang and Kong [4.37] do indicate that the depolarization cross section is much smaller than the copolar cross section for general random media. Results in [4.39] indicate that, in general, the depolarized backscattered signal is at least 30 dB below the copolar backscattered signal.

The results in this section show conclusively that copolar backscatter from rain is not a source of error for the radar path used in this experiment. While the situation for depolarized backscatter is far less certain, the available evidence indicates that this effect is much smaller than the copolar backscatter and therefore will not be a source of uncertainty in the experimental data.

5. DUAL-POLARIZED EXPERIMENTAL MODEL

This chapter describes a general theory and an experimental model developed to analyze the performance of a practical dual-polarized atomospheric propagation link including a crosspolar cancellation network. The major functions of this experimental model are to predict the dual-polarized link XPD performance and to separate, as far as possible, the depolarized signals resulting from the finite antenna/OMT isolations and the atmospheric propagation path. This type of analysis is especially important when comparing measured and predicted XPDs in this frequency range because the level of the rain depolarized signal is usually lower than the signal due to the uncancelled clear weather system isolation.

The basic idea of analyzing the XPD performance of a dual-polarized link by vector addition of all of the depolarized signals is not new and some references to previous work in this area are included in the next section. However, the model presented here has been extended to include a crosspolar cancellation network and the important effects of mismatches on the OMT ports. This model also incorporates a number of simplifications, approximations and a more descriptive notation which makes it easier to apply in a practical situation. Since they are not important in this experiment, the effects of antenna alignment errors and Faraday rotation are not included in this model.

A signal flow diagram for the dual-polarized experimental system to be described by this model is shown in Fig. 5.1. A number of simplifications, approximations and assumptions which were used to arrive at this system

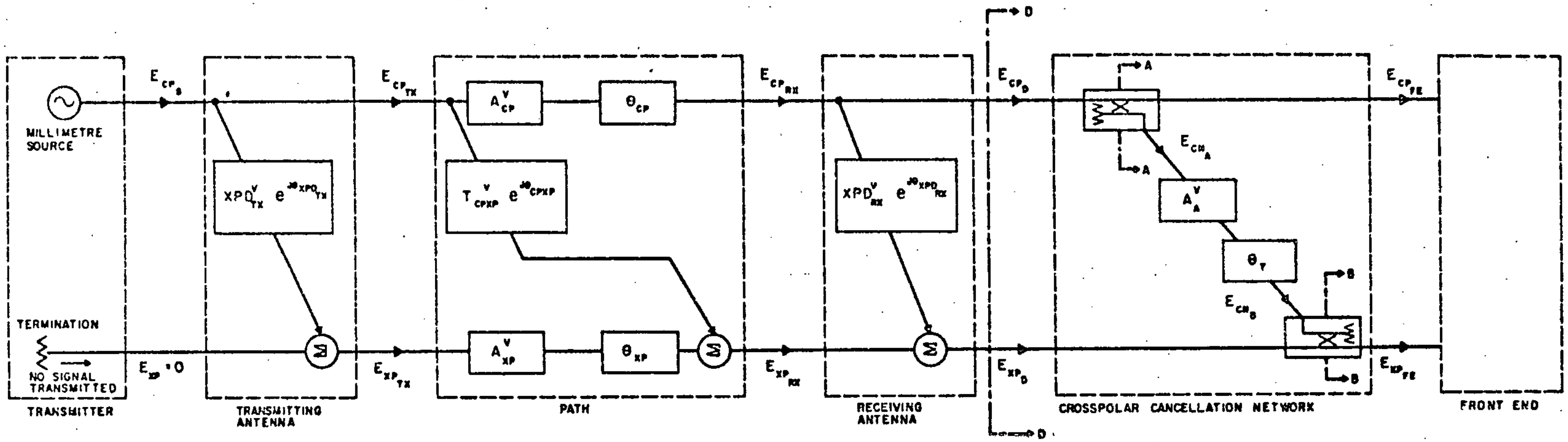

FIG. 5.1 EXPERIMENTAL SYSTEM SIGNAL FLOW DIAGRAM

diagram are discussed in Section 5.2. The symbols and notation in Fig. 5.1 are defined in Section 5.3. The equations describing the signals throughout the experimental system are discussed in Section 5.4. The rest of this chapter is devoted to the results and practical implications of the experimental model.

5.1 Previous Work

Several investigations have previously discussed some aspects of the problem of separating the antenna and path depolarized signals. Shkarofsky [5.1] and Shkarofsky and Moody [5.2] have included the effects of hydrometeors, antenna isolations, antenna misalignment and Faraday rotation in the XPD analysis of satellite links. Nowland and Olsen [5.3] have developed a simplified analysis of XPD including the same effects as discussed in the two previous references. Dintelmann [2.39] has investigated some aspects of the performance of dual-polarized links including crosspolar cancellation networks. Evans and Thompson [2.35] and Delogne and Sobieski [5.4] have presented graphs showing the error bounds on XPD measurements for conventional, uncancelled dual-polarized experimental systems.

5.2 Simplifications, Approximations and Assumptions

In order to reduce the complexity of the algebraic manipulations, only a single, fixed, transmitted polarization is included in the model. To facilitate the reading of the following equations, the two polarizations will be referred to as the copolar and crosspolar, rather than vertical or horizontal as is usually the case. These simplifications can be made without loss of generality up to the point where the actual meteorological parameters are substituted into the equations.

To make the following analysis feasible, it is necessary to make some assumptions and approximations. Most of these simplifications cause small losses, phase shifts and reflections to be ignored. Where it is felt to be necessary, a short explanation is included with the reasons why these approximations are justifiable.

Assumptions and approximations:

1. - the magnitude of the reflected signals throughout the cancellation network can be ignored. This is reasonable because the coupler ports are connected to either the well matched antenna ports or the isolators preceding the mixers.
2. - the effects of signals due to the finite directivity of the directional couplers are not significant. Even for relatively low directivities, this assumption is valid either because of the first assumption or because the undesired coupled signal is very much smaller than the desired signal.
3. - all signals are totally coherent. Only very small variations from ideal coherency occur due either to atmospheric turbulence or to multiple scattering.
4. - the planes A-A and B-B of Fig. 5.1 are the 3-port directional coupler reference planes and the signal coupled out of the main line is 10 dB lower in amplitude at planes A-A and B-B. It is also assumed that no

significant phase variation with frequency occurs as a result of the coupling at these reference planes.

5. - the phase shift introduced by the phase shifter has negligible variation with frequency over the bandwidth considered.

6. - the total length of the waveguide circuit between the directional coupler -10 dB ports can be considered as a section of uniform waveguide including the attenuator loss and phase shifter angle.

7. - the XPD of the antennas are independent of the atmospheric conditions i.e. near field antenna effects can be ignored.

8. - the clear weather attenuation and XPD of the propagation path are assumed to be zero and infinite, respectively.

9. - the waveguide losses before the directional couplers and the through-line losses of the couplers can be modelled as a reduction in receiving system sensitivity and otherwise ignored.

10. - the amplitude of the crosspolar signal depolarized to the copolar polarization can be ignored.

5.3 Notation and Units

The notation used in the following section was designed to reduce the number of times the symbol definitions would have to be consulted. This is accomplished in part by including the following descriptive subscripts.

Subscript definitions:

CP -copolar signal, i.e. signal of the same linear polarization (vertical or horizontal) as was originally transmitted.

XP -crosspolar signal, i.e. linear polarization orthogonal to CP.

CN -cancellation signal, referring to the signal in the attenuator - phase shifter line of the cancellation circuit.

CW -clear weather, value of a signal or quantity under clear weather conditions.

TX,RX -Transmitting and Receiving. When referring to signals, designates signals propagating on the path at the "output" of the transmitting antenna and at the "input" to the receiving antenna respectively. When referring to antenna parameters TX and RX refer to the individual antennas.

PATH -value of attenuation, phase shift or XPD resulting from the signal propagation over the path.

FE -front-end refers to signal at the input to the receiving system. These quantities are those recorded by the data acquisition system.

The units used in the following analysis are, whenever possible, those usually associated with the individual quantities. For example: attenuations are in dB, angles are in degrees and signal levels are in dB relative to the clear weather level of the received copolar signal. These familiar units and conventions are used when discussing data and analysis results and provide the most natural association with the actual measurement system. However, in the actual equations, where complex voltages are used, signal representation in dB is not convenient. To solve this problem, a superscript V is used, when necessary, on the attenuations and XPD's to designate a voltage ratio. For example, in the case of XPD:

XPD indicates the value in dB and XPD^V is the same value as a voltage ratio. i.e.

$$XPD^V \triangleq \left[10^{\frac{-XPD}{10}}\right]^{1/2} = \left[10^{\frac{-XPD}{20}}\right]$$

A similar situation arises when angles are written in the form $e^{j\theta_i}$, and in this case the angle is assumed to be in radians.

The symbol E is used to designate signals which are complex voltages, i.e. signals having a magnitude and angle.

Symbol definitions:

E_{CPCW_D} -refers to the clear-weather complex voltage of the copolar received signal at the input to the reference plane D-D of Fig. 5.1. E_{CPCW_D} is the 0 dB reference throughout the following analysis.

E_{CP_D} -the general received copolar signal at D-D, i.e. during anomolous propagation conditions.

E_{CP_S} -refers to the normalized signal generated by the millimetre source. This signal is normalized to include the clear weather transmission loss, i.e. antenna gains and dispersive path loss.

$E_{CP_{TX}}$ -refers to the copolar signal at the "output" of the transmitting antenna, i.e. at the path "input".

$E_{CP_{RX}}$ -refers to the copolar signal at the "input" to the receiving antenna after propagating the path.

$E_{CP_{FE}}$ -the copolar signal at the output of reference junctions A-A, i.e. the copolar signal at the front-end input.

E_{XPCW_B} -refers to the clear weather crosspolar received signal at the input of the reference junction B-B.

E_{XP_B} -refers to the same crosspolar signal under anamolous atmospheric conditions.

$E_{XP_{TX}}$ -refers to the crosspolar signal at the "output" of the transmitting antenna. This signal is due only to XPD_{TX}.

$E_{XP_{RX}}$ -refers to the crosspolar signal at the receiving antenna input.

$E_{CP_{FE}}$ -the signal at the output of reference junction B-B, i.e. the total signal into the crosspolar channel of the front-end. This will be the measured signal level of the crosspolar channel.

E_{CN_A} -refers to the copolar signal at the reference plane A-A which is coupled through the sampling coupler - 10 dB output, i.e. the cancellation signal before attenuation or phase shifting but after the - 10 dB coupling.

E_{CN_B} -refer to the cancellation signal at the input to the coupled port at reference junction B-B. This is the attenuated and phased shifted version of E_{CN_A} and includes the effect of both directional couplers.

XPD_{TX}, XPD_{RX}

XPD^V_{TX}, XPD^V_{RX} -refers to the crosspolar discrimination of the transmitting and receiving antennas (including the orthomode transducer) in dB and as a voltage ratio. These are for the transmitted polarization considered.

$\Theta_{XPD_{TX}}, \Theta_{XPD_{RX}}$ -refers to the angle of the phase shift added to the crosspolarized signal after it is depolarized by the antennas. The angle is relative to the copolar signal and includes any path length differences through the antenna for the two polarizations.

$\Delta\Theta_{XPD}$ -refers to the difference between $\Theta_{XPD_{TX}}$ and $\Theta_{XPD_{RX}}$ i.e. $\Delta\Theta_{XPD} = \Theta_{XPD_{TX}} - \Theta_{XPD_{RX}}$.

$\Delta\ell_{\Theta}$ -refers to the path length difference which causes

$\Delta\Theta_{XPD}$.

T_{CPXP}, T^{V}_{CPXP} -refers to the magnitude ratio of the path depolarized signal at the receiving antenna with respect to the copolar signal at the transmitting antenna. This is equal to the magnitude of T_{12} in the previous chapter.

Θ_{CPXP} -refers to the phase difference between the path depolarized signal at the receiving antenna and the copolar signal at the transmitting antenna. This is equal to the angle of T_{12}.

XPD_{CW}, XPD
XPD^{V}_{CW}, XPD^{V} -total system XPD including the effects of the antennas and path for clear weather and in general respectively.

A_{CP}, A^{V}_{CP} -excess path loss in (dB) and scalar voltage ratio, respectively for the copolar polarization, i.e. due to anamolous propagation only.

Θ_{CP} -electrical path length in degrees for the copolar polarization.

$A_{XP}, A^{V}_{XP}, \Theta_{XP}$ -similarly for the crosspolar polarization.

A_A, A^{V}_{A} -total attenuation in dB and as a voltage ratio, respectively, of the circuit connected between the - 10 dB coupler ports, including the attenuator phase shifter loss and waveguide loss.

Θ_{PS} -angle of the phase shift introduced by the phase shifter in degrees.

Θ_{ℓ} -total phase shift between reference planes A-A and B-B through the cancellation circuit excluding Θ_{PS}.

Θ_T -total phase shift between reference planes A-A and B-B through the cancellation circuit.

$\Theta_{D-A}, \Theta_{D-B}$ -the phase shift resulting from the waveguide connection between reference planes DD-AA and DD-BB respectively.

5.4 System Descriptive Equations

A signal flow diagram for the experimental system including most of the previous symbols was shown in Fig. 5.1. The following equations result directly from the previous definitions and Fig. 5.1.

The signal levels at the input to the front-end in terms of the signals at the receiving antenna orthomode transducer ports is given by:

$$\begin{bmatrix} E_{CP_{FE}} \\ E_{XP_{FE}} \end{bmatrix} = \begin{bmatrix} 1 & 0 \\ 0.1 \cdot A_A^V e^{j\Theta_T} & 1 \end{bmatrix} \begin{bmatrix} E_{CP_A} \\ E_{XP_B} \end{bmatrix} \tag{5.1}$$

This matrix completely describes the effects of the crosspolar cancellation network under the assumptions in Section 5.2.

The signal vectors at the receiving antenna ports can be expressed in terms of the transmitted signal by:

$$\begin{bmatrix} E_{CP_D} \\ \\ E_{XP_D} \end{bmatrix} = \begin{bmatrix} 1 & 0 \\ \\ XPD^V_{RX} e^{j\Theta_{XPD_{RX}}} & 1 \end{bmatrix} \begin{bmatrix} A^V_{CP} e^{j\Theta_{CP}} & 0 \\ \\ T_{CPXP} e^{j\Theta_{CPXP}} & A^V_{XP} e^{j\Theta_{XP}} \end{bmatrix}$$

$$\begin{bmatrix} 1 & 0 \\ \\ XPD^V_{TX} e^{j\Theta_{XPD_{TX}}} & 1 \end{bmatrix} \begin{bmatrix} E_{CP_S} \\ \\ 0 \end{bmatrix} \qquad (5.2)$$

These three matrices describe the effects of the receiving antenna, path and transmitting antenna.

One more matrix is required to include the phase shifts of the waveguide connections between the reference planes D-D, A-A and B-B. This phase shift will be important when analyzing the behaviour of the crosspolar cancellation network. (There is also a loss associated with these connections but it is negligible.) The receiving system in this experiment does not respond to the phases of the signals entering the front-end. For this reason, only the magnitudes of the copolar vector after plane A-A and the crosspolar vector after plane B-B are relevant. Accordingly, the phase shifts after plane A-A in the copolar line and plase B-B in the crosspolar line will be ignored. Thus, the following matrix includes all of the important phase shifts necessary to describe the signals after the receive antenna OMT:

$$\begin{bmatrix} E_{CP_A} \\ E_{XP_B} \end{bmatrix} = \begin{bmatrix} e^{j\Theta_{D-A}} & 0 \\ 0 & e^{j\Theta_{D-B}} \end{bmatrix} \begin{bmatrix} E_{CP_D} \\ E_{XP_D} \end{bmatrix} \tag{5.3}$$

In summary, these equations and the model in Fig. 5.1 describe the complex vector signals entering the receiver front-end in terms of the normalized transmitted signal. The general solution for the received signals is given by the product of the five matrices in equations (5.1), (5.2) and (5.3).

It should be noted that these expressions do not contain any terms not necessary for the practical "engineering" description of the experimental system. In the following sections, every effort will be made to consider only the equations necessary to analyze the system behaviour which is the topic of that section. Further assumptions and intermediate results will be used whenever possible to prevent unnecessary mathematical complexity.

5.5 Analysis Without the Crosspolar Cancellation Network

Without the crosspolar cancellation network, the signals at the input of the receiver will be E_{CP_D} and E_{XP_D}. In this case, the experimental system is described entirely by (5.2). Solving (5.2) for the received signals yields:

$$E_{CP_D} = E_{CP_S} A^V_{CP} e^{j\Theta_{CP}} \tag{5.4}$$

$$E_{XP_D} = E_{CP_S}[A^V_{CP}e^{j\Theta_{CP}} XPD^V_{RX}e^{j\Theta_{XPD_{RX}}}$$

$$+ T^V_{CPXP}e^{j\Theta_{CPXP}} + XPD^V_{TX}e^{j\Theta_{XPD_{TX}}} A^V_{XP}e^{j\Theta_{XP}}] \tag{5.5}$$

5.5.1 Contribution of Antenna XPD's to Clear Weather Crosspolar Signal Level

Both the transmitting and receiving antennas contribute to the crosspolar signal entering the receiver front-end. Reciprocity arguments show that the magnitude of the XPD coupling should be the same for transmitting or receiving using a particular antenna. The two antennas and orthomode transducers are identically constructed but minute mechanical differences, especially in the relative angular orientation of the side arm port and polarizing septum will cause differences in the individual antennas XPD values, as seen in Section 2.5. In addition, small variations in the angular alignment of the antenna assemblies and orthomode transducers will significantly affect the individual XPD's as discussed in Section 2.5.3.

It would be exceedingly difficult to quantify the complex XPDs of the antennas used in this experiment even using the most advanced millimetre wave measurement systems. The major difficulty would be isolating the effects of the antenna XPD angles (i.e. $\Theta_{XPD_{RX}}$ and $\Theta_{XPD_{TX}}$) from that of the free-space measurement set-up. Even measurements of the magnitude of the antenna XPD contain a significant uncertainty in this frequency range for antennas with XPDs as high as those used in this experiment.

For these reasons, the following analysis must use a range of values for the complex antenna XPDs. Reasonable estimates of the XPD magnitude range can be made based on the manufacturer's specifications, measurements made on the orthomode transducers connected back-to-back and measurements made on the complete antennas installed in the measurement system.

It is reasonable to assume that the differences between the angles of the two complex antenna XPD's can be any value between 0 and 360°. This is because path length differences of the order of a few millimetres can introduce relative phase shifts of up to 360°. In addition, these length dependent phase shifts will be a function of the operating frequency which is adjustable.

The following analysis, based on the results of the preceding section, will demonstrate how the interaction of the complex antenna XPD's can result in a wide range of values for the received crosspolar signal levels. In clear weather conditions, it can be assumed that T_{CPXP} is infinite, A_{CP} and A_{XP} are zero and that $\Theta_{CP}=\Theta_{XP}$ and can, therefore, all be ignored in this section of the analysis. Under these assumptions (5.5) can be rewritten:

$$E_{XP_D} = E_{XP_{FE}} = E_{CP_S}\left[XPD^V_{RX}\, e^{j\Theta_{XPD_{RX}}} + XPD^V_{TX} e^{j\Theta_{XPD_{TX}}}\right] \tag{5.6}$$

Equation (5.6) shows that during clear weather, in the system without a crosspolar cancellation network, the crosspolar signal entering the front-end has only two components, one resulting from each antenna.

To quantitively investigate the implications of (5.6) it will be assumed that:

1. $XPD_{TX} = 37$ dB
2. $XPD_{RX} = 33, 35, 37, 39, 41$ dB
3. $0 < \Delta\Theta_{XPD} < 360°$

Fig. 5.2 illustrates how the clear weather crosspolar signal level at the front-end input depends on the magnitudes and angles of the individual antenna XPDs. This graph shows that the received clear weather crosspolar signal level can vary between 6 dB higher than the individual antenna XPD's to infinity, depending on the relative XPD magnitudes and angles. The largest range of crosspolar signal levels occurs for the case when the magnitudes of the individual XPDs are equal.

The angle $\Delta\Theta_{XPD}=\Theta_{XPD_{TX}}-\Theta_{XPD_{RX}}$ will result from the different path lengths traversed by the two crosspolar signal components. Most of this differential path length will originate in the OMTs and will depend on the precise location of the depolarizing elements in the OMTs. (It is possible that depolarization occurs at more than one location within the OMT and that the individual OMT total XPDs result from the addition of more than one depolarized signal.) In this frequency range, the waveguide wavelengths are of the order of 5 mm. For these reasons it is not possible to make an accurate estimate of $\Delta\Theta_{XPD}$ from mechanical measurements of the OMTs. However, even though it is reasonable to assume that this angular difference is anywhere between 0 and 360°, it can be safely assumed that the path length difference is less than a few wavelengths. This is because the physical dimensions of the OMTs could not result in path length differences greater than a few millimetres.

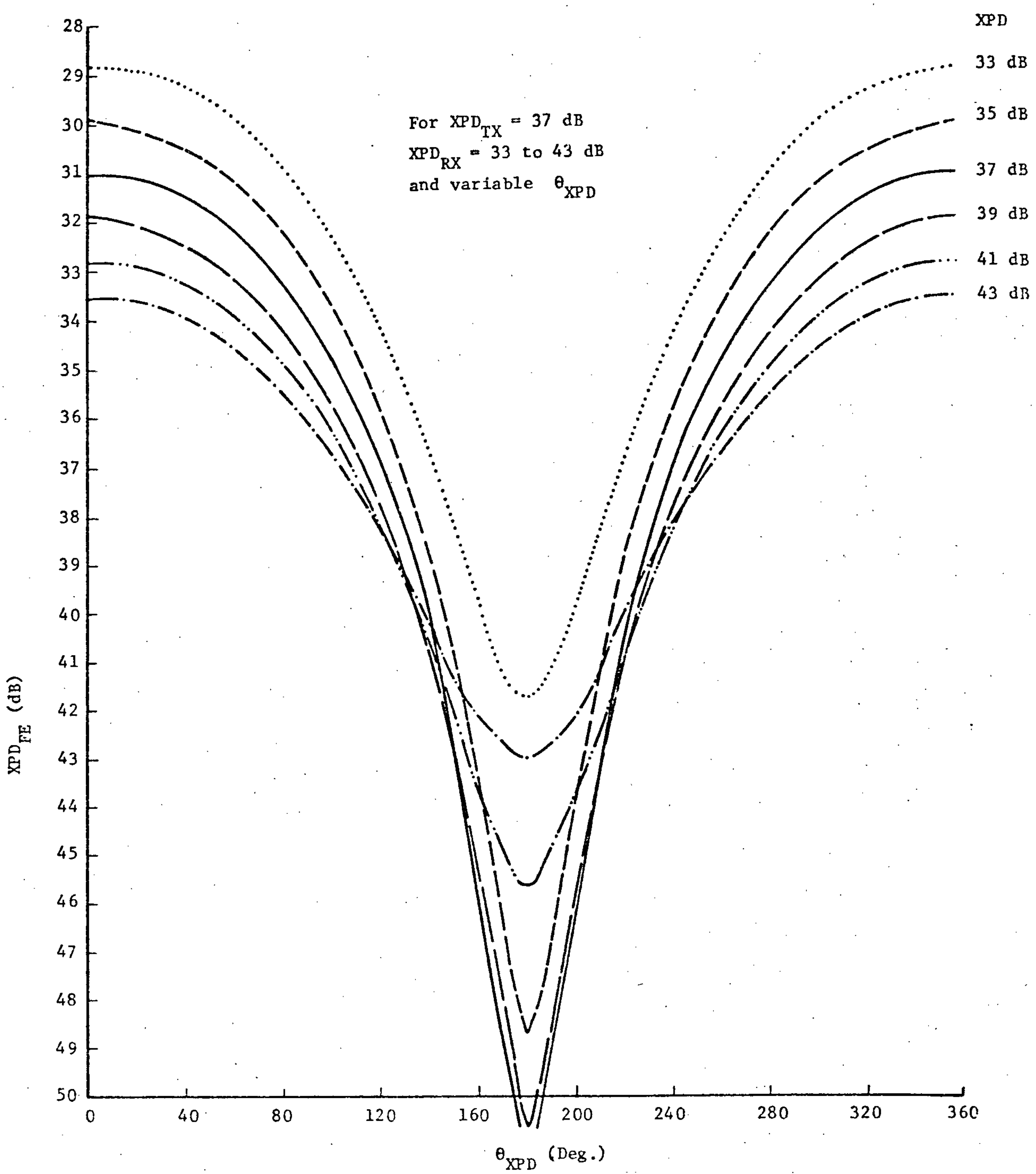

Fig. 5.2. Contribution of antenna XPDs to clear weather crosspolar signal at the front-end input.

Because $\Delta\Theta_{XPD}$ results from a path length difference, this angle will be a function of the operating frequency. If the physical path length difference creating $\Delta\Theta_{XPD}$ is denoted $\Delta\ell_\Theta$ the change in $\Delta\Theta_{XPD}$ at two different frequencies will be given by:

$$\left(\Theta_{XPD_{TX}} - \Theta_{XPD_{RX}}\right)\Big|_{f_1} - \left(\Theta_{XPD_{TX}} - \Theta_{XPD_{RX}}\right)\Big|_{f_2}$$
$$= \left(\beta(f1) - \beta(f2)\right)\Delta\ell_\Theta \qquad (5.7)$$

From (5.7) it is seen that the x-axis in Fig. 5.2 could be replaced by a frequency scale if $\Delta\ell_\Theta$ was known. Alternately, if the variation in the crosspolar signal level with frequency was measured, it would be possible to calculate the effective $\Delta\ell_\Theta$.

Fig. 2.35 is an example of this type of measurement. Both curves in this graph show a frequency response similar to that predicted by Fig. 5.2. However, a simple analysis will show that these responses cannot be satisfactorily explained from the results in this section. This is because these variations could only result from longer path lengths than those which could arise within the OMT s. To demonstrate this conclusion, it will be assumed that the path length different results from both OMTs is less than or equal to 2 cm. Using a 2 cm differential path length and assuming the path length difference occurs in rectangular waveguide propagating the TE_{10} mode, (5.7) predicts a 360° change in $\Delta\Theta_{XPD}$ for a frequency change from 62.8 to 75 GHz. This frequency change is much larger than that shown in Fig. 2.35 and therefore the observed effect must be due to another cause. In the next section it will be shown that the variation in crosspolar level in Fig. 2.35 probably arises from a mismatch within the back-to-back OMT circuit.

The klystron used in this experiment can be tuned over a frequency range from approximately 73.0 to 74.5 GHz. Over this frequency range (assuming TE_{10} mode), the change in $\Delta\Theta_{XPD}$ is approximately 15°. Fig. 5.2 shows that this will result in a change of only a few dB in the crosspolar signal level. Accordingly, in the following sections, the effect of changes in $\Delta\Theta_{XPD}$ due to frequency variation over the klystron tuning range (i.e. in Figs. 2.35, 2.36 and 2.38), will be ignored.

5.5.2 Effect of Reflected Signals on the Clear Weather Crosspolar Signal Level

The experimental results presented in Section 2.5 showed that the frequency variation of the crosspolar signal level at the front-end input was very dependent on the impedance connected to the orthomode transducer rectangular ports. No references to this phenomenon could be found in the literature and the antenna manufacturers did not have any explanation for these observations. It is believed that this impedance sensitive behaviour of the dual-polarized system can be explained using the model depicted in Fig. 5.1 with some additional clarification of the orthomode transducer operation.

5.5.2.1 Basic OMT Operation

Attempts to find OMT references with a mathematical description of their operation or mention of this mismatch sensitive behaviour have been unsuccessful. The OMT references which were located [5.5], [5.6], [5.7] contained only empirical discussions of OMT operation.

Fig. 5.3 shows the construction of the OMTs used in this experiment. This figure shows the basic OMT components and principals of operation [5.6].

Some aspects of the orthomode transducer operation will be quickly reviewed here to explain the expansion of the model required for this section of analysis. For simplicity, only the transmitting antenna OMT effects will be considered in this section. However, because the OMTs operate reciprocally, the entire discussion in this section applies equally well to the receiving OMT or to the combined pair of OMTs. If the transmitting signal is applied to the through arm port on the transmit OMT, almost all of this signal will leave the OMT via the antenna port unaffected by the septum and polarized in the copolar direction. Because the cross arm (or side arm) port is beyond cutoff for this polarization, virtually none of this copolar signal is coupled to the cross arm port. Small mechanical imperfections, principally in the alignment of the conducting septum, will create a small depolarized signal propagating in the circular waveguide within the OMT. This signal is generally considered to leave the OMT via the antenna port. However, the cross arm port, which is located after the septum in the direction of propagation, should also couple this depolarized waveguide mode. Measurements made on the OMTs used in this experiment showed that this, indeed, did occur

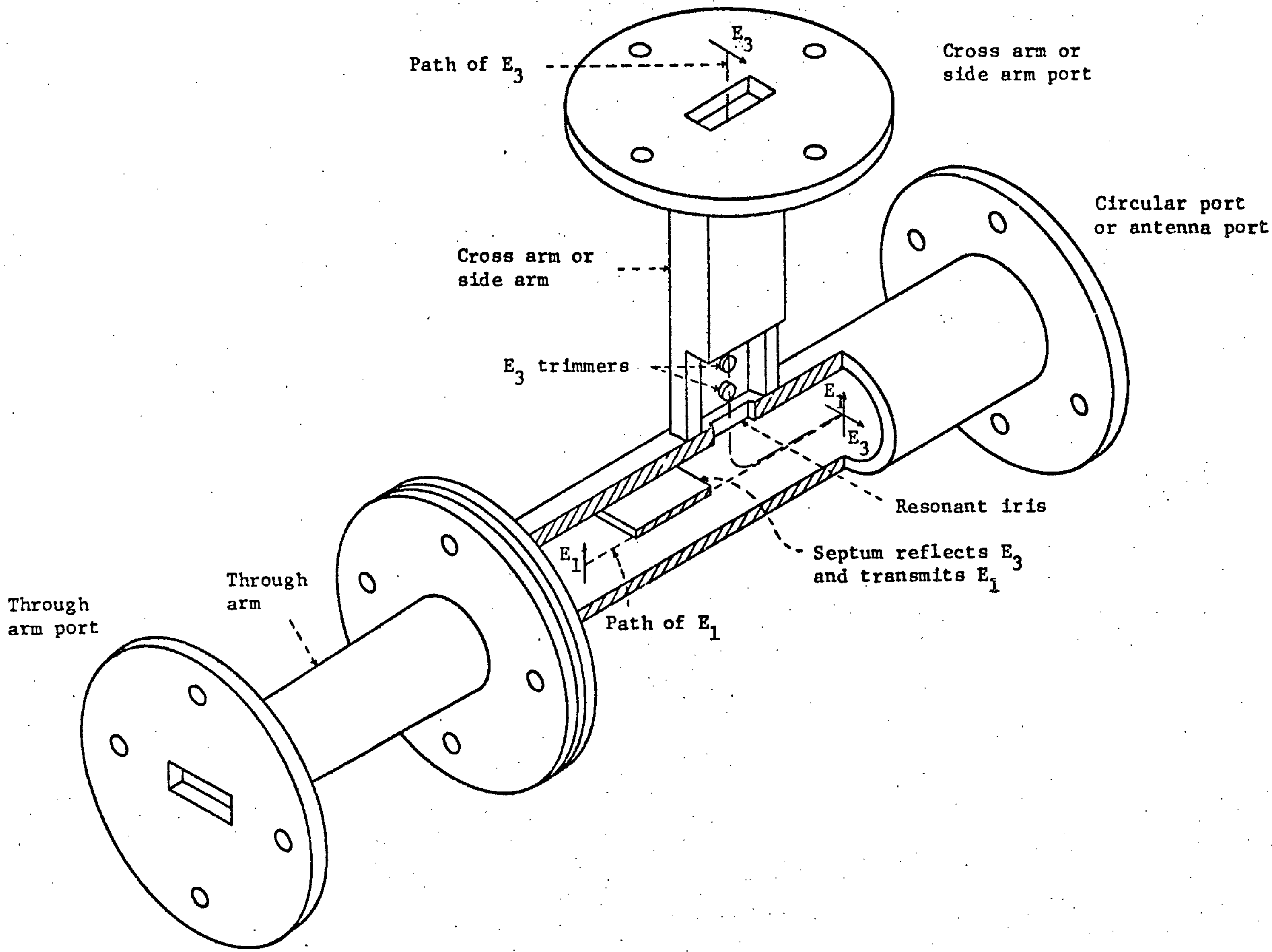

Fig. 5.3. Orthomode transducer construction and operation.

and that the crosspolar signal amplitude at the side arm and antenna ports were approximately equal. (Exact comparison could not be made because these measurements could only be performed with the OMTs back-to-back and the signals due to each OMT cannot be separated in this configuration.) If the transmitted signal is applied to the cross arm port, a similar situation occurs. In this case, approximately half of the crosspolar signal generated at the rectangular-circular waveguide junction propagates unimpeded past the septum into the through arm port.

This effect can be included in the model of Fig. 5.1 in two ways, depending on the directional properties attributed to the summing junctions in the OMT model. The directional properties of these summing junctions were not previously considered because they are unimportant if the experimental system is perfectly matched. If the summing junctions in the OMT models are assumed to be directional, the depolarized signal of amplitude $XPD^{V} e^{j\Theta_{XPD}}$ only couples to the antenna port. In this case, the OMT model requires an additional coupling element and directional summing junction which will account for the signal leaving the cross arm. This model configuration with the two coupling coefficients, XPD_{TX_1} and XPD_{TX_2}, is shown in Fig. 5.4(a). If the summing junction is considered to be bidirectional, the OMT can be modelled as shown in Fig. 5.4(b). Model (a) is more general and can include different couplings in each direction. Model (b) is simpler and more closely describes the actual OMT operation. For these reasons, model (b) will be used and it will be assumed that the OMT summing junctions in Fig. 5.1 are bidirectional. It should also be noted that the XPDs (power) in model (a) should be double that in model (b). However, to simplify the equations and

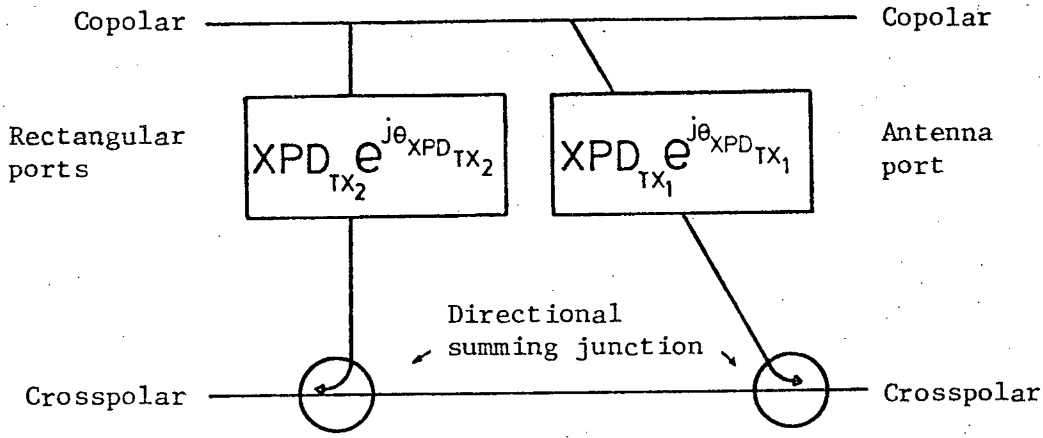

(a)

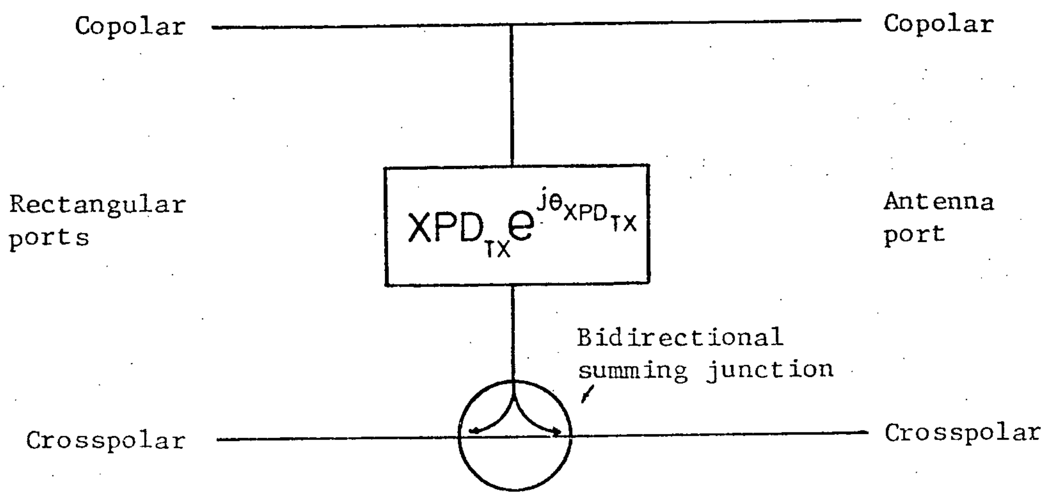

(b)

Fig. 5.4. OMT model options.

to conform to the usual definition of XPD, it will be assumed that the signal travelling in each direction from the bidirectional junction has amplitude XPD^{V}_{TX}.

5.5.2.2 Calculated Results and Comparisons to Experimental Data

If the crosspolar rectangular port is mismatched, another crosspolar signal component will be propagated in the direction of the receiver. The signal flow diagram for the mismatched transmit OMT model is shown in Fig. 5.5. A complex reflection coefficient Γ_L, completely describes the mismatch connected to the rectangular crosspolar OMT port. E_{XP_R} is the reflected signal at the OMT-load junction travelling in the direction of the receiving antenna. Plane C-C located at the bidirectional junction will be used as a local reference.

The reflected signal will propagate through plane C-C with negligible coupling in the "direction" of the copolar OMT ports (i.e. the reflected signal behaves like a transmitted signal injected into the side arm port). Now, the crosspolar signal at the output of the transmit antenna, designated $E'_{XP_{TX}}$, contains two components described by:

$$E'_{XP_{TX}} = XPD^{V}_{TX}\, e^{j\Theta_{XPD_{TX}}} + E_{XP_R}\, e^{-j2\beta\ell_R}$$

$$= XPD^{V}_{TX}\, e^{j\Theta_{XPD_{TX}}} \left(1 + \Gamma_L e^{-j2\beta\ell_R}\right) \qquad (5.8)$$

The angle of the second signal component with respect to the first at plane C-C is:

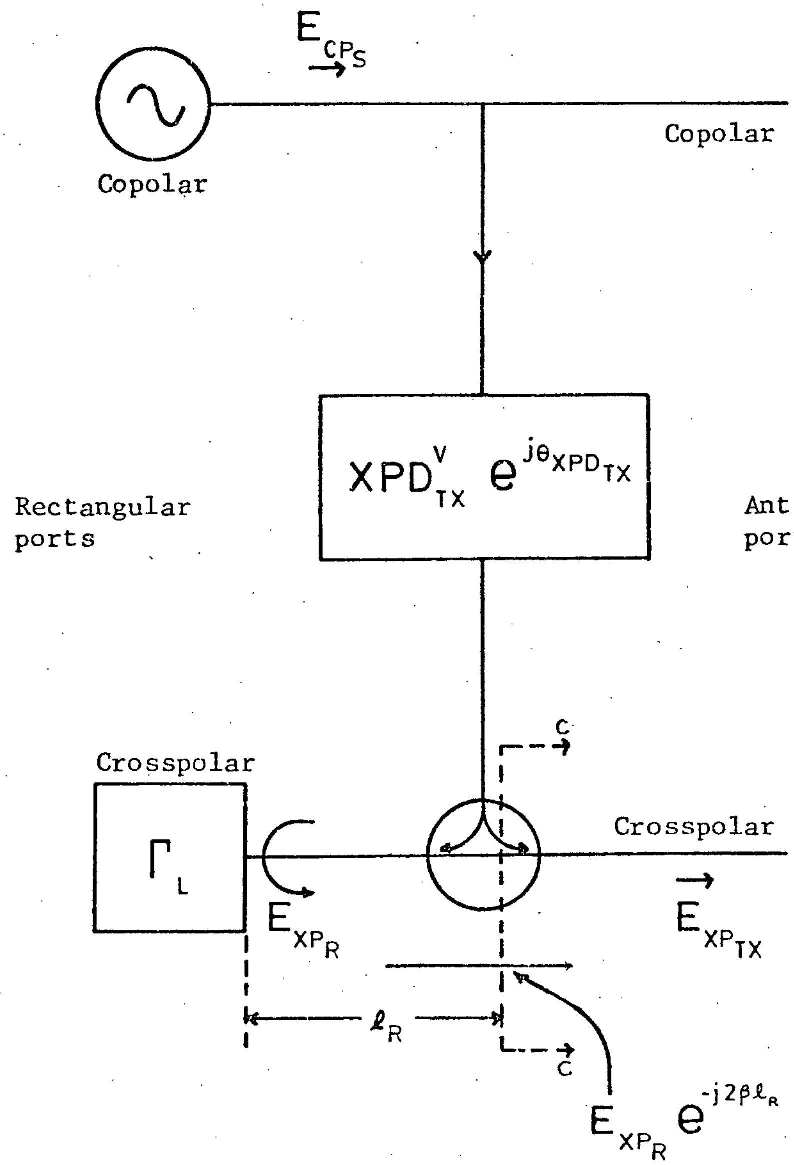

Fig. 5.5. Mismatched transmit OMT signal flow diagrams.

$$\Theta_R \stackrel{\Delta}{=} \mathrm{Arg}[\Gamma_L] - 2\beta\ell_R \tag{5.9}$$

where ℓ_R is the length of the waveguide connection between the OMT junction and the load represented by Γ_L. In practice, ℓ_R is much longer than several wavelengths and accordingly, $\mathrm{Arg}[\Gamma_L]$ variations with frequency can be ignored for practical purposes.

The effects of the mismatch will be illustrated by calculating a new, effective complex XPD_{TX} which includes the reflected signal generated at the crosspolar rectangular OMT port. Previously, i.e. without any mismatch:

$$XPD_{TX}^{V}\, e^{j\Theta_{XPD_{TX}}} = \frac{E_{XP_{TX}}}{E_{CP_S}} \tag{5.10}$$

Now, the effective transmit antenna XPD designated XPD'_{TX} is described by:

$$XPD_{TX}^{V'}\, e^{j\Theta'_{XPD_{TX}}} = \frac{E'_{XP_{TX}}}{E_{CP_S}} \tag{5.11}$$

Solutions to (5.8),(5.9) and (5.11) are presented graphically in Fig. 5.6. The effective XPD_{TX} magnitude is given in dB and the change in the angle of the XPD_{TX} is plotted as:

$$\delta\Theta_{XPD_{TX}} \stackrel{\Delta}{=} \Theta'_{XPD_{TX}} - \Theta_{XPD_{TX}} \tag{5.12}$$

Fig. 5.6 illustrates how the magnitude of the mismatch and distance from the OMT junction to the mismatch can change the effective OMT complex XPD. This graph shows that as the magnitude of the reflection coefficient on the unused rectangular port increases, the peak-to-peak variation of the

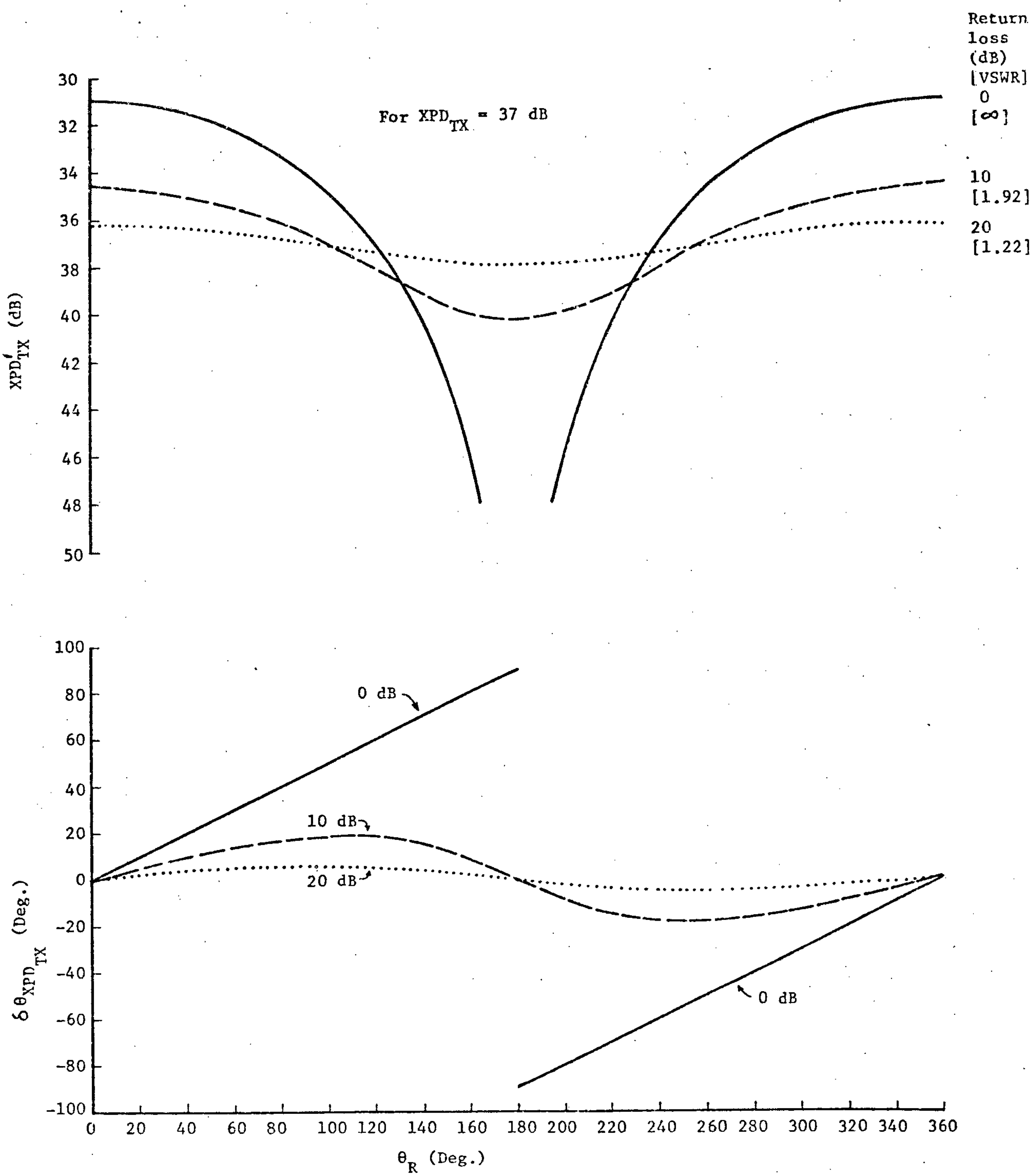

Fig. 5.6. Effect of a mismatch at the crosspolar rectangular OMT port on the effective transmit OMT complex XPD.

total OMT XPD also increases. The case where the return loss is 0 dB represents the situation which occurred when the transmit OMT was connected to the polarization switch without isolators as discussed in Section 2.2.4.3. For a 0 dB return loss, Fig. 5.6 shows that the OMT XPD can be degraded by up to 6 dB.

However, early tests on the complete experimental system showed that the severe mismatch on the transmit OMT caused by the polarization switch could degrade the system XPD by more than 6 dB (Section 2.2.4.3). This can be explained by solving (5.6) after substituting the new value of the transmit OMT given by (5.8) and (5.11). The solutions of these equations assuming equal antenna XPDs of 37 dB and a mismatch return loss of 10 dB (VSWR = 1.92) are shown in Fig. 5.7. Another set of solutions for the assumptions that the antenna XPDs are 37 dB and $\Theta_{XPD_{TX}} - \Theta_{XPD_{RX}} = 150°$ are shown in Fig. 5.8. These graphs show that mismatches can change the system XPD by considerably larger values depending on the exact values of the complex crosspolar signal vectors. It is interesting to note that in Fig. 5.8, the largest peak-to-peak variation in the crosspolar signal level occurs, in this case, when the return loss is 5 dB because the reflected signal is approximately the same magnitude as the sum of the antenna depolarized signals. The largest degradation still occurs for a 0 dB return loss.

In the case of a mismatch on the receive OMT copolar rectangular port, the effect on the system XPD is, of course, very similar to the results in Figs. 5.7 and 5.8 but the mechanism is slightly different than that shown in Fig. 5.5. A mismatch on this copolar port will result in a reflected copolar

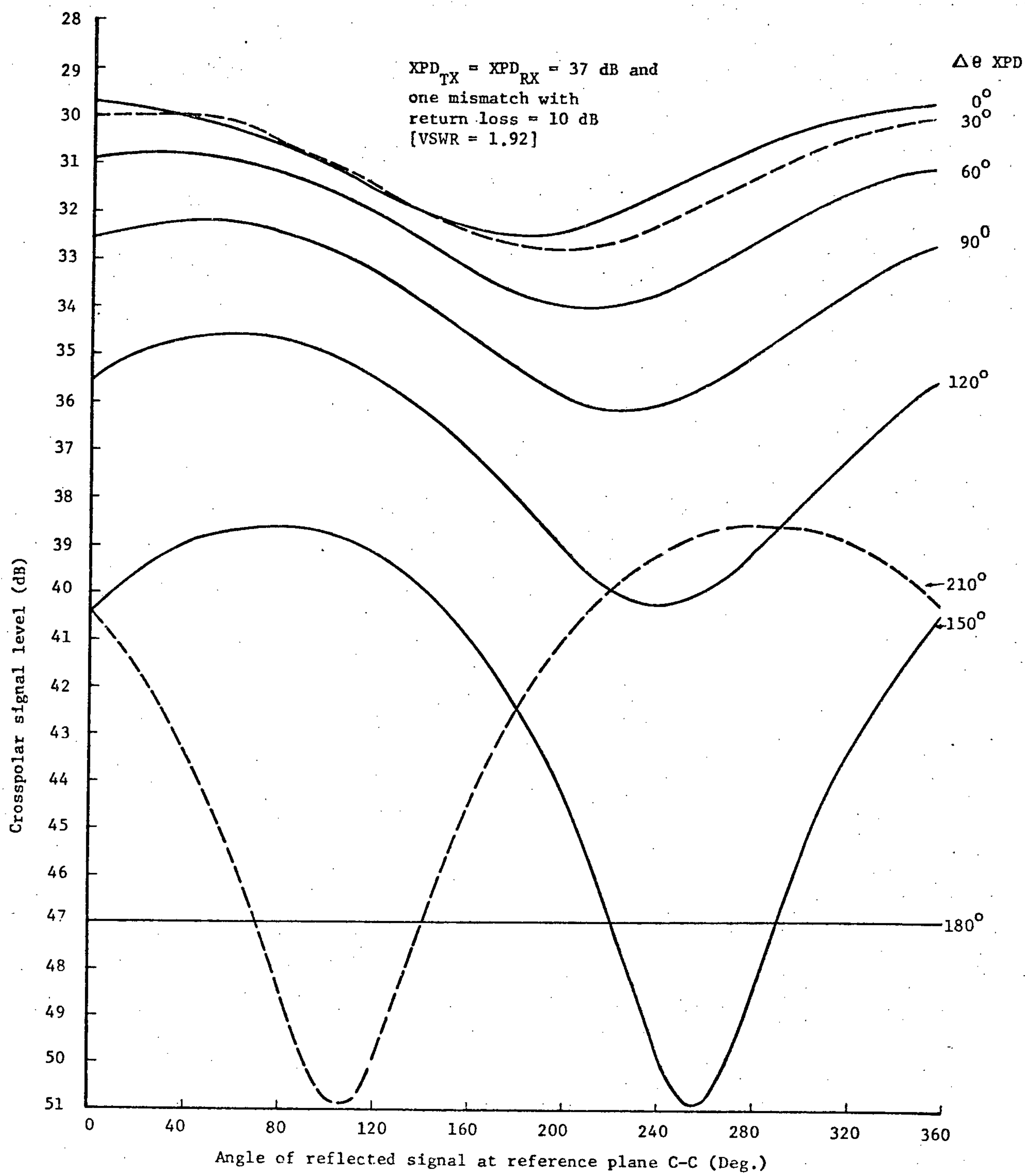

Fig. 5.7. Crosspolar signal level at plane D-D for $XPD_{TX}=XPD_{RX}=37dB$ and one mismatch with return loss = 10dB.

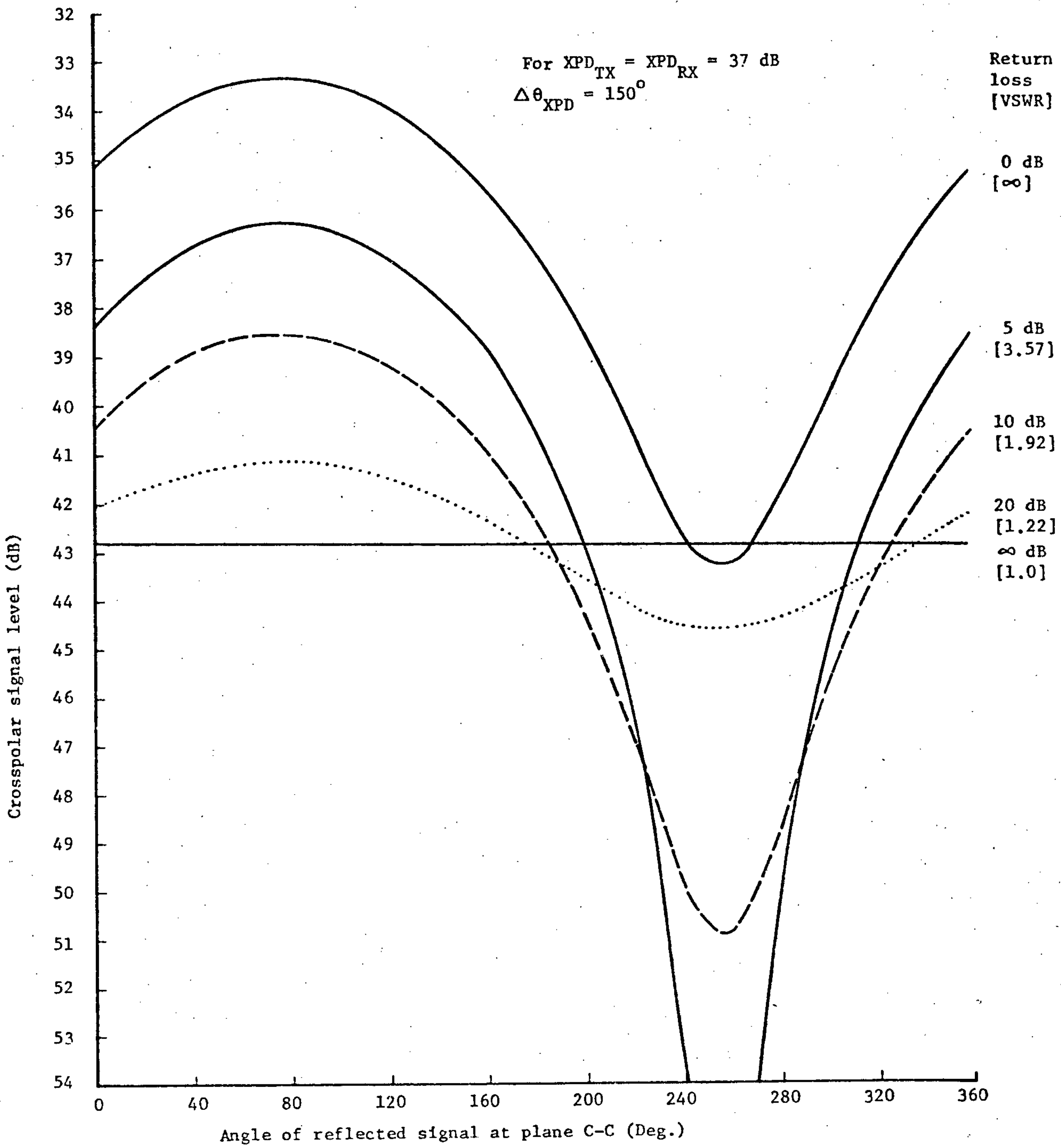

Fig. 5.8. Crosspolar signal level at plane D-D for $XPD_{TX}=XPD_{RX}=37$dB and $\Delta\theta_{XPD}=150^{o}$.

signal travelling toward the transmitter. As this signal passes through the receive OMT it will be depolarized and will result in approximately equal signals leaving via the "circular" and rectangular crosspolar ports. The signal leaving via the antenna feedhorn can be safely ignored. However, the signal leaving the crosspolar rectangular port will add to the other crosspolar signal components entering the front-end. For the same reflection coefficient and OMT XPD, this signal vector will have the same magnitude entering the front-end as the signal caused by a mismatch on the transmit OMT crosspolar rectangular port.

It is extremely difficult to quantitively compare the results of this section to a practical situation because all mismatches throughout the system will additively create effects similar to those shown in Figs. 5.7 and 5.8. Values could be chosen for this model which would generate results acceptably close to the experimental data shown in Figs. 2.35, 2.36 and 2.38. However, this would not be very meaningful because the model contains enough parameters to generate numerous solution sets which would fit the experimental data. If measuring apparatus were available to more completely characterize the individual components, accurate model parameters could be determined.

Nevertheless, some meaningful conclusions regarding the operation of the experimental system can be made with the aid of the results of this section. Fig. 2.35 presents the experimental results for the back-to-back OMT connection with terminations which were thought to be well matched. But this graph, especially the lower curve, shows a frequency response similar to those in Figs. 5.7 and 5.8. This response is believed to be due to the fact that the Hughes 44894H thermistor mount used in the crosspolar level measurement (connected to the OMT through arm in this case) has a specified VSWR of only 2:1 (return loss = 9.5 dB). Fig. 5.7 shows very similar variations in crosspolar level for $\Delta\Theta_{XPD}$ in the range 120°-150° with a 10 dB return loss and appears to explain the lower curve of Fig. 2.35. The smaller crosspolar variations in the upper curve could result either from the addition of two vectors or a reduction in the reflection caused by the thermistor mount due to some conjugate mismatch inherent in the receive OMT cross arm.

Fig. 2.36, where the transmit OMT cross arm was deliberately mismatched gives a response of the form shown in Fig. 5.8 for a return loss around 5 dB. The frequency response of Fig. 2.36 shows that the reflected signal angle (Θ_R) varies over approximately 180° over the frequency range 73.18-73.45 GHz, (a similar 180° frequency range occurs in Fig. 2.35). Over this frequency range, the change in the TE_{10} mode β is 7.0. Using (5.9), this gives ℓ_R, the distance from the combining reference plane to the mismatch as approximately 22 cm. This distance is reasonable for the circuit topology actually used to make the measurements. An exact correlation cannot be made due to the uncertainty of the location of the combining reference plane within the back-to-back OMT circuit.

Fig. 2.38 shows the variation of crosspolar signal level with frequency for the back-to-back OMTs connected to the front-end. The mixers in the front-end have a specified input VSWR of 2:1 typical (this will depend on the backshort tuning). With no isolation between the receive OMT and the front-end, large variations in the crosspolar level are observed. The variation with frequency in this case is more rapid than in the previous cases. This is due to the longer electrical path lengths between the OMT and the mismatches and may also partially be due to the addition of more than one reflected signal vector. With reasonable degrees of isolation between the OMT and the front-end, the crosspolar signal level shows very little variation with frequency. This verifies that the cause of the crosspolar signal variation with frequency is explained by the analysis presented in these sections.

5.5.2.3 System XPD Improvement Using Mismatches

This impedance sensitive behaviour of the OMTs can actually be used beneficially to increase the "uncancelled" system clear weather isolation at one frequency. Several methods were explored to change the OMT port mismatches in attempts to improve the system isolation. It was found that even with the isolators installed between the mixers and OMTs, the mixer backshort tuning and LO drive level would affect the system isolation. The most convenient method of adjusting the uncancelled system isolation was found to be a combination of operating frequency and copolar mixer LO adjustment. For certain combinations of antenna alignment and operating frequency, it was possible to improve the uncancelled system XPD from around 35 dB to 45 dB by slightly reducing the copolar mixer LO drive level. The required LO reduction only resulted in a few tenths of a dB reduction in copolar sensitivity. This method was successfully used during data acquisition for the results showing approximately 45 dB isolation on the "uncancelled" polarization. This technique has limited practical application, however, because of the difficulty of determining the advantageous combinations of antenna alignment, backshort tuning, LO level and operating frequency.

5.6 Crosspolar Cancellation Network Operation in Clear Weather

The theory presented in this section will be used to analyze the operation of the crosspolar cancellation network, examine the effects of amplitude and phase errors, and determine the cancellation frequency response - all under clear weather conditions. The previous sections introduced two pairs of crosspolar signal vectors, one pair due to the "matched" OMTs and a second pair resulting from mismatches on the OMT ports. These four signals are each actually the vector sum of more than one signal resulting from the same basic mechanism. The complex sum of these coherent signals propagates toward the front-end along the crosspolar signal path up to plane D-D in Fig. 5.1. Without the crosspolar cancellation network, this vector sum would be the clear weather received crosspolar signal. The magnitude of this signal under different conditions is shown in Figs. 5.7 and 5.8. In summary, it was shown that the crosspolar signal vector entering plane D-D, and thereafter junction B-B along the crosspolar signal line, can have any magnitude shown on Figs. 5.7 and 5.8 and any angle between 0 and 360°.

If the crosspolar cancellation network is adjusted so that the second signal entering the combining junction at plane B-B has exactly the same magnitude but opposite phase as the previously described signal, then the net signal leaving junction B-B, in the direction of the front-end, will be zero. Thus, perfect crosspolar signal cancellation can be achieved at one frequency under any clear weather conditions assuming the crosspolar cancellation network attenuation and phase can be adjusted with sufficient accuracy. In practice, however, it can be difficult to maintain the necessary cancellation signal phase and amplitude accuracy because of frequency shifts and ambient temperature variations.

5.6.1 Sensitivity to Amplitude and Phase Errors

The first step in analyzing the operating characteristics of the crosspolar cancellation network is to quantify the sensitivity of the received crosspolar signal to phase and amplitude errors. Fig. 5.9 shows the change in the crosspolar signal level at the front-end input for an error in the adjustment of the crosspolar cancellation circuit attenuation. Curves are given for uncorrected system isolations of 30, 35, 40 and 45 dB. This graph shows that the sensitivity of the crosspolar signal level to amplitude errors increases for lower levels of uncorrected system isolation. Fig. 5.10 is a corresponding plot for phase errors. It shows a similar increase in error sensitivity at lower uncorrected system isolations. The receiving system average noise level corresponds to a crosspolar signal level of approximately 65-70 dB below the copolar signal level, (ref. Section 2.8). From Figs. 5.9 and 5.10 it can be seen that to achieve a sufficient level of cancellation to ensure that the crosspolar signal level is below the noise level the adjustment errors must be maintained below ±0.3 dB and ±1.9 degrees for an uncorrected system isolation of 35 dB.

5.6.2 Cancelled System Frequency Response

To be able to analyze the frequency response of the cancelled systems, the mathematical expression for the crosspolar signal entering the front-end

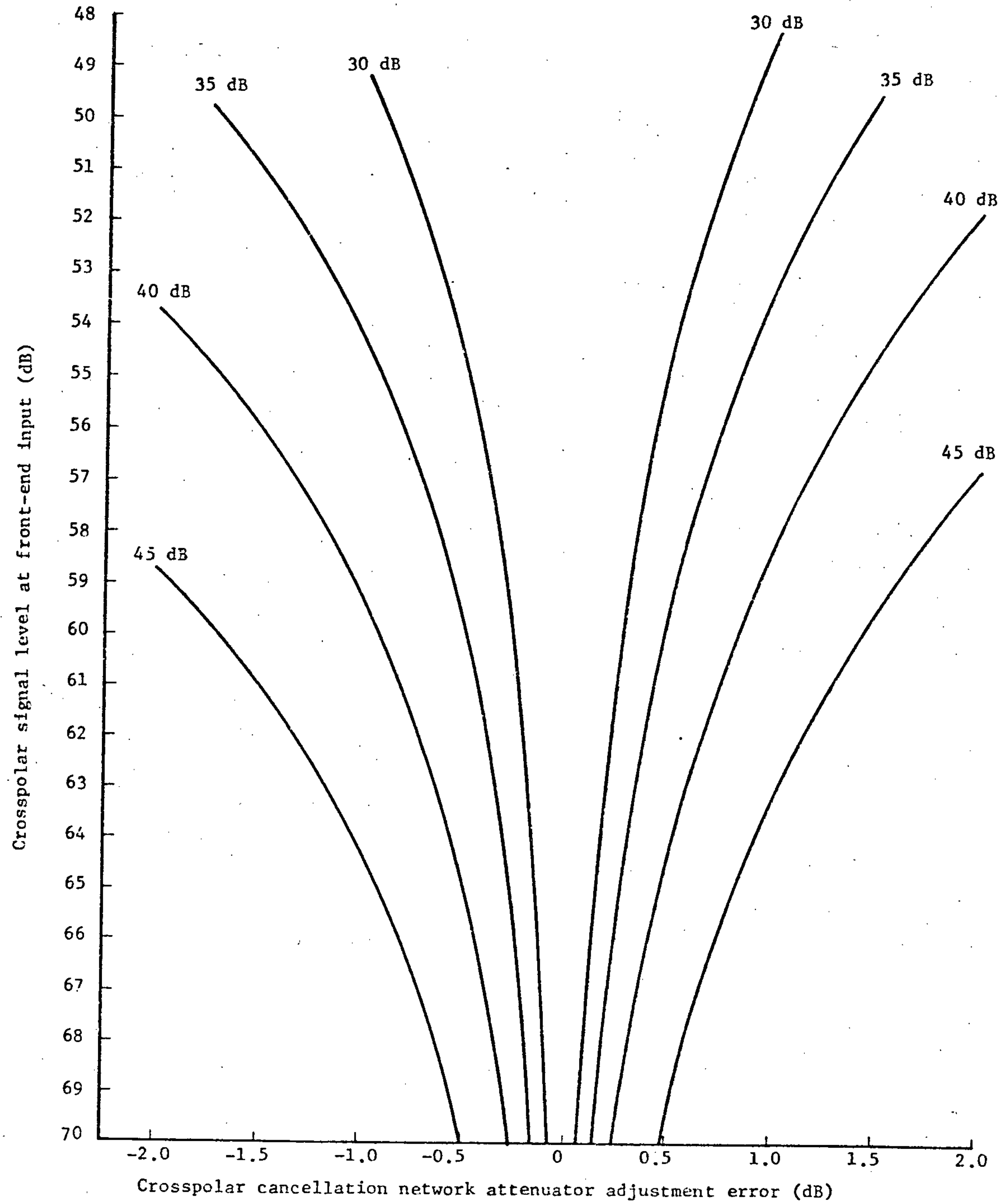

Fig. 5.9. Effect of crosspolar cancellation network amplitude errors.

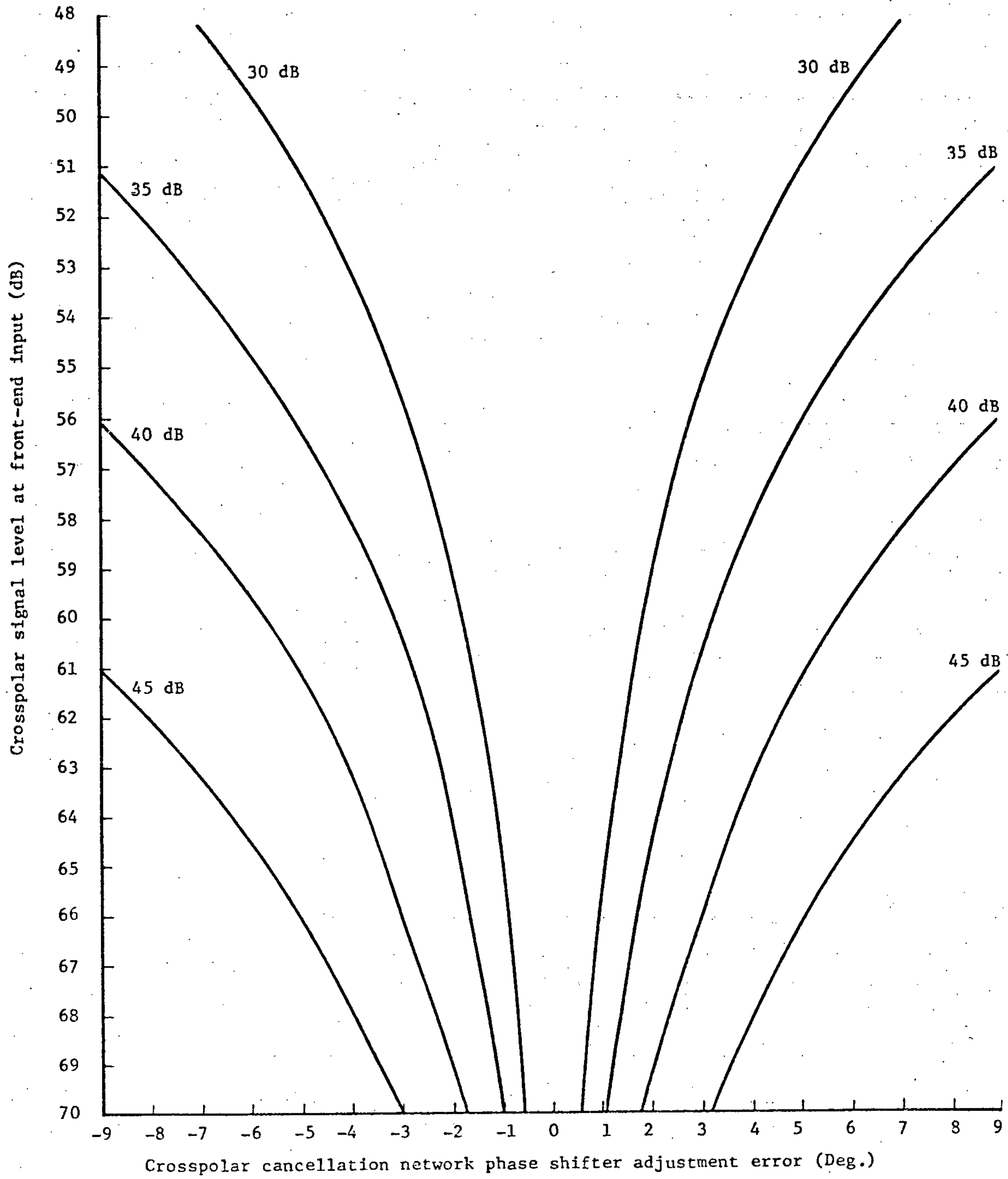

Fig. 5.10. Effect of crosspolar cancellation network phase errors.

must be derived. The matrix (5.1) describes the signals entering the front-end in terms of the signals at the reference planes A-A and B-B. Equation (5.3) relates the signals at plane D-D to the received signals at the directional coupler junctions (planes A-A and B-B). The signal set at the receiving antenna OMT ports (plane D-D) is described in general by (5.2) with the modifications introduced in Section 5.5.2 to include the effects of mismatches on the OMT ports. Because clear weather operation is again being considered, the simplifying assumptions made for (5.6) are still applicable. Thus, the clear weather signals at the front-end input are, in this case, described by:

$$\begin{bmatrix} E_{CP_{FE}} \\ E_{XP_{FE}} \end{bmatrix} = \begin{bmatrix} 1 & 0 \\ 0.1A_A^V e^{j\Theta_T} & 1 \end{bmatrix} \begin{bmatrix} e^{j\Theta_{D-A}} & 0 \\ 0 & e^{j\Theta_{D-B}} \end{bmatrix} \begin{bmatrix} E_{CP_D} \\ E_{XP_D} \end{bmatrix} \tag{5.13}$$

where the possible range of values for the signals at plane D-D has been analyzed for clear weather conditons in Section 5.5.

Solving (5.13) for the crosspolar signal at the front-end input yields:

$$E_{XP_{FE}}(f) = E_{CP_D}(0.1)A_A^V e^{j(\Theta_T+\Theta_{D-A})} + E_{XP_D}\, e^{j\Theta_{DB}}\Big|_f \tag{5.14}$$

If the crosspolar cancellation network is adjusted for total cancellation at a frequency f_o, (5.14) becomes:

$$E_{XP_{FE}}(f_o) = 0 = E_{CP_D}(0.1)A_A^V\, e^{j(\Theta_T+\Theta_{D-A})} + E_{XP_D}\, e^{j\Theta_{D-B}}\Big|_{f_o} \tag{5.15}$$

The solutions to (5.15) are:

$$|E_{XP_D}| = |E_{CP_D}| \; 0.1 \; A_A^V \Big|_{f_o} \tag{5.16}$$

and

$$(\mathrm{Arg}[E_{CP_D}] + \Theta_T + \Theta_{D-A}) - (\mathrm{Arg}[E_{XP_D}] + \Theta_{D-B}) = 180° \Big|_{f_o} \tag{5.17}$$

which describe the conditions necessary for complete cancellation, i.e. the cancellation signal must have equal amplitude and opposite phase.

The frequency sensitive behaviour of the cancelled system will be analyzed by solving (5.14), (5.16) and (5.17) after making the following simplfications:

- for practical purposes, the attenuator loss can be assumed to be constant over the frequency range under consideration.
- the clear weather, copolar, received signal level will also be assumed here to be constant over this frequency range.
- because the path length differences which give rise to the difference between $\mathrm{Arg}[E_{CP_D}]$ and $\mathrm{Arg}[E_{XP_D}]$ are small compared to other path length differences, it will be assumed that the change in these angles are negligible over the frequency range of interest. (Similar arguments were applied in Sections 5.5.1 and 5.5.2). These angles can be completely ignored in the frequency response calculation by considering their fixed values as a minute change in the length of the waveguide connections between A-D and B-D.
- from the symbol definitions, the total phase shift in the cancellation

circuit (Θ_T) is the sum of the phase shifter phase shift (Θ_{PS}) and the phase shift through the waveguide connection between the planes A-A and B-D (Θ_ℓ).

- it will also be assumed that the phase shift through the phase shifter is independent of frequency. (This is not strictly true but the phase shift change with frequency will be negligible compared to the change in the phase Θ_ℓ).

Now, using the symbol E_{CN_B} which represents the cancellation signal at plane B-B (and includes the effect of both couplers):

$$|E_{CN_B}| = |E_{XP_D}(f_o)| = |E_{CP_D}|(0.1)A_A^V \tag{5.18}$$

which according to the previous assumption, is constant with frequency. This allows (5.14) to be rewritten as:

$$E_{CP_{FE}}(f) = |E_{CN_B}|\, e^{j\Theta_{PS}}\, e^{j(\Theta_\ell + \Theta_{D-A})} + |E_{XP_D}(f)|e^{j\Theta_{D-B}} \tag{5.19}$$

To consolidate the $e^{j\Theta_i}$ terms, this may be rewritten:

$$E_{XP_{FE}}(f)e^{-j\Theta_{D-B}} = |E_{XP_D}(f)|e^{j0} + |E_{CN_B}|e^{j\Theta_{PS}}e^{j(\Theta_\ell+\Theta_{D-A})}e^{-j\Theta_{D-B}} \tag{5.20}$$

Because the phase of the crosspolar signal entering the front-end is not important, this equation may be rewritten:

$$|E_{XP_{FE}}|(f)| = \left|\,|E_{CN_B}| + |E_{XP_D}(f)|e^{j\Theta_{PS}}\, e^{j(\Theta_\ell + \Theta_{D-A} - \Theta_{D-B})}\right| \tag{5.21}$$

where Θ_ℓ, Θ_{D-A} and Θ_{D-B} are, of course, also functions of frequency. Thus, the magnitude of the crosspolar signal in the cancelled system can be calculated at any frequency by the complex addition of a scalar constant and a vector dependent on frequency. The angle between these two vectors is given by:

$$\Theta_{DIF}(f) \triangleq \Theta_{PS} + \Theta_{\ell}(f) + \Theta_{DA}(f) - \Theta_{DB}(f) \tag{5.22}$$

Therefore the constant angle Θ_{PS} is equal to:

$$\Theta_{PS} = 180° - \Theta_{\ell}(f_o) - \Theta_{D-A}(f_o) + \Theta_{D-B}(f_o) \tag{5.24}$$

The three angles Θ_{ℓ}, Θ_{D-A} and Θ_{D-B} can all be expressed in radians, by equations of the form:

$$\Theta_{\ell}(f) = \Theta_{\ell}(f_o) + [\beta(f) - \beta(f_o)]\ell \tag{5.25}$$

where ℓ is the appropriate length, i.e. ℓ, ℓ_{D-A} or ℓ_{D-B} and $\beta = \frac{2\pi}{\lambda_g}$. Therefore, (5.22) can be rewritten:

$$\begin{aligned} \Theta_{DIF}(f) = \Theta_{PS} &+ \Theta_{\ell}(f_o) + [\beta(f) - \beta(f_o)]\ell \\ &+ \Theta_{D-A}(f_o) + [\beta(f) - \beta(f_o)]\ell_{D-A} \\ &- \Theta_{D-B}(f_o) - [\beta(f) - \beta(f_o)]\ell_{D-B} \end{aligned} \tag{5.26}$$

Substituting (5.24) into (5.26):

$$\Theta_{DIF}(f) = \pi + [\beta(f) - \beta(f_o)]\ell_{\Theta} \tag{5.27}$$

where:

$$\ell_{\Theta} \triangleq \ell + \ell_{D-A} - \ell_{D-B} \tag{5.28}$$

and now (5.21) can be written:

$$|E_{XP_{FE}}(f)| = \left| |E_{CN_B}| e^{j0} + |E_{XP_D}(f)| e^{j[\beta(f_o)-\beta(f)]\ell_\Theta} \right| \qquad (5.29)$$

Equation (5.29) gives the magnitude of the crosspolar signal at the front-end input at any frequency in terms of measurable quantities. The results from these equations can now be compared to actual measurements made with the crosspolar network connected to the front-end.

Fig. 5.11 shows the results of a frequency response measurement made on the bench with the OMTs connected back-to-back and the crosspolar cancellation network connected to the front-end. The experimental set-up was identicial to Fig. 2.37 without the isolator and variable attenuation but with the crosspolar cancellation network connected as shown in Fig. 2.39. The first measurement was made with the cancellation network attenuator at maximum attenuation to determine the uncancelled system XPD. This value varied between 32 and 37 dB over the measurement frequency range. This magnitude and rate of XPD variation indicates that the entire system was fairly well matched in this configuration (i.e. compared to Fig. 2.38). The crosspolar cancellation network was then adjusted for a null at 73.125 GHz and the second set of measurements were made.

The calculated values of XPD were obtained using (5.29) with:

- $|E_{XP_D}(f)|$ are the values of XPD for the uncancelled system.

- $|E_{CN_B}|$ = 36 dB which is the value of uncancelled XPD at 73.125 GHz.

- $\ell_\Theta = \ell + \ell_{D-A} - \ell_{D-B}$ = 77 cm which resulted from ℓ = 91 cm ± 1 cm (the length of the waveguide connection between the two directional

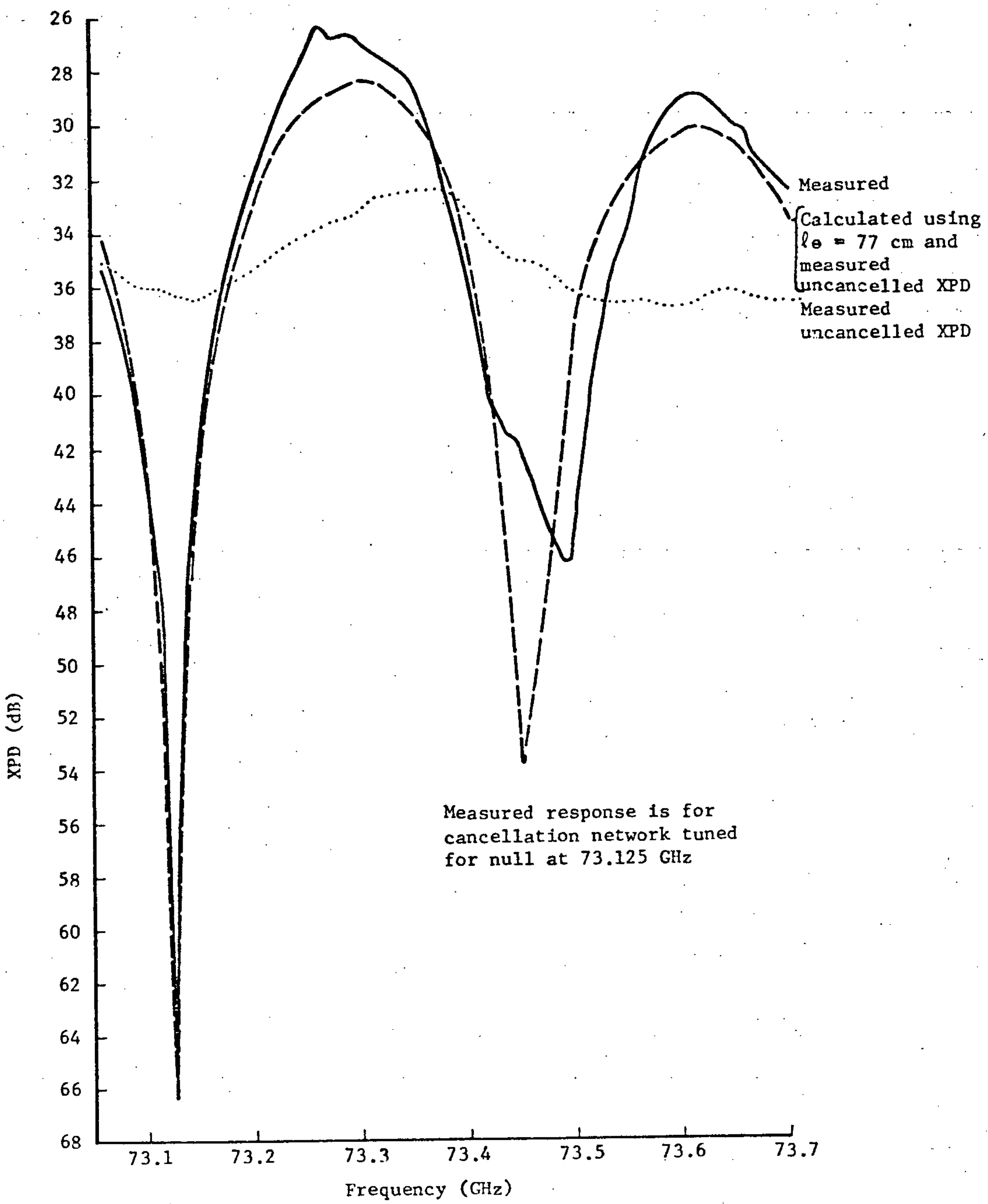

Fig. 5.11. Clear weather cancelled system XPD vs. frequency.

coupler junctions through the cancellation network) and $\ell_{D-B} - \ell_{D-A} = 14$ cm. $\pm$ 1 cm (the difference in the length of the waveguide connection between the OMT ports and the directional coupler "input" ports).

and

- β calculated for WR-15 waveguide.

The agreement between the measured and calculated cancelled system frequency responses is considered to be very good. Both curves show differences between the maximum and minimum XPD values which result from changes in the uncancelled system XPD magnitude. Differences between the two curves presumably result from: small changes in angles not due to waveguide lengths, small mismatches and small frequency dependent amplitude changes in the OMTs, couplers, attenuators and front-end.

The typical peak-to-peak variation in the free running klystron frequency in a one hour period is approximately 3.5 MHz. This is the calculated average of the difference between the maximum and minimum frequency values recorded by the data acquisition system over several, typical one hour periods. Many records show much smaller variations but some also show larger variations, probably due to different changes in ambient temperature. The specified temperature coefficient of the klystron is −1.0 MHz/°C typical.

This variation in the klystron frequency could cause the cancelled system clear weather XPD to drift to approximately 55-60 dB, from a value below the noise level, over a typical one hour period. This effect can be compounded by the fact that it is possible to have cumulative klystron frequency drifts over longer periods due to a consistent change in the ambient temperature. Operational experience with the cancellation network also uncovered changes in the cancelled XPD level which could not be accounted for by frequency drift. For this reason the effects of temperature variation on the cancellation network were also investigated.

5.6.3 Cancelled System Temperature Drift

It is also possible to use the previously derived theoretical results to estimate the change in the cancelled system XPD due to temperature variation. Equations (5.27) to (5.29) show how the lengths of the waveguide connections associated with the cancellation network can affect the cancelled system XPD. The net critical length, ℓ_Θ, was measured to be 93 cm for the network topology used in the vicinity of the receiving antenna and front end. Coin silver waveguide is used for these interconnections. The linear coefficient of thermal expansion for silver is $19.1 \cdot 10^{-6}$/°C over the temperature range 0-100°C. This will result in a net change in ℓ_Θ of approximately 0.018 mm/°C. At 73 GHz this will translate to a change in the cancellation circuit angle of approximately 1.3 degrees/°C. From Fig. 5.10, it can be seen that a change in the ambient temperature of a few °C can result in significant changes in the crosspolar signal level. It is also likely that other components in the crosspolar cancellation network or associated millimetre-wave circuitry have significant temperature coefficients which could also affect the cancelled system XPD. Unfortunately, no specifications for temperature effects are available for these devices.

5.6.4 Phase Compensation of the Crosspolar Cancellation Network

The previous theory indicates that the frequency and temperature dependence of the cancelled system XPD can be improved by selecting the lengths of the important waveguide connections in the vicinity of the crosspolar cancellation network. From (5.28) and (5.29) if $\ell_\Theta = 0$, then the XPD frequency variation is only due to the variation in the uncancelled system XPD and the frequency variation of the circuit components. In addition, if $\ell_\Theta = 0$ the temperature dependent XPD variation will result only from the temperature effects on the millimetre-wave components, i.e. the attenuator, phase shifter, etc. and not the change in the waveguide lengths.

It is a simple matter to set $\ell_\Theta = 0$ by selecting the length of the waveguide connection ℓ_{D-B} (i.e. the connection between the receiving antenna OMT crosspolar port and the cancellation network summing coupler) to be equal to the sum of the lengths ℓ_{D-A} and ℓ (i.e. the connections between the OMT copolar port and sampling coupler and total length between the coupler junctions, respectively), as shown in Fig. 2.39.

To test the efficacy of this phase compensation scheme, a 93 cm length of WR-15 waveguide was added to the length, ℓ_{D-B}. This length was calculated, after measuring the relevant waveguide lengths in the circuit, to give $\ell_\Theta = 0$. Fig. 5.12 shows the measured XPD for the uncancelled, cancelled but not phase corrected and cancelled and phase corrected systems. The improvement was less than what was hoped for but the phase compensation section did result in an approximate increase of 100% in the useful bandwidth. The reason that the phase compensated response is not flat is that even though the major source of the frequency sensitive response was the length ℓ_Θ, other

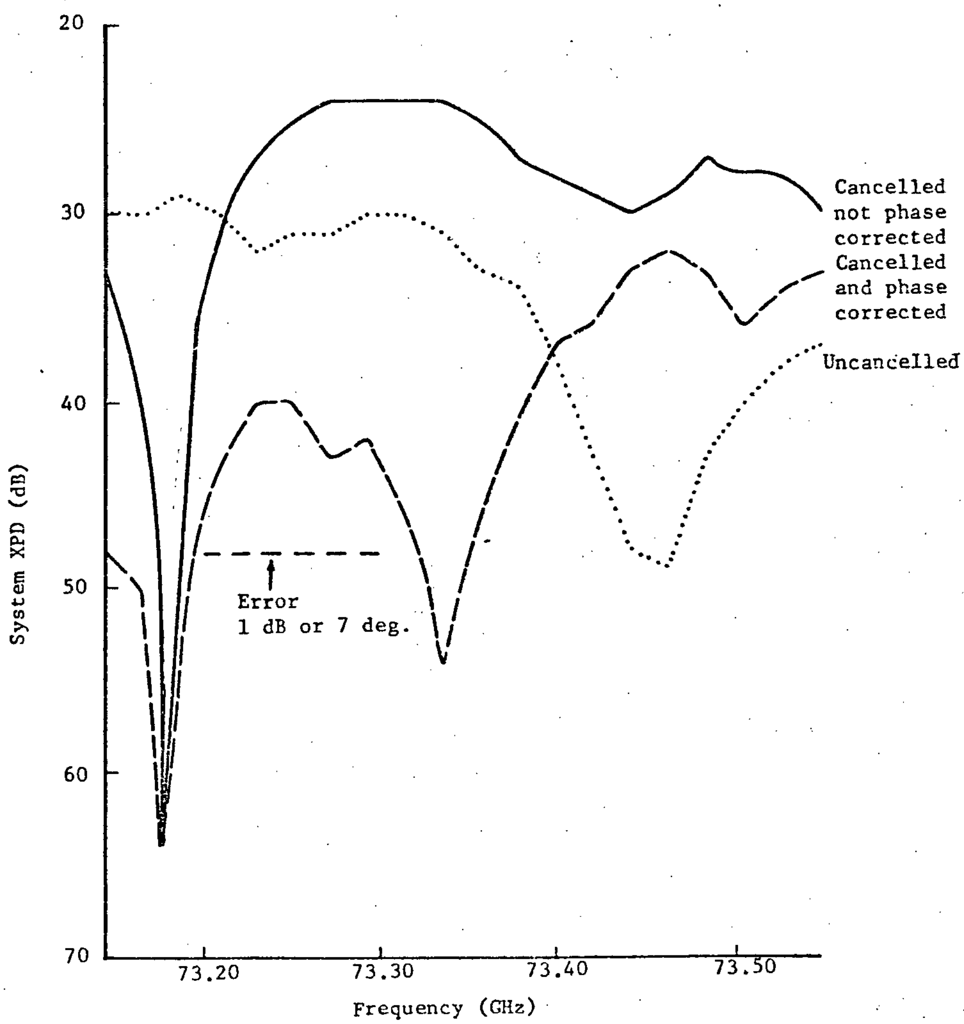

Fig. 5.12. Effect of phase compensation on uncancelled system XPD

circuit components also produce variations with frequency. Also shown in Fig. 5.12 is the predicted XPD level (i.e. 48 dB) for a cancellation network imbalance of approximately 1 dB or 7 Deg. (ref. Figs. 5.9 and 5.10). This effect can easily explain the phase compensated response. For example, the uncancelled system XPD does show a 1 dB variation within the frequency range where the compensated response degrades to approximately 48 dB.

While the bandwidth improvement of approximately 100% is very beneficial, the overall improvement in the stability of the cancellation appears to be much greater. This extra improvement is thought to be due to the temperature compensation effect discussed in Section 5.6.3. Before the phase compensation section was added, it was occasionally necessary to readjust the cancellation network every hour or so to maintain the system XPD below 55 dB. With phase compensation, the XPD level has often remained in the 60 dB range for many hours and does not usually require adjustment after the warm up period.

5.7 Model Predicted System XPD Performance

In this section, the previously described experimental model will be used to predict the system XPD response during rain. It will be shown that for a given set of meteorological conditions, a range of system XPD values could possible be observed. This application of the model allows a more accurate comparison to be made between the theoretically predicted and measured XPD during rain.

This type of mathematical procedure is very important when measuring XPD in the shorter millimetre range because path XPD values are usually more than the uncancelled system clear weather isolation. As a result, the observed system XPD during rain can be very different than that predicted for ideal antennas because of the addition of the path and antenna/OMT depolarized signals. The observed system XPD can vary over a range of values for a fixed path depolarization depending on the relative phases of the depolarized signals. Even though the theoretical methods can predict the relative phase of the path depolarization, this uncertainty cannot be resolved because the angles of the antenna depolarized signals are not known.

The use of the model is also essential to predict the change in the measured system XPD due to path differential attenuation and phase shift. It will be shown that for different measurement system configurations, the differential attenuation and phase shift also cause a change in the system XPD because of their relative effect on the transmit antenna depolarized signal. This effect would cause an apparent change in XPD even for the case of equi-oriented drops with zero canting angle. For this reason, it is important to take into consideration this effect when comparing XPD predictions and measurements.

The basic procedure to be followed in this section is to use the model to calculate the possible system XPD values for a range of the unknown depolarization angles. The model inputs are a set of predicted path propagation parameters and estimated values for the antenna XPDs. Values for the magnitudes of the antenna depolarized signals will be estimated from previous measurements and the observed clear weather system XPD. In some cases, it is also possible to estimate the difference between the antenna XPD angles from the clear weather system isolation and the antenna XPDs in Fig. 2.33. Path propagation parameters are calculated for a set of assumed meteorological conditions using the techniques described in Chapter 4. These data are then used as the input for a model implementation program written for an HP-41-CV programmable calculator. The program outputs the signal levels throughout the measurement system and XPD values for cancelled or uncancelled systems. This basic method was also used in the next chapter when experimental data are compared to theoretical predictions.

In the following sections, example predictions will be used to demonstrate the use of the model and to show the interrelation between the path propagation parameters and the experimental system. The effects of path attenuations and phase shifts on the measured XPD will be illustrated. An example showing the range of XPD values possible for cancelled and uncancelled systems will also be discussed. A complete, rigorous investigation of the relationship between the path propagation parameters and the measured system XPD, as predicted by the model under all propagation conditions, would be extremely tedious. Instead, the results in the next chapter also include discussions of the experimental model in conjunction with actual experimental data.

5.7.1 Effects of Polarization Insensitive Attenuation or Phase Shifts

Sample model calculations show that a polarization insensitive path attenuation or phase shift will have no effect on the cancelled or uncancelled system XPD, as would be expected intuitively. Even though a polarization insensitive attenuation or phase shift could only occur for the unrealistic case of spherical rain drops, it is necessary to verify that the polarization insensitive portions of the path propagation do not affect the measured XPD. When performing these calculations it is important to remember that these attenuations and phase shifts must also be included in T_{CPXP}.

5.7.2 Effects of Differential Attenuation and Phase Shift

Path differential attenuation and phase shift cause a change in the system XPD because of their effect on the transmit antenna depolarized signal. The system XPD can increase or decrease depending on whether vertical or horizontal polarization is transmitted. Fig. 5.13 shows the model predicted effects of differential attenuation for several system configurations with no path depolarizaton. Because the model uses copolar and cross-polar polarizations, differential attenuation is positive and negative for vertical and horizontal transmitted polarizations, respectively. The largest variation due to differential attenuation occurs for the cancelled system. This would appear at first glance, to be a disadvantage of the cancellation system, but Fig. 5.14 shows that for the case where there is a path depolarized signal, the cancelled system gives a much more accurate response. (The superiority of the cancelled system will also be demonstrated in further model predictions.)

Fig. 5.14 shows that for both the cancelled and uncancelled systems, the XPD variation due to differential attenuation is lower for higher transmit antenna XPDs. For this reason, the antenna/OMT assembly with the slightly better isolation was used for the transmit antenna in this experiment.

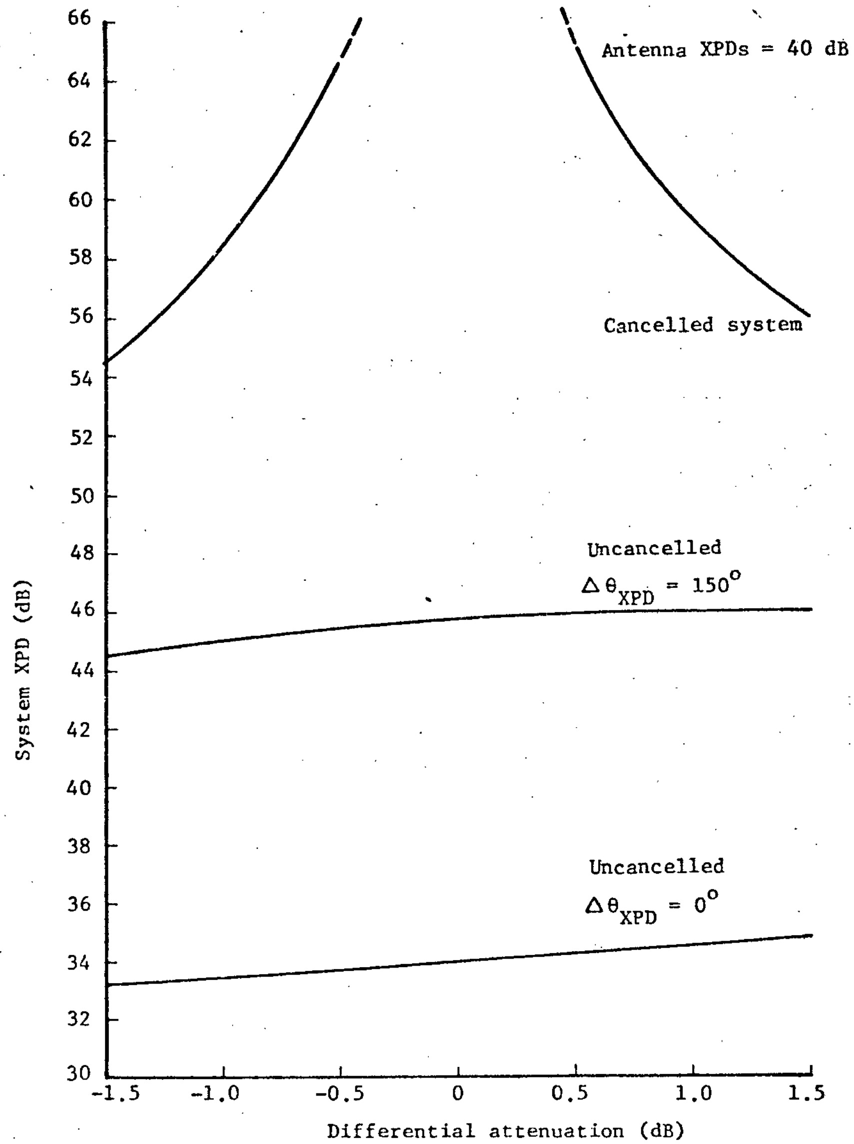

Fig. 5.13. Effects of differential attenuation on system XPD for no path depolarization.

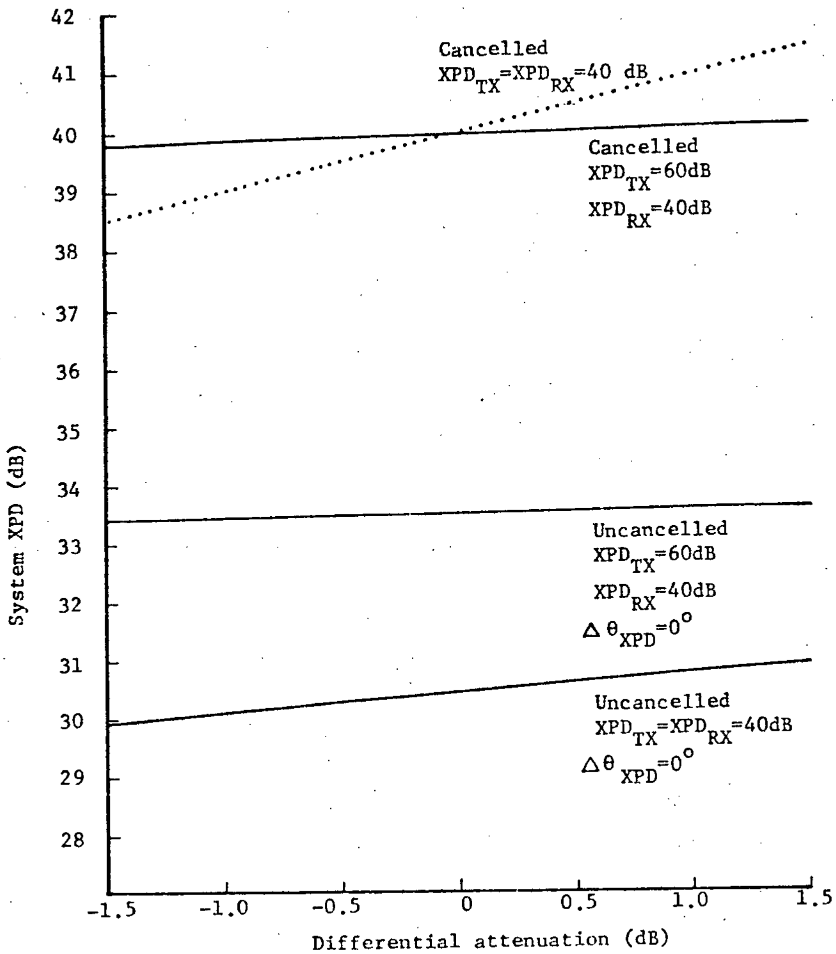

Fig. 5.14. Effects of differential attenuation on system XPD for path XPD = 40 dB $\angle 0^{\circ}$

These graphs show that for accurate comparisons between predicted and measured XPD, it is necessary to include the effects of differential attenuation on the system XPD. Path differential phase will produce similar results. To illustrate, and to compare the effects of differential attenuation and phase, a realistic set of path propagation parameters will be used. For this example, the following meteorological conditions will be assumed: rainrate = 10 mm/h, Joss/Olsen Widespread drop size distribution, canting angle = 2°, path length = 1.8 km., horizontal transmitted polarization and antenna XPDs = 40 dB $\underline{/}$ 0°. For this set of conditions, the path XPD is predicted to be 54.3 dB. Table 5.1 shows the system XPD response for cancelled and uncancelled systems with no differential attenuation or phase shift, differential attenuation only included, differential phase only included and both included. These results show that, for this case, the effect of differential phase is less than the effect of differential attenuation for both cancelled and uncancelled systems.

5.7.3 Effects of Antenna XPD Angle

The largest uncertainty in XPD measurement is due to the unknown relative angles between the antenna/OMT and path depolarized signals. The model shows that a rain depolarized signal can cause the measured uncancelled system XPD to increase or decrease depending on this relative angle. This effect has been demonstrated theoretically by Evans and Thompson [2.35] and Delogne and Sobieski [5.4]. Experimental observations of system XPD improvement during rain, presumably due to this effect, have been observed and

System XPD (Measured)	Ignoring differential attenuation and phase shift	Including differential attenuation only	Including differential phase shift only	Including both differential attenuation and phase shift
Uncancelled	34.8	34.5	34.8	34.5 dB
Cancelled	54.3	56.5	54.6	57.2 dB

Meteorological conditions:

$R = 10$ mm/h

$\phi = 2°$

Joss/Olsen Widespread drop size distribution

Path length = 1.8 km

T_X = Horiz.

$XPD_{TX} = XPD_{RX} = 40$ dB $\angle\ 0°$

Clear weather uncancelled isolation = 34 dB

Copolar atten = 11.28dB $\angle\ -106.1°$

Diff. atten.=-.43 dB

Diff. phase=1.25 Deg

Path XPD = 54.3 dB

Table 5.1 Effects of Differential Attenuation and Phase Shift on Cancelled and Uncancelled Systems.

commented on by De Lange, Dietrich and Hogg [1.74] and seem to appear but were not discussed in Shimba and Morita [1.81].

For an experimental system with constant antenna XPD angles, it is possible to observe system XPD increases or decreases because the angle of T_{CPXP} (i.e. T_{12}) can change depending on the canting angle. Equation (4.15) shows that the angle of the depolarizing element in the transmission matrix will change by 180° for opposite canting angle signs. In actual rain, the angle of T_{CPXP}, shown in Fig. 4.8, depends on rainrate and dropsize distribution and is quite variable. As a result, when analyzing this effect, it is necessary to consider all relative angles between the path and antenna/OMT depolarized signals.

To demonstrate this effect for the cancelled and uncancelled systems used in this experiment, the system XPD response for the meteorological conditions used in the previous section will be predicted again. In this case, the antenna XPD angles will be varied to illustrate the range of possible measured XPD values. The maximum and minimum XPD values were determined by incrementing the antenna XPD angles by n degrees for the same set of path propagation parameters.

Table 5.2 shows the range of XPD values for different sets of antenna XPD angles. Again, it is important to note that the same range of values could occur if the antenna XPDs were held constant and the path depolarization angle varied. These results again show the reduced uncertainty when using the crosspolar cancellation network. The uncertainty when using the cancellation network is due to differential attenuation and phase shift. For the uncancelled system, a very large range of system XPD values is possible.

	Antenna XPD Angles (DEG)	Uncancelled System Clear Weather XPD (dB)	Uncancelled System XPD range (dB)	Cancelled System XPD range (dB)
1.	$\underline{/}XPD_{RX} = 24.5 + n$ $\underline{/}XPD_{TX} = 23.2 + n$	34	33-34.6	52.1-57.2
2.	$\underline{/}XPD_{RX} = 24.5$ $\underline{/}XPD_{TX} = 23.2 + n$	34-NOISE LEVEL	34.6-52.2	52.1-57.2
3.	$\underline{/}XPD_{RX} = 24.5 + n$ $\underline{/}XPD_{TX} = 23.2$	34-NOISE LEVEL	34.6-56.9	56.8
4.	$\underline{/}XPD_{RX} = 204.5$ $\underline{/}XPD_{TX} = 23.2 + n$	34-NOISE LEVEL	33-56.9	52.1-57.2
5.	$\underline{/}XPD_{RX} = 24.5 + n$ $\underline{/}XPD_{TX} = 203.2°$	34-NOISE LEVEL	33-52.2	52.2
6.	$\underline{/}XPD_{RX} = 150 + n$ $\underline{/}XPD_{TX} = n$	45.7	42.5-48.9	52.1-57.2

Antenna XPD magnitudes = 40 dB
Meteorological conditions given in Table 5.1
Path XPD = 54.3 dB

Table 5.2 Range of Possible System XPDs for Different Antenna XPD Angles.

Case 1 in Table 5.2 is for the situation where the antenna depolarized signals are in phase at plane D-D. This is likely to be very close to the actual situation when clear weather isolations are observed to be about 34 dB. Case 6 represents the situation where a clear weather XPD improvement has been obtained by altering the relative antenna XPD angles. This is thought to be similar to the situations when received OMT mismatches were used to improve the clear weather system XPD.

5.7.4 Effects of Antenna XPD Magnitudes

Table 5.3 shows the range of XPD values for the situation in case 1 of Table 5.2 but with different antenna XPD magnitudes. These results show that the uncertainty in the cancelled system XPD decreases as the transmit antenna XPD increases. The receiving antenna XPD has no effect because the cancellation network can compensate for the receiving antenna without degradation due to differential attenuation and phase.

For the uncancelled system, the system XPD is closer to the path XPD for higher antenna isolations. The range of possible XPD values increases for higher isolations in this case because the relative magnitude of the path depolarized signal has increased. This trend would of course reverse if the path XPD was smaller than the clear weather system XPD.

These results show that in cancelled systems, if the available antennas have different isolations the higher isolation antenna should be used for transmitting. In this experiment the transmit antenna XPDs are a few dB higher than those for the receive antenna.

Antenna XPD magnitudes (dB)	Uncancelled Clear weather System XPD (dB)	Uncancelled System XPD (dB)	Cancelled System XPD (dB)
XPD_{TX} = 40 dB XPD_{RX} = 40 dB	34	33-34.6	52.1-57.2
XPD_{RX} = 40 dB XPD_{TX} = 42 dB	35	33.9-35.6	52.5-56.5
XPD_{RX} = 42 dB XPD_{TX} = 42 dB	36	34.8-36.8	52.5-56.5

Table 5.3 Range of Possible System XPDs for Different Antenna XPD Magnitudes.

Practical applications of the experimental model developed in this chapter will be included in the next chapter in conjunction with the actual experimental observations.

6. EXPERIMENTAL RESULTS

6.1 Preliminary Discussion

During the period this experimental system was being developed, several hundred hours of data were recorded. Only single polarization CPA and rainrate, however, were observed during the early phases of this project. Dual-polarized, uncancelled XPD measurements were made later. Finally, when the crosspolar cancellation network was added and the final version of the disdrometer system operational, many hours of complete data were recorded.

For the majority of this time, however, rainrates were below 5 mm/h (as predicted by Fig. 3.4). At low rainrates, it is more difficult to make accurate XPD measurements (due to small changes from the clear weather value) and rainrate measurements (because of raingauge averaging). In addition, reasonably high rainrates were often accompanied by low wind velocities which resulted in path XPD values too high to be accurately measured.

The number of data files which could be completely analyzed and included in this report was limited by the finite monetary resources available and the great deal of time required to thoroughly analyze each hour of data. Most of the files were subjected to a preliminary analysis. The majority of these showed very similar results, with high path XPDs and CPAs in agreement with the "standard" predictions, especially during periods with low wind velocities. For this reason, the files which were chosen to be presented in this report contain either comparatively low path XPDs and/or CPAs beyond the range of the "standard" predictions.

Eight different data periods will be analyzed in Sections 6.2-6.9. Each section includes the results from a portion of a one hour data file. These data files are described by an eight digit code, e.g. 81.11.30.18 which, in this case, designates the file recorded November 30, 1981. The last pair of digits are the hour of the day during the first data sample. Most plot headers contain: this file number, the date, the file starting time in hours and minutes, and the data averaging period.

Before analyzing the first data file, a short discussion of some experimental characteristics common to all files may be useful.

6.1.1 Disdrometer Data

All of the drop size data included in this report were recorded using:

- the standard (i.e. Laws and Parsons) drop diameter categories
- a minimum measurable drop diameter of approximately 0.30-0.35 mm diameter and
- a one minute averaging interval.

The drop data are presented as the number density, i.e. number of drops per cubic meter in a 1 mm drop diameter interval, to conform to the standard definition of N_D. These values of N_D are plotted against drop diameter along with the similar standard drop distributions for similar rain-rates. On these curves, and throughout this chapter, the following abbreviations are used for the standard distributions:

JOD for Joss/Olsen Drizzle

JOW for Joss/Olsen Widespread, which is the same as the Marshall and Palmer, and JOT for Joss/Olsen Thunderstorm.

Propagation data intervals are segmented during analysis into hundredth hour periods. Because drop data are recorded for one minute periods, the number of drop distribution samples displayed on each graph will vary depending on where in the hour the decimal divisions occurred. Some one-to-three minute gaps also occur in the drop data because the transducer grid was periodically cleared of small droplets clinging to the wires by blowing air over the grids.

The accuracy of the disdrometer data was periodically checked by comparison to the rainrate and water accumulation indicated by tipping-bucket gauge number 1, which was located about 10 m from the disdrometer. Three comparisons are shown in Figs. 6.1.1 to 6.1.3. Typically, the disdromter indicated rain accumulations were 5 to 8% higher than that indicated by the raingauge. This was at least partially due to a simplification in the water accumulation calculation, which assumed a uniform distribution of drop sizes in each category.

The number of drops in the smallest category was usually lower than expected from the standard distributions. To a small extent, this was due to the minimum measurable drop size of approximately 0.30-0.35 mm in diameter. The major portion of this discrepancy is believed, however, to be due to the lower gauge catch efficiency for the smaller drops. Fig. 3.3 shows the reduction in precipitation gauge catch efficiency for different horizontal wind speeds. This reduction is due to wind flows carrying the drops up and over the gauge aperture, which is obviously a more pronounced problem for smaller drops.

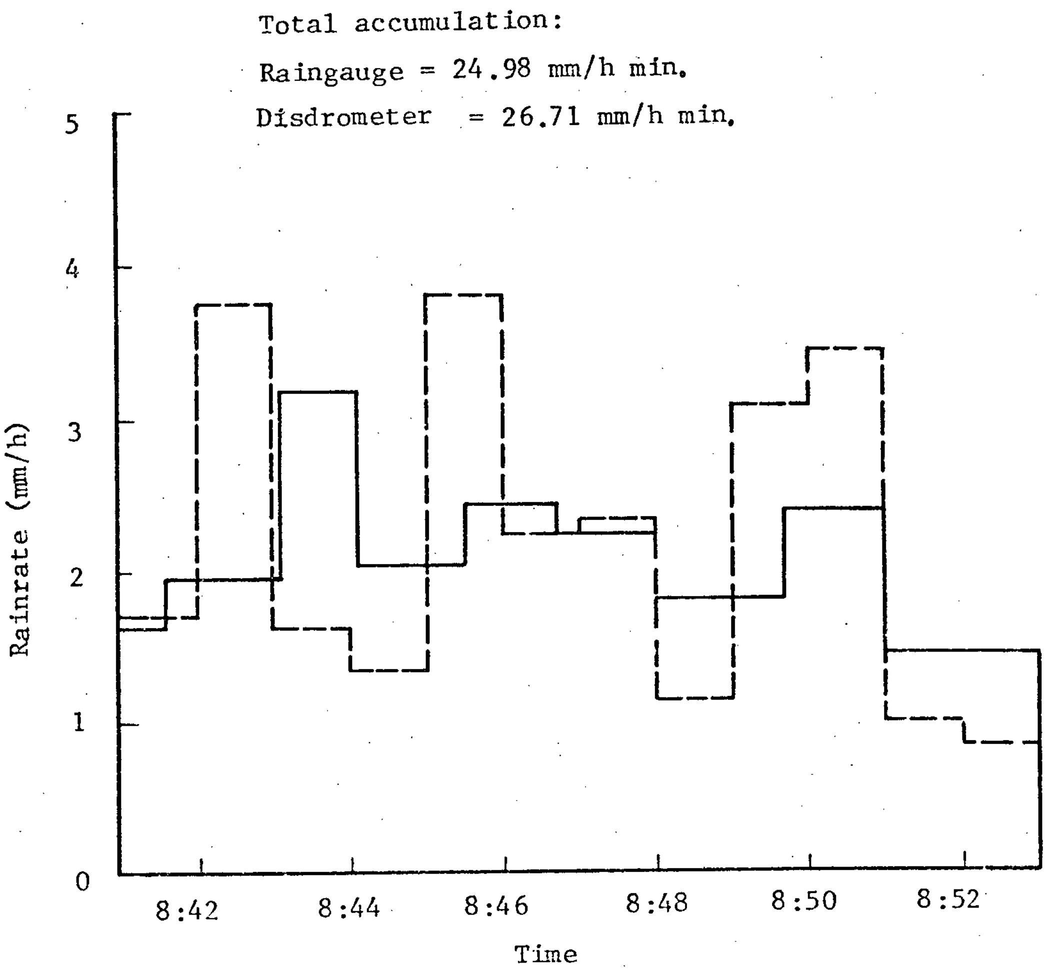

Fig. 6.1.1. Disdrometer-raingauge #1 comparison, Nov. 14, 1981.

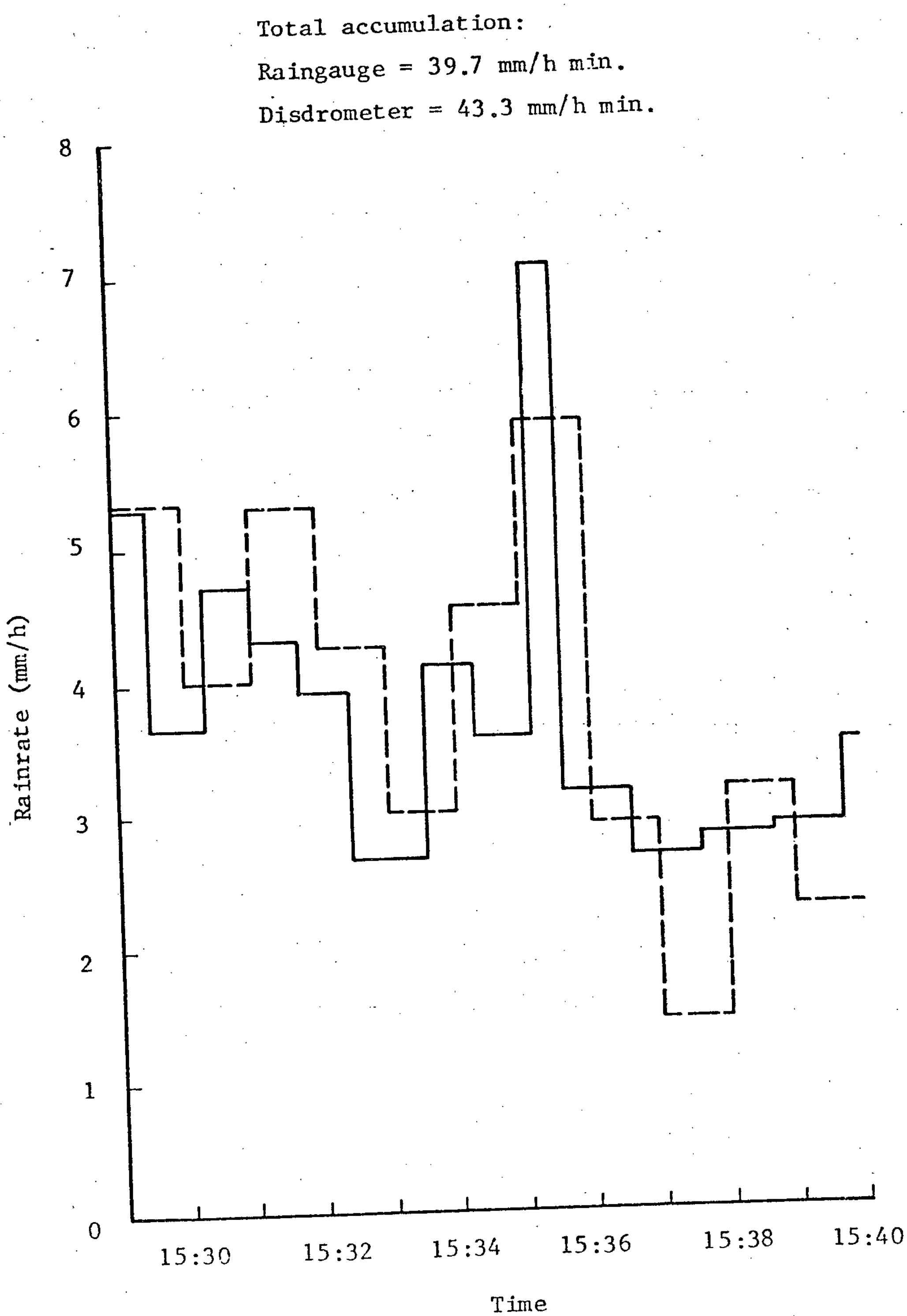

Fig.6.1.2. Disdrometer-raingauge #1 comparison, Nov. 15, 1981.

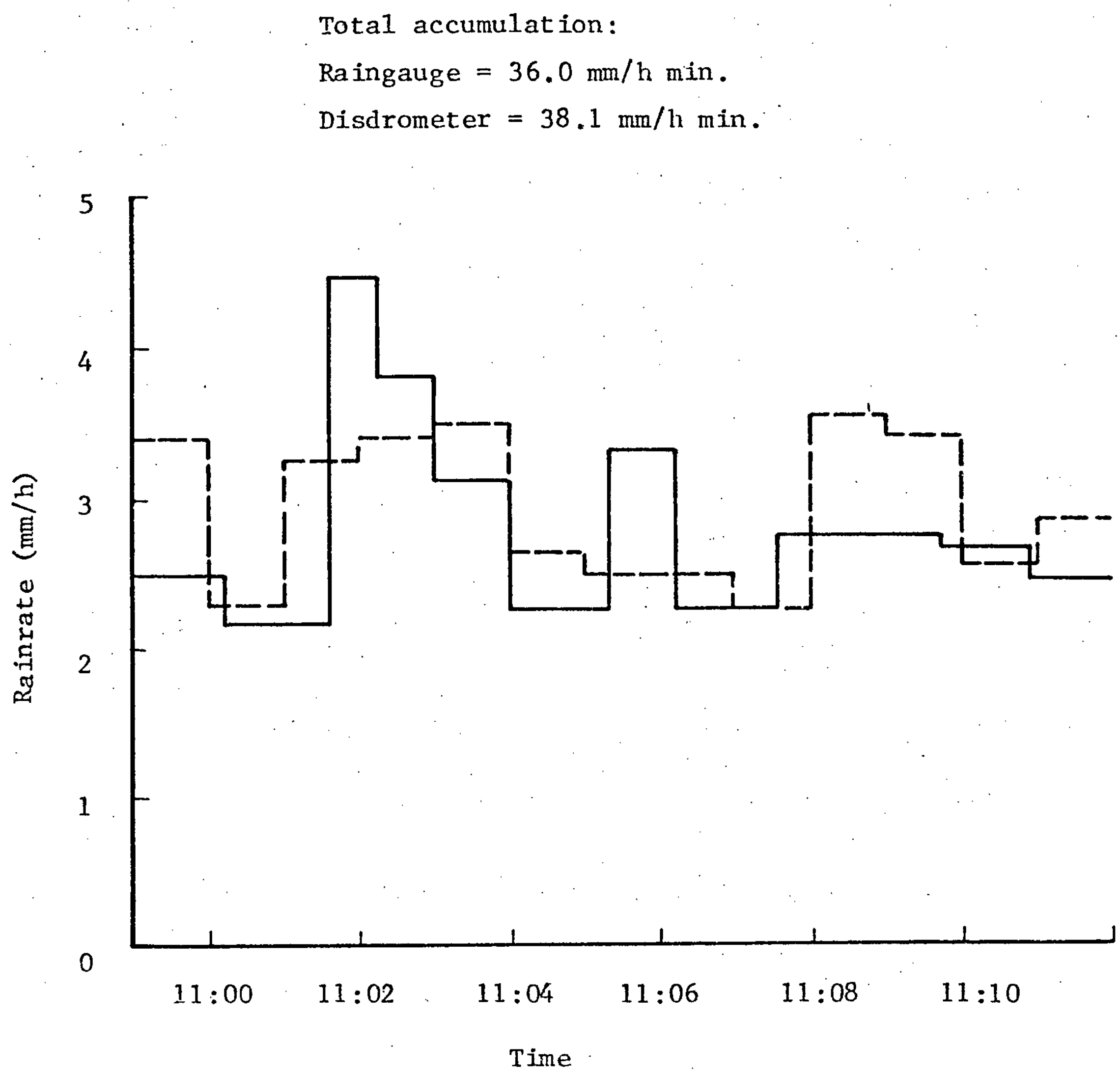

Fig. 6.1.3. Disdrometer-raingauge #1 comparison, Nov. 30,1981.

6.1.2 Receiving System Noise Levels

For the gains used for most data periods, the receiving system average noise levels were approximately -78 dB and -76 dB on the vertical and horizontal channels, respectively. At very low rainrates, these noise levels may have introduced inaccuracies in the cancelled XPD data as discussed in Section 6.2.2. They also set the minimum measurable path XPD. This level was, on occasion, exceeded during high rainrates with low canting angles, as discussed in Sections 6.4.2 and 6.9.2.

6.1.3 Differential Attenuation Calculations

The differential attenuation results presented in this chapter were calculated from the sequential samples of CPA for each polarization. For the data presented here, the polarization switching period was 15 s. During analysis, the data from one second before and two seconds after the polarization change were discarded to allow time for the receiving system to settle. This resulted in 12 s of accurate data for each polarization during every 30 s of real time. Differential attenuation results were calculated by averaging two calculated differential attenution samples. Each sample was the calculated difference between 6 samples of one polarization, the next 12 samples of the other polarization and the next 6 samples of the first polarization. This calculation was performed starting with both polarizations, and the average value was plotted. This method eliminates calculated differential attenuation errors due to linear time variations in CPA and greatly reduces inaccuracy due to quadratic CPA changes. However, it is possible that some inaccuracy still occurred when the CPA was changing rapidly or, increasing and decreasing, in a 30 second period.

6.2 Experimental Results for 81.11.30.10.

This data file is the first of a series which were recorded on Nov. 30, 1981. As this day progressed, a wide variety of meteorological and propagation conditions were observed. Because these data contain examples of most types of anomalous propagation observed during the course of this experiment and because the entire experimental system was operating satisfactorily and without interruption, several data files recorded on this date will be thoroughly analyzed in the following sections.

The first file of this series was recorded November 30, 1981 from 10:59 to 11:46. Rainrates for the individual raingauges and the path average are shown in Fig. 6.2.1. Rainrates were reasonably uniform over the raingauge network and changed relatively slowly. The path average rainrate during this period of widespread rain varied between 2 and 4 mm/h.

During this period, the wind direction was constantly from the east and therefore blowing directly perpendicular to the path. The horizontal wind velocity, shown in Fig. 6.2.2(a) on a 10 s average and in Fig. 6.2.2(b) over a 30 s average, varied between 2 and 8.2 m/s. Vertical wind velocities during this period were generally positive, (i.e. upward) as shown in Figs. 6.2.3(a) and (b) for 30 s and 60 s averages, respectively. The vertical wind velocity often changed rapidly and had 30 s average values over 1.0 m/s.

Signal levels for horizontal transmitted polarization are shown in Figs. 6.2.4(a) and (b) (10 s and 30 s averages). Fig. 6.2.5 is a time series

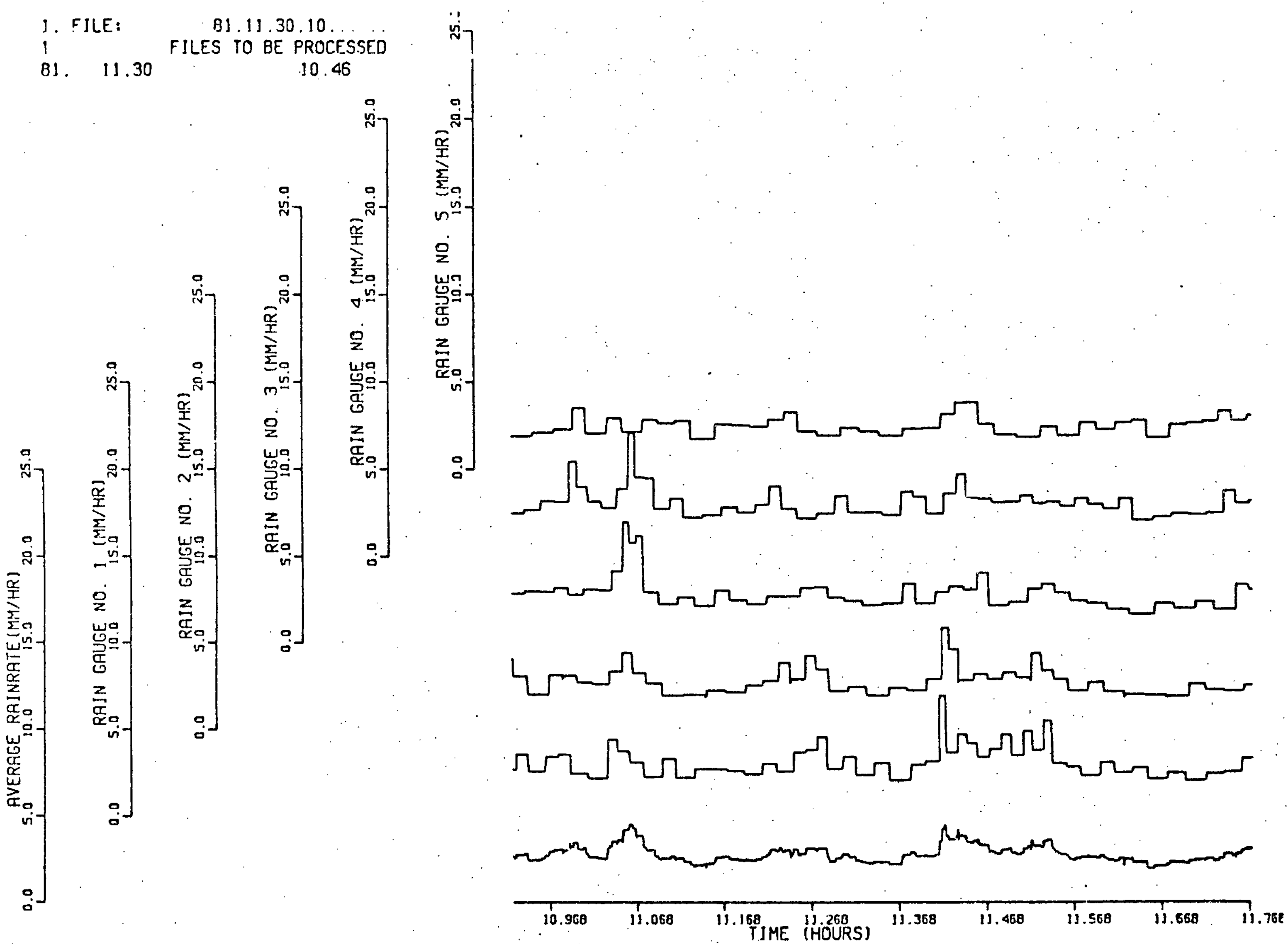

Fig. 6.2.1. Rainrates for 81.11.30.10.

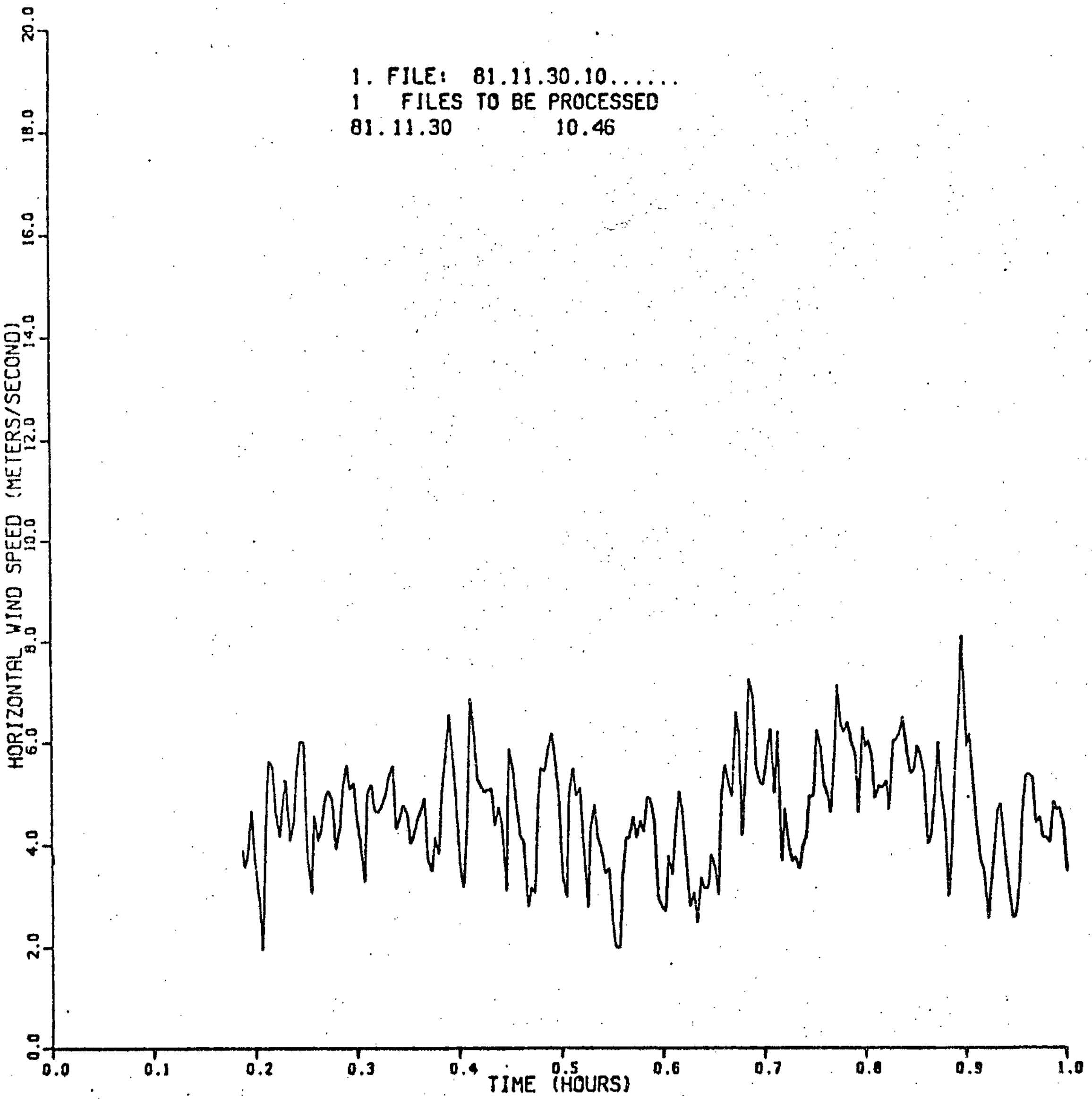

Fig. 6.2.2(a). Horizontal wind velocity, 10 s avg. for 81.11.30.10.

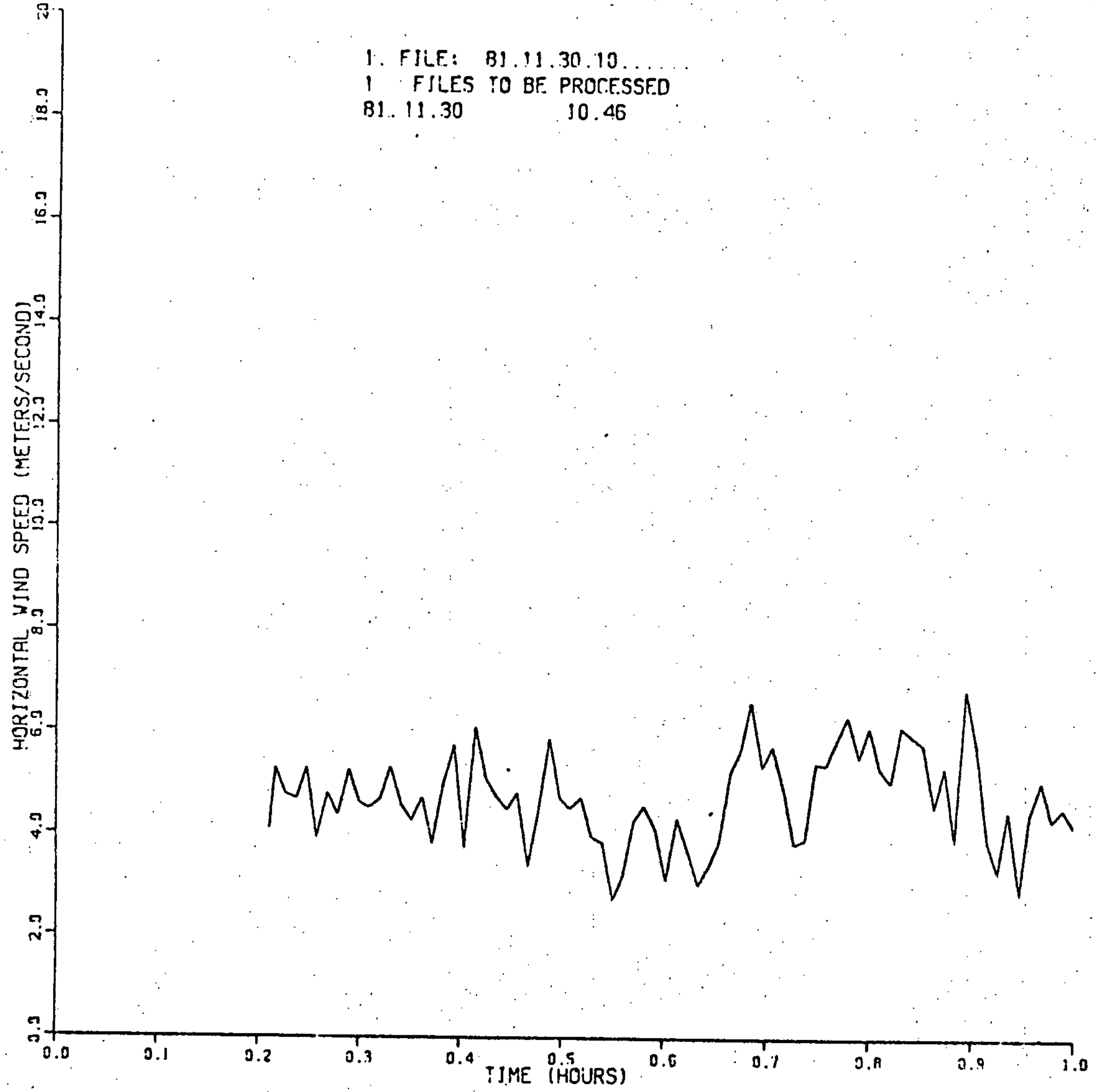

Fig. 6.2.2.(b). Horizontal wind velocity, 30s avg. for 81.11.30.10.

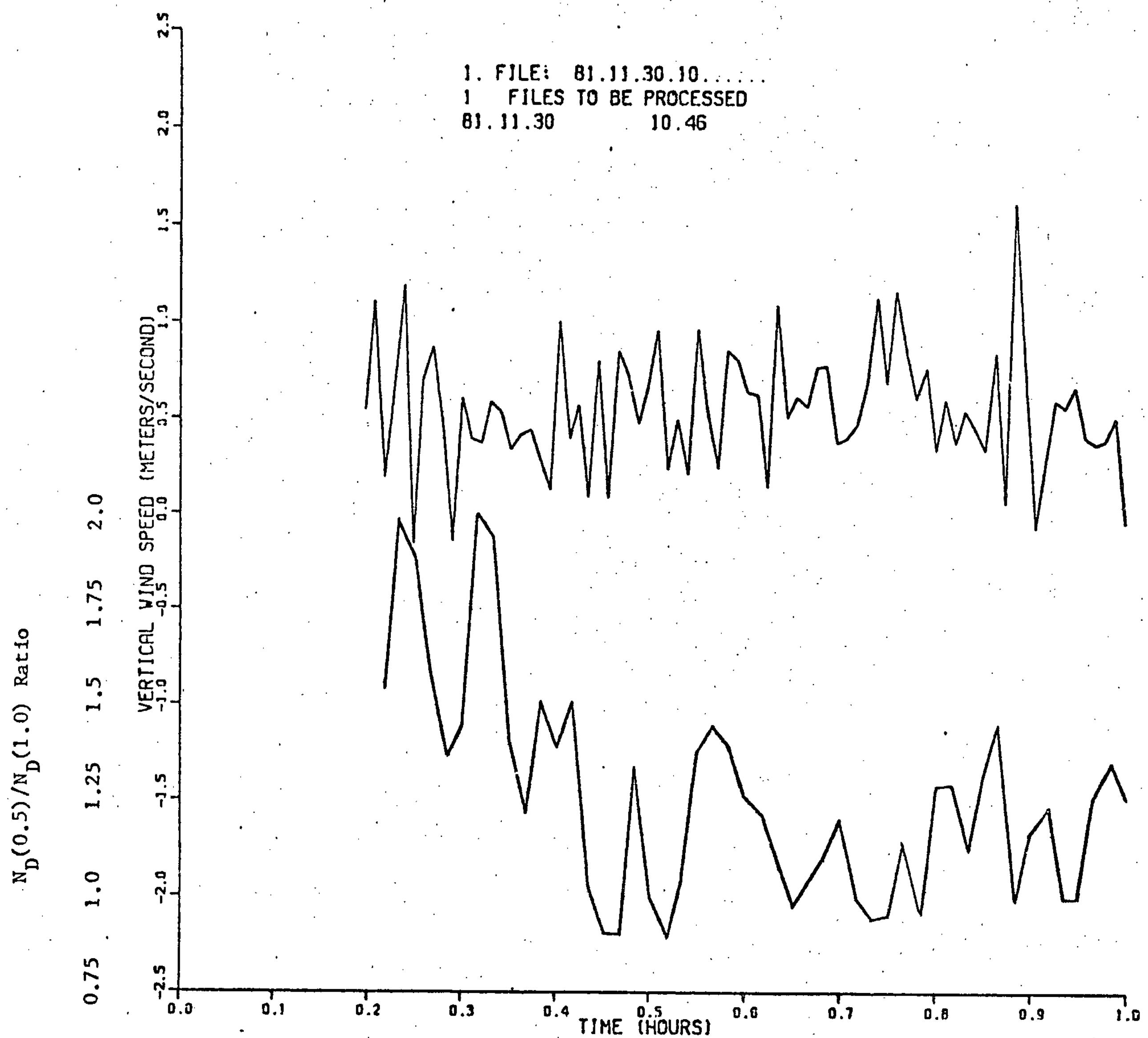

Fig. 6.2.3.(a). Vertical wind velocity, 30 s avg. and $N_D(0.5)/N_D(1.0)$ ratio for 81.11.30.10.

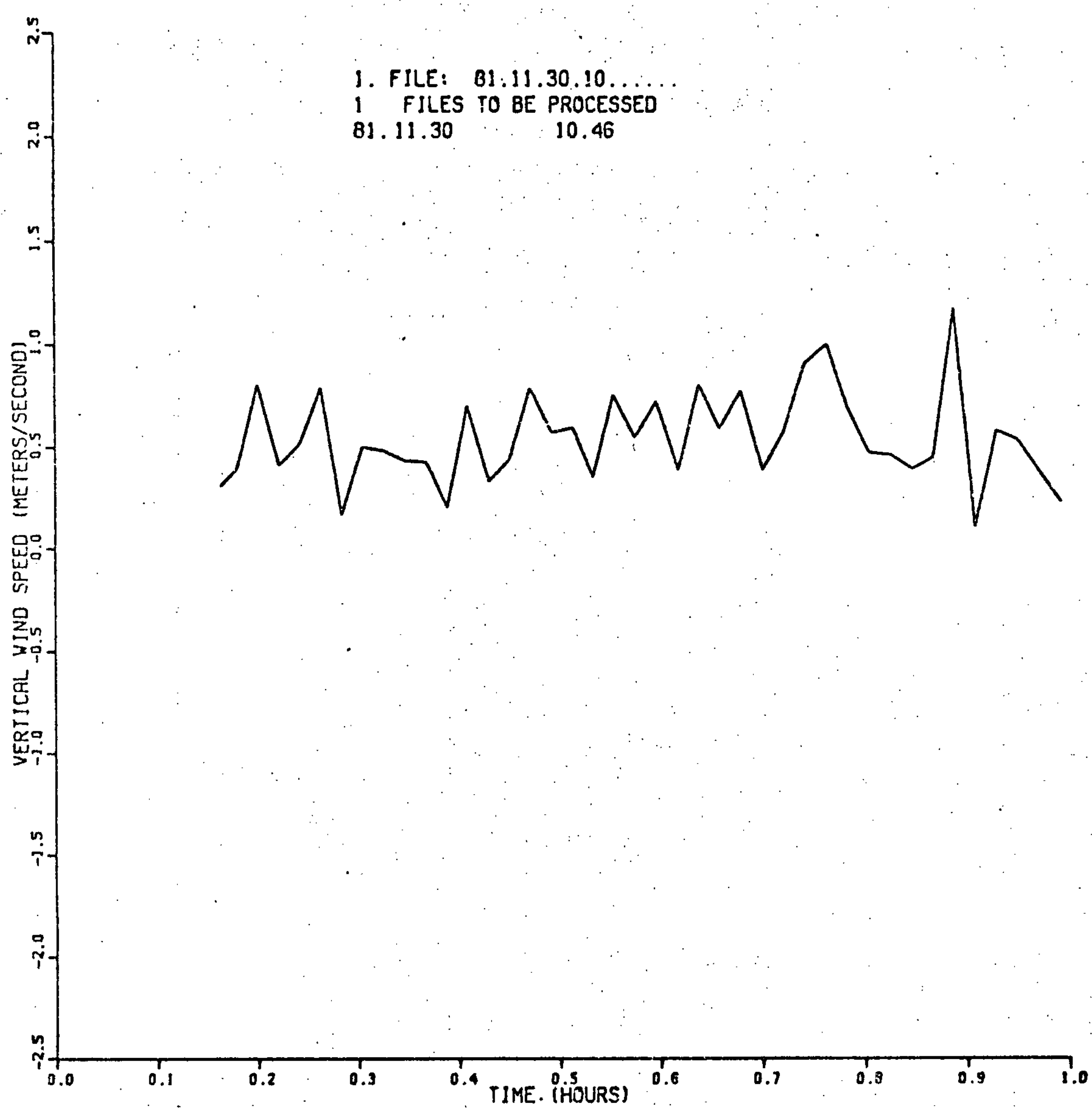

Fig. 6.2.3(b). Vertical wind velocity, 60 s avg. for 81.11.30.10.

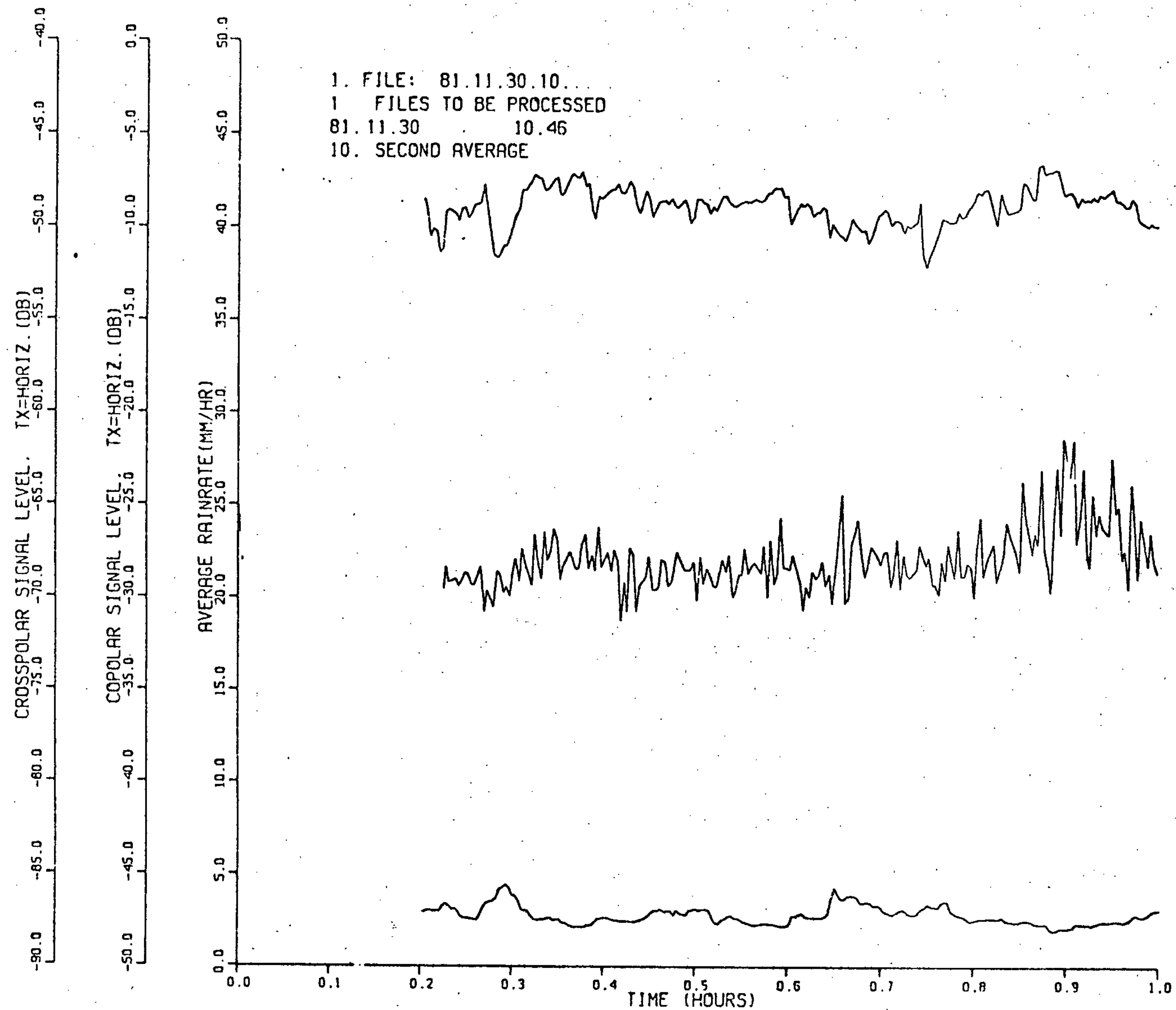

Fig. 6.2.4(a). Signal levels for horizontal polarization transmitted, 10s avg. for 81.11.30.10.

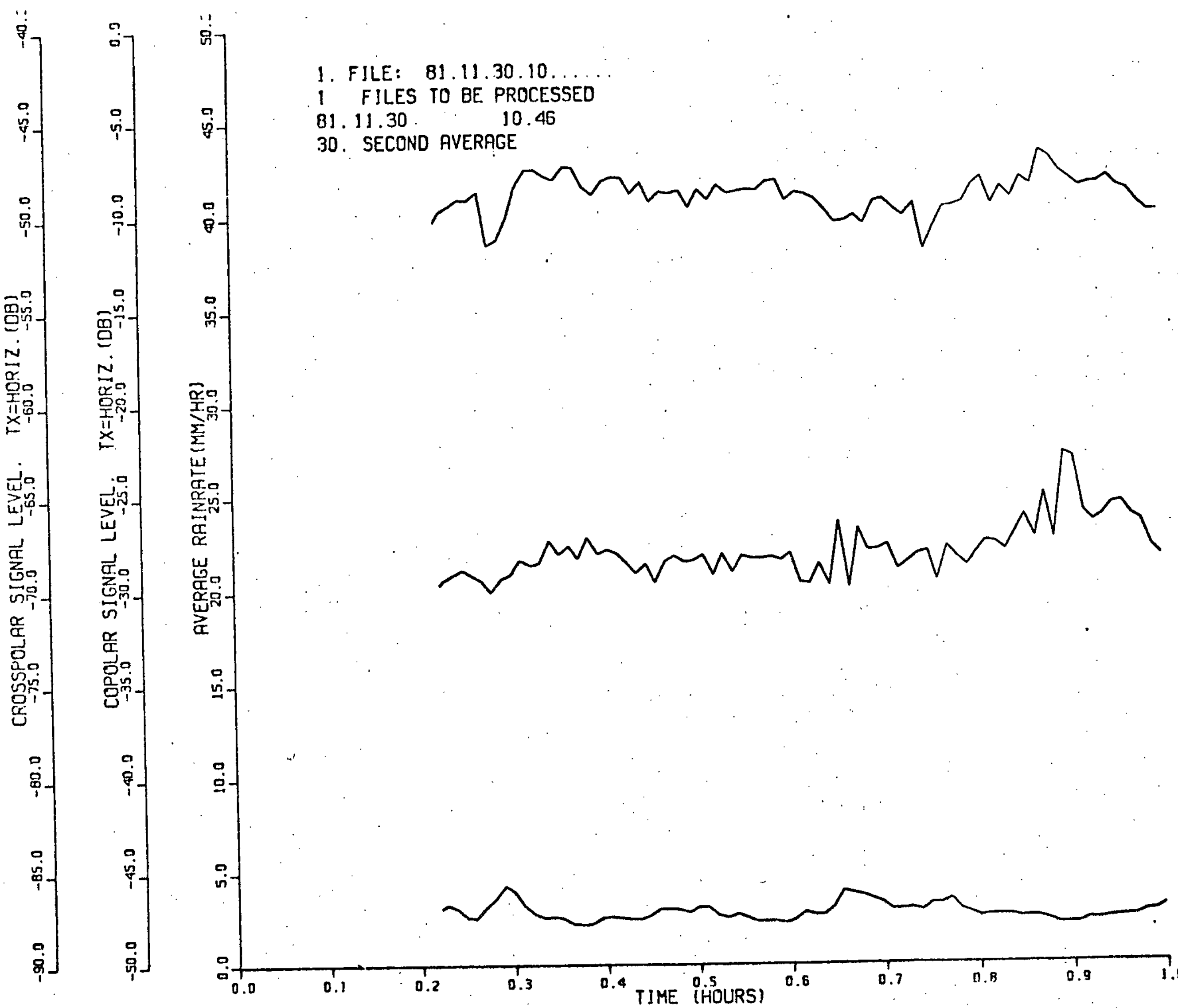

Fig. 6.2.4(b). Signal levels for horizontal polarization transmitted, 30 s avg. for 81.11.30.10.

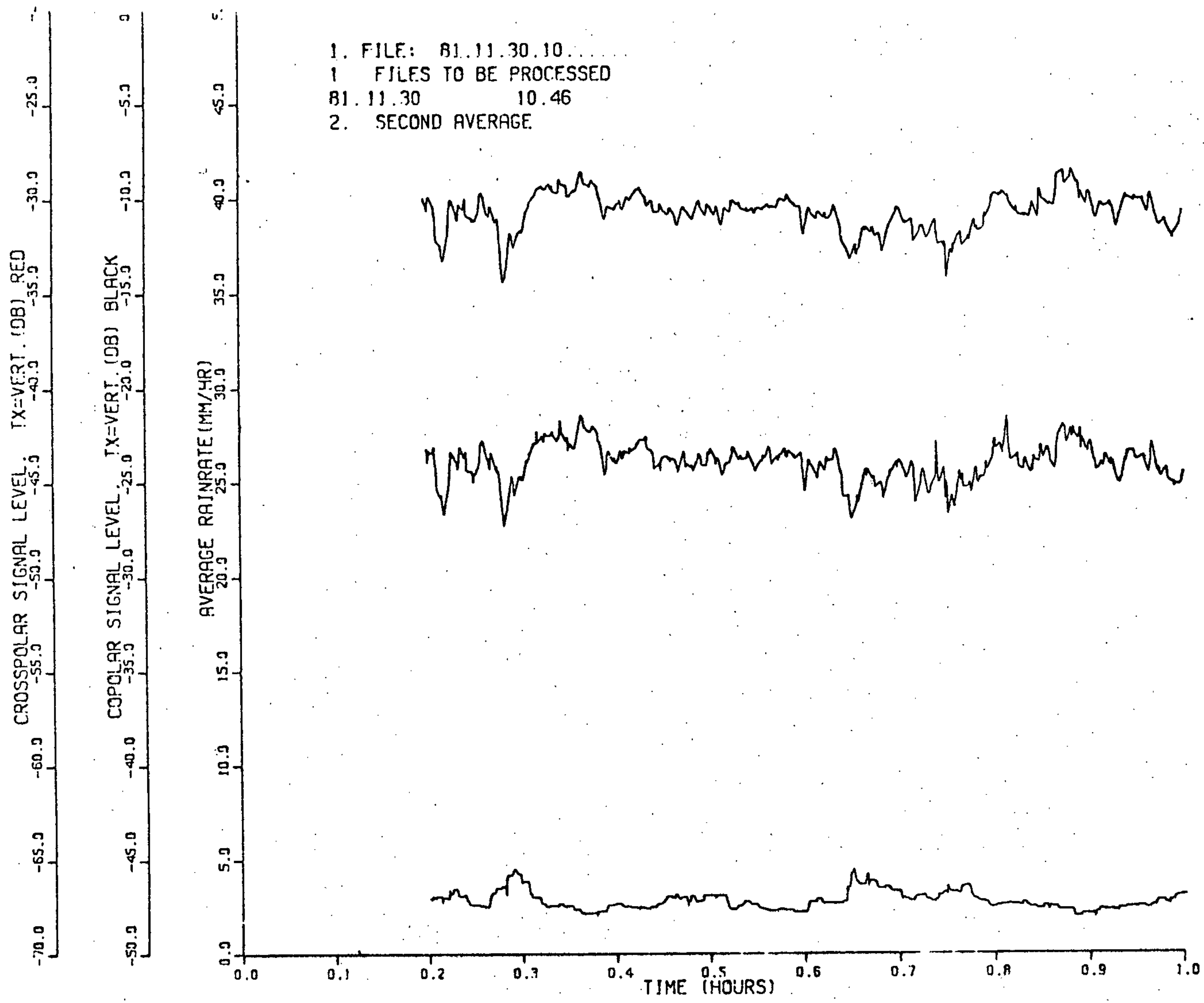

Fig. 6.2.5. Signal levels for vertical polarization transmitted, 2 s avg. for 81.11.30.10.

plot of the 2 s average signal levels for vertical transmitted polarization.

6.2.1 Attenuation Data for 81.11.30.10, 10:59-11:41

This data file contains several excellent examples of the effects of vertical wind on copolar attenuation. Included are periods of attenuation as low as that predicted for the JOT distribution and considerably higher than predicted for the JOD distribution. These occurred even though almost all of the measured drop distributions generally conformed to the JOW distribution. Significant variation did occur, however, in the relative number of drops in the smallest categories, as indicated by the ratio: $N_D(0.5)/N_D(1.0)$ shown in Fig. 6.2.3(a). The vertical wind effects can be clearly isolated in this file because the rainrate was reasonably uniform along the path, slowly varying and relatively constant over this entire period. A summary of the attenuation results for this file are given in Table 6.2.1. A legend for the numbered comments for this and all of the similar summaries immediately follows Table 6.2.1.

Period	Measured Attenuation Compared to Standard Predictions	Measured Drop Distribution	Vertical Wind During Rain	Data is in Approximate Agreement with Predictions for:	Comments
T_1 0.20--0.23 h	Varied from JOW to greater than JOD Fig. 6.2.6	JOW, 1 Fig. 6.2.7	Decreased from +1.2 m/s to +0.2 m/s then started to increase. Fig. 6.2.3(a),(b)	Rainrate ≅ constant. Attenuation correlated with vertical wind decrease. Figs. 6.2.3(a), 6.2.4(a), 6.2.6.	3,
T_2 0.23-0.26 h	Between JOD and JOW Fig. 6.2.8	JOW, 1 Fig. 6.2.9	Variable, rapidly increased, decreased and increased. avg ≅ 0.6 m/s Fig. 6.2.3(a),(b)	JOW and vert. wind 0 to +1.0 m/s Fig. 6.2.8	Ref. Section 6.2.1.2
T_3 0.27-0.29 h	Varied from JOD to JOT Fig. 6.2.10	Between JOW and JOT, more large drops that T1 & T2 Fig. 6.2.11	Decreased from +0.85 to -0.15 m/s Fig. 6.2.3(a)	Rainrate ≅ constant attenuation variable due to vertical wind. Figs. 6.2.3(a), 6.2.4(a), 6.2.10	3,
T_4 0.31-0.34 h	Between JOW and JOT Fig. 6.2.12	JOW, 1 Fig. 6.2.13	Relatively constant ≅+0.5 m/s avg. Fig. 6.2.3(a)	JOT and JOW with zero vert. wind. Fig. 6.2.12	Anomolously low attenuation. Ref. Section 6.2.14
T_5 0.72-0.74 h	Close to JOD Fig. 6.2.14	JOW, 1 & 5 Fig. 6.2.15	Increased from +0.5 to +1.15 m/s, ≅0.70 m/s avg. Fig. 6.2.3(a)	JOW and vert. wind =+1.0 m/s Fig. 6.2.14	4, 5.

. . . continued

Period	Measured Attenuation Compared to Standard Predictions	Measured Drop Distribution	Vertical Wind During Rain	Data is in Approximate Agreement with Predictions for:	Comments
T_6 0.74-0.78 h	Varied from JOW to much higher than JOD Fig. 6.2.16	Basically JOW, 1, but few more large drops. Fig. 6.2.17	Decreased, increased and decreased between +0.6 and +1.15 m/s Fig. 6.2.3(a)	Rainrate ≅ constant Range of attenuation due to vertical wind. Figs. 6.2.3(a), 6.2.4(a), 6.2.16	3 and 4
T_7 0.78-0.84 h	Between JOW and JOD Fig. 6.2.18	JOW, 1 Fig. 6.2.19	Relatively constant ≅+0.5 m/s avg. Fig. 6.2.3(a)	JOW and vert. wind = +0.5 m/s. Fig. 6.2.18	
T_8 0.87-0.89 h	JOT, lower than T_7 Fig. 6.2.20	JOW, 1 & 5 Fig. 6.2.21	Increased from +0.1 to 1.6 m/s Fig. 6.2.3(a)	JOT and zero vert. wind. See comments Fig. 6.2.20	8 Ref. Section 6.2.1.8
T_9 0.89-0.93 h	Between JOW and JOD, higher that T_8. Fig. 6.2.22	JOW, 1 Fig. 6.2.23	Decreased from ≅1.0 m/s to 0 and then increased. Fig. 6.2.3(a)	JOW and vert. wind = 0.5 m/s Fig. 6.2.22	3

Table 6.2.1 Summary of Attenuation Data for 81.11.30.10, 10:59-11:41

Legend for Summary Tables.

1. Number of drops in the smallest category was actually larger than indicated by disdrometer because of horizontal wind velocity. This is discussed in Section 6.1.1.
2. Actual or "effective" vertical wind velocity appears to be approximately double measured vertical wind velocity. This is discussed in Section 6.4.1.1.
3. Attenuation was unusually high because small drops were "stored" above the path by a vertical wind flow before this period and then, during this period, "released" by a reduced or decreasing vertical wind velocity. This is discussed in Section 6.2.1.1.
4. Attenuation was relatively high because vertical wind was increasing or was near a peak and this was increasing the number of small drops per m^3 in the propagation path, as discussed in Section 6.2.1.5.
5. Number of drops in smallest or two smallest categories measured by the disdrometer were low because vertical wind was increasing during this period, transiently reducing the number of small drops falling into the disdrometer.
6. Measured attenuation was relatively low for measured path rainrate because of an unusually large number of large drops which considerably

increase measured rainrate but did not affect attenuation as significantly at this frequency.

7. During this interval the drop size distribution changed rapidly. Because this distribution was measured at one end of the path, the attenuation and drop size data have been time shifted by up to one minute to obtain a more realistic correlation between the path average attenuation and the measured drop size distribution. This delay is discussed in Section 6.2.1.3.

8. Attenuation and number of drops in the smallest categories were both temporarily low due to an unusually rapid increase in vertical wind velocity. This vertical wind transient temporarily reduced the number of drops falling to the level of the propagation path, as discussed in Section 6.2.1.8.

9. Some inaccuracy may occur when comparing XPD values during low rainrates to theoretical predictions because:
   - the clear weather cancelled system XPD is just over 60 dB and this value agrees with the theoretical predictions for $\phi \cong 3°$ at a rainrate of 2.5 mm/hr.
   - at low crosspolar signal levels (i.e. close to −70 dB) the proximity of the receiver noise floor can introduce errors (expecially for short averaging periods).

6.2.1.1 Attenuation During T_1, 0.20-0.23 h.

During the interval T_1, Fig. 6.2.6 shows that the CPA was quite variable and at times was considerably higher than predictions for the JOD distribution even though the measured drop sizes were in agreement with the JOW distribution, as shown in Fig. 6.2.7. This is thought to be due to the vertical wind velocity, which decreased rapidly from +1.1 m/s to +0.2 m/s, and then began to increase again at the end of this period. Figs. 6.2.3(a) and 6.2.4(a) show that the attenuation was high during the decreasing vertical wind and then decreased when the vertical wind began to increase. It is believed that the high attenuation was due to a large number of small drops (which attained a reduced velocity above the path during an immediately previous period of upward vertical wind) being "released" as the vertical wind decreased. When the vertical wind increased near the end of this period, the attenuation was reduced as the drops were again temporarily "suspended" above the propagation path.

6.2.1.2 Attenuation During T_2, 0.23-0.26 h.

In the interval T_2, the attenuation, Fig. 6.2.8, was less variable than during T_1, even though the variations in the 30 s average vertical wind velocity, Fig. 6.2.3(a), were greater. This is thought to be because the

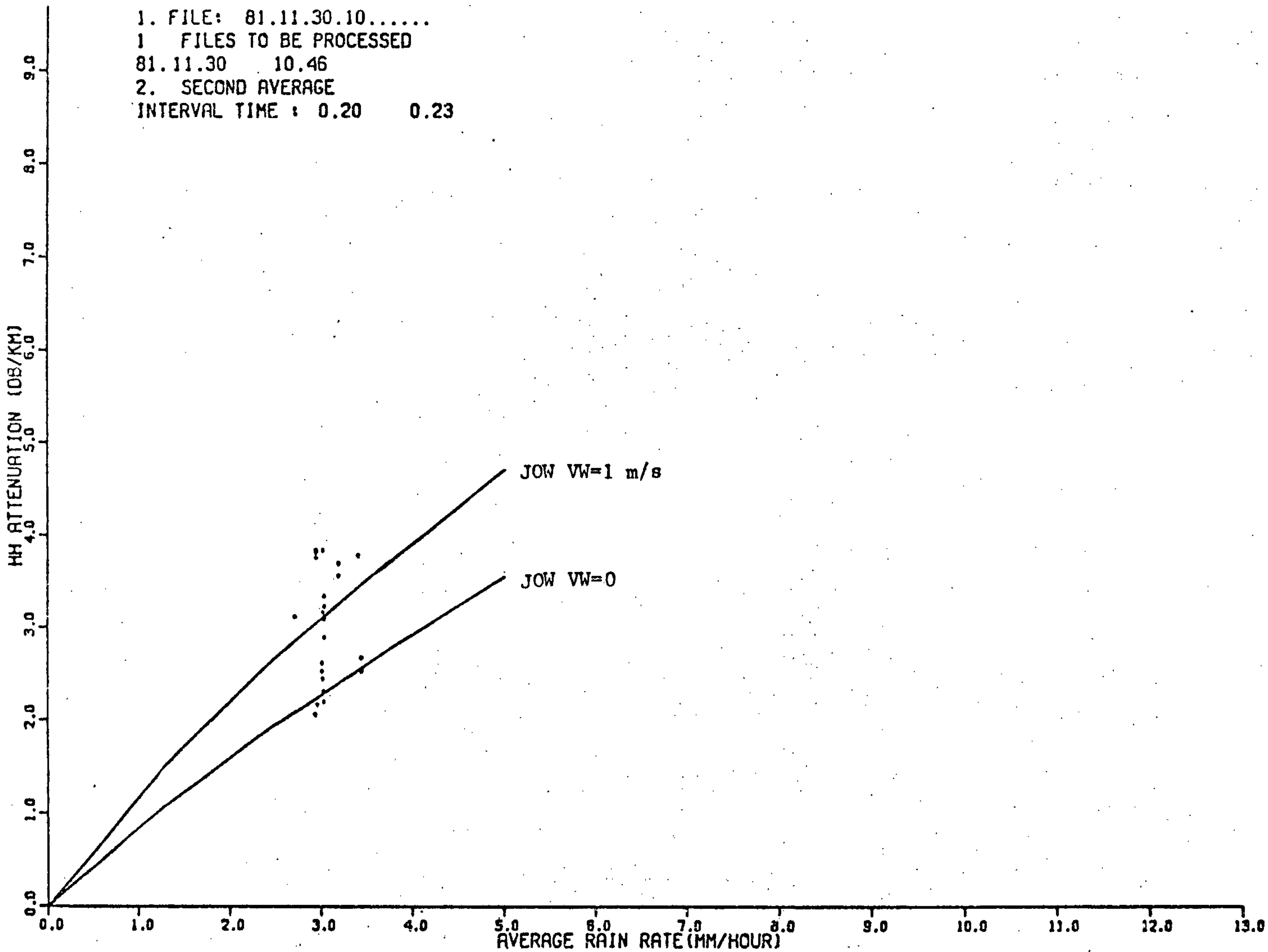

Fig. 6.2.6. CPA during T_1.

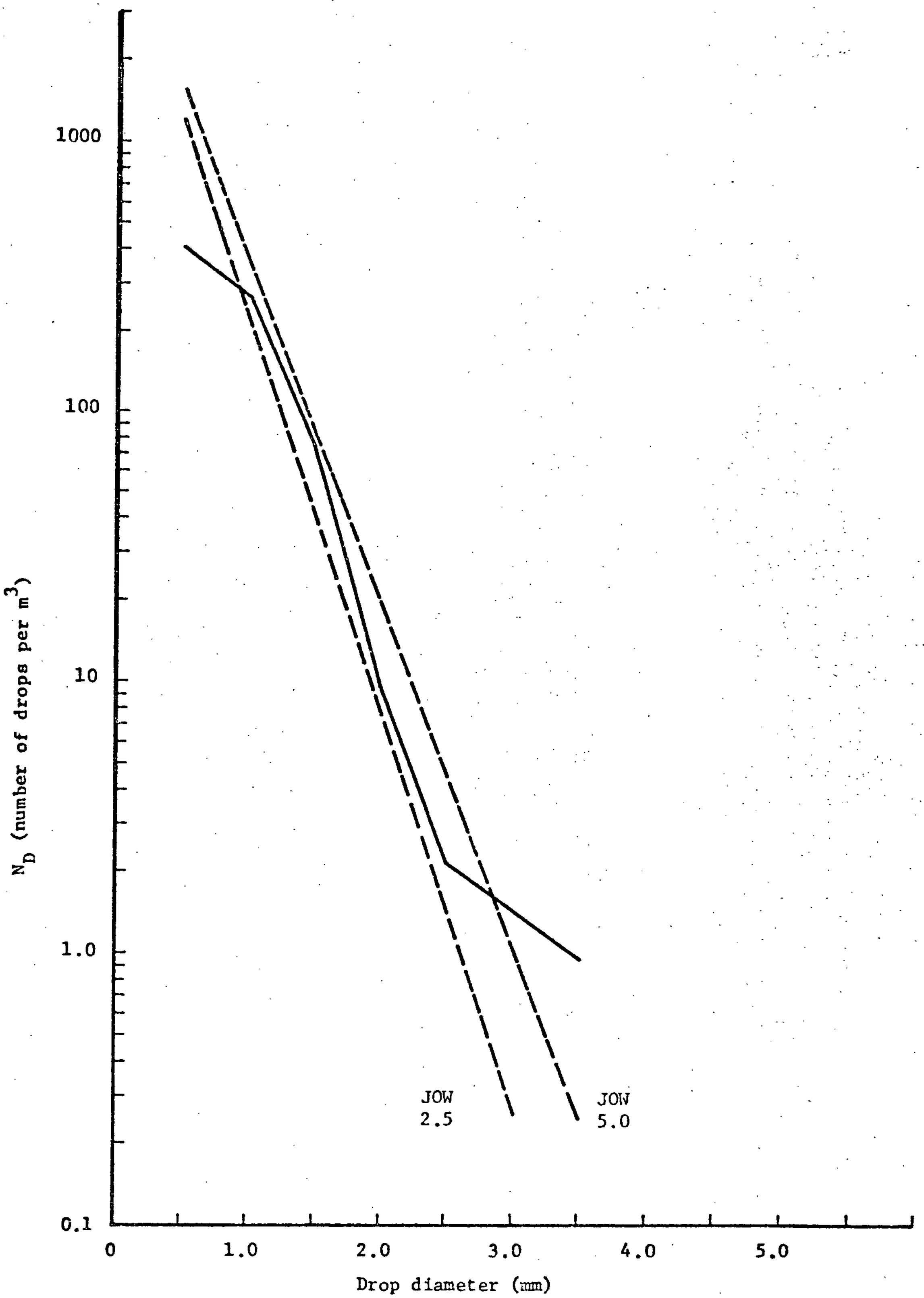

Fig. 6.2.7. Drop distributions for T_1.

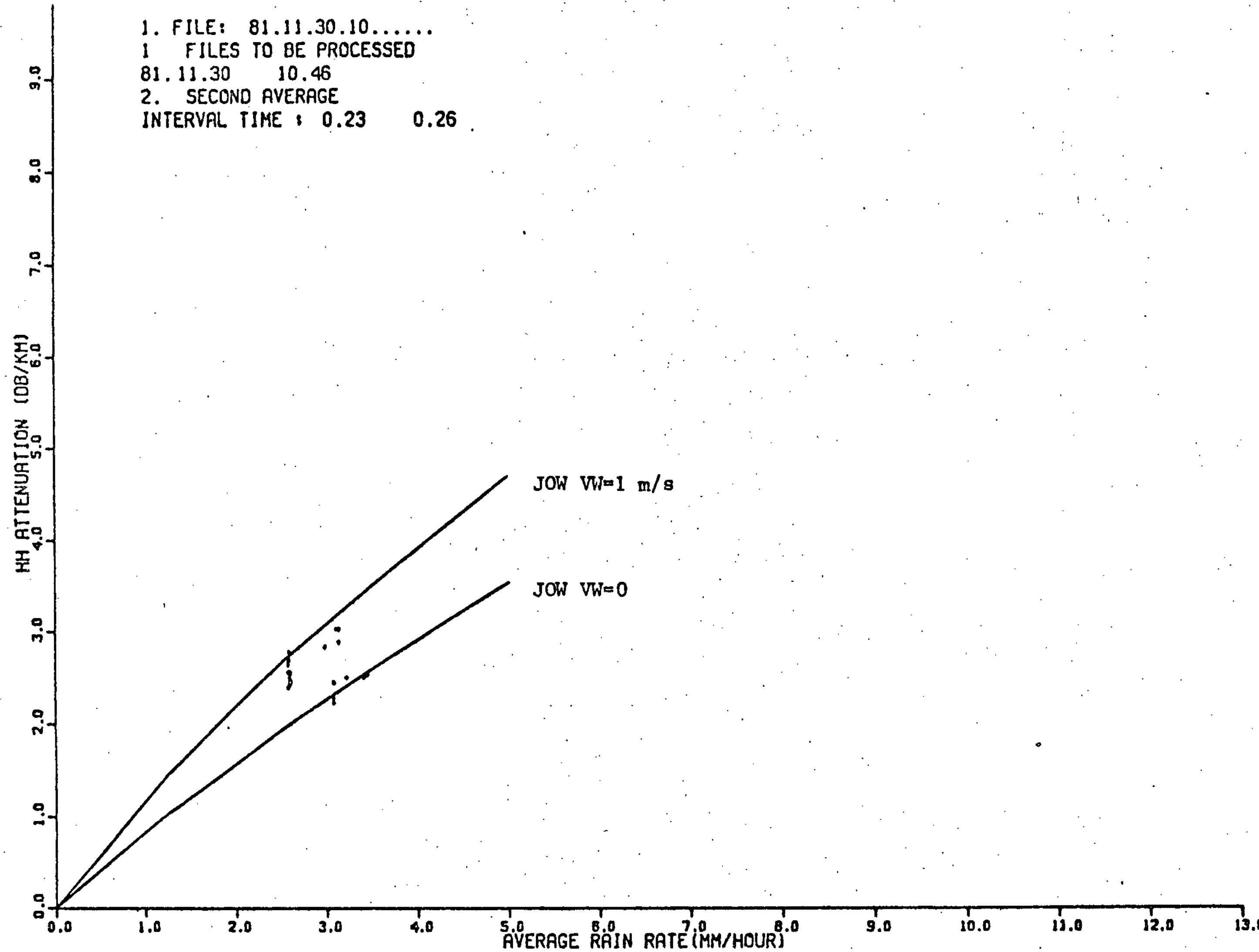

Fig. 6.2.8. CPA during T_2.

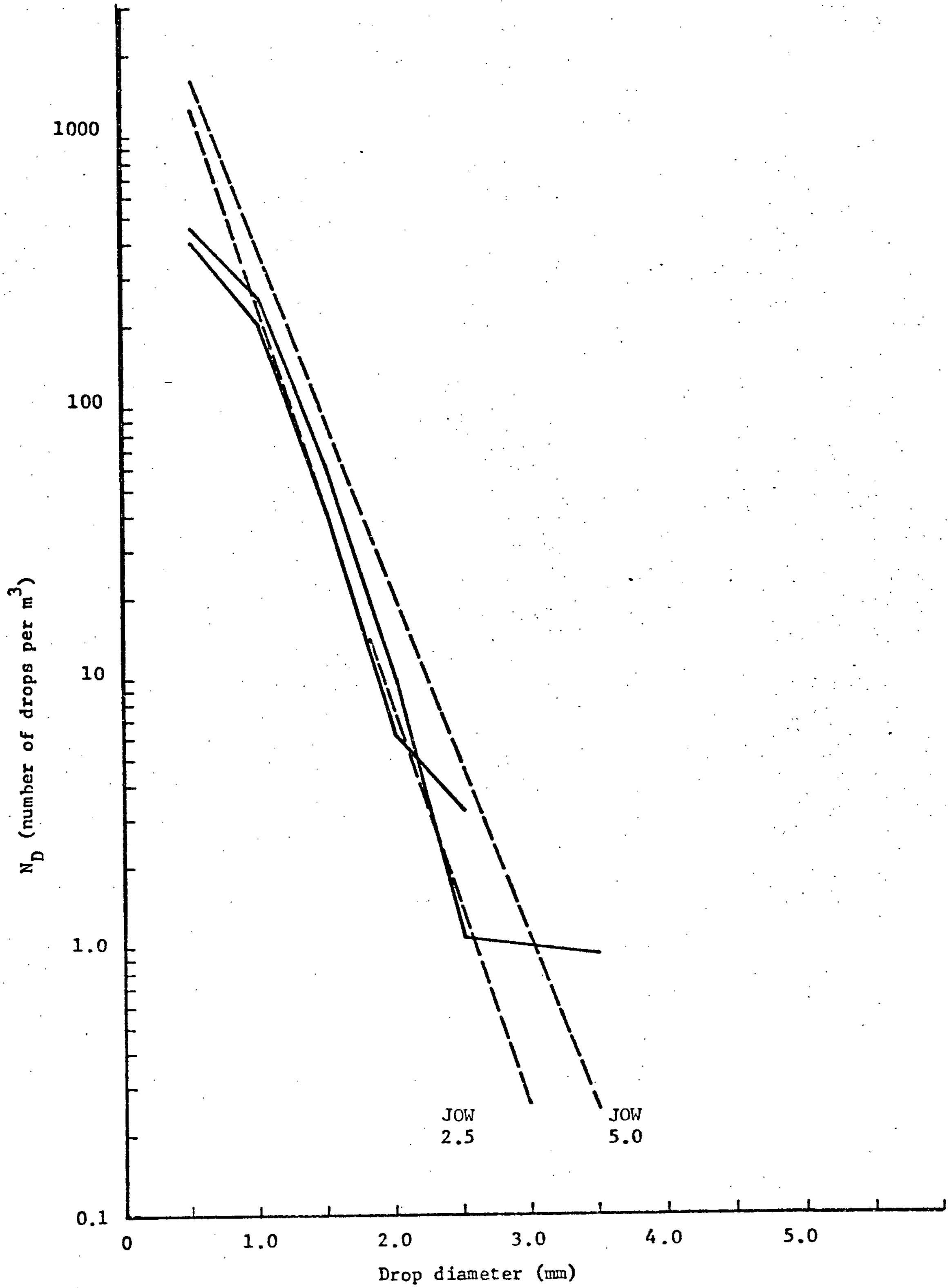

Fig. 6.2.9. Drop distributions for T_2.

vertical wind velocity during T_2 increased, decreased and then increased again without sufficient time for a significant change in the drop size distribution at the height of the antenna beams. The 60 s average vertical wind velocity, Fig. 6.2.3(b), shows more clearly the general decrease during T_1 and a slightly smaller and more gradual variation during T_2.

6.2.1.3 Attenuation During T_3, 0.27-0.29 h.

During T_3 the attenuation, Fig. 6.2.10, again varied over a wide range, in this case, between predictions for the JOT, to slightly higher than the JOD, distributions. The vertical wind velocity during this period rapidly decreased from +0.85 to −0.15 m/s after a period of upward flow, Fig. 6.2.3(a), in a manner very similar to T_1. The slightly lower absolute values of attenuation during T_3 compared to T_1 were due to a larger proportion of large drops during T_3, as shown in Fig. 6.2.11. Fig. 6.2.3(a) also shows the ratio: $N_D(0.5)/N_D(1.0)$. This curve shows the increase in the number of smaller drops approximately one minute after the vertical wind decrease and attenuation increase, for both periods T_1 and T_3. The reason for this delay is not entirely clear, but is believed to be due to the fact that the disdrometer is at one end, which is also the lowest point, of the path. The disdrometer is 30 m lower than the reflector, Fig. 2.31. If an average vertical wind velocity of 1 m/s is assumed, this height difference could

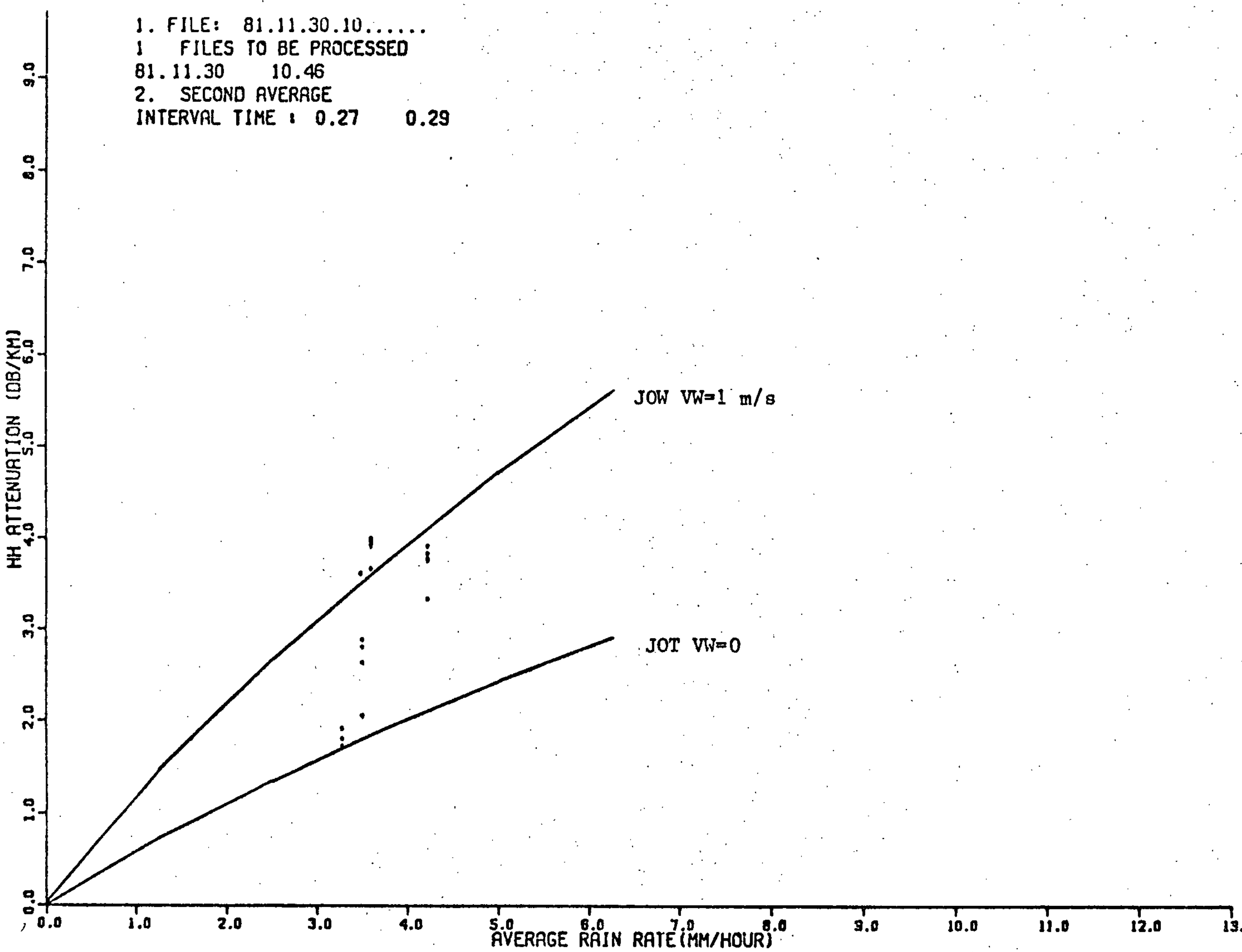

Fig. 6.2.10. CPA during T_3.

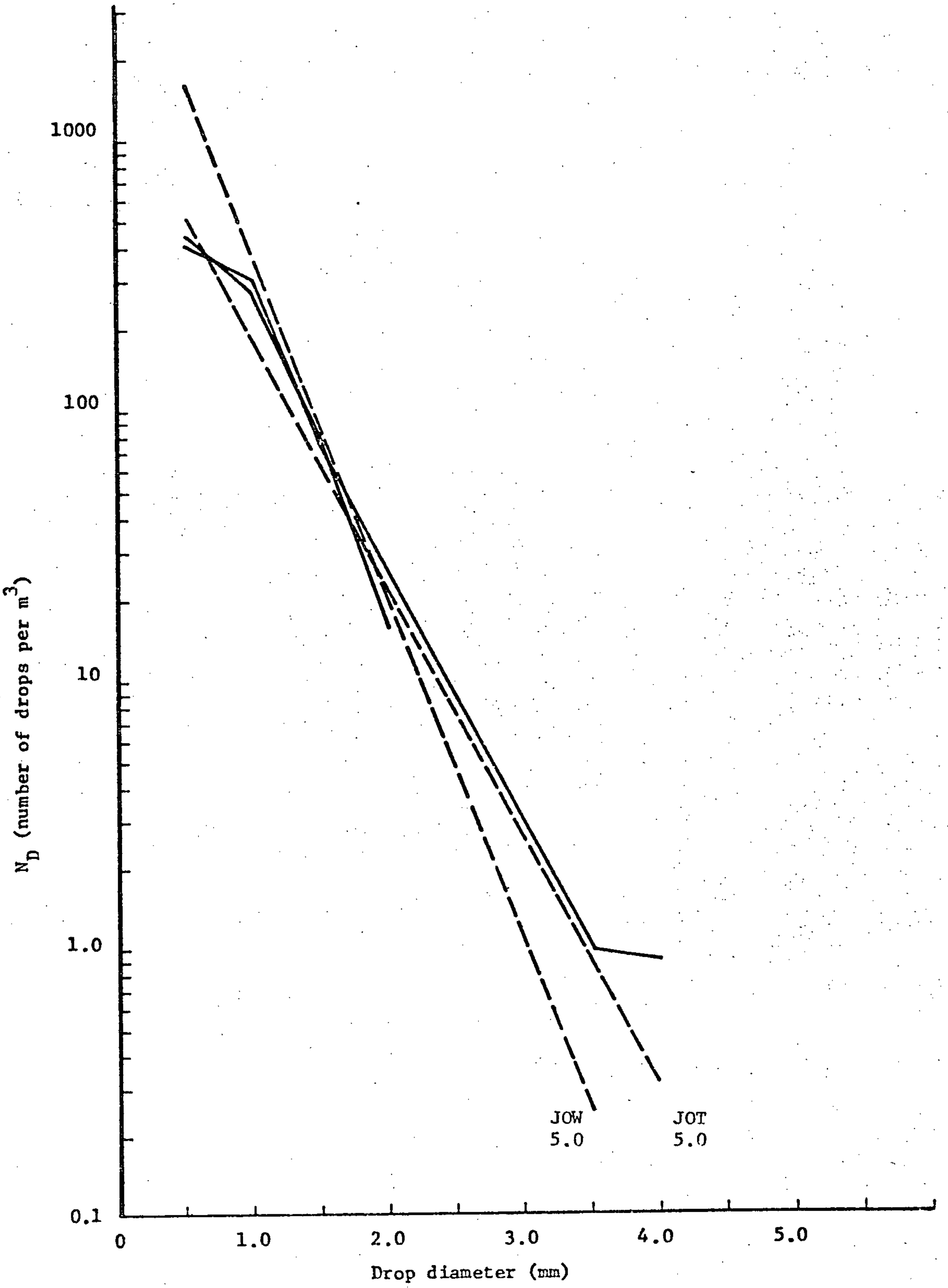

Fig.6.2.11. Drop distributions for T_3.

account for an average 30 s delay in the arrival time of the increased number of drops in the smallest category, at the reflector, compared to the disdrometer. This delay would also be considerably larger for the smaller drops in this category which would also have undergone the greatest degree of "storage" due to the previous upward air flow. It is also possible that there is a general movement, during these periods, of rain medium change from the reflector end of the path towards the end of the path where the disdrometer is located. This would probably be related to a southerly component of rain cell movement but this is difficult to verify for these periods because the rainrate along the path is quite uniform.

6.2.1.4 Attenuation During T_4, 0.31-0.34 h.

Attenuation during period T_4, Fig. 6.2.12, was anomolously low. Vertical wind during this period was relatively constant at +0.5 m/s, Figs. 6.2.3(a) and (b), which should have resulted in a slightly increased attenuation. The drop sizes measured by the disdrometer during this period were close to the JOW distribution. The only possible explanation for this low attenuation is the relatively smaller number of small drops shown in Fig. 6.2.3(a) immediately after this interval. If the theory about a delay in the disdrometer data for these periods, presented in the previous section, was correct, then this change in drop distribution might adequately explain these attenuation results.

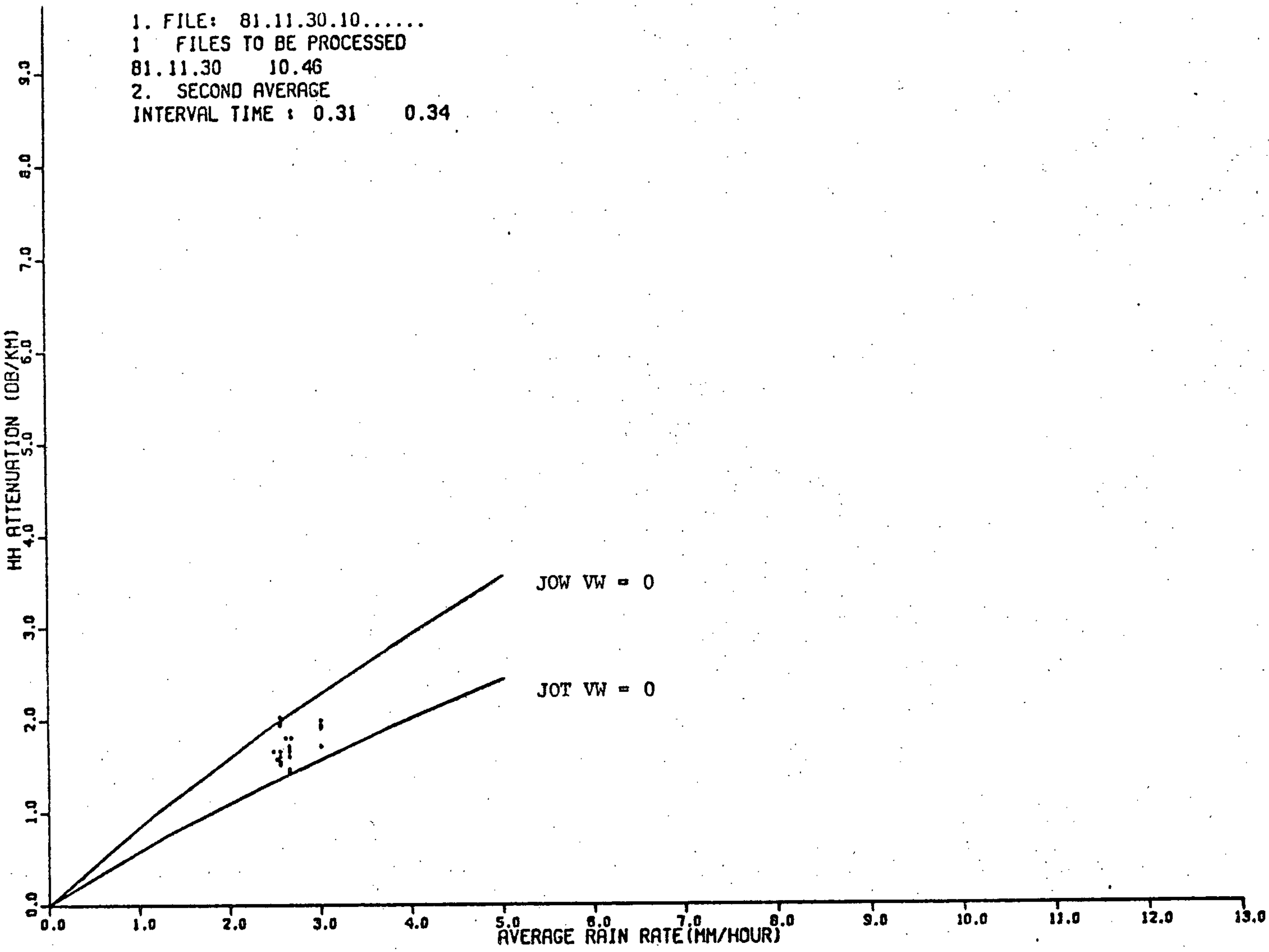

Fig. 6.2.12. CPA during T_4.

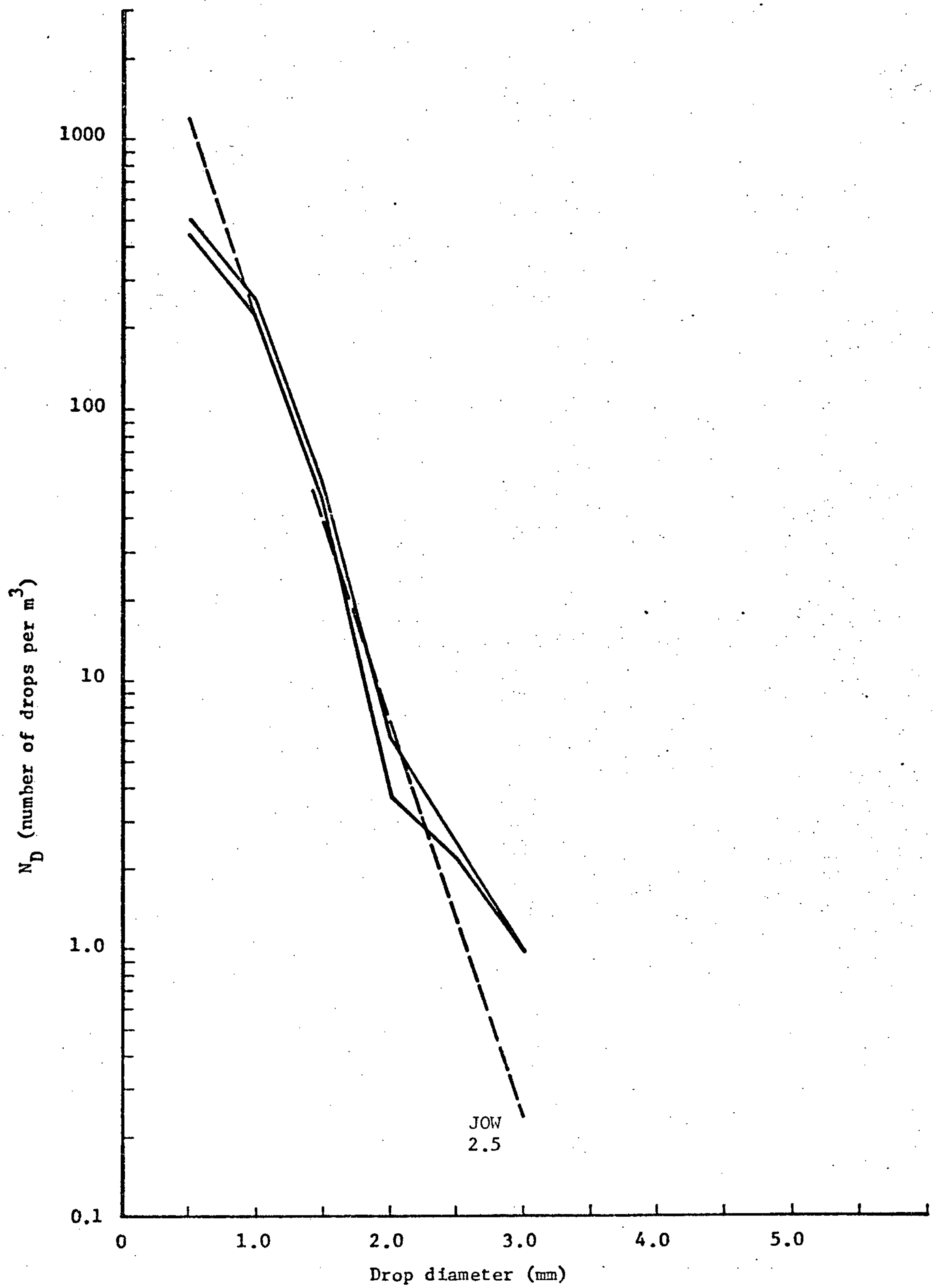

Fig. 6.2.13. Drop distributions for T_4.

6.2.1.5 Attenuation During T_5, 0.72-0.74 h.

During interval T_5, Fig. 6.2.14 shows that the attenuation was similar to that predicted for the JOD distribution but the measured drop sizes, Fig. 6.2.15, generally corresponded to the JOW distribution. The unusually small number of drops in the smallest category is believed to be due to the vertical wind, which was increasing from +0.5 to +1.15 m/s during this period. It is thought that the increasing vertical wind temporarily reduced the number of small drops falling to the height of the disdrometer. This reduction in the number of small drops is clearly shown in Fig. 6.2.3(a). The attenuation during T_5 agrees with that predicted for the JOW distribution and a vertical wind velocity of +1.0 m/s. Thus, it appears that the upward vertical wind during this period temporarily increased the number of drops in the path while simultaneously reducing the number of drops falling to the height of the disdrometer. Some suggestions as to the cause of this phenomena include:

- a simple, vertical wind induced transient in the number of small drops at the location of the disdrometer
- the different heights along the path
- a complex, vertically-circular, turbulent airflow along the path due to the buildings below the path, or
- the vertical wind velocity near the building on which the disdrometer is mounted further reducing the small drop catch efficiency of the disdrometer as discussed in Section 6.1.1.

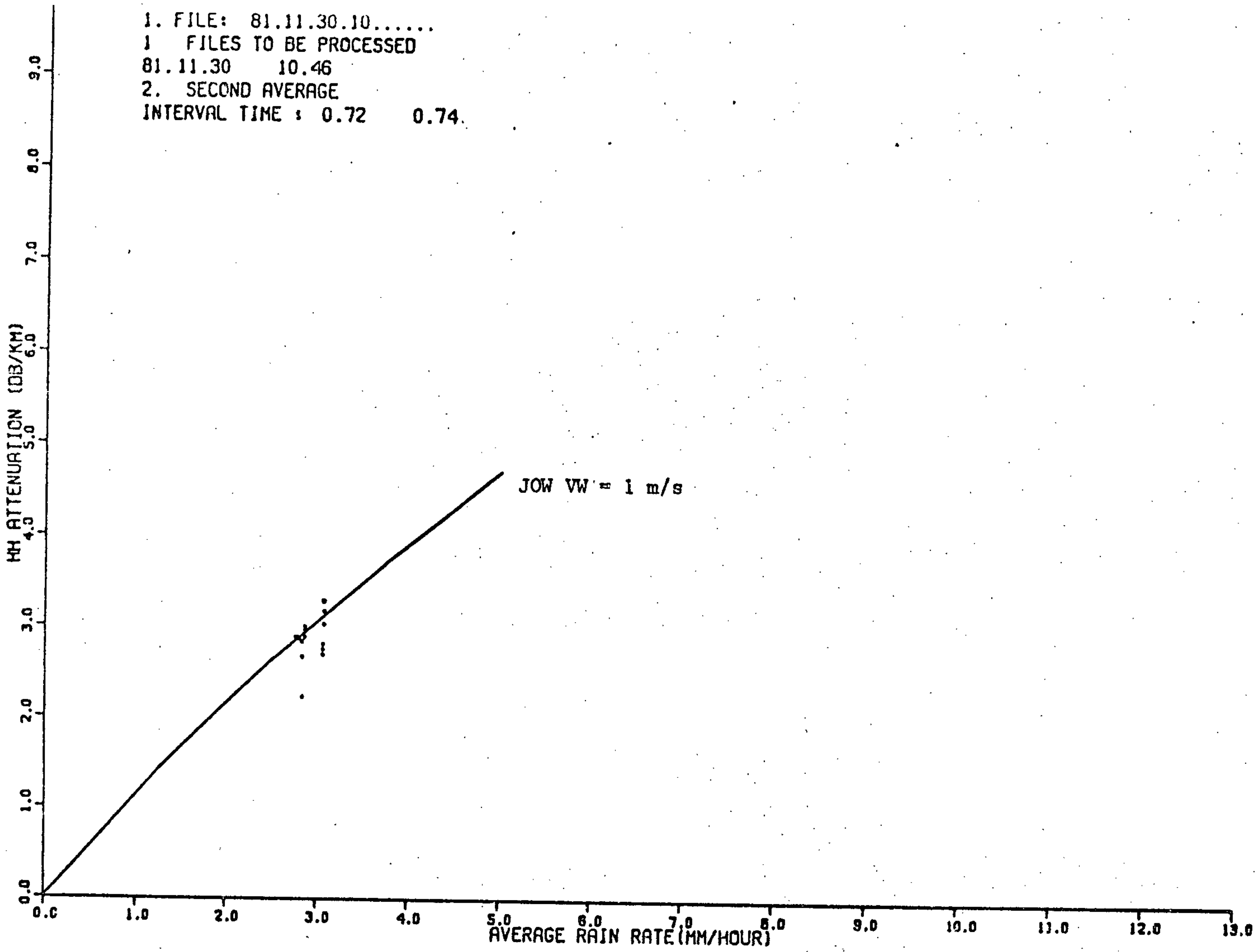

Fig. 6.2.14. CPA during T_5.

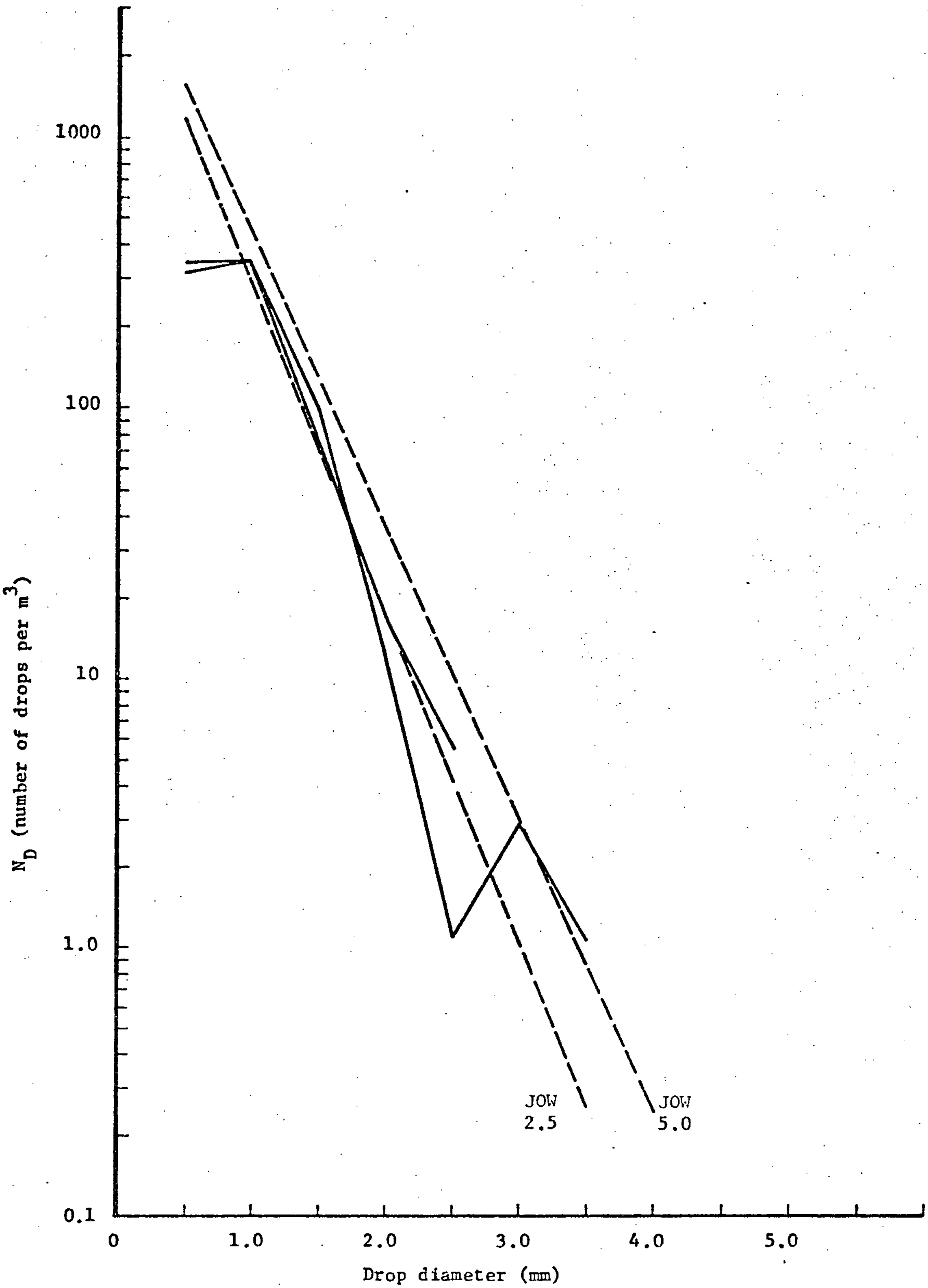

Fig. 6.2.15. Drop distributions during T_5.

6.2.1.6 Attenuation During T_6, 0.74–0.78 h.

Interval T_6 is another clear example of attenuation much higher than that predicted for the JOD distribution, Fig. 6.2.16. The highest attenuations occurred at 0.75 h, Fig. 6.2.4(a), at the same time as the vertical wind decreased in Fig. 6.2.3(a). Again, Fig. 6.2.3(a) shows an increase in the number of small drops one minute later. This attenuation peak is believed to be relatively large because the vertical wind was steadily increasing for the 2.5 minutes before 0.75 h, resulting in a large accumulation of small drops.

6.2.1.7 Attenuation During T_7, 0.78–0.84 h.

During T_7, the attenuation, Fig. 6.2.18, was generally higher than that predicted for the JOW distribution. This is believed to be due to the relatively constant +0.5 m/s vertical wind and possibly some small drops which were held suspended by the previously higher vertical wind velocity. These results agree, on the average, with predictions for the measured distribution and vertical wind velocity.

6.2.1.8 Attenuation During T_8, 0.87–0.89 h.

Attenuation during T_8, Fig. 6.2.20, agreed with the standard predictions for the JOT distributoin. This very low attenuation was due to an extremely fast increase in the vertical wind velocity from +0.1 to +1.6 m/s, Fig. 6.2.3(a). In this case, the disdrometer indicated the decrease in the $N_D(0.5)/N_D(1.0)$ ratio within approximately 30 s. This period is in contrast to T_5, which had higher attenuation during a period of increasing

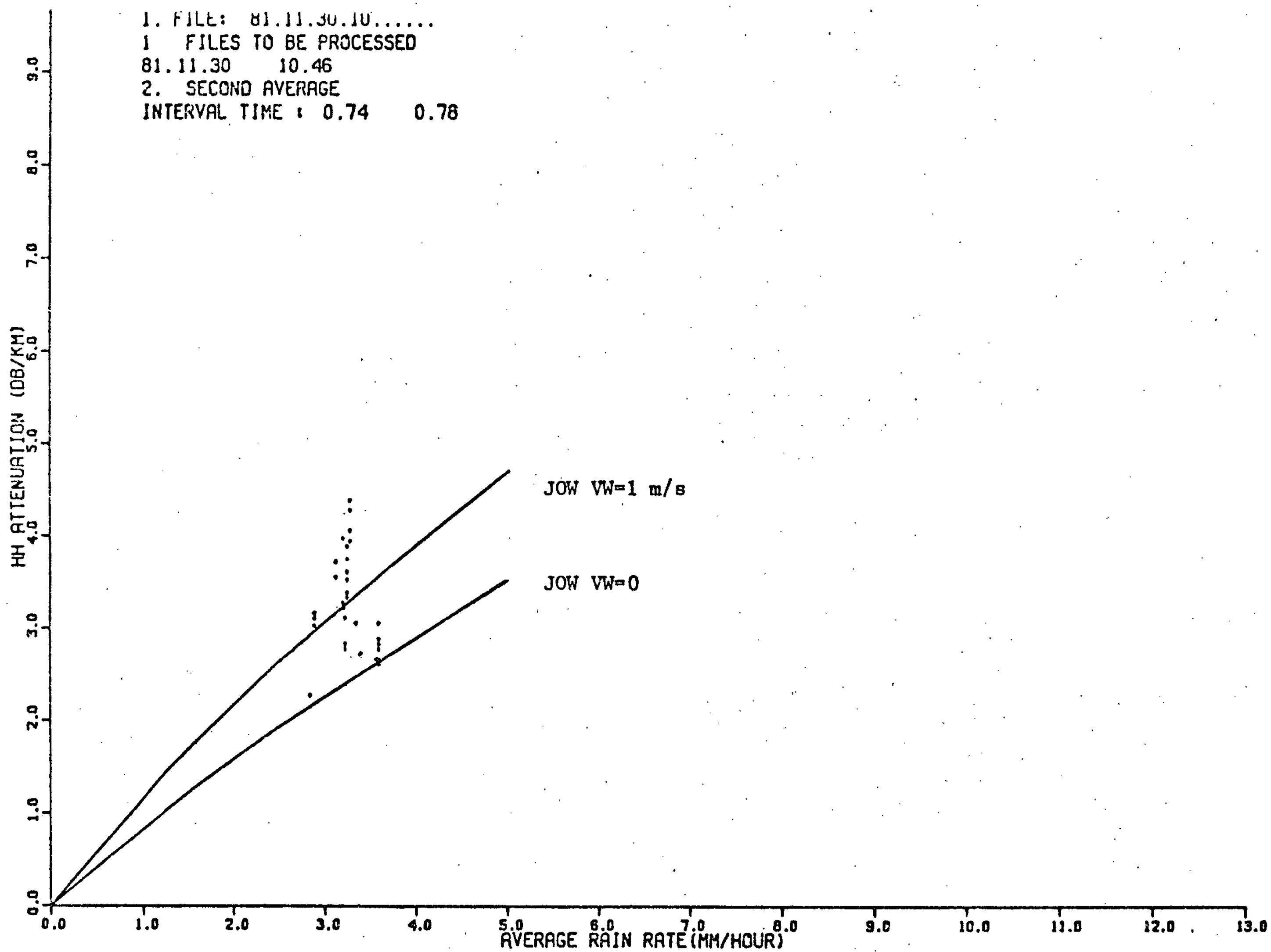

Fig. 6.2.16. CPA during T_6.

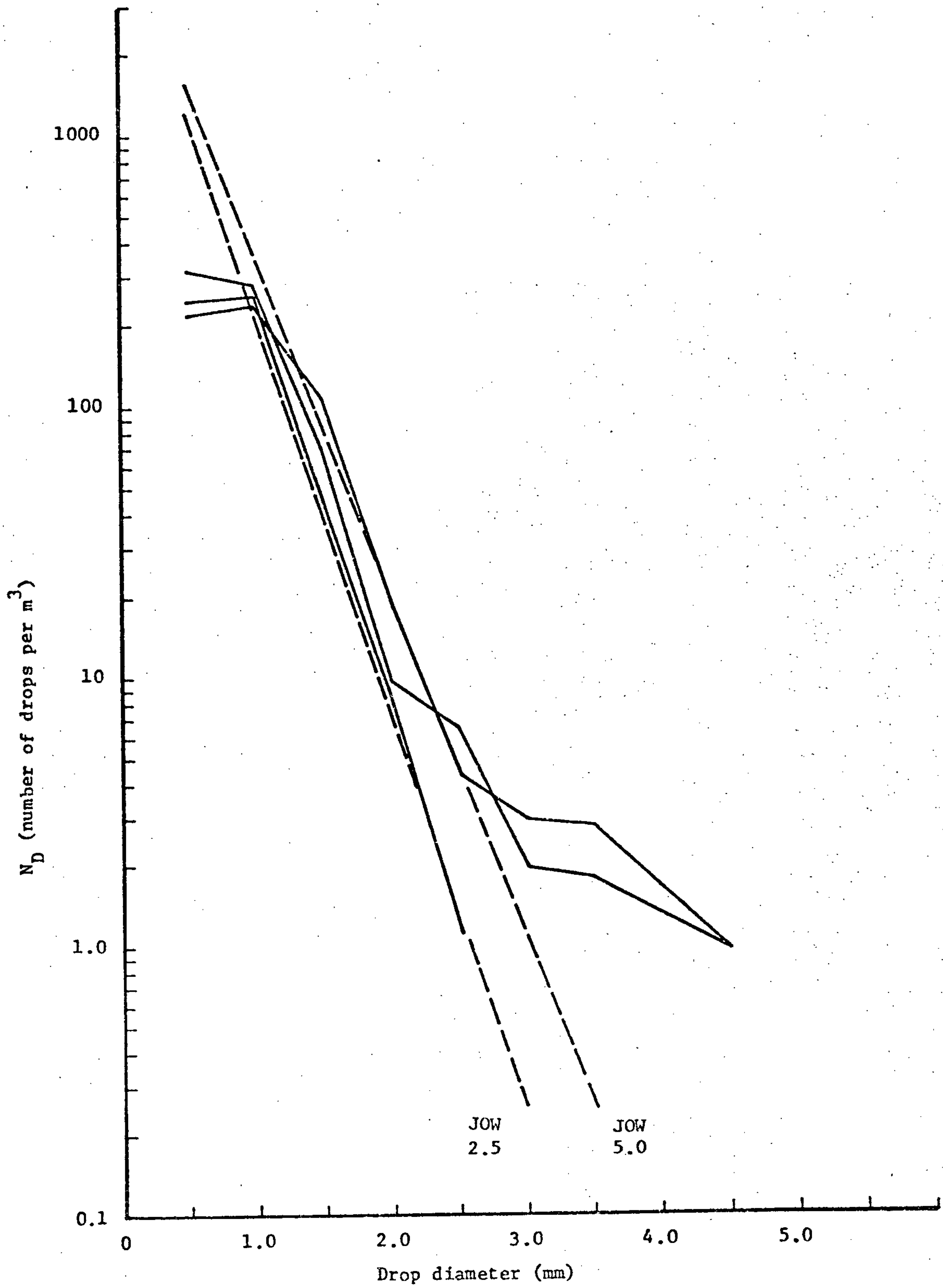

Fig. 6.2.17. Drop distributions for T_6.

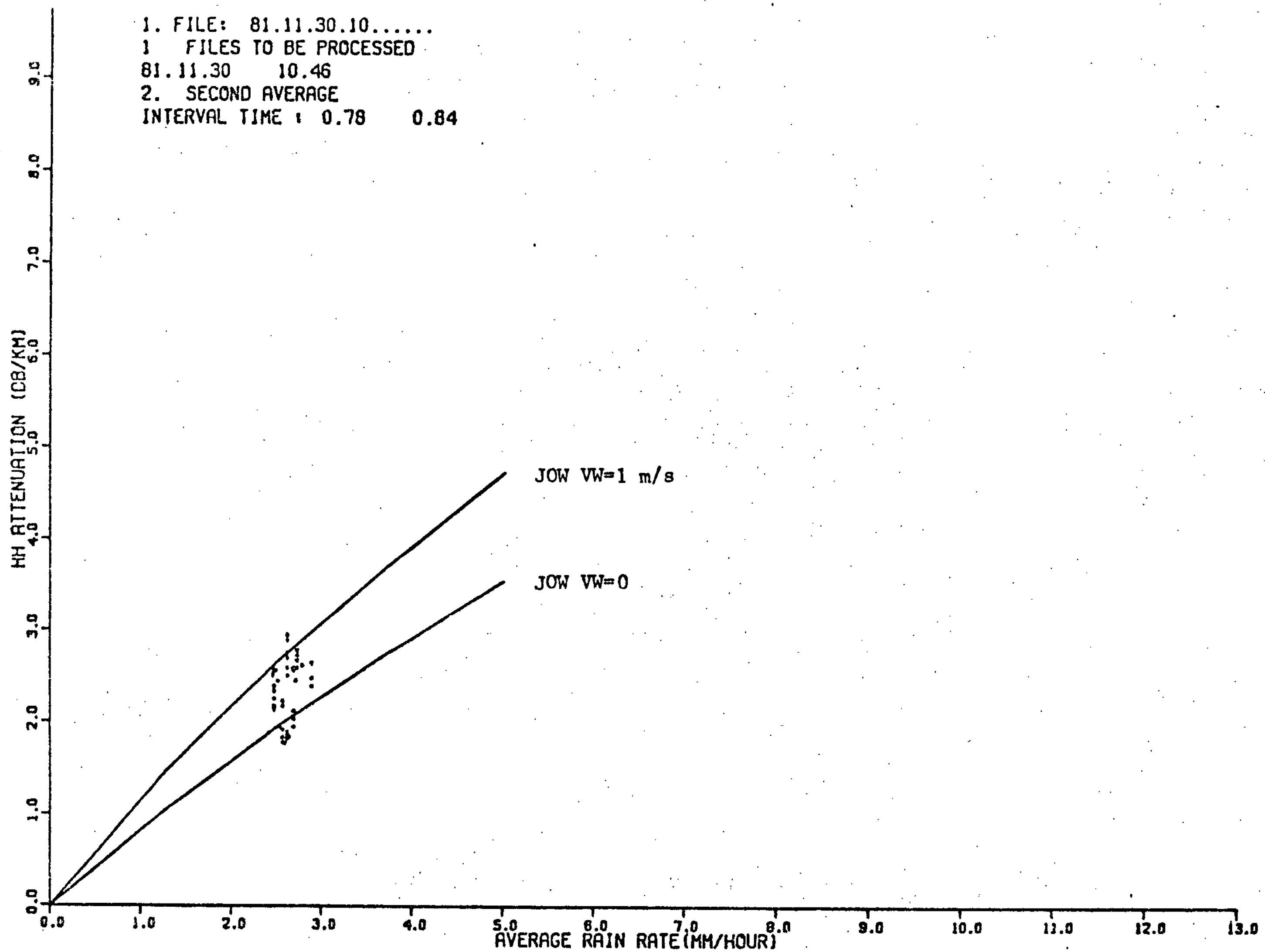

Fig. 6.2.18. CPA during T_7.

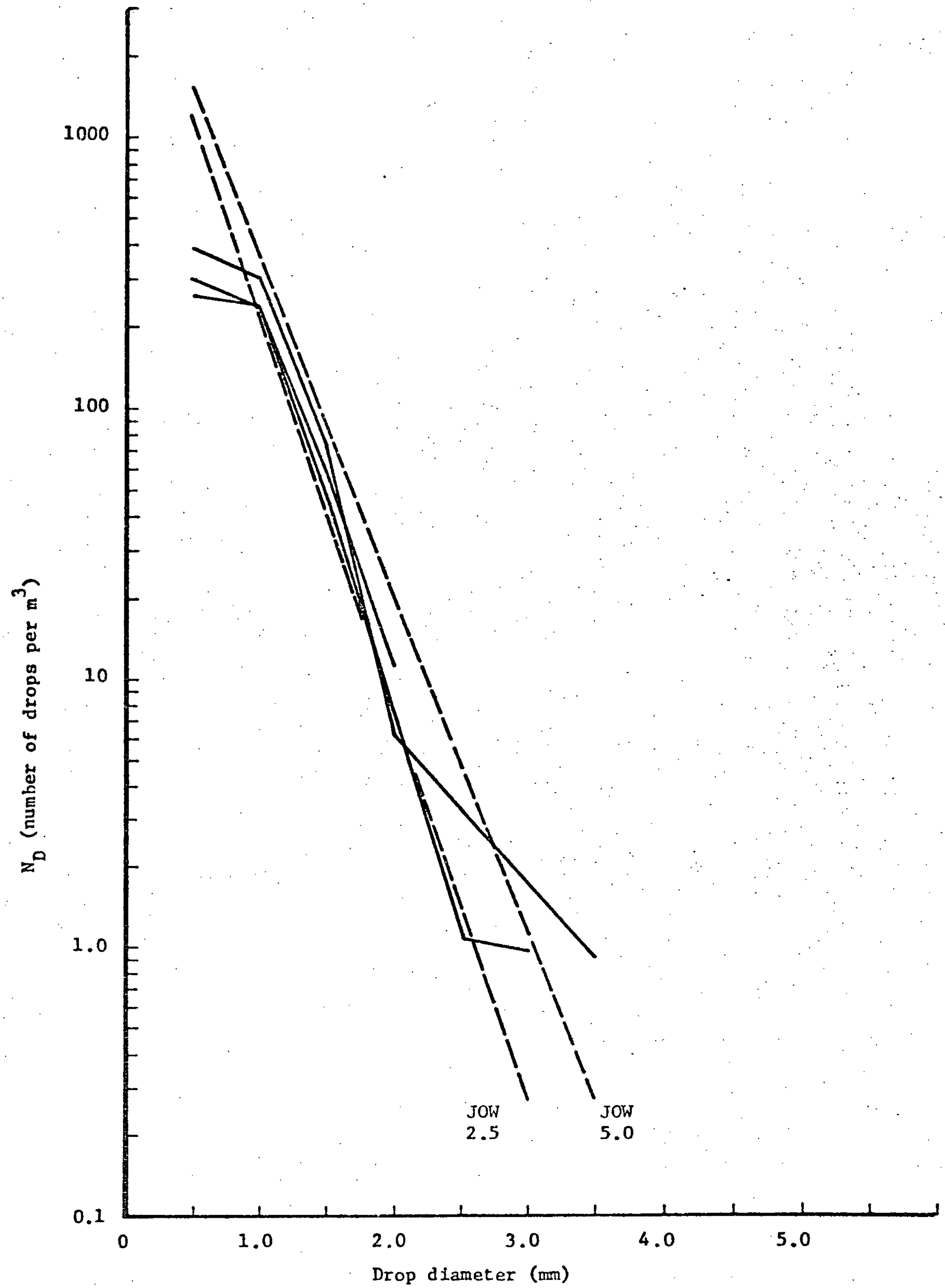

Fig.6.2.19. Drop distributions for T_7.

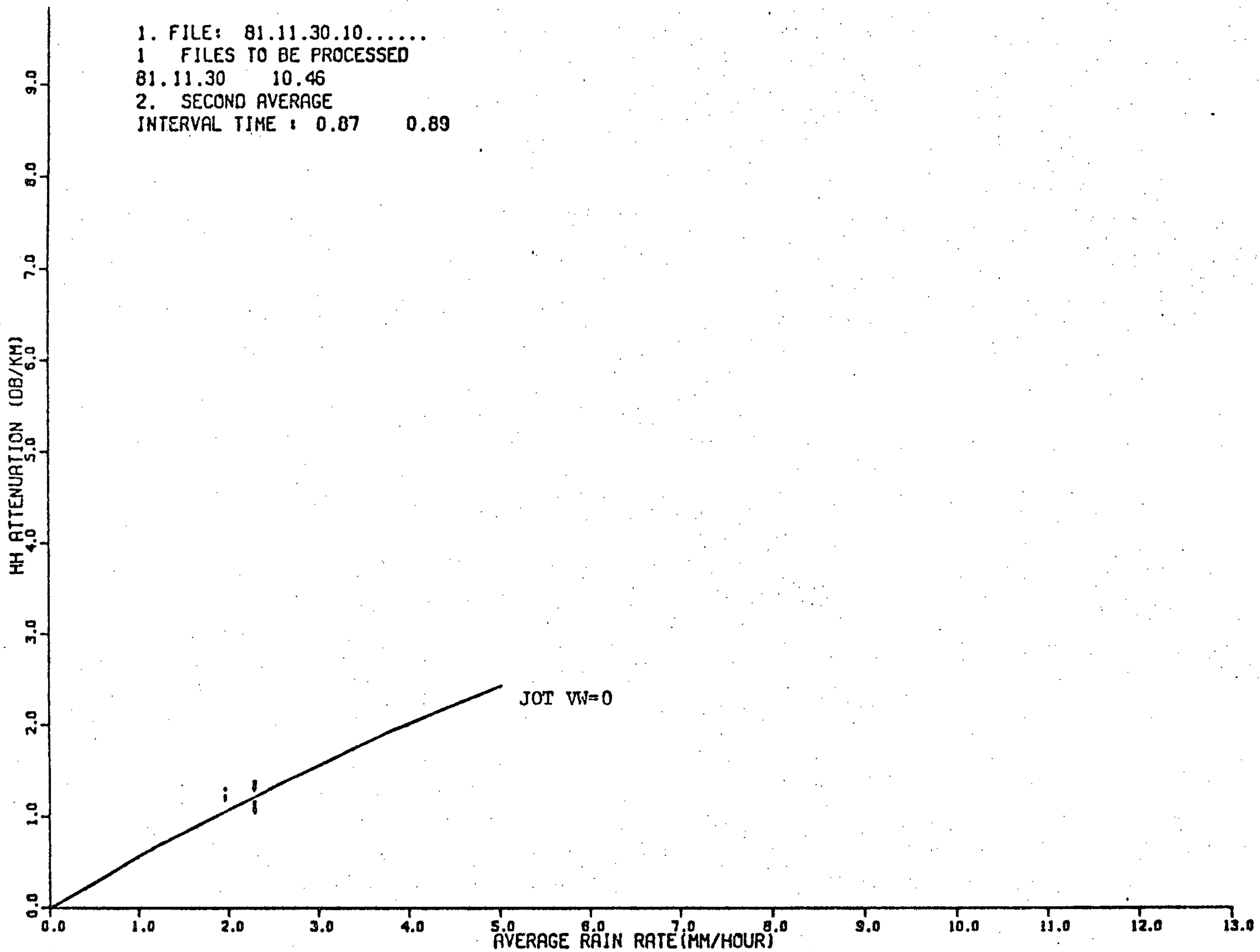

Fig. 6.2.20. CPA during T_8.

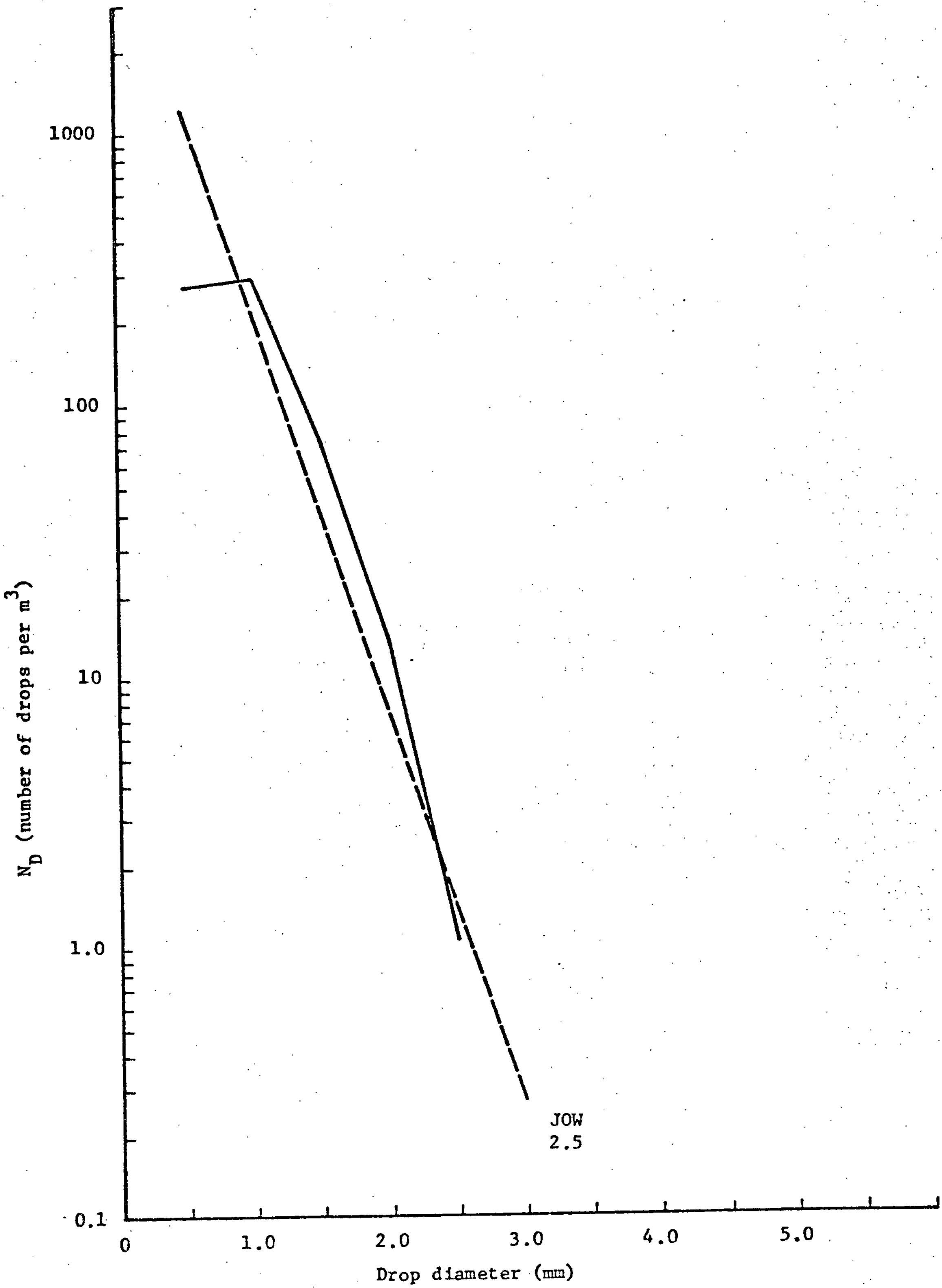

Fig. 6.2.21. Drop distributions for T_8.

vertical wind velocity. In this case, it is thought that the significantly larger and faster vertical wind increase was sufficient to temporarily reduce the number of small drops at the height of the propagation path. It is probable that the transient decrease in the number of small drops was actually lower than that indicated by the disdrometer because of averaging over the one minute sample period.

6.2.1.9 Attenuation During T_9, 0.89-0.93 h.

During T_9, Fig. 6.2.22 shows that the attenuation was higher than that predicted for the JOW distribution. The attenuation is not as large as that observed during T_6, even though the vertical wind decrease at the beginning of this period is larger than during T_6. This is thought to be because the period of upward flow preceeding the decrease was much shorter in this case, and therefore fewer drops were "stored" above the path by the upward flow.

6.2.2 XPD and Differential and Attenuation Data for 81.11.30.10

The cancelled system XPD, for horizontal transmitted polarization, is shown in Fig. 6.2.24 for a 30 s averaging period. During this period, the crosspolar cancellation network provided a clear weather system XPD of slightly over 60 dB (an exact value cannot be determined because it rained constantly during this period). The uncancelled XPD, for vertical transmitted polarization, is shown in Figs. 6.2.25(a) and (b) for 2 s and 30 s averages respectively. For this polarization, the clear weather system XPD was approximately 33 dB.

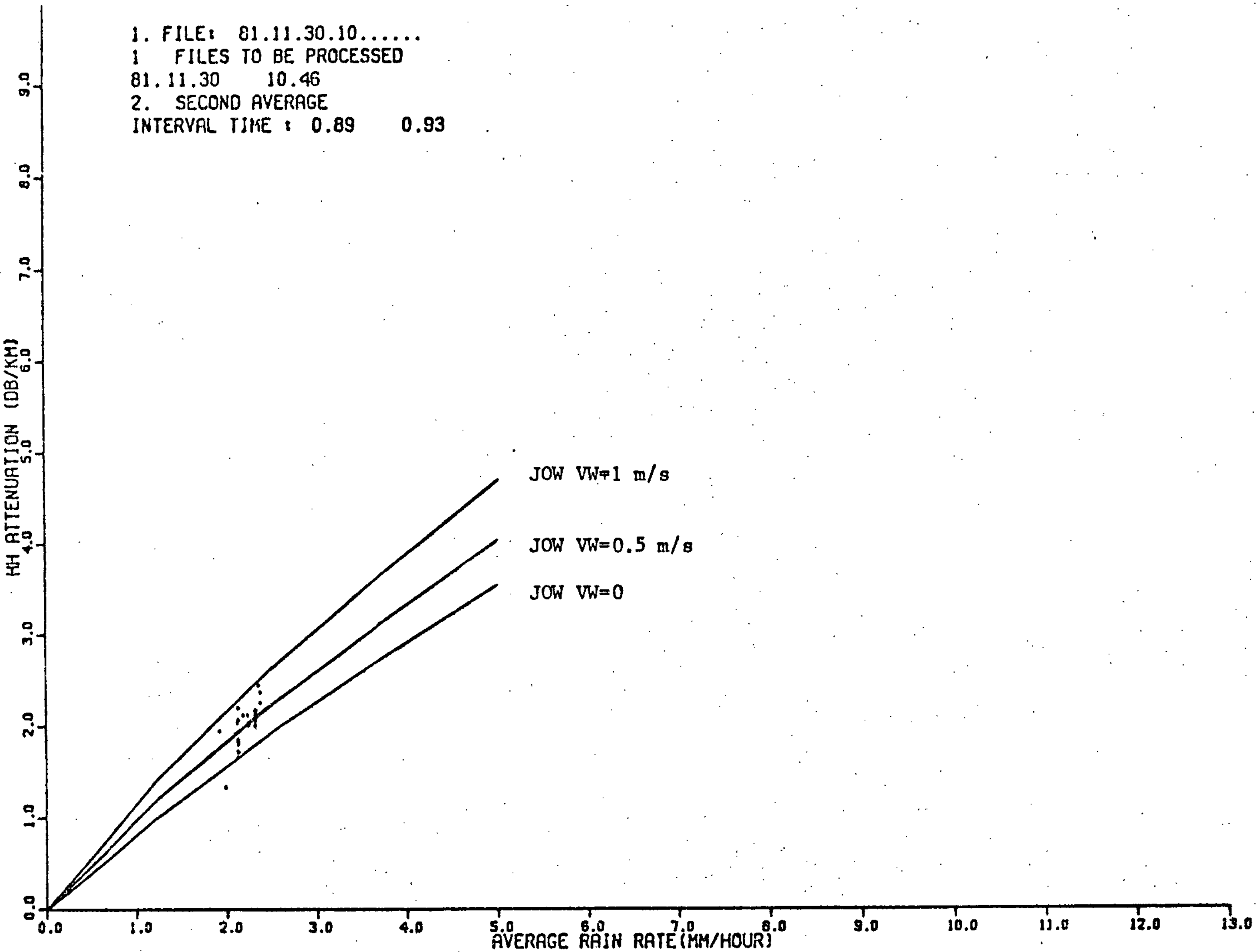

Fig. 6.2.22. CPA during T_9.

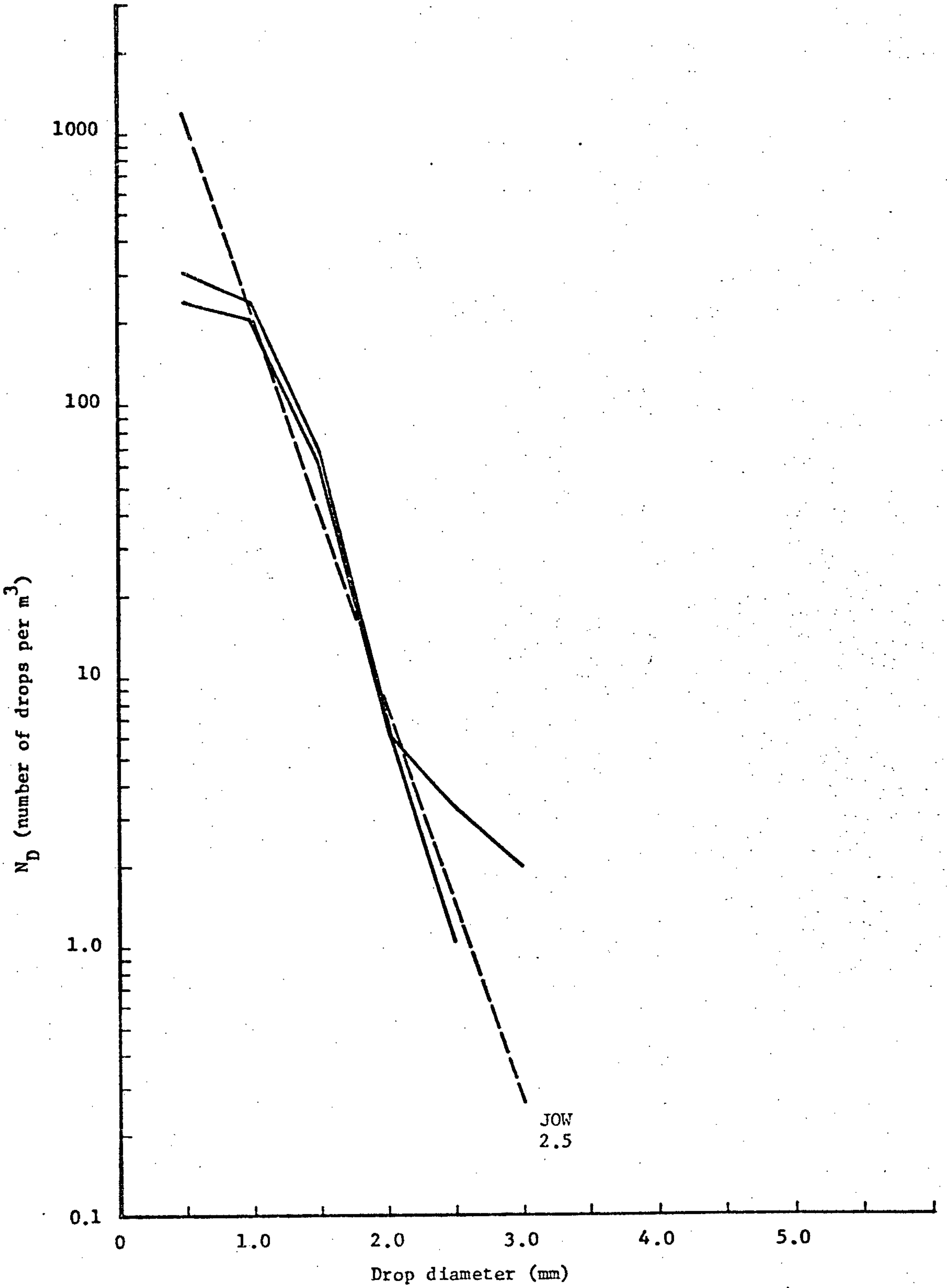

Fig. 6.2.23. Drop distributions during T_9.

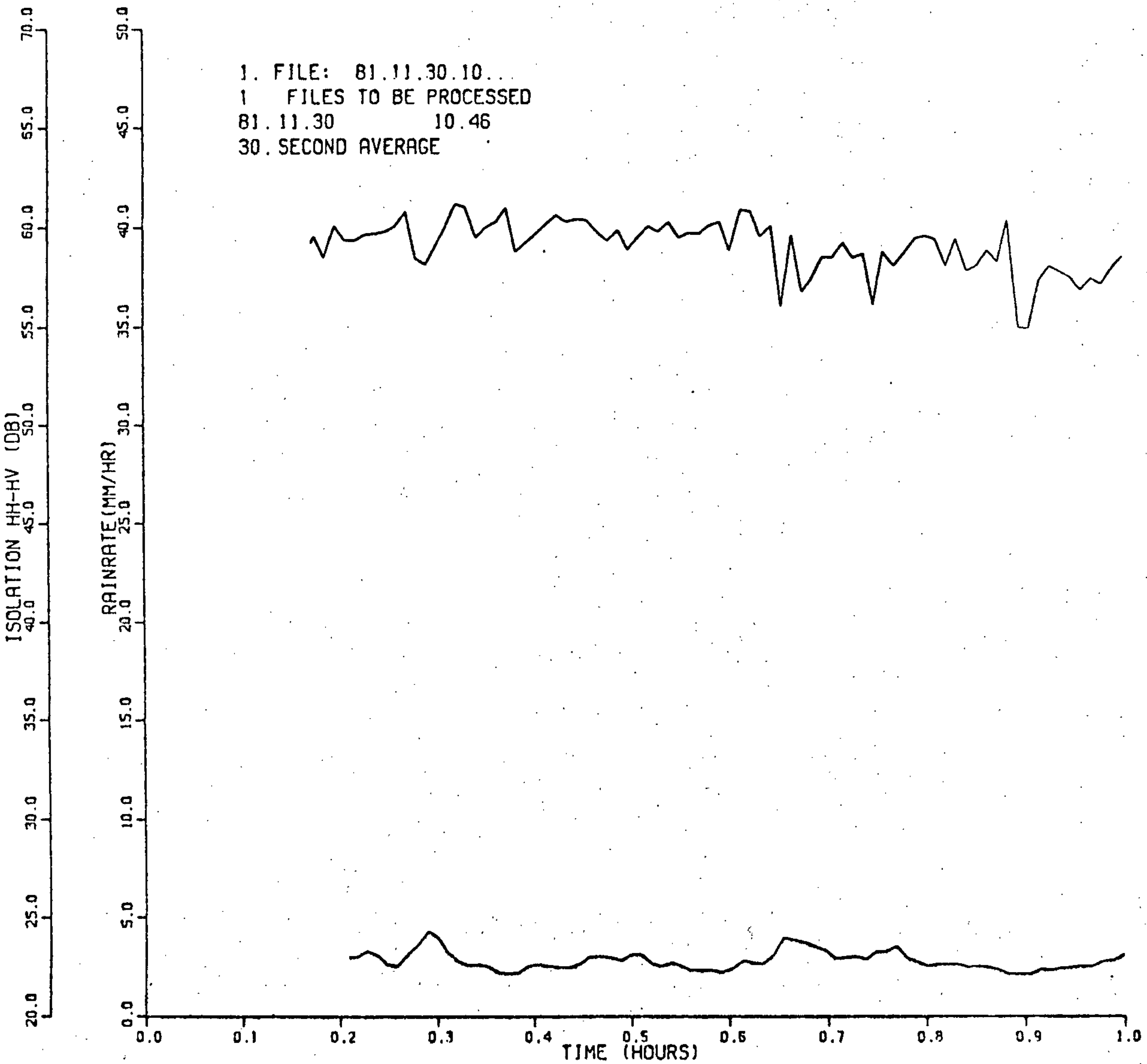

Fig. 6.2.24. XPD for horizontal transmitted polarization, 30 s avg. for 81.11.30.10.

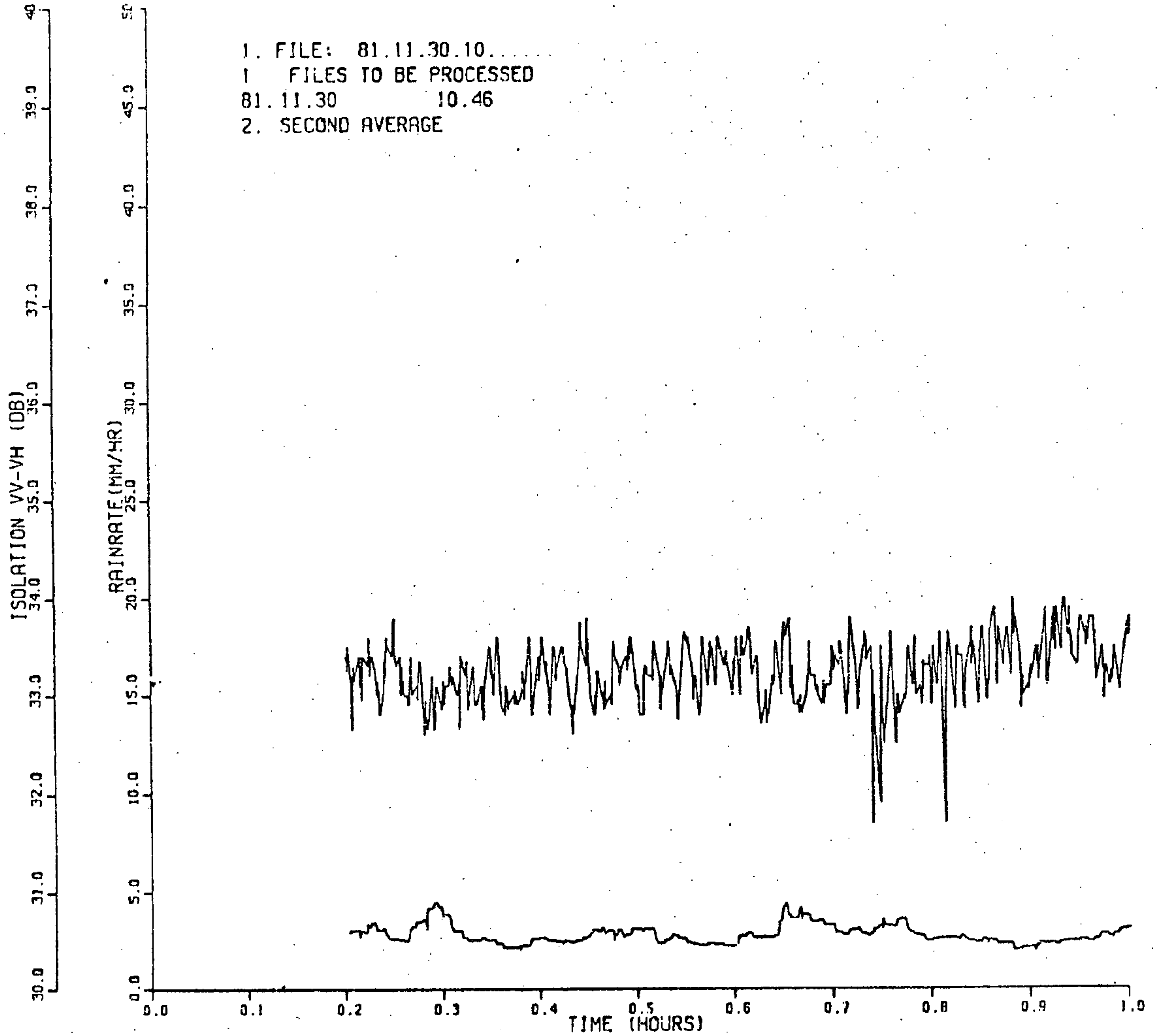

Fig. 6.2.25(a). XPD for vertical transmitted polarization, 2 s avg. for 81.11.30.10.

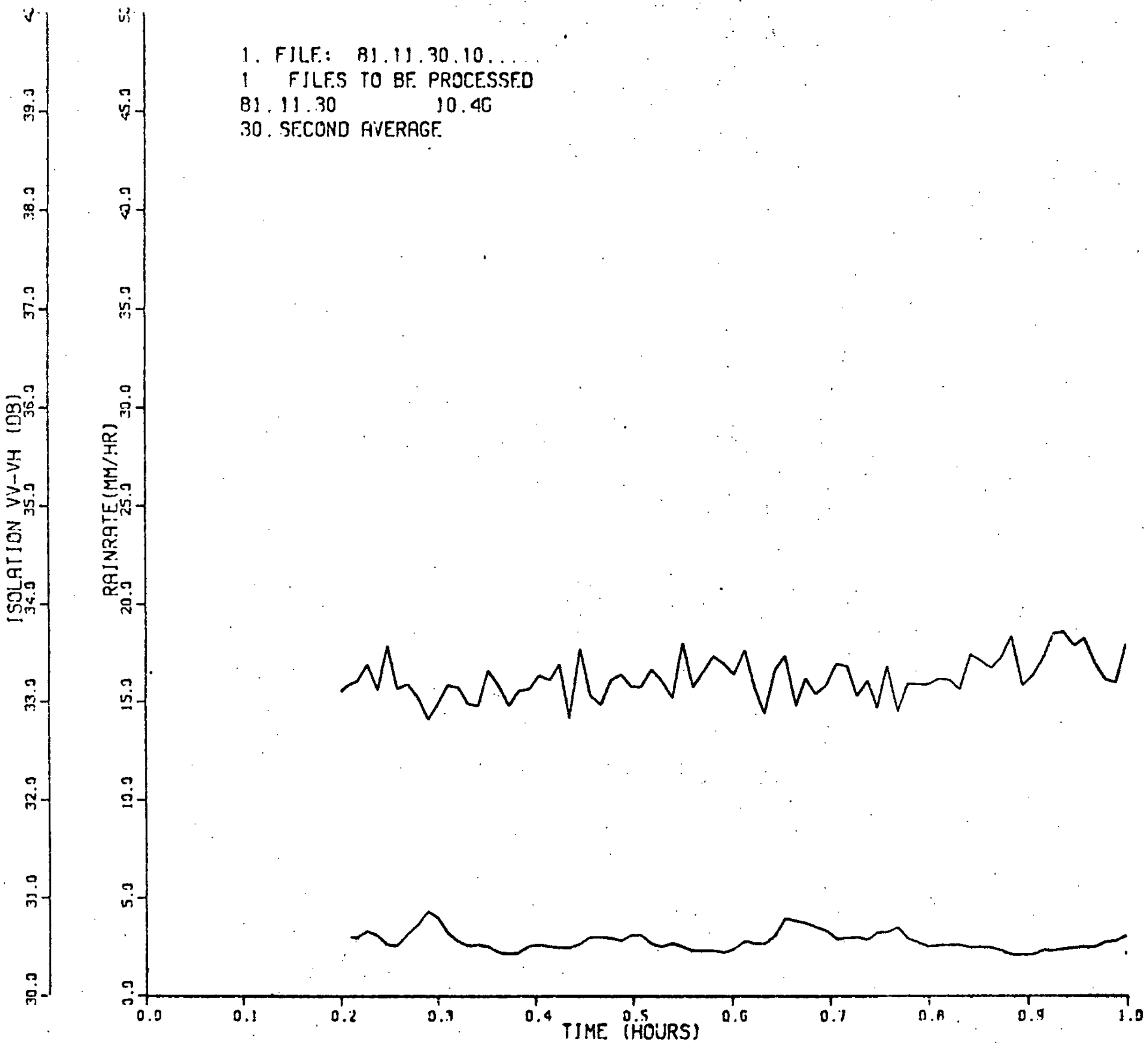

Fig. 6.2.25(b). XPD for vertical transmitted polarization, 30s avg. for 81.11.30.10.

Both the cancelled and uncancelled XPDs show the greatest change from clear weather values near the end of this file, during the periods of largest horizontal wind velocity. During this file, as during most observations from this experiment, the uncancelled XPD increases and decreases from the clear weather value. As an example, at 0.29 h during a rainrate maxima, both XPDs decreased. However, in contrast, the uncancelled XPD generally increased prior to 0.89 h and then decreased at 0.90 h. The cancelled system XPD continually decreased during these periods. This uncancelled system XPD behaviour is believed to be due to changes in the angle of T_{CPXP} (i.e. T_{12}). These changes in angle result in the path depolarized signal adding with the antenna depolarized signal to either increase or decrease the total system XPD. The cancelled XPD is relatively immune to these changes in angle. It is believed that the path XPD did, in fact, sharply decrease at 0.90 h as observed on the cancelled channel. This change was not clearly observed as a change from the clear weather value on the uncancelled channel because it is believed that the horizontal wind transient responsible for this path XPD minimum also changed the path XPD angle. This change in angle caused the uncancelled XPD to change from increasing to decreasing resulting in a net value close to the clear weather XPD. This type of behaviour makes it very difficult to compare the uncancelled XPD to model predictions during variable wind conditions. Better examples of the phase effects on the uncancelled XPD are included in other sections.

Some caution must be applied when comparing the cancelled XPD during low rainrates to the model predictions because these values are close to the clear weather system XPD. For example, at a rainrate of 2.5 mm/hr, the clear weather XPD (which would also be observed for a zero canting angle) corresponds to an effective mean canting angle of approximately 3°. As a result, the absolute value of the calculated canting angle is likely smaller than the value obtained by a direct comparison to the data during low rainrates.

The differential attenuation during this file is shown in Fig. 6.2.25. This plot shows that the differential attenuation was often negative (for periods up to 2 minutes) in contradiction to the basic theory and drop shape assumptions. Similar negative differential attenuations were observed during most rainstorms over the course of this experiment. While some caution is necessary in interpreting the differential attenuation data from this experiment because of the data sampling as discussed in Section 6.1.3, it is believed that these negative differential attenuations did, in fact, occur. Similar negative differential attenuations were observed in [1.74].

A summary of the XPD and differential attenuation data analyzed during this file is shown in Table 6.2.2. The legend for the comments follows Table 6.2.1.

6.2.2.1 XPD and Differential Attenuation During T_{10}, 0.62-0.72 h.

The cancelled system XPD during T_{10} was reasonably well correlated with the rainrate and horizontal wind during this period, i.e. the lower XPDs occurred during the higher rainrates and horizontal wind velocities. During this period, the average horizontal wind velocity was approximately 5.0 m/s, Fig. 6.2.2(b). The cancelled system XPD agrees well with the model predictions for an equivalent mean canting angle of 4°, as shown in Fig. 6.2.27.

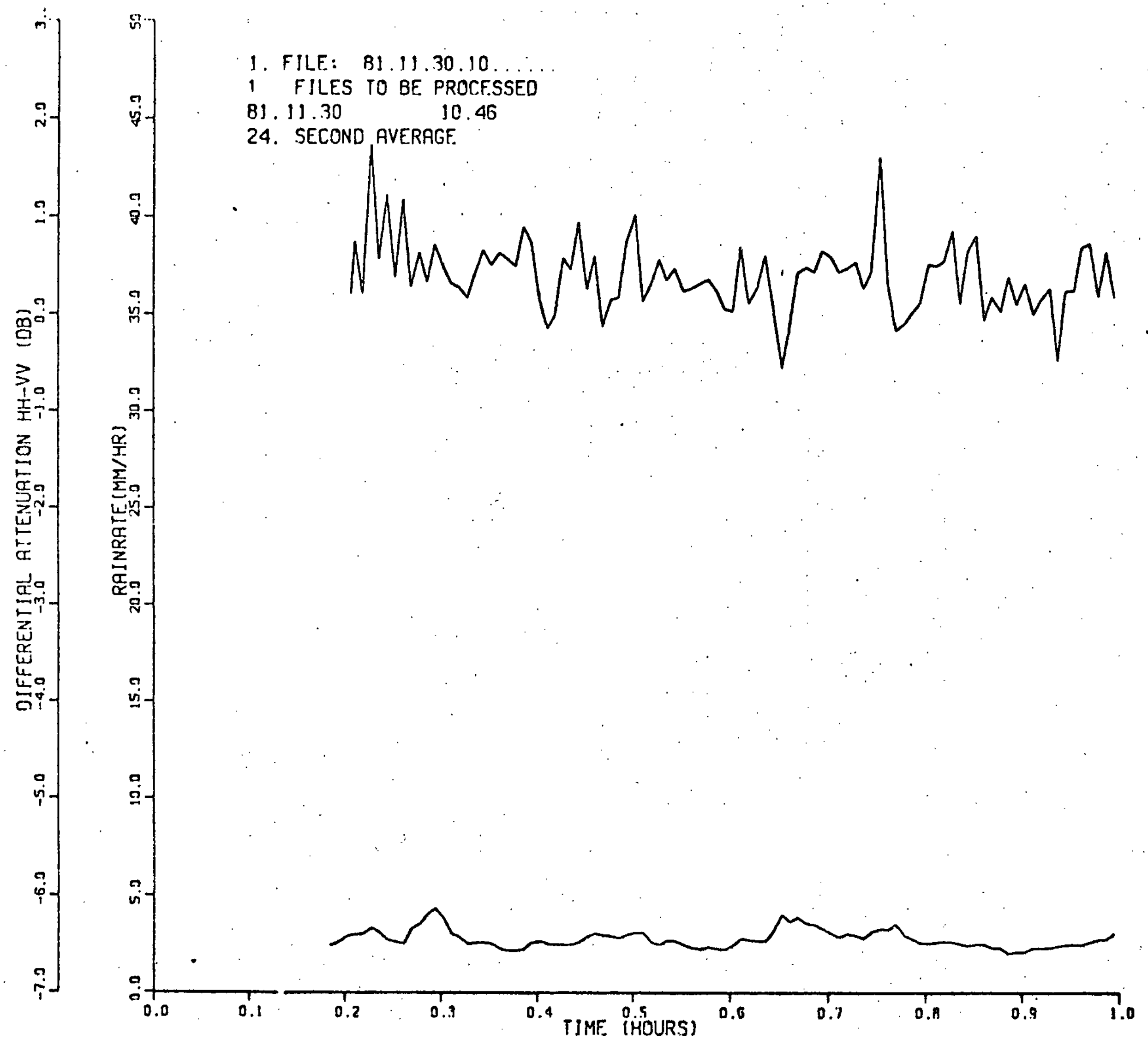

Fig. 6.2.26. Differential attenuation for 81.11.30.10.

Period	XPD	Differential Attenuation	Wind Velocities During Rain	XPD is in Approximate Agreement with Model Predictions for:	Comments
T_{10} 0.62–0.72 h	56.0–60.8 dB XPD generally decreased as rainrate increased and horiz. wind increased. Figs. 6.2.2(b), 6.2.24, and 6.2.27.	Peaks at -0.9dB at 0.66 h during horiz. wind increase. Small and positive during latter part of period. Max. pos. value occurred during horiz. wind local max. Fig. 6.2.2(a) and 6.2.26.	Horiz. wind max. = 7.3 m/s. Fig. 6.2.2(a) Horiz. wind ≅ 5.0 m/s avg. Fig. 6.2.2(b)	XPD follows $\phi \cong 4°$ predictions , 9. Fig. 6.2.27	XPD well correlated with rainrate and horiz. wind variations.
T_{11} 0.72–0.78 h	56.0–59.3 dB XPD min. at 0.75 h. Fig. 6.2.24 Uncancelled XPD also min. at 0.75 h. Fig. 6.2.25(a)	Peaks at +1.2dB at a 0.75 h, Fig. 6.2.26	Horiz. wind generally increased from 4-7 m/s Fig. 6.2.2(a) ≅5.0 m/s avg. Fig. 6.2.2(b). Moderate horiz. wind peak (6.2 m/s) and large vert. wind peak (1.2 m/s) at 0.75 h. Figs. 6.2.2(a) and 6.2.3(a)	For most of period $\phi \cong 4°$, during peak $\phi \cong 5-6°$, 9. Fig. 6.2.28	XPD and diff. att. peaks during vert. and horiz. wind peaks.

. . . continued

Period	XPD	Differential Attenuation	Wind Velocities During Rain	XPD is in Approximate Agreement with Model Predictions for:	Comments
T_{12} 0.78-0.85 h	57.9-59.7 dB cancelled XPD rel. const. Fig. 6.2.24 and 6.2.29 Uncancelled XPD has fast decrease at 0.81 h Fig. 6.2.25(a)	Varied between -0.5 to +0.4 dB Fig. 6.2.26	Horiz. wind rel. const. ≅ 5.8 m/s avg. Fig. 6.2.2(b)	$\phi \cong 5°$ Fig. 6.2.29	
T_{13} 0.88-0.93 h	54.9-60.5 dB XPD min. at 0.9 h Figs. 6.2.24 and 6.2.30 Uncancelled XPD also has local min. at 0.9 h Fig. 6.2.25(b)	Rel. const. ≅ -0.3 dB Fig. 6.2.26	Horiz. wind peaks at 8.2 m/s at 0.9 h Fig. 6.2.2(a) ≅ 5.0 m/s avg. Fig. 6.2.2(b) large vert. wind peak just before 0.9 h.	$\phi = 10°$ during horiz. wind max. at 0.9 h During rest of period $\phi \cong 6°$. Fig. 6.2.30	Cancelled XPD correlated well with horiz. wind.
T_{14} 0.93-0.99 h	57-58.1 dB Fig. 6.2.31 Uncancelled XPD has increased from average value Fig. 6.2.25(b)	Varied -0.8 to +0.3 dB. Both extreme values occur during local horiz. wind peaks. Fig. 6.2.26	≅ 4.3 m/s avg. Fig. 6.2.2(b)	$\phi = 6°, 9$ Fig. 6.2.31	Cancelled XPD correlated with horiz. wind.

Table 6.2.2 Summary of XPD and Differential Attenuation Data for 81.11.30.10, 10:30-10:46.

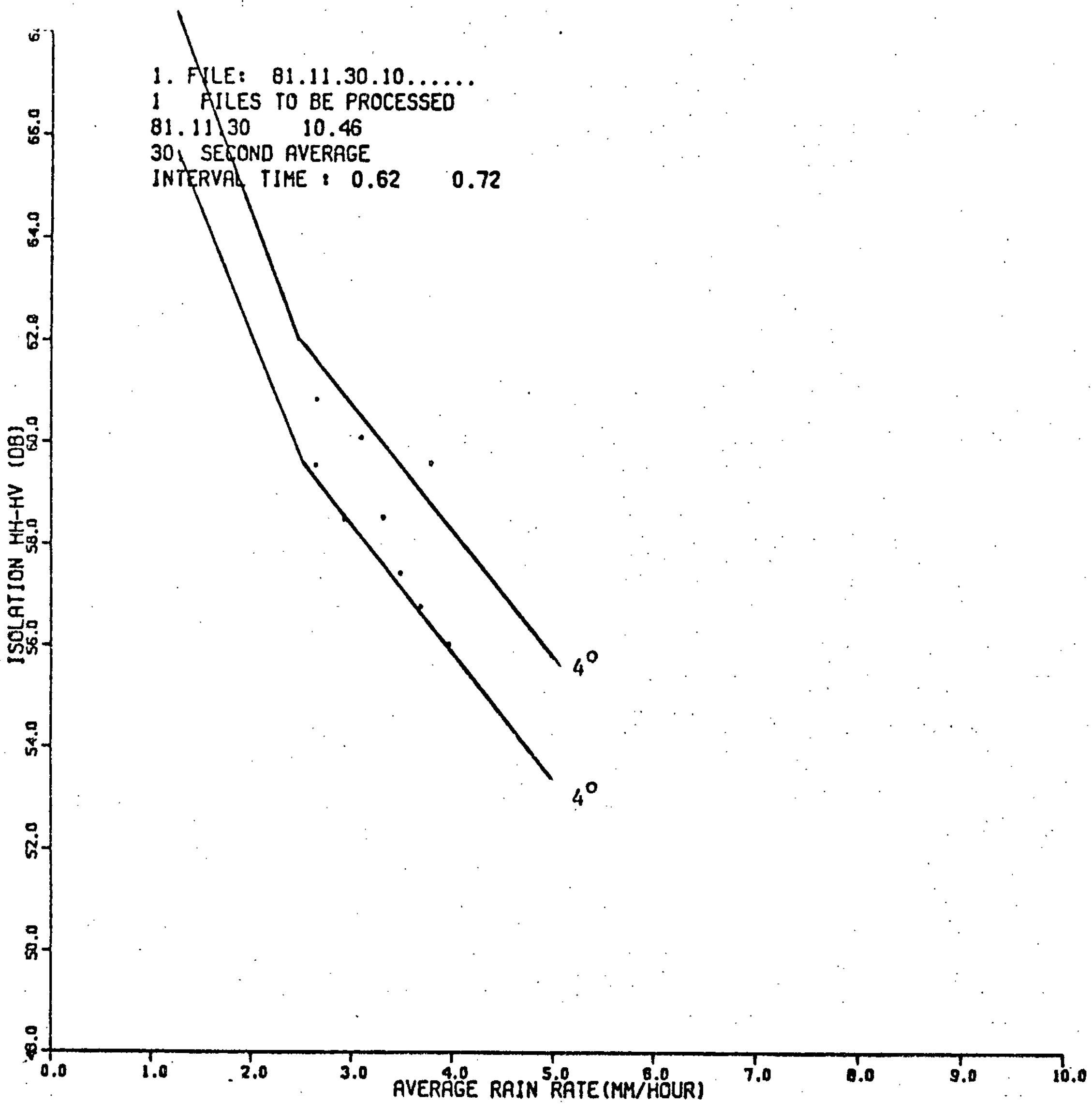

Fig. 6.2.27. XPD_H during T_{10}.

The differential attenuation, Fig. 6.2.26, reached a negative value of -0.9 dB at 0.66 h during a period of rapidly increasing horizontal wind velocity, Fig. 6.2.2(a). During the latter part of this period, the differential attenuation was positive with a range of values close to the theoretical predictions.

6.2.2.2 XPD and Differential Attenuation During T_{11}, 0.72-0.78 h.

The cancelled system XPD during this period also generally agreed with predictions for an effective canting angle of 4°. At 0.75 h, however, both XPDs rapidly decreased, Figs. 6.2.24 and 6.2.25(a). During this decrease, the horizontal wind reached a maximum of 6.2 m/s, Fig. 6.2.2(a), and the vertical wind peaked at +1.2 m/s, Fig. 6.2.3(a). This minimum value of cancelled XPD confirmed to predictions for a 5 to 6° canting angle, Fig. 6.2.2.

The plotted differential attenuation reached a peak value of +1.2 dB at 0.75 h, but this unusually large value must be considered suspect because of the rapid, vertical wind induced, change in the CPA.

6.2.2.3 XPD and Differential Attenuation for T_{12}, 0.78-0.85 h.

During T_{12}, the cancelled system XPD was relatively constant and agreed with predictions for an equivalent mean canting angle of 5°, Fig. 6.2.29. This slightly larger canting angle is apparently associated with the increased horizontal wind velocity, which averaged about 5.8 m/s during this period. It should, however, be reiterated that the absolute value of these calculated canting angles may be too large due to the proximity of these data to the cancelled, clear-weather XPD.

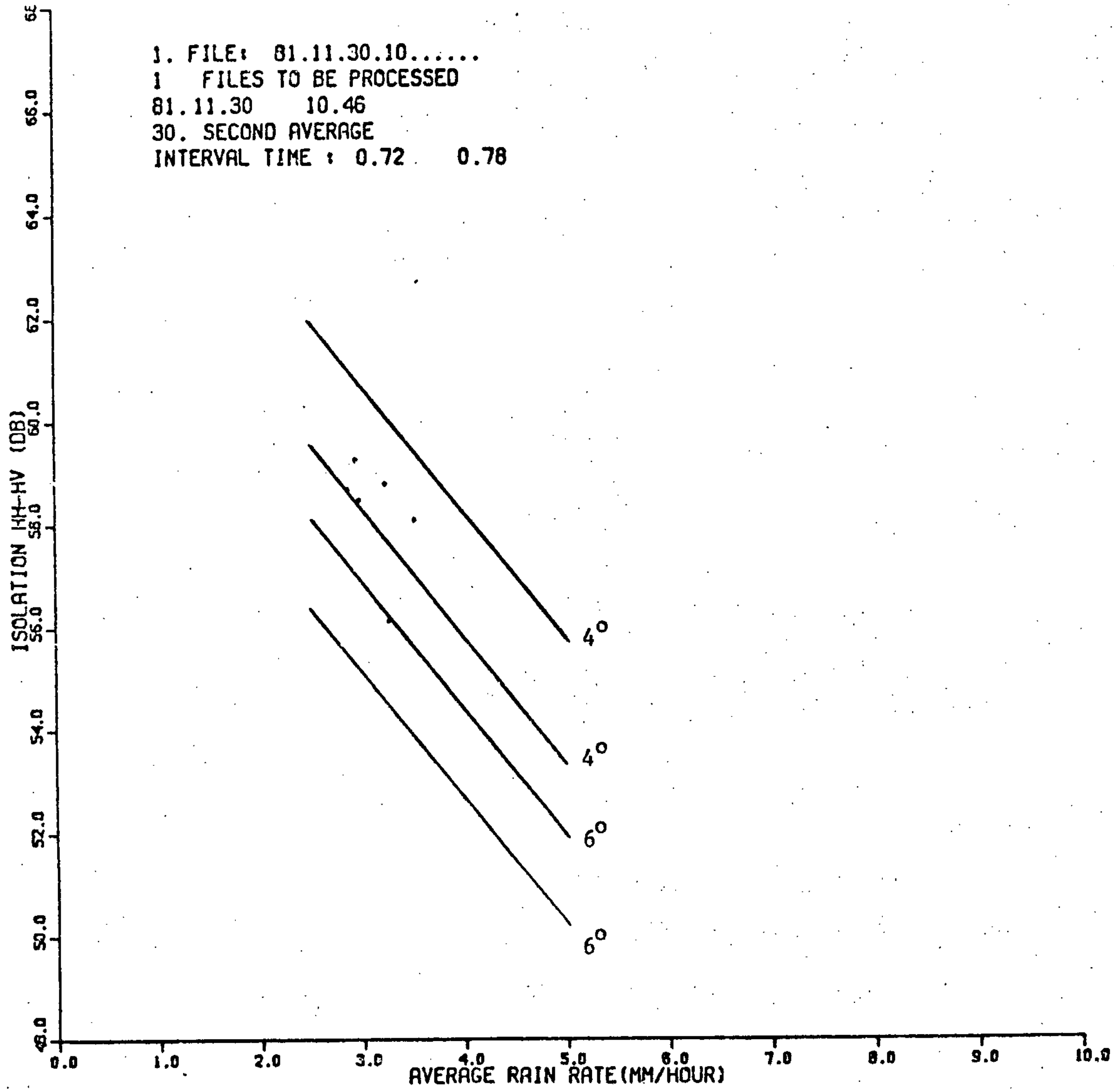

Fig.6.2.28. XPD_H during T_{11}.

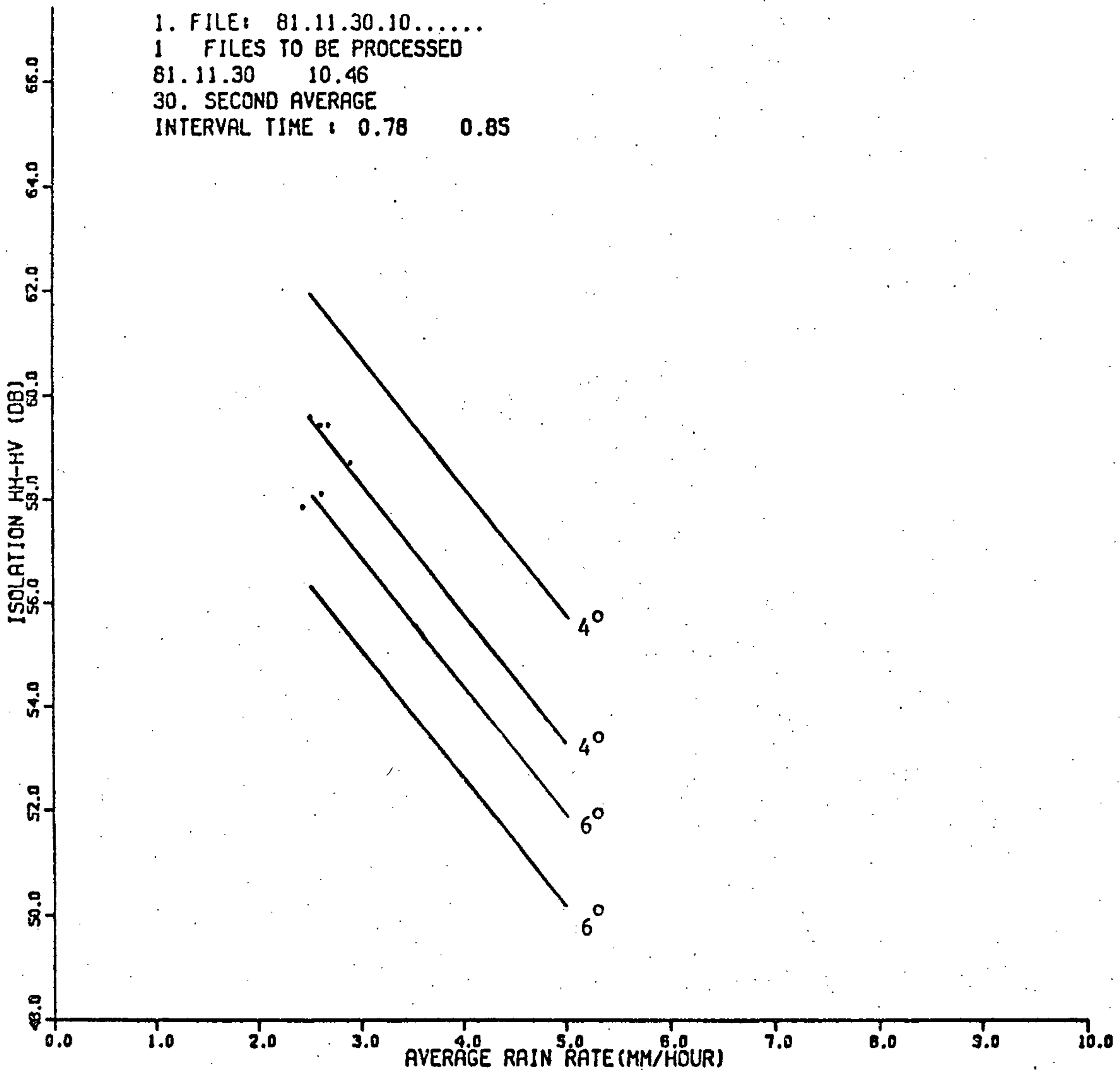

Fig. 6.2.29. XPD_H during T_{12}.

The uncancelled XPD, Fig. 6.2.25(a) rapidly decreased at 0.91 h, in a manner similar to the decrease at 0.75 h. The reasons for this decrease are not clear, but it did occur at the same time as a fast, but relatively small, decrease in the horizontal wind velocity.

The differential attenuation during this period increased from approximately -0.5 dB to +0.4 dB. Negative values occurred just after and during a period of increasing horizontal wind and during a period of comparatively high horizontal wind velocity.

6.2.2.4 XPD and Differential Attenuation During T_{13}, 0.88-0.93 h.

At 0.90 h the cancelled XPD decreased to the lowest value observed during this data file. This decrease coincided with the maximum horizontal wind during this file, 8.2 m/s, Fig. 6.2.2(a). It also occurred immediately after the largest vertical wind velocity, which was +1.6 m/s, Fig. 6.3.3(a). During this wind peak, the cancelled XPD agreed with predictions for a canting angle of approximately 10°. The explanation for the cancelled XPD behaviour during this wind maxima were given in Section 6.2.3.

The differential attenuation during T_{13} was relatively constant and averaged approximately -0.3 dB.

6.2.2.5 XPD and Differential Attenuation During T_{14}, 0.93-0.99 h.

During interval T_{14}, both XPDs showed relatively large changes from their clear weather values, Figs. 6.2.24 and 6.2.25(b). The cancelled system XPD data agreed with predictions for a canting angle of approximately 6°, Fig. 6.2.31, and correlated reasonably well with the horizontal wind velocity.

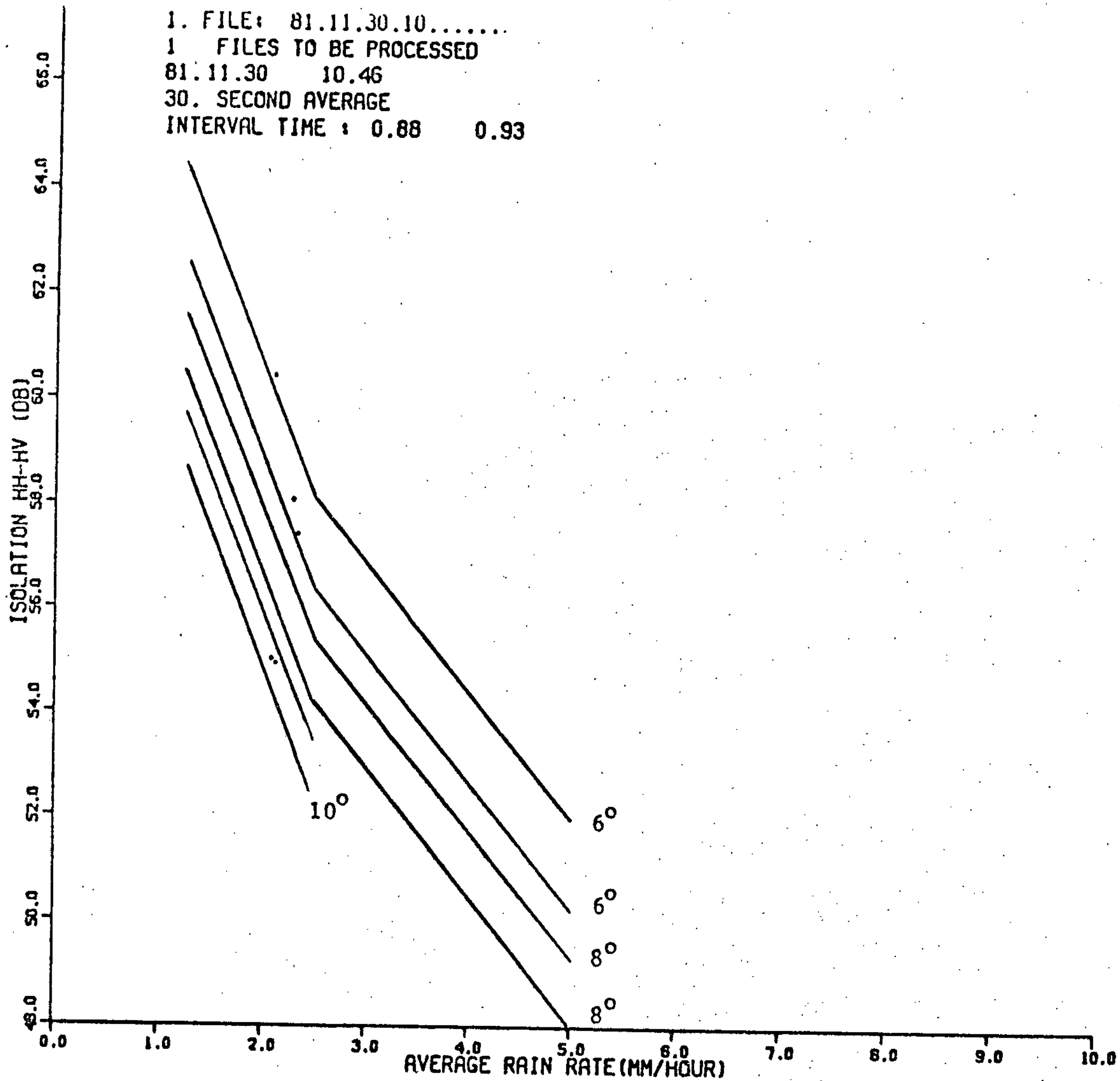

Fig. 6.2.30. XPD_{H} during T_{13}.

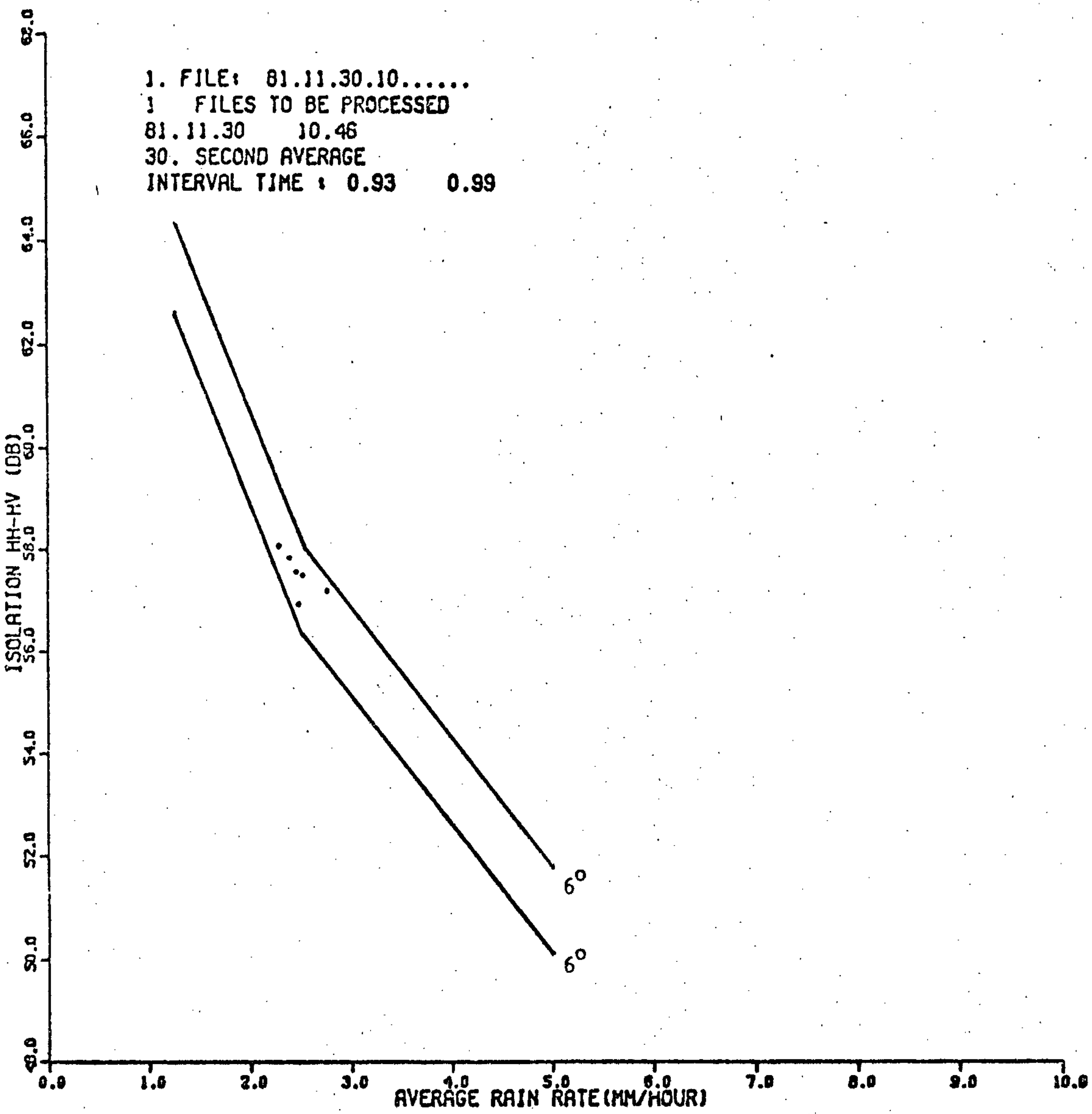

Fig. 6.2.31. XPD_H during T_{14}.

Differential attenuation during T_{14} varied from -0.8 to +0.3 dB, even though the rainrates and CPAs were only changing very slowly. The most negative and two most positive maximum values all occurred during local maximums in the horizontal wind velocity.

6.3 Experimental Results for 81.11.30.18

This data file was included because it was the best example observed during this experiment of the variability of propagation phenomena which can occur during rapidly changing wind conditions. Rainrates for this file are shown in Fig. 6.3.1. The individual rainrates were relatively constant on a long term basis, but were moderately variable over short periods. Some of this short term rainrate variability is believed to be due to varying wind velocities which could affect drop velocities and raingauge capture efficiencies (Fig. 3.3).

The 10 s average wind direction during this period was constantly from the east, as shown in Fig. 6.3.2. Time series plots of horizontal wind velocity for 2 s, 10 s, and 99 s averages are shown in Figs. 6.3.3(a), (b) and (c). The 10 s average horizontal wind velocity varied between 2 and 15 m/s during this file and was unusually variable. Vertical wind velocities for this period with 10 s and 30 s averages are shown in Fig. 6.3.4(a) and (b). The vertical wind velocity was (subjectively) even more variable and ranged from -0.9 to +2.5 m/s with a 10 s average.

Three samples of the drop size distribution from this file are shown in Figs. 6.3.5-6.3.8. These are included mainly to show the unusual peak in

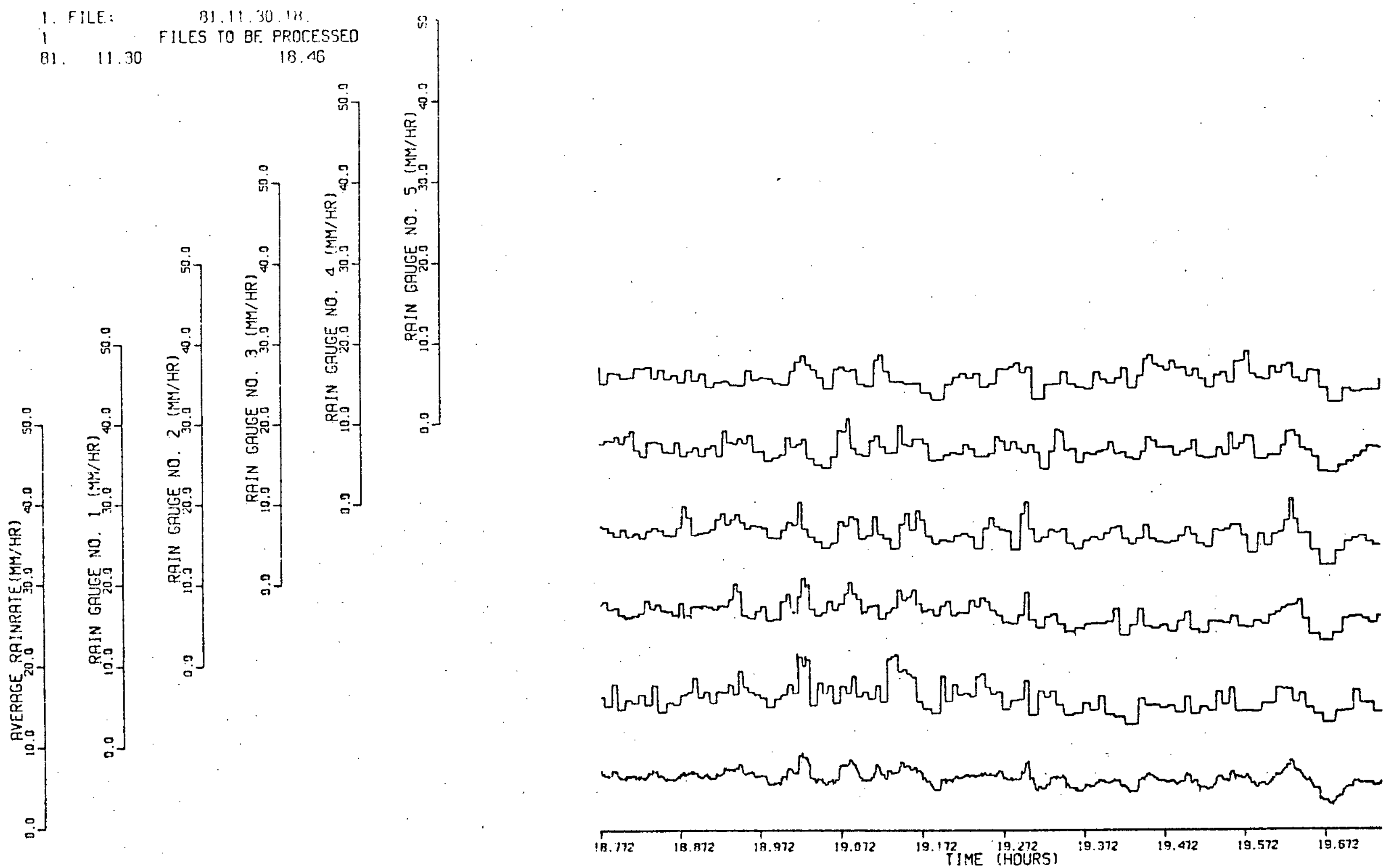

Fig. 6.3.1. Rainrates for 81.11.30.18.

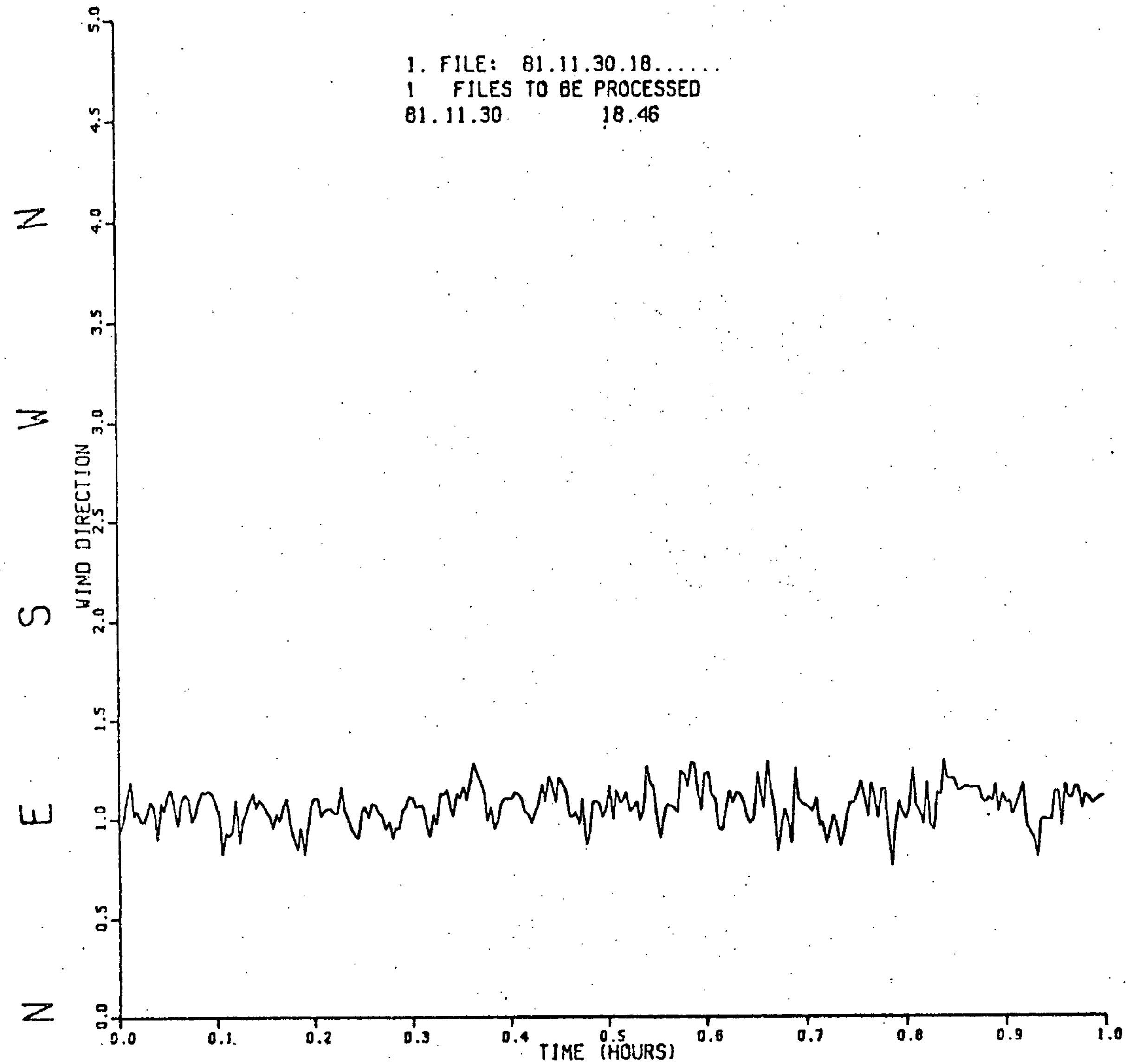

Fig. 6.3.2. Wind direction, 10 s avg. for 81.11.30.18.

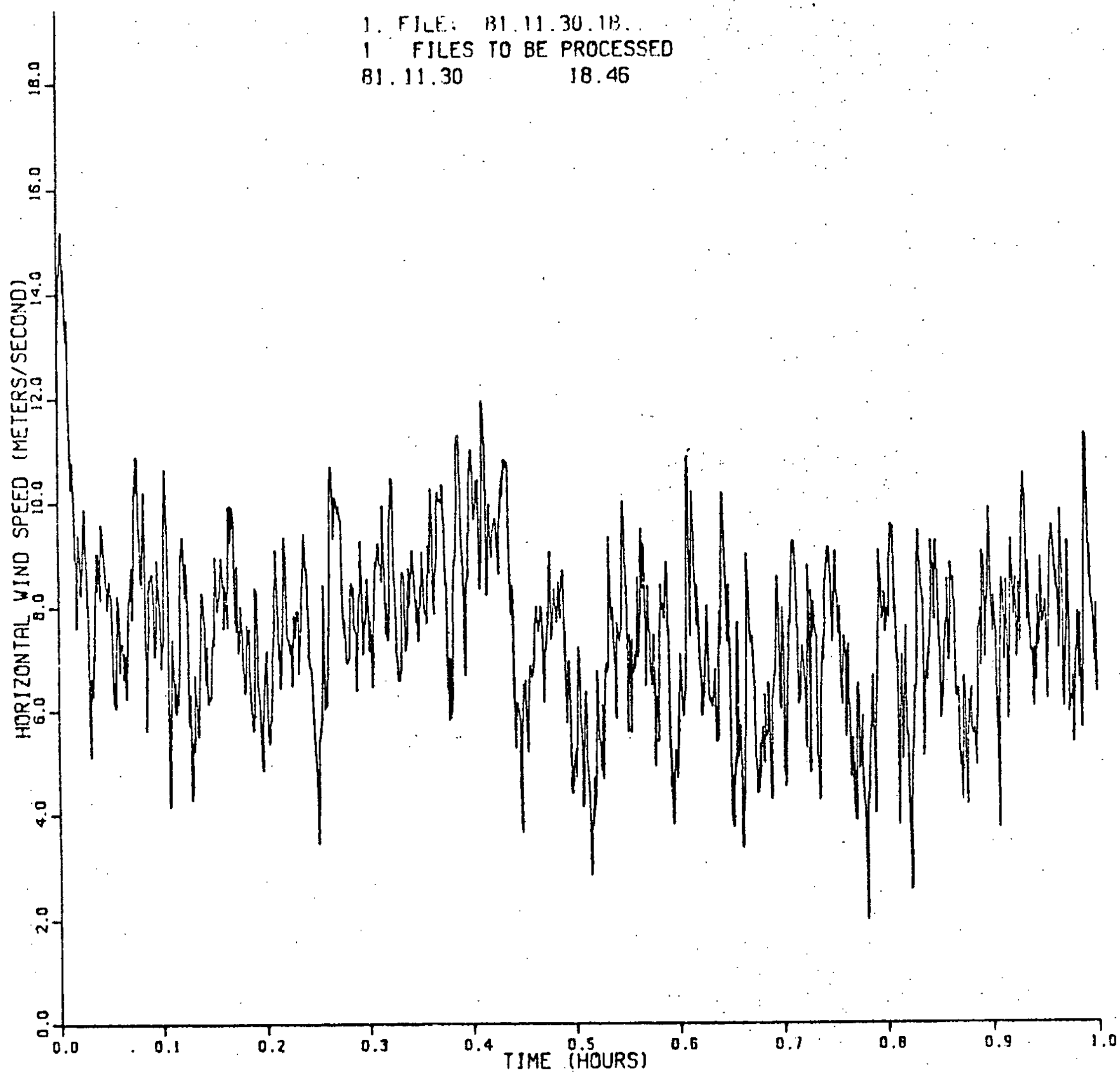

Fig. 6.3.3(a). Horizontal wind velocity, 2 s avg. for 81.11.30.18.

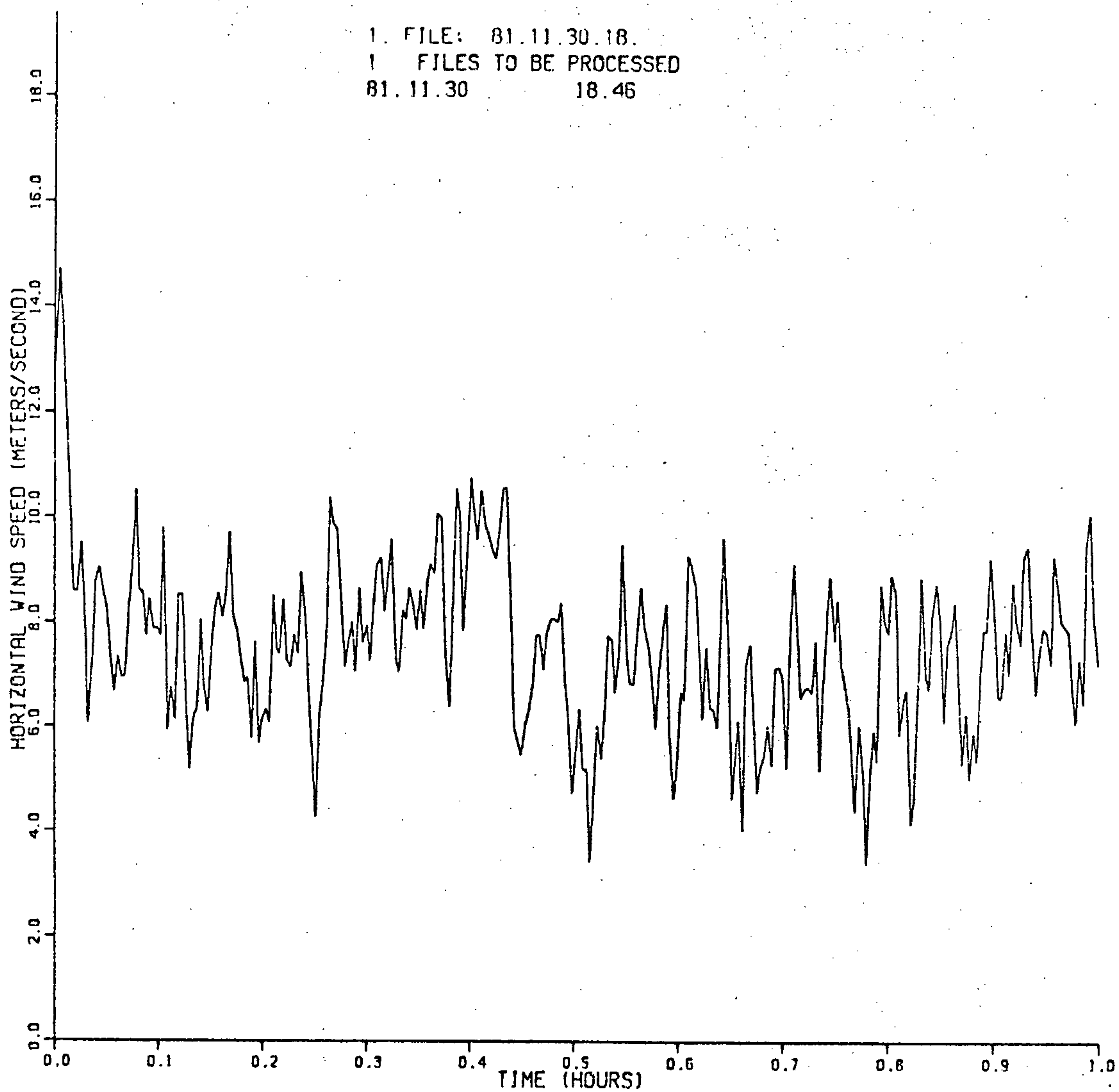

Fig. 6.33(b). Horizontal wind velocity, 10 s avg. for 81.11.30.18.

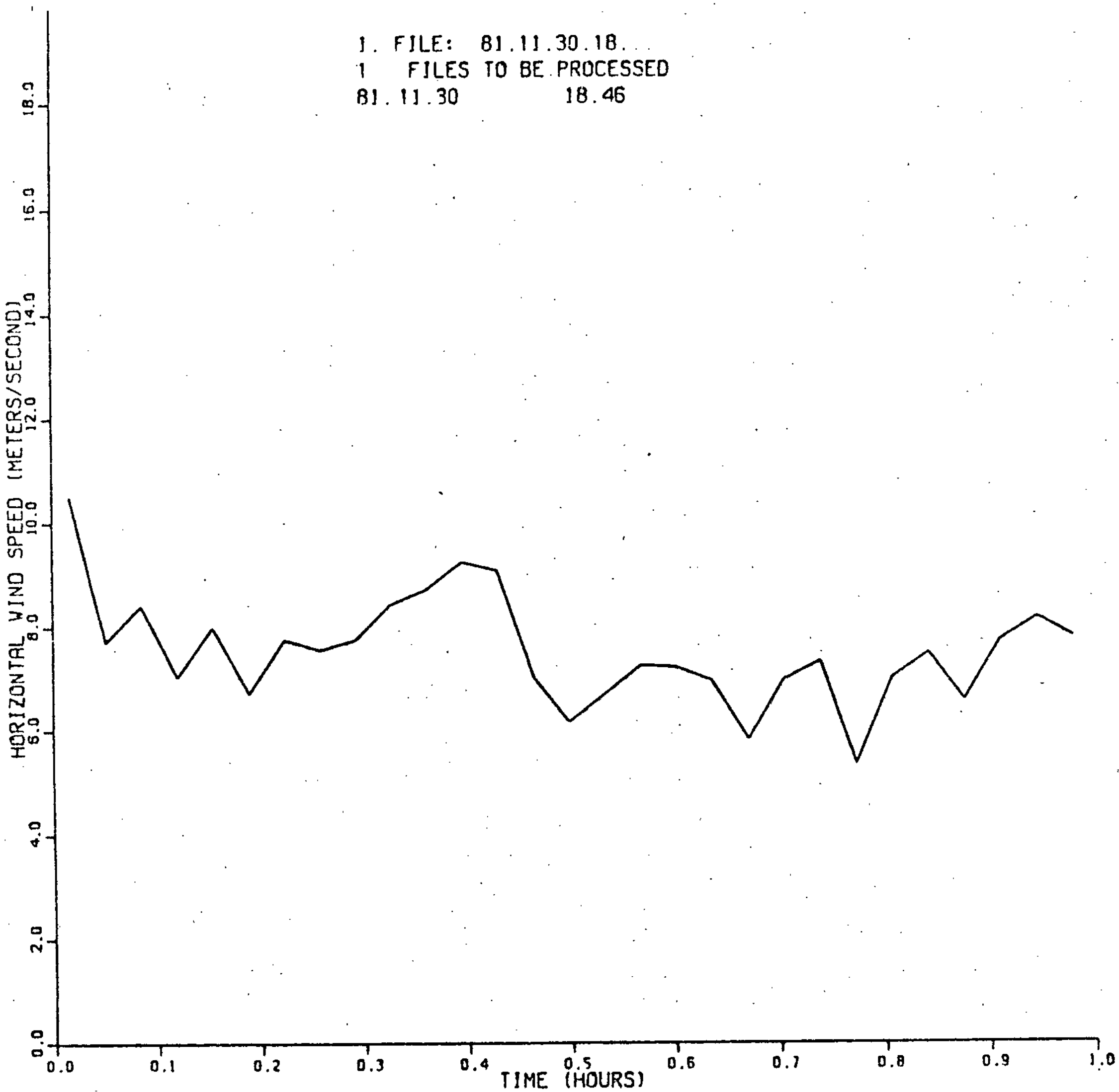

Fig. 6.3.3.(c). Horizontal wind velocity, 99 s avg. for 81.11.30.18.

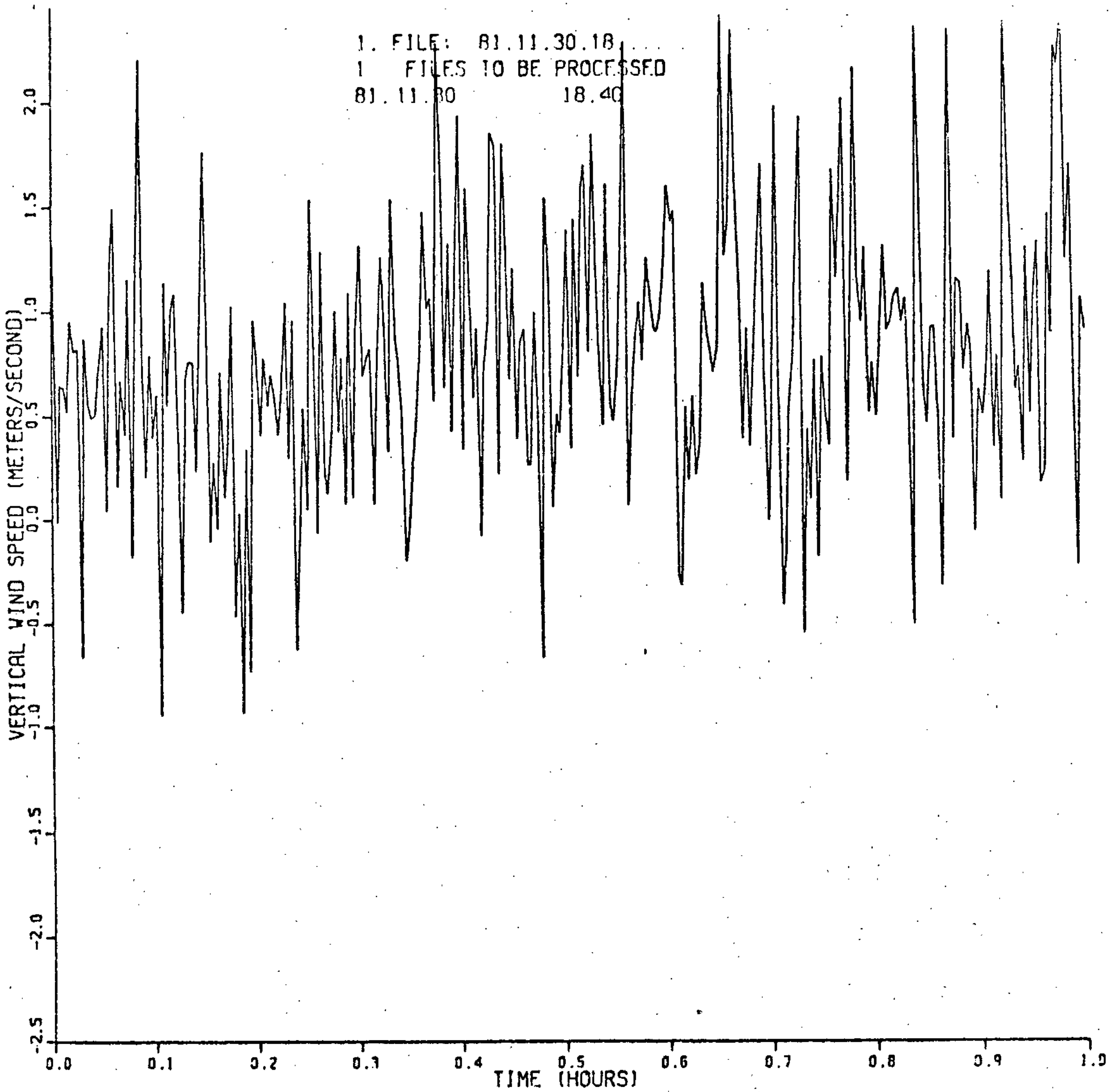

Fig. 6.3.4(a). Vertical wind velocity, 10 s avg. for 81.11.30.18.

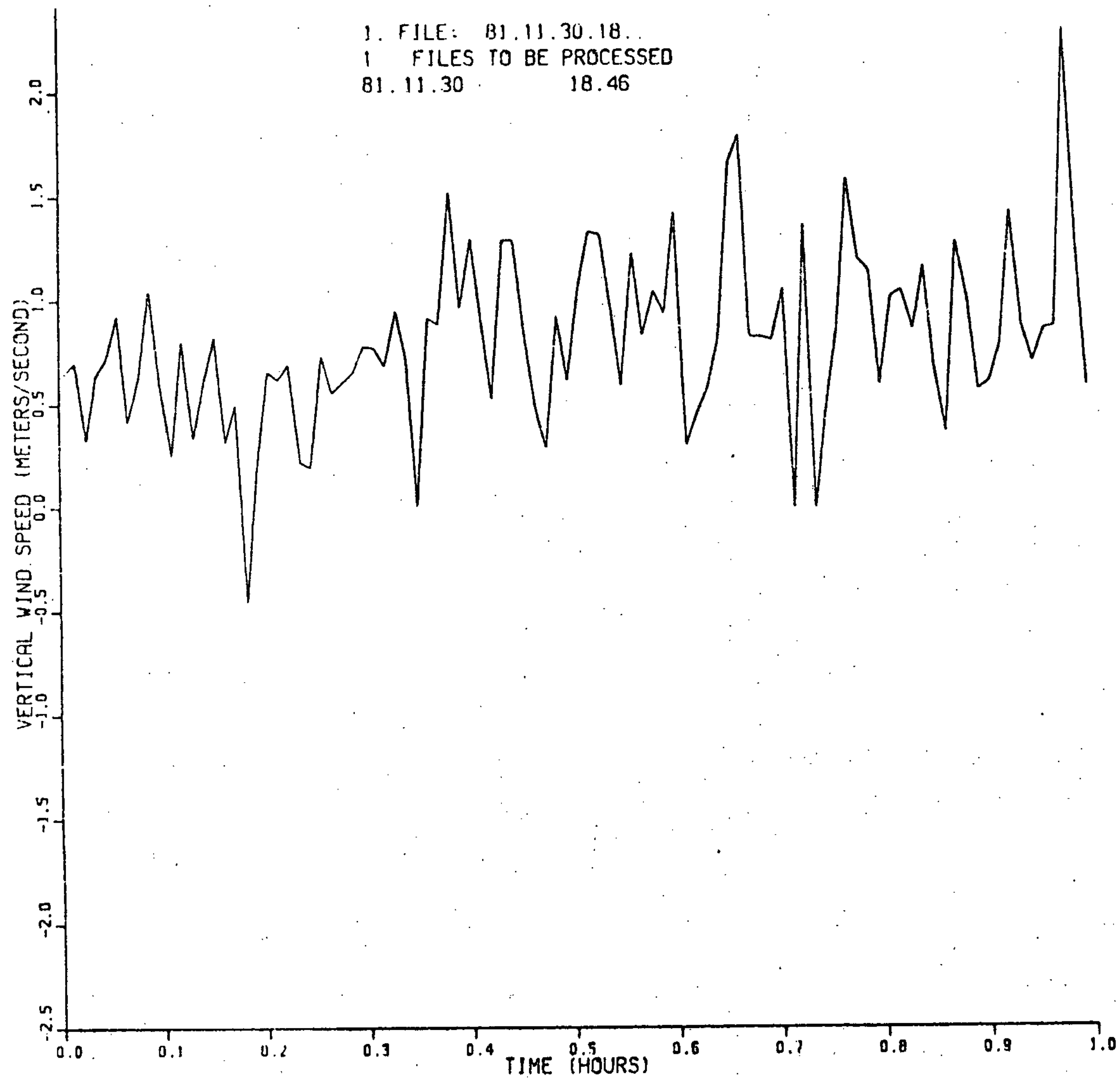

Fig. 6.3.4(b). Vertical wind velocity, 30 s avg. for 81.11.30.18.

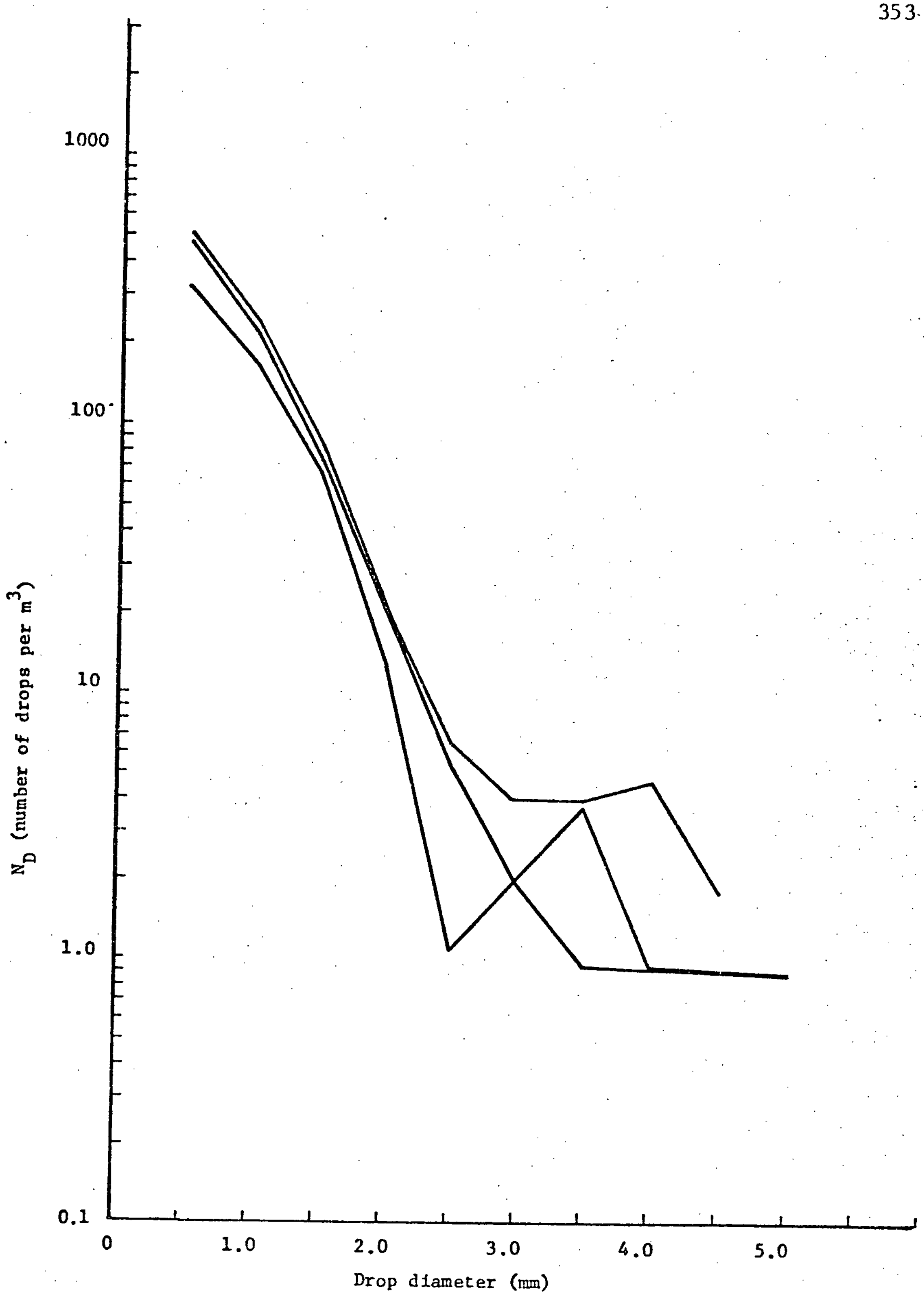

Fig. 6.3.5. Drop distributions for T_1.

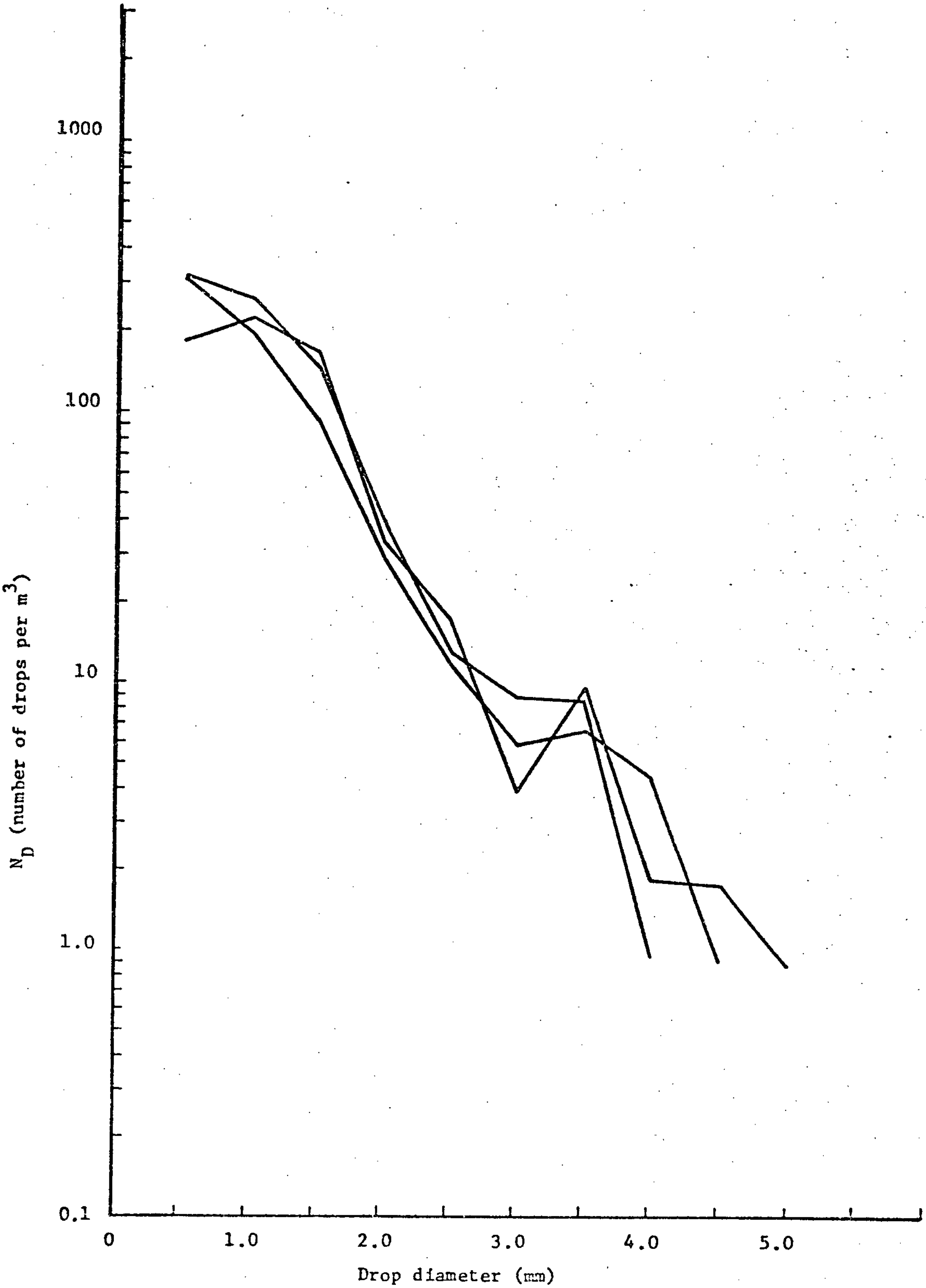

Fig. 6.3.6. Drop distributions for T_2.

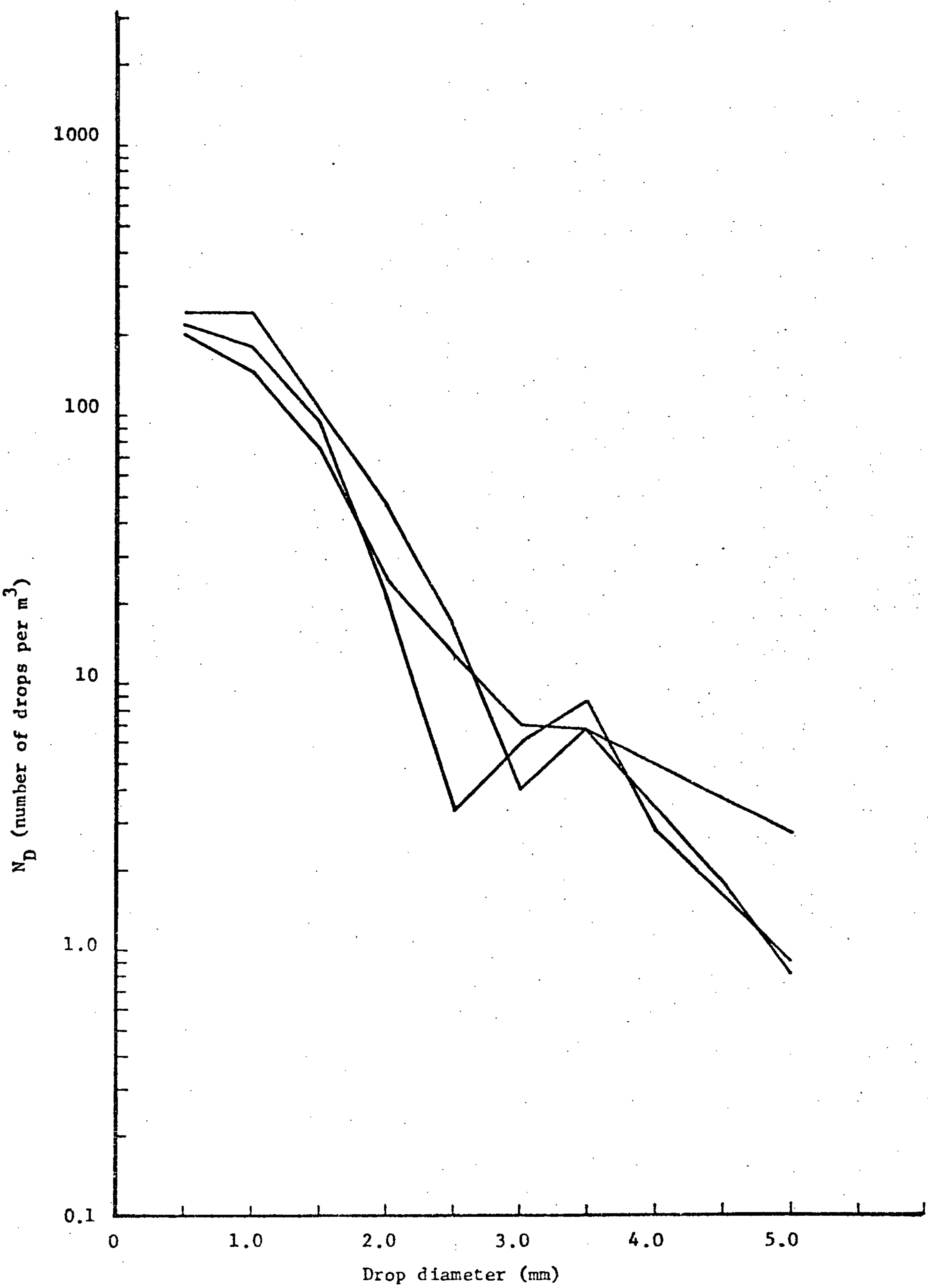

Fig. 6.3.7 Drop distributions for T_3.

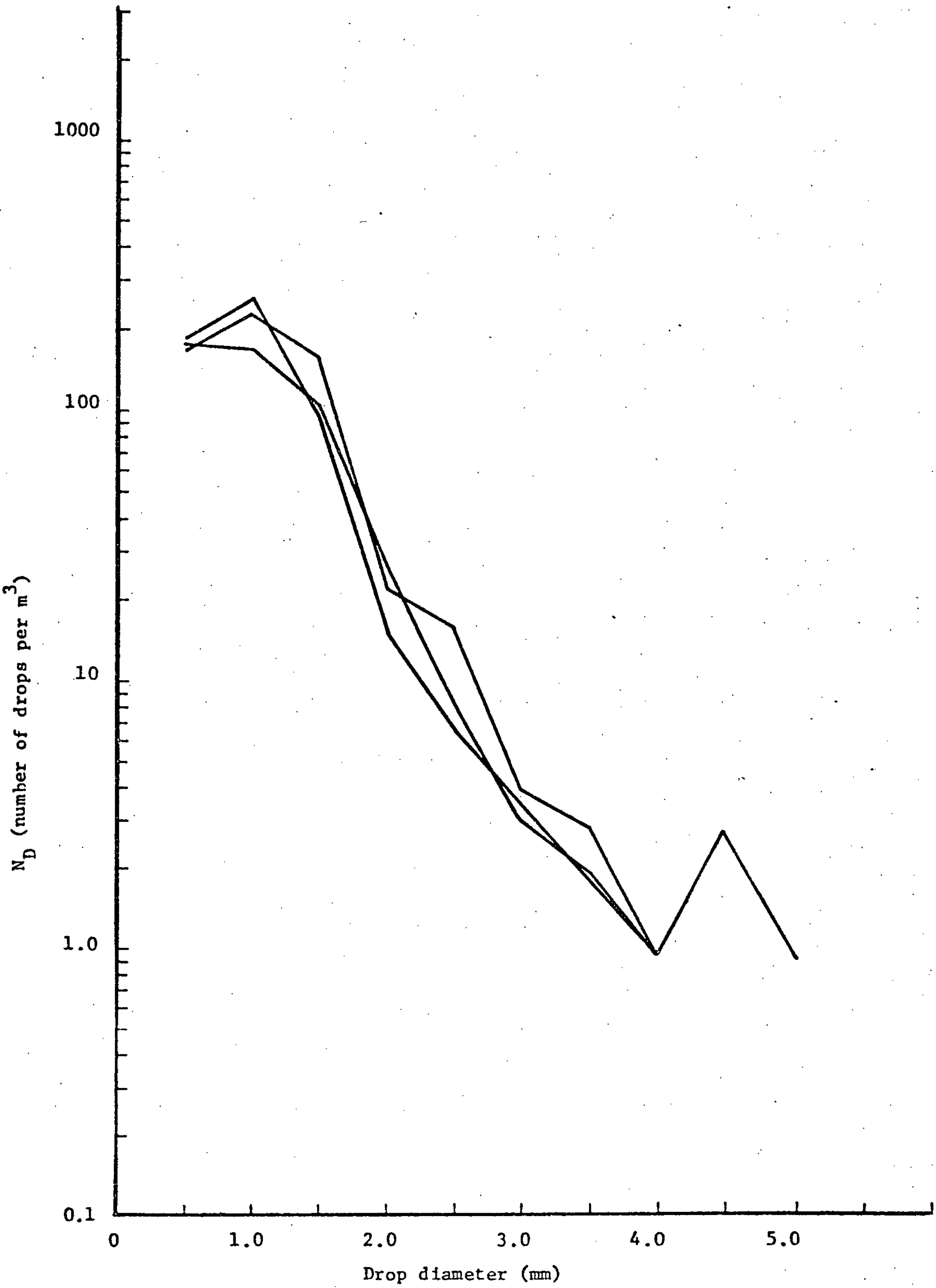

Fig. 6.3.8. Drop distributions for T_4.

the distribution at diameters between 3.5 and 4.5 mm. Similar distribution peaks were observed in [3.39], [6.1], [6.2], [6.3] and [6.4].

The four 10 s average signal levels for this file are shown in Figs. 6.3.9 and 6.3.10.

6.3.1 Attenuation Data for 81.11.30.18, 18:46-19:46

The large and extremely variable horizontal and vertical wind velocities during this file resulted in a large range of attenuation values over relatively short periods. Attempts to analyze the attenuation data recorded in this file in a manner similar to that used on other files was unsuccessful because the wind variations were too rapid to permit clear correlations between attenuation and meteorological observations. Three examples of this variability are shown in Figs. 6.3.11 to 6.3.13. During all of these periods, the attenuation varied over a range greater than that between the predictions for the JOT and JOD distributions.

6.3.2 XPD and Differential Attenuation Data for 81.11.30.18.

The XPDs for horizontal and vertical transmitted polarizations for 10 s and 99 s averages are shown in Figs. 6.3.14 and 6.3.15, (a) and (b) respectively. The 10 s average XPDs both exhibit large short term variations, again preventing any accurate correlations with meteorological observations. Referring to the 99 s averages, however, there does appear to be a similar long term variation in both the cancelled and uncancelled XPDs. These variations appear to be loosely correlated with the 99 s avg. horizontal wind velocity.

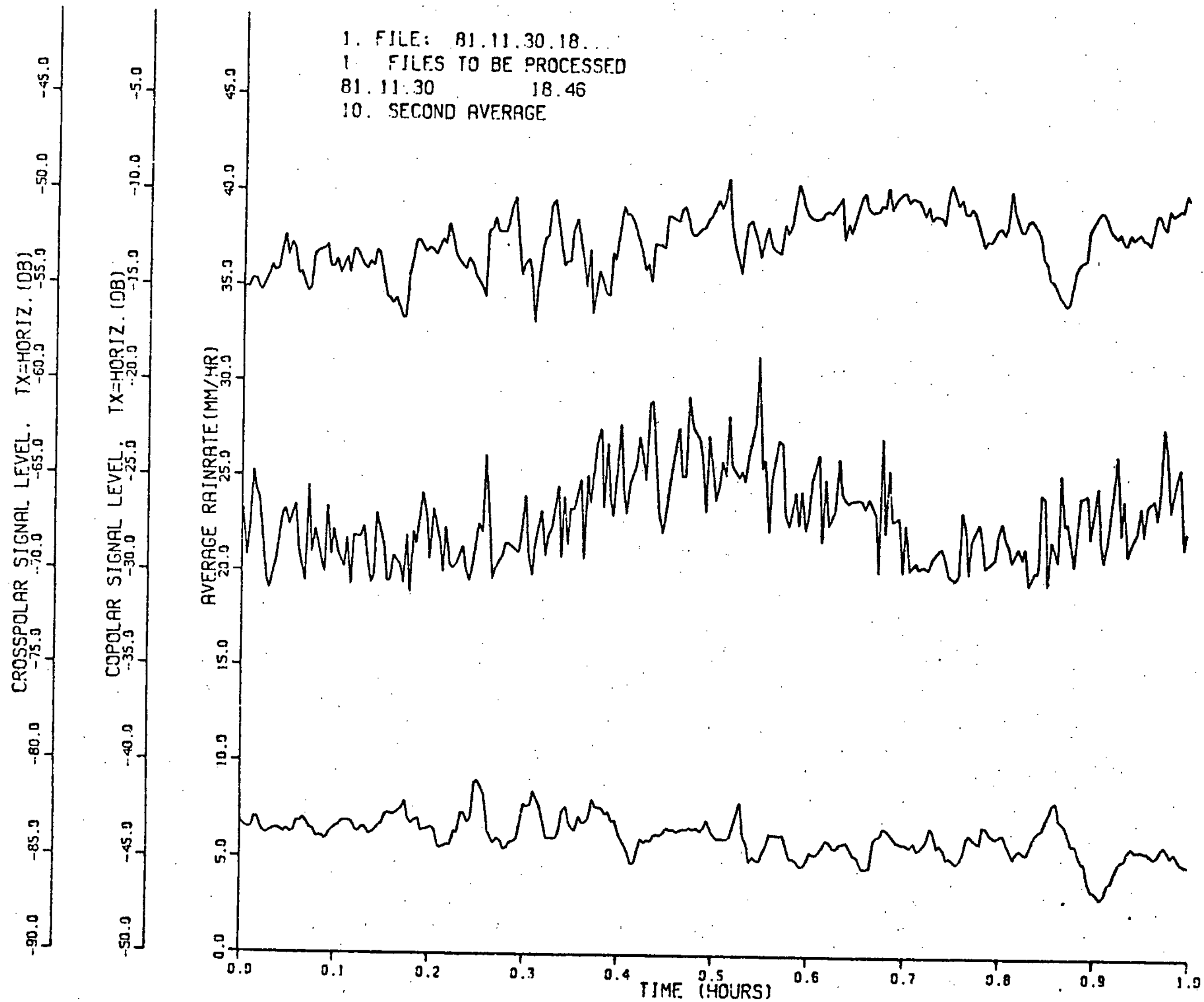

Fig. 6.3.9. Signal levels for horizontal polarization transmitted, 10 s avg, for 81.11.30.18.

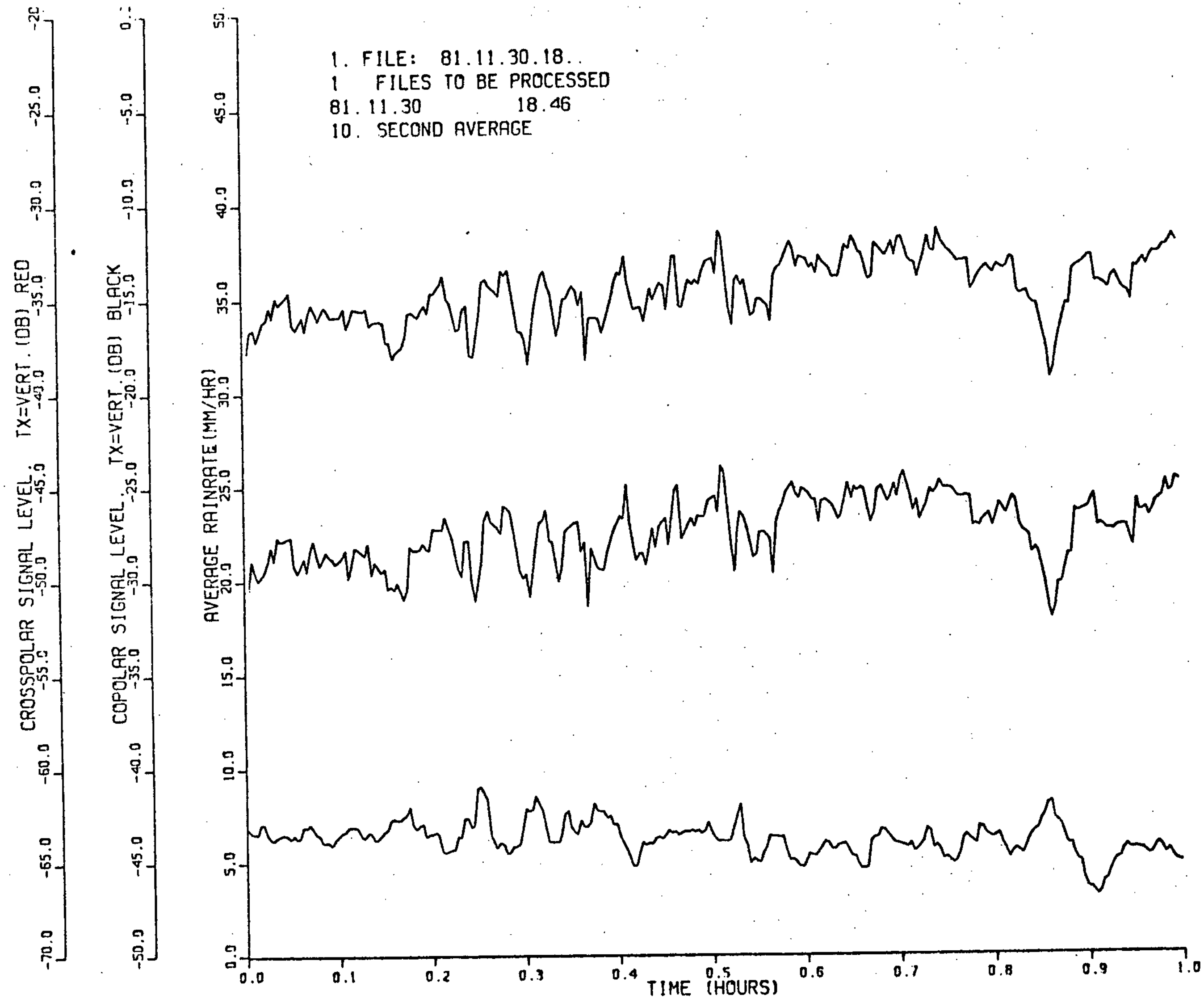

Fig. 6.3.10. Signal levels for vertical polarization transmitted, 10 s avg. for 81.11.30.18.

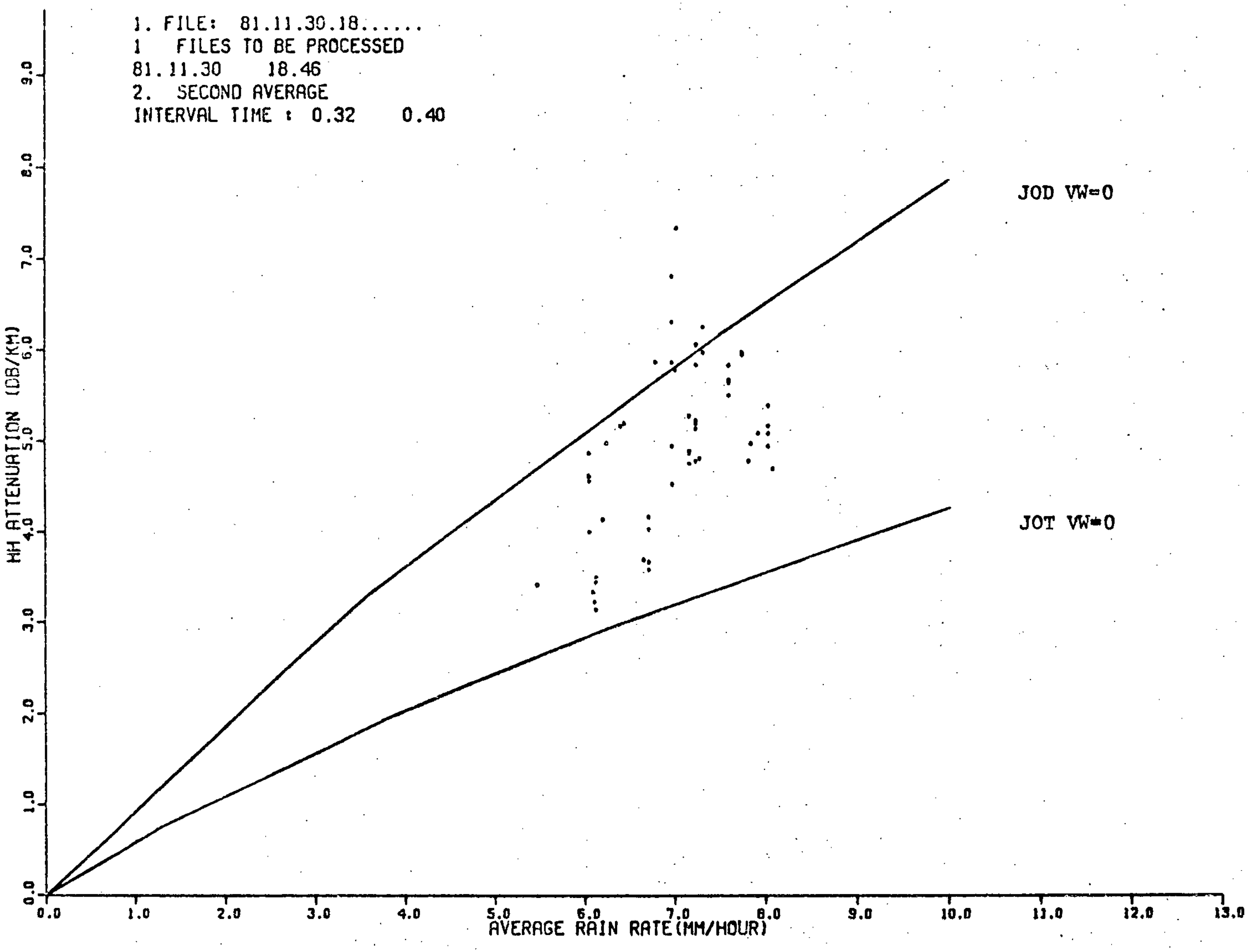

Fig. 6.3.11. CPA during T_5.

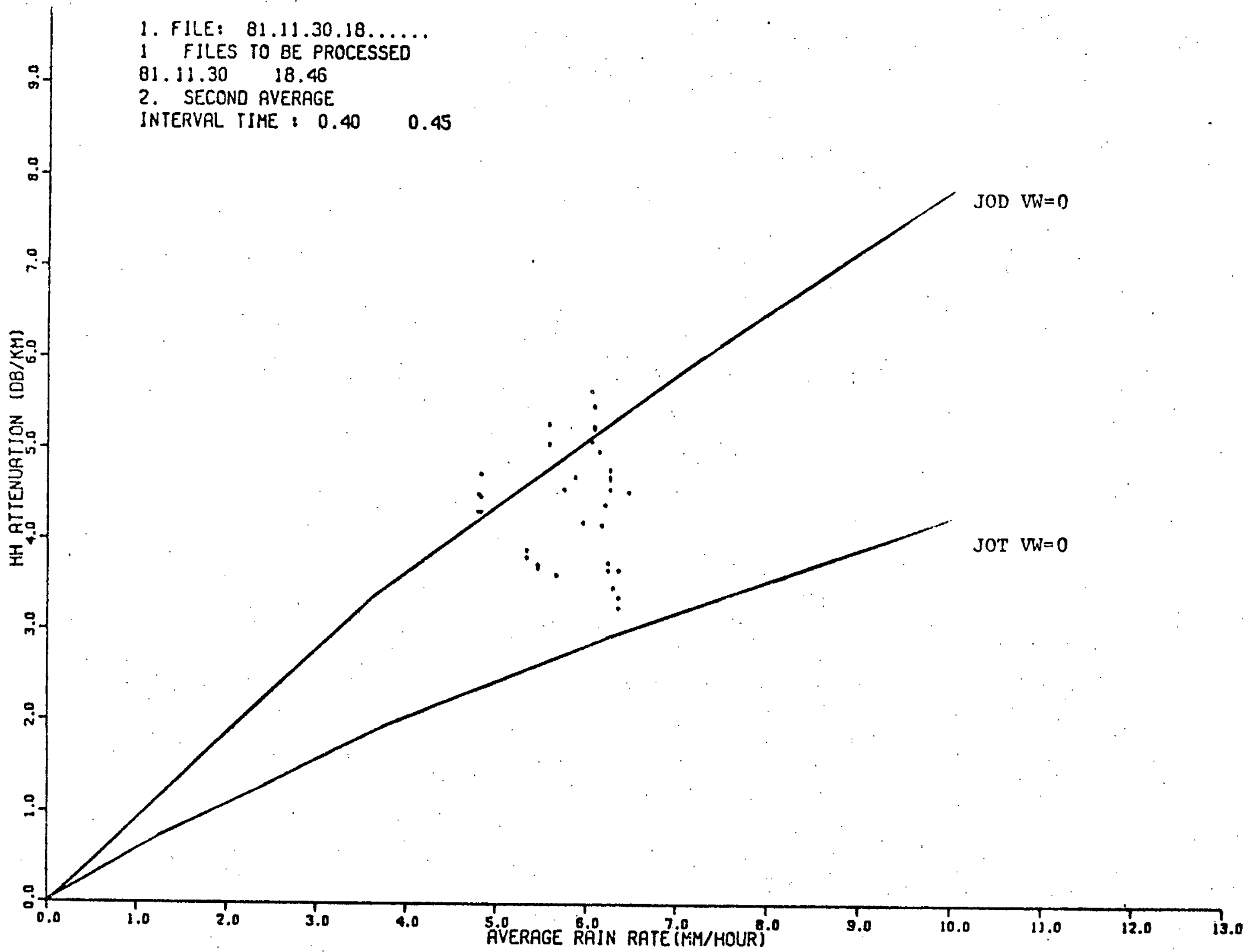

Fig. 6.3.12. CPA during T_6.

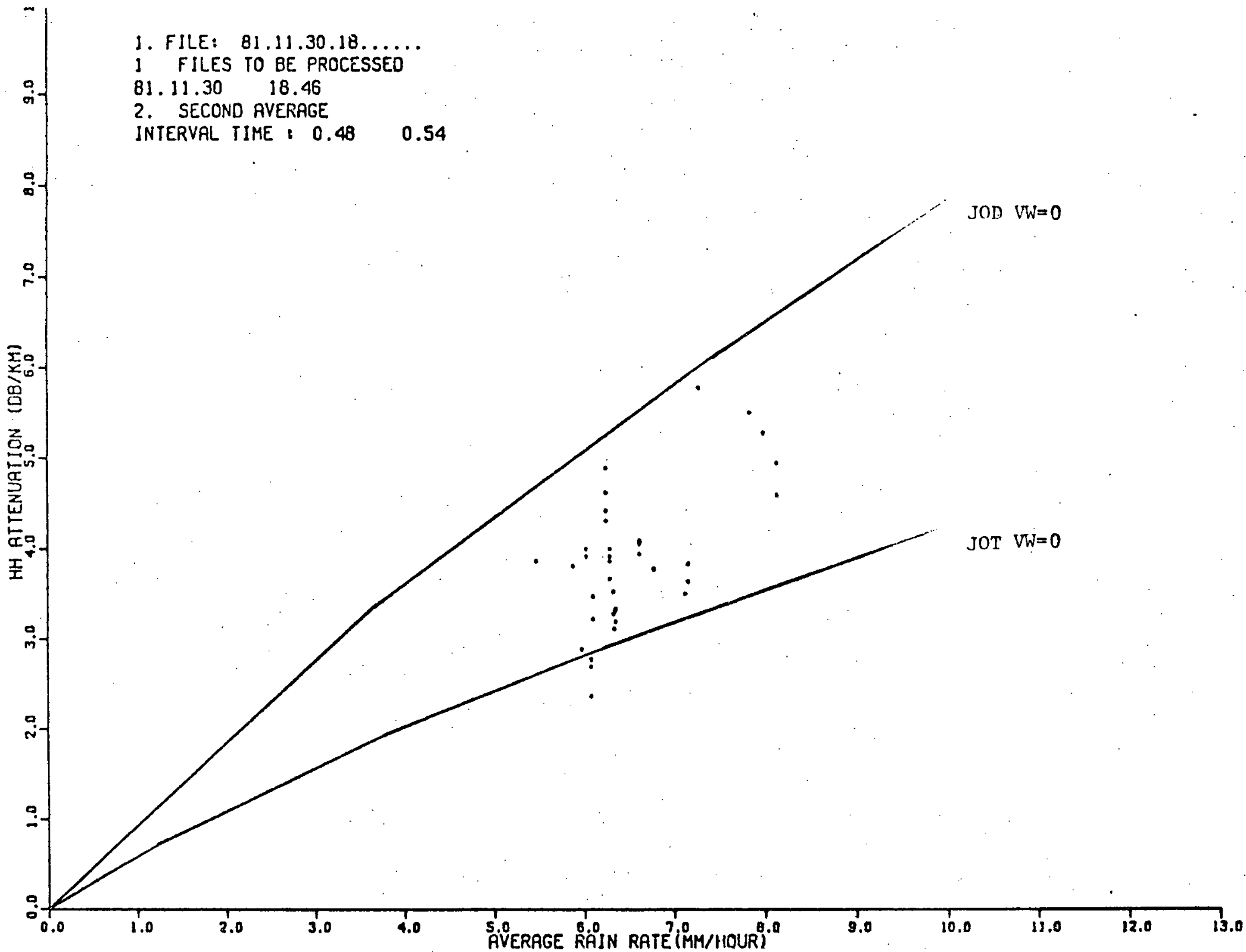

Fig. 6.3.13. CPA during T_7.

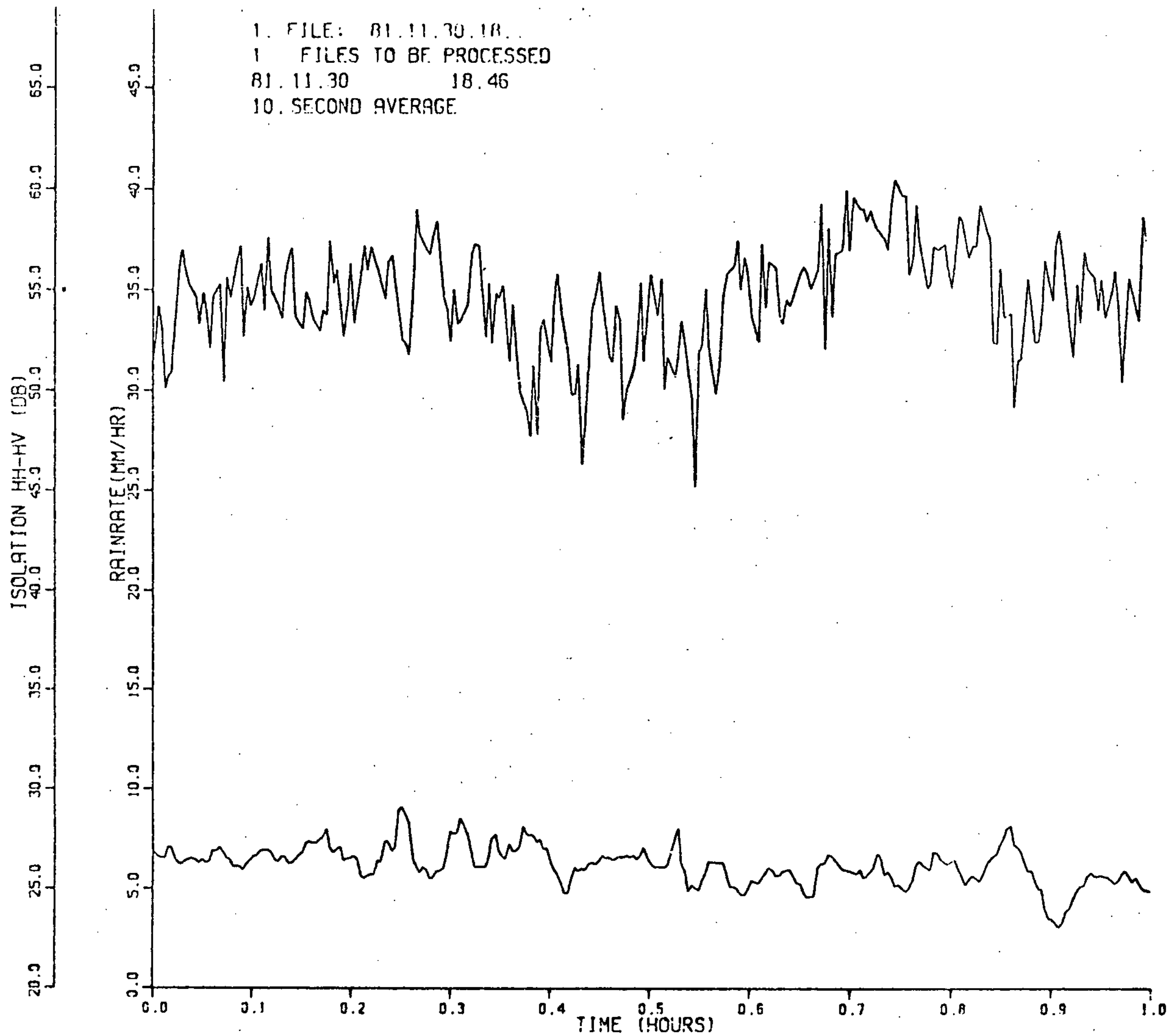

Fig. 6.3.14(a). XPD for horizontal transmitted polarization, 10 s avg. for 81.11.30.18.

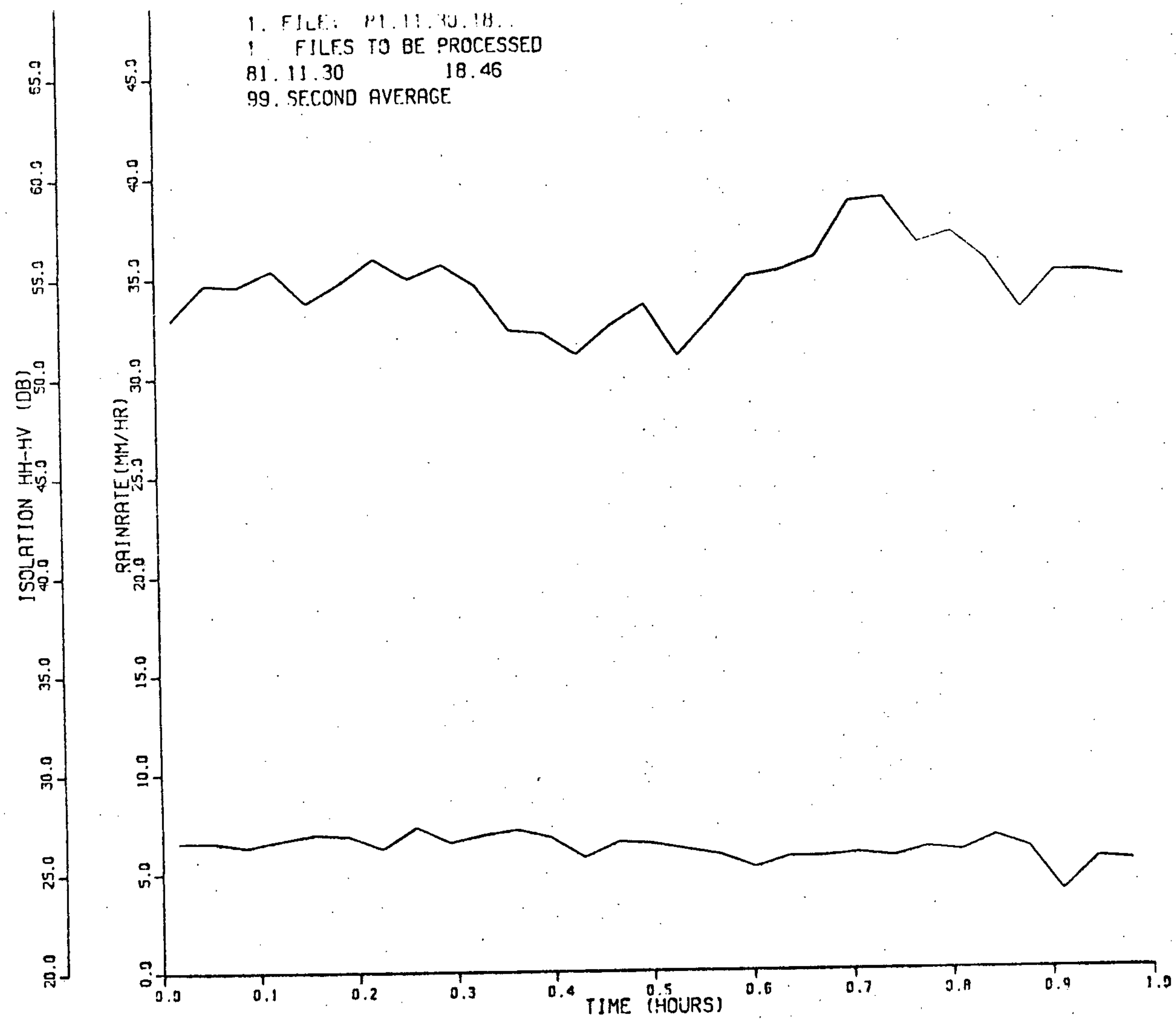

Fig. 6.3.14(b). XPD for horizontal polarization transmitted, 99 s avg. for 81.11.30.18.

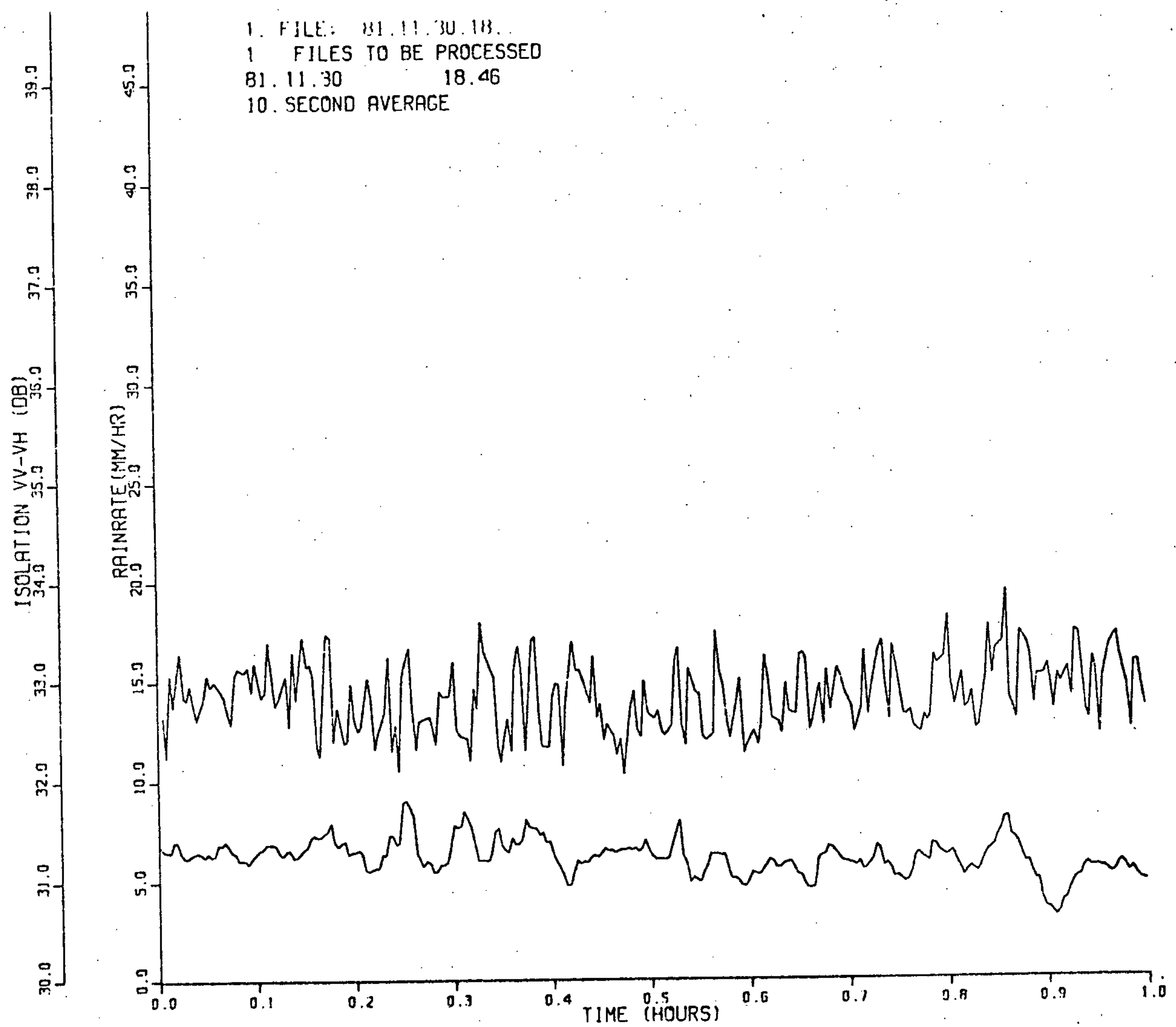

Fig. 6.3.15(a). XPD for vertical transmitted polarization, 10 s avg. for 81.11.30.18.

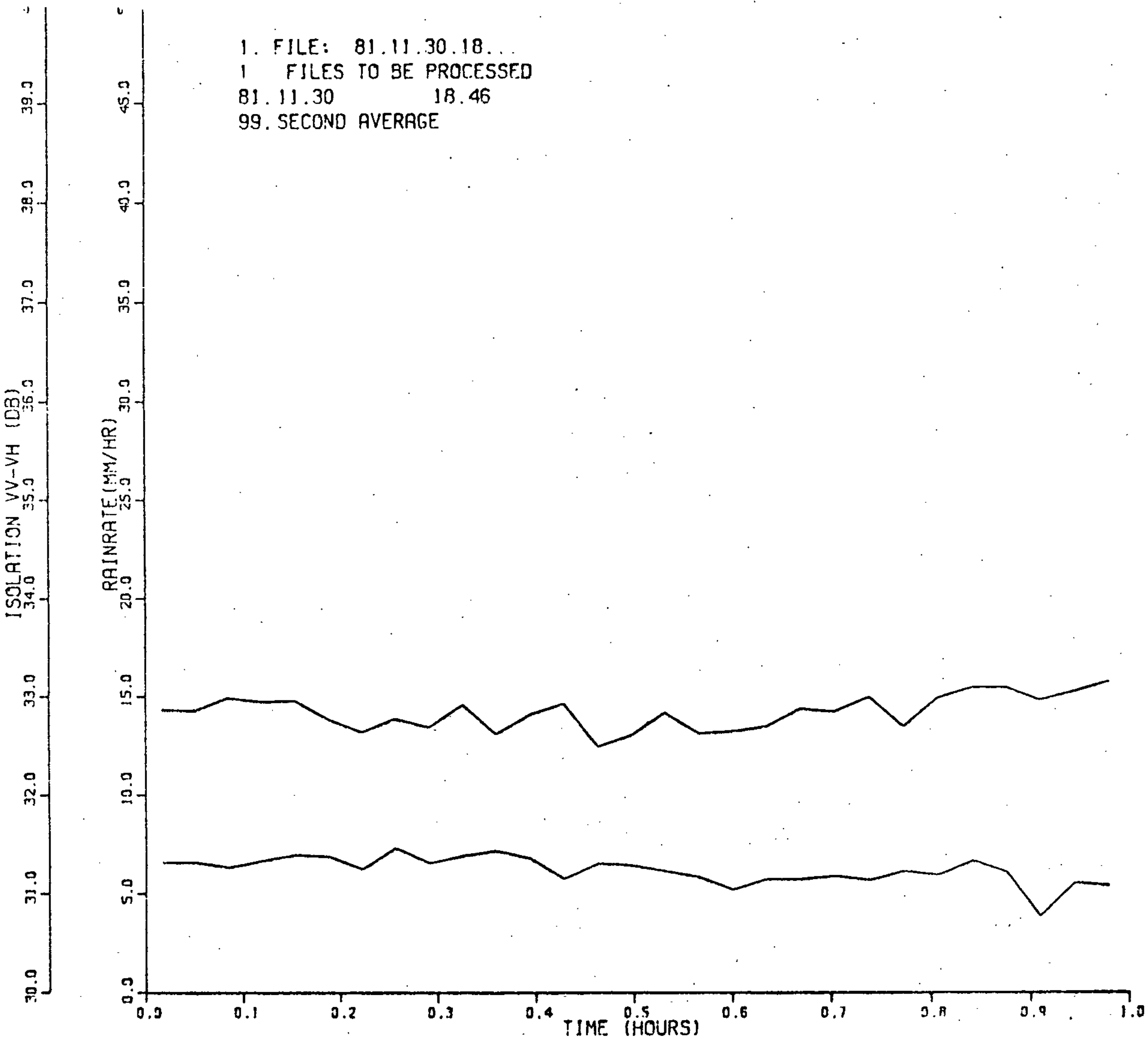

Fig. 6.3.15(b). XPD for vertical transmitted polarization, 99 s avg. for 81.11.30.18.

The differential attenuation data in Fig. 6.3.16 displays a wide range of values, both positive and negative. While these data must be interpreted with the usual caution, the general similarity of this plot to Fig. 6.3.15(a) (which, of course, also includes the effects of differential attenuation on the transmitted copolar and transmit antenna depolarized signals) means that much of the variation in Fig. 6.3.16 is, in fact, what would be observed without polarization sampling.

6.4 Experimental Results for 81.11.30.19.

This data file was recorded during a period of widespread, relatively uniform rain of medium intensity and moderately high wind velocities. During the latter part of this file, there was an interesting change in the drop size distribution which apparently affected the XPD as well as the CPA. Rainrates for this file are shown in Fig. 6.4.1. The path average rainrate during this period varied from 3 to 13 mm/h.

The wind direction during this file was again constantly from the east, i.e. perpendicular to the path. Horizontal wind velocities for 10 s and 30 s averages are shown in Figs. 6.4.2(a) and (b). Over this period the 10 s average horizontal wind varied from 4.2 to 10 m/s. Vertical wind velocities are shown in Figs. 6.4.3(a) to (c) for 10 s, 30 s and 60 s averages. The 30 s horizontal wind velocity varied between -0.2 to +1.3 m/s.

Time series plots for the four signal levels with 10 s averages are shown in Figs. 6.4.4 and 6.4.5.

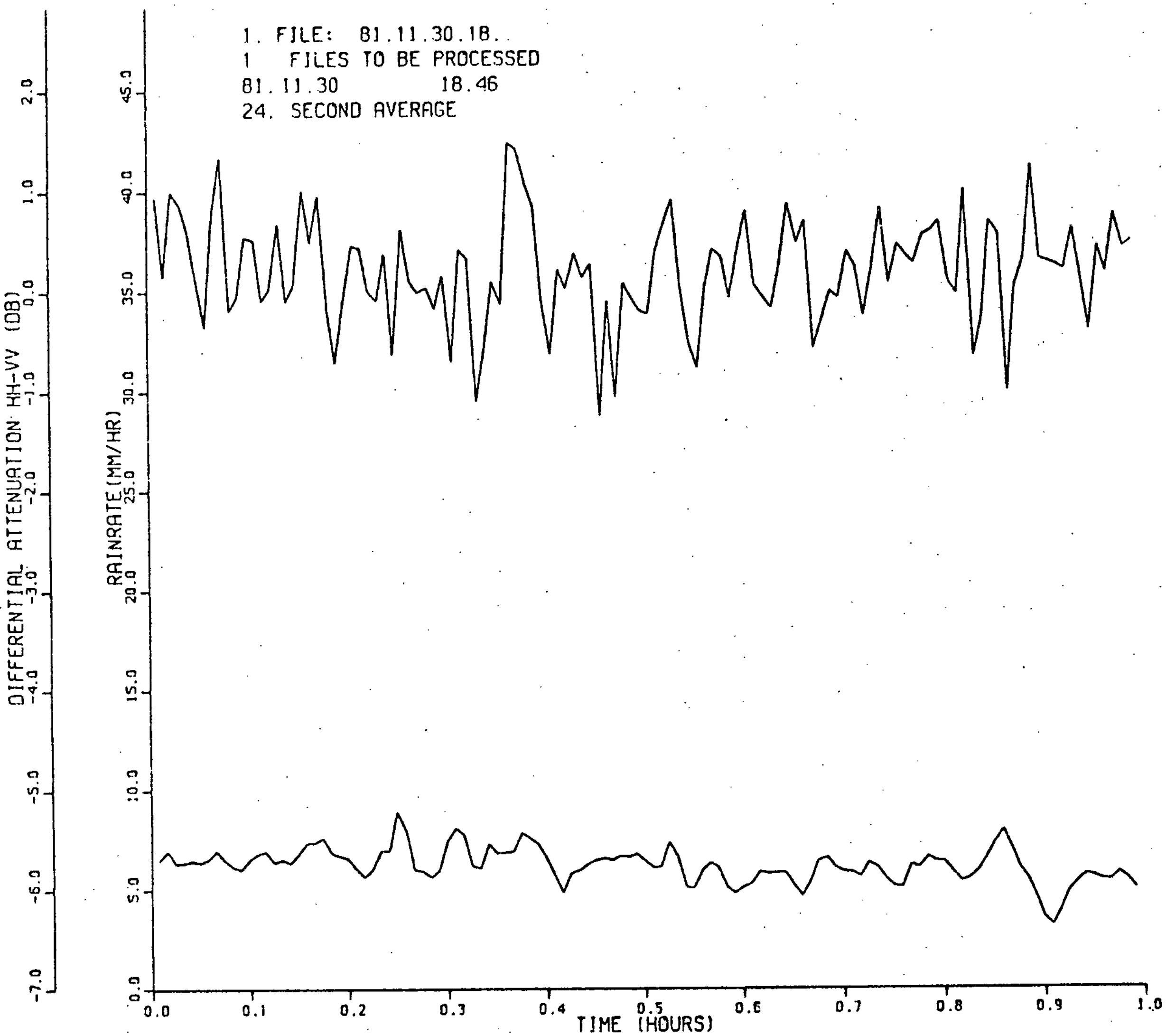

Fig. 6.3.16. Differential attenuation for 81.11.30.18.

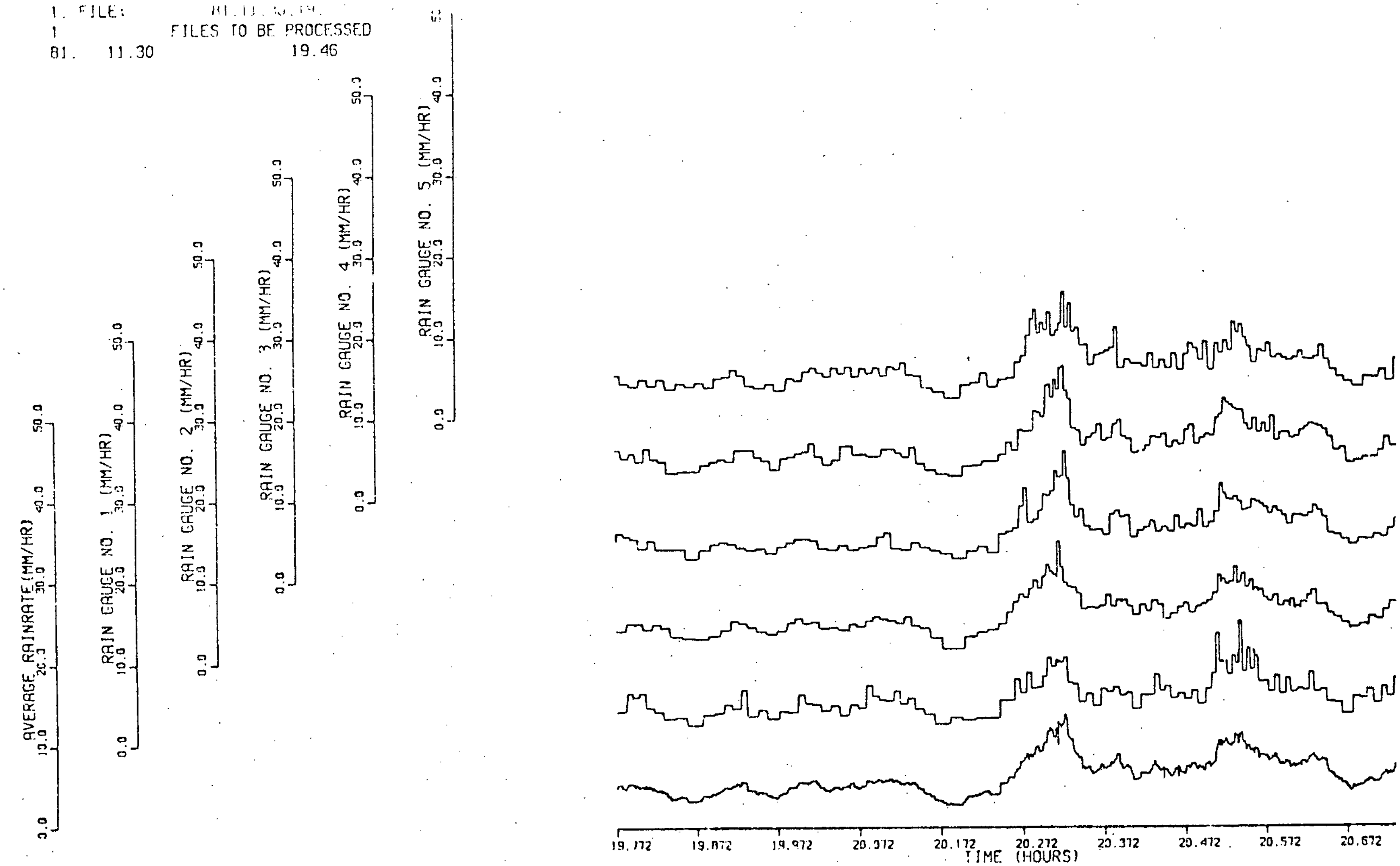

Fig. 6.4.1. Rainrates for 81.11.30.19.

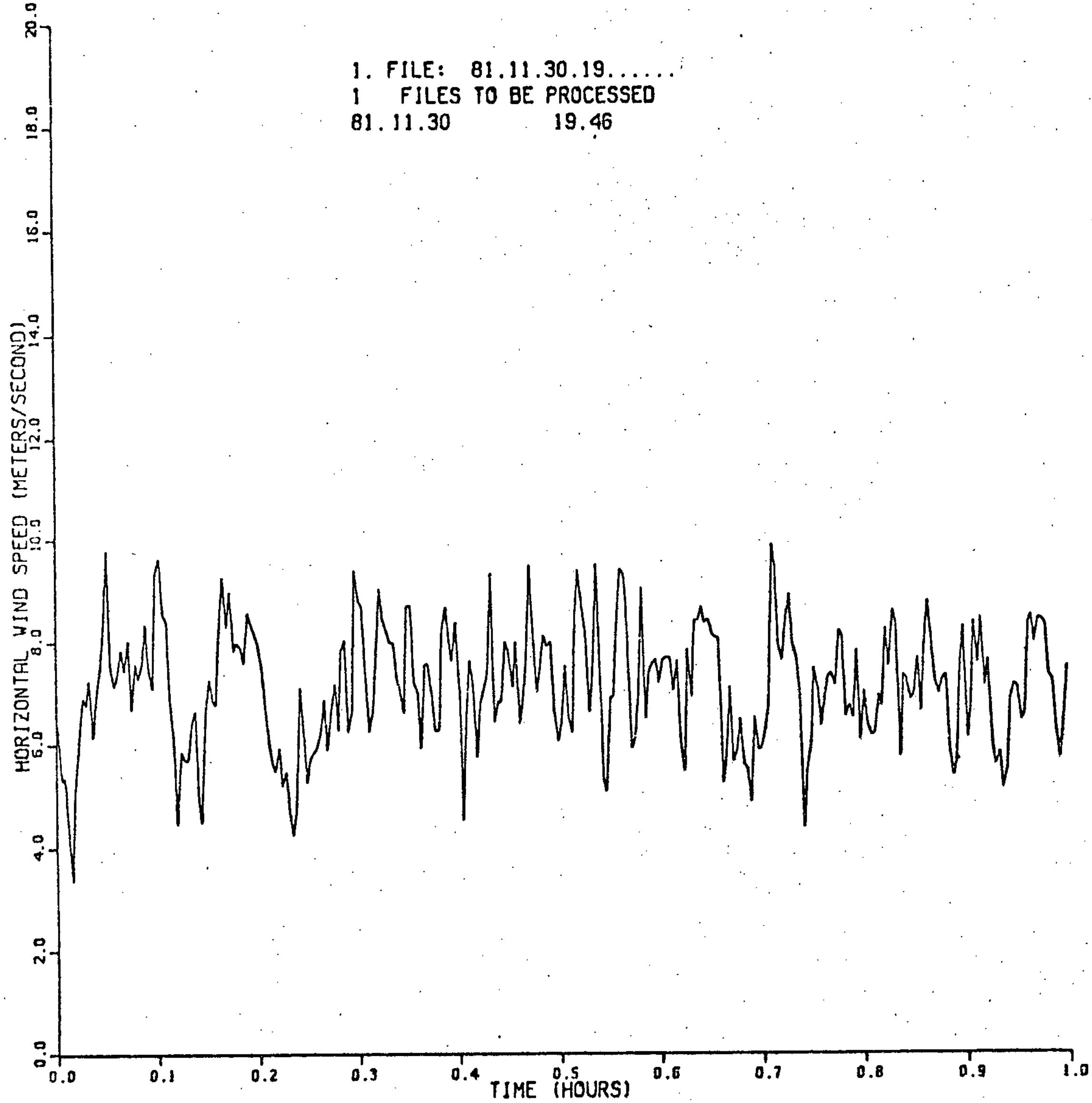

Fig. 6.4.2(a). Horizontal wind velocity, 10 s avg. for 81.11.30.19.

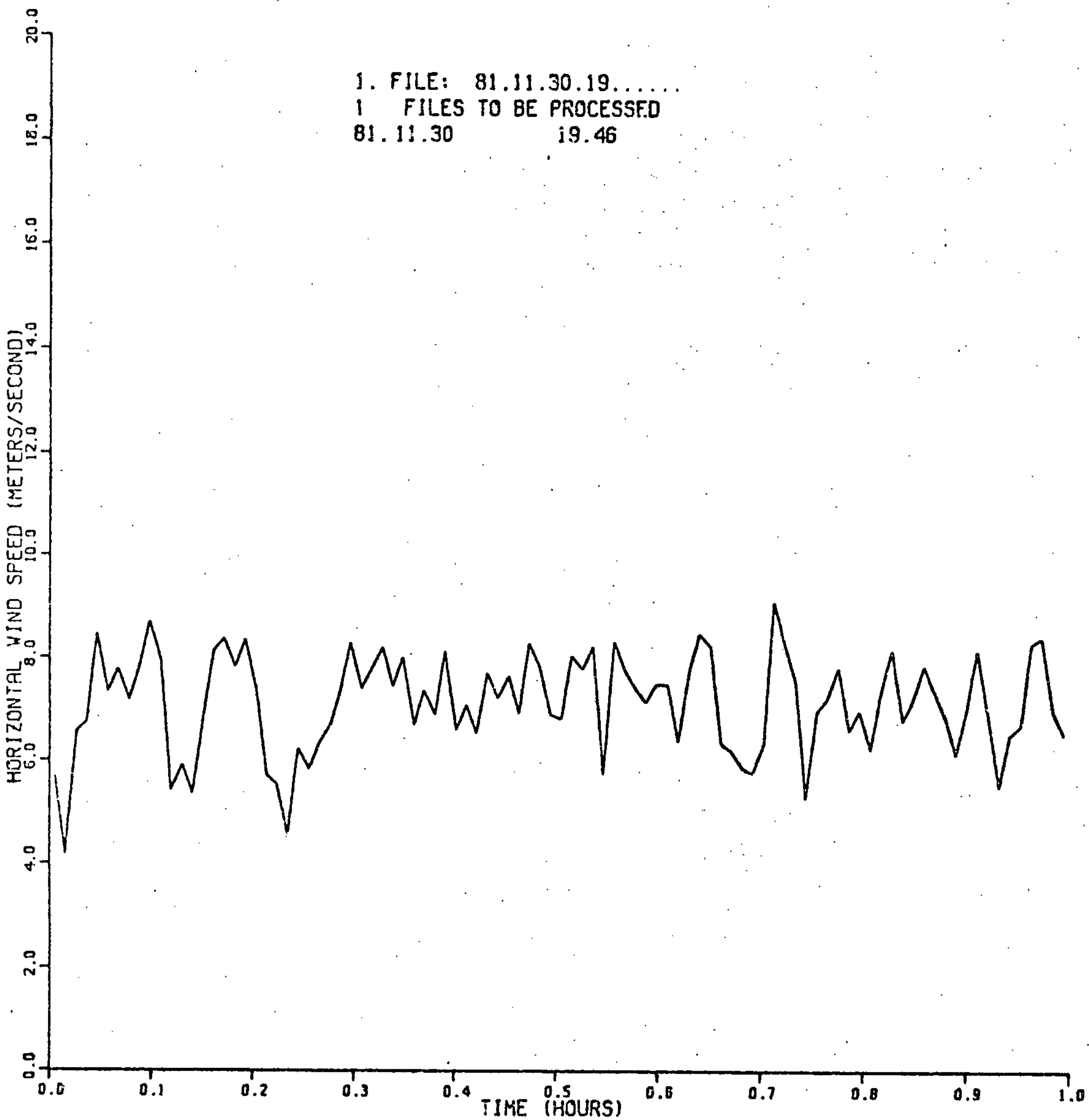

Fig. 6.4.2(b). Horizontal wind velocity, 30 s avg. for 81.11.30.19.

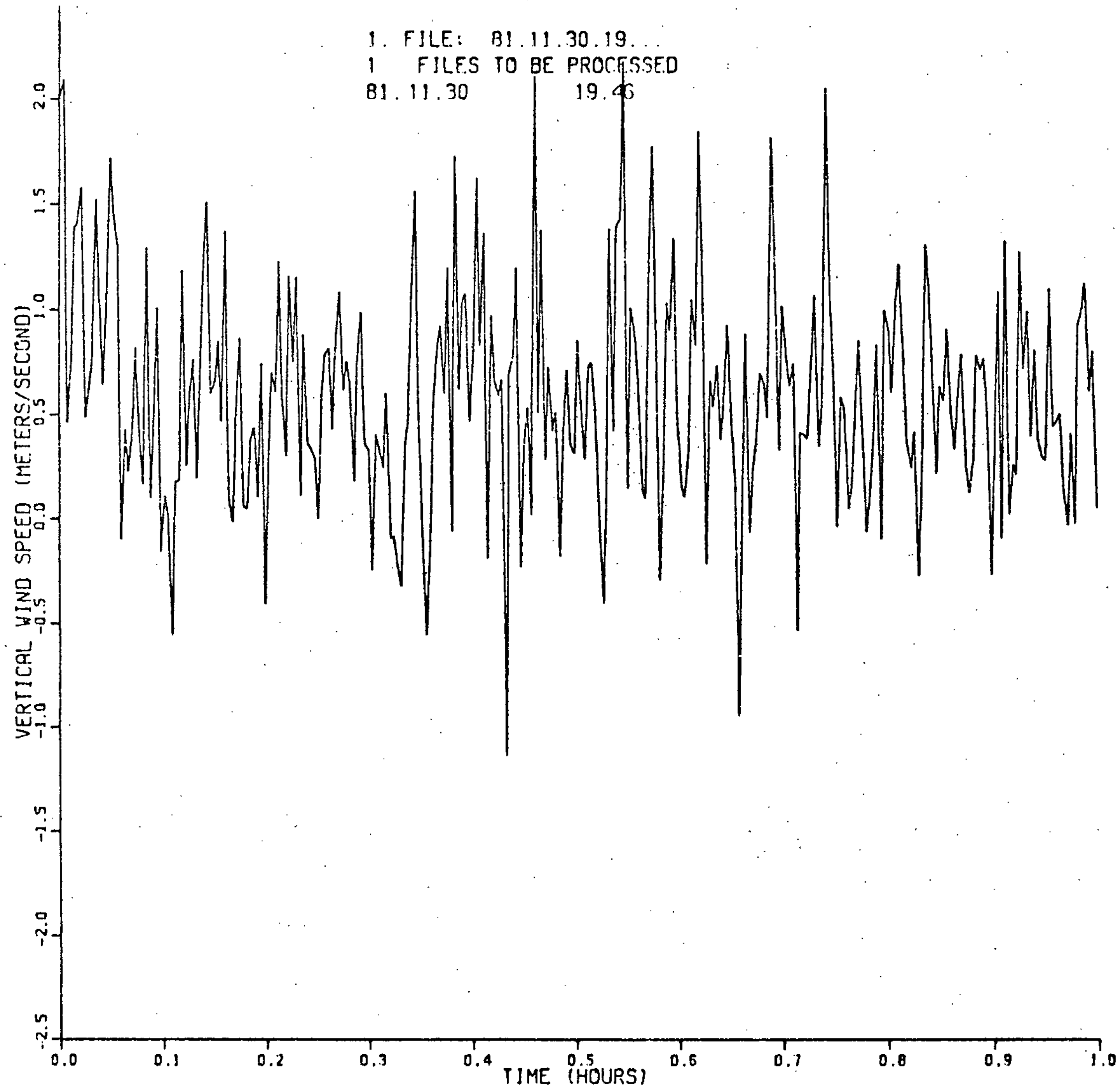

Fig. 6.4.3(a). Vertical wind velocity, 10 s avg. for 81,11,30,19.

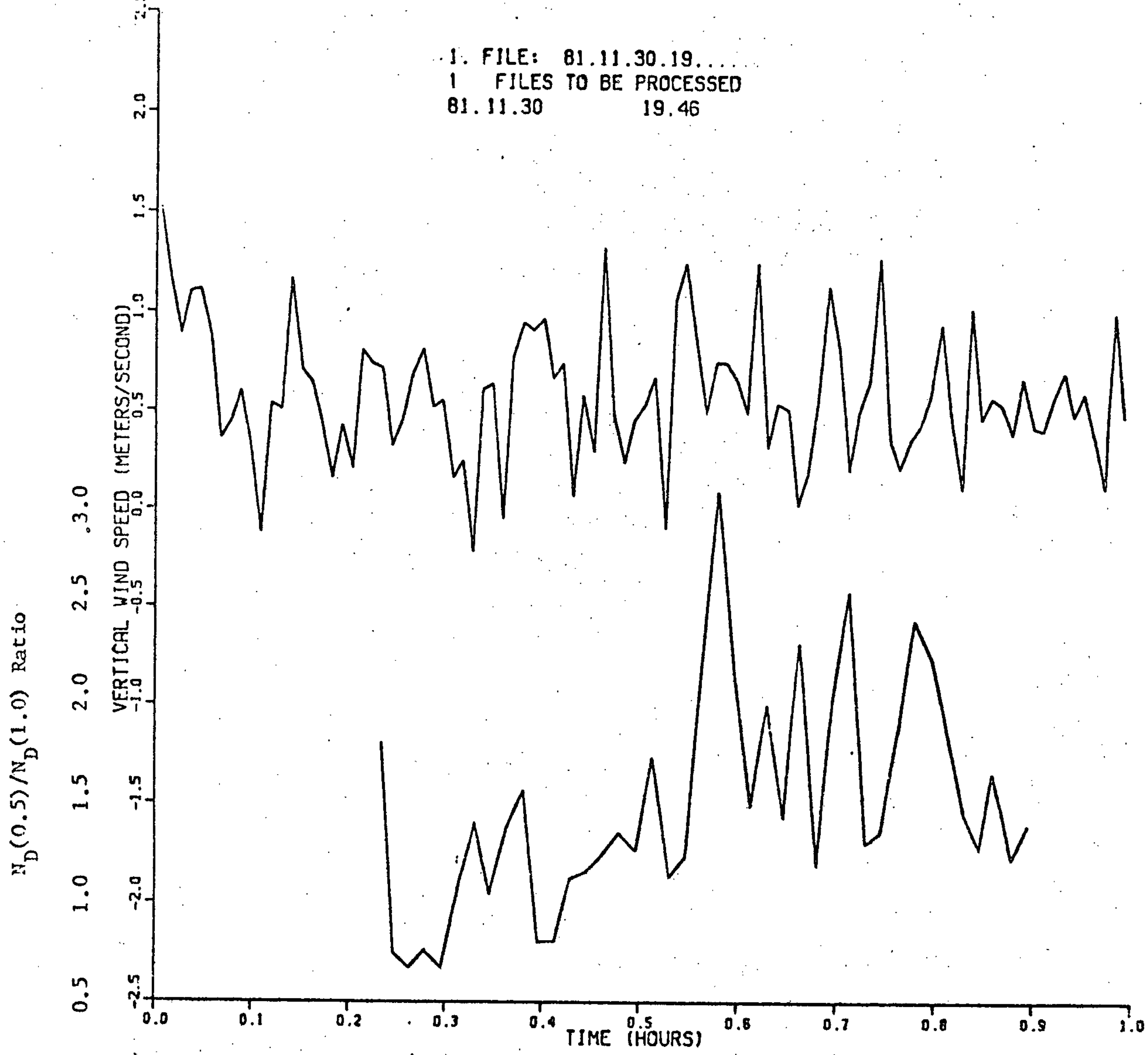

Fig. 6.4.3.(b). Vertical wind, 30 s avg. and $N_D(0.5)/N_D(1.0)$ ratio, for 81.11.30.19.

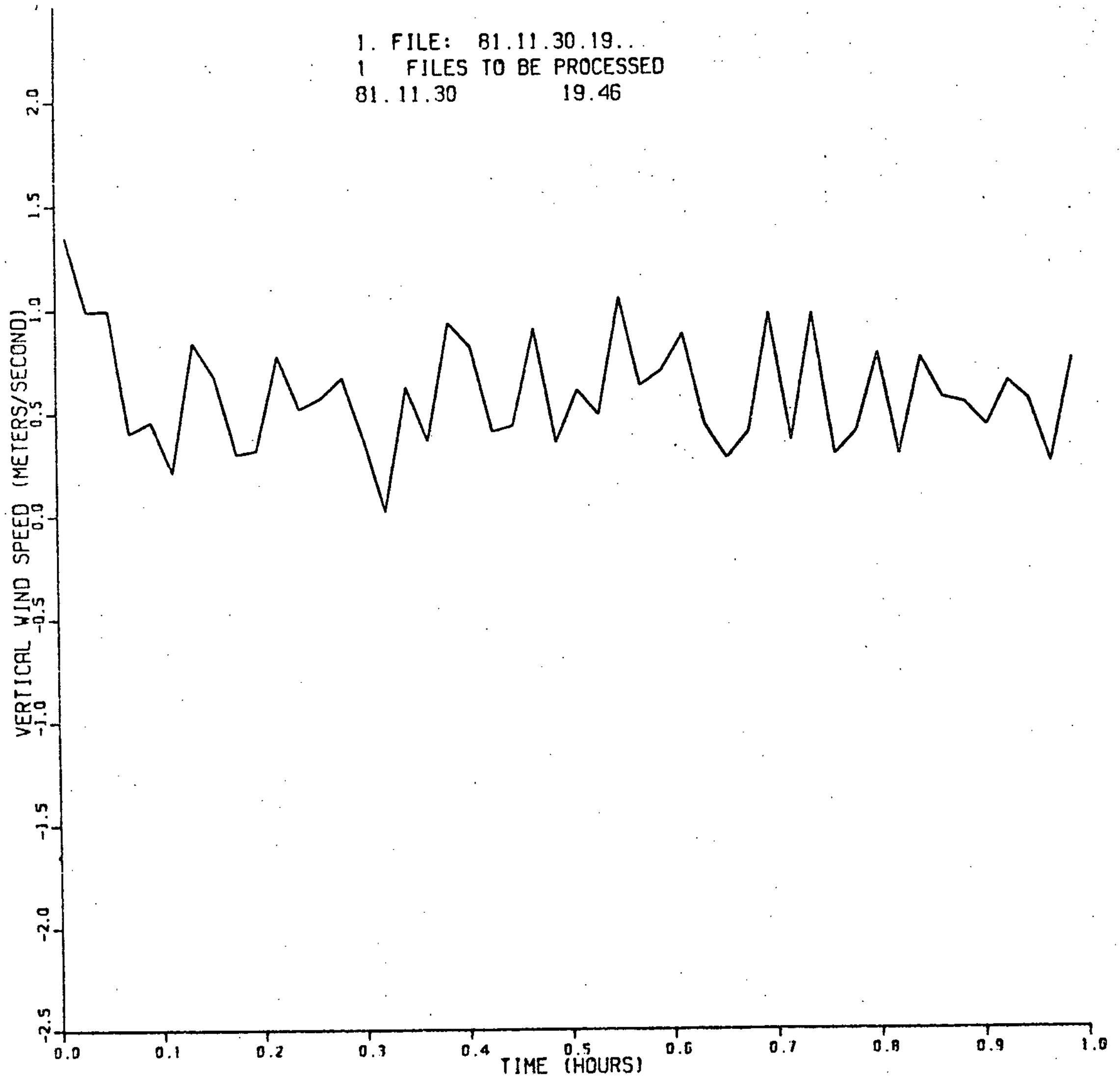

Fig. 6.4.3(c). Vertical wind velocities, 60-s avg. for 81.11.30.19.

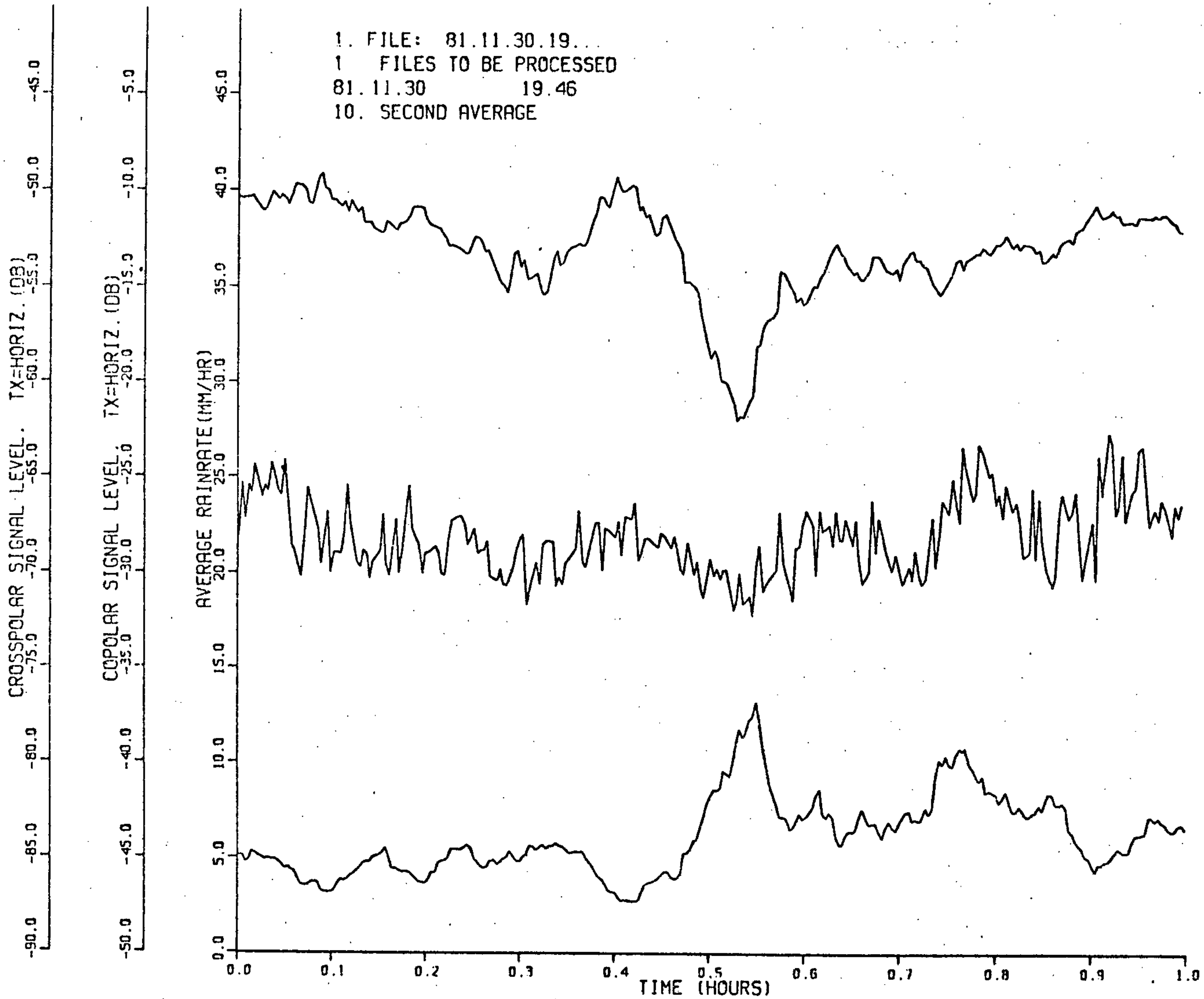

Fig. 6.4.4. Signal levels for horizontal polarization transmitted, 10 s avg. for 81.11.30.19.

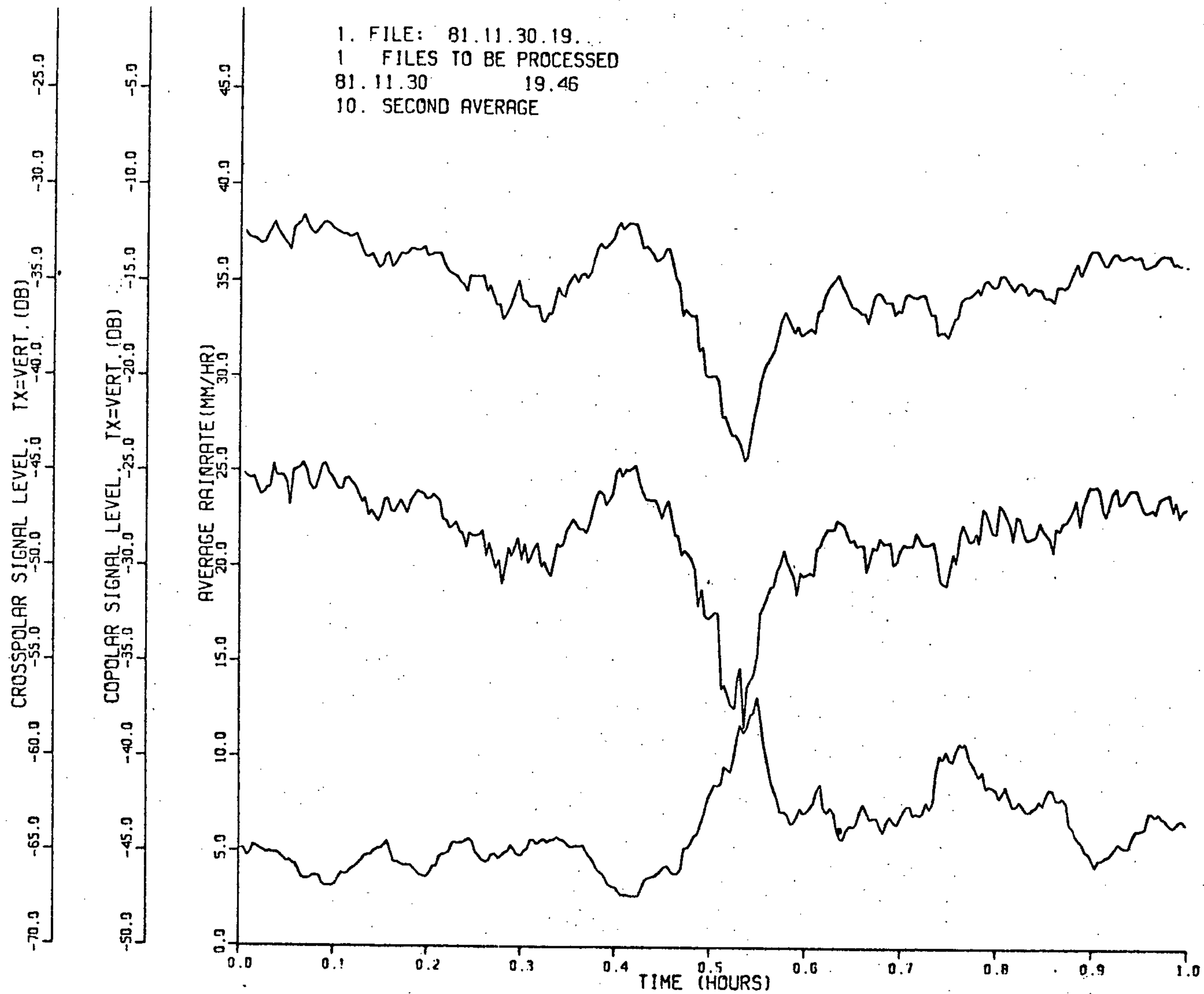

Fig.6.4.5. Signal levels for vertical polarization transmitted, 10 s avg. for 81.11.30.19.

6.4.1 Attenuation Data for 81.11.30.19, 20:20-20:34

This data file includes examples of high attenuations due to vertical wind and changes in the drop size distribution. Included are examples of vertical wind induced attenuation consistently higher than standard predictions for the JOD distribution and an example of consistently decreasing attenuation with increasing rainrate due to a vertical wind transient. During the latter part of this file, there was a general trend to simultaneously increasing numbers of very small and medium-large drops. Over this period, the distribution changed from close to the JOW to having more medium and large drops than the JOT distribution. A summary of the attenuation results for this file are given in Table 6.4.1.

6.4.1.1 Attenuation During T_1, 0.24-0.28 h

During interval T_1, the CPA, Fig. 6.4.6, was higher than that predicted for the JOD distribution. The measured drop sizes were similar to the JOW distribution with a few more large drops, Fig. 6.4.7. Attenuation was higher than that predicted using standard techniques and the measured distribution because of the upward vertical wind. The 30 s average wind, Fig. 6.4.3(b) was slowly increasing during T_1 and had an average value of approximately +0.6 m/s, Fig. 6.4.3(c). The measured data is in agreement with the predictions using the vertical wind modification discussed in Section 4.4 with a vertical wind velocity of slightly greater than +1.0 m/s.

This vertical wind velocity is approximately double that measured by the anemometer. In most of the files with similar, relatively constant, vertical wind velocities it was found that best agreement was obtained for an

Period	Measured Attenuation Compared to Standard Predictions	Measured Drop Distribution	Vertical Wind During Rain	Data is in Approximate Agreement with Predictions for:	Comments
T_1 0.24-0.28 h	Higher than JOD Fig. 6.4.6	Basically JOW but few more large drops, 1 Fig. 6.4.7	≅+0.6 m/s avg. Fig. 6.4.3(b), (c)	JOW and vert. wind = +1 m/s Fig. 6.4.6	2
T_2 0.28-0.33 h	Higher than JOD and slightly higher than T_1 Fig. 6.4.8	Agrees with JOW, 1 Fewer large drops than T_1 Fig. 6.4.9	Decreasing +0.6 to -0.2 m/s Fig. 6.4.3(b), (c)	Slightly higher than JOW and vert. wind = +1 m/s Fig. 6.4.8	3
T_3 0.33-0.43 h	Close to JOD, lower than T_2 Fig. 6.4.10	Basically JOW but few more large drops Fig. 6.4.11	≅ +0.7 m/s avg. Fig. 6.4.3(b)	JOW and vert. wind = +1 m/s Fig. 6.4.10	2
T_4 0.47-0.53 h	Consistently higher than JOD Fig. 6.4.12	Agrees with JOW, 1, more small drops than during T_3 Fig. 6.4.13	Generally decreasing from +1.3 to -0.1 m/s Fig. 6.4.3(b)	Consistently higher than JOW and vert wind = +1 m/s Fig. 6.4.12	3
T_5 0.53-0.55 h	Higher than JOD decreasing to JOW as rainrate increased. Fig. 6.4.14	Basically JOW but fewer drops in two smallest categories, 1, 4. Fig. 6.4.15	Increasing from -0.1 to +1.25 m/s Fig. 6.4.3(b) or -0.4 to +2.2 m/s Fig. 6.4.3(a)	Between JOW and zero vert. wind and vert. wind = +1 m/s lower attenuations at 0.55 h due to increasing vert. wind Figs. 6.4.3(a), 6.4.4, Fig. 6.4.14	8 as period progresses

. . . continued

Period	Measured Attenuation Compared to Standard Predictions	Measured Drop Distribution	Vertical Wind During Rain	Data is in Approximate Agreement with Predictions for:	Comments
T_6 0.555-0.59 h	Slightly higher than JOW Fig. 6.4.16	Basically JOW but more large drops, 1 Fig. 6.4.17	≅ +0.7 m/s avg. Fig. 6.4.3(b)	JOW and vert. wind = 0.5 m/s Fig. 6.4.16	6,
T_7 0.59-0.71 h	Slightly higher than JOW, lower than T_6 Fig. 6.4.16	Basically JOW but more large drops, 1. Fig. 6.4.19	≅ 0.6 m/s avg. Fig. 6.4.3(b)	JOW and vert. wind = +0.5 m/s. Fig. 6.4.18	6,
T_8 0.71-0.83 h	Slightly lower than JOW. Lower than T_7 Fig. 6.4.20	Basically JOT but even more large drops Fig. 6.4.21	≅ 0.5 m/s avg. Fig. 6.4.3(b)	JOT and vert. wind = +1 m/s Fig. 6.4.20	2, 6

Table 6.4.1 Summary of Attenuation Data for 81.11.30.19, 20:00-20:34

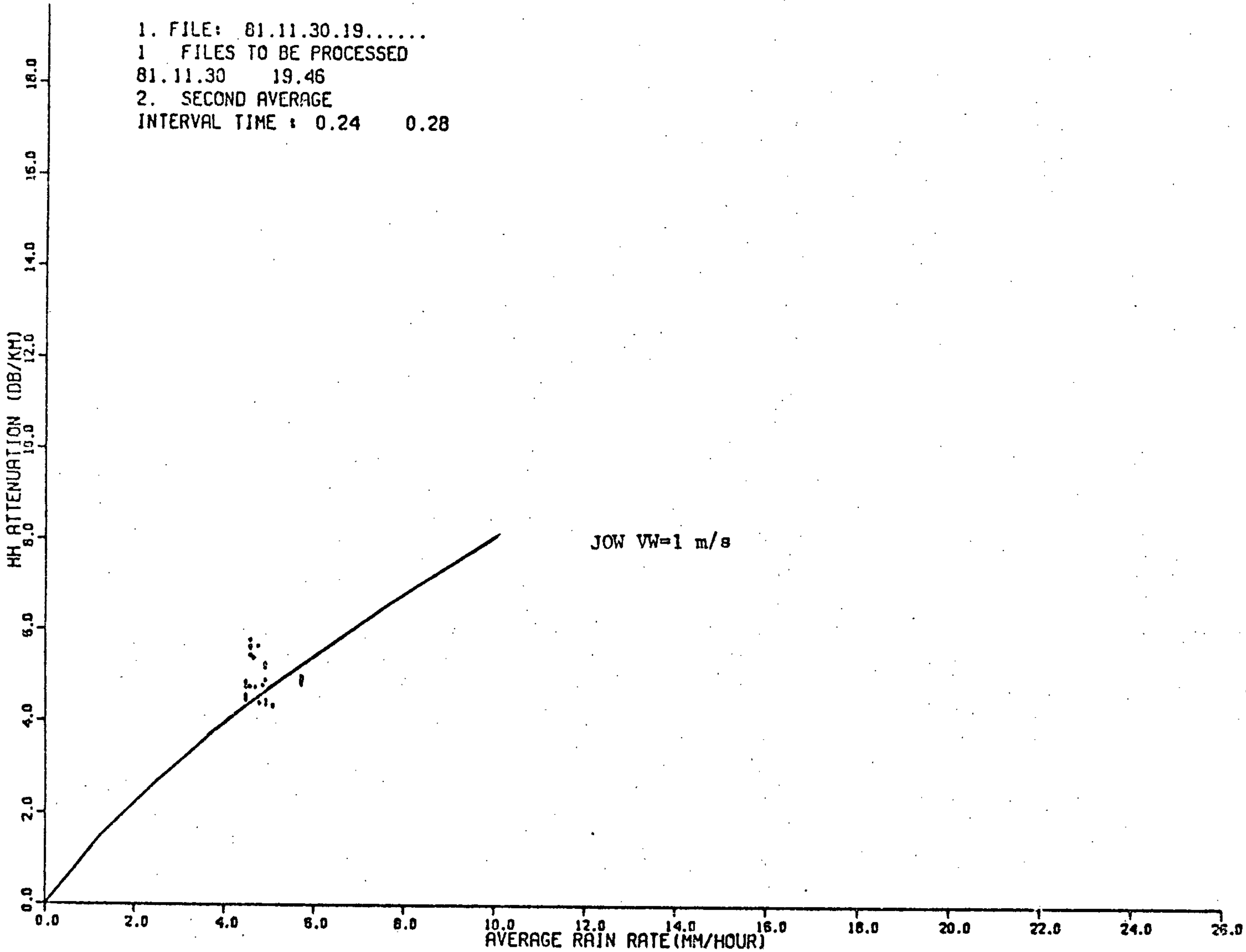

Fig. 6.4.6. CPA during T_1.

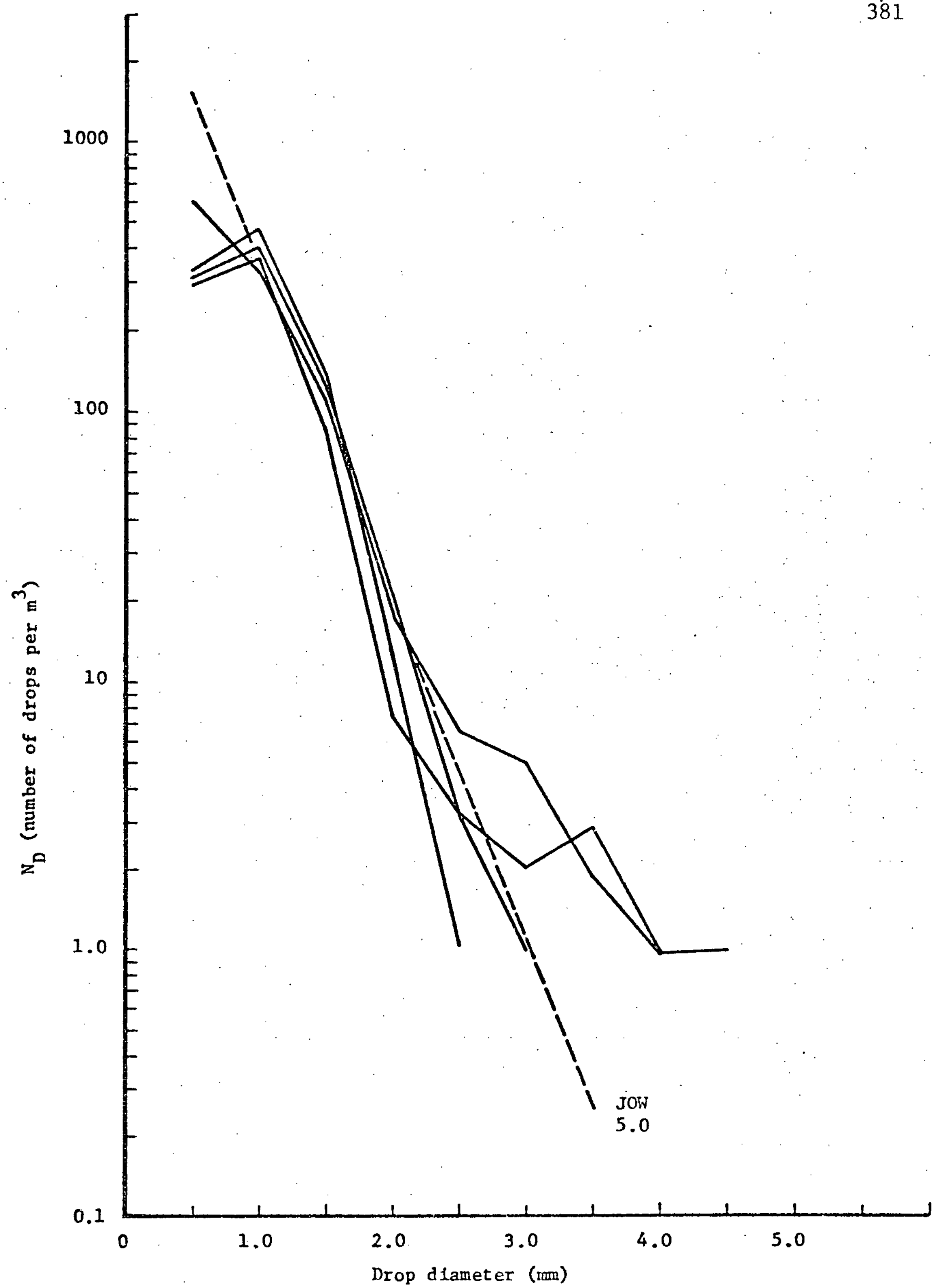

Fig. 6.4.7 Drop distributions for T_1.

"effective" vertical wind velocity approximately double the measured velocity. This observation is probably due to two factors. First, the anemometer may have indicated a lower vertical wind velocity because of the boundary effects caused by the building below the anemometer, despite the 8 m tower on which the anemometer was mounted. Another cause is a simplification used in the model presented in Section 4.4 which assumes an equal velocity for all drops in one size category. The actual drop distributions usually contain many more drops in the smaller diameter range within each category. These greater numbers of smaller drops will have lower terminal velocities than the velocity of the mid-range diameter which was used to estimate the velocity for all drops in the category. These smaller drops, which will have a significant affect on CPA at this frequency, will be correspondingly affected to a greater degree by the vertical wind velocity, resulting in a lower predicted attenuation increase due to vertical wind.

6.4.1.2 Attenuation During T_2, 0.28-0.33 h

In interval T_2, Fig. 6.4.8 shows that the attenuation was slightly higher than during T_1, even though the average vertical wind velocity during this period was lower, Fig. 6.4.3(c). This is believed to be due to the decreasing vertical wind velocity during this period, Fig. 6.4.3(b). As discussed previously, this decreasing vertical wind after a period of upward flow has increased the relative number of small drops in the path during this interval, Figs. 6.4.3(b) and 6.4.9. The increasing attenuation toward the end of this period, Fig. 6.4.4, correlates well with the decreasing vertical wind velocity and corresponding, undelayed, increase in the $N_D(0.5)/N_D(1.0)$

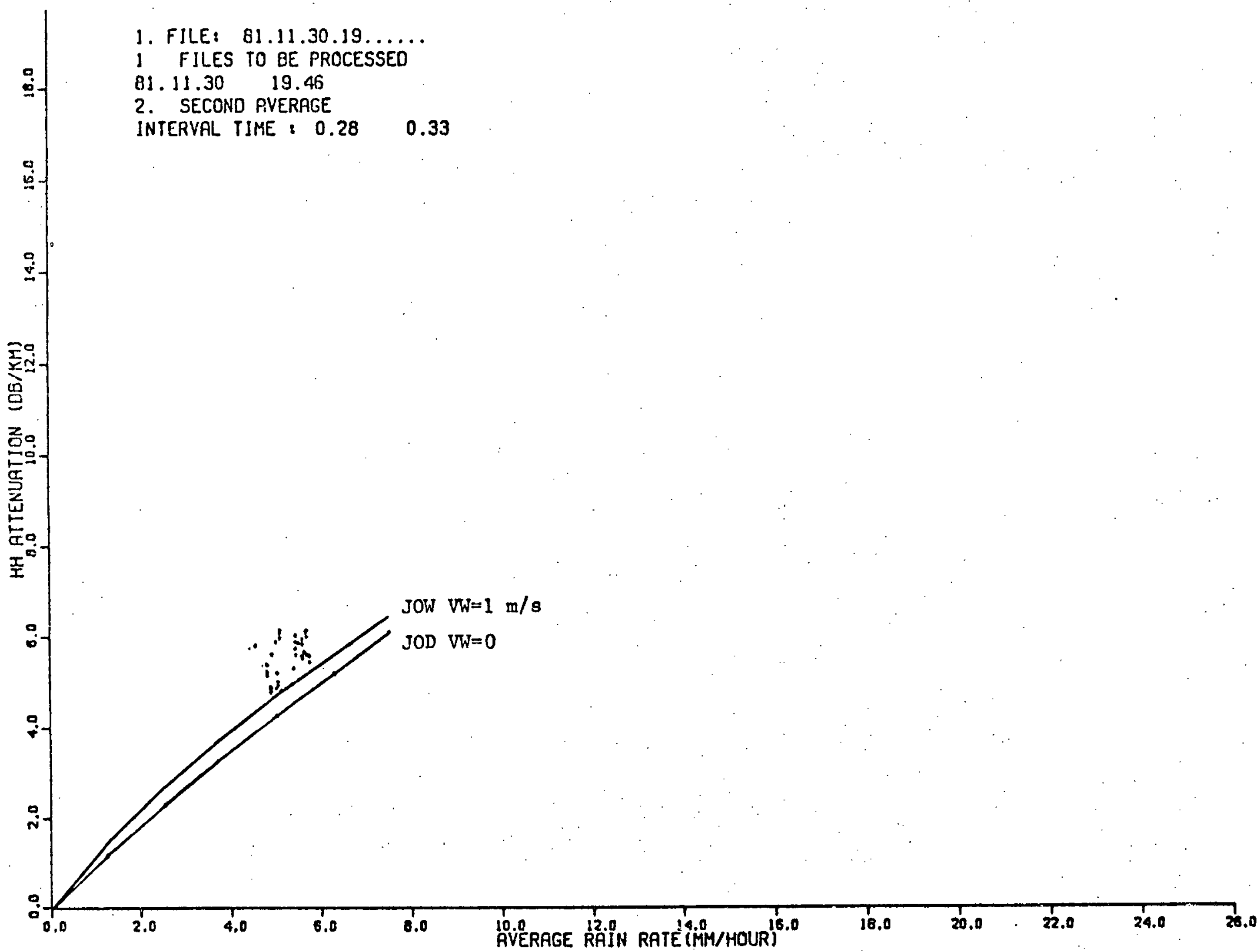

Fig.6.4.8. CPA during T_2.

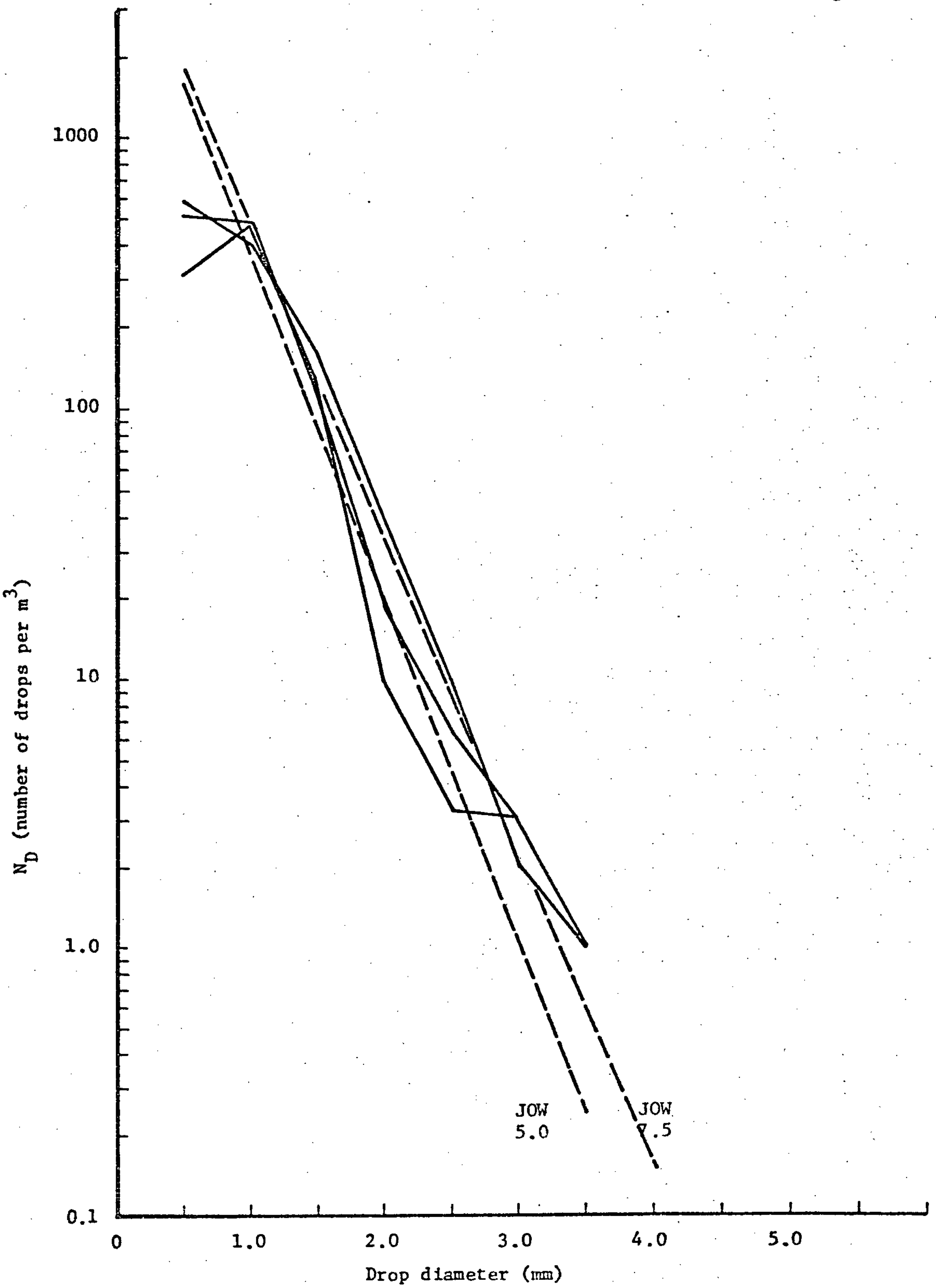

Fig. 6.4.9. Drop distributions for T_2.

ratio, Fig. 6.4.3(b).

6.4.1.3 Attenuation During T_3, 0.33-0.43 h

Attenuation during T_3, Fig. 6.4.10, was lower than during T_2 because the vertical wind velocity was generally increasing during most of this period, Fig. 6.4.3(b). The CPA was higher at the lower rainrates which occurred near the end of this period because the vertical wind began to decrease. This attenuation increase is difficult to resolve in Fig. 6.4.4 because the rainrate is also decreasing. On the average, these attenuation data agree with the modified predictions for a vertical wind velocity of +1.0 m/s, which is similar to T_1.

6.4.1.4 Attenuation During T_4, .047-.053 h

During T_4, the attenuation was consistently higher than the standard predictions for the JOD distributions, Fig. 6.4.12. Again, this is due to the vertical wind which generally decreased from +1.3 to -0.1 m/s over this period. Figs. 6.4.3(b) and 6.4.13 show the increasing number of small drops during this interval with no delay.

6.4.1.5 Attenuation During T_5, 0.53-0.555 h

As period T_5 progressed, the rainrate generally increased but the attenuation consistently decreased, Figs. 6.4.4 and 6.4.14. This was due to the vertical wind velocity rapidly increasing, on a 30 s average, from -0.1 to +1.25 m/s (Fig. 6.4.3(b)) or -0.4 to 2.2 m/s for a 10 s average (Fig. 6.4.3(a)). This vertical wind transient temporarily reduced the number of

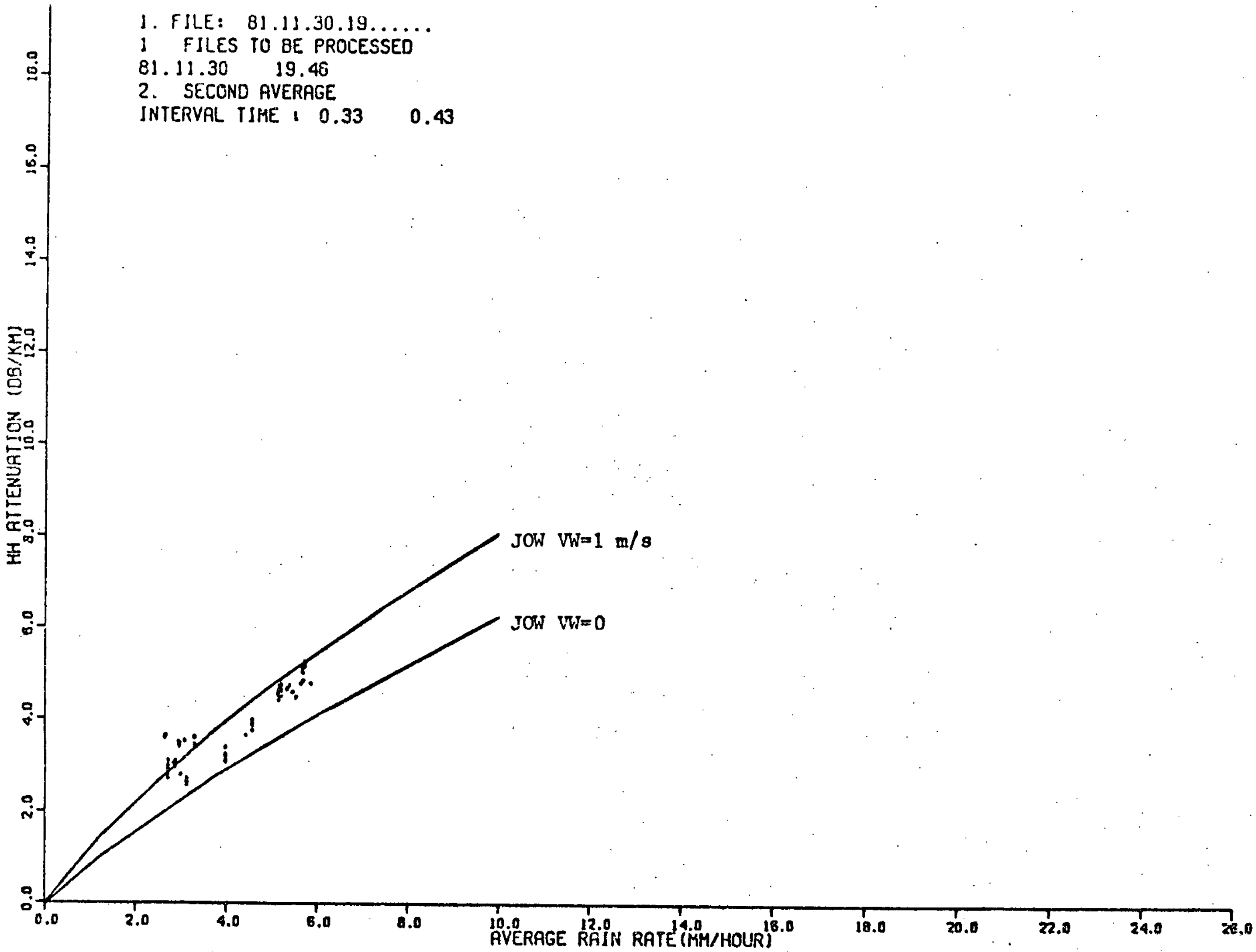

Fig. 6.4.10 CPA during T_3.

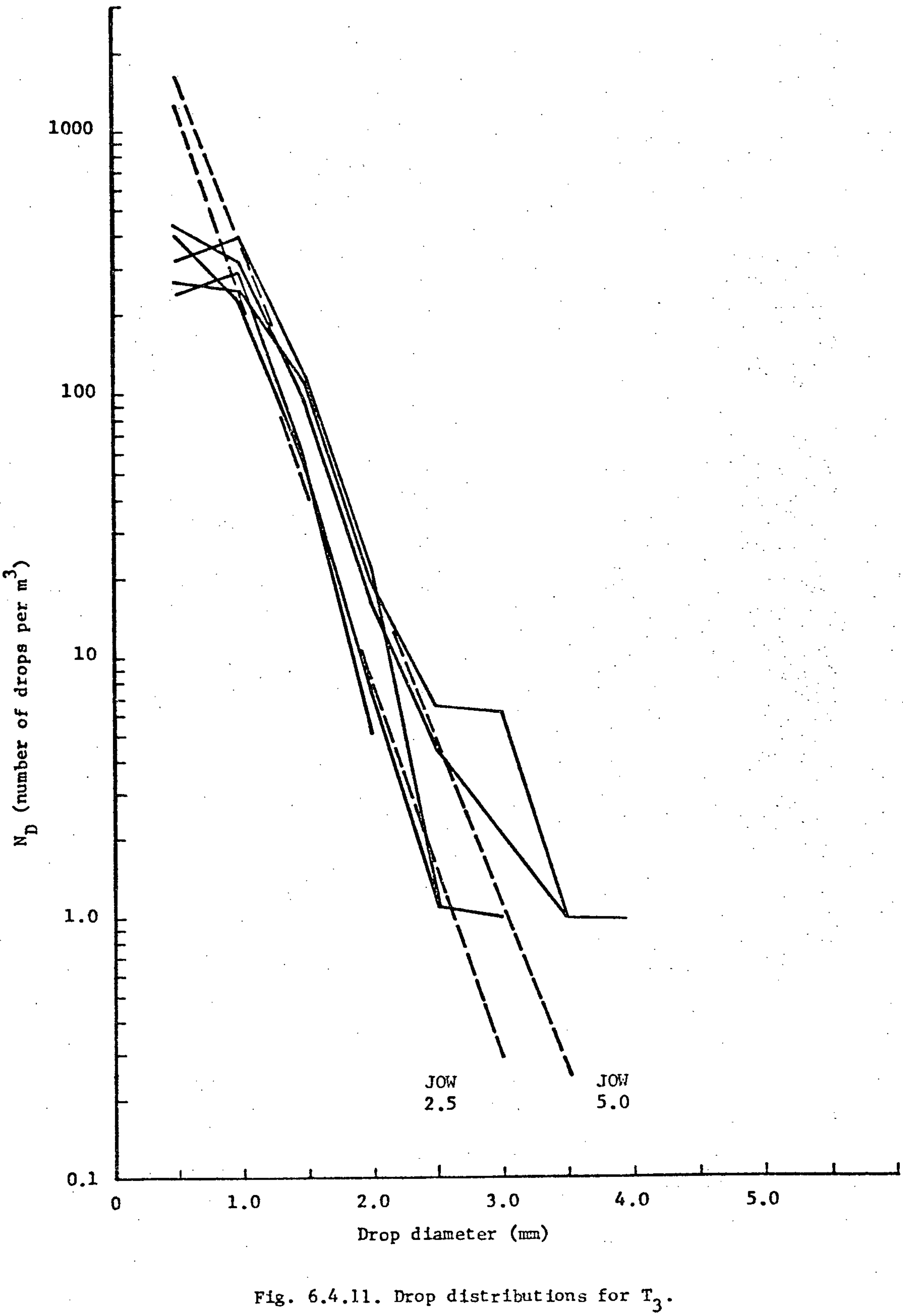

Fig. 6.4.11. Drop distributions for T_3.

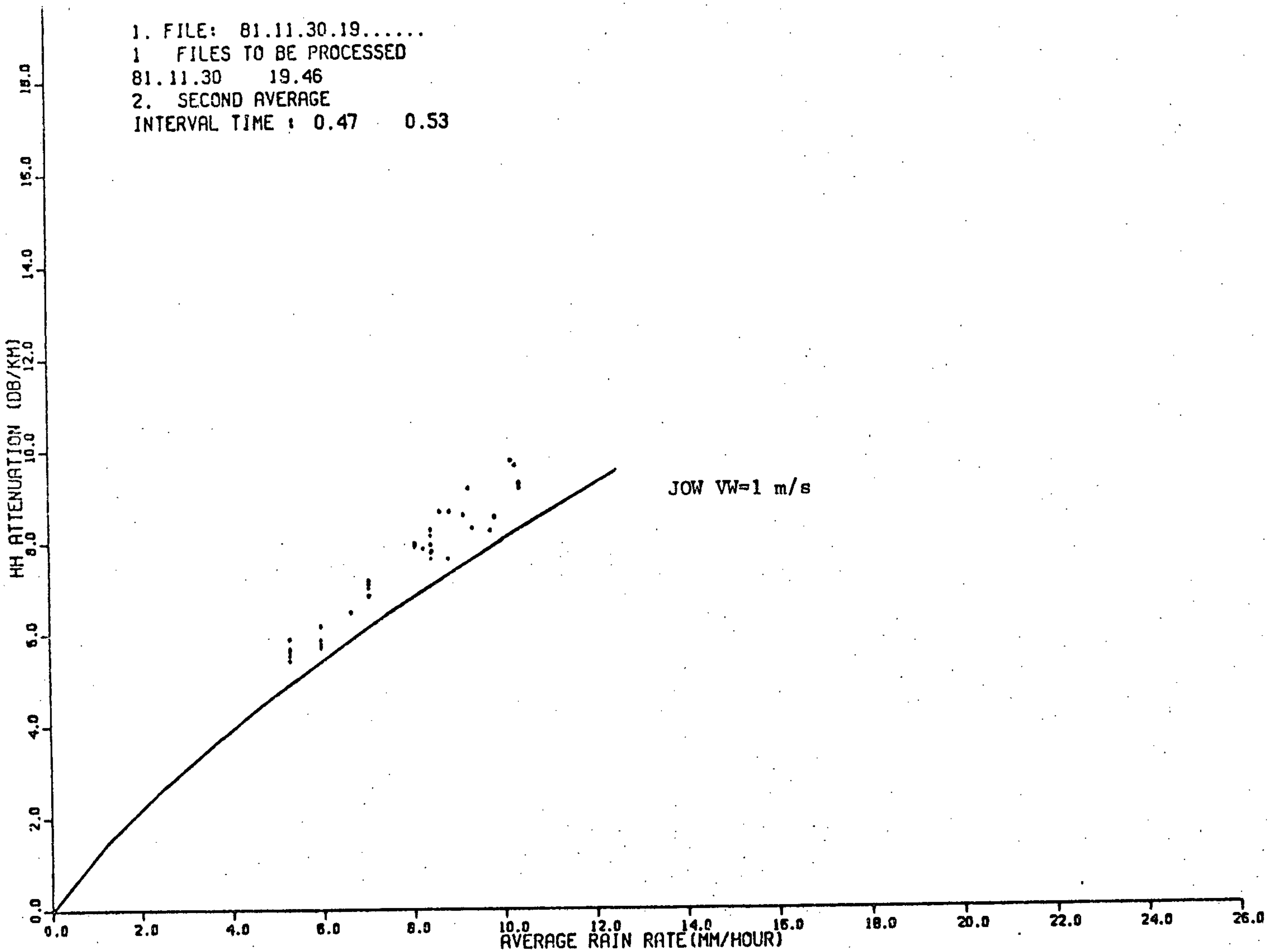

Fig. 6.4.12. CPA during T_4.

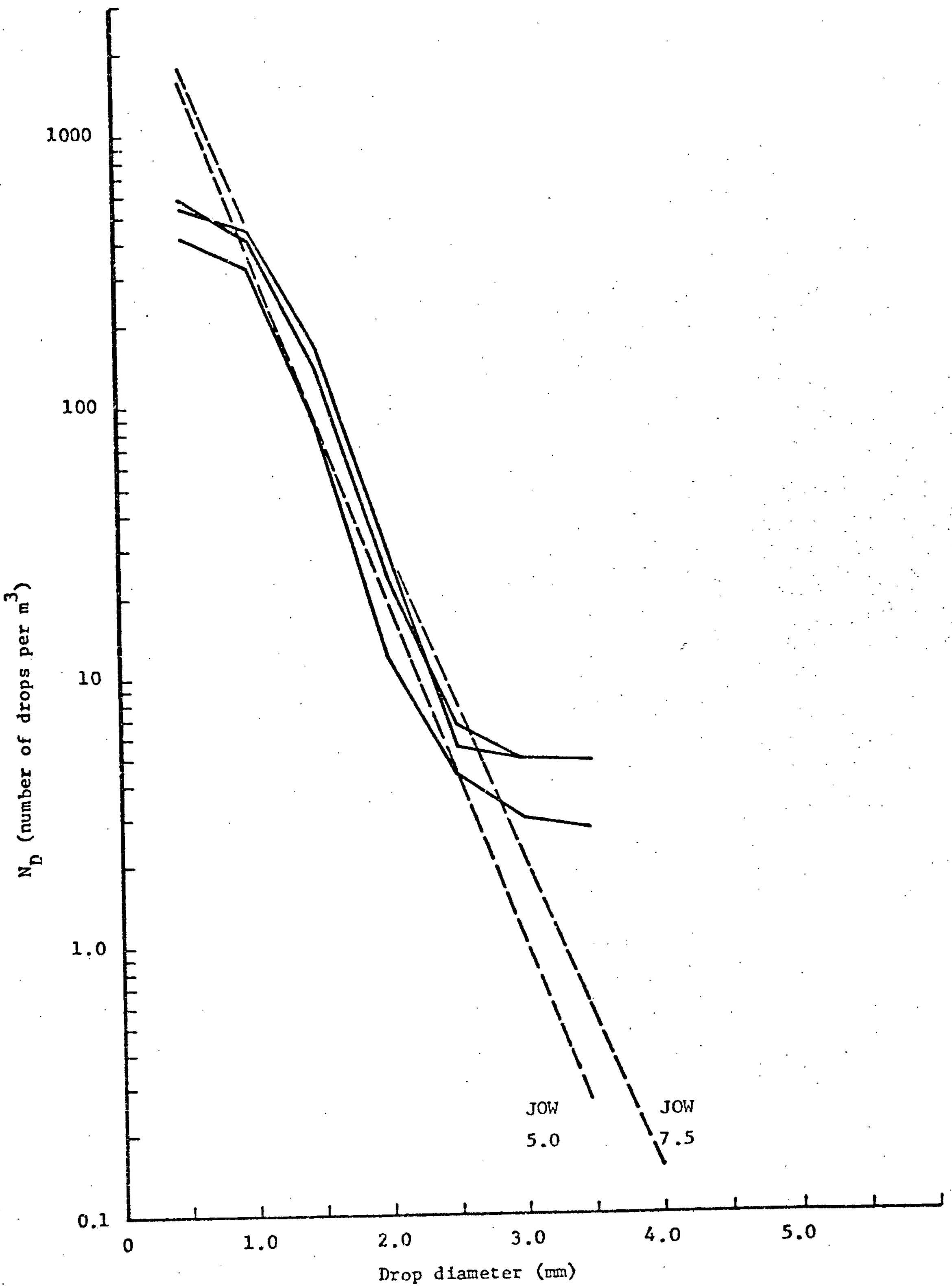

Fig. 6.4.13. Drop distributions for T_4.

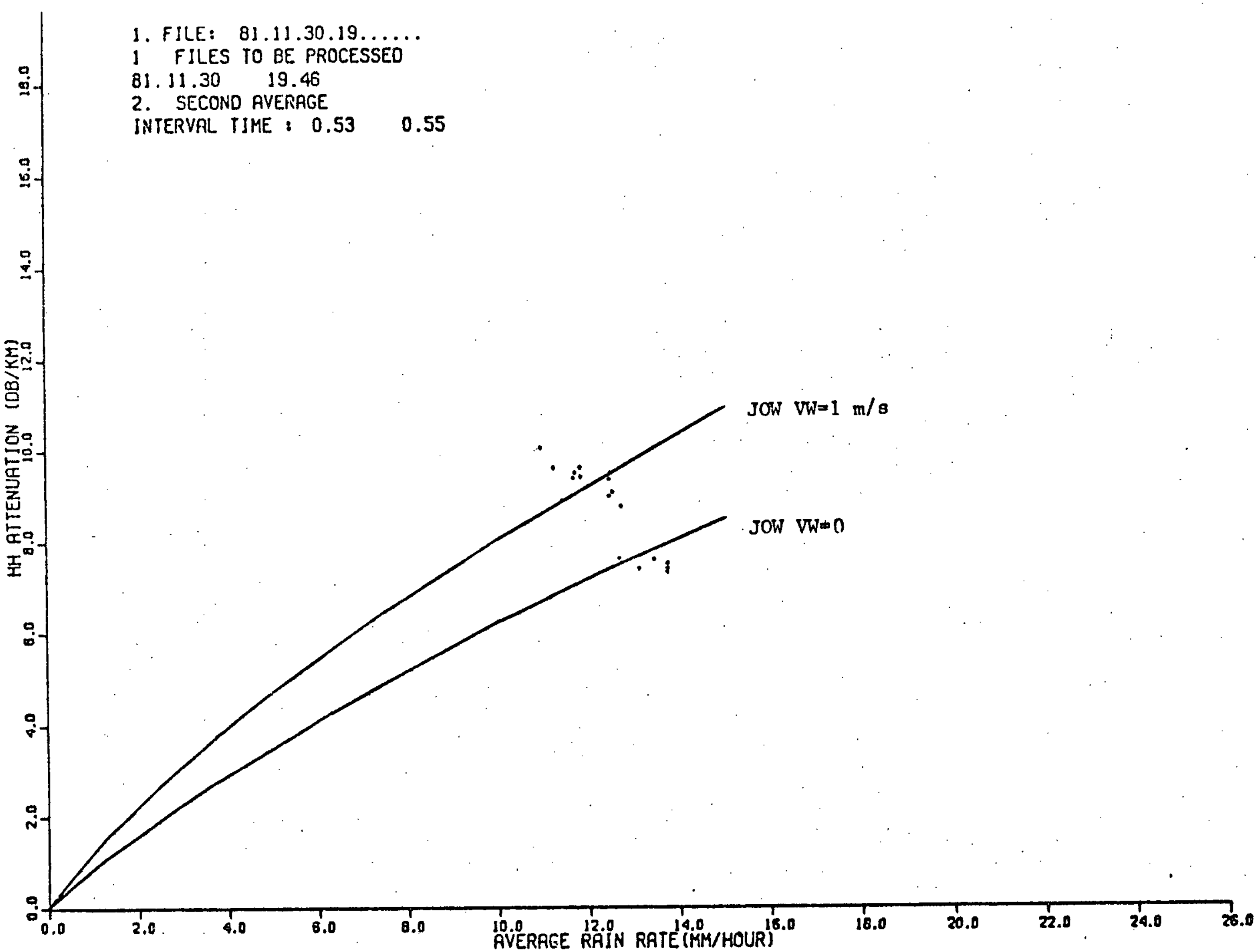

Fig. 6.4.14. CPA during T_5.

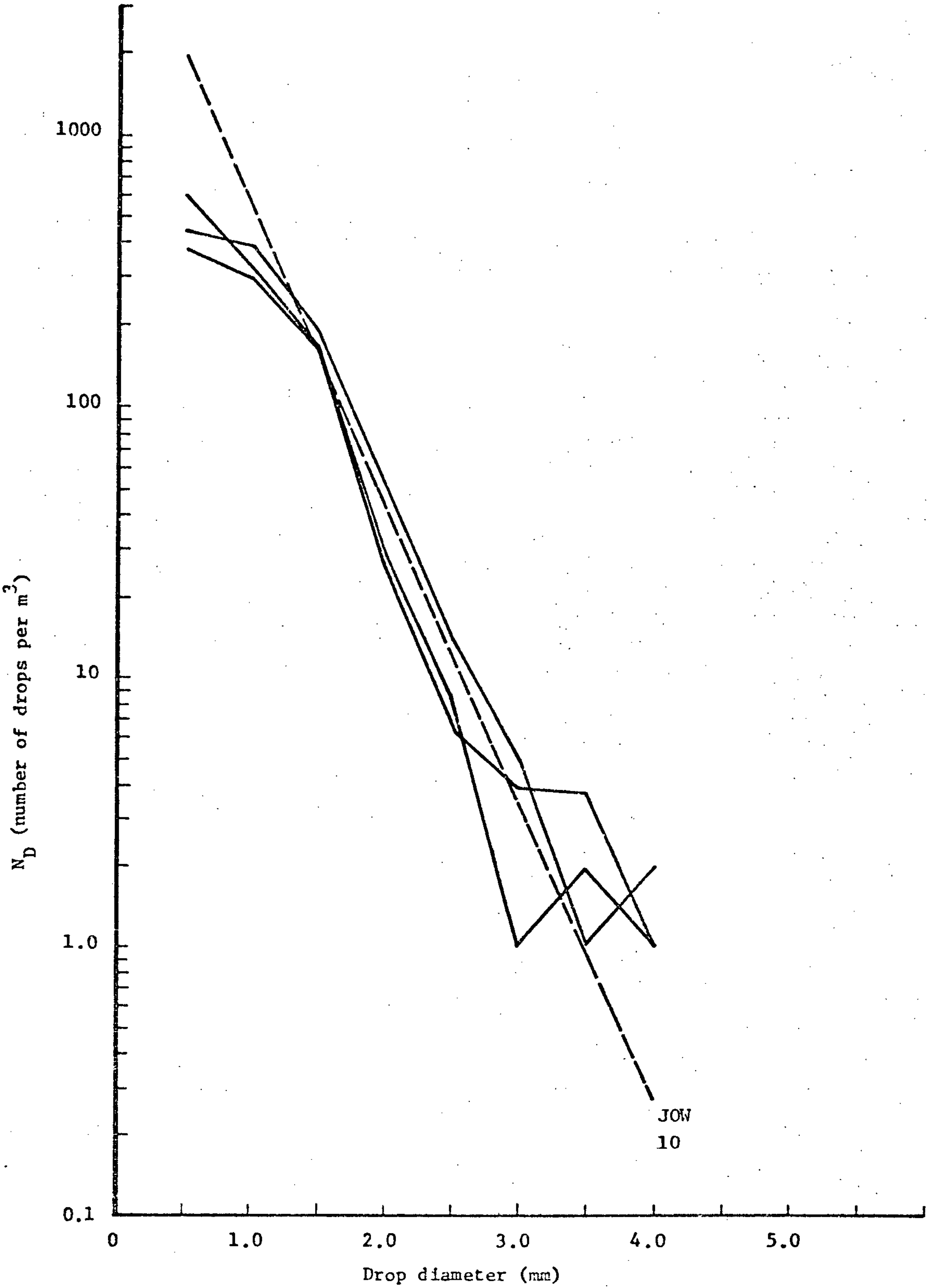

Fig. 6.4.15. Drop distributions for T_5.

small drops falling to the level of the antenna beams. Fig. 6.4.3(b) shows the change in the $N_D(0.5)/N_D(1.0)$ ratio with little or no delay. Fig. 6.4.14 shows that the number densities, $N_D(0.5)$ and $N_D(1.0)$, also both decreaseddue to this wind transient.

6.4.1.5 Attenuation During T_6, 0.555-0.59 h

During T_6 the attenuation/rainrate relation was slightly lower than previous periods in this file because the number of drops in the largest categories had increased, Figs. 6.4.16 and 6.4.17. These large drops significantly increase measured rainrate but do not greatly affect attenuation at this frequency. Fig. 6.4.3(b) and 6.4.17 show a vertical wind created increase in the number of drops in the smallest category near the end of this period, during the lowest rainrates. This does increase the attenuation around 0.57 h, Fig. 6.4.4, but it is difficult to see because the rainrate is decreasing relatively rapidly.

The large increase in the $N_D(0.5)/N_D(1.0)$ ratio during this period is believed to be partly due to a general change in the drop distribution during the second half of this data file. The next two periods also had drop distributions with relatively large numbers of drops in the smallest category. These distributions, however, also had increasingly larger numbers of drops in the largest categories.

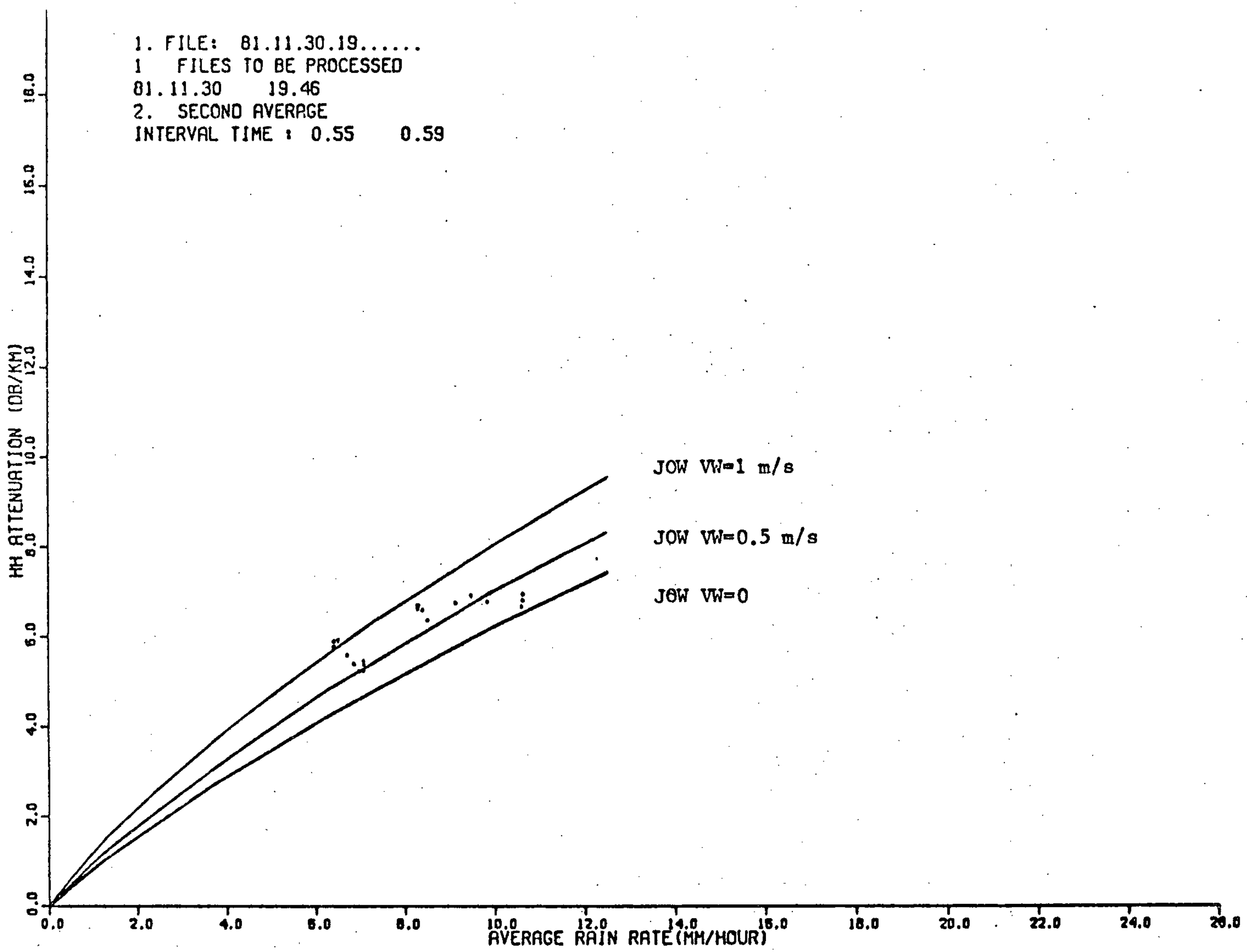

Fig. 6.4.16. CPA during T_6.

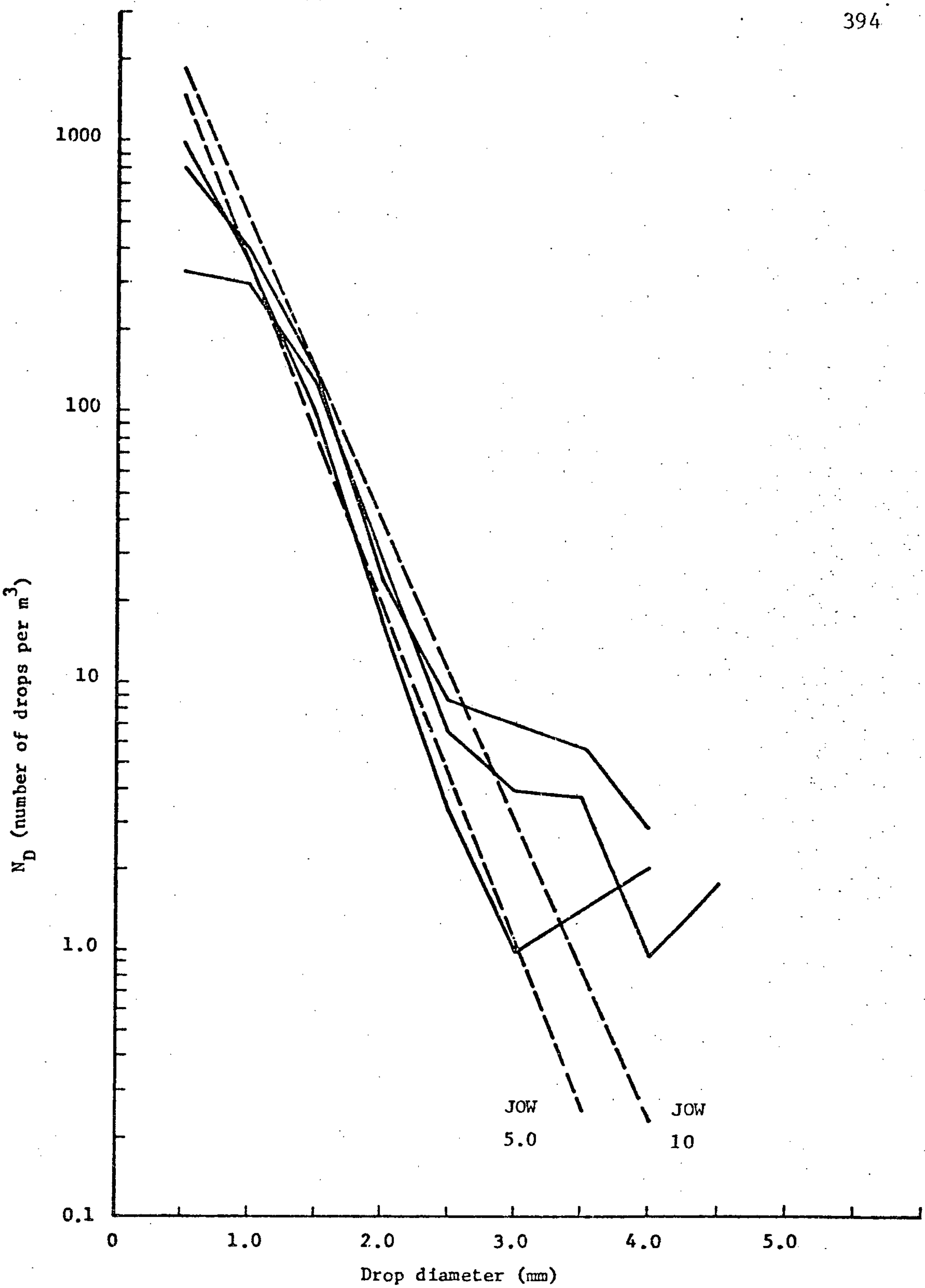

Fig. 6.4.17. Drop distributions for T_6.

6.4.1.7 Attenuation During T_7, 0.59-0.71 h

During T_7, the CPA was again generally lower than during the previous period because the number of large drops further increased, Figs. 6.4.18 and 6.4.19.

6.4.1.8 Attenuation During T_8, 0.71-0.83 h

During T_8, the trend to larger drops continued until the distribution had even more medium and large size drops than the JOT distribution, Fig. 6.4.21. On the average, the measured attenuation was in agreement with the modified predictions for the JOT distribution and a vertical wind velocity of +1.0 m/s, Fig. 6.4.20. The range of attenuation values is due to the variability of the vertical wind during this period, Fig. 6.4.3(b). The CPA and drop distributions during the next period were very similar to the ones during this period and therefore were not included.

6.4.2 XPD and Differential Attenuation Data for 81.11.30.19

The cancelled system XPD, for horizontal transmitted polarization during this file, is shown in Figs. 6.4.22(a) and (b) for 10 s and 30 s averages, respectively. Corresponding plots for uncancelled XPD and vertical transmitted polarization are given in 6.4.23(a) and (b). Differential attenuation is shown in Fig. 6.4.24.

The XPD data during this file appears to indicate lower values of XPD for drop distributions with larger numbers of medium-large drops. Referring to Fig. 6.4.4, the largest values of crosspolar signal level occur during the latter portions of this file. In Section 6.4.1, it was shown that the

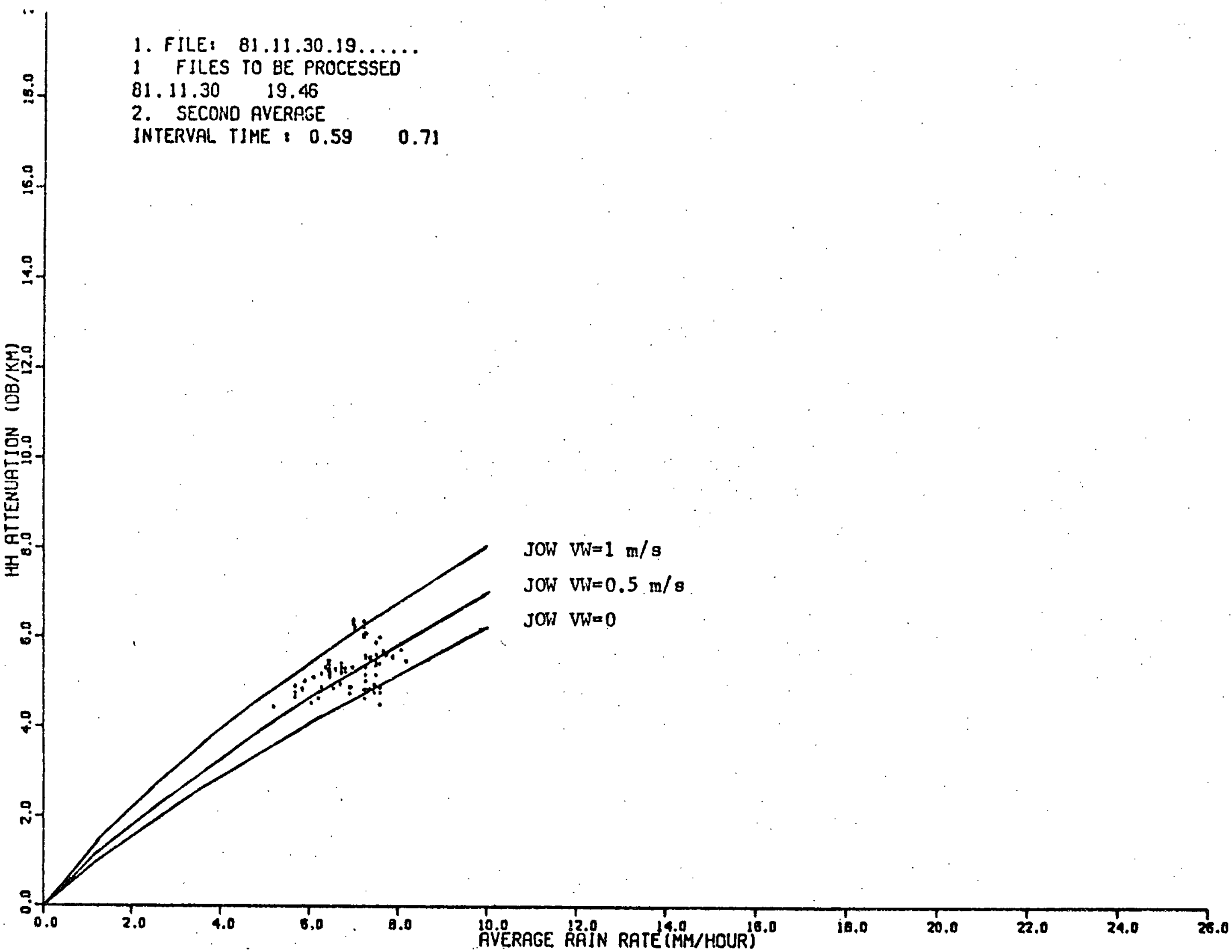

Fig. 6.4.18. CPA during T_7.

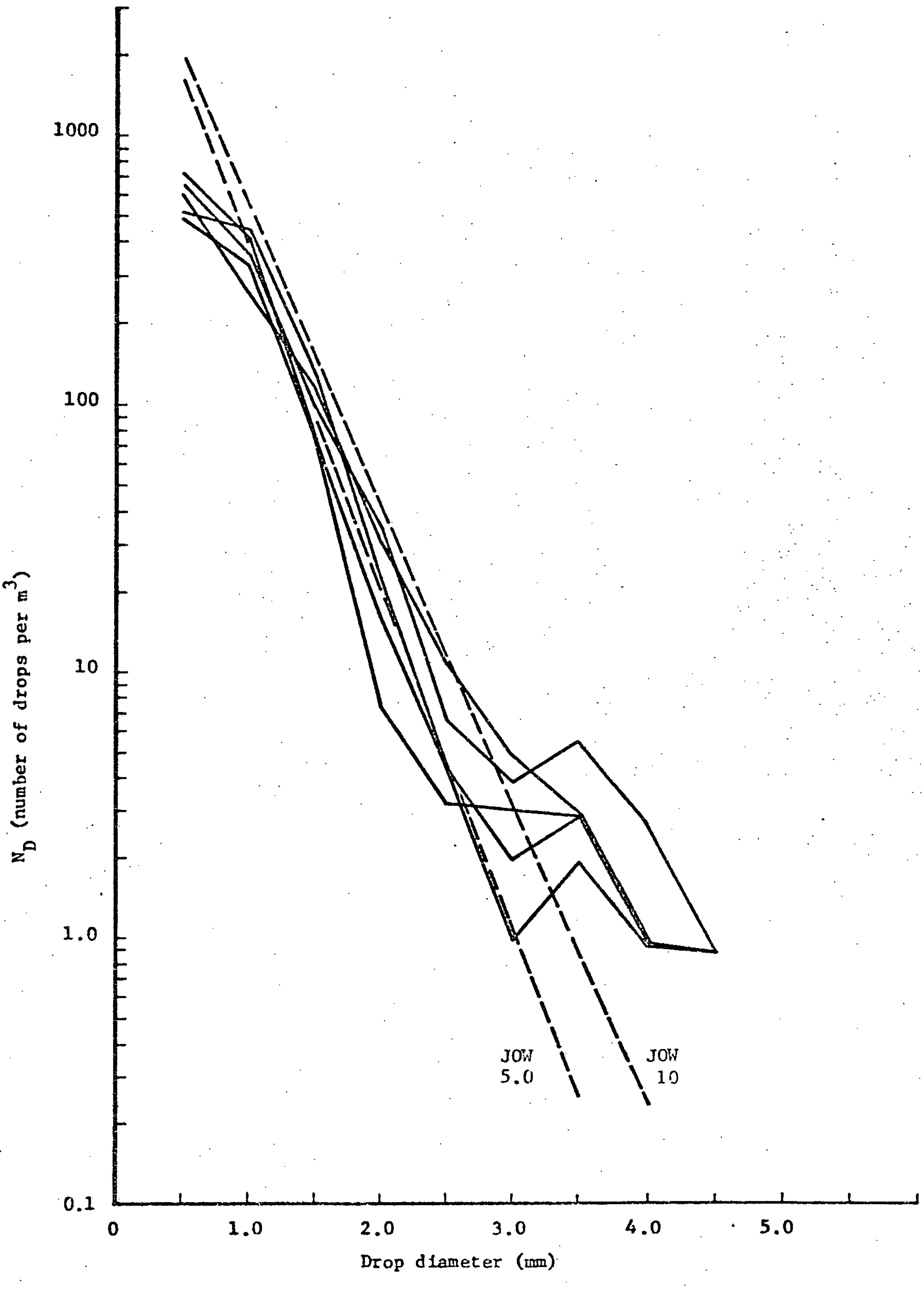

Fig. 6.4.19. Drop distributions during T_7.

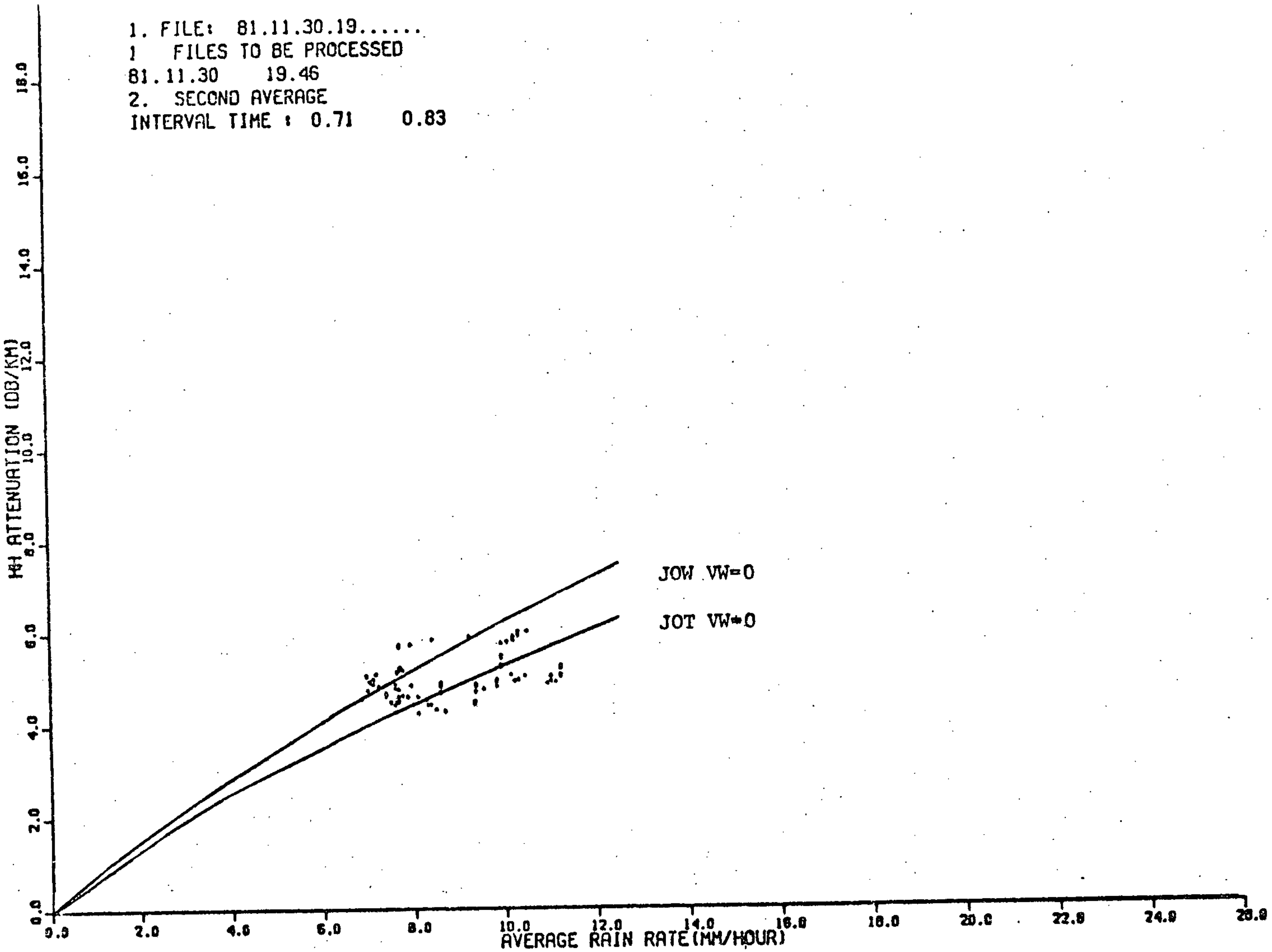

Fig. 6.4.20. CPA during T_8.

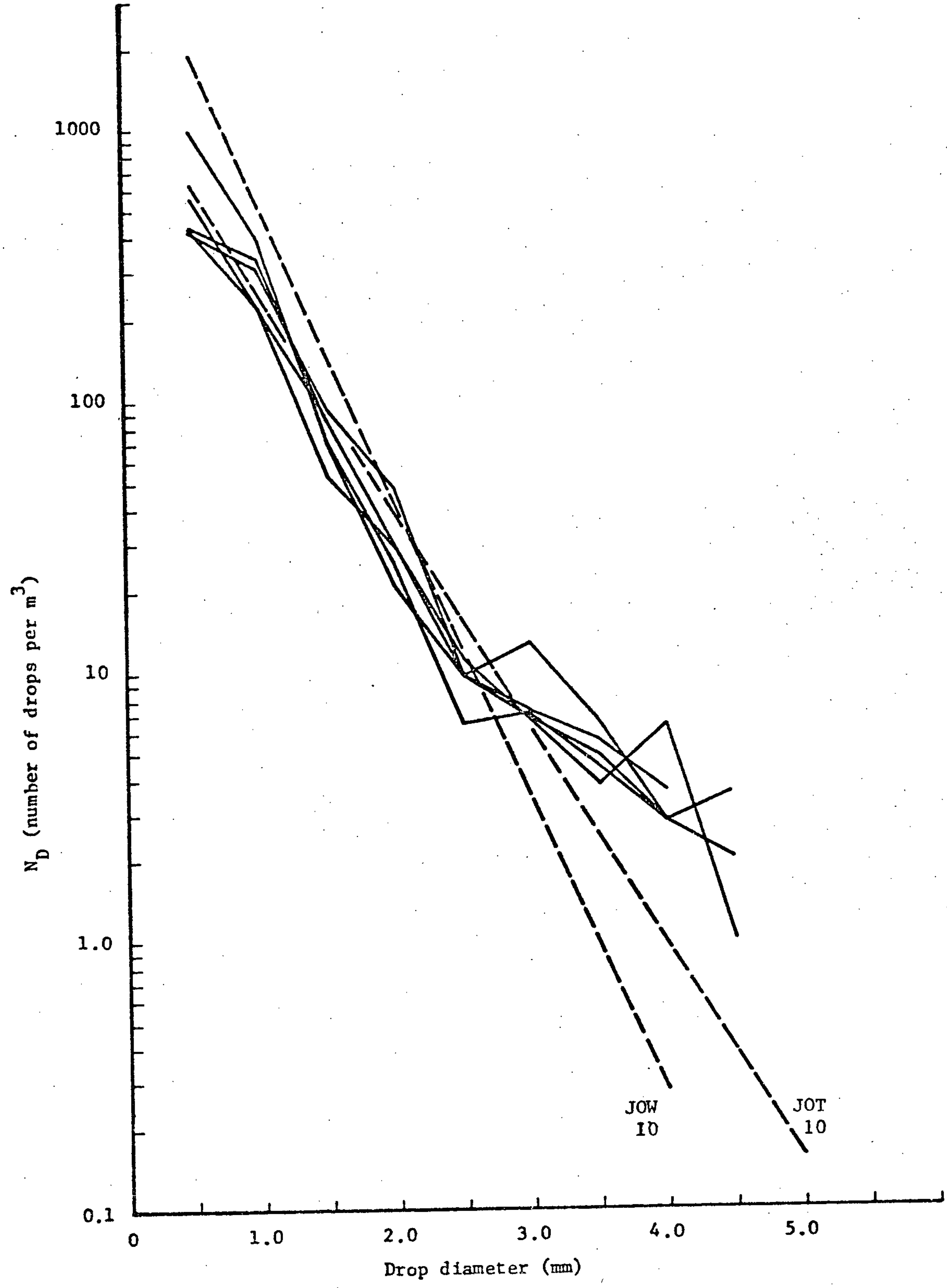

Fig. 6.4.21. Drop distributions for T_8.

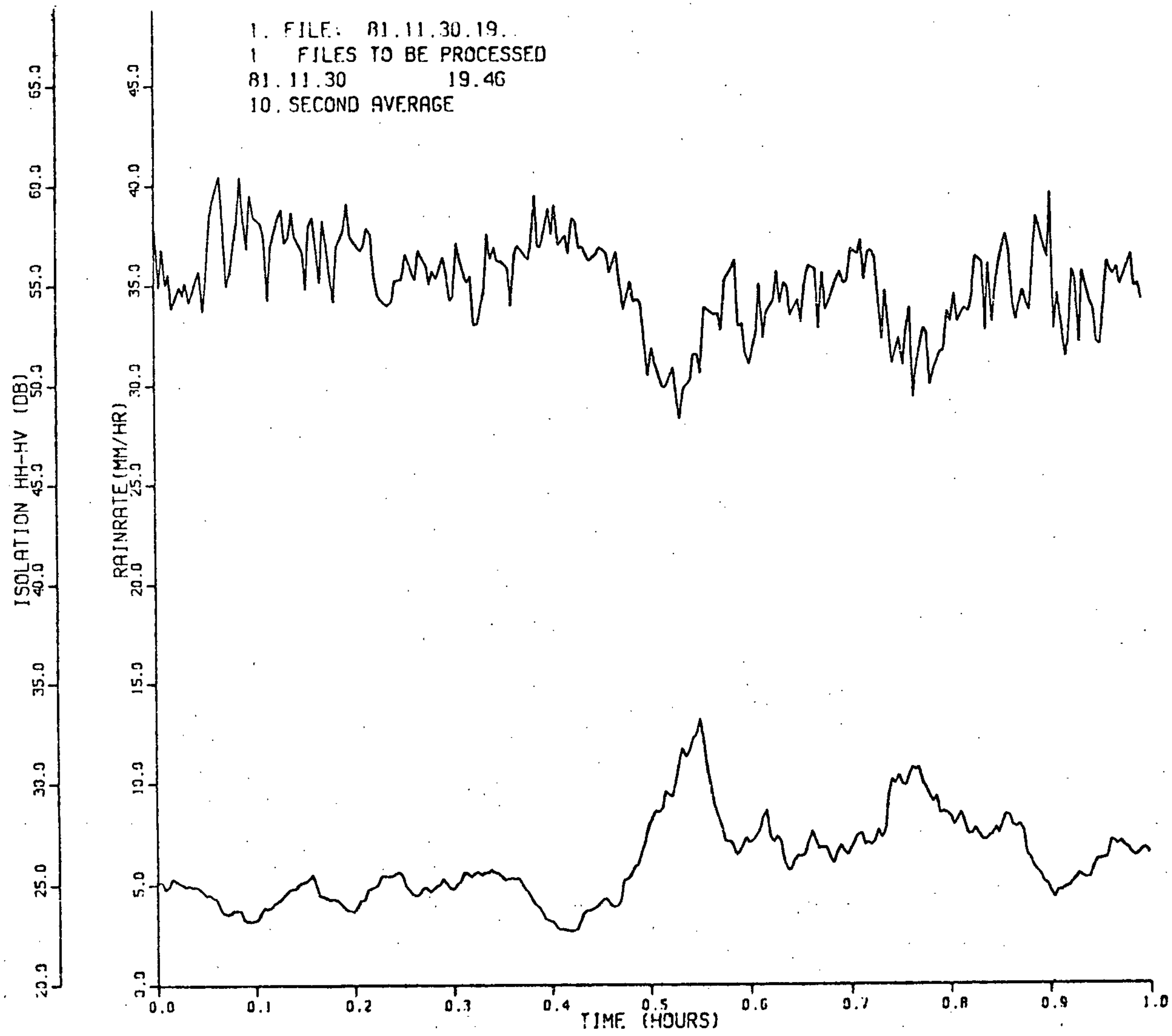

Fig. 6.4.22(a). XPD for horizontal transmitted polarization, 10 s avg. for 81.11.30.19.

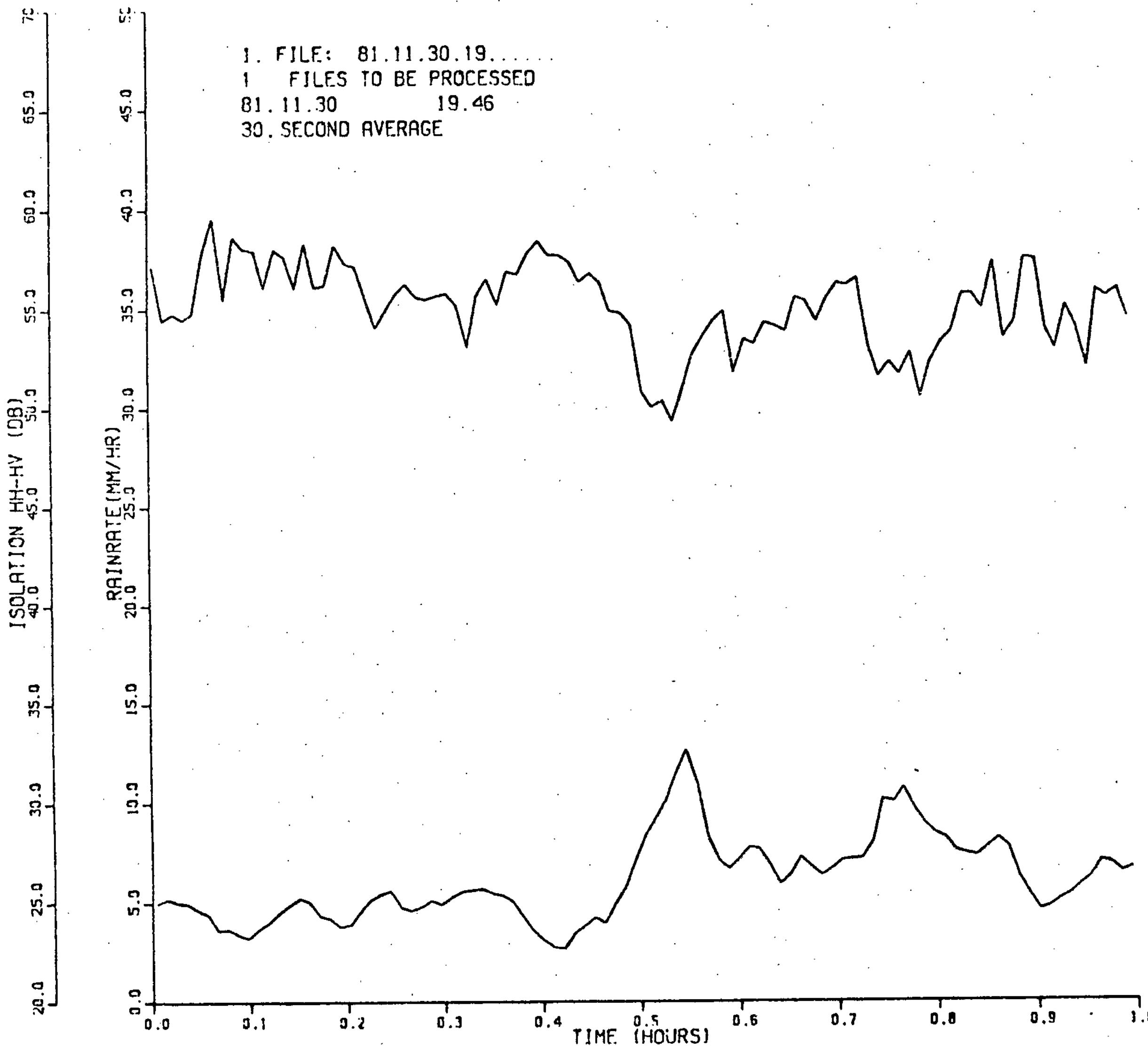

Fig. 6.4.22(b). XPD for horizontal transmitted polarization, 30 s avg. for 81.11.30.19.

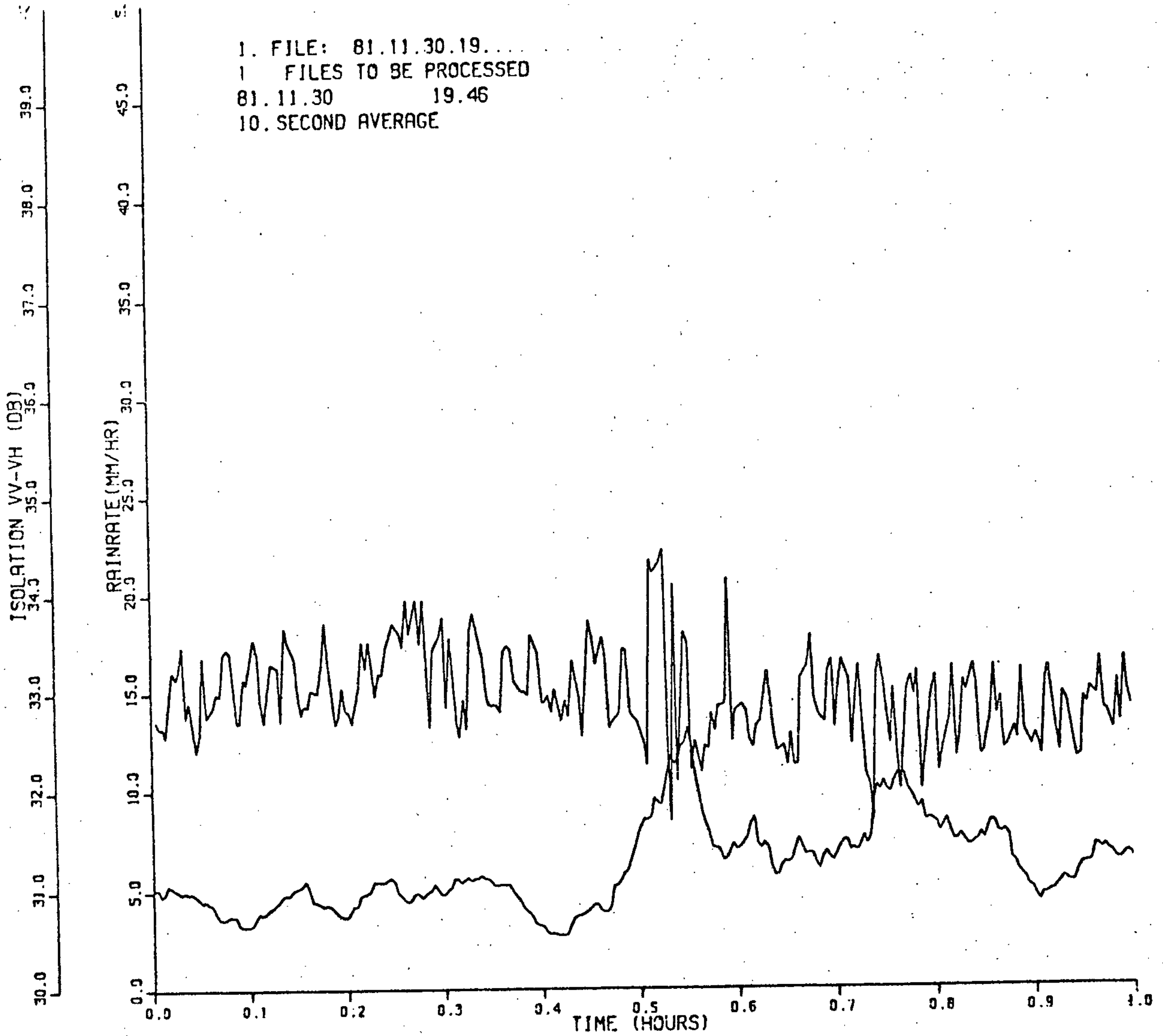

Fig. 6.4.23(a). XPD for vertical transmitted polarization, 10 s avg. for 81.11.30.19.

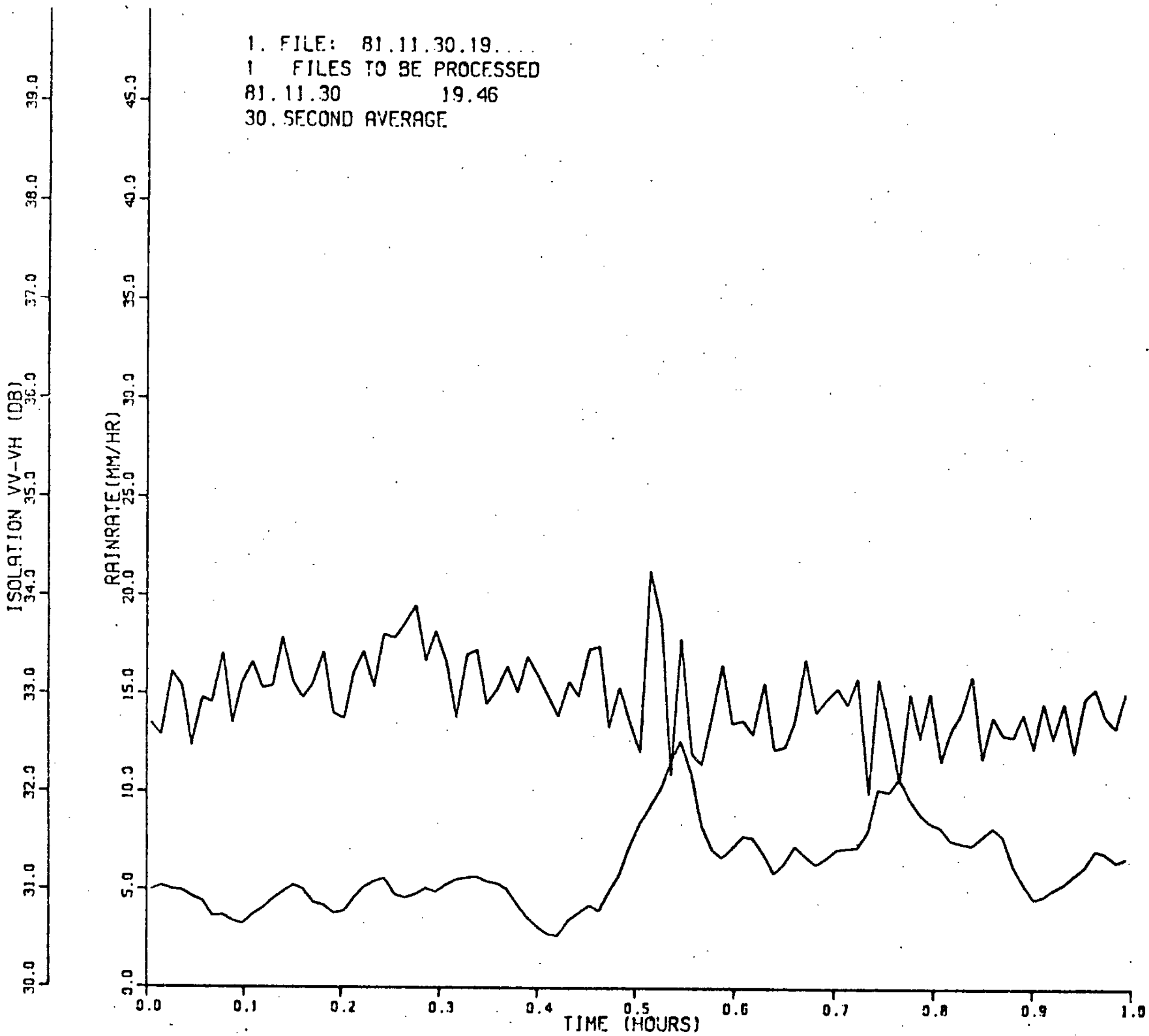

Fig. 6.4.23(b). XPD for vertically transmitted polarization, 30 s avg. for 81.11.30.19.

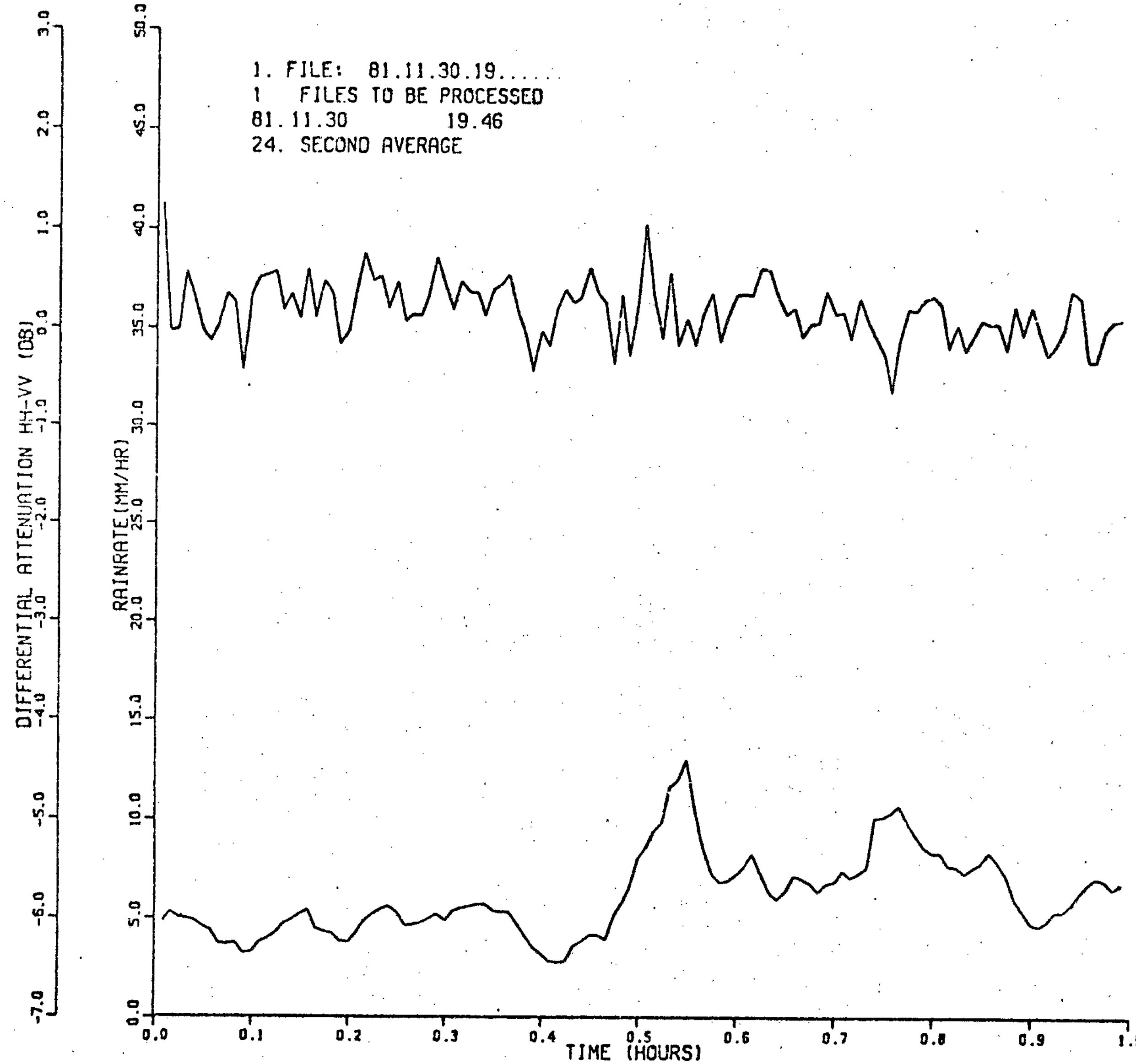

Fig. 6.4.24. Differential attenuation for 81.11.30.19.

numbers of medium-large drops was increasing during the same periods. This decrease in XPD is not predicted by the basic theory for the JOT distribution compared to the JOW distribution. However, this may not be a contradiction because the drop distributions observed during these periods, expecially T_8, had significantly more large drops than even the JOT distribution, and it may be that, for the measured distribution the calculated XPD would be lower.

It should be pointed out that, for the period 0.50-0.56, during the highest rainrates in this file, the cancelled system XPD measurement range has been exceeded. Referring to Fig. 6.4.4 it can be seen that the cross-polar signal level has been reduced to 72 dB, which is within 4 to 6 dB of the noise level. Accordingly, the XPD data in Figs. 6.4.22(a) and (b) over this period are not reliable.

A summary of the XPD and differential attenuation data for this file is given in Table 6.4.2.

6.4.2.1 XPD and Differential Attenuation During T_8, 0.71-0.83 h

The cancelled system XPD during T_8 was correlated with the rainrate and horizontal wind. It is also interesting to note the correlation between the crosspolar signal level, and rainrate, Fig. 6.4.4, and the horizontal wind, Fig. 6.4.2(a),(b), during the interval 0.74-0.83 h. The crosspolar signal level increases as the rainrate and horizontal wind increase from 0.73 to 0.77 h. At 0.77 h the rainrate begins to decrease but the crosspolar signal level continues to increase, and remain high, until approximately

Period	XPD	Differential Attenuation	Wind Velocities During Rain	XPD is in Approximate Agreement with Model Predictions for:	Comments
T_8 0.71-0.83 h	49.4-57.2 dB XPD variation correlated with rain and horiz. wind. Figs. 6.4.2(a), 6.4.22(b) Uncancelled XPD also had lowest values during this period. Fig. 6.4.23(b)	Neg. peak =-0.7 m/s at 0.76 h during horiz. wind increase. Also decreases at ≅0.71 and 0.82 h during increasing horiz. wind. Fig. 6.4.2(a) and 6.4.24	Horiz. wind max. at 0.71 h ≈ 10.0 m/s Horiz. wind increased from 4.3 to 8.2 m/s from 0.73 h to 0.78 h Fig. 6.4.2(a) Horiz. wind ≅7.0m/s avg. Fig. 6.4.2(b)	$\phi \cong 2°$ at low rainrates during lower horiz. wind. $\phi \cong 3°$ at higher rainrate during higher horiz. wind. Fig. 6.4.25.	Drop distribution basically JOT, but even more large drops. Crosspolar signal level increases from 0.74 - 0.78 as horiz wind increases. Fig. 6.4.4
T_9 0.83-.091 h	52.6-59.8 dB Cancelled XPD roughly correlated to horiz. wind. Figs. 6.4.2(a) and 6.4.22(b)	Varied between +0.3 and -0.3dB First and last periods of neg. diff. atten. associated with increasing horiz. wind. Second period of neg. diff. atten. occurred during horiz. wind decrease. Figs. 6.4.2(a) and 6.4.24	Horiz. wind ≅7.0 m/s avg. Fig. 6.4.2(b)	Varied between $\phi \cong 2°$ to $3°$. Fig. 6.4.26	Drop distribution similar to T_8, but rainrates lower.

Table 6.4.2 XPD and Differential Attenuation Data for 81.11.30.19

0.83 h apparently because the horizontal wind was increasing and was causing a continuing increase in the canting angle.

At the lower rainrates, during the lower wind velocities, the cancelled system XPD agreed with the model predictions for an approximate canting angle of 2°. During most of the period, the cancelled XPD agreed with the model predictions for an equivalent mean canting angle of approximately 3°, as shown in Fig. 6.4.25. The average horizontal wind velocity during T_8 was roughly 7.0 m/s.

The uncancelled XPD also had the lowest 30 s avg. values observed in this file during 0.72-0.79 h, Fig. 6.4.23(b). Comparison to predictions are not feasible, however, because the uncancelled XPD is increasing and decreasing during this period apparently due to path XPD phase variations. These phase variations are even more apparent through 0.50 h to 0.57 h during the highest rainrates in this file.

The differential attenuation during T_8 displays a -0.7 dB minima at 0.76 h during the highest rainrate in this period. This occurred during an interval of increasing horizontal wind velocity. The differential attenuation also decreased to negative values at 0.71 and 0.82 h, again during increasing horizontal wind velocities.

6.4.2.2 XPD and Differential Attenuation During T_9, 0.83-0.99 h

During T_9, the cancelled system XPD was roughly correlated to the horizontal wind velocity. The data are also in reasonable agreement with the

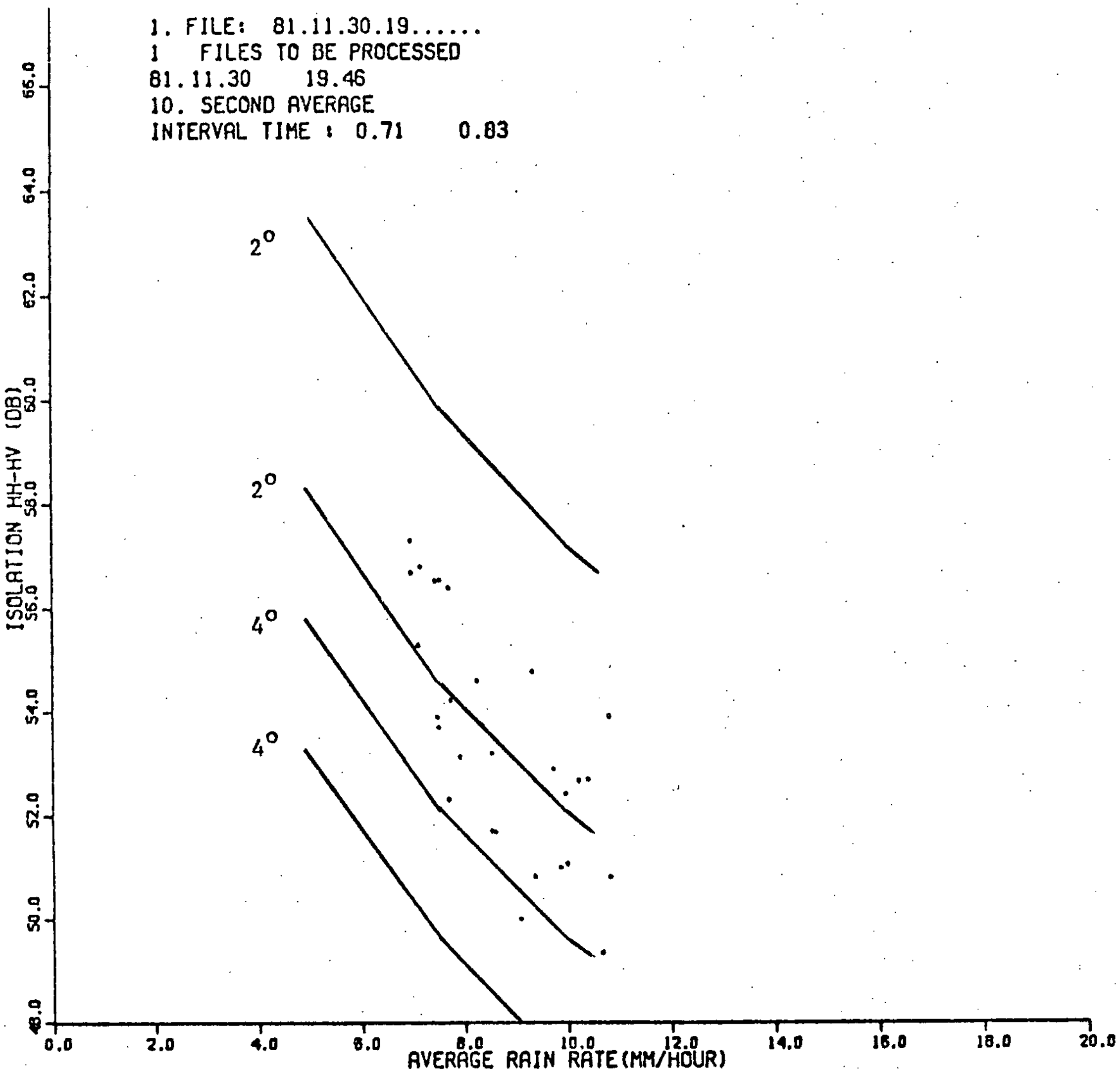

Fig. 6.4.25. XPD_H during T_8.

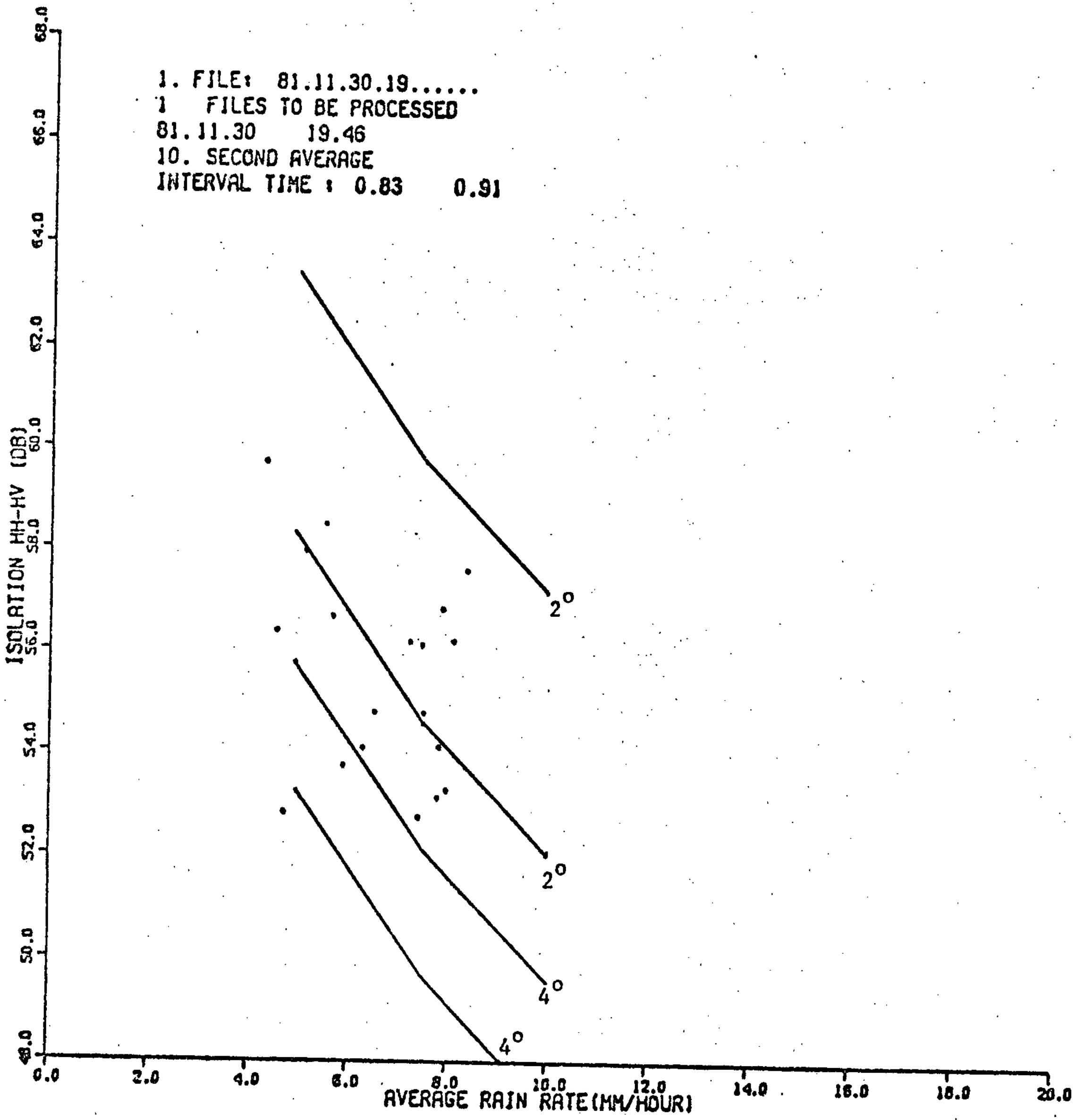

Fig. 6.4.26. XPD_H during T_9.

predictions for a canting angle of 2-3°. The horizontal wind velocity and drop distributions were similar to the previous period but the rainrate was generally lower.

Differential attenuation during T_9 varied between +0.3 dB and -0.3 dB. The first and last periods of negative differential attenuation were associated with periods of increasing horizontal wind velocity. However, the period in between occurred during a measured decrease in horizontal wind velocity.

6.5 Experimental Results for 81.11.30.21

This file contains an example of the leading edge of a rainstorm and includes periods of rapidly changing drop size distribution. Fig. 6.5.1 shows the rainrates during this data file. The path average rainrate increased from zero to 12 mm/h as the leading edge of the storm passed over the raingauge network.

The wind direction during this file was again directly from the east. Fig. 6.5.2 shows the 10 s average horizontal wind velocity for this period. The 30 s and 60 s vertical wind velocities are shown in Figs. 6.5.3(a) and (b). Both wind velocities were relatively constant during the periods of rain.

The 10 s average signal levels for this file are given in Figs. 6.5.4 and 6.5.5 for horizontal and vertical transmitted polarizations, respectively.

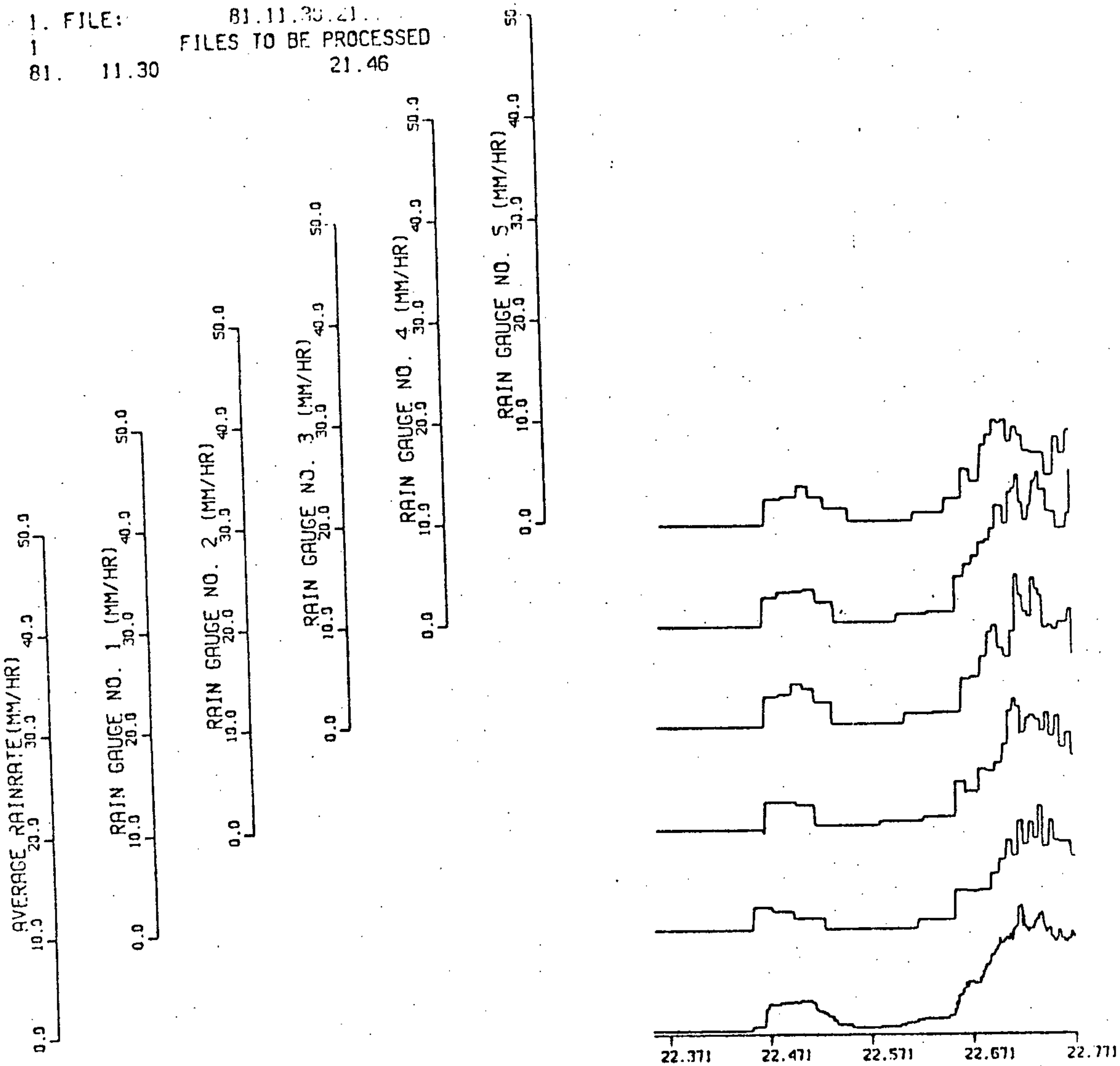

Fig. 6.5.1. Rainrates for 81.11.30.21.

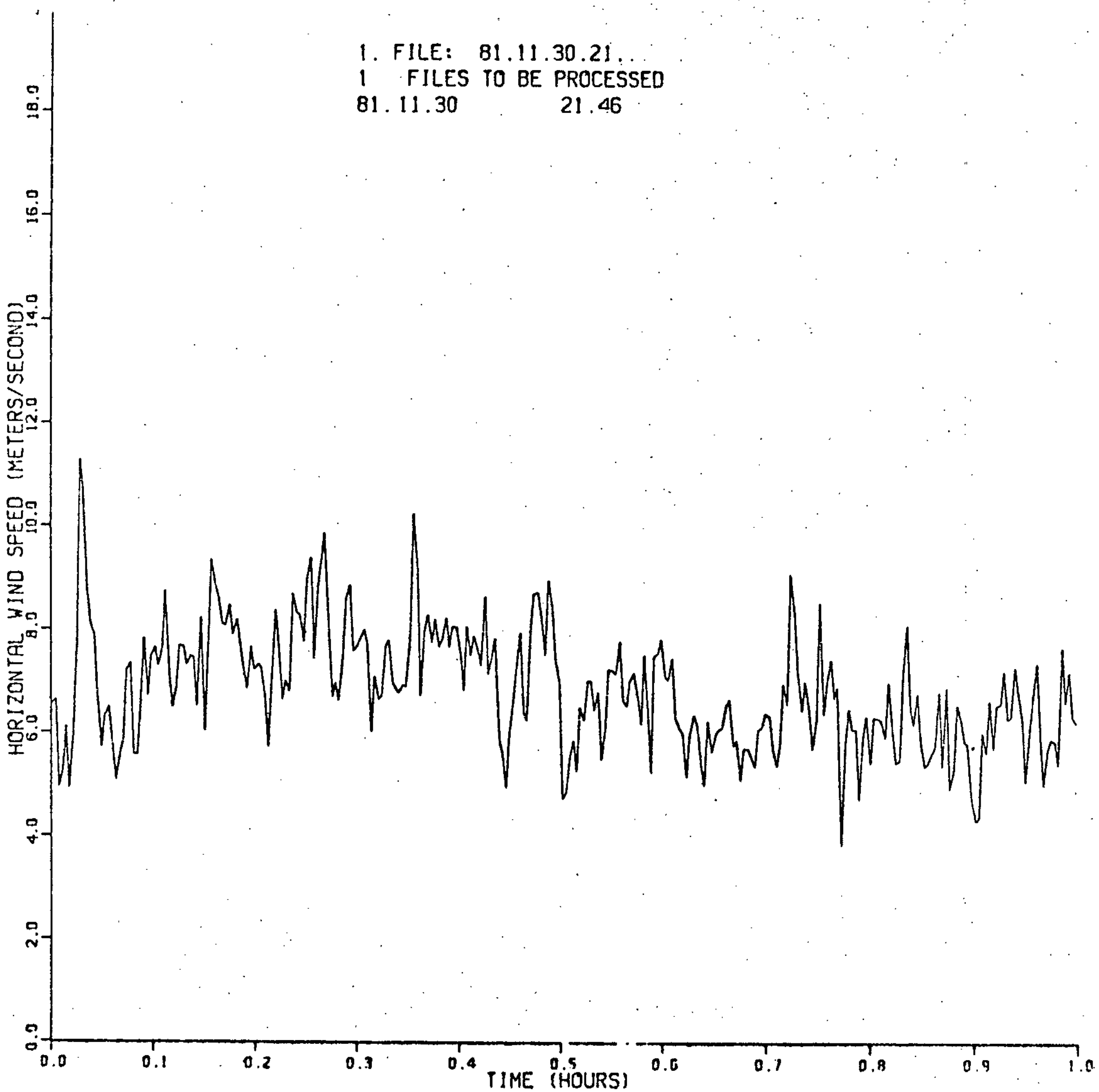

Fig. 6.5.2. Horizontal wind velocity, 10 s avg. for 81.11.30.21.

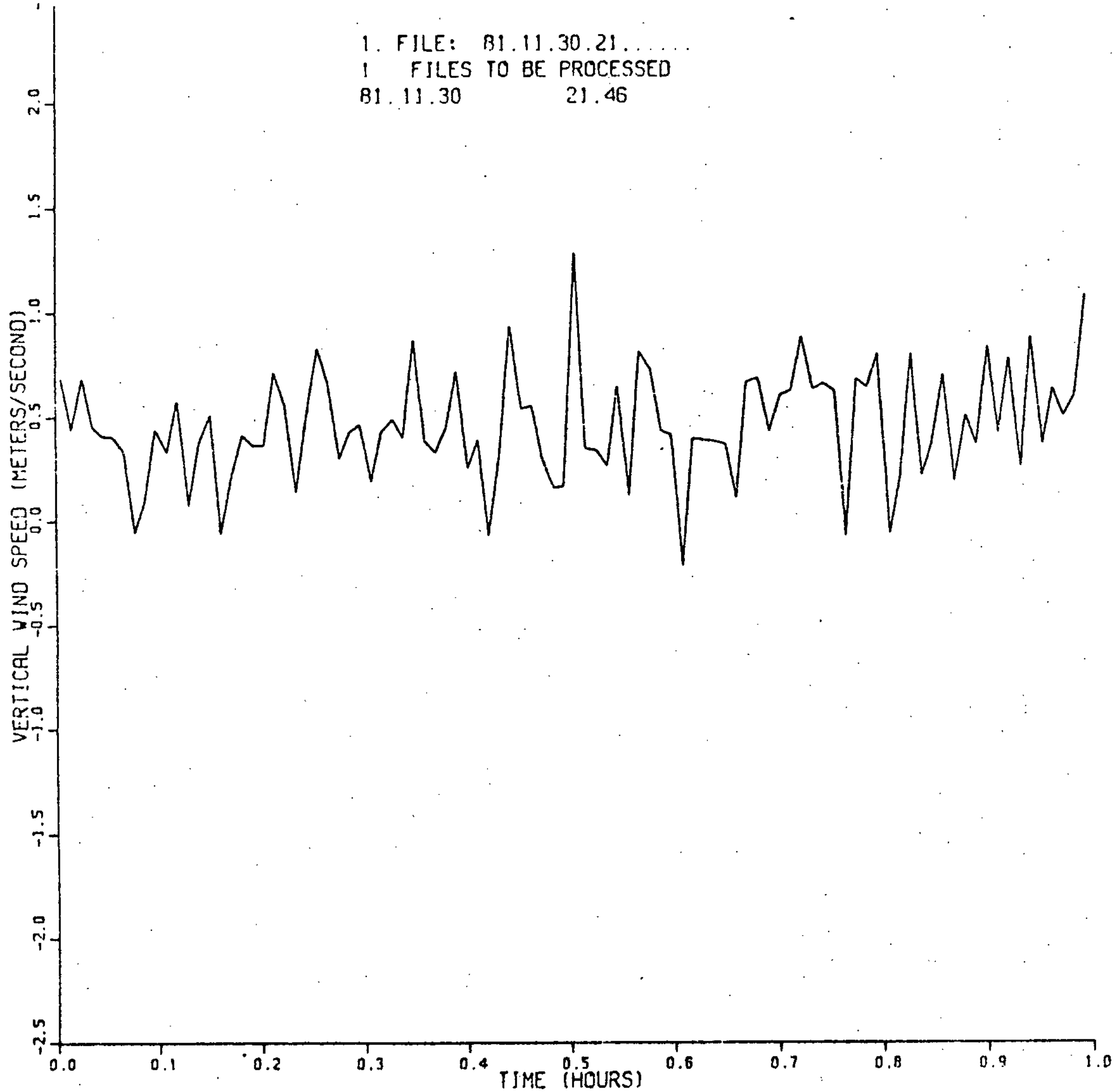

Fig. 6.5.3(a). Vertical wind velocity, 30 s avg. for 81.11.30.21.

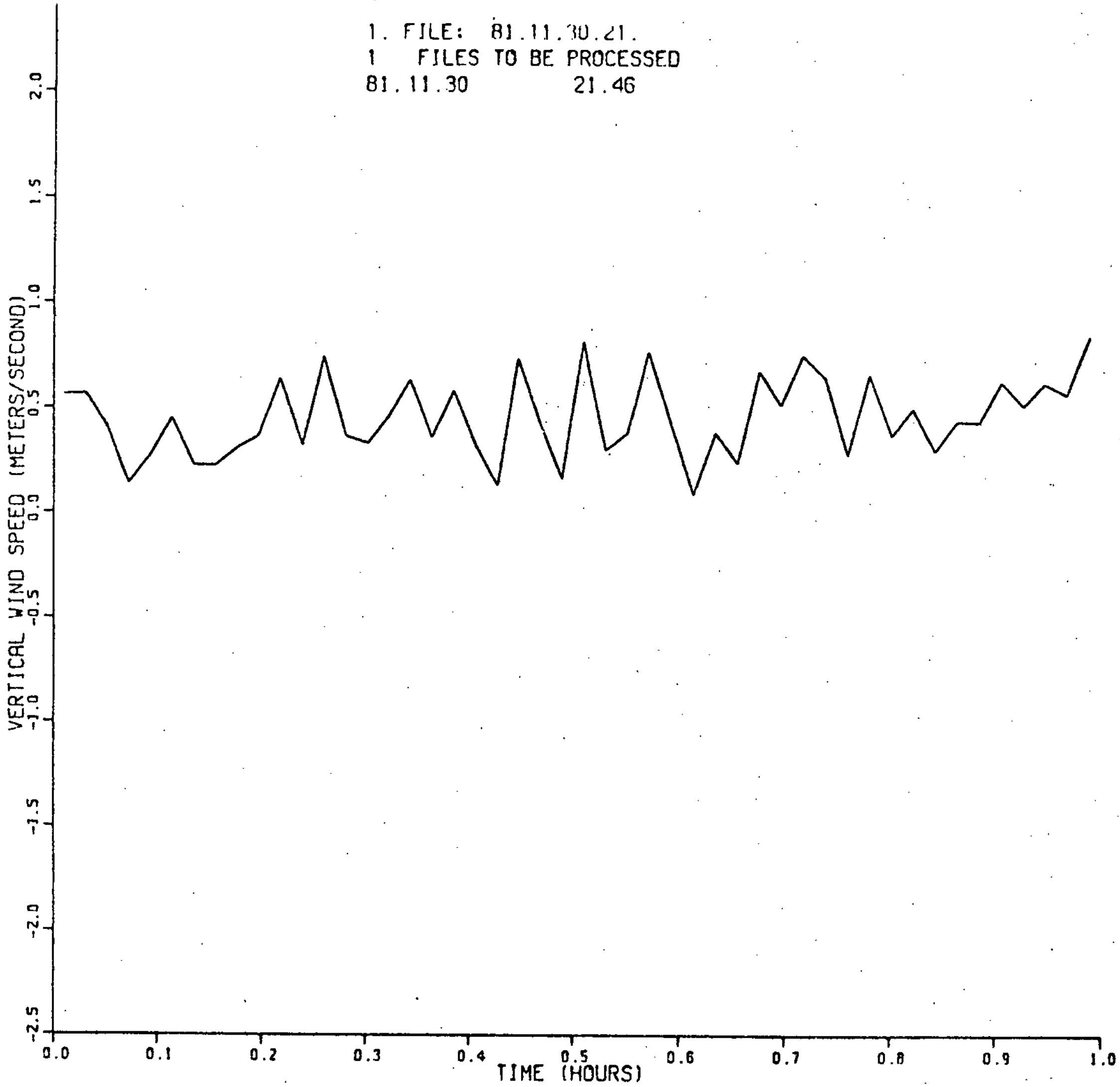

Fig. 6.5.3(b). Vertical wind velocity, 60 s avg. for 81.11.30.21.

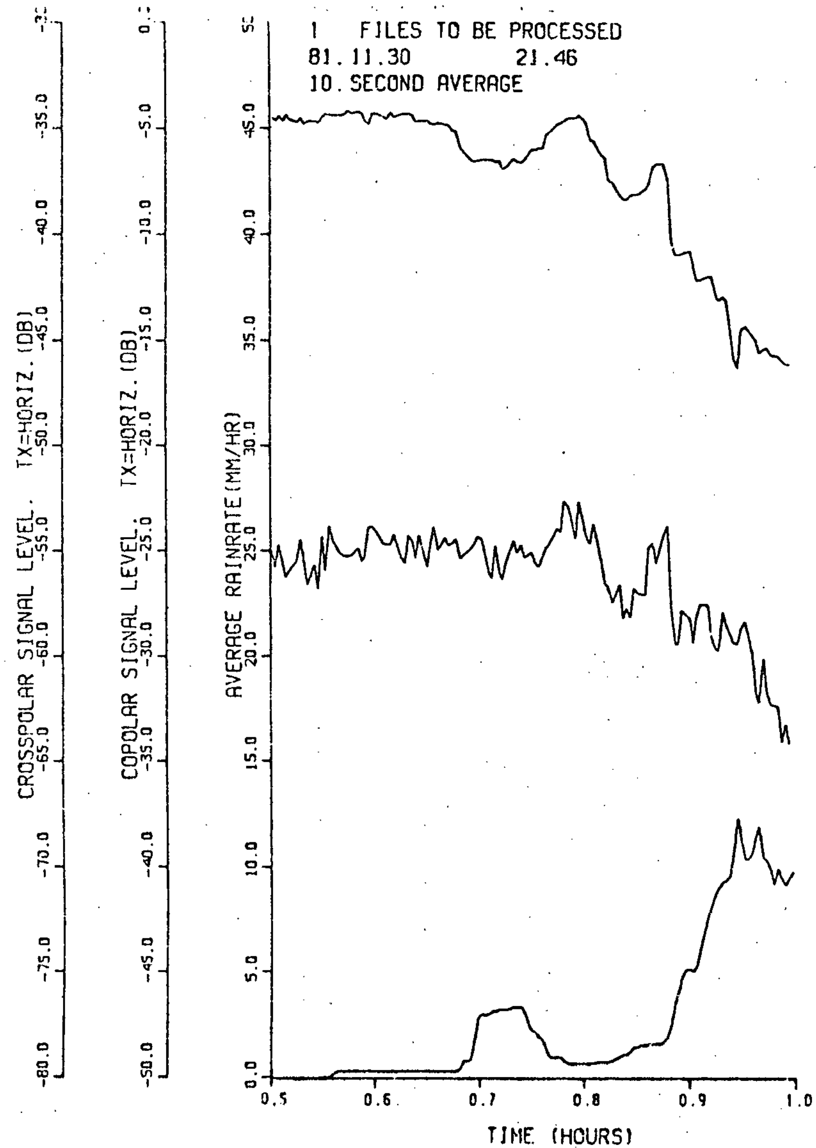

Fig. 6.5.4. Signal levels for horizontal transmitted polarization, 10 s avg for 81.11.30.21

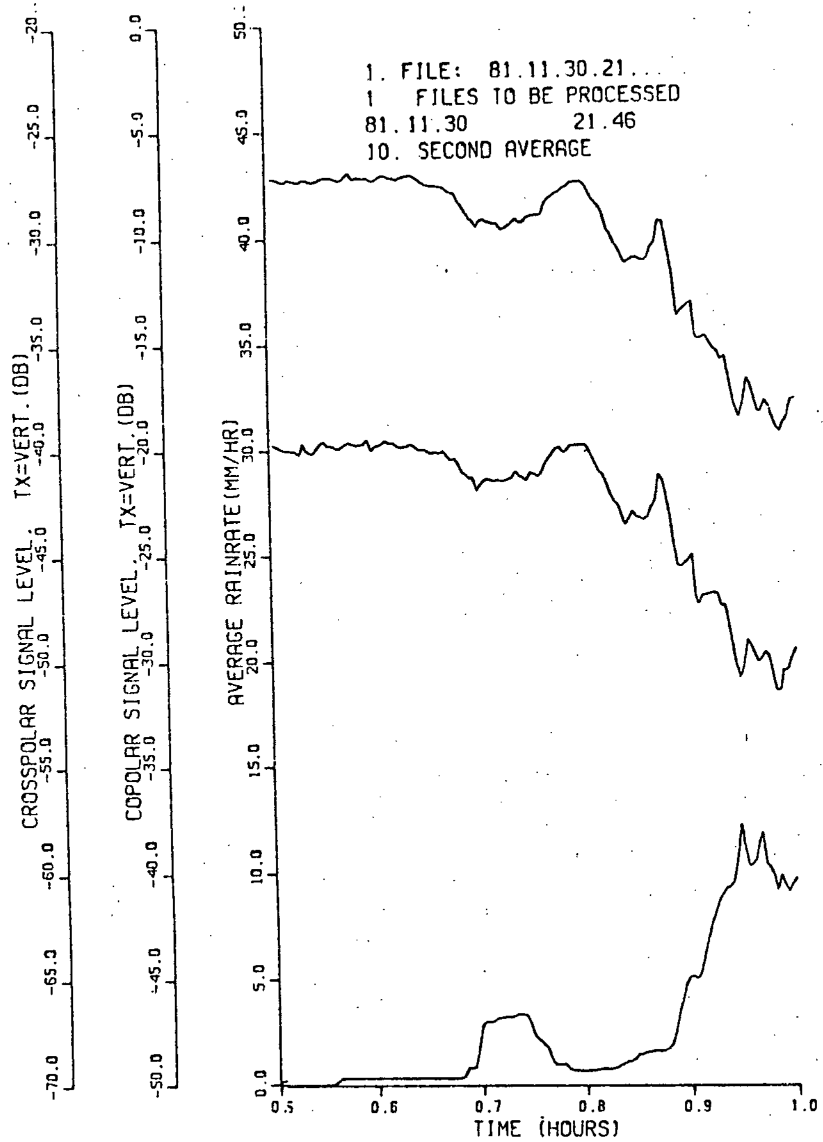

Fig. 6.5.5. Signal levels for vertical transmitted ploarization, 10 s avg. for 81.11.30.21.

6.5.1 Attenuation Data for 81.11.30.21, 22:16-22:45

This data file includes attenuation examples with rapidly changing drop size distributions and relatively constant vertical wind velocities. At the leading edge of this storm, the measured attenuation was much lower than that predicted for the JOT distribution. In the next period, the attenuation rapidly changed to be higher than that predicted for the JOW distribution. These changes were due to corresponding variations in the drop size distributions. Table 6.5.1 gives a summary of the attenuation data for this file.

6.5.1.1 Attenution During T_1, 0.50-0.80 h

During T_1, at the leading edge of this storm, Fig. 6.5.6 shows that the CPA was even lower than that predicted for the JOT distribution. This was due to the drop size distribution, shown in Fig. 6.5.7, which had an unusually small number of small drops and a large number of large drops. Distributions of this type at the leading edges of some storms have been discussed by [1.57], [1.59], [1.85], [4.17] and [6.5]. The attenuation predicted from the measured drop size distribution is also shown in Fig. 6.5.6. Measured values of attenuation were slightly higher than this prediction because of the 0.6 m/s average upward wind velocity during this period.

Period	Measured Attenuation Compared to Standard Predictions	Measured Drop Distribution	Vertical Wind During Rain	Data is in Approximate Agreement with Predictions for:	Comments
T_1 0.50-0.80 h	Lower than JOT Fig. 6.5.6	Fewer small and more large drops than JOT Fig. 6.5.7	≅+0.6 m/s avg. Fig. 6.5.3(a), (b)	Measured drop distribution and measured vert. wind. Fig. 6.5.6	Leading edge of storm.
T_2 0.80-0.89 h	Higher than JOW Fig. 6.5.8	Agreed with JOW, 1 Fig. 6.5.9	≅+0.4 m/s avg. Fig. 6.5.3(a), (b)	JOW and vert. wind = +1 m/s Fig. 6.5.8	2
T_3 0.89-0.99 h	Higher than JOT Fig. 6.5.10	Agreed with JOT, 1 Fig. 6.5.11	≅+0.6 m/s avg. Fig. 6.5.3(a), (b)	JOT and vert. wind = +1 m/s Fig. 6.5.10	2

Table 6.5.1 Summary of Attenuation Data for 81.11.30.21, 22:16-22:46

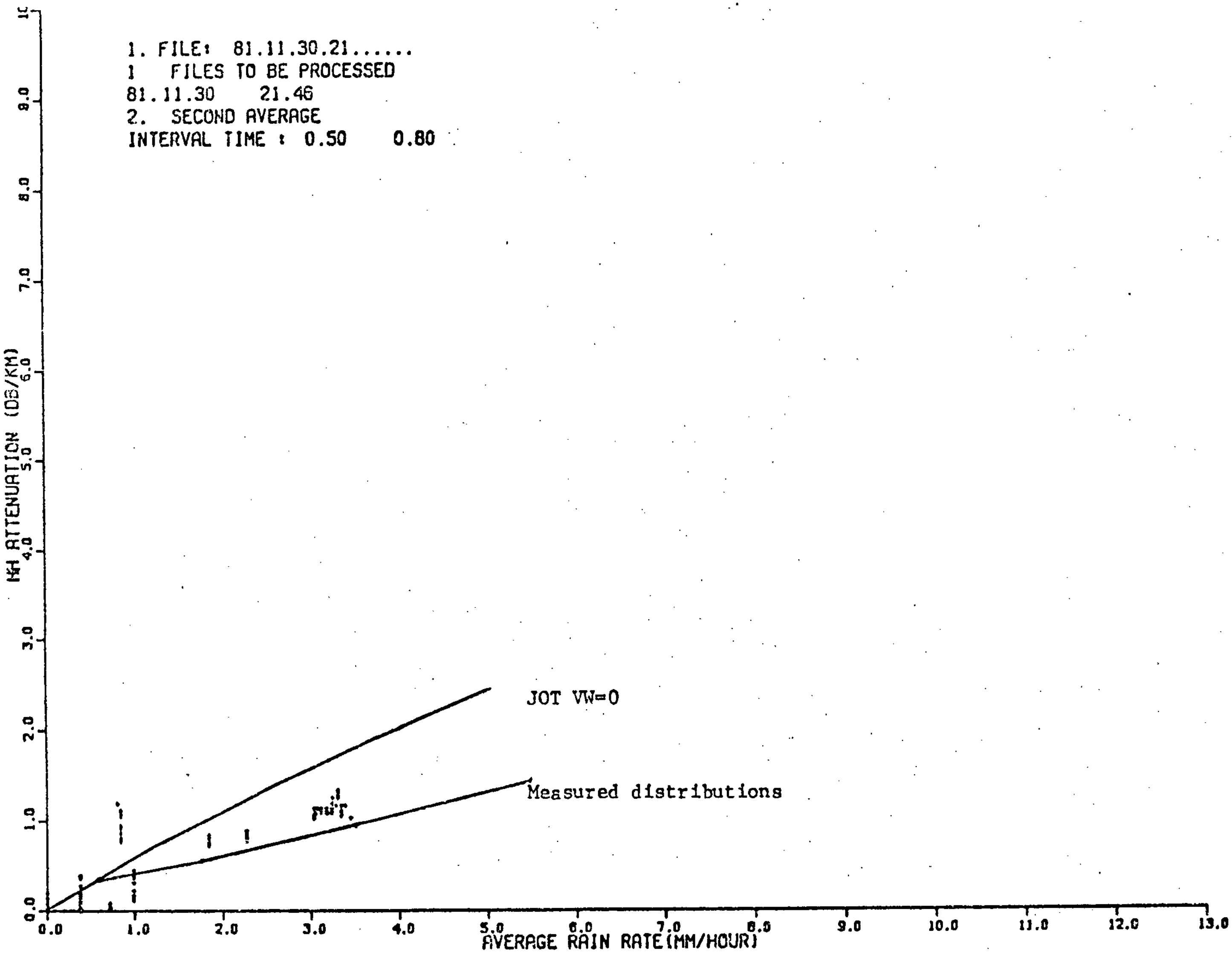

Fig. 6.5.6. CPA during T_1.

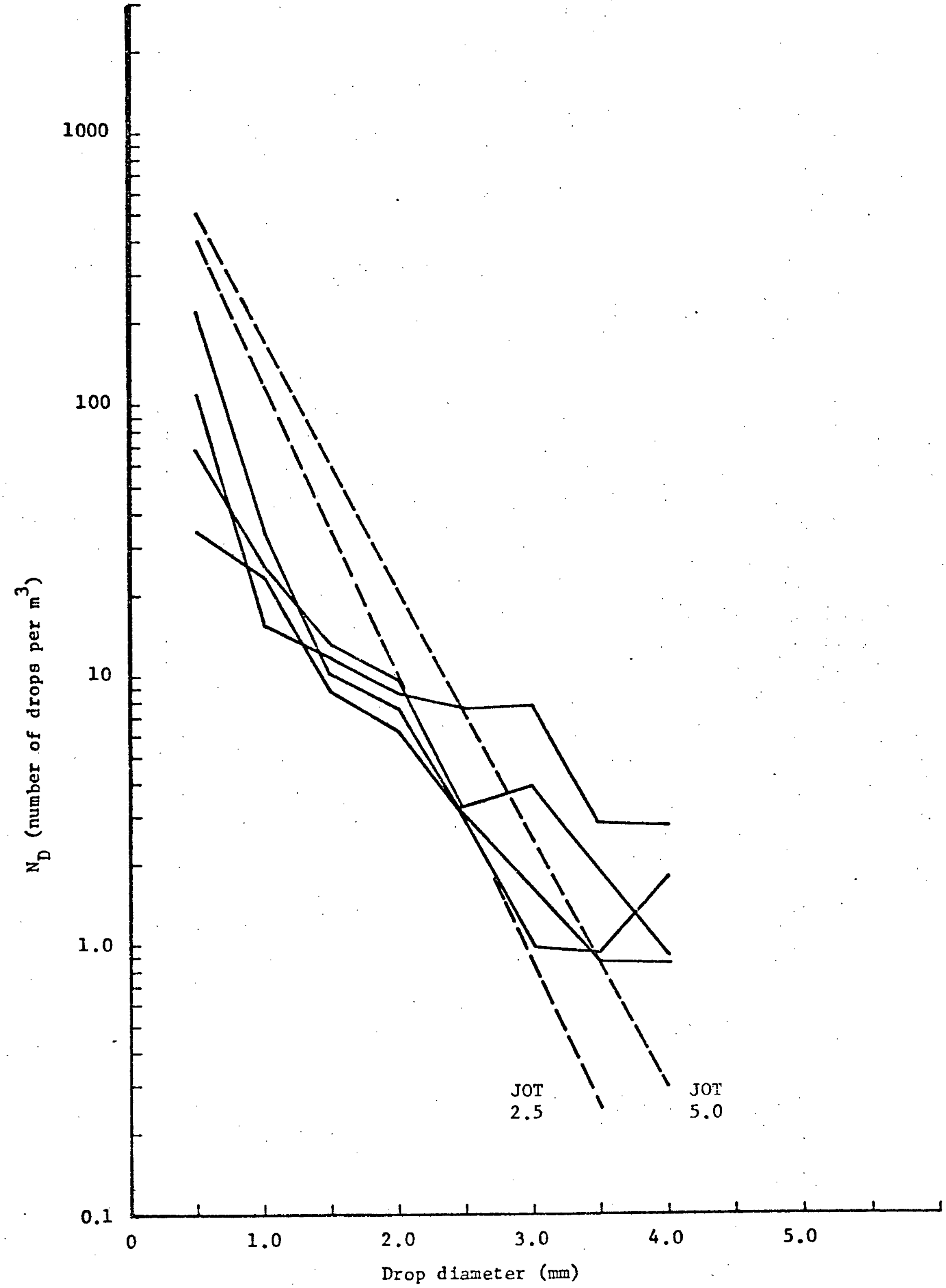

Fig. 6.5.7. Drop distributions for T_1.

6.5.1.2 Attenuation During T_2, 0.80–0.89 h

During interval T_2 the CPA was higher than during T_1, even though the rainrate during T_2 was much lower. This was due to the change in the drop size distribution, which is shown in Fig. 6.5.9. During this period, the distribution was quite close to the JOW (or Marshall and Palmer) distribution for similar rainrates. The lower numbers of drops in the smallest category are believed to be due to the moderately high horizontal wind velocity during this interval as discussed in Section 6.1.1. Figure 6.5.8 shows the attenuation/rainrate scatterplot for this interval. The attenuation was higher than that predicted for the measured distribution because of the vertical wind velocity, Fig. 6.5.3(a), which varied between −0.05 to +0.8 m/s during this period. Vertical wind effects for this distribution will be considerably larger than during the previous period because of the larger number of small drops. The best agreement with the measured attenuation is for the predicted values with an upward vertical wind of 1.0 m/s which is somewhat higher than the average measured vertical wind velocity for the reasons discussed in Section 6.4.1.1.

6.5.1.3 Attenuation During T_3, 0.89–0.99 h

During T_3, the drop size distribution, Fig. 6.5.11, had changed to agree with the JOT distribution for a similar range of rainrates. The vertical wind during this period, Fig. 6.5.2(a), varied between +0.25 to +1.1 m/s upward and has an average value of about 0.6 m/s. The measured attenuation, shown in Fig. 6.5.10 agreed with predictions for the Joss/Olsen Thunderstorm and a 1.0 m/s constant upward wind velocity.

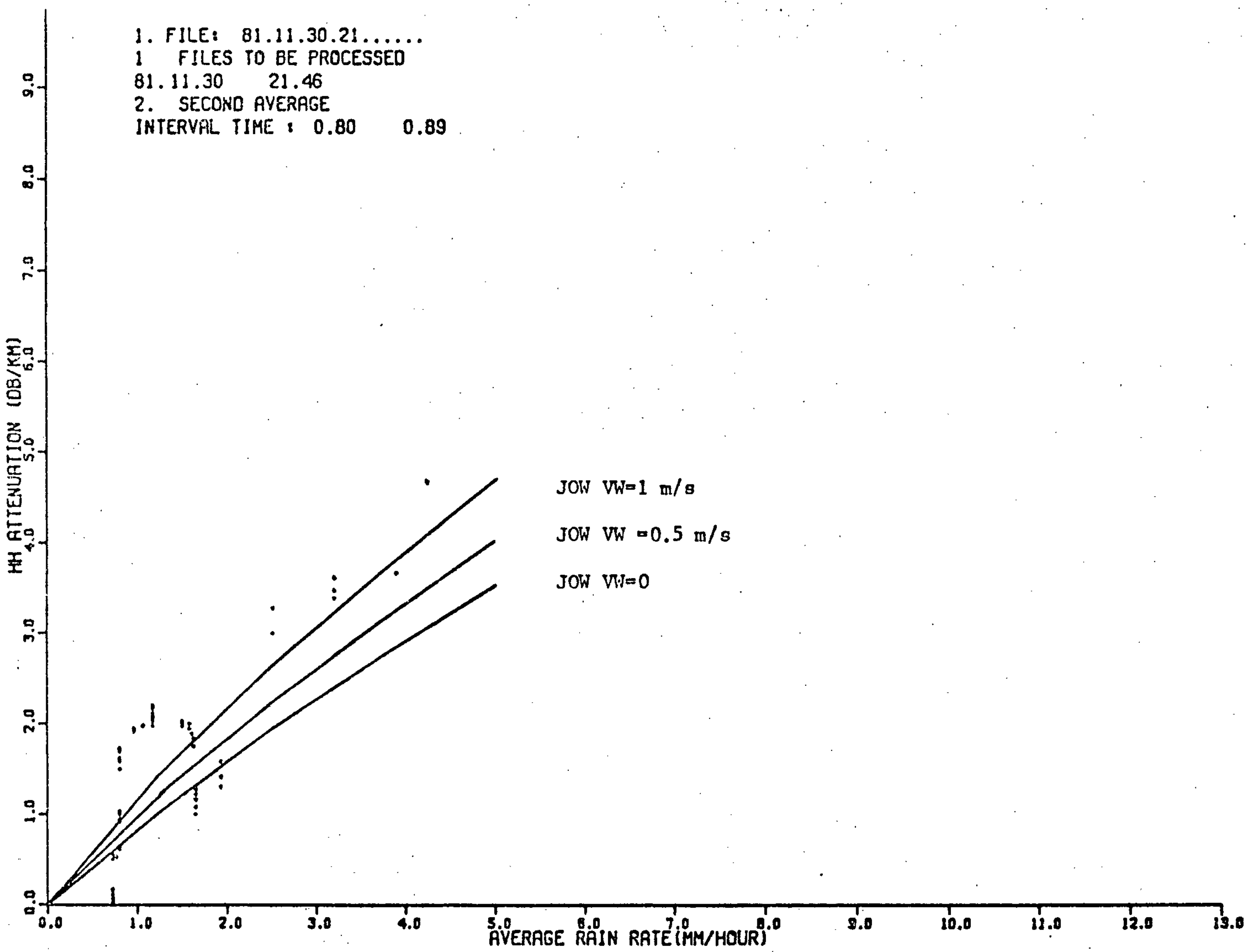

Fig. 6.5.8. CPA during T_2.

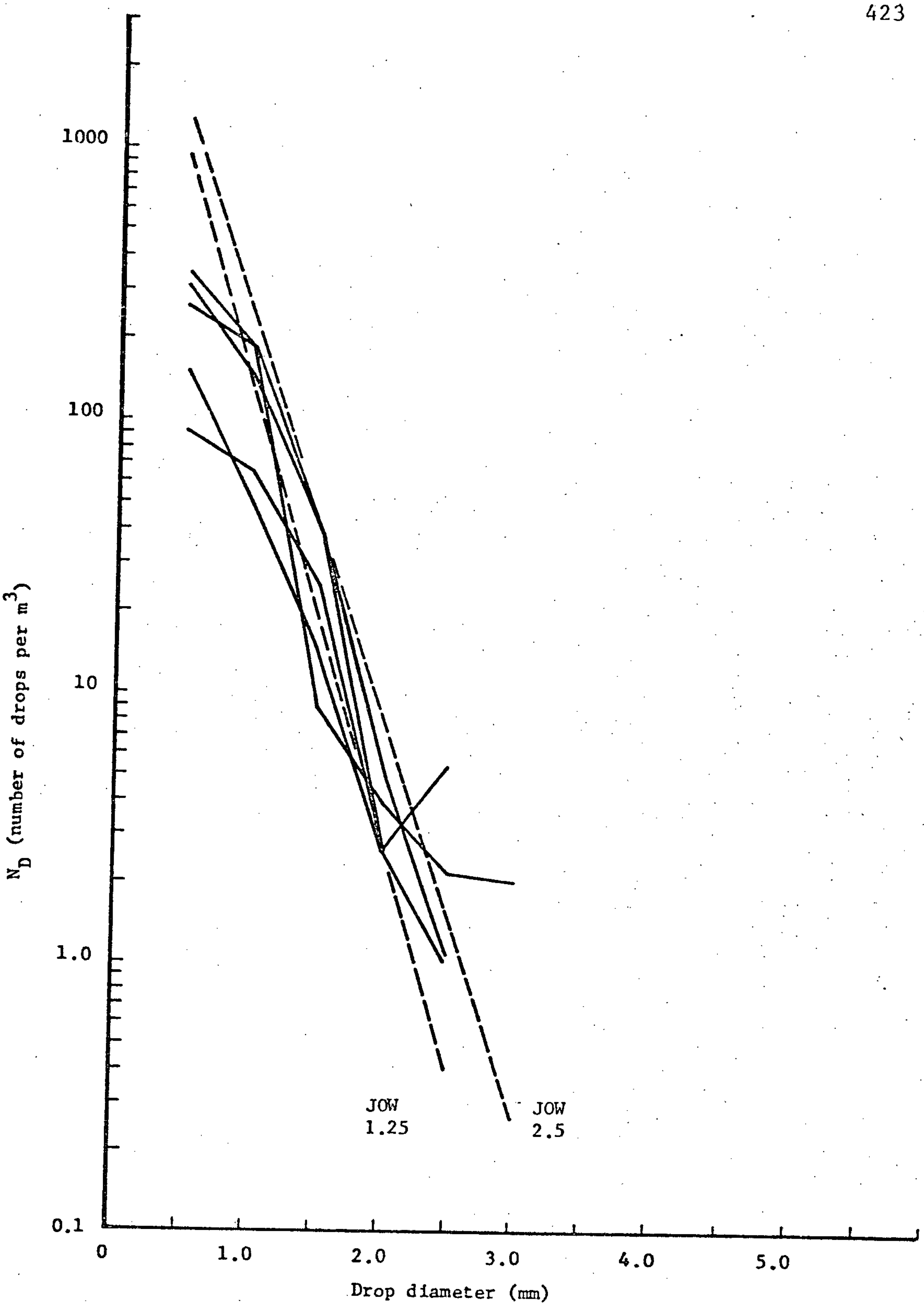

Fig. 6.5.9 Drop distributions for T_2.

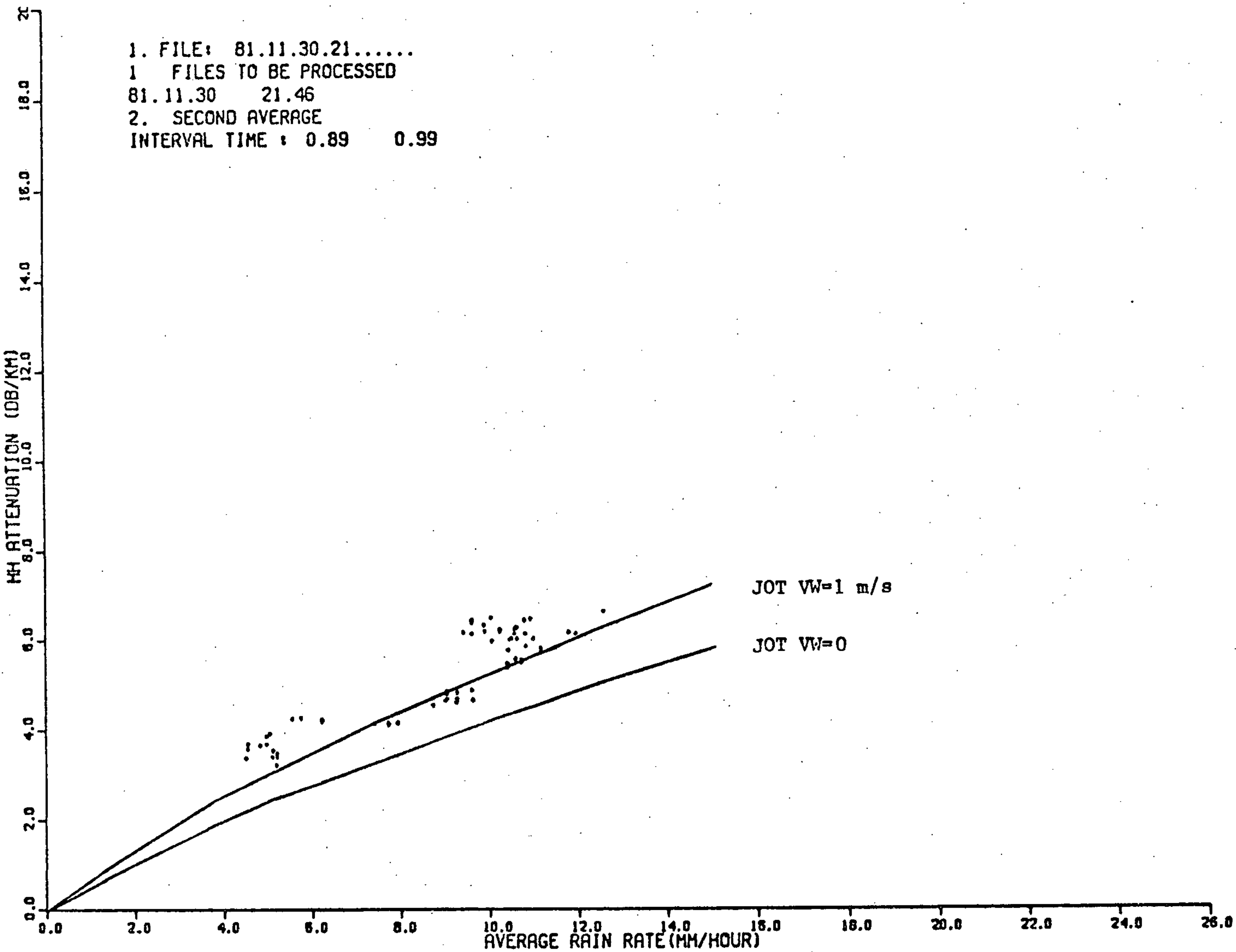

Fig. 6.5.10. CPA during T_3.

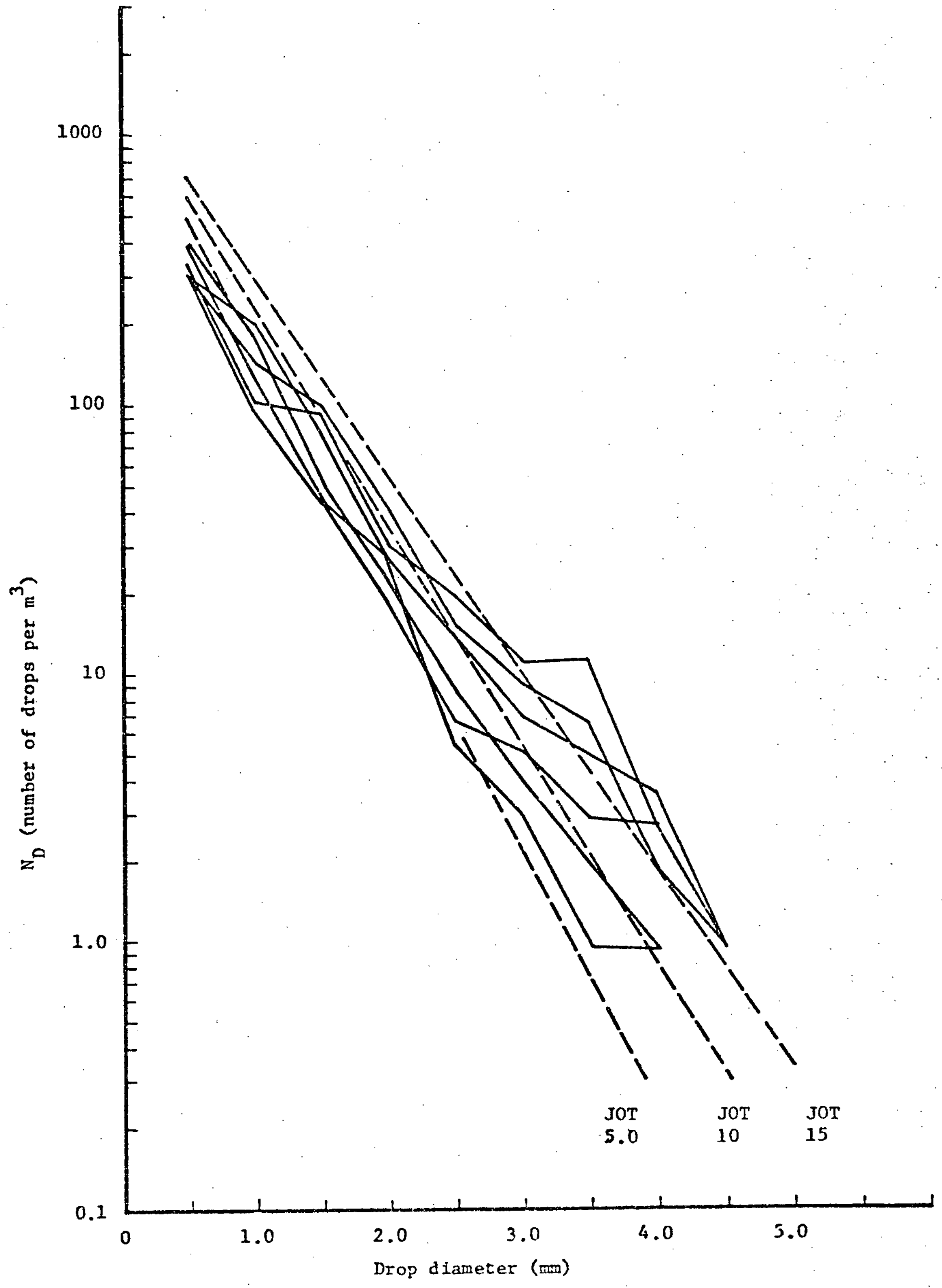

Fig. 6.5.11. Drop distributions during T_3.

6.5.2 XPD and Differential Attenuation Data for 81.11.30.21

Time series plots of system XPD for horizontal and vertical transmitted polarization during this file are shown in Figs. 6.5.12 and 6.5.13. The clear weather XPD for horizontal transmitted polarization is approximately 50 dB due to a long term drift of the crosspolar cancellation network. To compensate for this during the comparisons to the theory, the model parameters for the crosspolar cancellation network were adjusted to give the same clear weather XPD. The clear weather XPD for the uncancelled channel is approximately 32.5 dB. Estimates for the model parameters in this case were obtained from this clear weather isolation and the antenna XPD specifications in Fig. 2.33. Assuming the antennas are aligned reasonably close to the crosspolar minimums this clear weather isolation could only result from the antennas adding approximately in phase. The antenna parameters used in the model calculations were 40 dB<0° and 37.3 dB<0° for the transmit and receive antennas, respectively.

The differential attenuation for this period is shown in Fig. 6.5.14. These results are much closer to what would be expected from the basic theory and assumed drop shapes than the data in the previous files.

A summary of XPD and differential attenuation data for the file is shown in Table 6.5.2.

6.5.2.1 XPD and Differential Attenuation During T_4, 0.65-0.80 h

During this period, the horizontal XPD, Fig. 6.5.15, generally agrees with the model predictions for a canting angle of 2 to 3°. The vertical XPD, Fig. 6.5.16, appeared to conform to canting angles of 3-4°. This difference could be due to different relative angles between the path and antenna XPDs

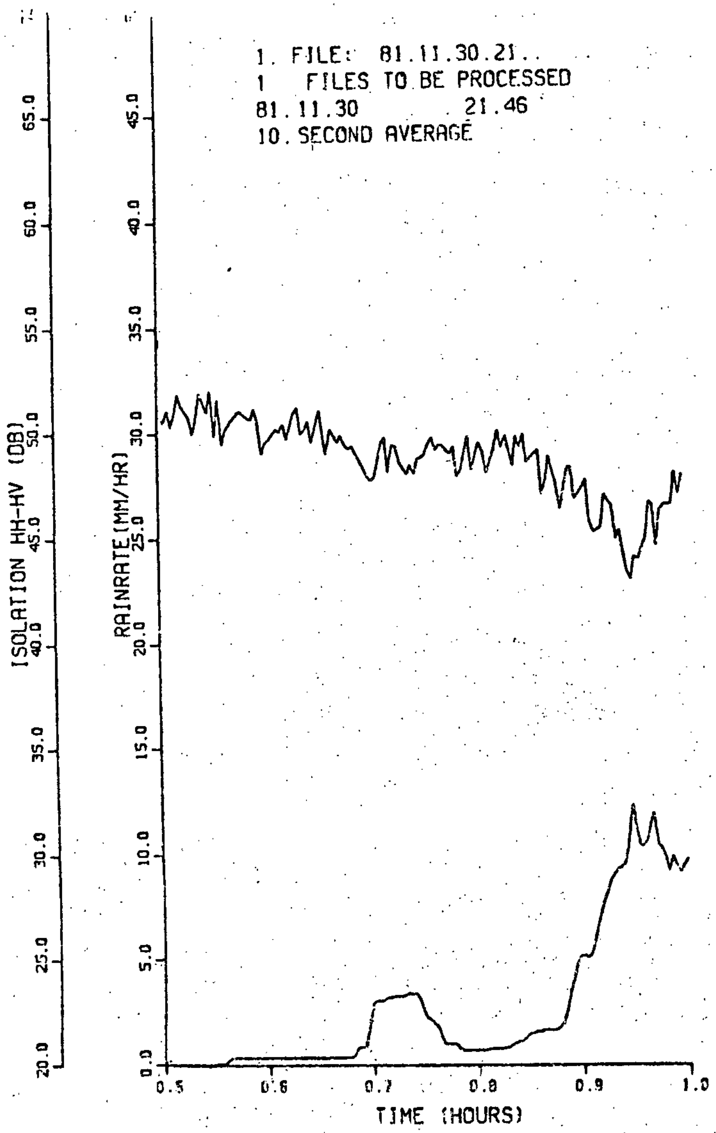

Fig. 6.5.12. XPD for horizontal transmitted polarization, 10 s avg, for 81.11.30.21.

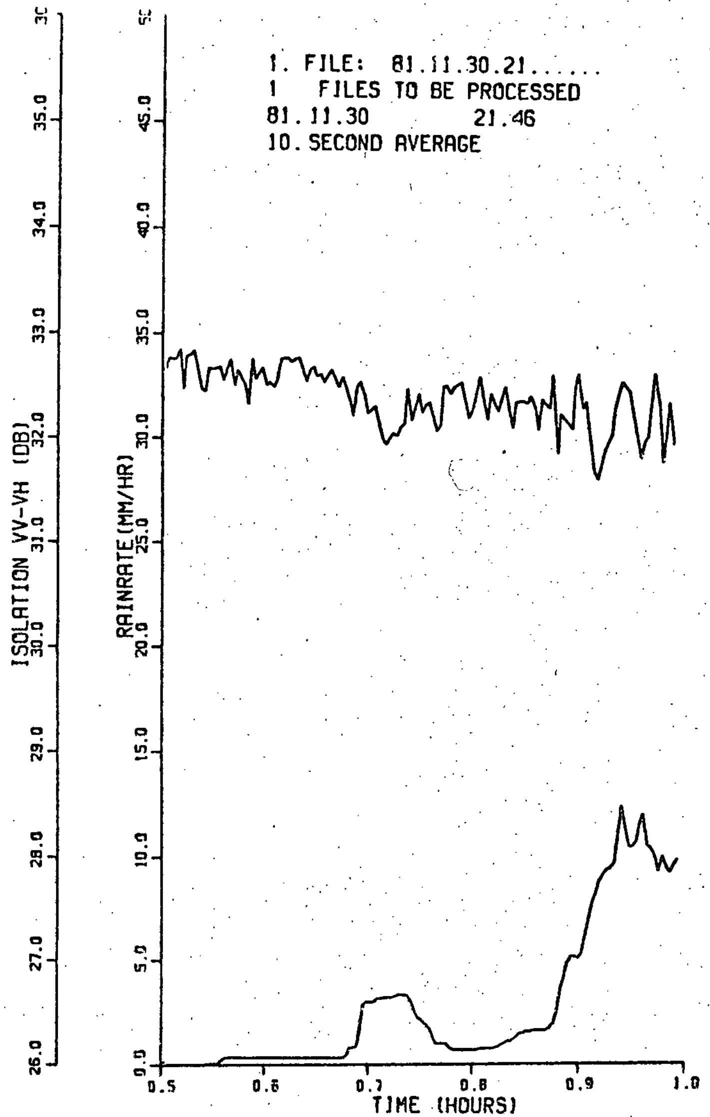

Fig. 6.5.13. XPD for vertical transmitted polarization, 10 s avg. for 81.11.30.21.

Period	XPD	Differential Attenuation	Wind Velocities During Rain	XPD is in Approximate Agreement with Model Predictions for:	Comments
T_4 0.65-0.80 h	50.7-48 dB clear weather XPD ≅ 50 dB Fig. 6.5.15 32.5-31.9 dB clear weather XPD = 32.5 dB Fig. 6.5.16	Varied between -0.1 and +0.2 dB. Fig. 6.5.14	Horiz. wind ≅ 7.0 m/s avg. during lowest XPD data, Fig. 6.5.2	"Cancelled" XPD $\phi \cong 2° - 3°$ Uncancelled XPD $\phi \cong 3° - 4°$ Figs. 6.5.15 and 6.5.16	Reasonable agreement between XPDs for both Uncancelled polarizations. XPDs agree with slightly higher canting angles.
T_5 0.80-0.99 h	50-43.5 dB clear weather XPD ≅50 dB Fig. 6.5.17 32.5-31.7 dB clear weather XPD = 32.5 dB Uncancelled XPD not correlated to rainrate. Fig. 6.5.18	Varied between -0.2 and +0.5dB generally positive Fig. 6.5.14	Horiz. wind ≅6.5 m/s avg. during lowest XPD data. Fig. 6.5.2	"Cancelled" XPD $\phi \cong 2° - 4°$ Uncancelled XPD $\phi \cong 2° - 4°$ Figs. 6.5.17 and 6.5.18	Reasonable agreement between XPDs for both polarizations. Uncancelled XPDs agree with slightly higher canting angles.

Table 6.5.2 XPD and Differential Attenuation Data for 81.11.30.21

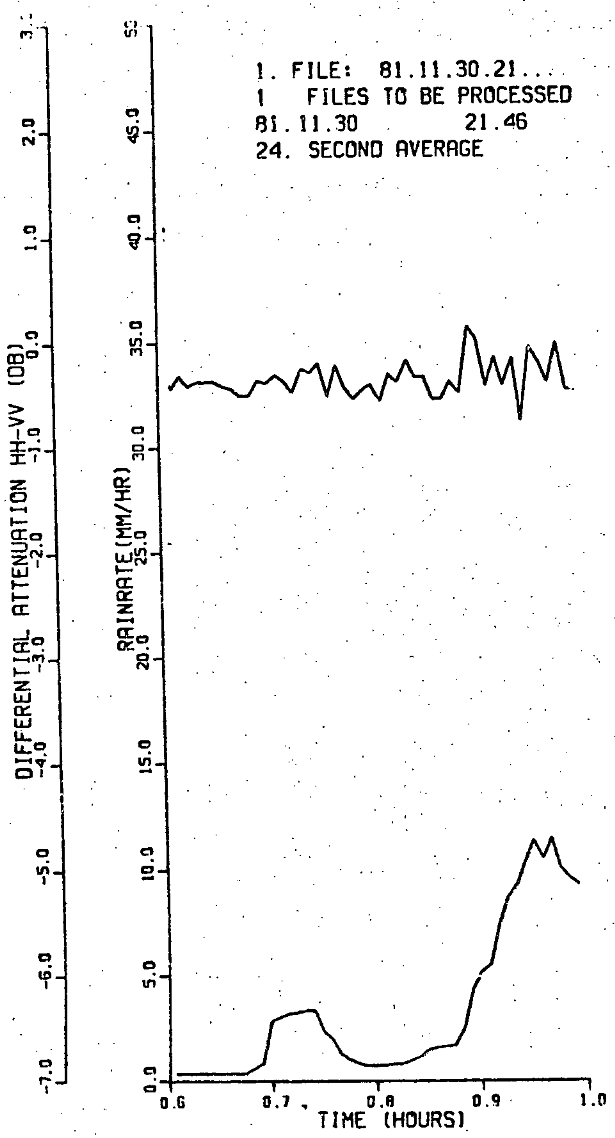

Fig. 6.5.14. Differential attenuation for 81.11.30.21.

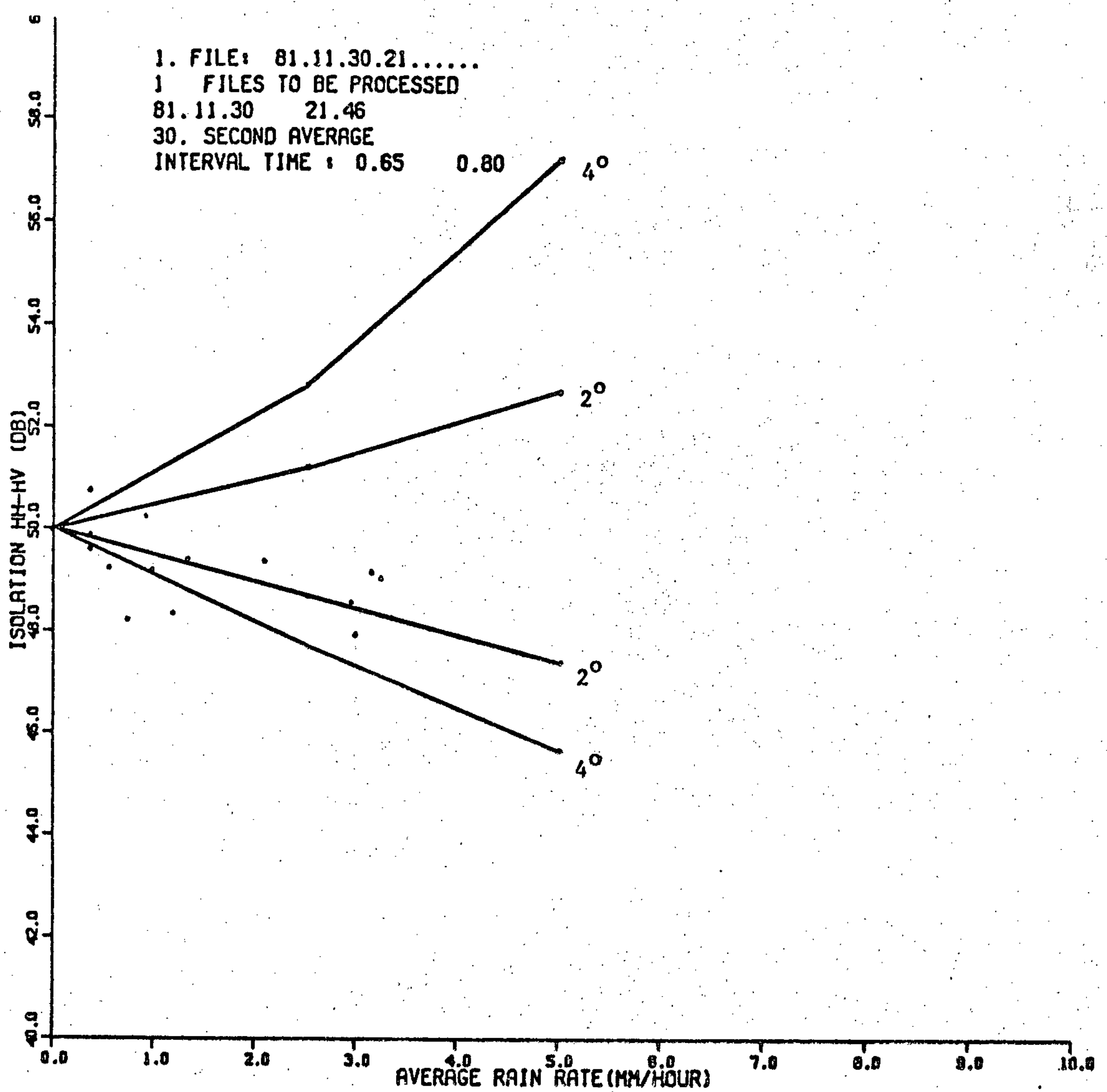

Fig. 6.5.15. XPD_H during T_4.

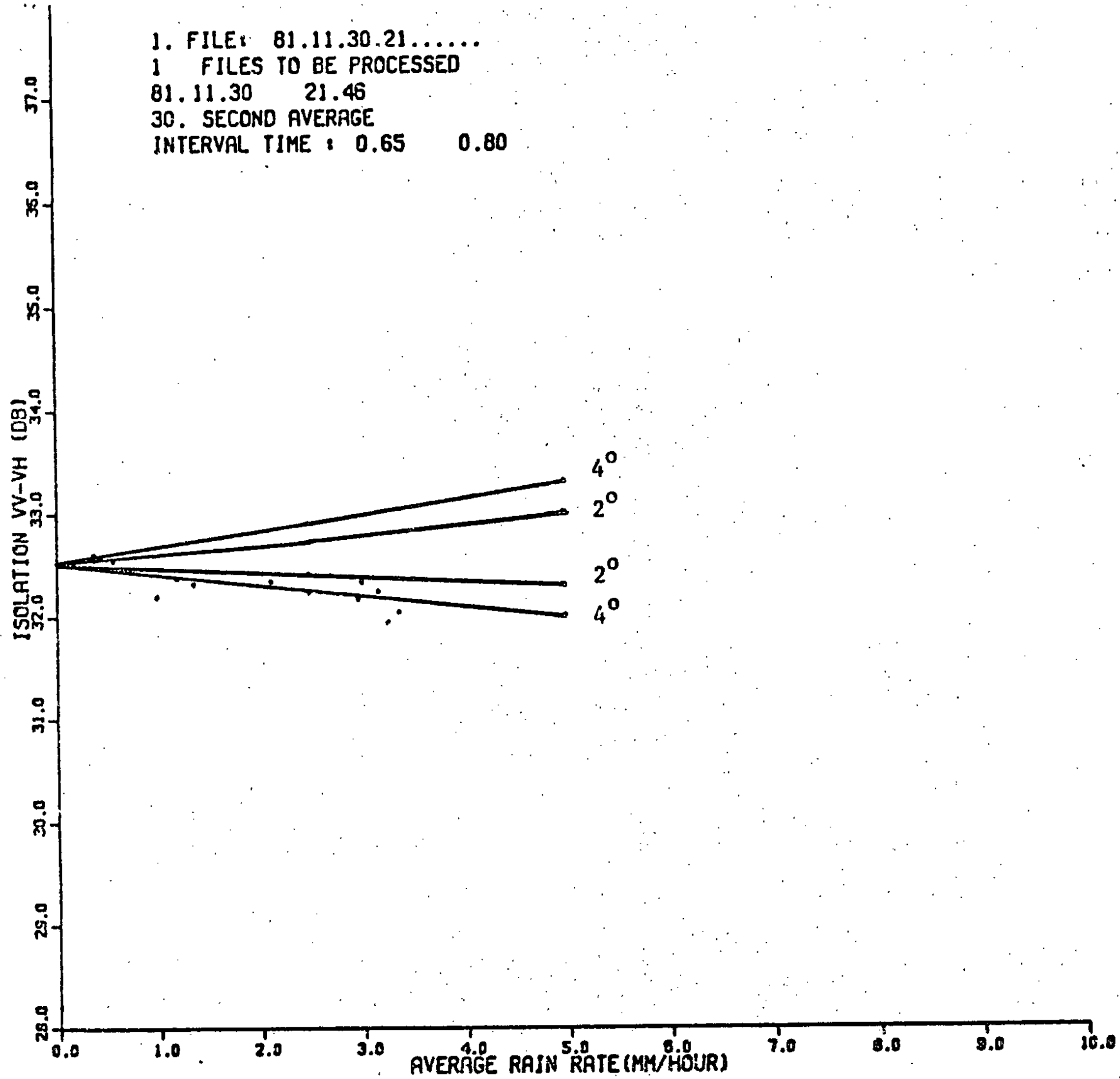

Fig. 6.5.16. XPD_V during T_4.

but a definite conclusion is not possible because the total change from the clear weather value on the uncancelled channel is too small for accurate comparisons. During the periods of lower XPD, the average horizontal wind velocity was approximately 7.0 m/s.

The differential attenuation during T_4 varied between -0.1 dB and +0.2 dB. For these small values and rainrates it is only possible to conclude that these data are within the range of values predicted from the basic theory and experimental-system differential-attenuation measurement uncertainty.

6.5.2.2 XPD and Differential Attenuation During T_5, 0.80-0.99 h

During T_5, the rainrates were much higher than during T_4, but the average horizontal wind velocity was similar (≅6.5 m/s average). Both XPDs agree reasonably with model predictions for canting angles between 2 and 4°, with the uncancelled XPDs again conforming to slightly larger canting angles, Figs. 6.5.17 and 6.5.18. The uncancelled XPD was at times close to the clear weather value during high rainrates, apparently due to path XPD phase variations, Figs. 6.5.13 and 6.5.18. This behaviour of the uncancelled XPD was discussed in Section 6.2.2.

The differential attenuation during T_5 was generally positive, Fig. 6.5.14. A single small negative peak occurred around 0.95 h during a rapid decrease in the horizontal wind velocity. The largest values of the positive differential attenuation during the higher rainrates were in reasonable agreement with the theoretical predictions.

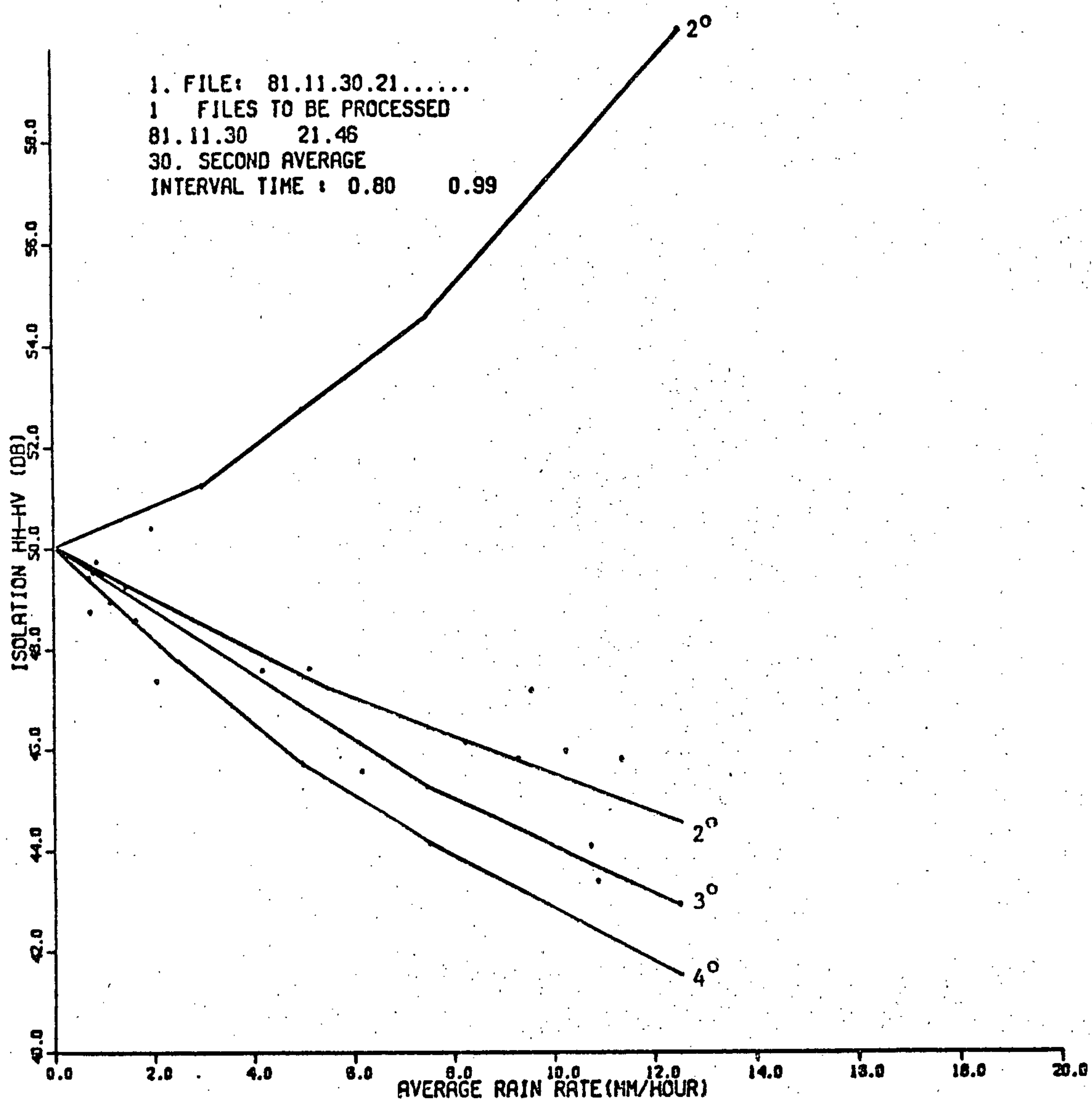

Fig. 6.5.17. XPD_H during T_5.

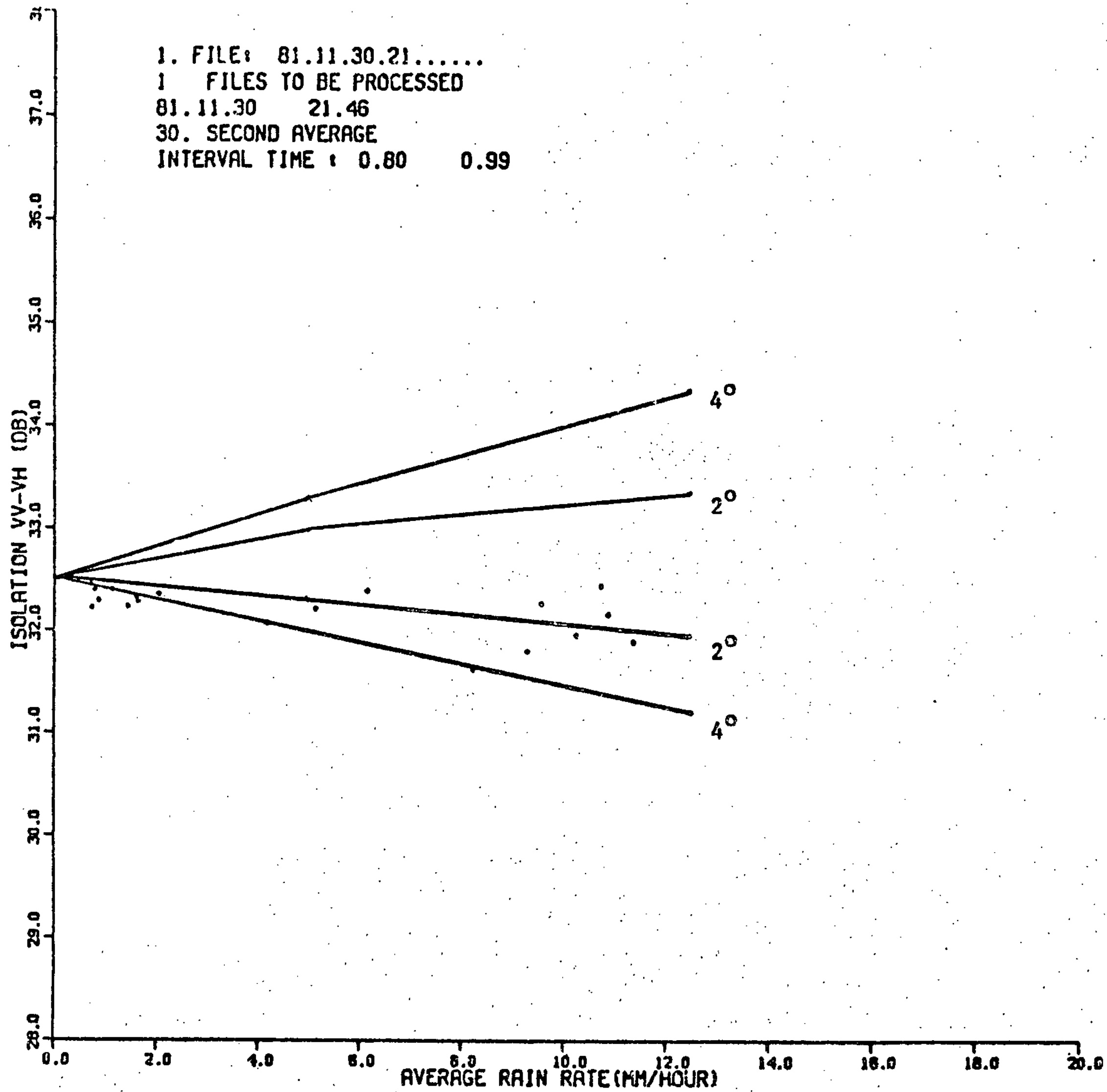

Fig. 6.5.18. XPD_V during T_5.

6.6 Experimental Results for 81.11.30.22

This data file includes examples of distinct rain cell structure. The rainrates for this file are shown in Fig. 6.6.1. During this period the rainrate varied between 0 and 10 mm/h. An interesting increase in the number of drops in the smallest category was observed during this file at the trailing edge of the small, high intensity raincells. This increase is clearly shown in $N_D(0.5)/N_D(1.0)$ ratio, Fig. 6.6.4(a).

Unusual wind conditions were also observed during this file. The 10 s average wind direction, Fig. 6.6.2, was extremely variable during this period in sharp contrast to the previous files. Horizontal wind velocities, Fig. 6.6.3, were also relatively variable on a medium to long term scale. The vertical wind velocities shown in Figs. 6.6.4(a) and (b) were unusual in that during the first half of the file the vertical wind is upward but during the latter half of the file it is generally downward. This variability in wind direction and the change from upward to downward vertical wind direction are believed to be due to the passage of a cold front similar to the one described by Semplak and Turrin [4.29], (see also Section 4.4).

Time series, 10 s average, signal levels for this file are shown in Figs. 6.6.5 and 6.6.6.

6.6.1 Attenuation Data for 81.11.30.22, 22:46-23:30

The attenuation data for this file includes examples of attenuation as low as the standard predictions for the JOT distribution and higher than the predictions for the JOD distribution. During this file, the drop size

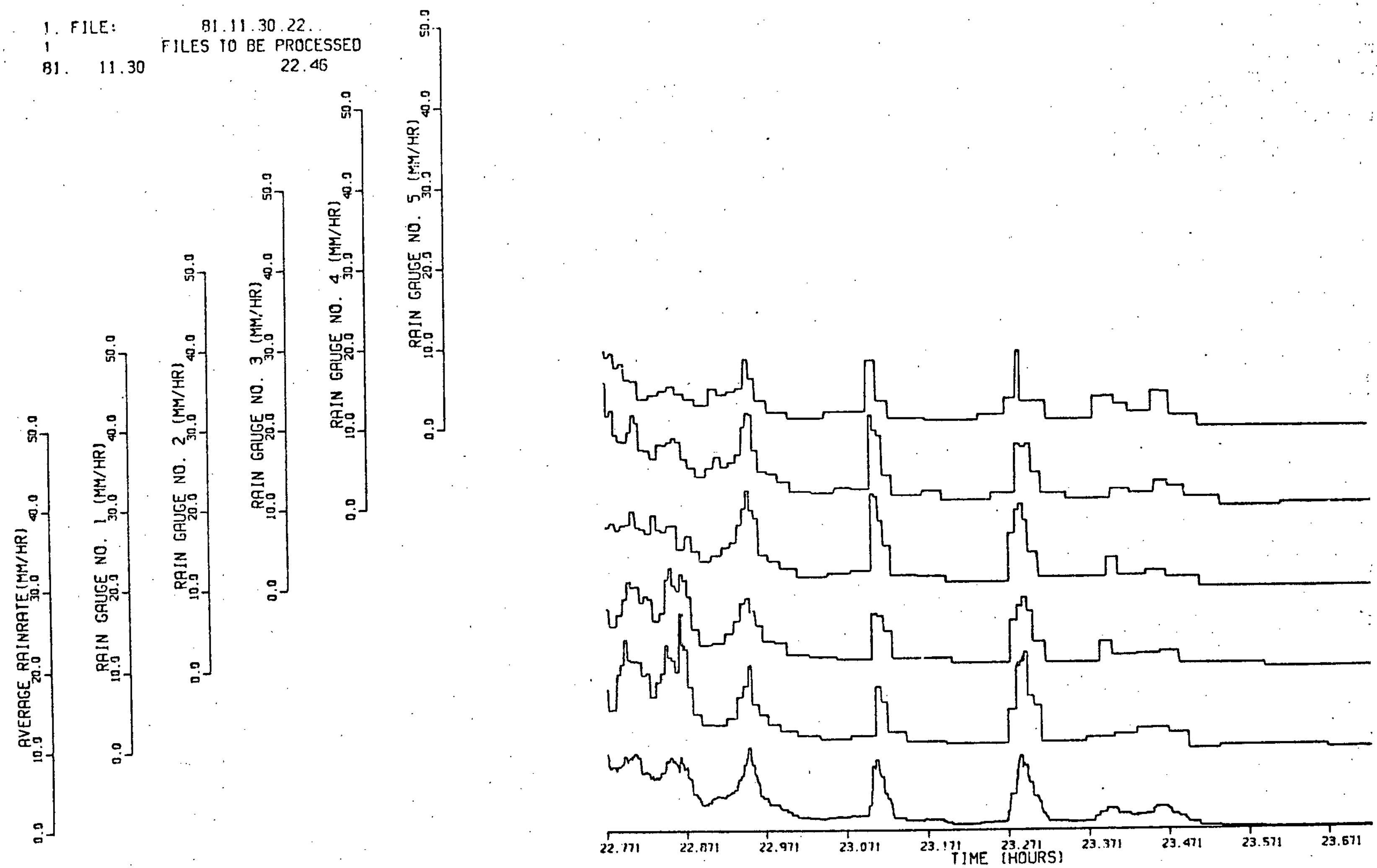

Fig. 6.6.1. Rainrates for 81.11.30.22.

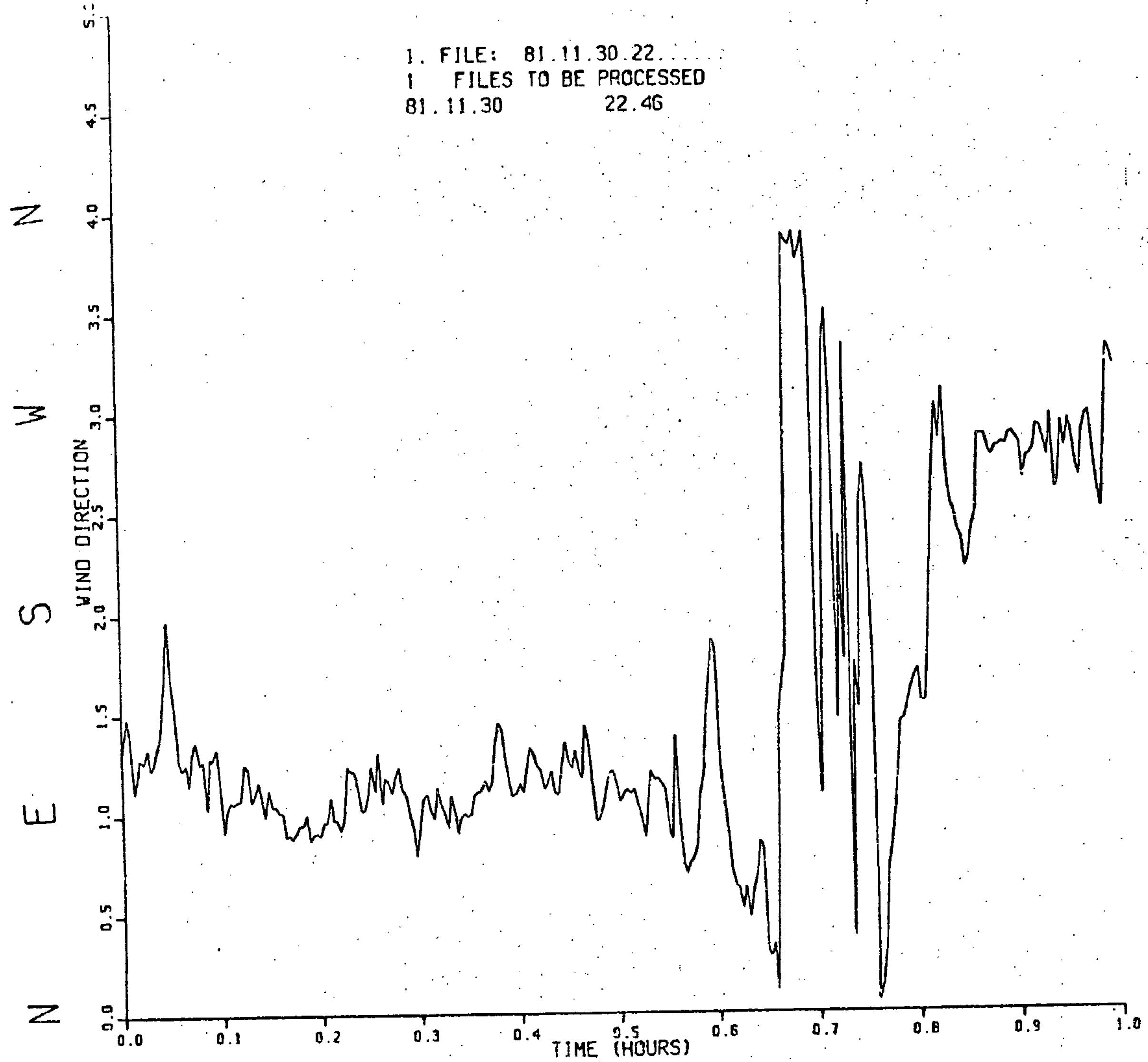

Fig. 6.6.2. Wind direction, 10 s avg. for 81.11.30.22.

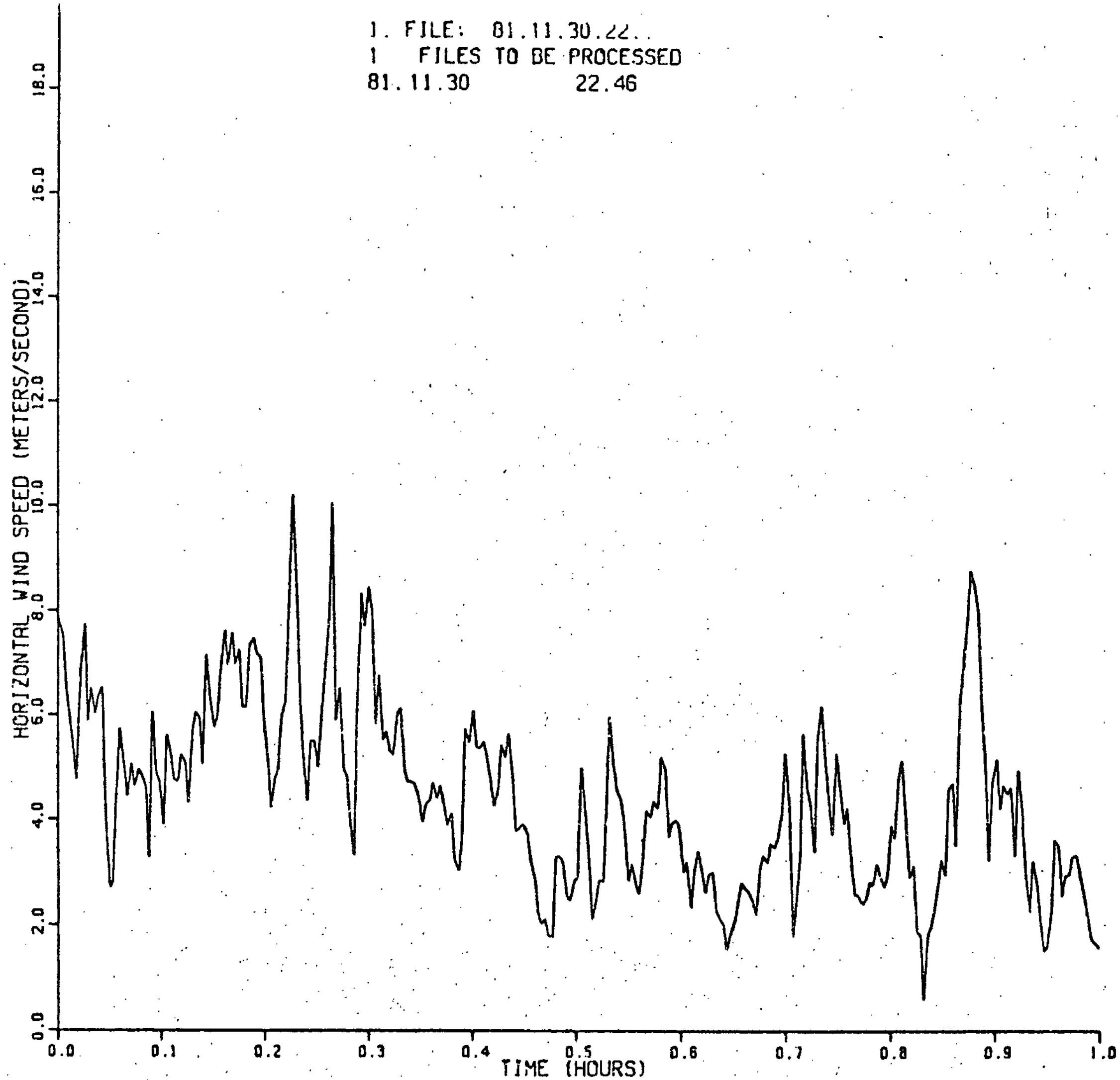

Fig. 6.6.3 Horizontal wind velocity, 10 s avg. for 81.11.30.22.

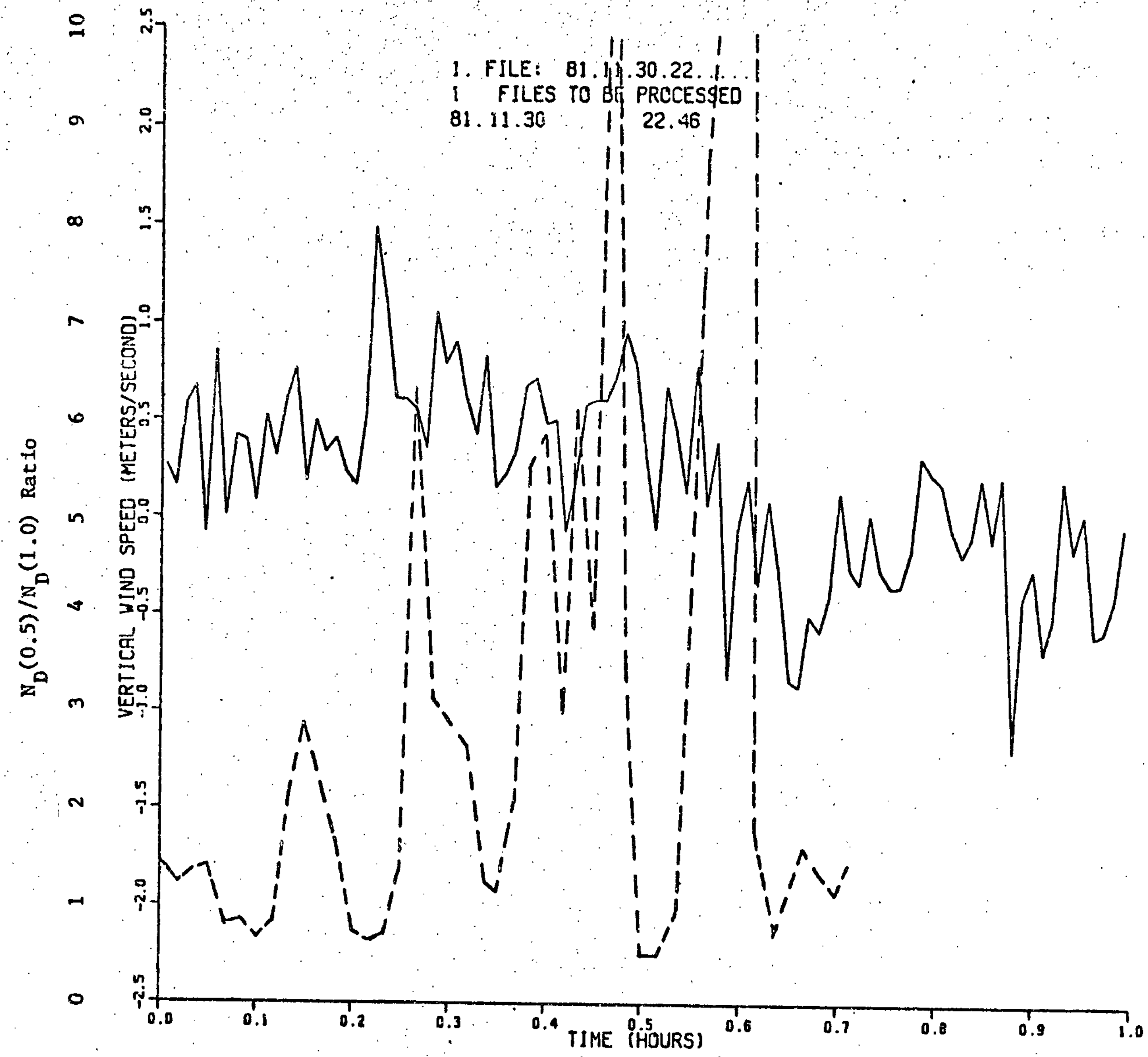

Fig. 6.6.4(a). Vertical wind, 30 s avg. and $N_D(0.5)/N_D(1.0)$ ratio for 81.11.30.22.

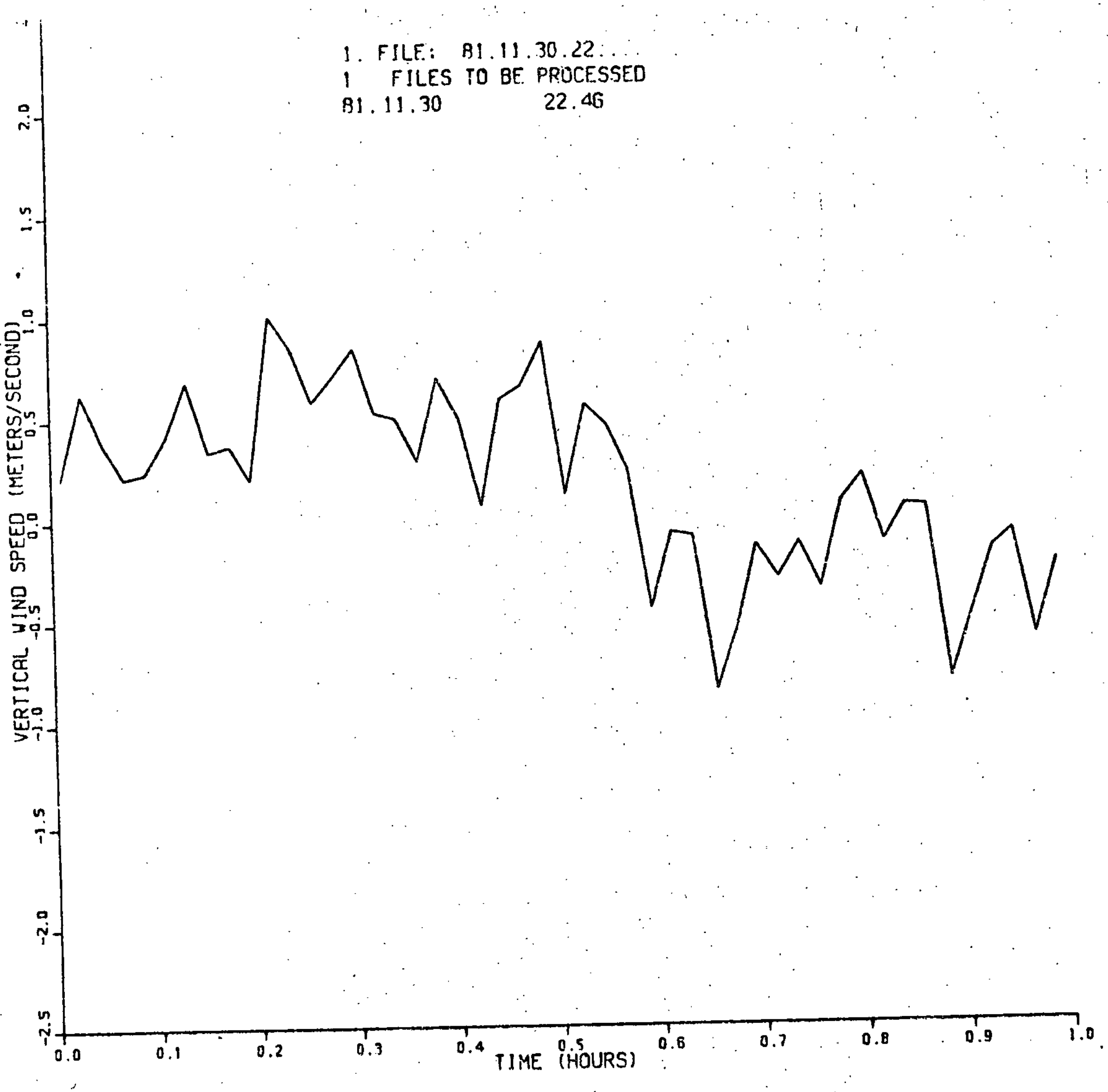

Fig. 6.6.4(b). Vertical wind velocity, 60 s avg. for 81.11.30.22.

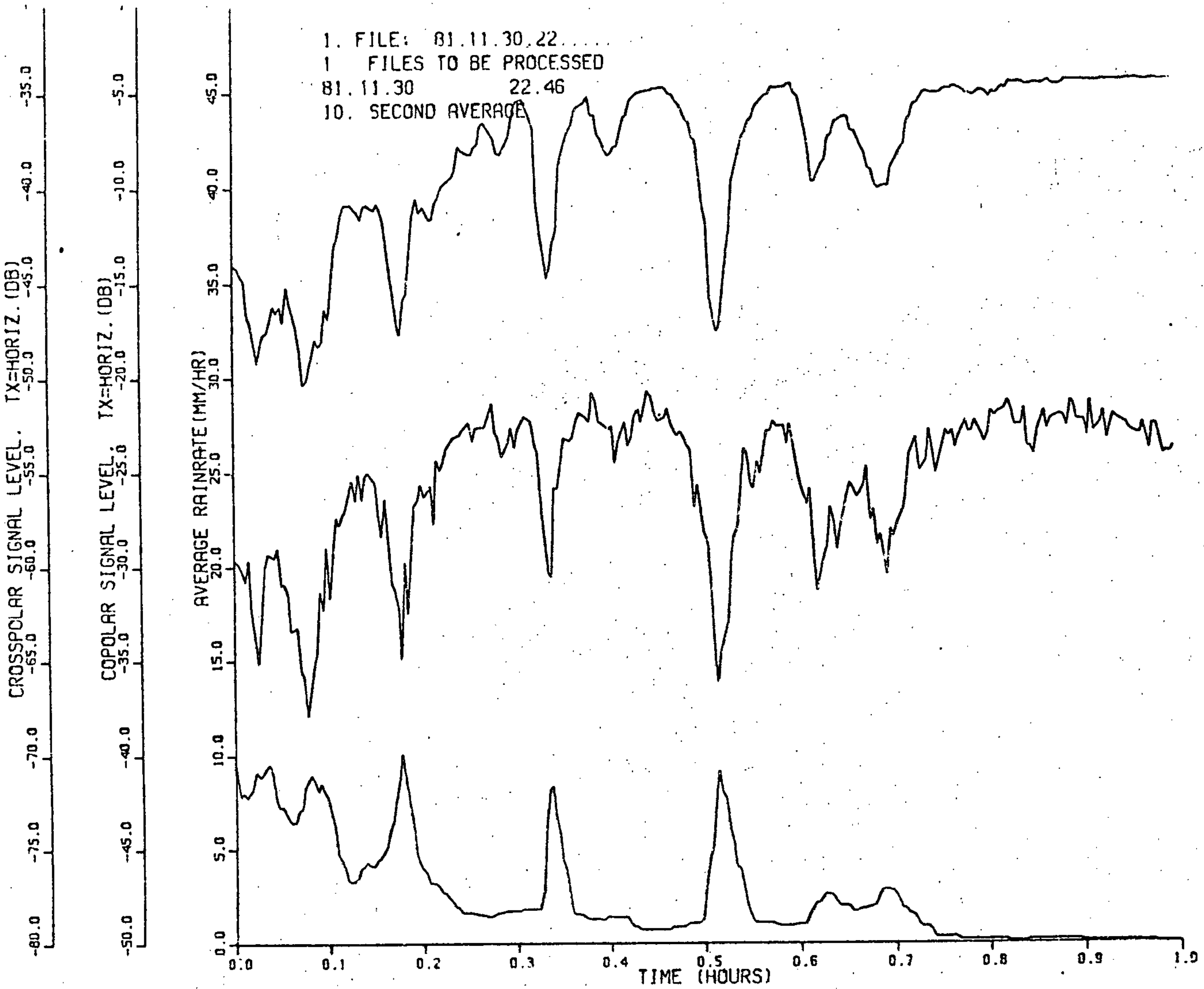

Fig. 6.6.5. Signal levels for horizontal transmitted polarization, 10 s avg. for 81.11.30.22.

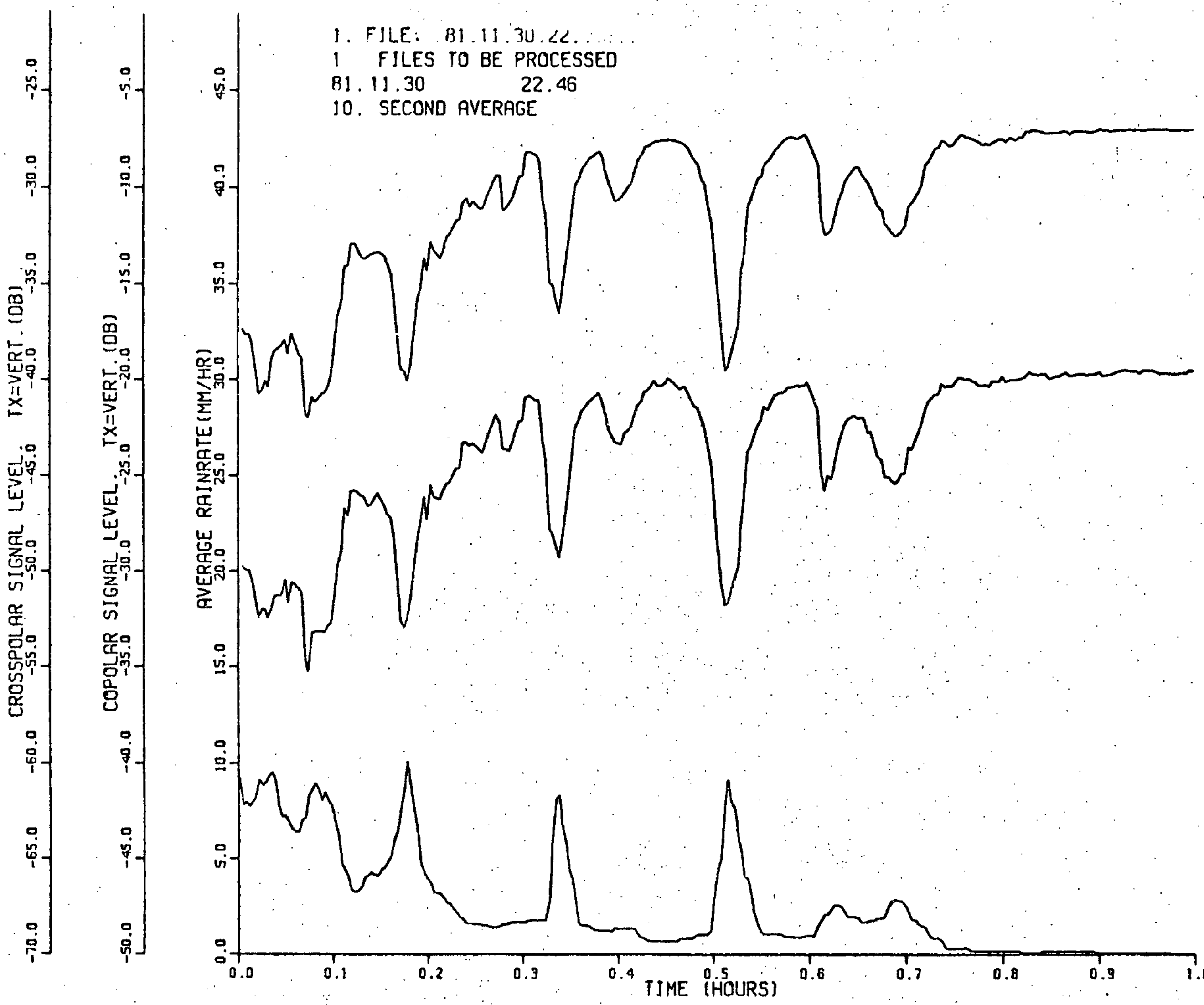

Fig. 6.6.6. Signal levels for vertical transmitted polarization, 10 s avg. for 81.11.30.22.

distribution was quite variable and often changed rapidly. There was also a large increase in the number of small drops after the passage of each individual rain cell. Excellent examples of the effects of vertical wind on attenuation were observed at times during this file. A summary of the attenuation results for this file is shown in Table 6.6.1

6.6.1.1 Attenuation During T_1, 0.00-0.13 h

During T_1, the CPA, Fig. 6.6.7, varied between the standard predictions for the JOW distribution to higher than the predictions for the JOD distribution. This variation is thought to be partially due to the rapidly changing vertical wind velocity, Fig. 6.6.4(a). The drop size distributions for this period also varied over a relatively wide range. This may have been partly due to the vertical wind but the variations in the medium to large size drops indicates that the distribution variation was mainly caused by the rapidly changing rain conditions during this period. These variations in drop distribution also contributed to the variability in the attenuation/rainrate relationship.

6.6.1.2 Attenuation During T_2, 0.13-0.26 h

Attenuation during this period, Fig. 6.6.9, was moderately higher than the standard predictions for the JOW distribution at the higher rainrates. However, at the lower rainrates on the trailing edge of the rain peak, the attenuation was considerably higher because of the large vertical wind peak near 0.22 h and the increasing number of small drops after 0.25 h, Fig.

Period	Measured Attenuation Compared to Standard Predictions	Measured Drop Distribution	Vertical Wind During Rain	Data is in Approximate Agreement with Predictions for:	Comments
T_1 0.0-0.13 h	Varied between JOW and higher than JOD Fig. 6.6.7	Basically JOW slightly more large drops, variable, 1. Fig. 6.6.8	Variable, vertical wind peaks of +0.7 and +0.4 m/s during rain peaks Fig. 6.6.4(a)	Between JOW and zero vertical wind and JOW and vert. wind = +1.0 m/s Fig. 6.6.7	Range of attenuations due to variable vertical wind and drop distribution.
T_2 0.13-0.26 h	Close to JOD at higher rainrates. Higher atten. at lower rainrates. Fig. 6.6.9	JOW, 1. Large numbers of small drops at low rain-rates. Fig. 6.6.10	≅0.3 m/s avg. during high rainrates. Strong peaks at 0.14 and 0.22 h during low rainrates. Fig. 6.6.4(a)	JOW and vert. wind +0.5 to +1 m/s during high rainrates. Higher during low rainrates.	2 during high rainrates, 3 or 4 during low rainrates
T_3 0.26-0.31 h	Higher and lower than JOW. Rain-rate is constant Fig. 6.6.11	JOW, 1. Relatively large numbers of small drops Fig. 6.6.12	Vertical wind peak =+1.0m/s at 0.28 h same time as attena-tion peak. Fig. 6.6.4(a) 6.6.5 and 6.6.6	Rainrate is constant, attenuation correlates with vertical wind peak. Fig. 6.6.4(b), 6.6.5, and 6.6.6.	4
T_4 0.31-0.37 h	Agrees with JOW except higher for R ≅ 2 to 3 mm/h. Fig. 6.6.13	Similar to JOW but quite variable, 1. More large drops at high rainrate. Fig. 6.6.14	Generally decreases up to 0.34 h. after a period of upward flow. ≅+0.25 m/s avg. during rain peak. Fig. 6.6.4(a)	Agrees with JOW except for R ≅ 2 to 3 mm/h on leading edge of rain peak where atten. is higher. Figs. 6.6.5, 6.6.6 and 6.6.13	3 during leading edge of rain peak, i.e. up to 0.34 h.

. . . continued

Period	Measured Attenuation Compared to Standard Predictions	Measured Drop Distribution	Vertical Wind During Rain	Data is in Approximate Agreement with Predictions for:	Comments
T_5 0.37-0.45 h	Higher and lower than JOW. Rainrate is ≅ constant. Fig. 6.6.15	JOW, 1 Large number of small drops	Vertical wind peak = +0.7 m/s at 0.39 h. same time as attenuation peak Figs. 6.6.4(a), 6.6.5, 6.6.6	Rainrate is ≅ const. Attenuation correlated with vertical wind peak. Figs. 6.6.4(b), 6.6.5 and 6.6.6	4
T_6 0.45-0.54 h	Generally higher than JOD Fig. 6.6.17	JOW, 1	Decreasing from +0.9 to 0, up to 0.52 hrs ≅ time of rain peak Fig. 6.6.4(a)	Higher than JOW and vert. wind = 1 m/s at high rainrates.	3 before and during rain peak.
T_7 0.54-0.63 h	Variable (see comments) Fig. 6.6.19	Similar to JOD, 1 Many more small drops than T_8 Fig. 6.6.20	Generally decreasing after a period of upward wind Fig. 6.6.4(a)	See comments	3,7 Disdrometer measured rainrates lower than indicated by raingauges. Fig. 6.6.5 shows higher attenuation during 0.59-0.62 due to small drops

. . . continued

Period	Measured Attenuation Compared to Standard Predictions	Measured Drop Distribution	Vertical Wind During Rain	Data is in Approximate Agreement with Predictions for:	Comments
T_8 0.63-0.66 h	JOT Fig. 6.6.21	Similar to JOT, 1. Many fewer small drops than T_7 Fig. 6.6.22	Vertical wind negative	JOT and zero vertical wind	7
T_9 0.66-0.73 h	Between JOW and JOT Fig. 6.6.23	Similar to JOW, 1. Fig. 6.6.24	Vertical wind increasing from $\cong -0.75$ m/s to $\cong 0$ and then negative again Fig. 6.6.4(a)	Varied between JOW and zero vert. wind and JOW and vert. wind = +1.0 m/s	

Table 6.6.1 Summary of Attenuation Data for 81.11.30.22, 22:46-23:30

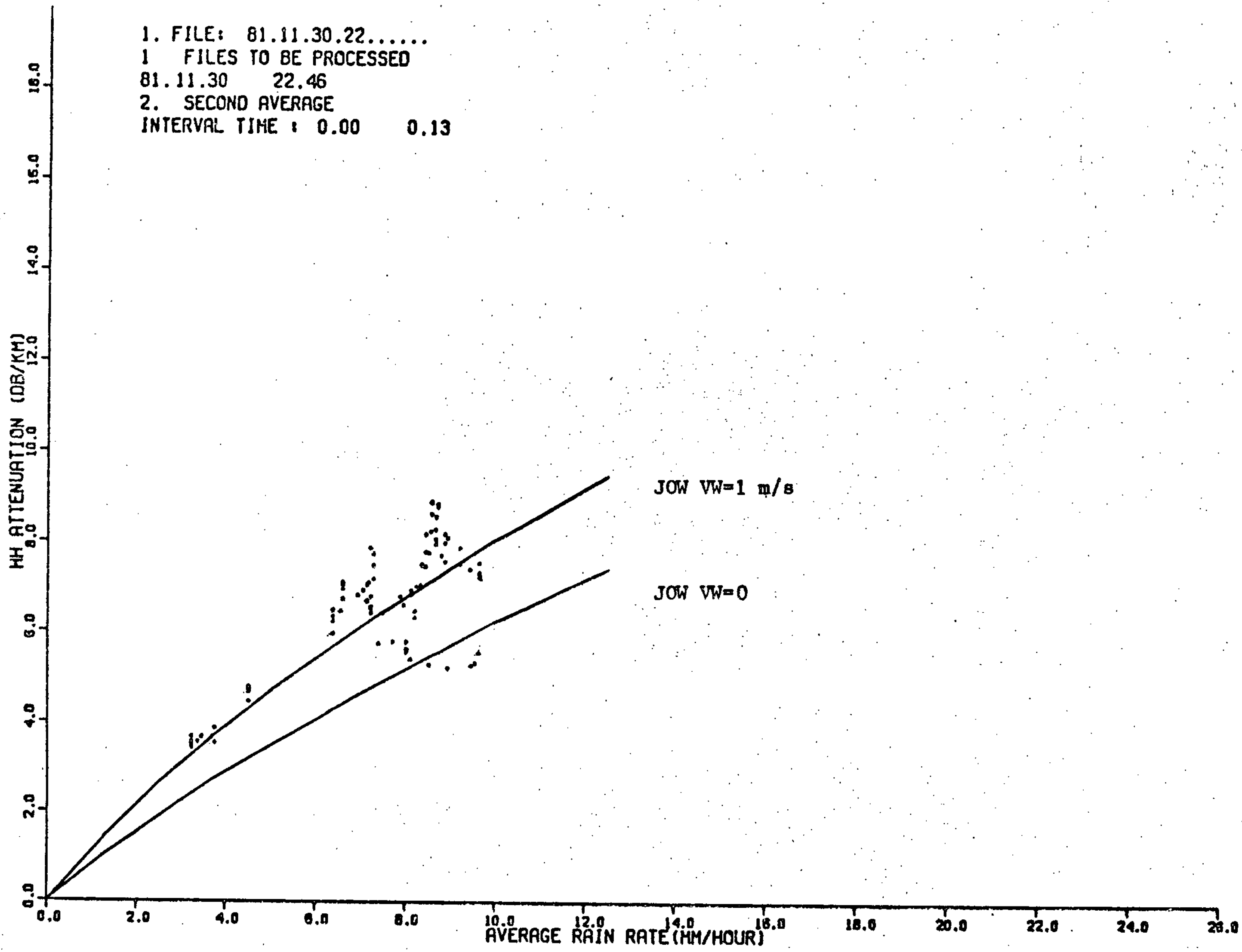

Fig. 6.6.7. CPA during T_1.

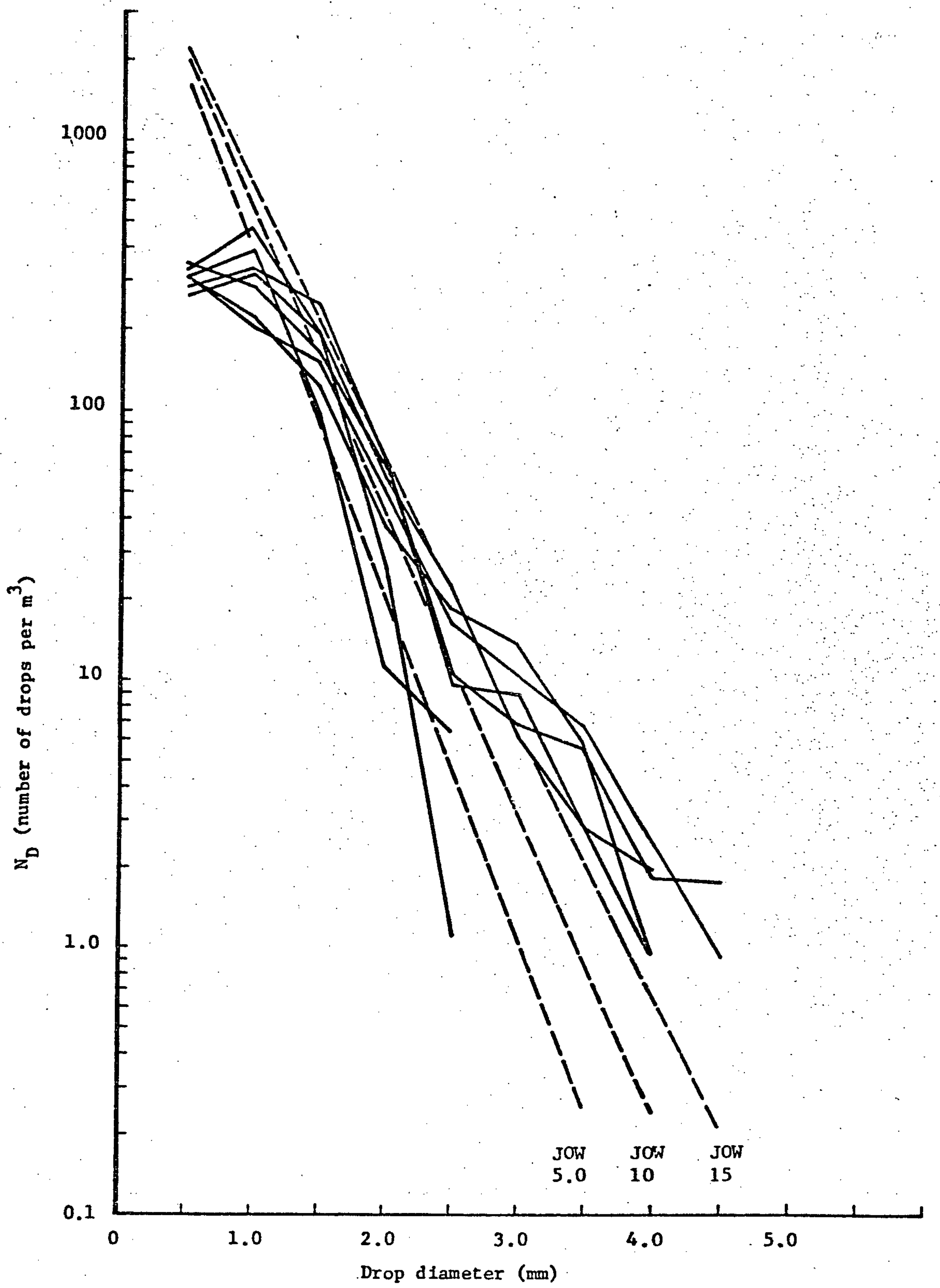

Fig. 6.6.8. Drop distributions for T_1.

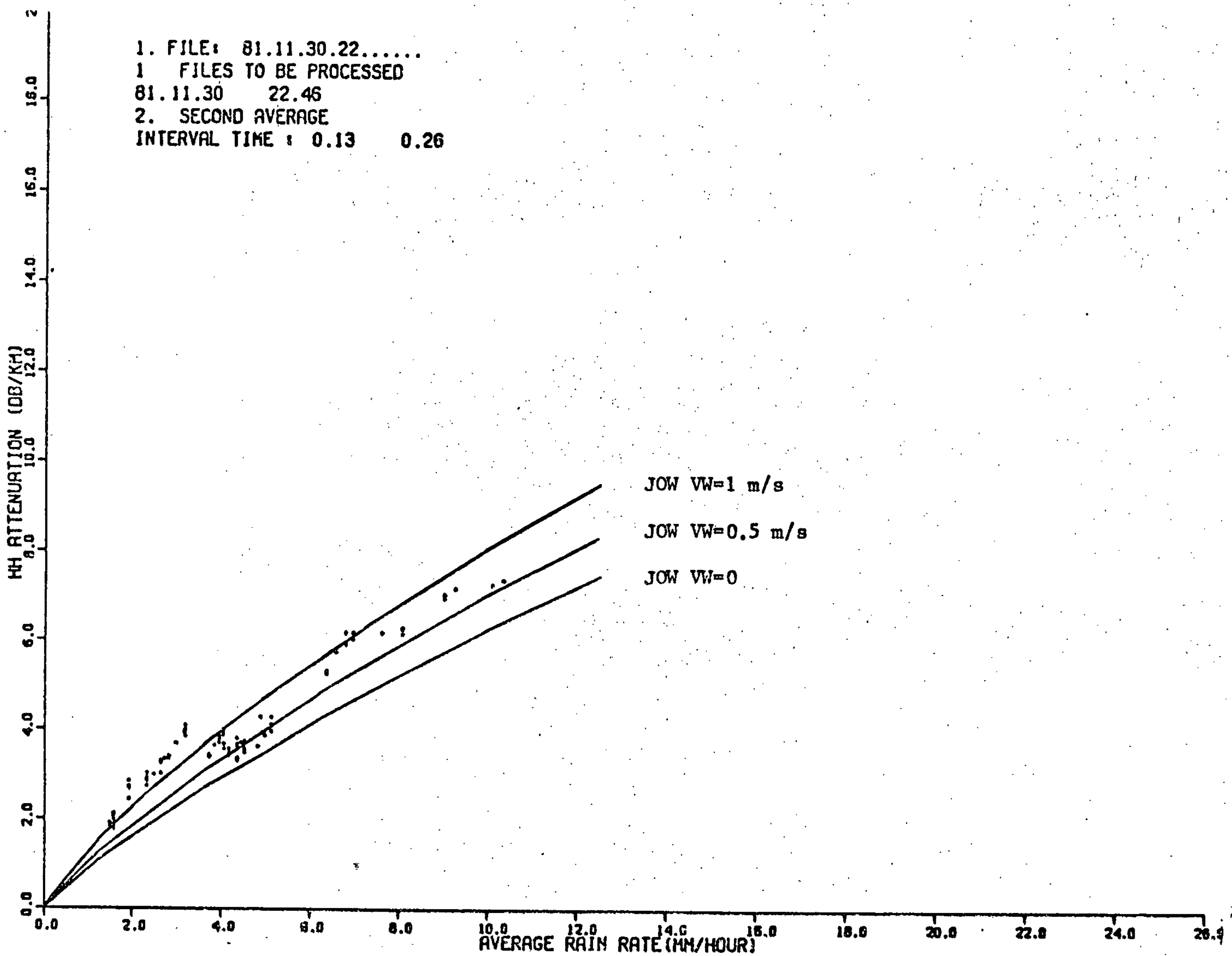

Fig. 6.6.9. CPA during T_2.

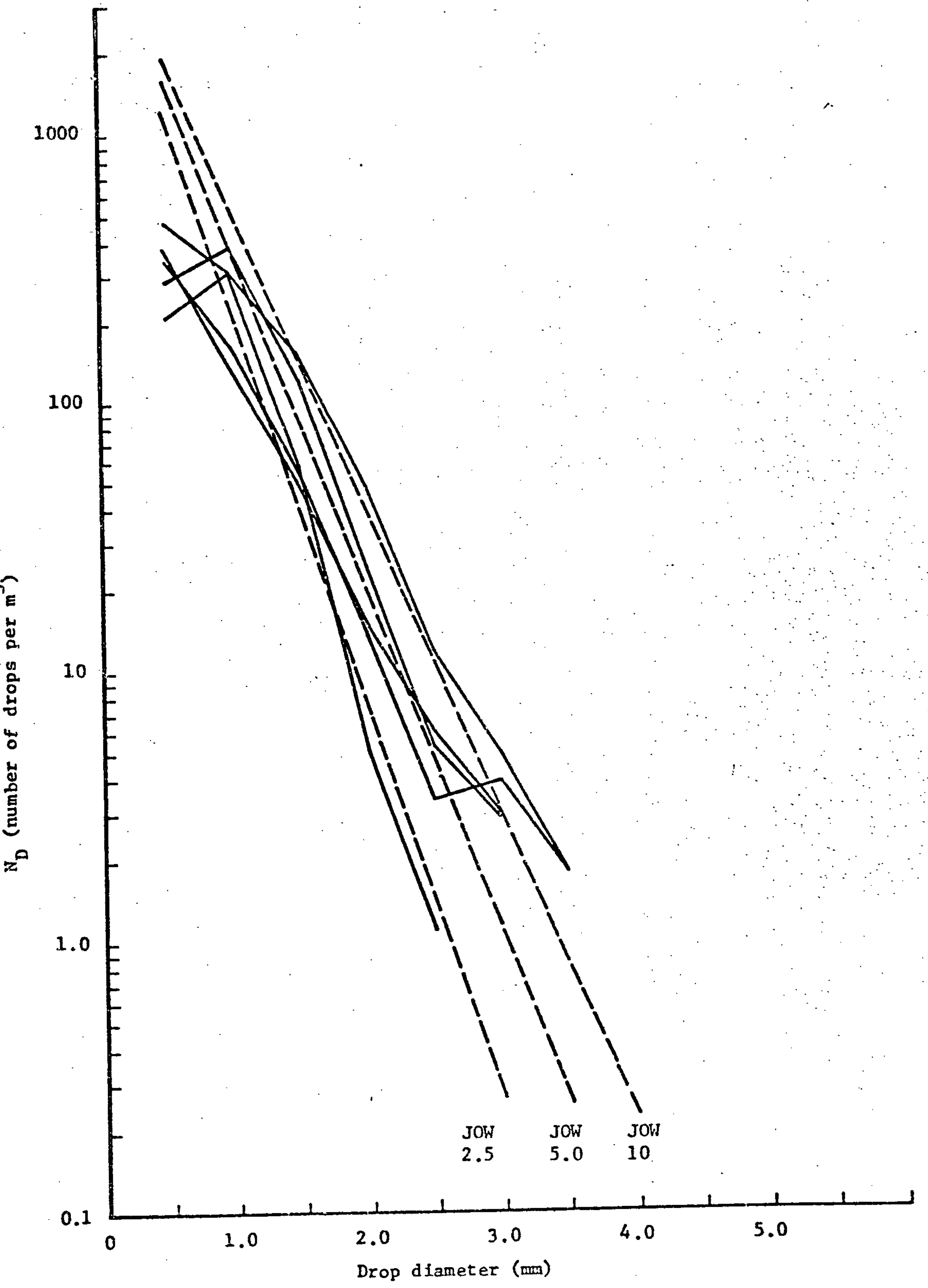

Fig. 6.6.10. Drop distributions for T_2.

6.6.4(a). During the higher rainrates the attenuation agrees with the modified prediction for the JOW distribution and a vertical wind velocity between +0.5 and +1.0 m/s.

6.6.1.3 Attenuation During T_3, 0.26-0.31 h

During T_3, the rainrate was constant but the attenuation, Fig. 6.6.11, varied from much lower to much higher than the standard JOW predictions. This is due to the increasing vertical wind, which peaks at +1.0 m/s near 0.28 h at the same time as the attenuation increase in Fig. 6.6.5. The vertical wind effects are pronounced because of the relatively large number of small drops during this period, Figs. 6.6.4(a) and 6.6.12.

6.6.1.4 Attenuation During T_4, 0.31-0.37 h

The CPA during T_4 generally agreed with predictions for the JOW distribution except for the 2-3 mm/h rainrates during the leading edge of the rain cell, Figs. 6.6.5, and 6.6.13. These higher attenuations are the result of the decreasing vertical wind up to 0.34 h which occurred after a period of upward flow. The drop size distribution was quite variable during this period, Fig. 6.6.14, presumably due to the rapidly changing rain conditions as this small cell passed over the disdrometer.

6.6.1.5 Attenuation During T_5, 0.37-0.45 h

Period T_5 is an excellent example of a vertical wind induced change in attenuation. The rainrate during this period was almost constant but the

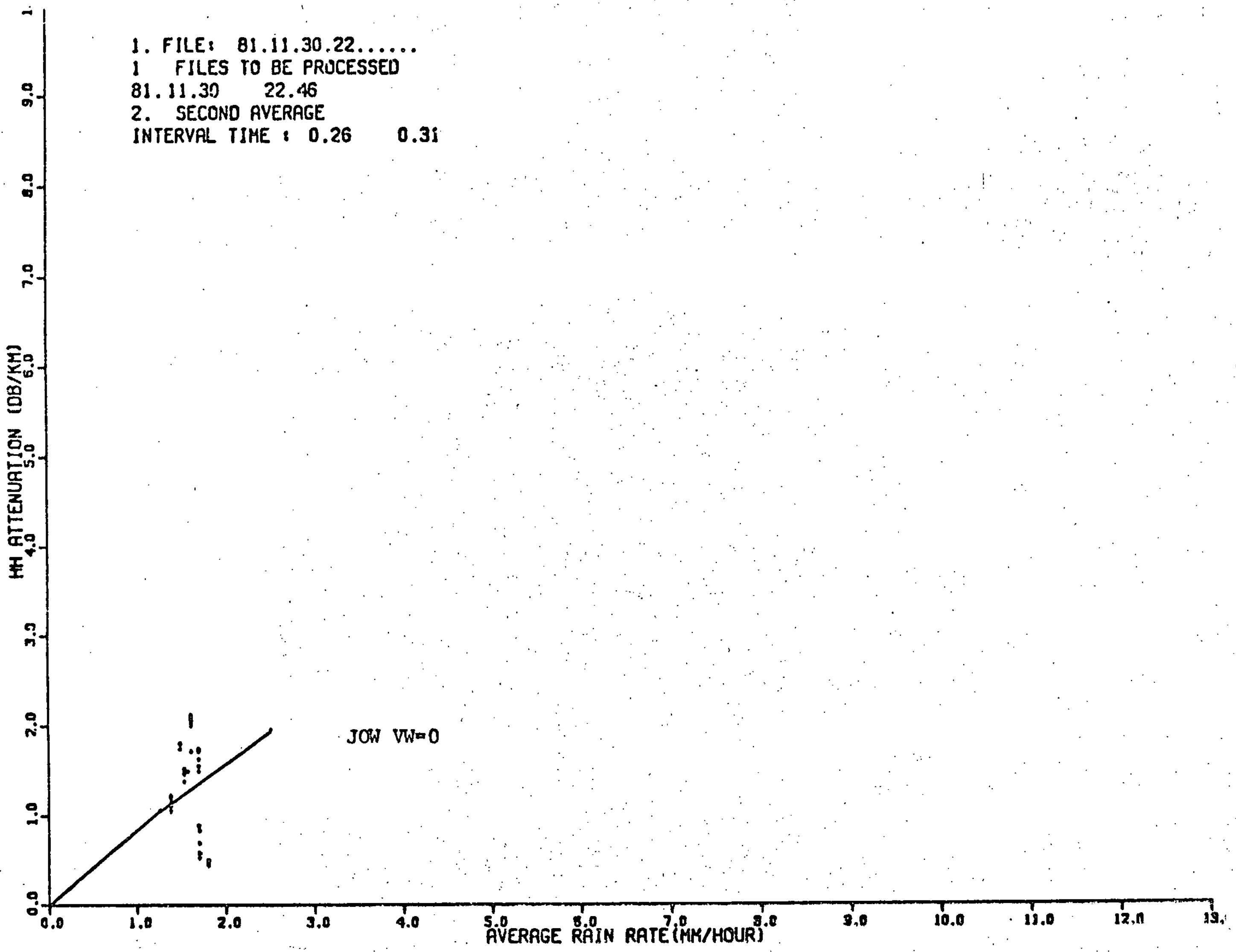

Fig. 6.6.11. CPA during T_3.

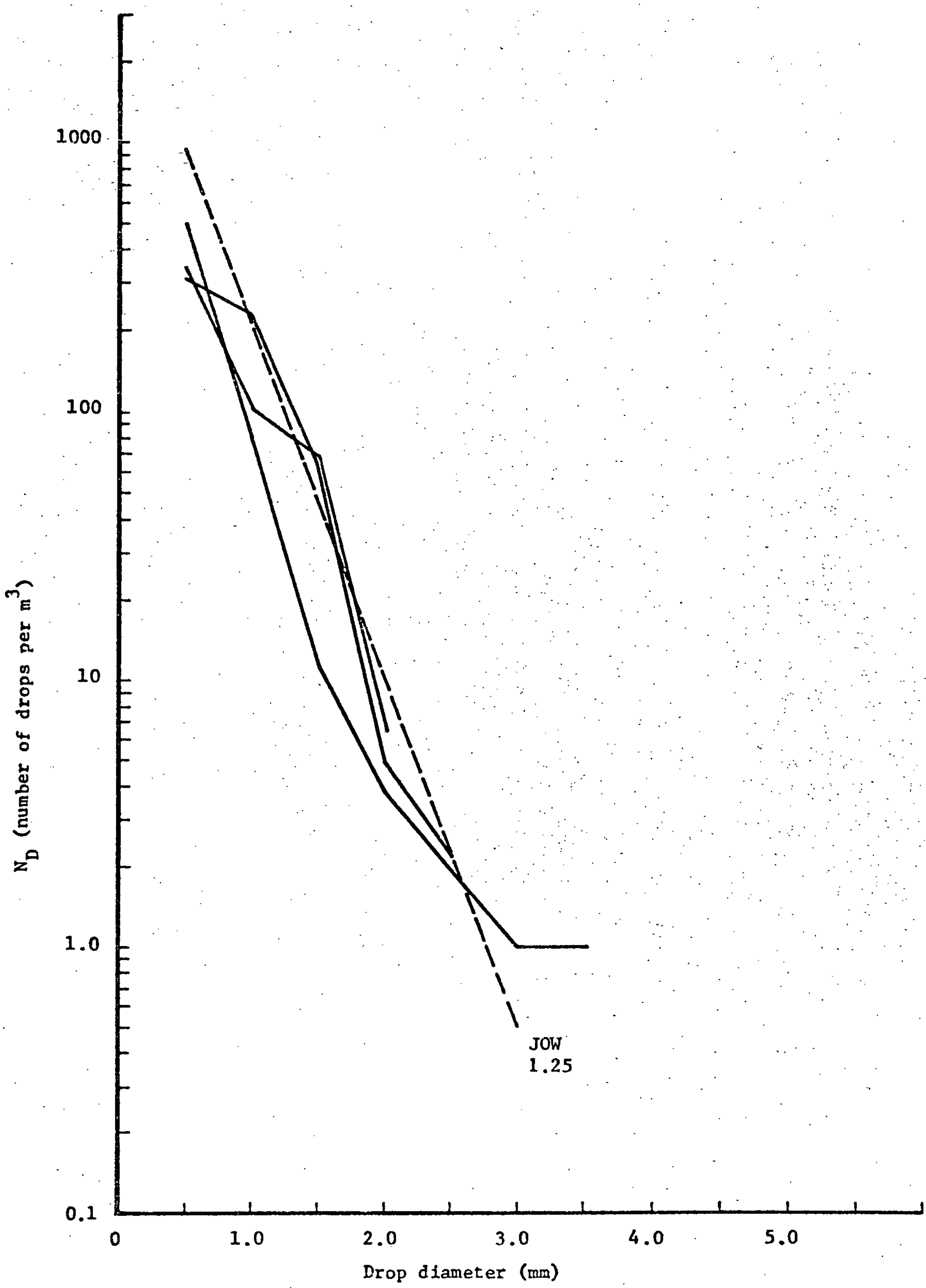

Fig. 6.6.12. Drop distributions for T_3.

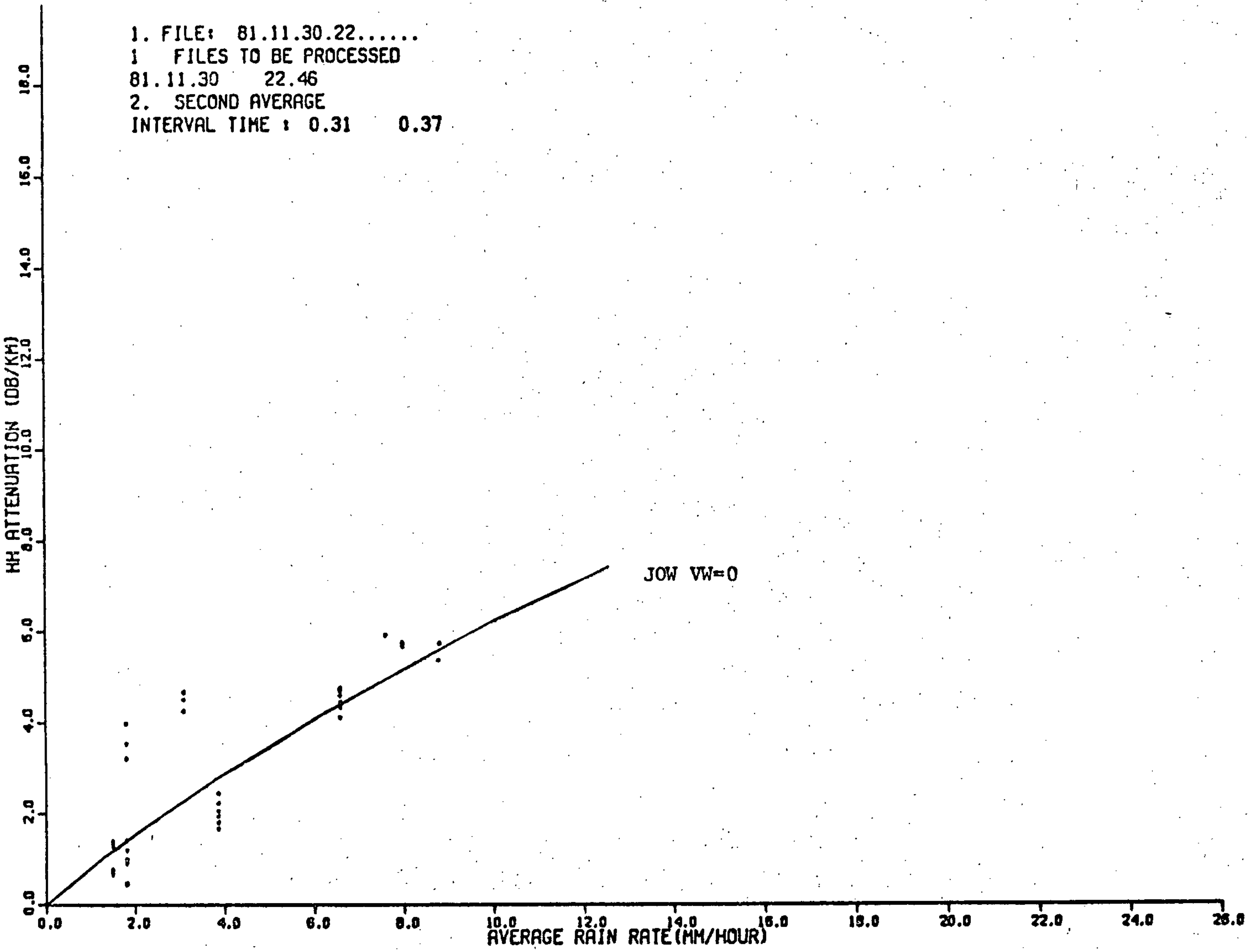

Fig. 6.6.13. CPA during T_4.

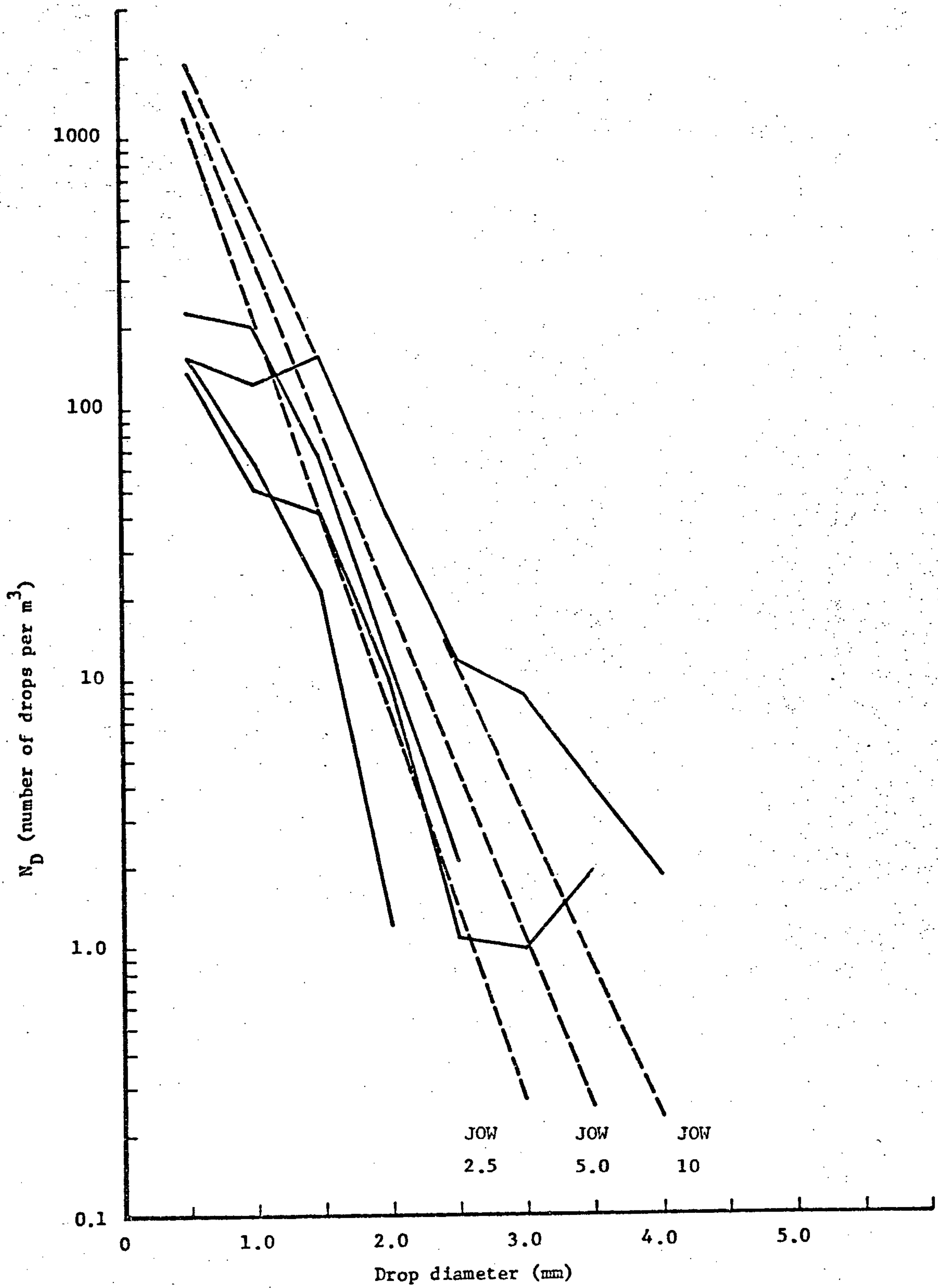

Fig. 6.6.14. Drop distributions for T_4.

attenuation varied over a wide range, Fig. 6.6.15. This variation in attenuation, Fig. 6.6.5, is well correlated with the vertical wind peak between 0.35-0.42 h, Fig. 6.6.4(a). The attenuation variation with vertical wind was very pronounced for this period because of the relatively large number of small drops which were observed at the trailing edge of this cell, Fig. 6.6.16.

6.6.1.6 Attenuation During T_6, 0.45-0.54 h

The CPA during T_6, Fig. 6.6.17 was generally higher than the JOD predictions. This is believed to be due to the decreasing vertical wind velocity up to 0.52 h. The drop distributions, Fig. 6.6.18, however, show a smaller number of small drops at the higher rainrates. This is believed to be due to the previously discussed delay in the disdrometer data under similar conditions (ref. Section 6.2.1.3). The wide range of drop sizes is again thought to be associated with the rapidly changing rain conditions during the passage of this cell.

6.6.1.7 Attenuation During T_7, 0.54-0.63 h

During T_7, at the trailing edge of this cell, the wind direction, Fig. 6.6.2, began to change and the vertical wind was at times negative (i.e. downward). The drop size distribution, Figs. 6.6.4(a) and 6.6.20 show an unusually large number of small drops. These small drops could be due to: the generally decreasing vertical wind velocity before and during this period up to 0.59 h and some delayed disdrometer indication of small drops from the preceeding period and/or a general trend to smaller drops at the trailing

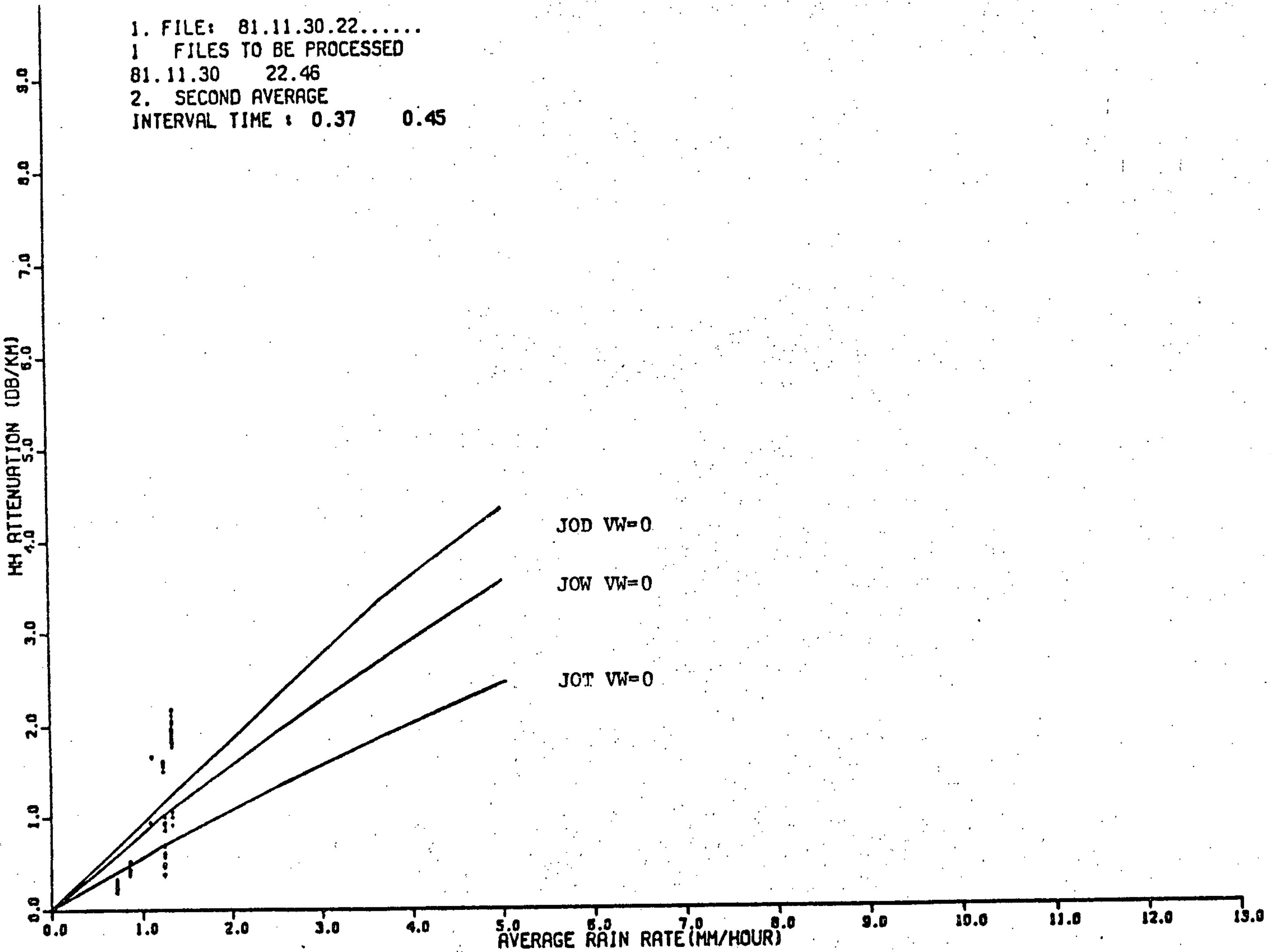

Fig. 6.6.15. CPA during T_5.

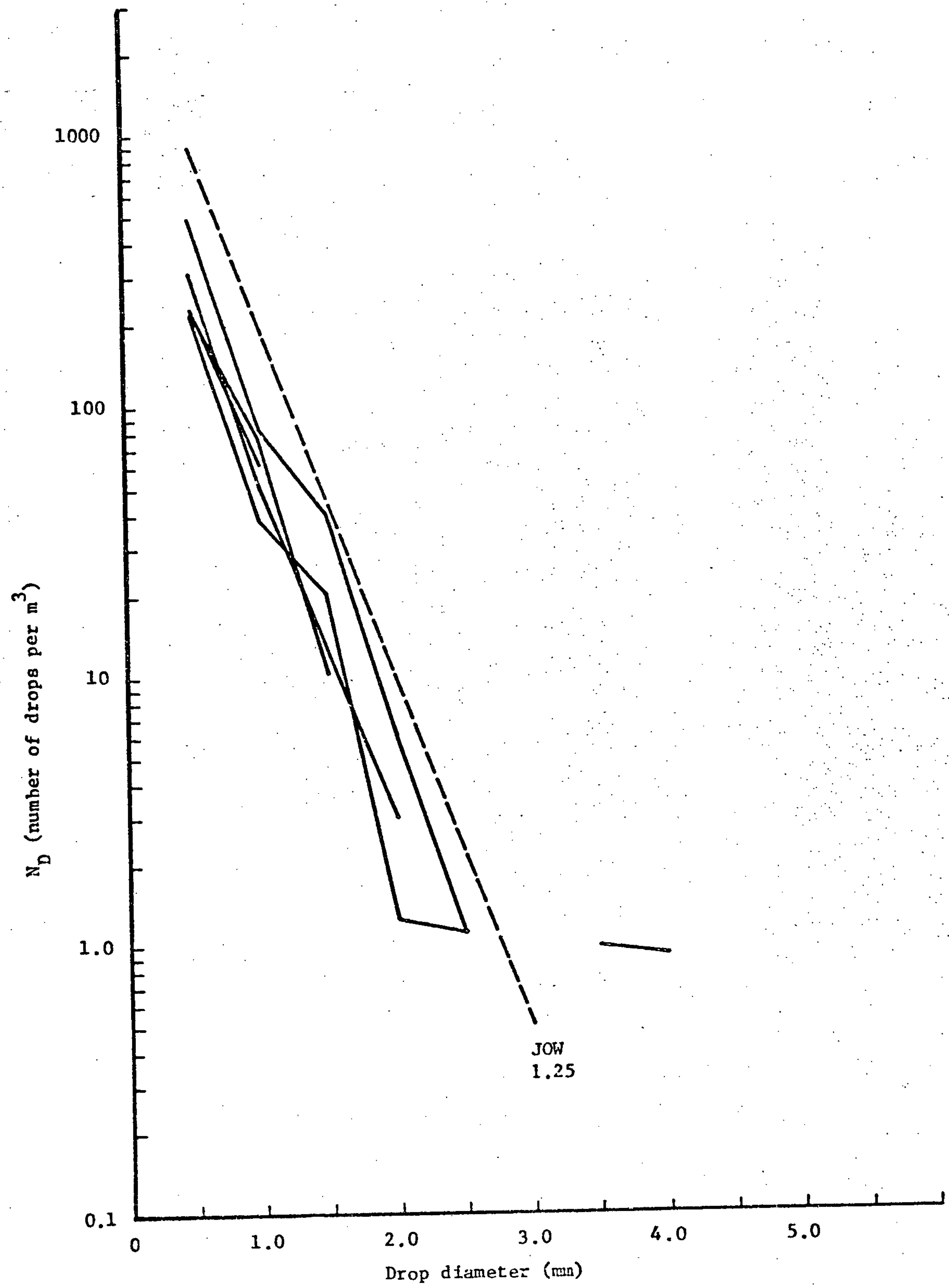

Fig. 6.6.16. Drop distributions for T_5.

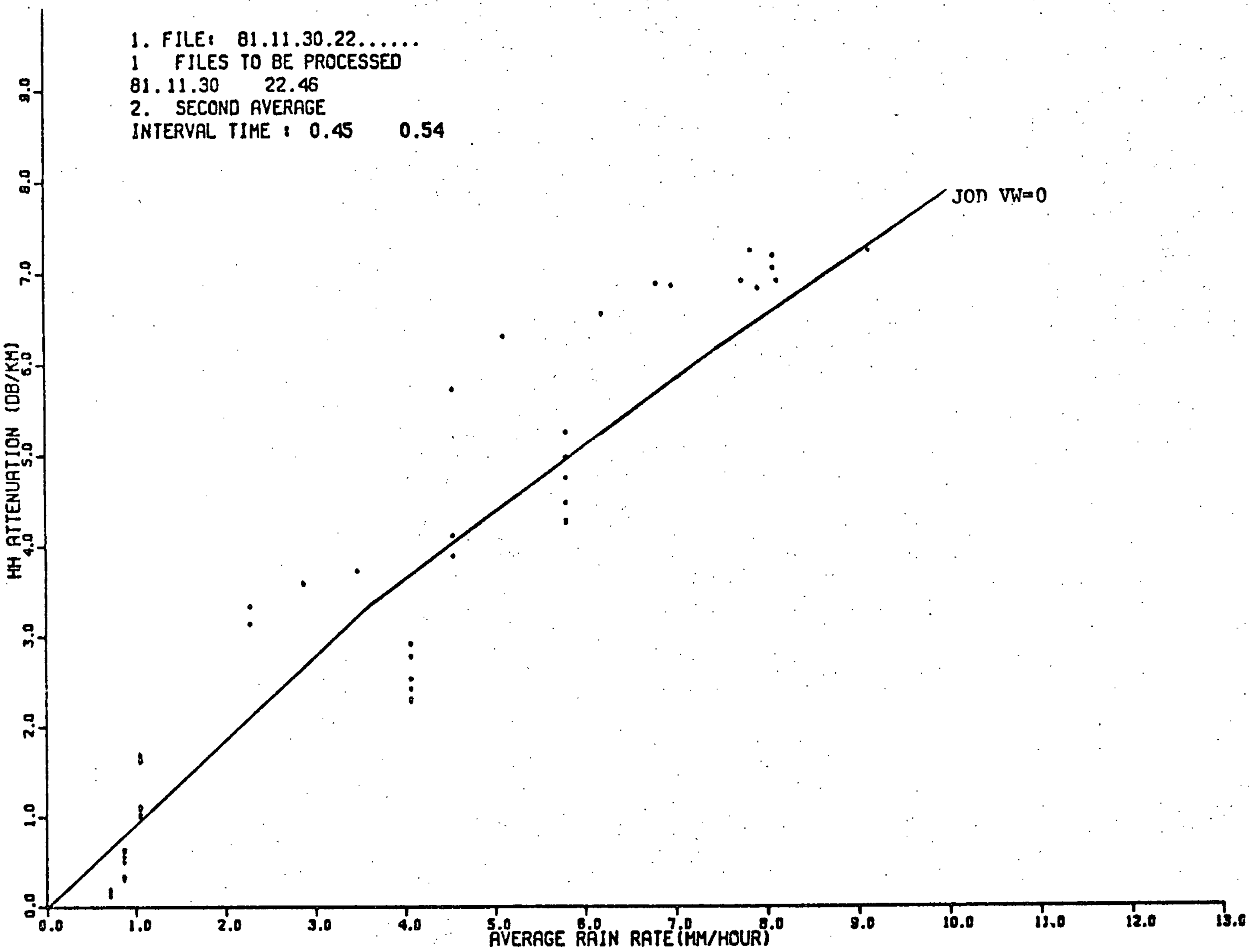

Fig. 6.6.17. CPA during T_6.

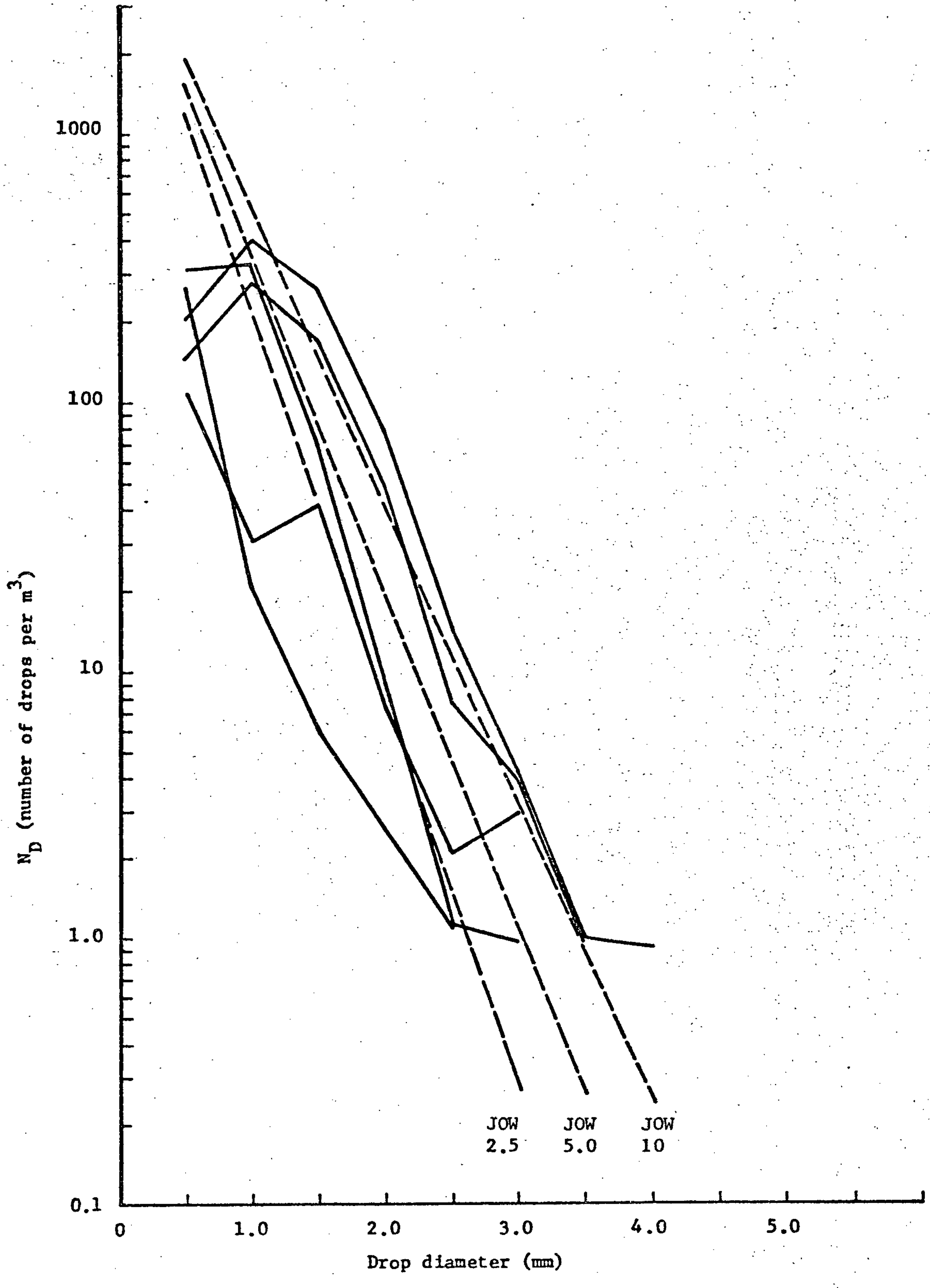

Fig. 6.6.18. Drop distributions for T_6.

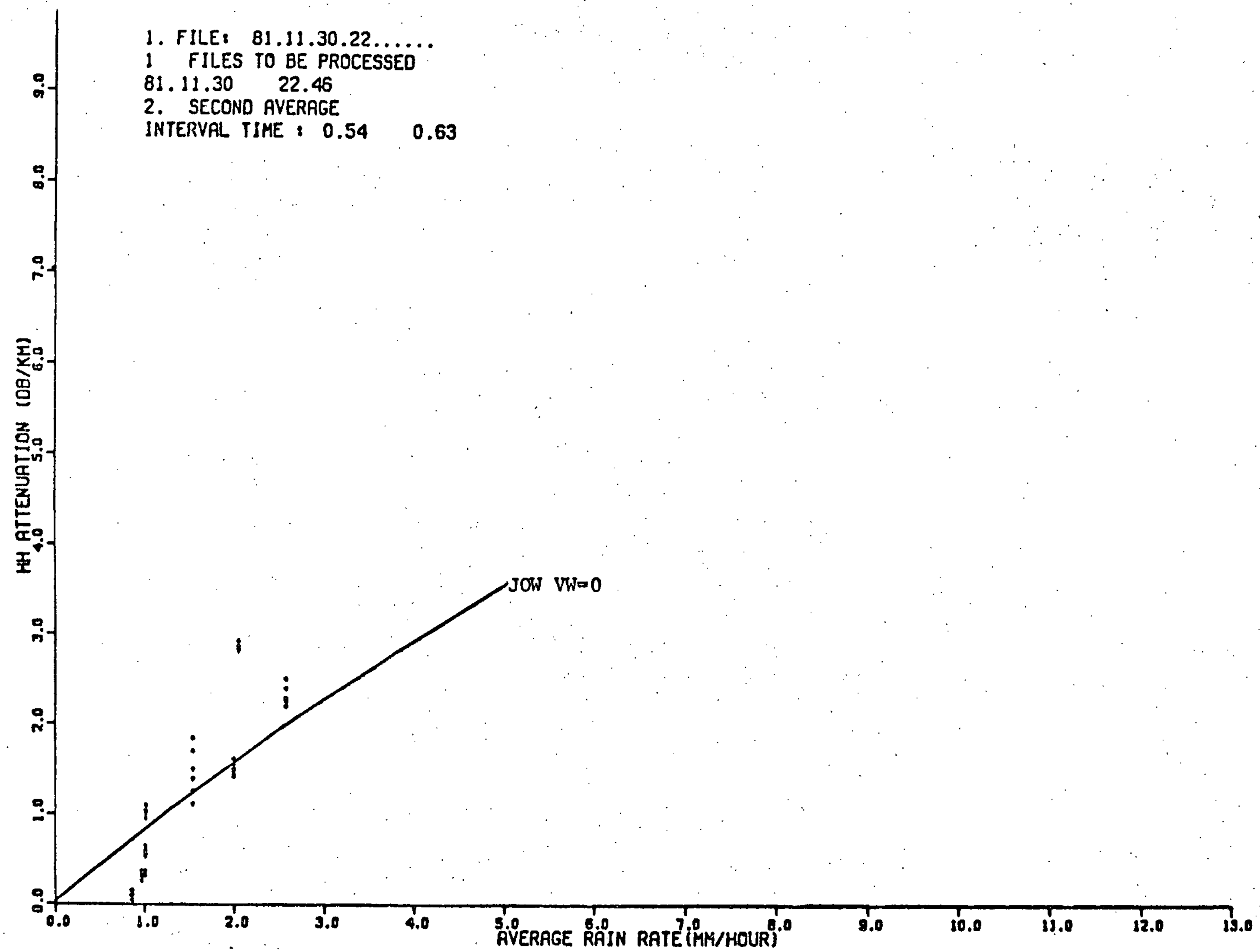

Fig. 6.6.19. CPA during T_7.

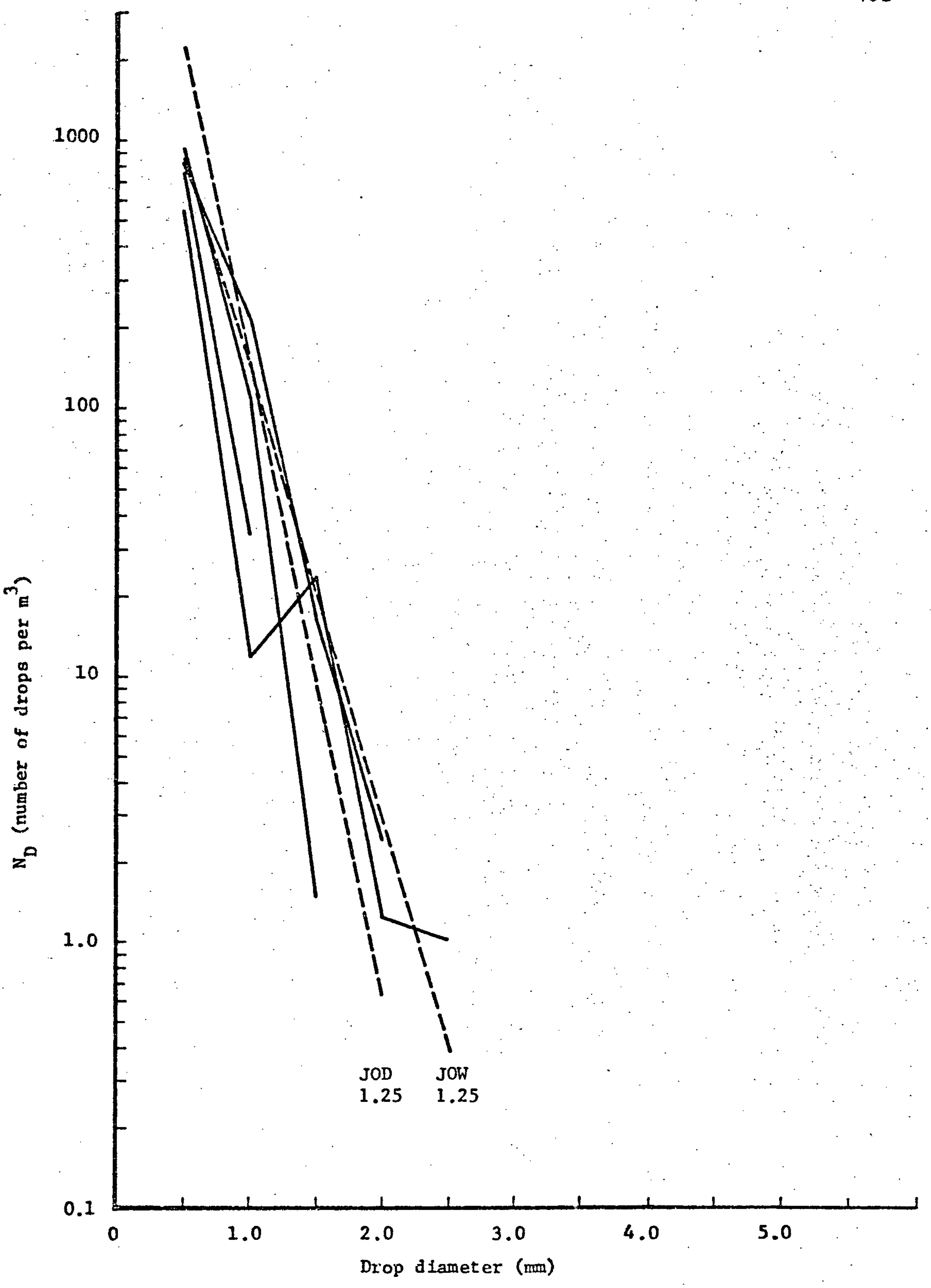

Fig. 6.6.20 Drop distributions for T_7.

edge of these rain cells, as in T_2, T_3 and T_5. The attenuation is not as high as would be expected for this large number of small drops because of the generally negative wind velocity.

6.6.1.8 Attenuation During T_8, 0.63-0.68 h

During T_8, the vertical wind was negative and the drop size distribution changed to conform to the JOT distribution but with even fewer small drops, Fig. 6.6.22. Correspondingly, the CPA was very low and generally agreed with predictions for the JOT distribution.

6.6.1.9 Attenuation During T_9, 0.66-0.73 h

During T_9, the attenuation, Fig. 6.6.23 and drop distributions, Fig. 6.6.24 have quickly changed to be very similar to the first two periods in this file. The drop size distribution is close to JOW and the attenuation varied from the standard predictions for the JOW distribution to slightly higher.

6.6.2 XPD and Differential Attenuation Data for 81.11.30.22

The XPD data for this file will not be analyzed in detail because the results were generally similar to previous periods and because the crosspolar cancellation network had drifted as discussed in Section 6.5.2. The time series uncancelled XPD, Fig. 6.6.25, is included because it shows the XPD reversals observed in other files and a short period of clear weather XPD for comparison.

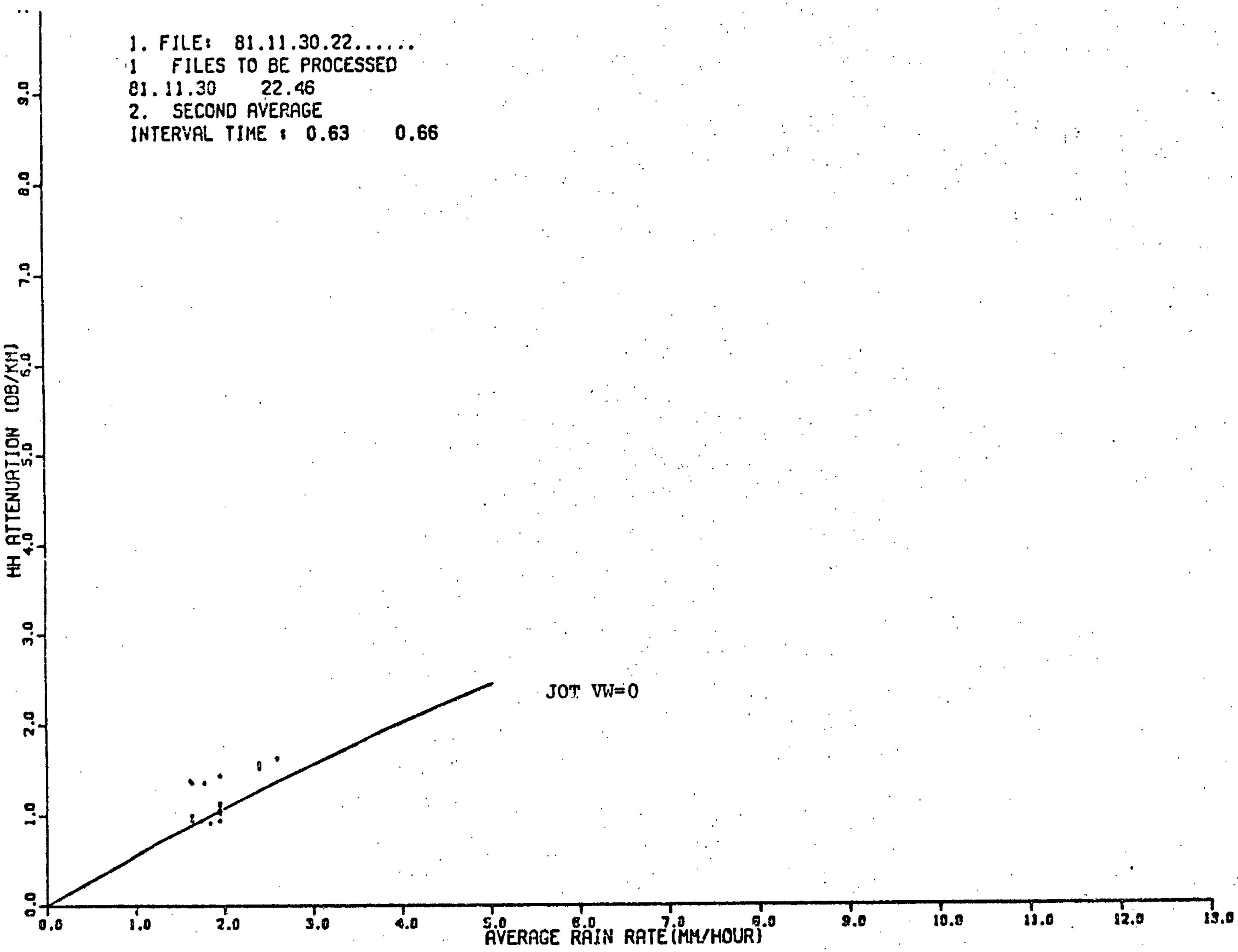

Fig. 6.6.21. CPA during T_8.

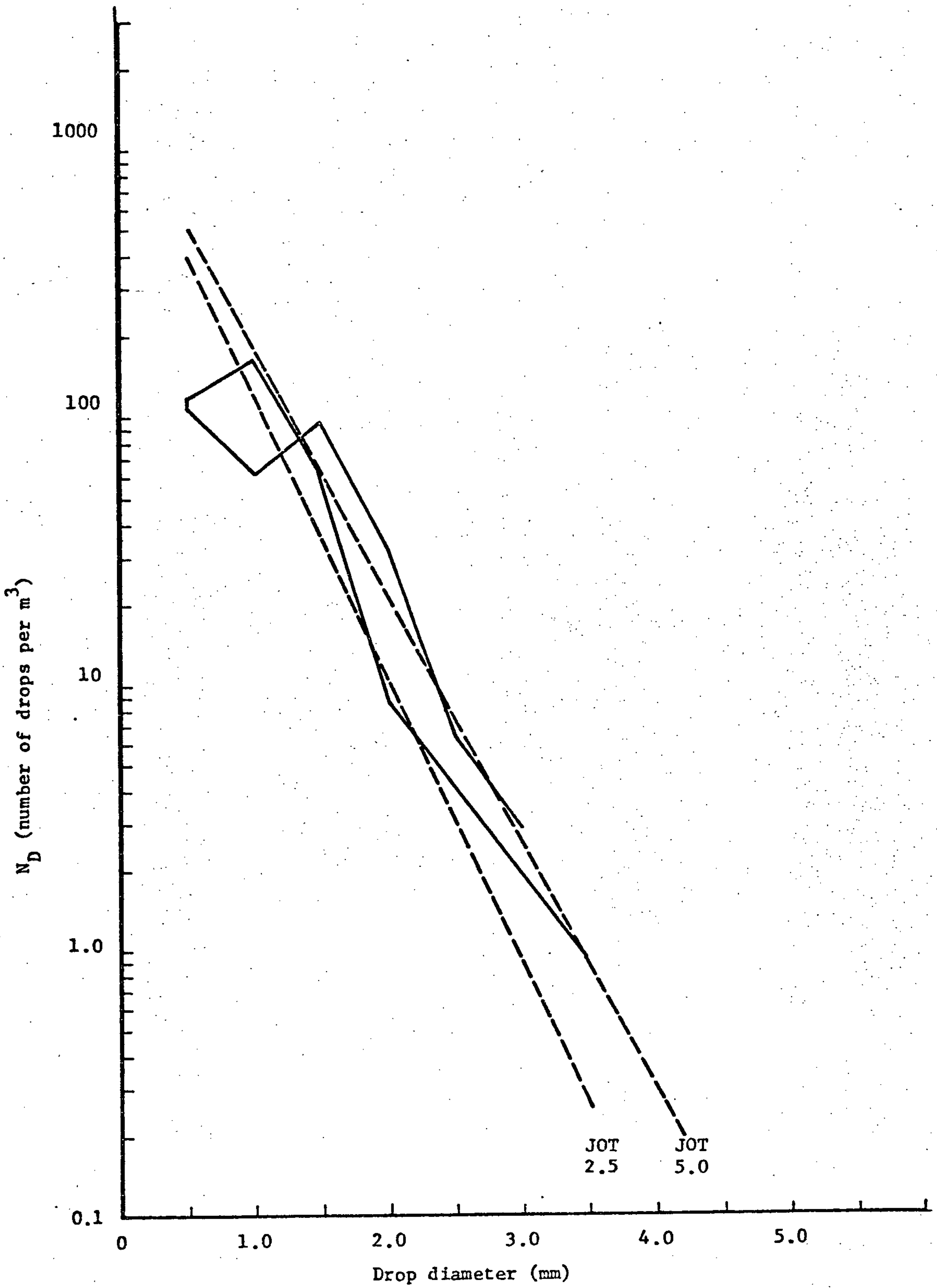

Fig.6.6.22. Drop distributions for T_8.

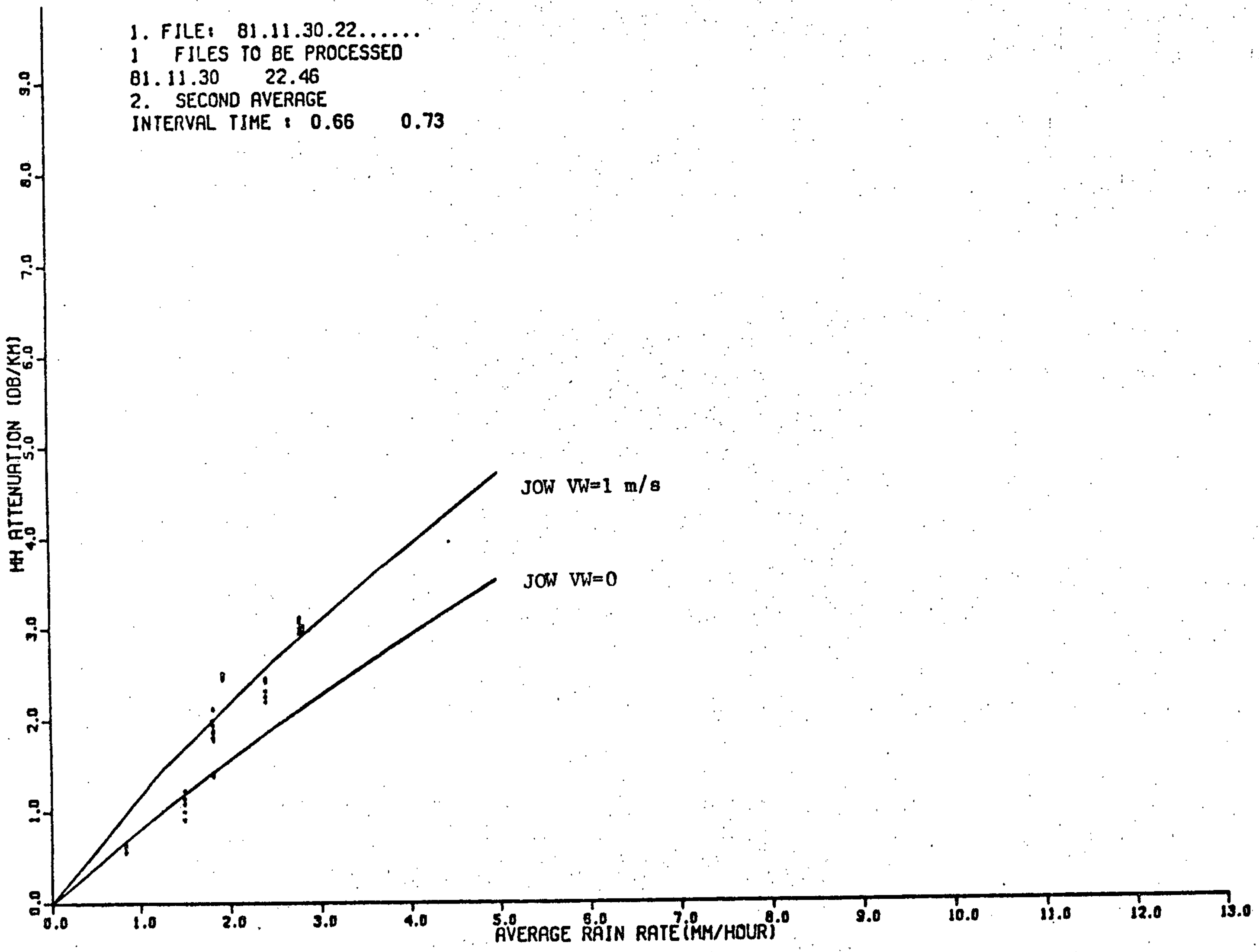

Fig. 6.6.23. CPA during T_9.

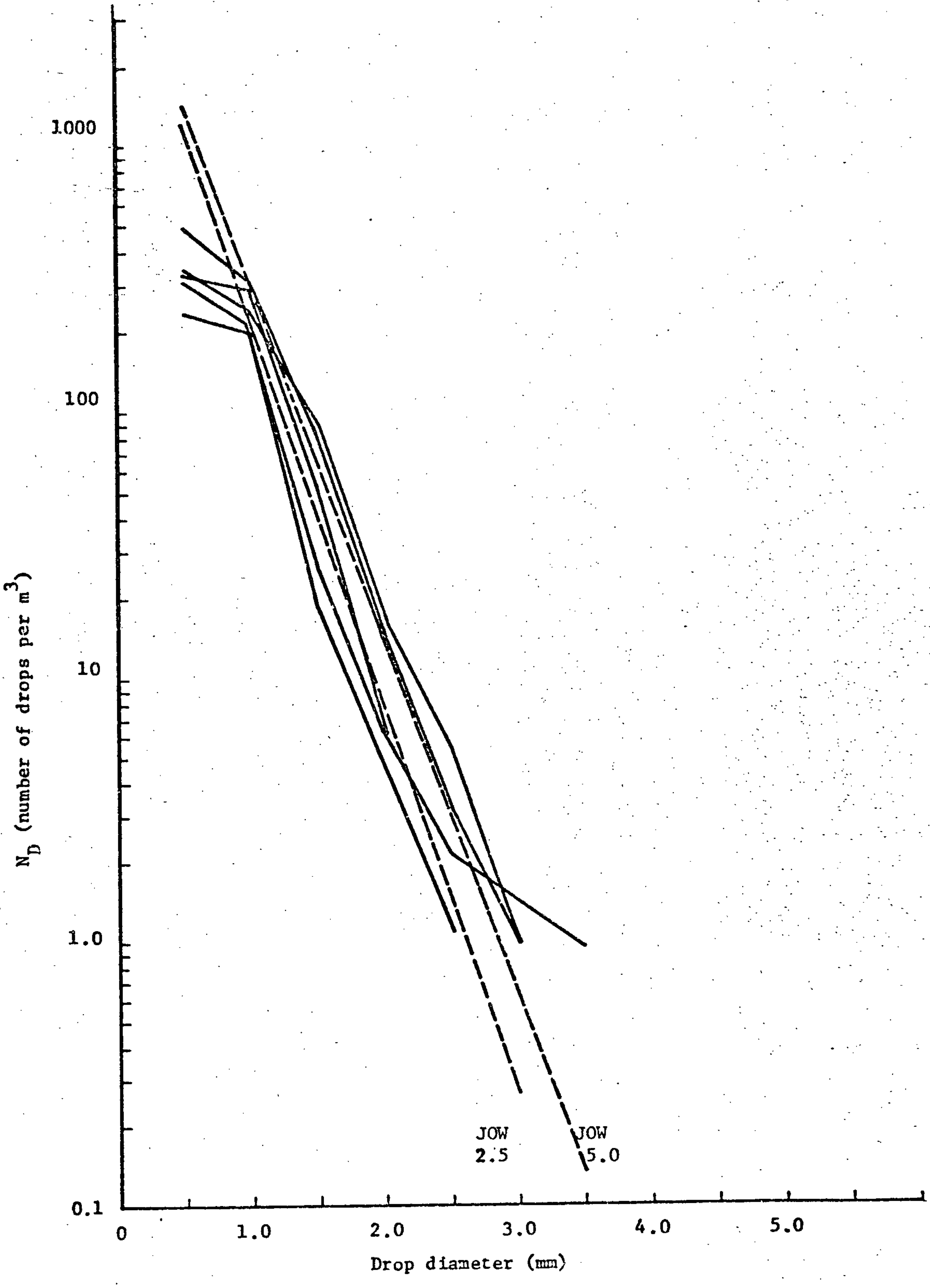

Fig. 6.6.24. Drop distributions for T_9.

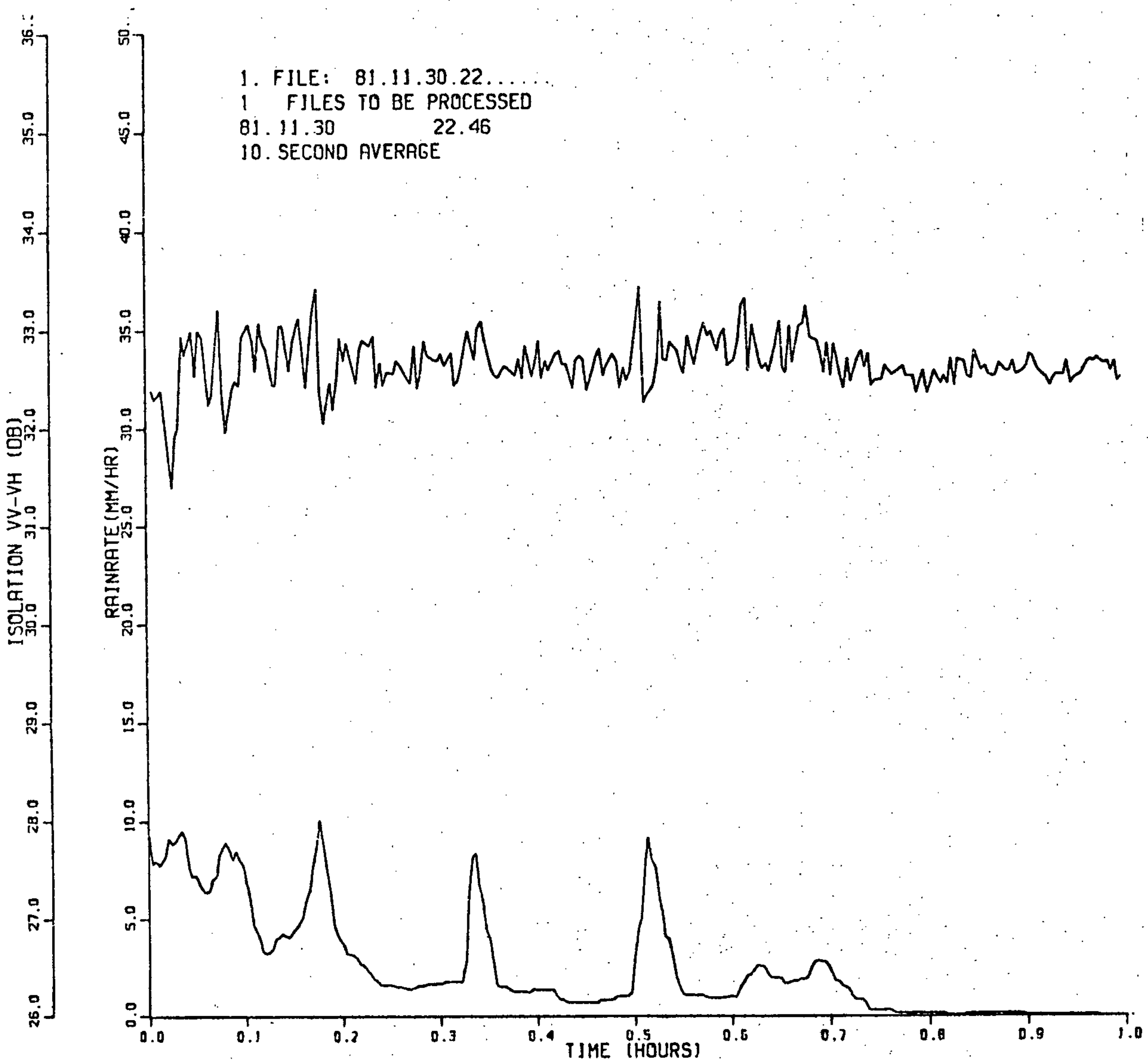

Fig. 6.6.25. XPD for vertical transmitted polarization, for 81.11.30.22.

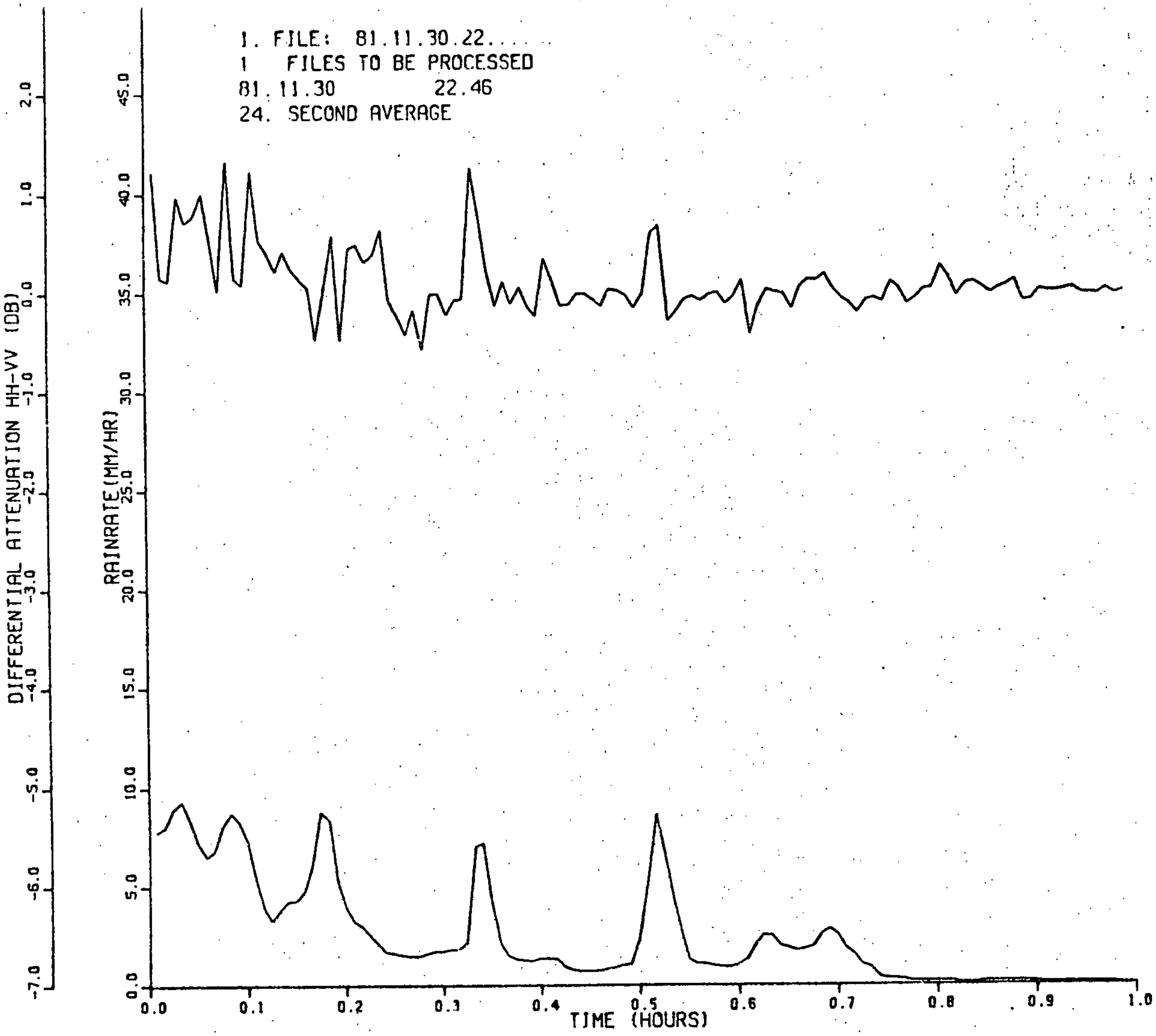

Fig. 6.6.26. Differential attenuation for 81.11.30.22.

Differential attenuation, Fig. 6.6.26, is also similar to previous files, (i.e. includes periods of negative differential attenuation) but in this case a clear weather baseline is also shown. The maximum values of differential attenuation during this file are approximately double (in dB) the values predicted by the theory for similar rainrates.

6.7 Experimental Results for 80.05.22.10

The data interval discussed in this section extends from 10.19 to 11.07 hours on May 22, 1980. Fig. 6.7.1 shows the rainrates recorded along the propagation path. Rainrates during this file varied from 0 to 27 mm/h. This rainstorm was typical of what is commonly referred to as a thunderstorm, i.e. had high peak rainrates and a distinct cellular structure with small cell area. Figs. 6.7.2 to 6.7.4 show the wind directions, horizontal velocity and vertical velocity, respectively. Figs. 6.7.2(a) and 6.7.2(b) give the 2 second and 10 second average wind directions. Two averaging periods for wind direction are included to more clearly illustrate the unusual variability of the measured wind direction. Fig. 6.7.3 shows that the horizontal wind velocity was low to moderate over this period. The vertical wind velocity, shown in Fig. 6.7.4, was roughly half of the horizontal velocity, an unusually large proportion. The vertical wind direction at the anemometer location is totally downward. These variations in wind direction and large downward vertical wind are again believed to be due to the passage of a cold front as discussed in Section 6.6.

Fig. 6.7.1 clearly shows the raincells moving with some velocity components along the raingauge network from south to north. This has

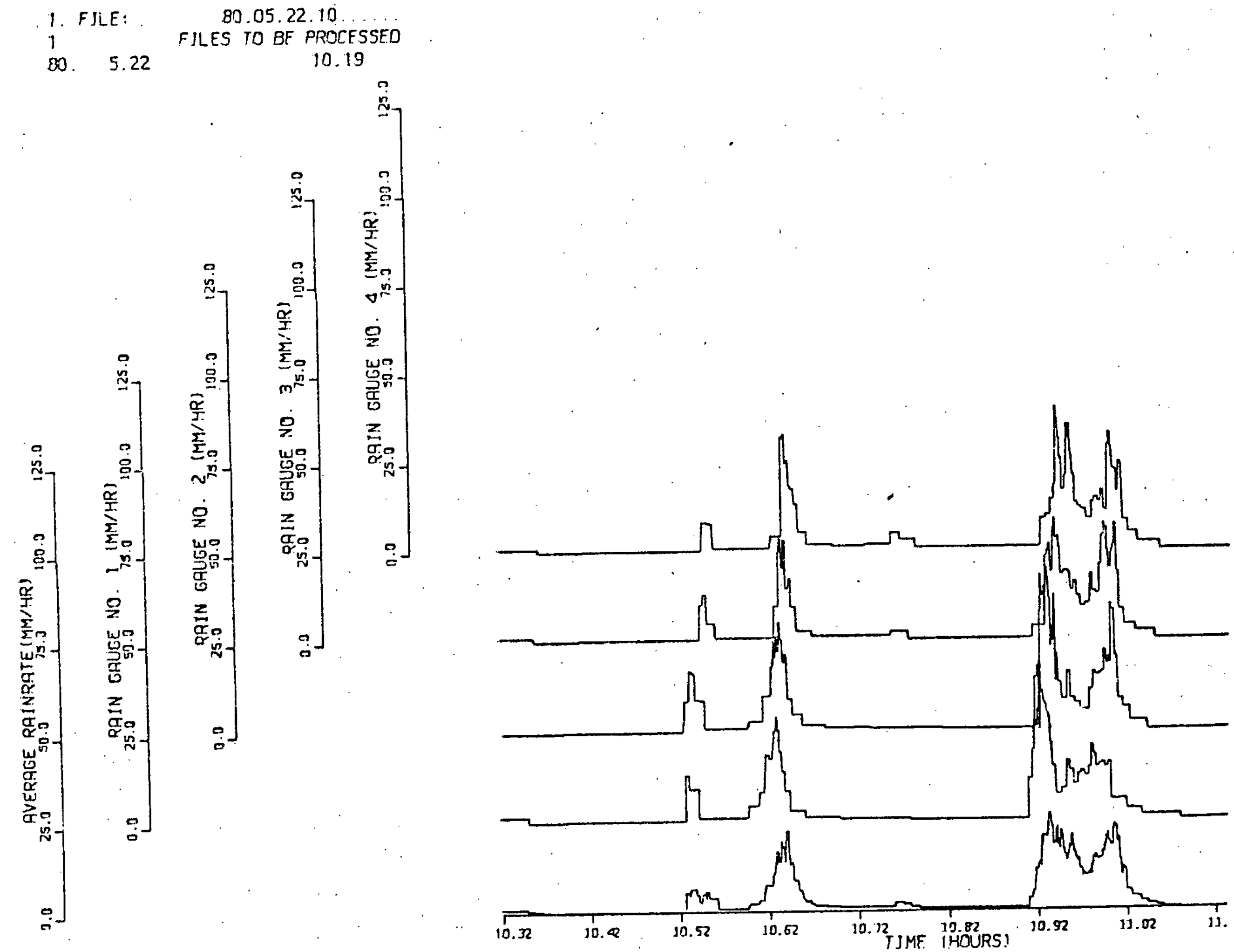

Fig. 6.7.1. Rainrates for 80.05.22.10.

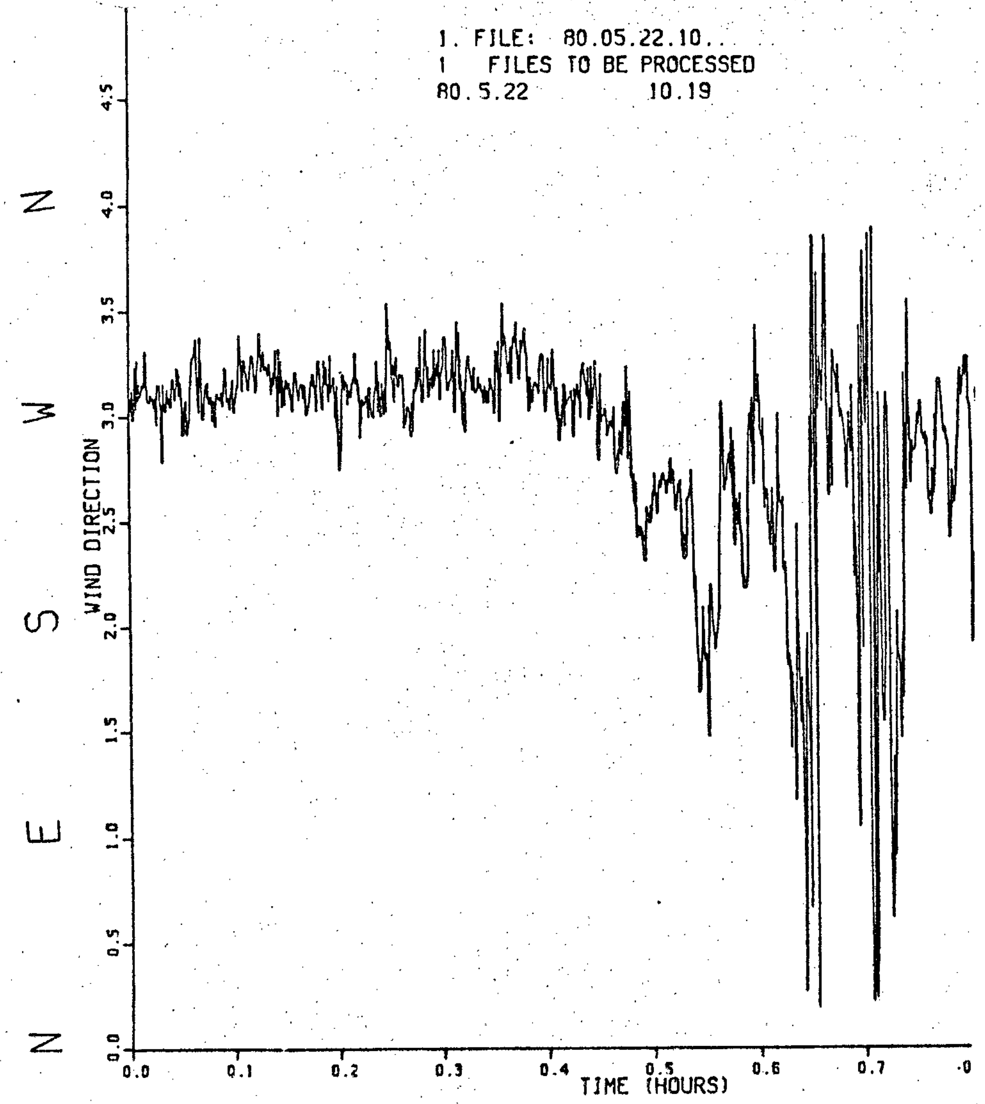

Fig. 6.7.2(a). Wind direction 2 s avg. for 80.05.22.10.

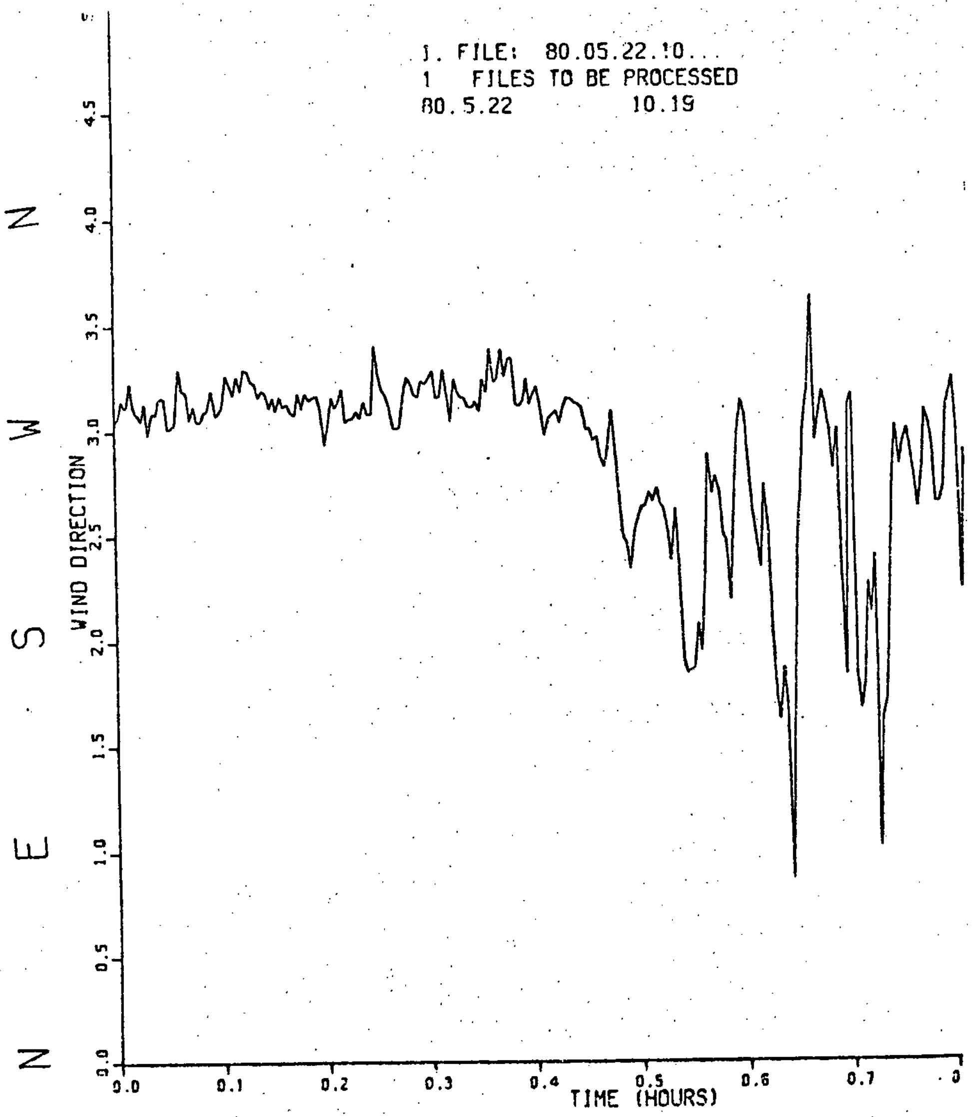

Fig. 6.7.2(b). wind direction 10 s avg. for 80.05.22.10.

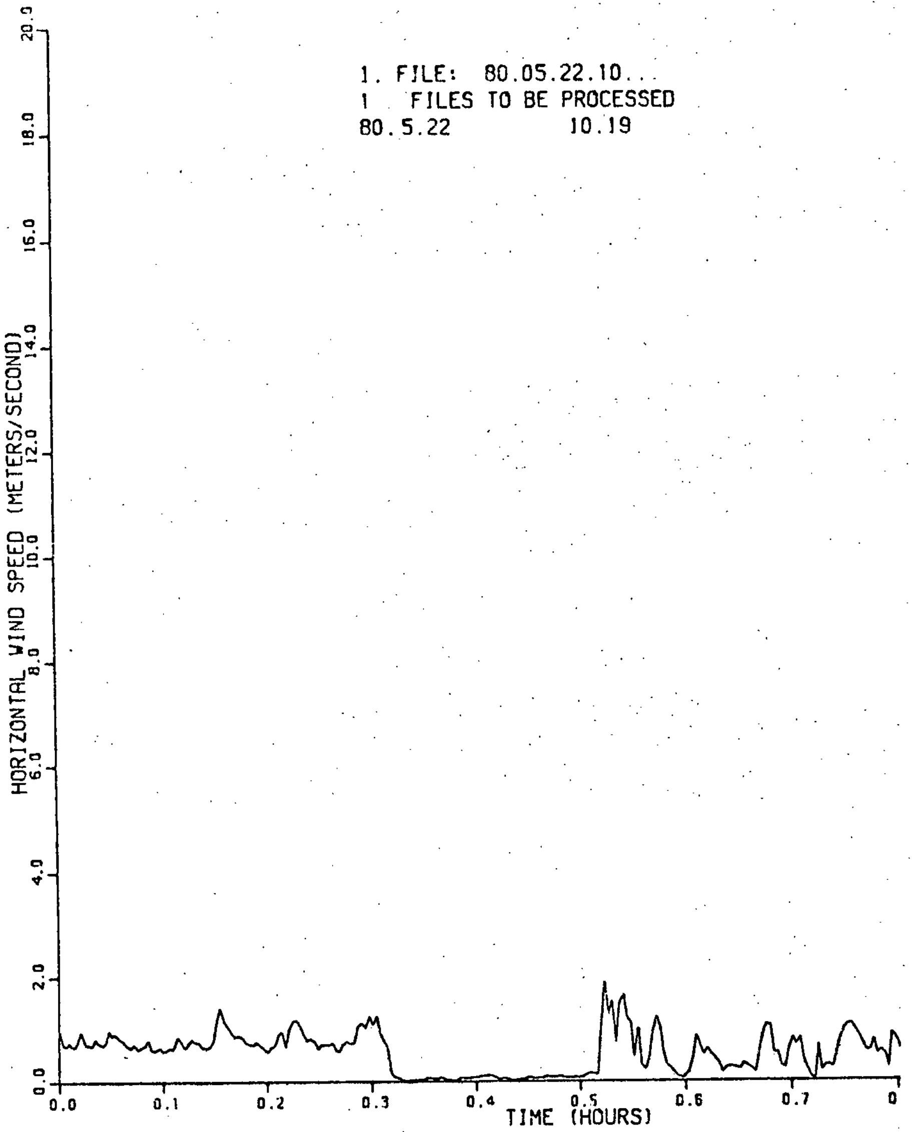

Fig. 6.7.3. Horizontal wind velocity 10 s avg. for 80.05.22.10.

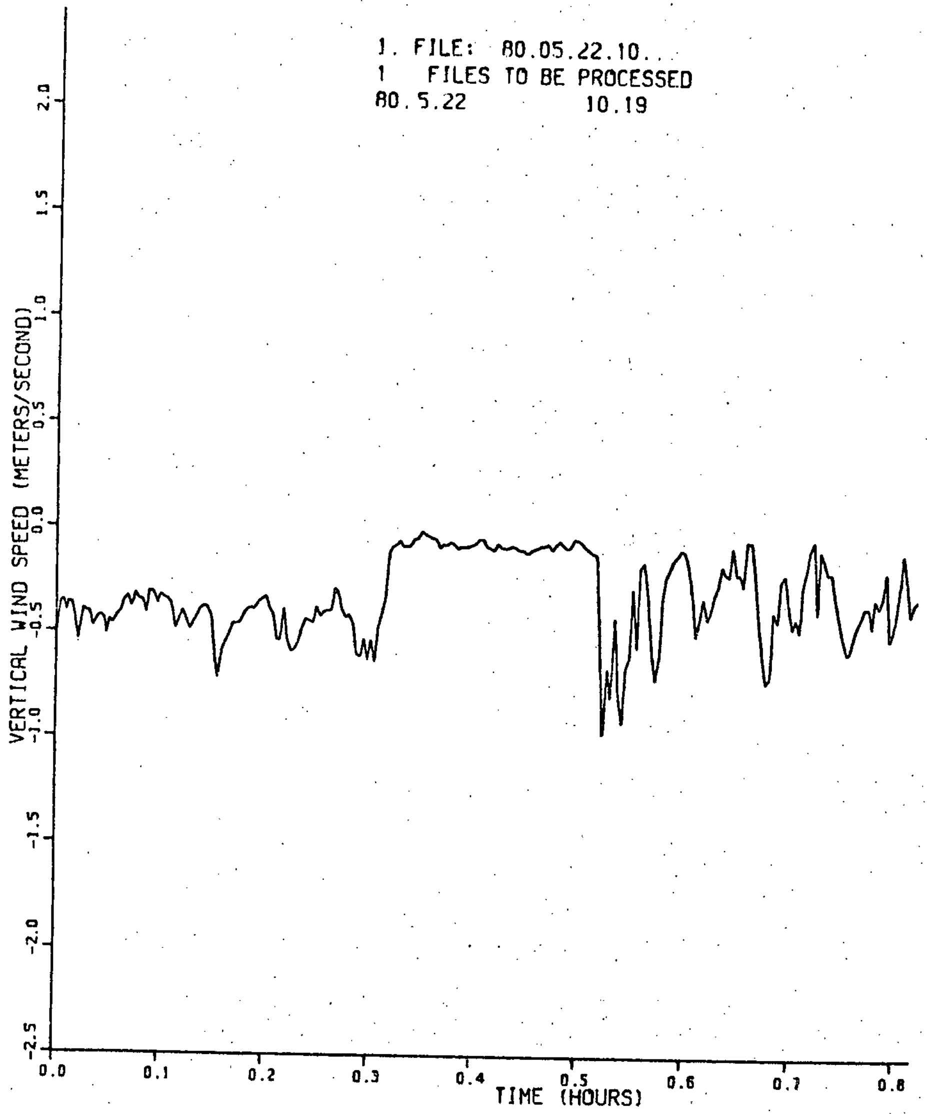

Fig. 6.7.4. Vertical wind velocity, 10 s avg. for 80,05.22.10.

occurred even though the measured wind direciton is mainly from the west. However, the variability of wind direction measured by the anemometer leaves considerable doubt as to its applicability to measuring wind direction at the height of the raincell. The time taken for the raincells to travel the approximately 0.65 km across the raingauge network from raingauge 1 to 4 is estimated as 1.0 to 1.5 minutes. This translates to a northerly cell velocity component approximately 7-11 m/s (26-40 km/h).

Time series plots of the four signal levels with 10 s averages are shown in Figs. 6.7.5 and 6.7.6 for horizontal and vertical transmitted polarizations, respectively.

6.7.1 Attenuation Data for 80.05.22.10

This data file contains examples of very low attenuation at the leading edge of a storm and attenuations lower than the standard predictions for the JOT distribution as a result of downward vertical wind velocities. A summary of the attenuation results for this file are given in Table 6.7.1.

The low attenuation at the leading edge of this storm can be clearly seen in Figs. 6.7.5 and 6.7.6 by comparing the fade depths and rainrates for the periods T_1 and T_4. During these intervals the attenuations were very similar but the rainrate in interval T_1 was more than double that in T_4.

It is also interesting to note that during T_5 there was a deeper fade than in either T_1 or T_3 but no indicated increase in rainrate on any of the raingauges. This attenuation increase at T_4 and a similar decrease at 0.38 h, again with no indicated increase in rainrate, are believed to be due to

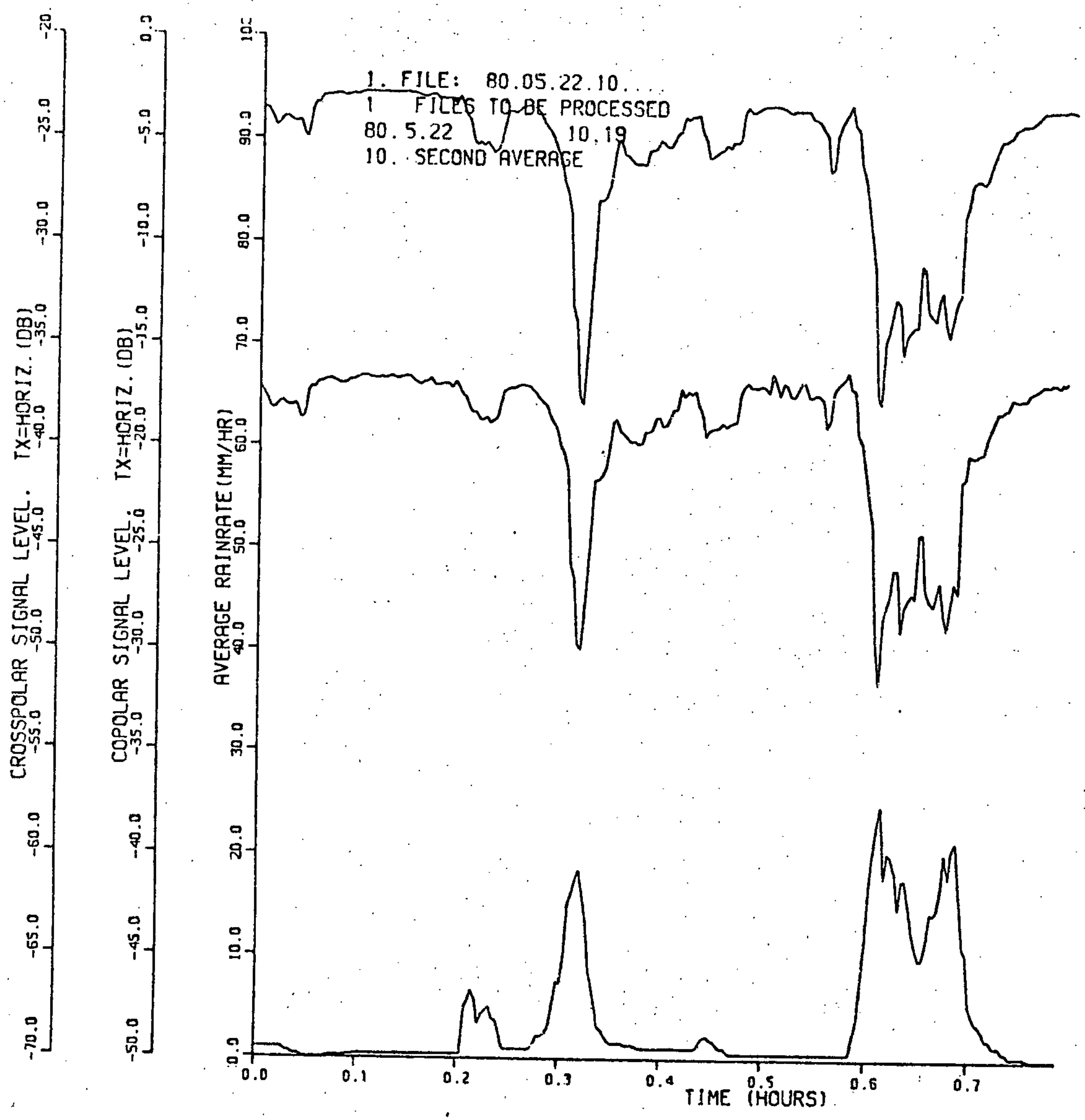

Fig. 6.7.5. Signal levels for horizontal transmitted polarization, 10 s avg.

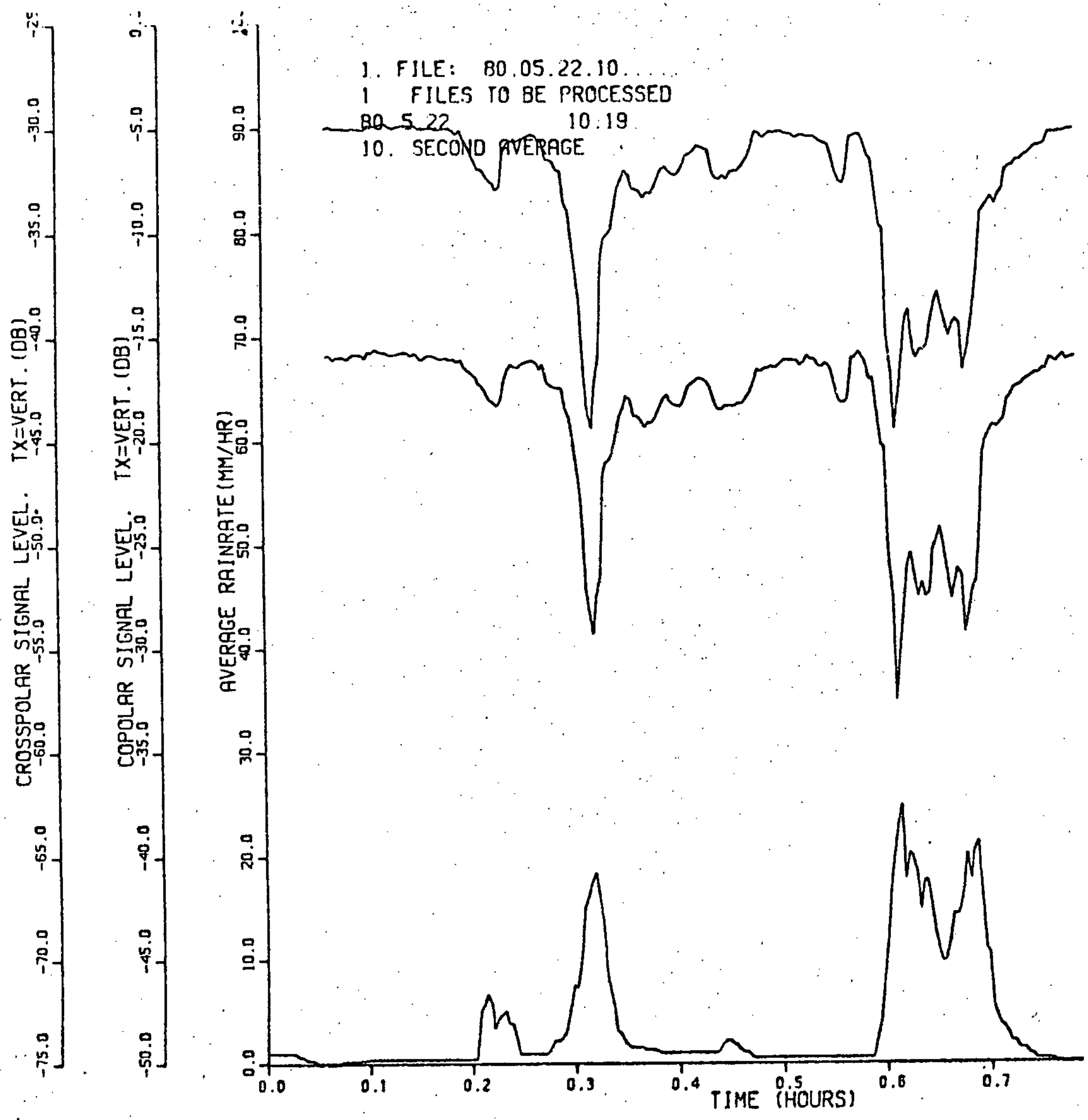

Fig. 6.7.6. Signal levels for vertical transmitted polarization, 10 s avg.

Period	Measured Attenuation Compared to Standard Predictions	Vertical Wind During Rain	Data is in Approximate Agreement with Predictions for:	Comments
T_1 0.20-0.25 h	Much lower than JOT Fig. 6.7.7	≅-0.5 m/s avg. Fig. 6.7.4	See comments	Attenuation unusually low due to large number of large drops at leading edge of storm
T_2 0.25-0.31 h	Lower than JOT Fig. 6.7.8	≅0.6 m/s Fig. 6.7.4	JOT and vert. wind ≅-1.0 m/s	2
T_3 0.31-0.35 h	Generally higher than JOT. Higher than T_2 Fig. 6.7.9	Almost zero. Fig. 6.7.4	Between JOW and JOT and zero vertical wind	
T_4 0.42-0.47 h	Attenuation similar to T_1 but rainrates much lower. Fig. 6.7.10	Almost zero Fig. 6.7.4	Higher than JOD at low rainrates. Between JOW and JOT at higher rainrates.	

. . . continued

Period	Measured Attenuation Compared to Standard Predictions	Vertical Wind During Rain	Data is in Approximate Agreement with Predictions for:	Comments
T_5 0.48-0.61 h	Atten. ≅ 2 dB/km at 0.56 h with no indicated increase in rainrate. During rest of period, close to JOT. Figs. 6.7.5, 6.7.6, and 6.7.11	Variable, increased from ≅ 0 to -0.5 m/s during rainrate increase. Fig. 6.7.4	JOT during most of period. Fig. 6.7.11	Attenuation increase assumed to be due to large number of small drops, similar to 81.11.30.22.
T_6 0.61-0.75 h	Generally agreed with JOT but much lower at highest rainrates Fig. 6.7.12	Variable, peaks: -0.5 m/s at 0.61 h and -0.7 m/s at 0.68 h during highest rainrates.	Generally JOT and zero vert., wind but JOT and vert. wind ≅ -2 m/s during high rainrates	2

Table 6.7.1 Summary of Attenuation Data for 80.05.22.10, 10:19-11:19

the same effects as the similar attenuation increases at 0.3 and 0.4 h in 81.11.30.22.

6.7.1.1 Attenuation During T_1, 0.20-0.25 h

The path average rainrate vs. horizontal attenuation scatterplot for the period T_1, Fig. 6.7.7, shows much lower attenuation than predicted, even for the JOT distribution. This unusual result is believed to be due to a large number of large drops at the leading edge of this storm and the downward vertical wind velocity. The measured attenuation during T_1 was almost identical to that measured during T_1 in 81.11.30.21 at the leading edge of that storm. Because this storm was recorded before the disdrometer was complete, no drop data are available. However, the similarity to this other example leaves little doubt as to the main cause of this unusually low attenuation being the drop distribution at the leading edge of this storm. Fig. 6.7.7 shows the relative effect of the measured vertical wind, assuming the JOT distribution. The actual vertical wind effects were probably even lower because of the large number of large drops.

6.7.1.2 Attenuation During T_2, 0.25-0.31 h

During T_2, the CPA was lower than predicted for JOT, Fig. 6.7.8, presumably because of the negative vertical wind. The data are in agreement with the modified predictions for a vertical wind velocity of -1.0 m/s. This is again approximately double the measured vertical wind for the reasons discussed in Section 6.4.1.1.

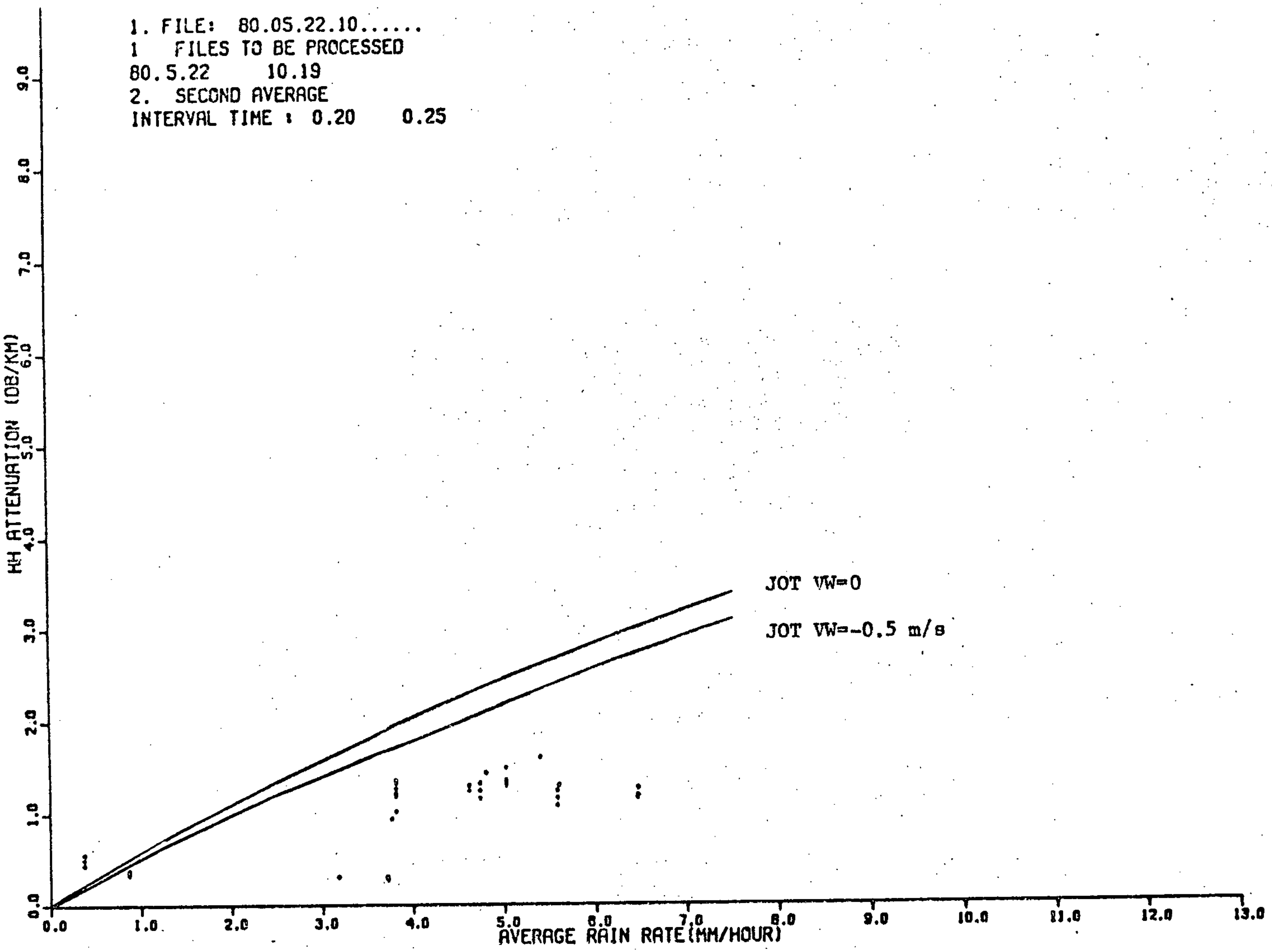

Fig. 6.7.7 CPA during T_1.

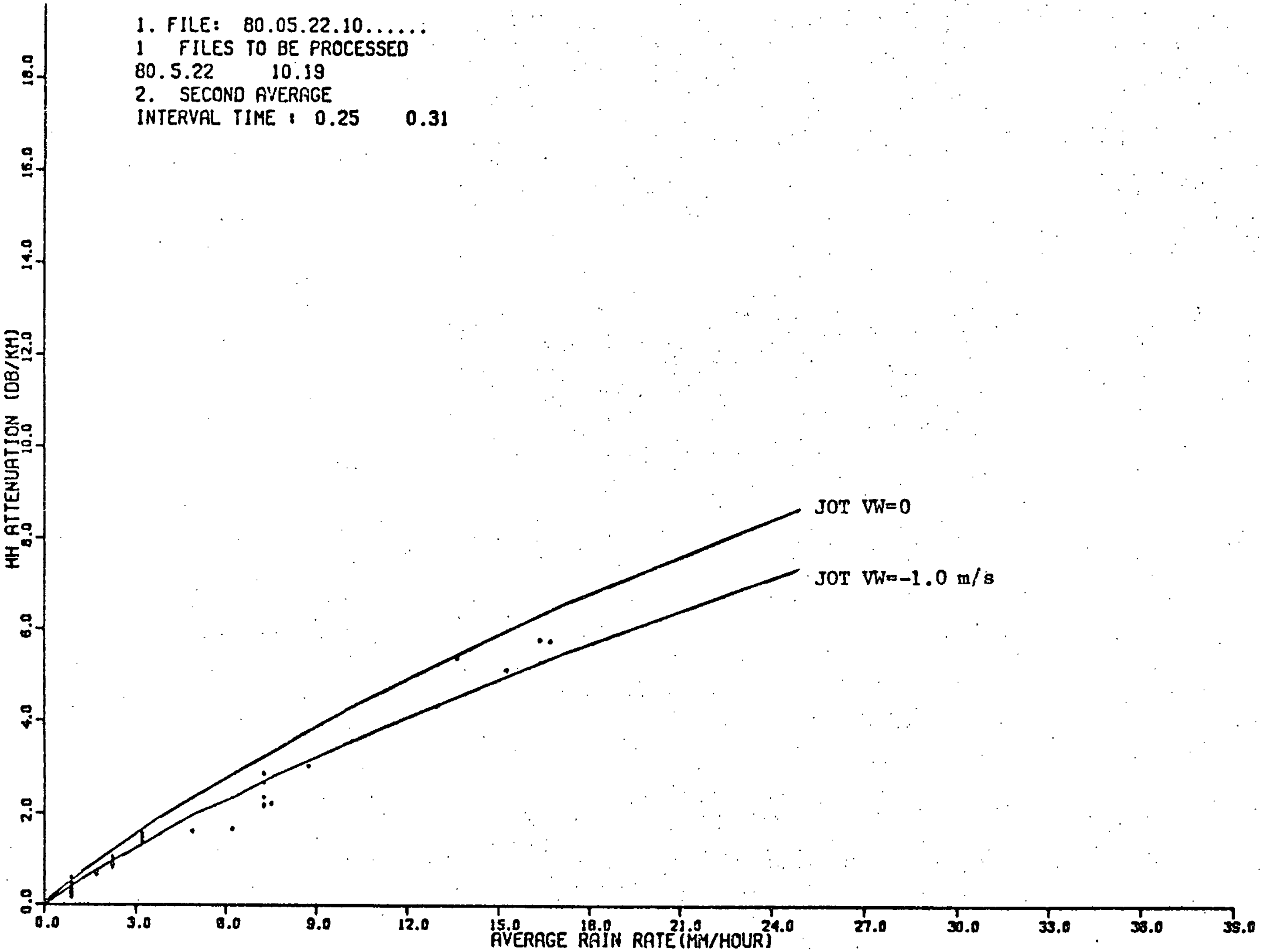

Fig. 6.7.8. CPA during T_2.

6.7.1.3 Attenuation During T_3, 0.31-0.35 h

During T_3, the attenuation, Fig. 6.7.9, is generally higher than during T_2 becasue the vertical wind has decreased to approximately zero. The measured attenuation falls between the predictions for the JOW and JOT distributions with zero vertical wind.

6.7.1.4 Attenuation During T_4, 0.42-0.47 h

Fig. 6.7.10 shows that during T_4, the attenuation was similar to T_1 even though the rainrates were much lower. This is due to the relatively larger number of small drops and zero vertical wind during this period.

6.7.1.5 Attenuation During T_5, 0.48-0.61 h

Around 0.56 h during this file, there was an attenuation increase to almost 2 dB/km with no indicated increase in rainrate, Figs. 6.7.5, 6.7.6 and 6.7.11. This is assumed to be due to a large number of small drops like those which occurred during similar rain conditions in file 81.11.30.22. During the rest of this period, the attenuation generally agreed with the standard predictions for the JOT distribution. The lower attenuation as the rainrate increased may be partially due to the simultaneously decreasing vertical wind velocity.

6.7.1.6 Attenuation During T_6, 0.61-0.75 h

Attenuation during period T_6, Fig. 6.7.12, shows a large number of points well below that predicted for the JOT distribution, especially at the

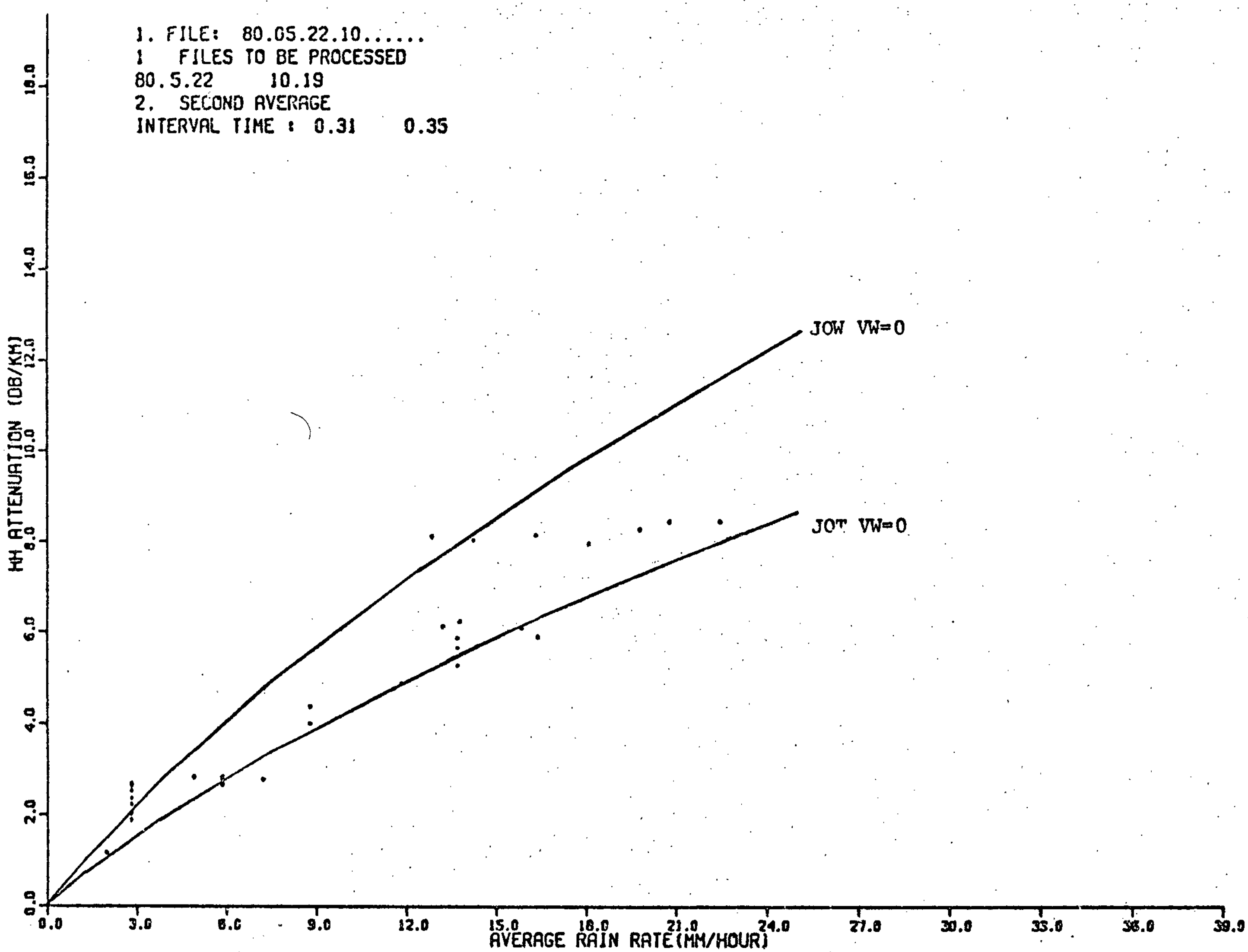

Fig. 6.7.9. CPA during T_3.

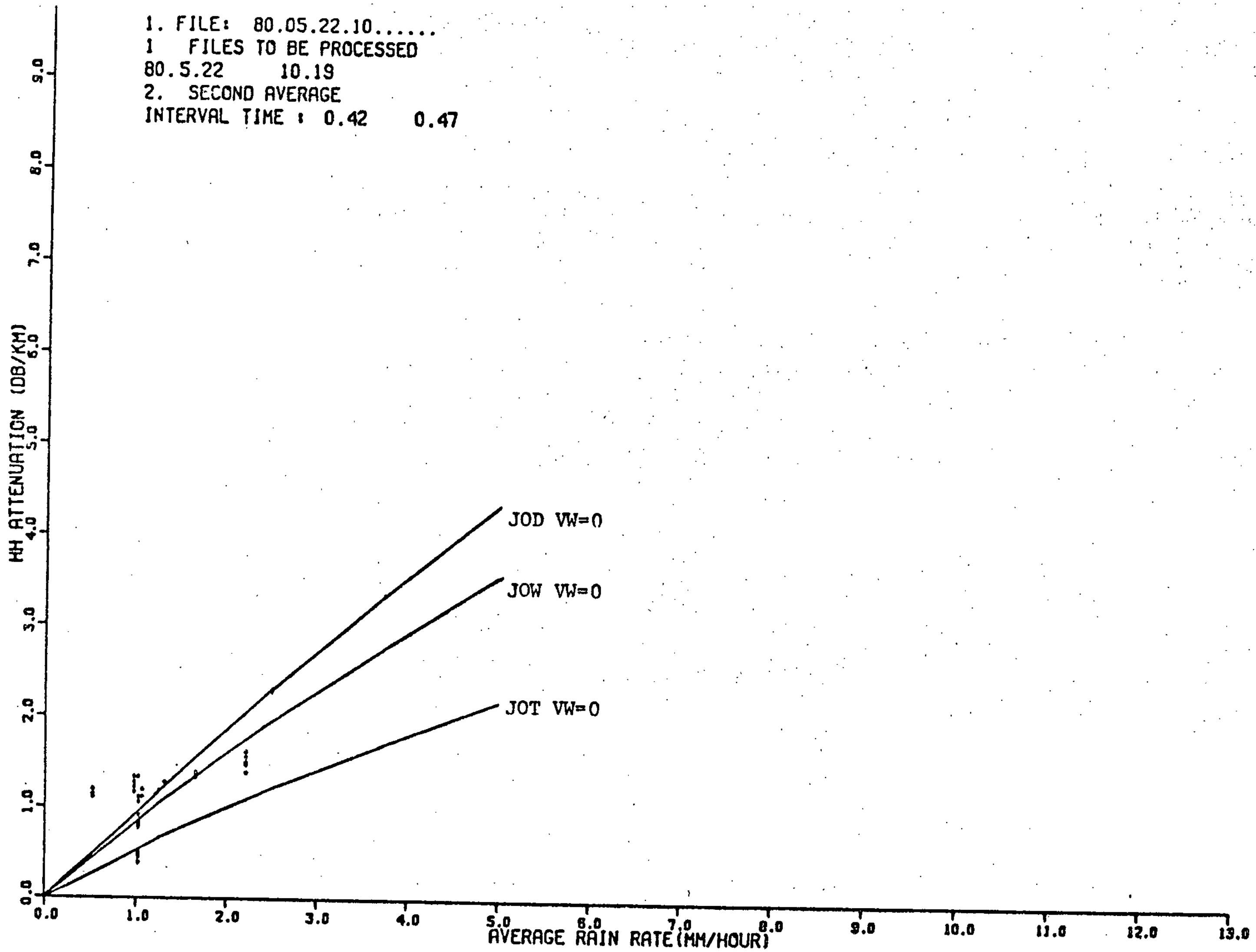

Fig. 6.7.10. CPA during T_4.

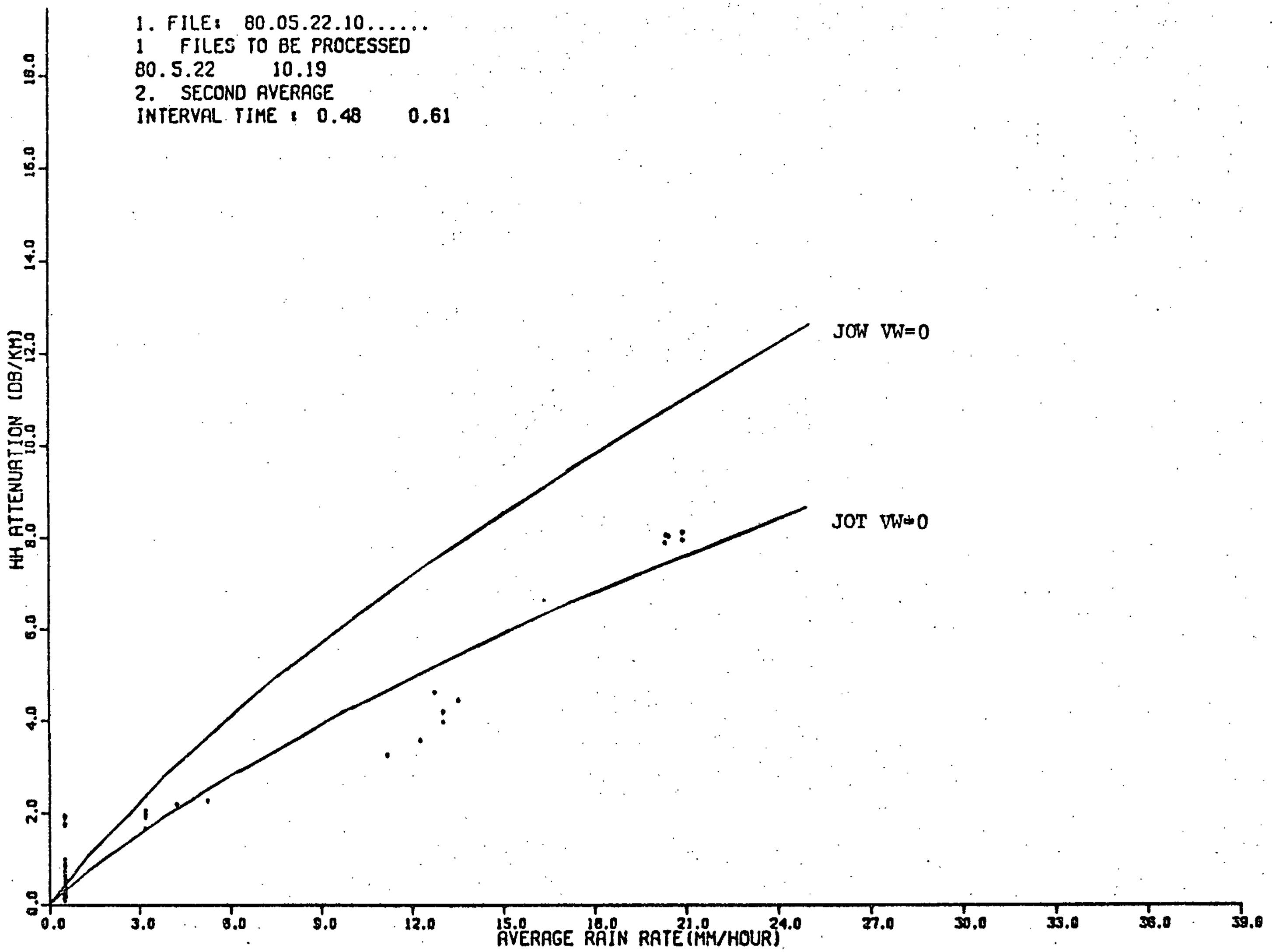

Fig. 6.7.11. CPA during T_5.

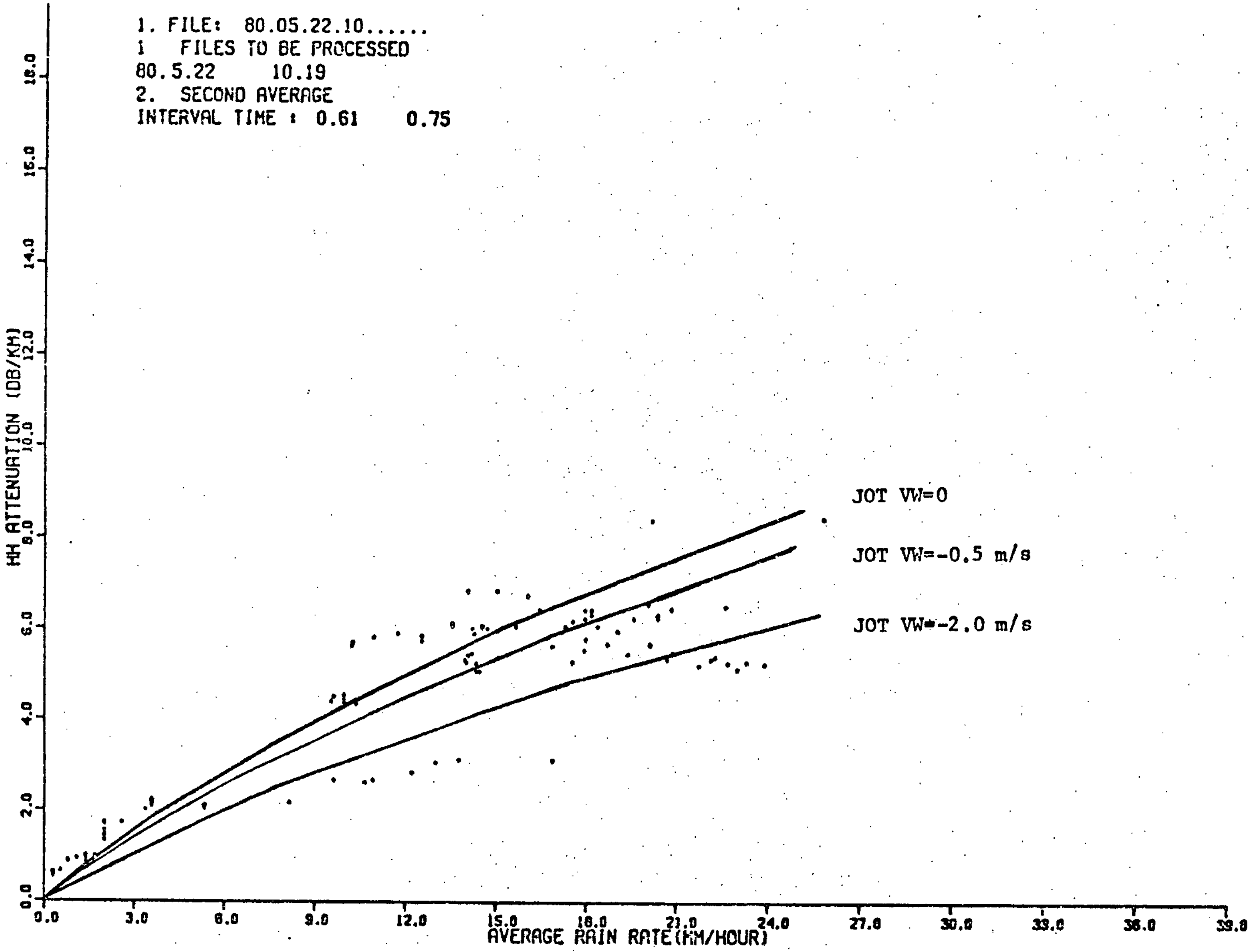

Fig. 6.7.12. CPA during T_6.

higher rainrates. These low attenuations were associated with the downward vertical wind peaks which are coincident with the peak rainrates at 0.61 and 0.68 hours. The attenuation at the higher rainrates is in approximate agreement with the modified predictions for the JOT distribution and a vertical wind velocity of -2.0 m/s, again considerably higher than measured for the reasons discussed in Section 6.4.1.1.

6.7.2 XPD and Differential Attenuation Results for 81.05.22.10

This data file contains an excellent example of uncancelled system XPDs increasing and decreasing from the clear weather value due to changes in the path XPD angle. A summary of the XPD and differential attenuation data for this file is shown in Table 6.7.2.

The time series system XPD plots for this storm are shown in Figs. 6.7.13 and 6.7.14. This file was recorded before the crosspolar cancellation network was installed and accordingly, both channels are uncancelled. These plots clearly show the system XPD decreasing as rainrate increases during T_1 to T_3 and increasing as rainrate increases during T_6. During T_1 to T_3 the wind direction was from the west and reasonably constant but during T_6 the wind direction was extremely variable and does not appear to have had any preferred direction. This extremely interesting XPD behaviour is believed to be due to a consistent change in the sign of the mean canting angle. In Section 4.3.2, it was shown that a change in the sign of the effective mean canting angle would change the angle of T_{12} by 180°. It was then demonstrated in Chapter 5 that the experimental model predicted that a change in the angle of T_{12} would cause a change from increasing to decreasing (or vice

Period	XPD	Differential Attenuation	Wind Velocities During Rain	XPD is in Approximate Agreement with Model Predictions for:	Comments
T_1-T_3 0.20-0.35 h	Both XPDs well correlated to rainrate. XPDs decrease as rainrate increases. Figs. 6.7.16 and 6.7.17	Generally positive. Maximum value ≅+0.8 dB Fig. 6.7.15	Wind constantly from the west. Horiz. wind ≅ 1.0 m/s avg. Figs. 6.7.2 and 6.7.3	Over entire period varied from $\phi \cong 1$ to $4°$ See T_2 and T_3 below.	Results for both polarizations conform similarly to model predictions.
T_2 0.25-0.31 h	Generally lower XPD than T_3 Fig. 6.7.18	See T_1 - T_3	Westerly Horiz. wind ≅ 1.2 m/s avg. Fig. 6.7.2 and 6.7.3	Conforms to model predictions for $\phi \cong 2$-$4°$	Higher horizontal wind velocity than T_3
T_3 0.31-0.35 h	XPD closer to clear weather value than during T_2. Fig. 6.7.19	See T_1 - T_3	Horiz. wind approx. zero. Figs. 6.7.2 and 6.7.3	Generally conforms to predictions for $\phi \cong 1$-$2°$	
T_6 0.61-0.75 h	Both XPDs increased with increasing rainrate. Figs. 6.7.20 and 6.7.21	Generally positive. Maximum value ≅ 0.8 dB Fig. 6.7.15	Wind direction variable. Horiz. wind velocity varied between 0 and 1.2 m/s. Figs. 6.7.2 and 6.7.3	Within predictions for canting angle of 2°.	Average horizontal wind velocity lower than T_2

Table 6.7.2 XPD and Differential Attenuation Data for 80.05.22.10

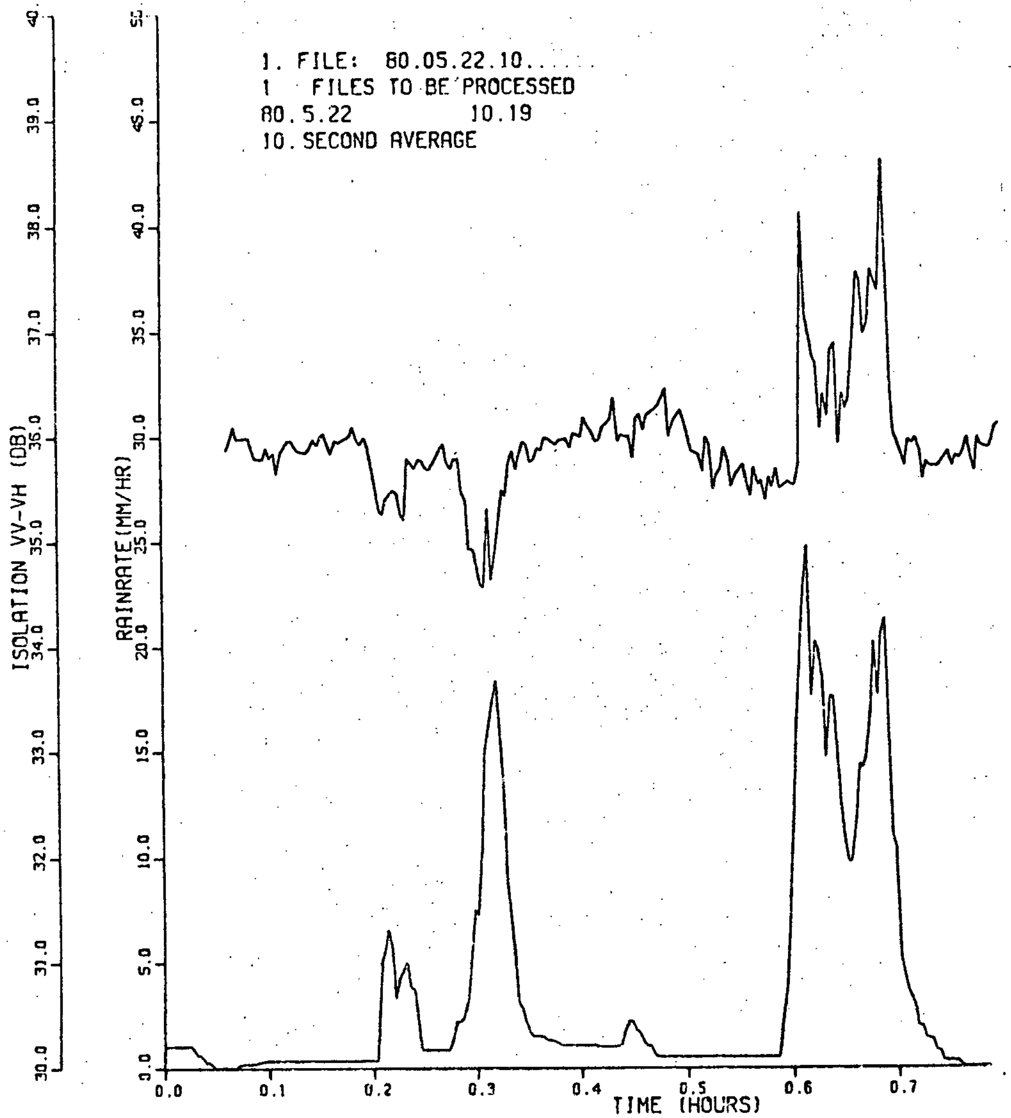

Fig. 6.7.13. XPD for vertical transmitted polarization, 10 s avg. for 80.05.22.10.

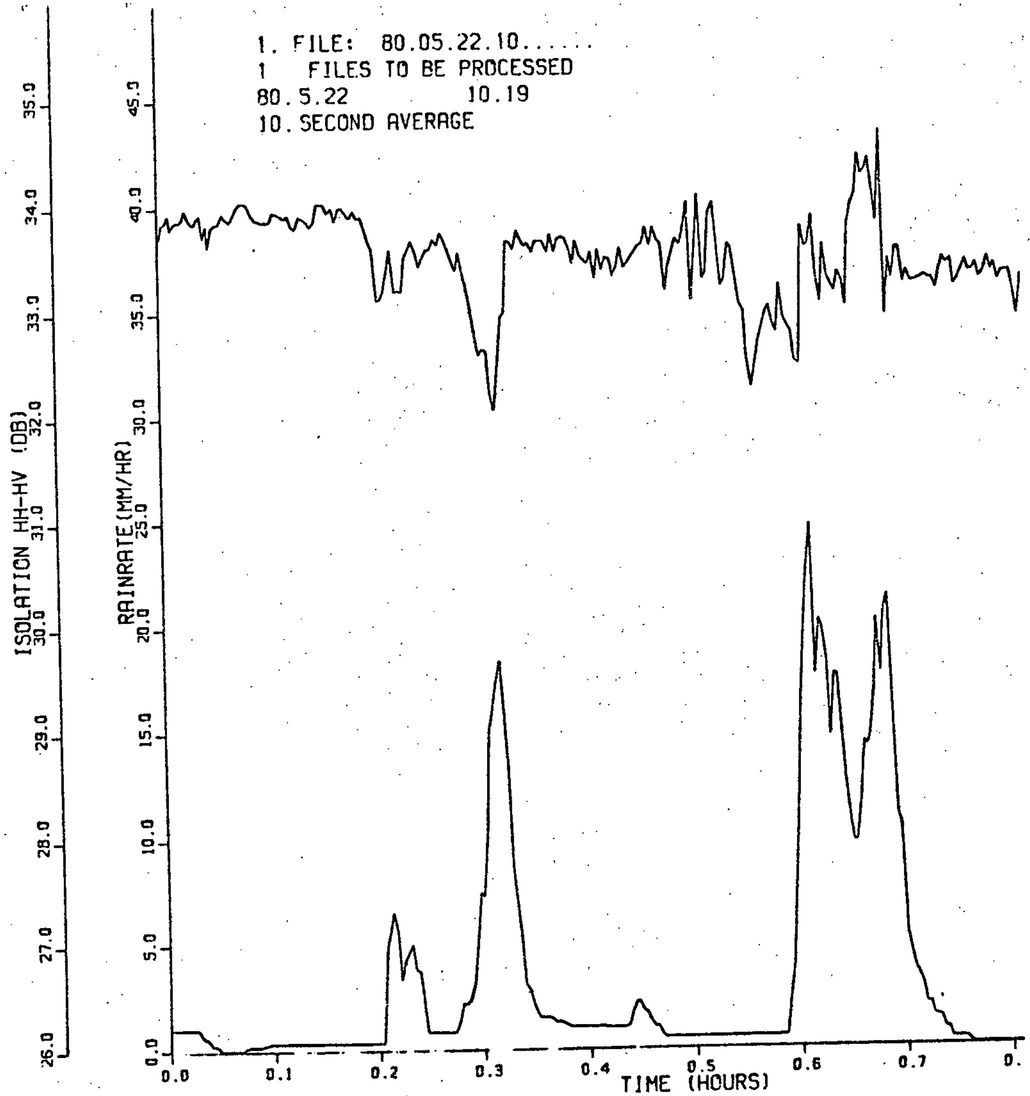

Fig. 6.7.14. XPD for horizontal transmitted polarization, 10 s avg. for 80.05.22.10.

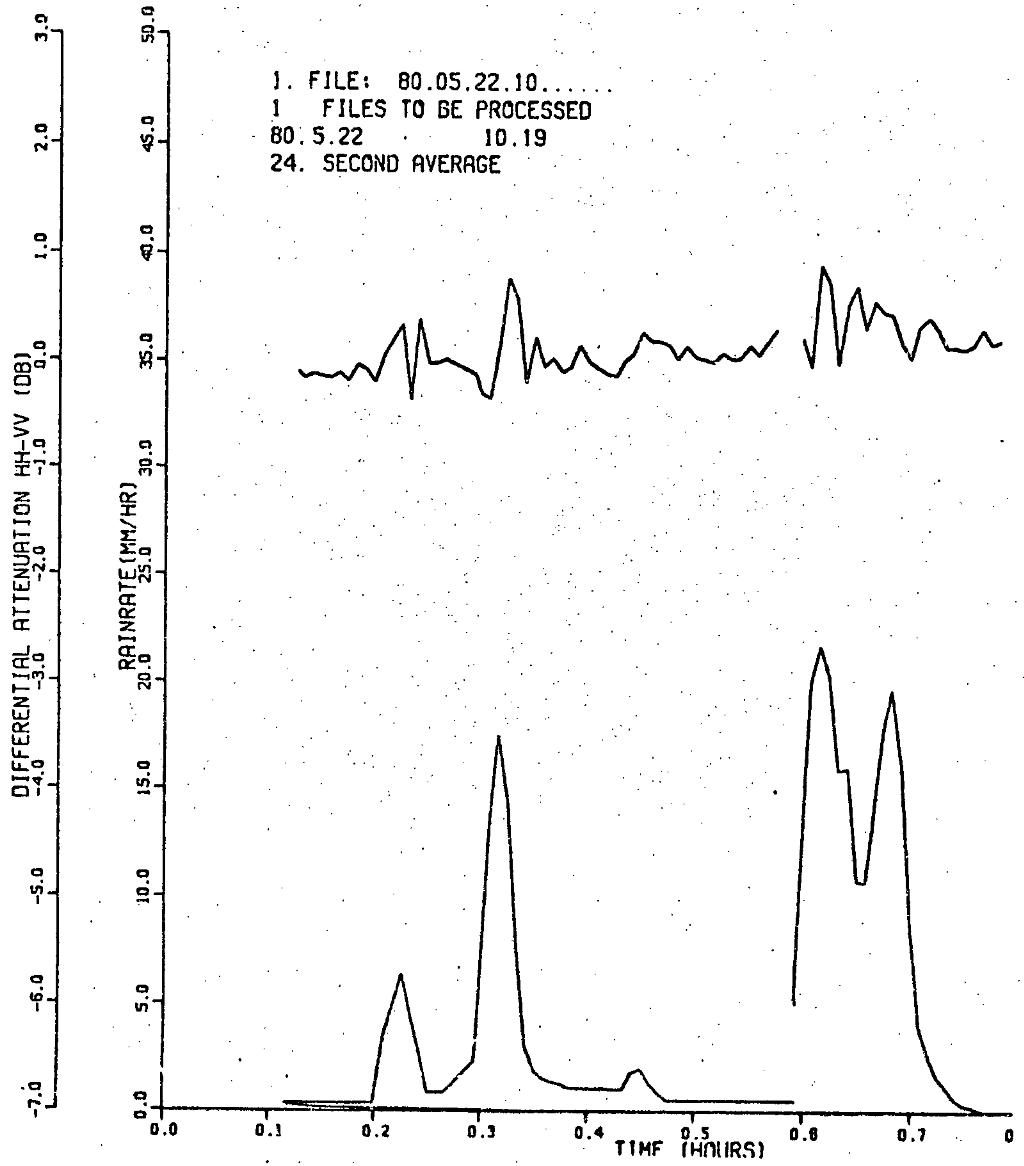

Fig. 6.7.15. Differential attenuation for 80.05.22.10.

versa) system XPD with increasing rainrate in an uncancelled system. Whether the system XPD increased or decreased with rainrate was shown to be dependent on the relative angle between the path and antenna depolarized signals. It is believed that the change in canting angle between periods T_1-T_3 and T_6 is due to the measured changes in wind direction.

The interval T_4 includes some unexpected variations in system XPD especially in Fig. 6.7.19 which shows the results for horizontal transmitted polarization. These unusual XPD variations occur just prior to and during the unusual fade at 0.56 h, which was discussed earlier. This XPD behaviour starts at approximately the same time as the erratic wind direction changes and occurred during a period of very low indicated rainrate. No satisfactory explanation has been found for this short period of XPD behaviour.

Before analyzing the individual scatterplots of XPD vs. rainrate, it is necessary to discuss the model inputs used for comparing the results of this storm to the theory. To be able to compare the theoretically predicted results from Chapter 4 to the experimental results, it is necessary to estimate values of the effective complex antenna XPDs for use in the experimental model. The magnitudes of the antenna XPDs, for a well matched system, are reasonably accurately known from the manufacturer's data shown in Fig. 2.33. When this storm was recorded, the antennas were aligned for best simultaneous horizontal and vertical isolations and the antenna ports were known to be well matched because the variations of system XPD with frequency were low. The clear weather system isolations were approximately 33.6 and 35.8 dB for horizontal and vertical transmitted polarizations, respectively. From these clear weather system isolations and the individual antenna XPDs in Fig. 2.33, it is clear that the antenna depolarized signals are adding with an approximately zero (or very small) phase difference. Assuming a zero phase difference ($\Delta\Theta_{XPD} = 0$) the antenna isolations for the horizontal transmitted polarizations case were estimated to be 38 and 41.7 dB for the receive and transmit antennas, respectively. For vertical transmitted polarization the antenna XPD's were estimated to be 41.7 and 42.0 dB. These values are consistent with the data in Fig. 2.33 and gives the correct clear weather isolations.

It is still not possible to estimate the relative phase between the path and antenna depolarized signals. This means that for an assumed canting angle, the system XPD could increase or decrease from the clear weather value. As a result, all possible values for this angle were used in the model calculations and the maximum and minimum values used for comparison to the experimental observations. Because all possible angles between the path and antenna crosspolar signals were used in the model calculations, the resulting range of values will automatically include the possible range for positive and negative canting angles. In other words, in an uncancelled system, a change in the sign of the canting angle has the same effect as a 180° phase change in both antenna XPD angles.

The model calculations used the results from Chapter 4 for a 1.8 km path length and the Joss/Olsen Thunderstorm distribution. The Joss/Olsen Thunderstorm distribution was used to conform to the observed attenuation results but the data in Fig. 4.9 shows that the drop size distribution will have a very small effect on the XPD/rainrate relationship. System XPD values were calculated for ±1°, ±2° and ±4° effective mean canting angles.

6.7.2.1 XPD and Differential Attenuation During T_1-T_3, 0.20-0.25 h

Figs. 6.7.16 and 6.6.17 are the system XPD vs. rainrate scatterplots for the combined periods T_1 to T_3. The XPD behaviour for both polarizations is very similar, and shows a decreasing system XPD with increasing rainrate. Because the clear weather isolations and path XPDs are different for the two polarizations, this data tends to verify that the model correctly predicts uncancelled system XPD behaviour.

The differential attenuation, Fig. 6.7.15, was generally positive during T_1-T_3. The maximum differential attenuation was approximately 0.8 dB which is in good agreement with the theoretical predictions for this maximum rainrate.

6.7.2.2 XPD During T_2, 0.25-0.31 h and T_3, 0.31-0.35 h

The different XPDs during these periods clearly show the effect of horizontal wind on canting angle and XPD. For both periods, the wind was from the west, i.e. perpendicular to the path. During T_2 the average horizontal wind velocity was approximately 1.2 m/s and the XPD data agreed with the model predictions for a 2 to 4° canting angle. At the beginning of T_3, the horizontal wind decreases almost to zero and the XPD then generally agreed with canting angles between 1 and 2°.

6.7.2.3 XPD and Differential Attenuation During T_6, 0.61-0.75 h

Figs. 6.7.20 and 6.7.21 are XPD/rainrate scatterplots for the period T_6. As discussed previously, the system XPD increased with rainrate in this

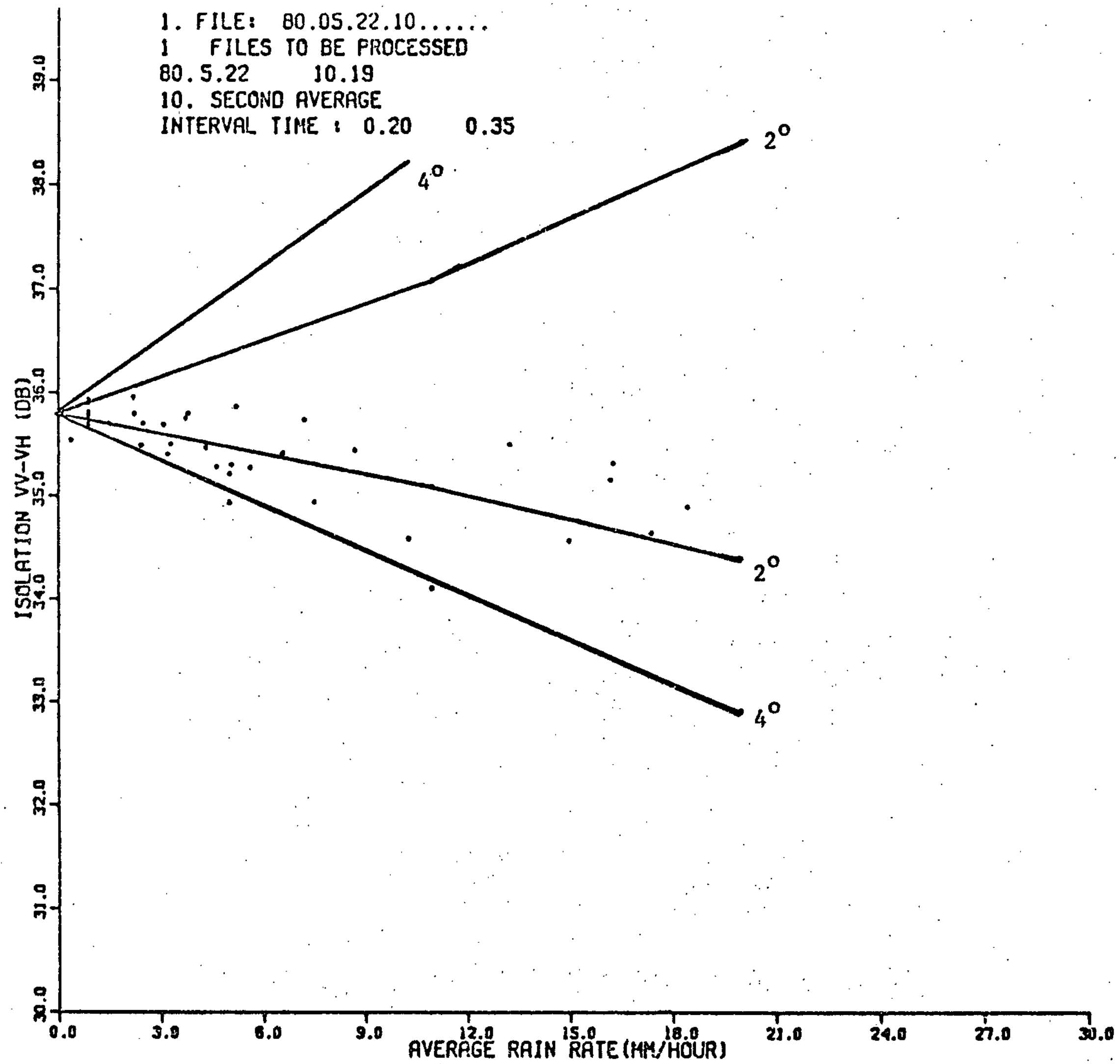

Fig. 6.7.16. XPD_V for $T_1 - T_3$.

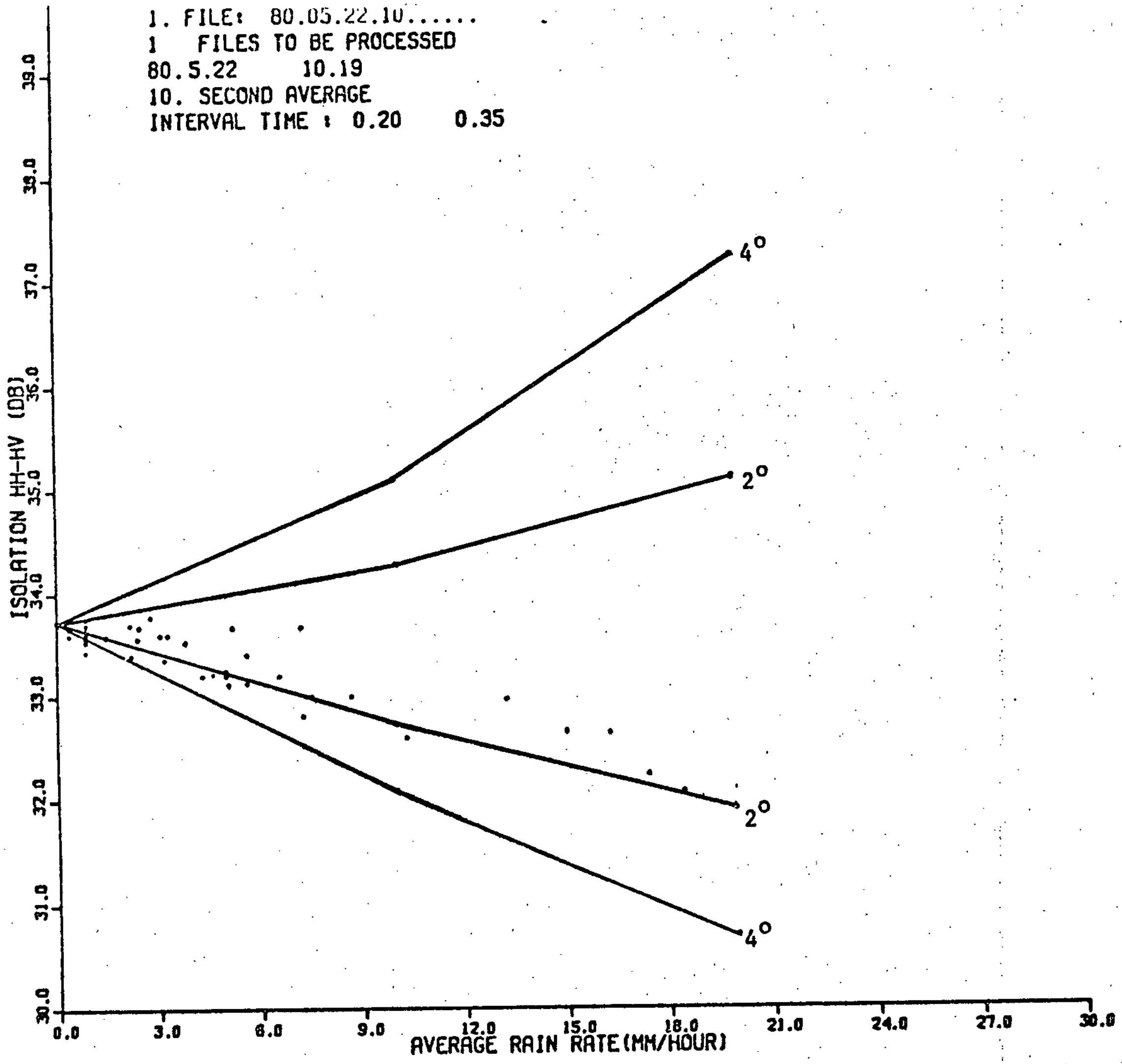

Fig. 6.7.17. XPD_H for $T_1 - T_3$.

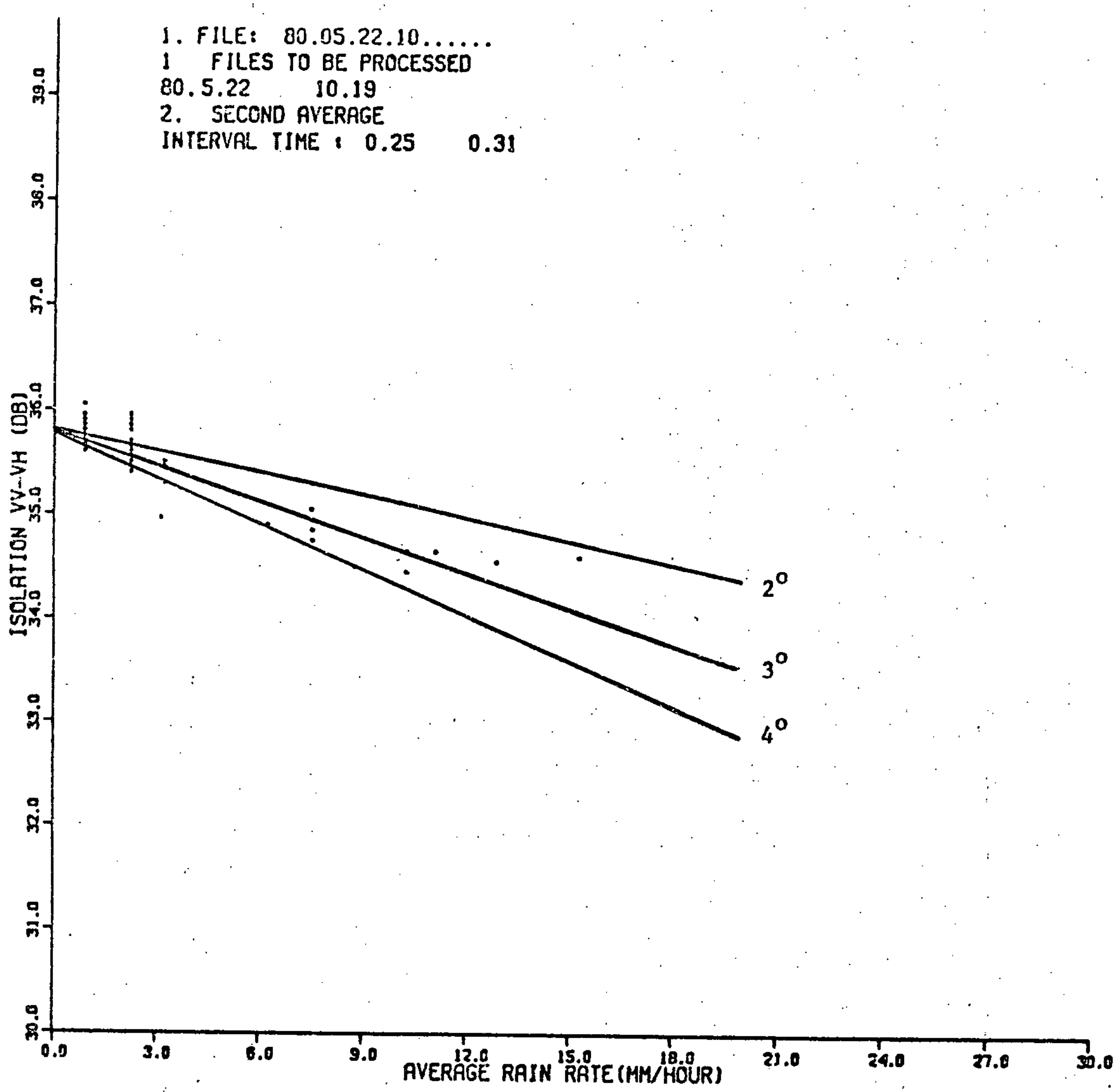

Fig. 6.7.18. XPD_V for T_2.

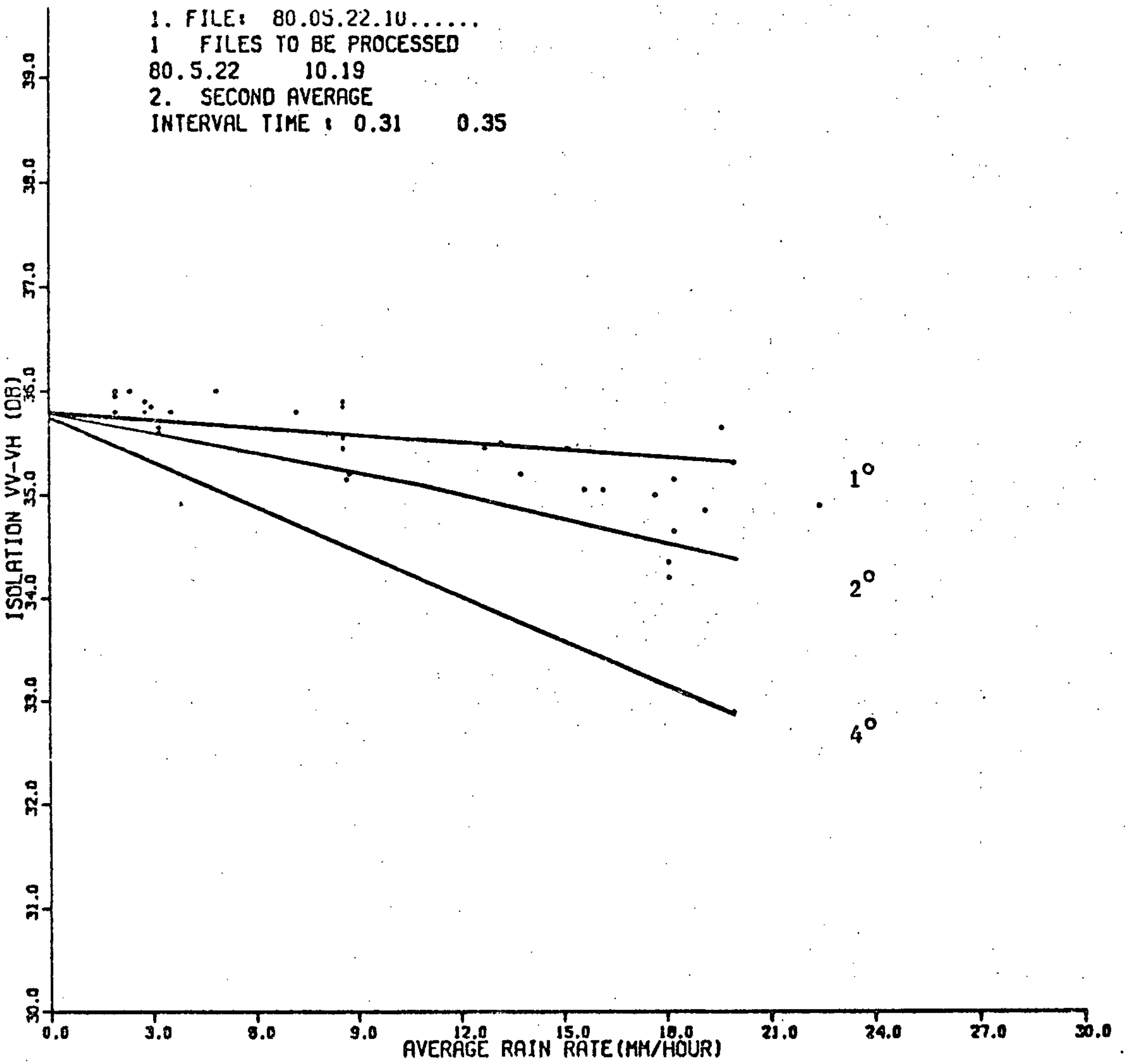

Fig. 6.7.19. XPD_V for T_3.

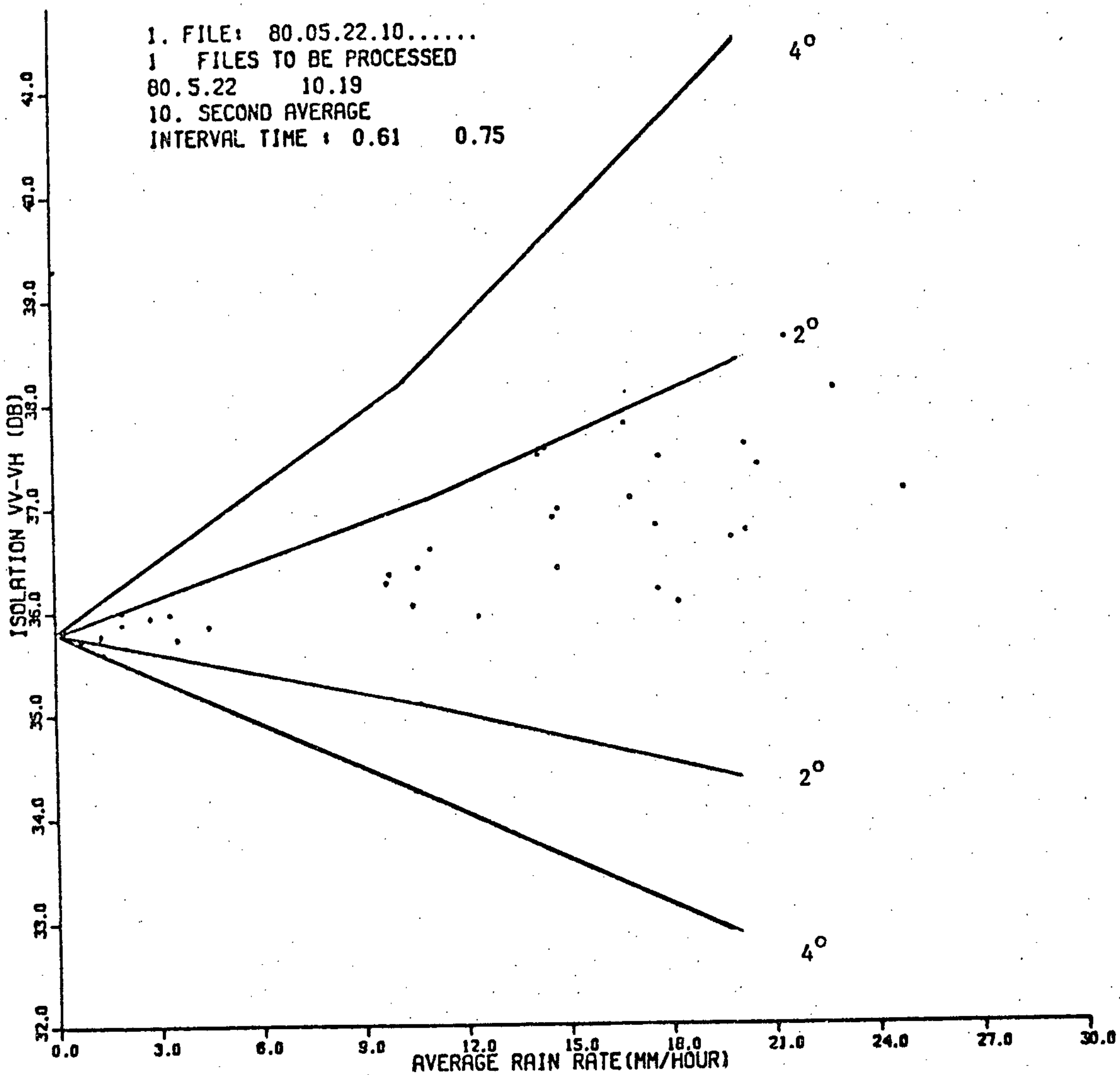

Fig. 6.7.20. XPDV for T_6.

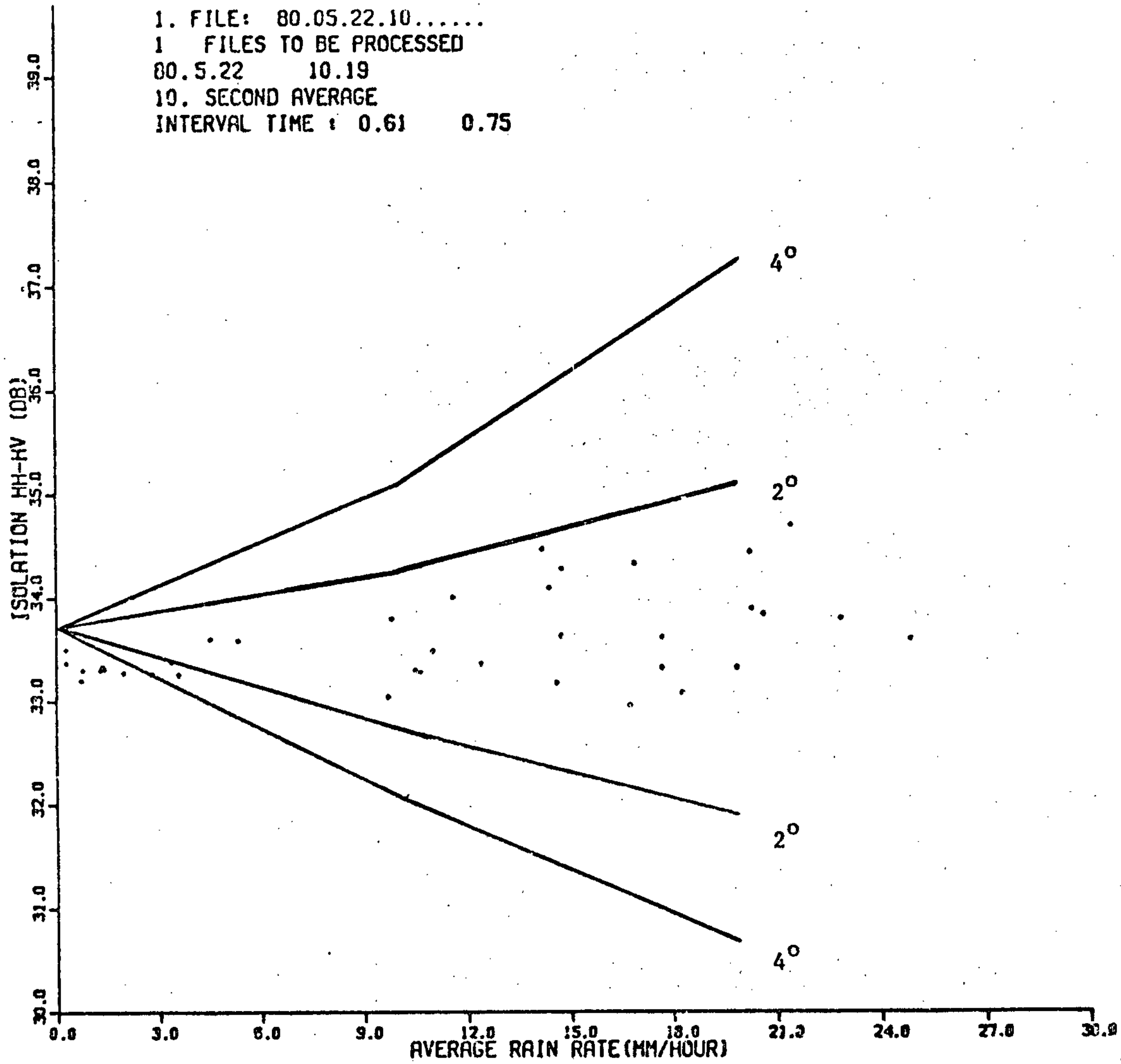

Fig. 6.7.21. XPD_H for T_6.

interval due to a change in the sign of the mean canting angle. The results for this period again show similar agreement to the model predictions for both polarizations. In this period, the effective mean canting angle was less than during T_2 because of the lower average horizontal wind velocity. The effective mean canting angle magnitudes can be compared for similar rainrates in these two different intervals because the change in the sign of the canting angle will only add 180° to the angle of the path depolarized signal. This will result in similar relationships for the same mean effective canting angle between the two limiting cases predicted by the model and the actual experimental observations in each period.

The differential attenuation during T_6 was similar to that during T_1-T_3 and again shows reasonable agreement with the theoretical predictions.

6.8 Experimental Results for 81.06.18.15

This data file, covering the period June 18, 1981, 15:36-16:24 hours, is included because it contains a period of good correlation between XPD and rainrate. The rainrates for this file are shown in Fig. 6.8.1. During this period, the rainrate was relatively uniform over the path and varied slowly from less than 1 to approximately 9 mm/h. The wind direction, horizontal velocity and vertical velocity are shown in Figs. 6.8.2 to 6.8.4. During the period of significant rainrate (0.35-0.80 hours), the wind direction was from ENE and changed very little. The horizontal windspeed during this period ranged from approximately 3 to 6 m/s and was relatively constant. It is interesting that, during the rain interval, the vertical windspeed was almost

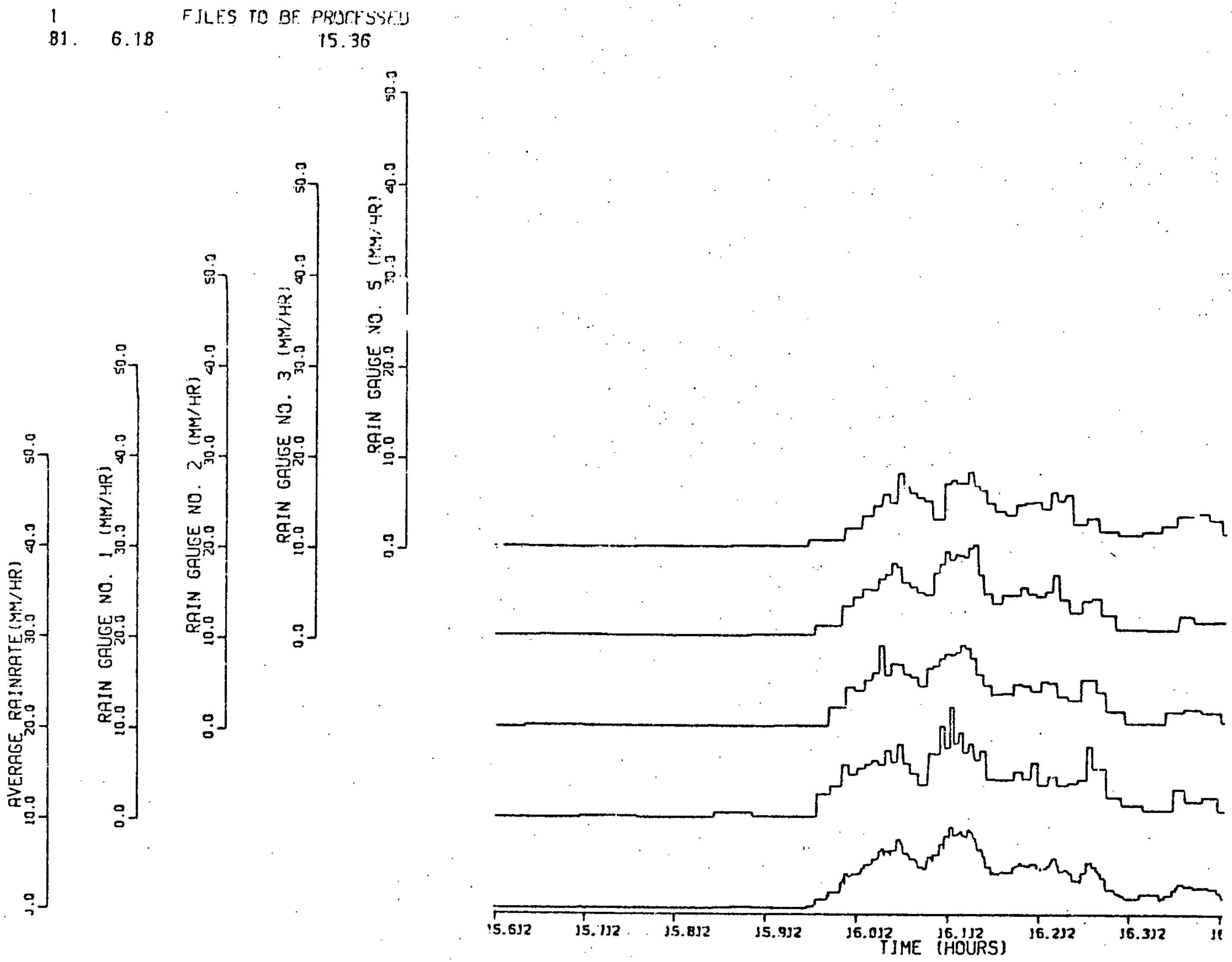

Fig. 6.8.1. Rainrates for 81.06.18.15.

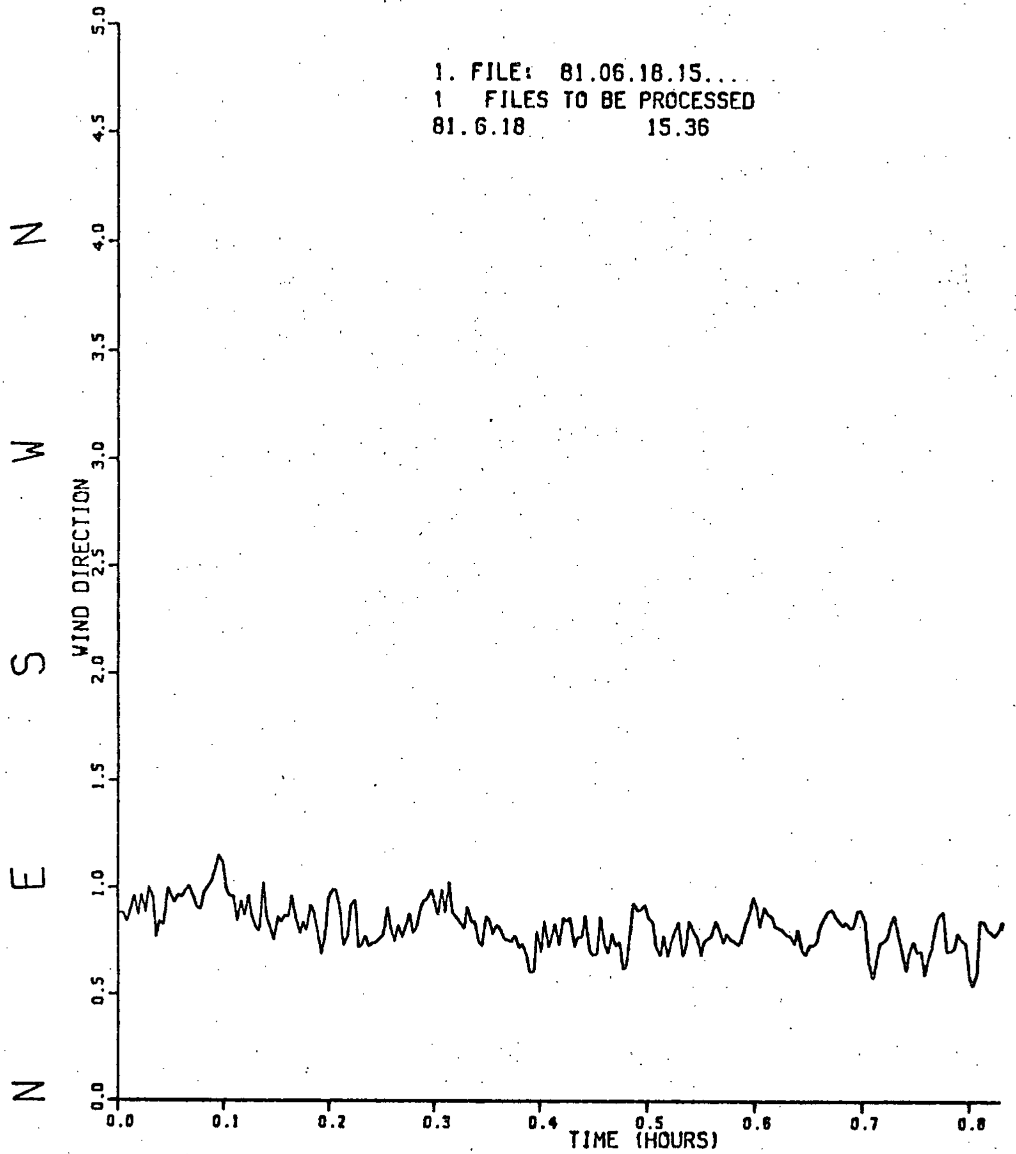

Fig. 6.8.2. Wind direction 10 s avg. for 81.06.18.15.

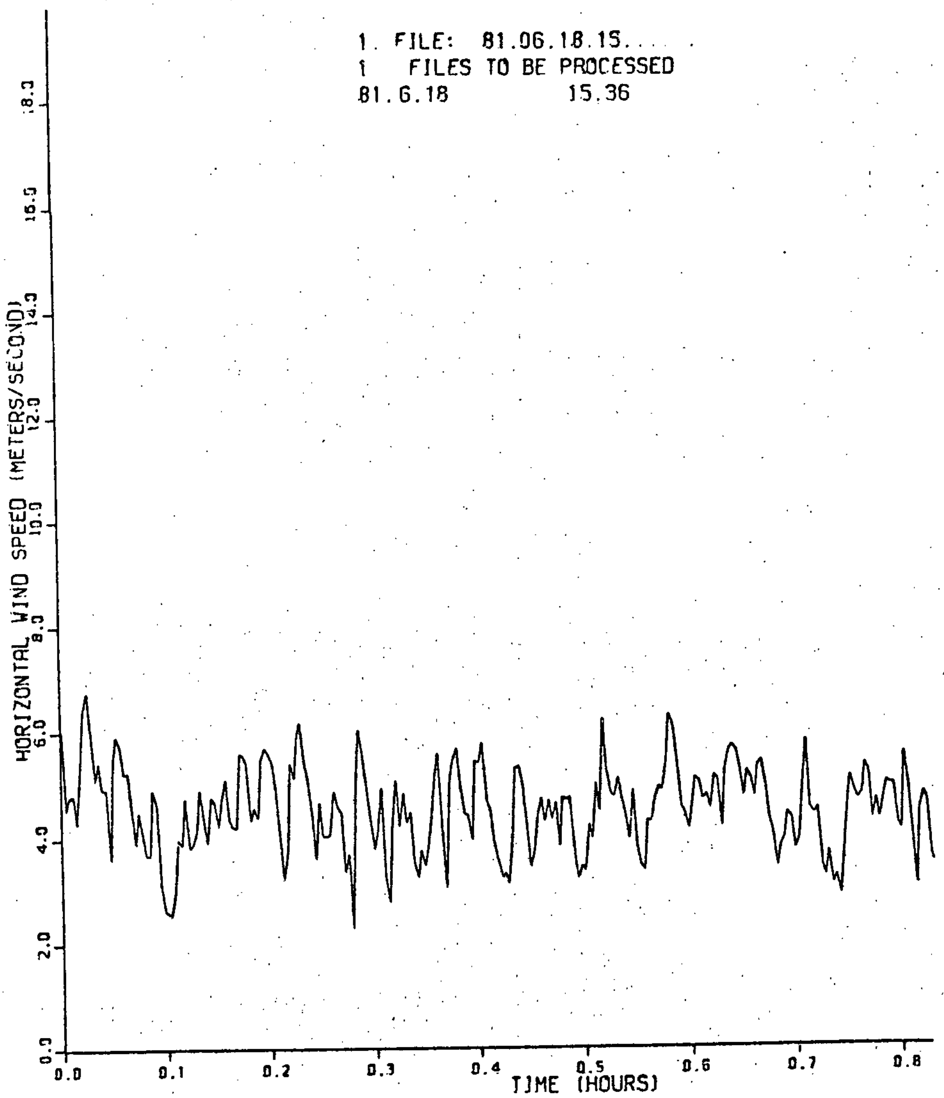

Fig. 6.8.3. Horizontal wind velocity, 10 s avg. for 81.06.18.15.

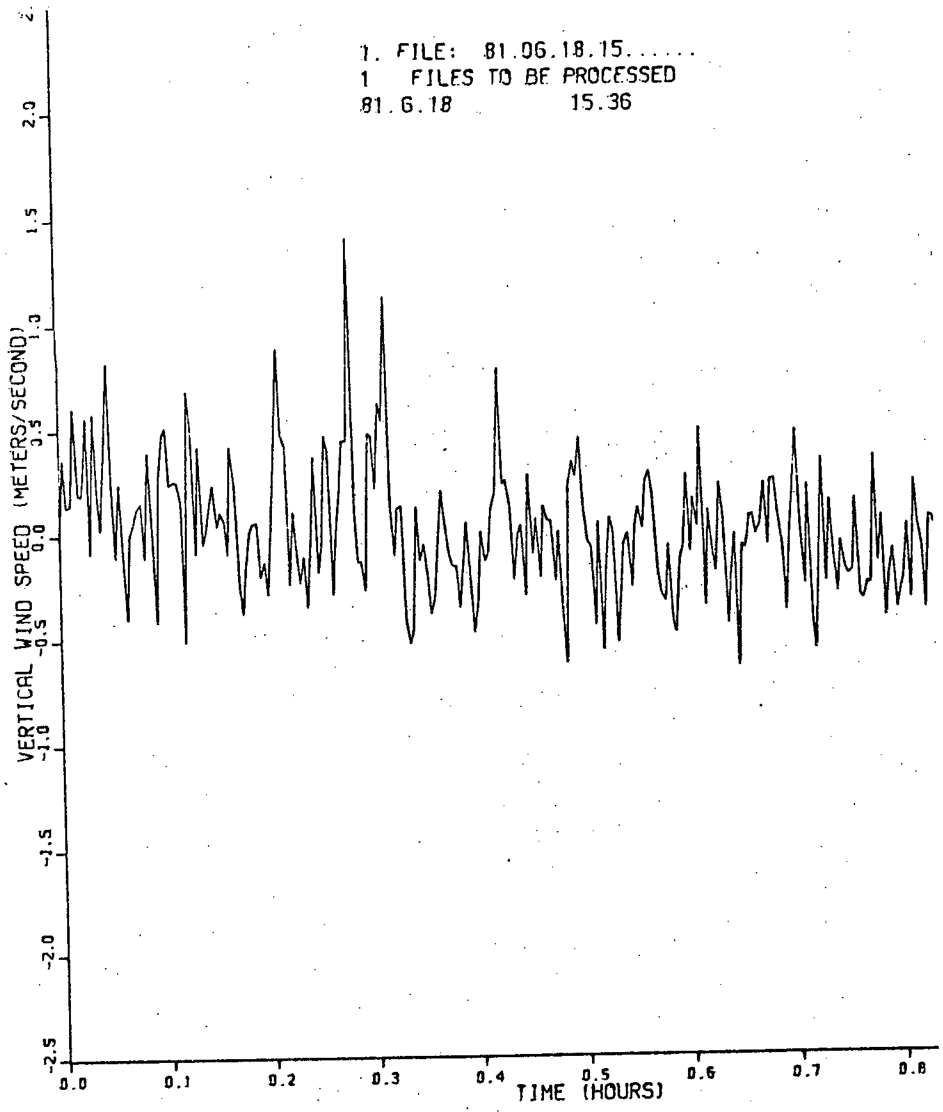

Fig. 6.8.4(a). Vertical wind velocity, 10 s avg. for 81.06.18.15.

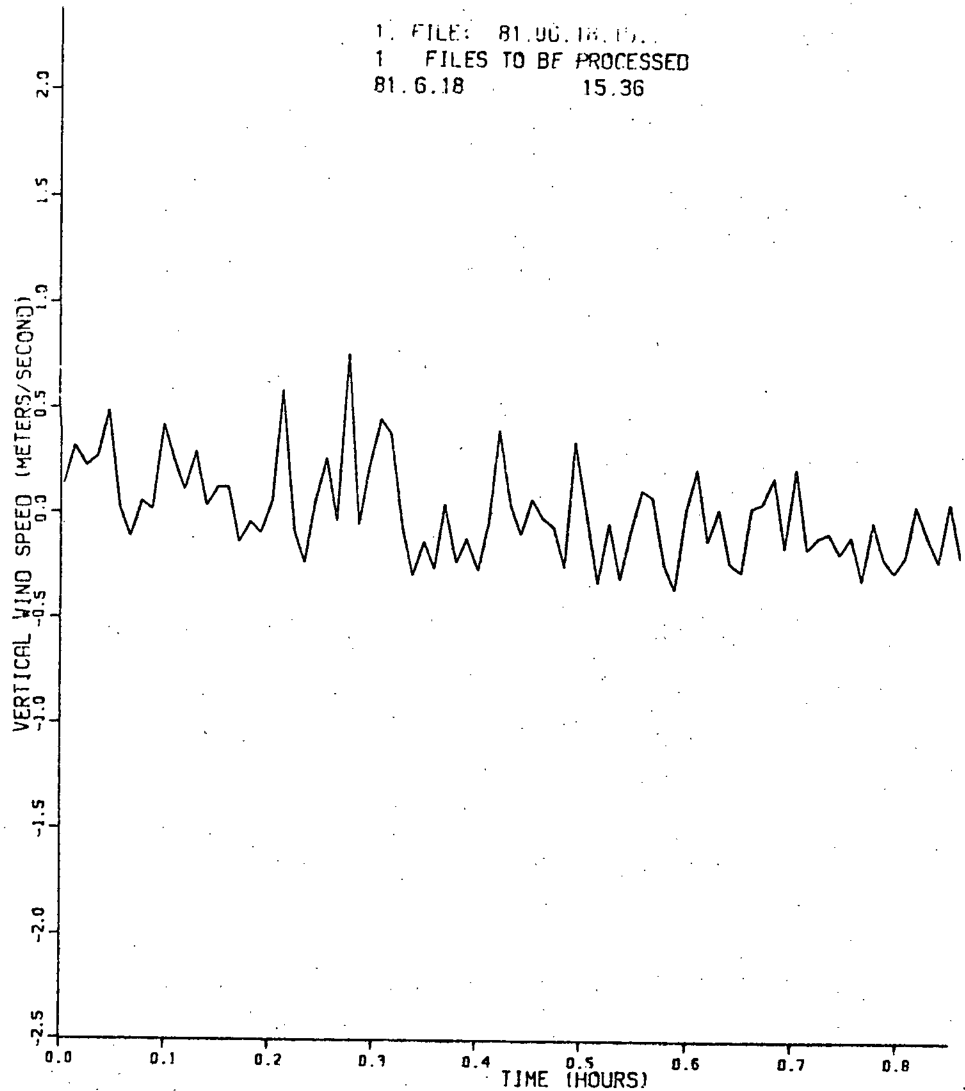

Fig. 6.8.4(b). Vertical wind velocity, 30 s avg. for 81.06.18.15.

always close to zero and never exceeded ±0.75 m/sec even though there was a comparatively high horizontal wind velocity.

Time series signal level plots for horizontal transmitted polarization, with 10 s and 30 s averages, are shown in Figs. 6.8.5(a) and (b). Corresponding levels for vertical transmitted polarization, 10 s average, are shown in Fig. 6.8.6.

6.8.1 Attenuation Data for 81.06.18.15

Fig. 6.8.7 is the horizontal attenuation vs. rainrate scatterplot for this entire period. These results are almost all within the area defined by the predicted attenuations for the standard drop size distributions. The degree to which these observations conform to the standard predictions is mainly due to the lack of significant vertical wind velocities.

6.8.2 XPD and Differential Attenuation Data for 81.06.18.15

Time series plot of system XPD and rainrate for horizontal transmitted polarization is shown in Fig. 6.8.8(a) and (b) for 10 s and 30 s averages. These data were recorded using the crosspolar cancellation network described in Chapters 2 and 5. The cancelled system XPD decreases from an average of approximately 62 dB during the period of very light rain to 51 dB at a rainrate of 9 mm/hr.

It is difficult to establish an accurate clear weather system XPD and therefore minimum measurable path XPD for this record for several reasons. Once complicating factor is the reasonably constant indicated path average rainrate from 0.0 to 0.35 hours. At this indicated rainrate, there will have

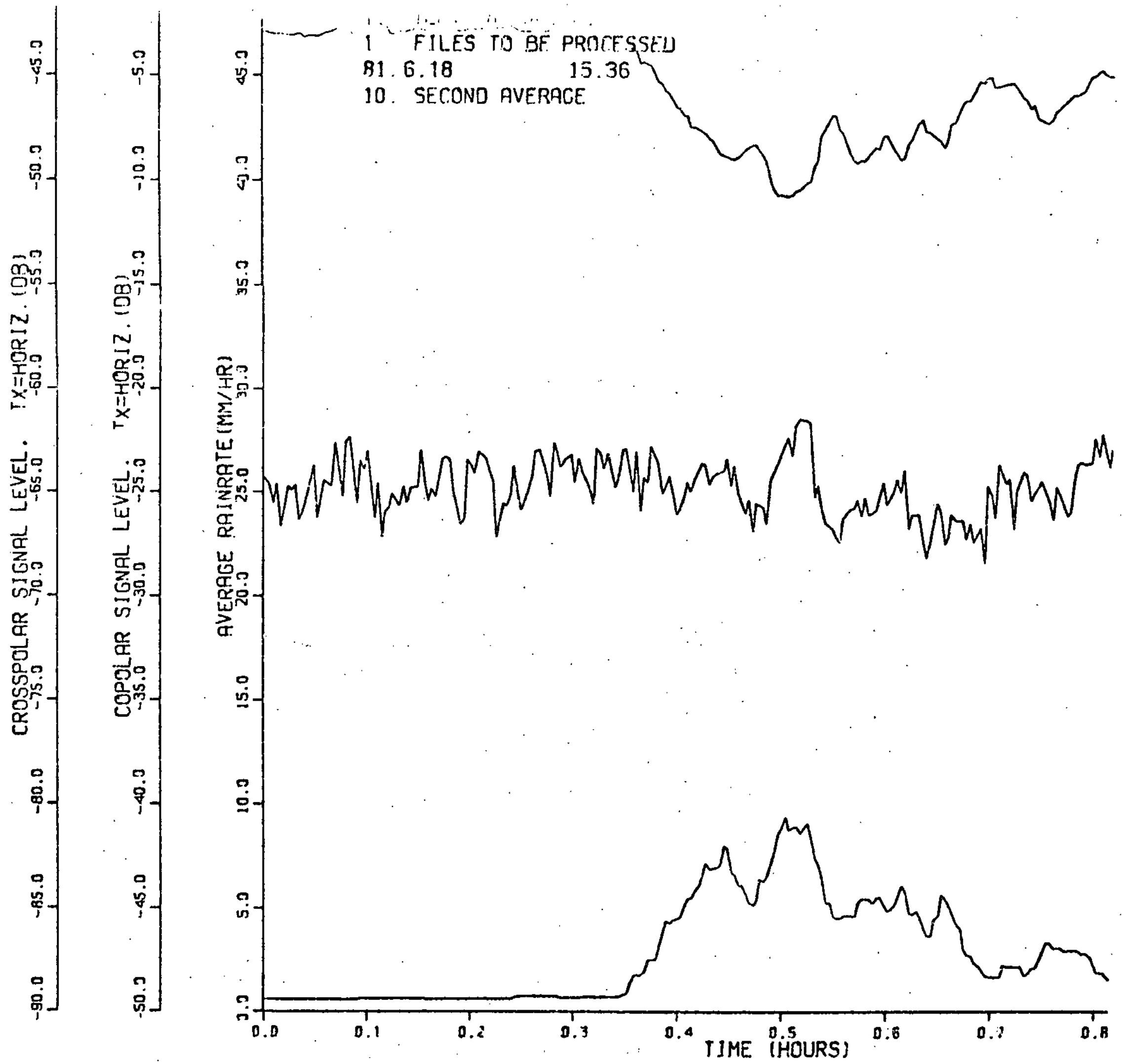

Fig. 6.8.5(a). Signal levels for horizontal polarization transmitted, 10 s avg.

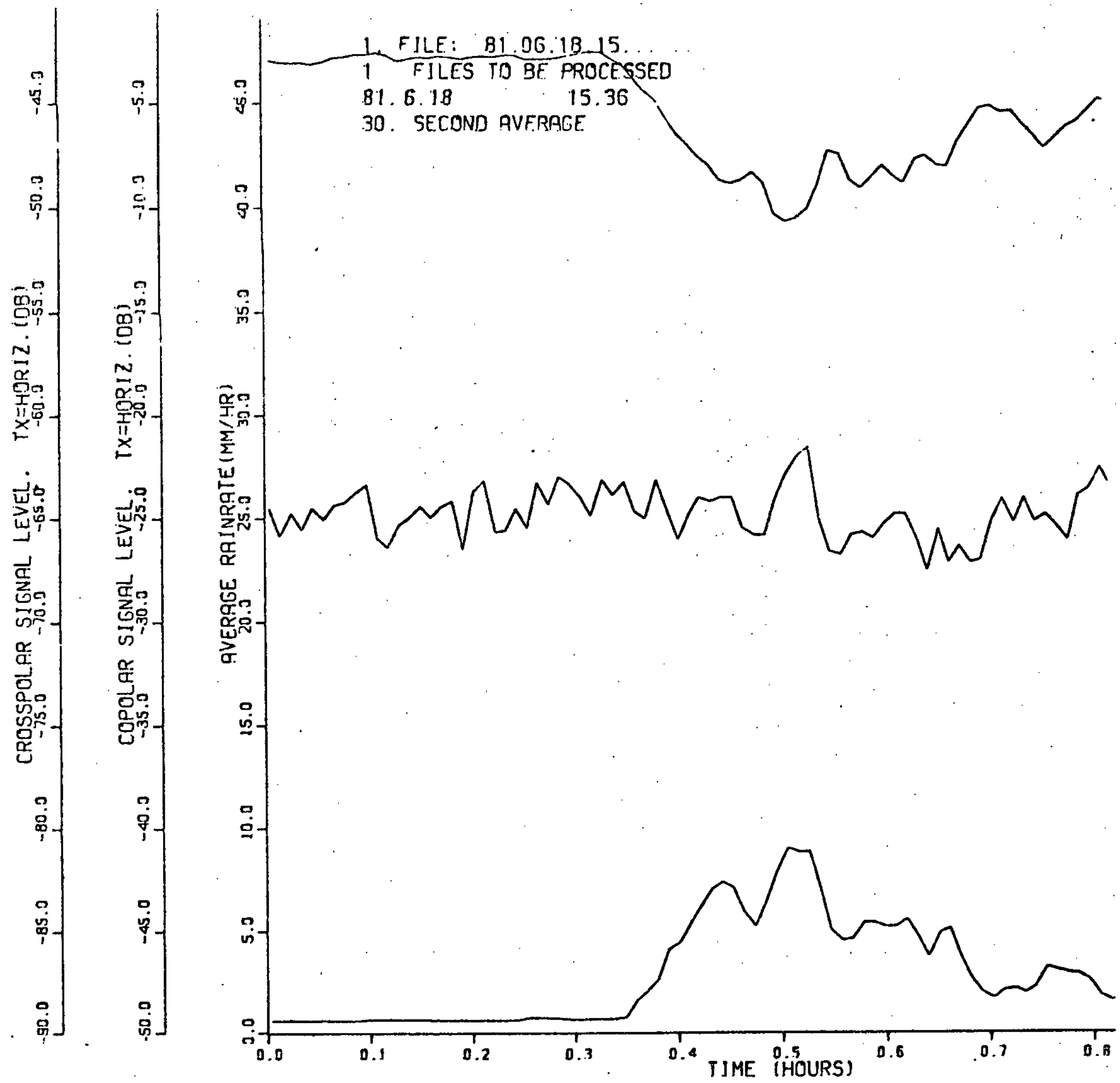

Fig. 6.8.5(b). Signal levels for horizontal polarization transmitted, 30 s avg.

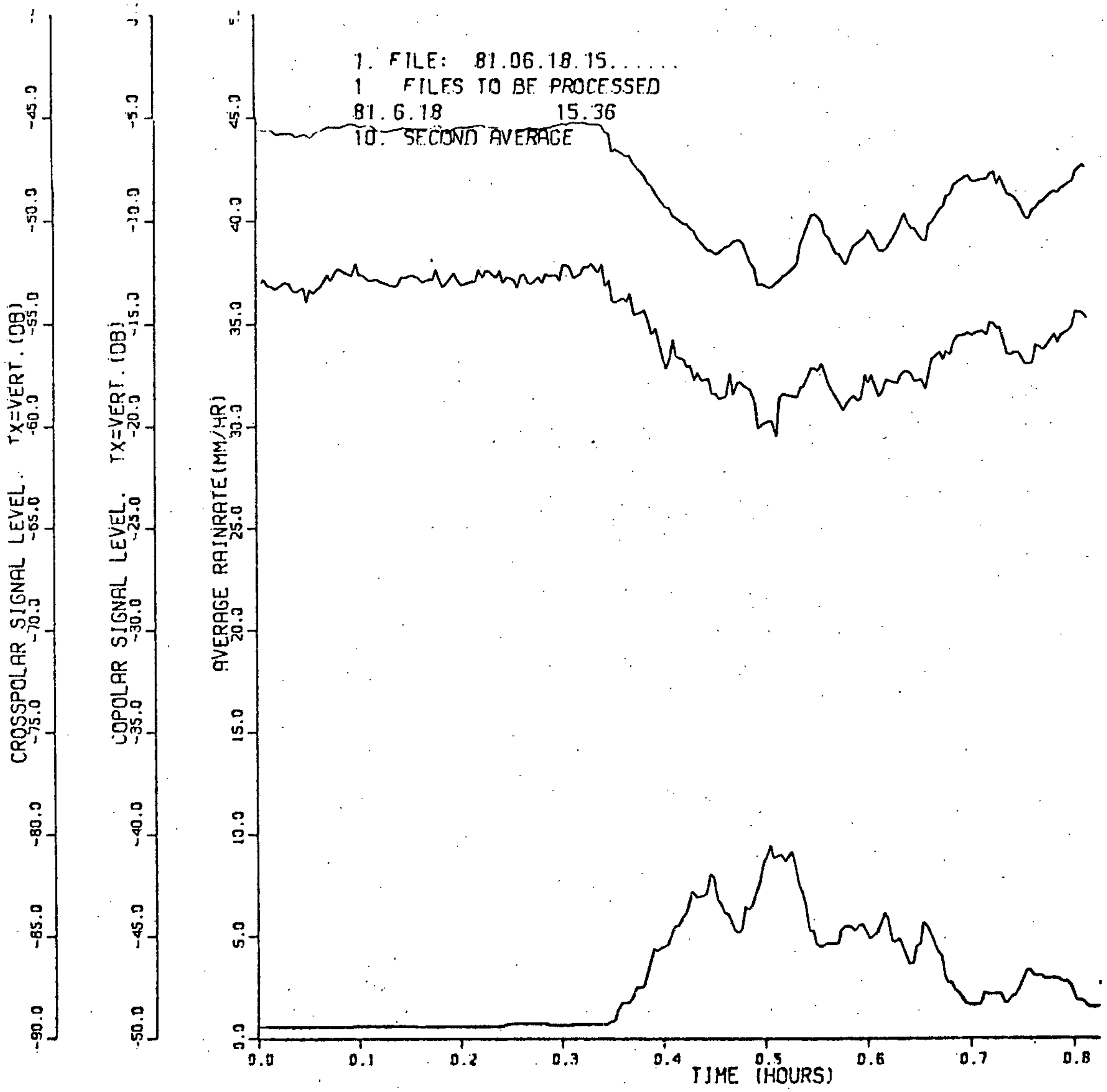

Fig. 6.8.6 Signal levels for vertical polarization transmitted, 10 s avg.

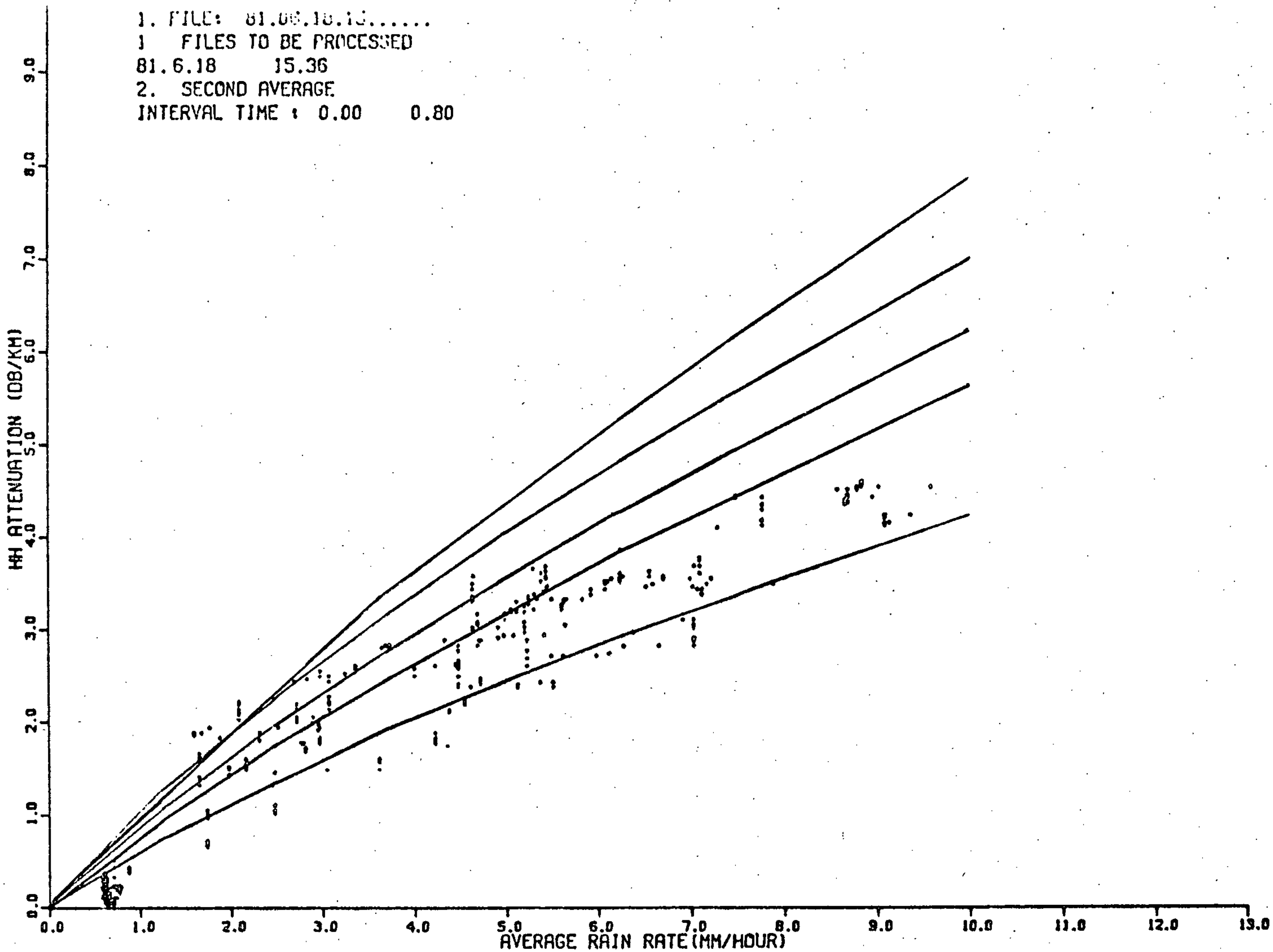

Fig. 6.8.7. CPA during 81.06.18.15.

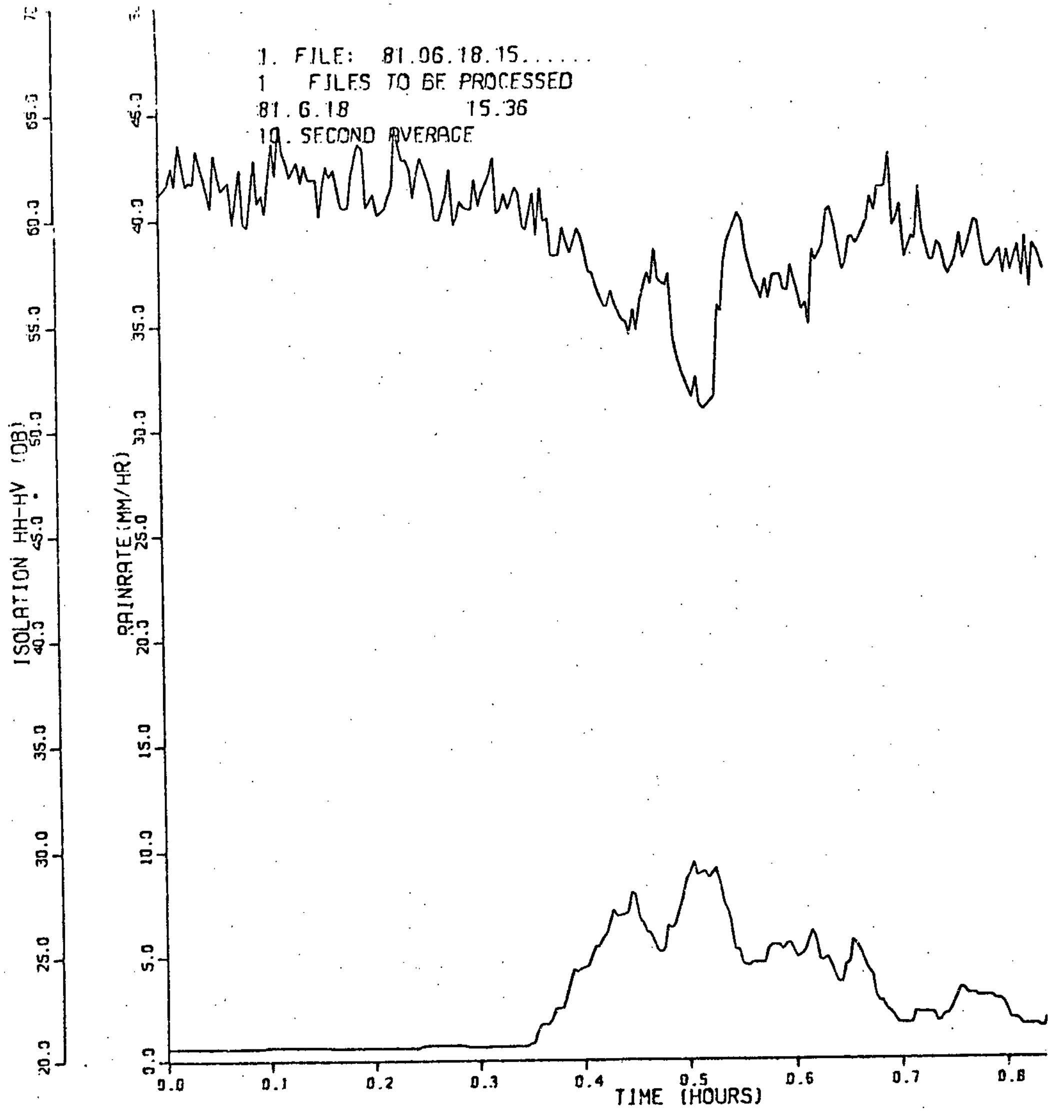

Fig. 6.8.8(a). XPD for horizontal transmitted polarization, 10 s avg.

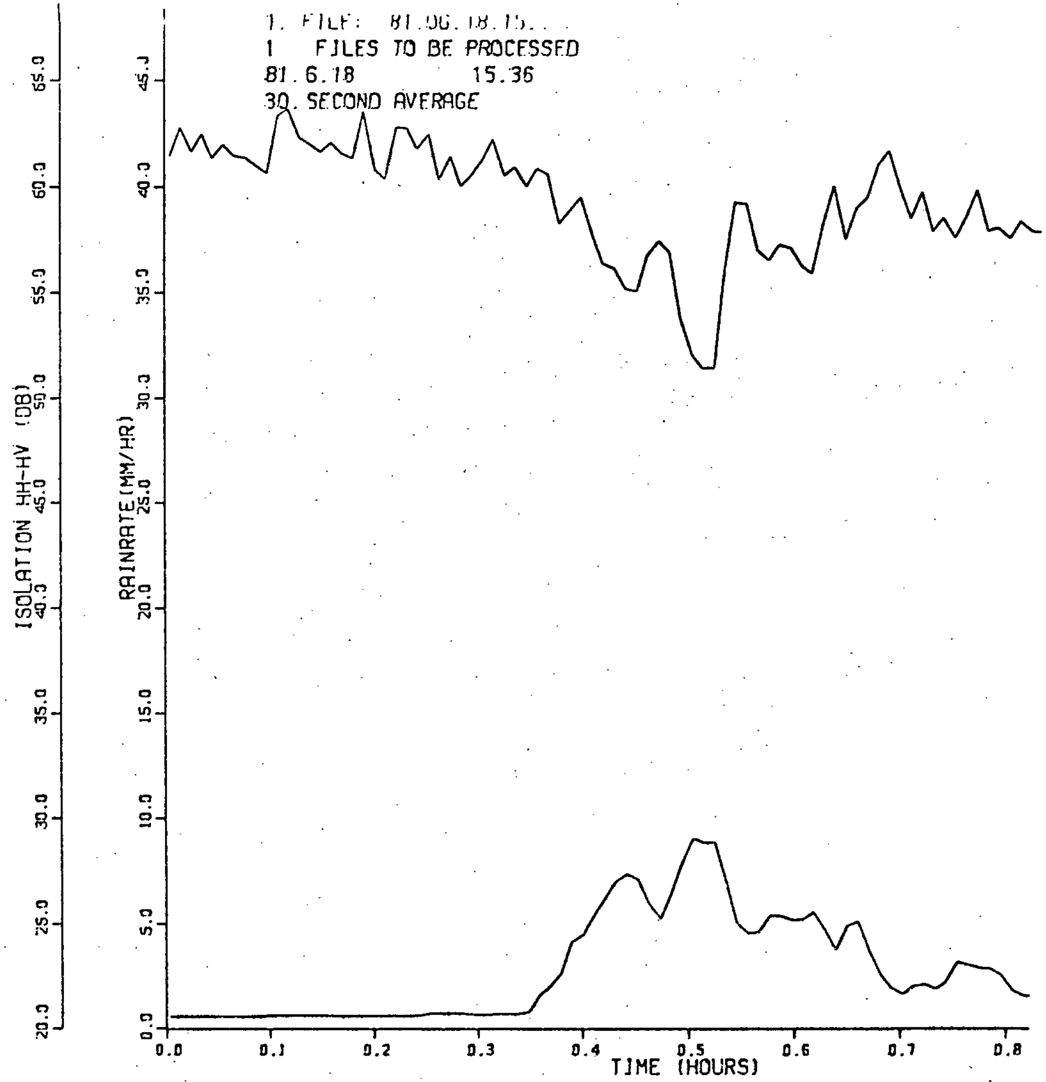

Fig. 6.8.8 (b). XPD for horizontal transmitted polarization, 30 s avg.

been considerable time averaging of the actual rainrate. As a result, some of the XPD variations in this plot may be due to small rainrate changes. Another problem is that even though the average noise level for this cross-polar channel is approximately 10 dB lower, it does not seem to be possible to achieve a stable, cancelled-crosspolar signal-level much below that shown in Figs. 6.8.8(a) (10 sec. avg.) and 6.8.8(b) (30 sec. avg.). This is definitely not due to insufficient adjustability on the cancellation attenuator and phase shifter. It is believed to be due to small short term phase and amplitude fluctuations over the path. For this reason it is not possible to be confident in the highest measured XPD values.

The scatterplot for this data, over the period 0.35-0.70 hours, with the theoretically predicted path and model predicted system XPDs are shown in Fig. 6.8.9. Calculated values are shown for the Joss/Olsen Widespread (or Marshall and Palmer) distributions for ±2° and ±4° canting angles.

The greatly improved measurement accuracy resulting from the cross-polar cancellation network is clearly demonstrated by the calculated values in Fig. 6.8.9. The values for an ideal experimental system, from Chapter 4, are included for comparison. For an ideal system, the measured XPDs would be identical for positive or negative effective mean canting angles. The maximum and minimum cancelled system XPDs calculated from the experimental model are reasonably symmetric around the ideal values. In addition, the range of possible XPD values decreases for the larger canting angles and is reasonably constant for the rainrates in Fig. 6.8.9. This is in contrast to the uncancelled system which shows larger variations in possible system XPD

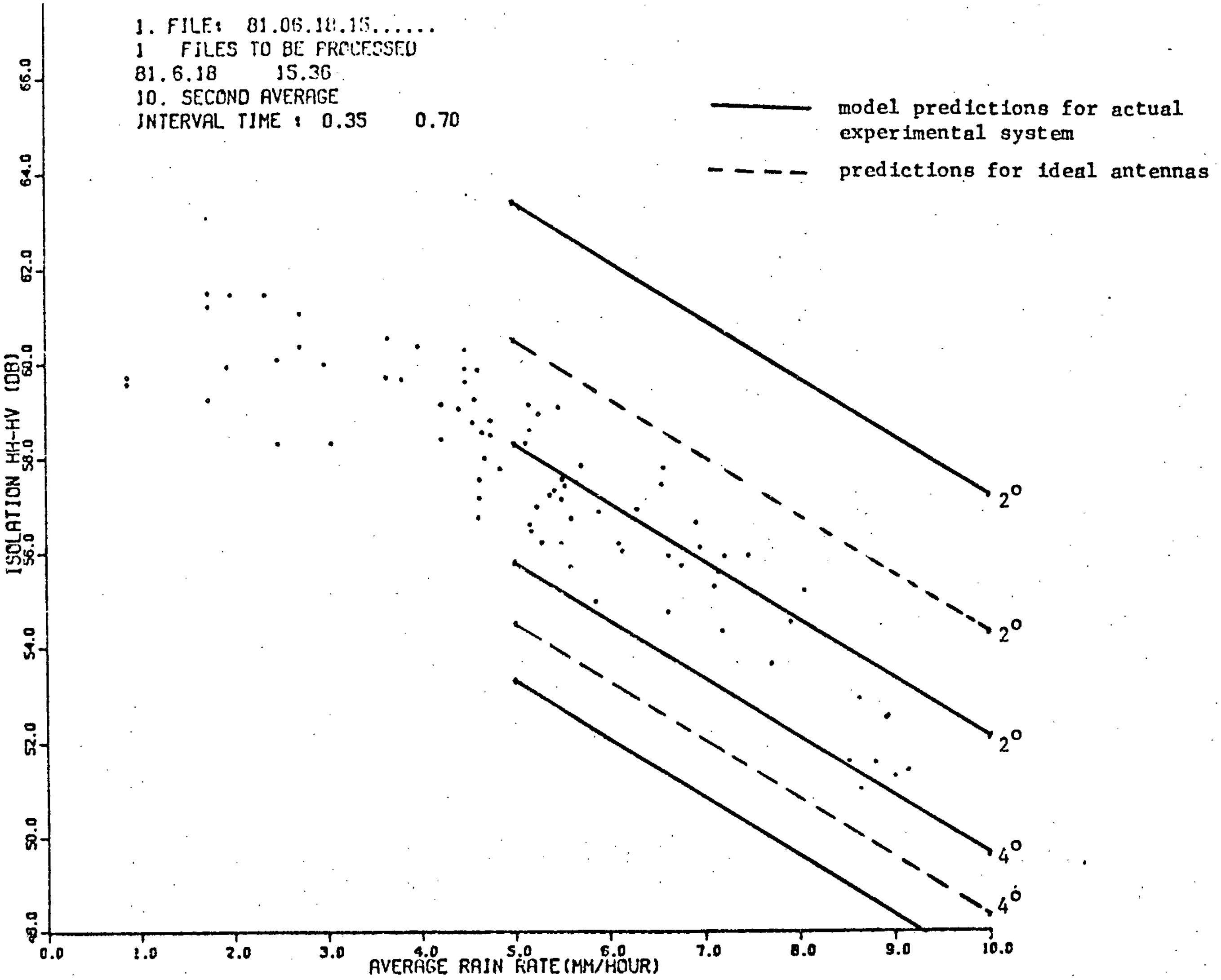

Fig. 6.8.9. XPD_H during T_1.

for larger canting angles and rainrates (for this experimental system).

From Figs. 6.8.12 and it can be seen that the differential attenuation for this even had only a small effect on the possible cancelled system XPD values. The maximum differential attenuation observed for this storm was approximately 0.4 dB. Fig. 5.13 shows this would only result in an imbalance corresponding to a 66 dB system XPD. This effect is of course, already included in the model calculations shown in Fig. 6.8.9.

The data shown in Fig. 6.8.9 indicates that the effective mean canting angle during this period was close to 3°. This is one of the larger effective mean canting angles clearly observed during many similar hours of recorded data over this path. The relatively large canting angle is believed to be due to the constant cross-path wind direction and reasonably steady, relatively high horizontal wind velocity.

Figs. 6.8.10 and 6.8.11 show the system XPD values and rainrates for vertical transmitted polarization. For this data a clear weather system XPD of 47 dB was achieved using the reflection cancellation methods discussed in Section 5.5.2.3. The observed change in the system XPD for this case was very low because of the relative angle between the path and antenna depolarized signals. In addition, the model predictions show that a very large range of system XPD values are possible even for a 2° canting angle. This is because the antenna and path depolarized signals are similar for this degree of cancellation. This data and several similar events resulted in the conclusion that, for this experiment, this type of partial cancellation was not advantageous.

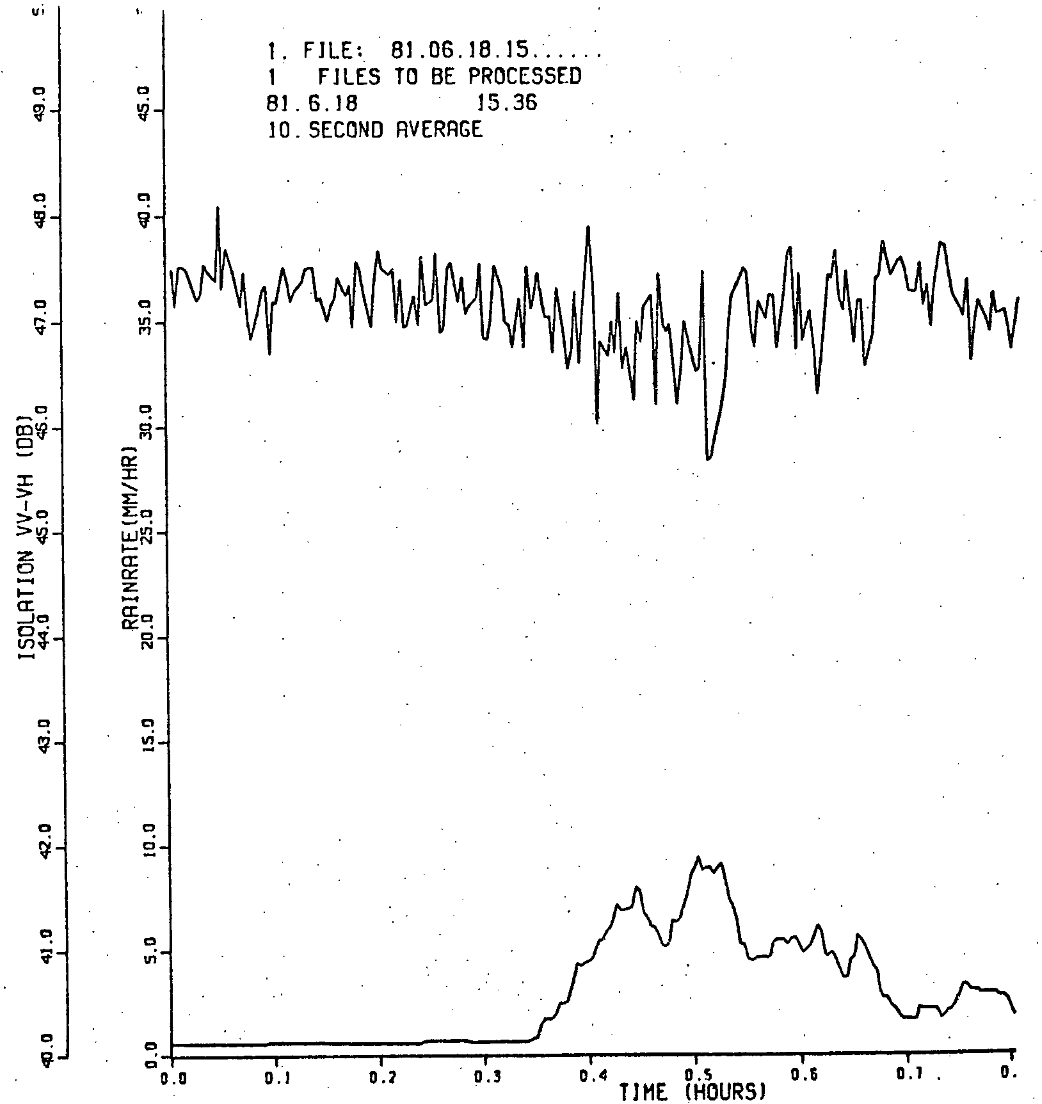

Fig. 6.8.10. XPD_V for vertical transmitted polarization, 10 s avg.

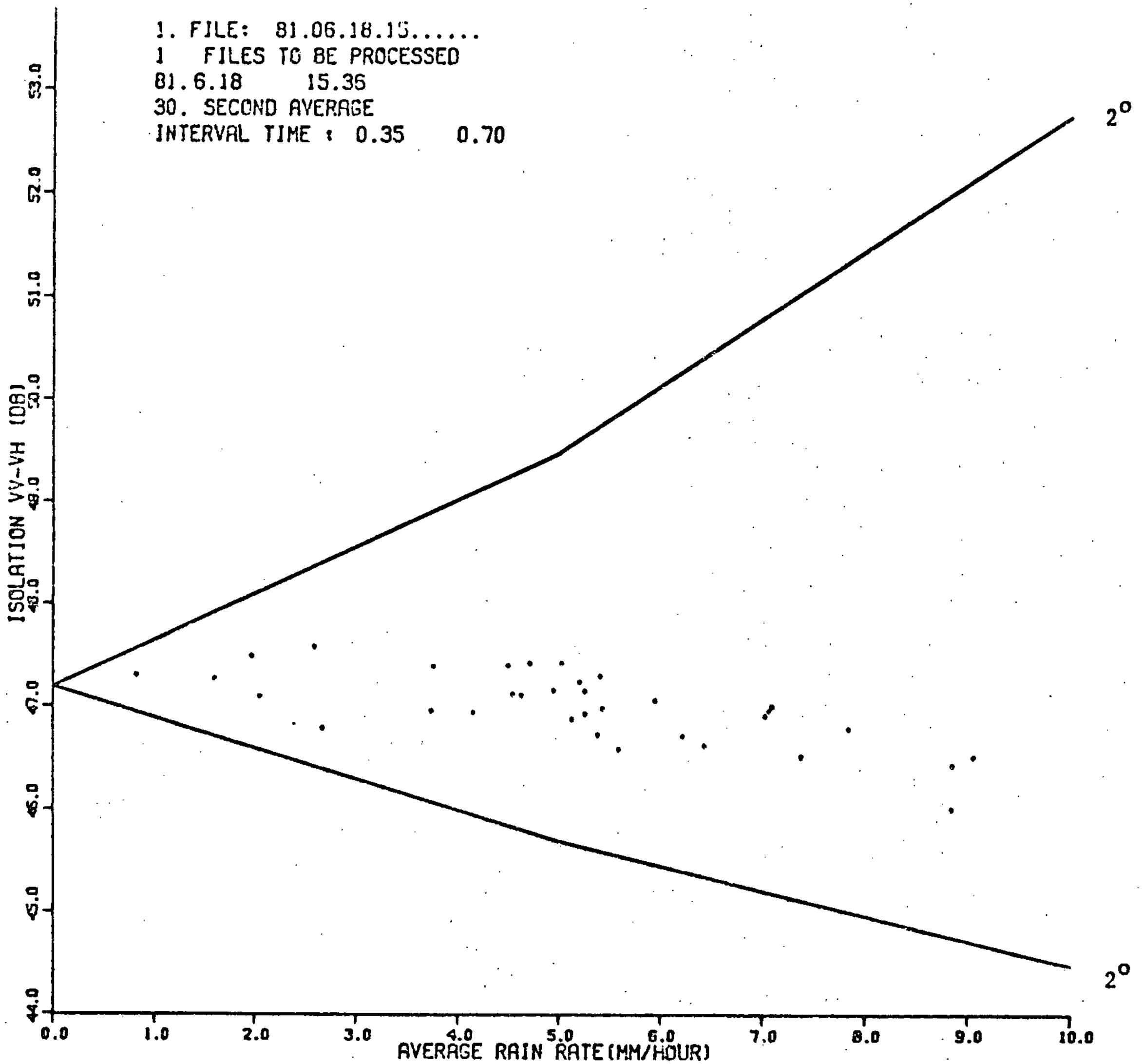

Fig. 6.8.11. XPD_V during T_1.

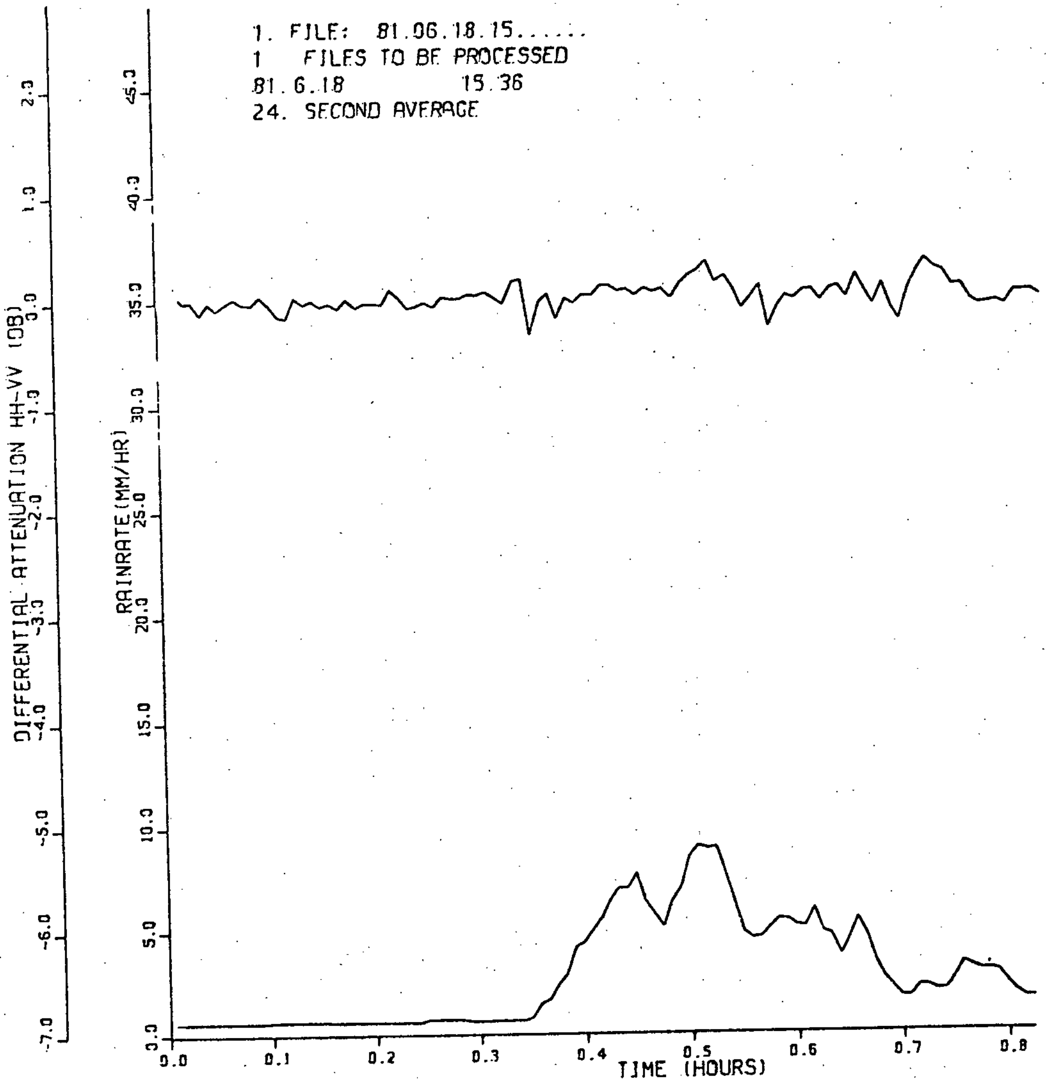

Fig. 6.8.12. Differential attenuation during 81.06.18.15.

The differential attenuation for this period, Fig. 6.8.12, is generally positive. During the highest rainrates the maximum differential attenuation is approximately 0.4 dB which is in good agreement with the theoretical predictions for this rainrate. A similar positive differential attenuation also occurs near a lower rain maxima around 0.75 h. No reason for this relatively high differential attenuation could be determined. The differential attenuation is believed to be generally positive during this file because the wind velocities were relatively constant.

6.9 Experimental Results for 81.11.14.07

This file had the highest path average rainrate - 37 mm/h - observed during the several years this experiment was operational. Individual rainrates are shown in Fig. 6.9.1.

The wind data for this period are shown in Figs. 6.9.2 to 6.9.4. During the first 30 min. of this record, the wind direction was generally ESE. At approximately 0.5 hours, when the heavy rainfall began, the wind direction changed to generally SSE. The horizontal wind velocity during the heavy rain increased from about 3 to 5 m/s during T_1, to 4 to 7 m/s during T_2 and to 6 to 8 m/s during T_3. The 30 s average vertical wind velocity, Fig. 6.9.4(b), shows a general decline as a percentage of the horizontal wind velocity in the latter portion of this record. This is believed to be at least partially due to the change in the wind direction, indicating that the vertical wind in this case, was probably caused by some topographical feature, as discussed in Section 4.4.

Signal levels for horizontal polarization transmitted are shown in Fig. 6.9.5(a) and (b) for 10 s and 30 s averages, respectively.

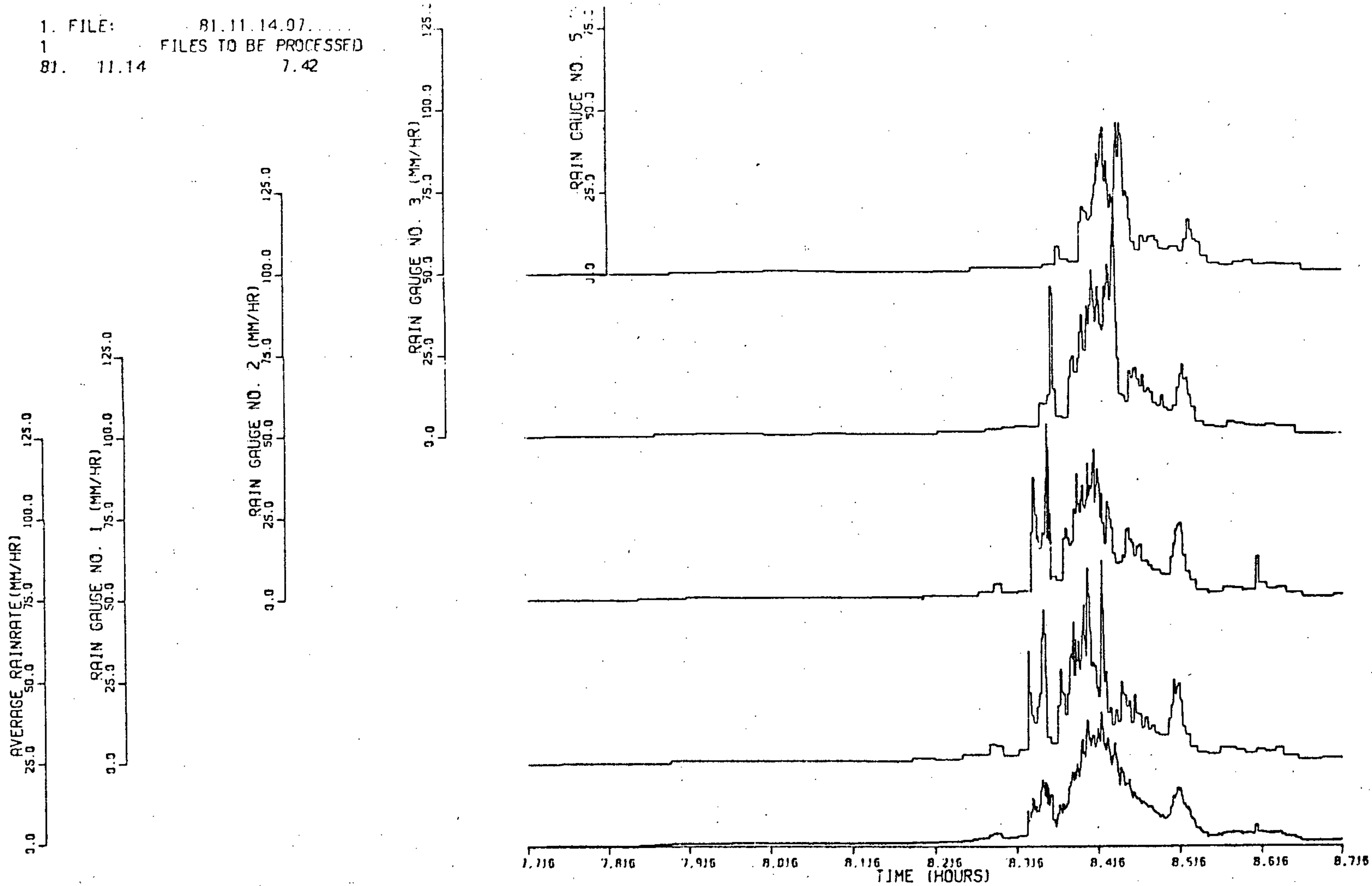

Fig. 6.9.1. Rainrates for 81.11.14.07.

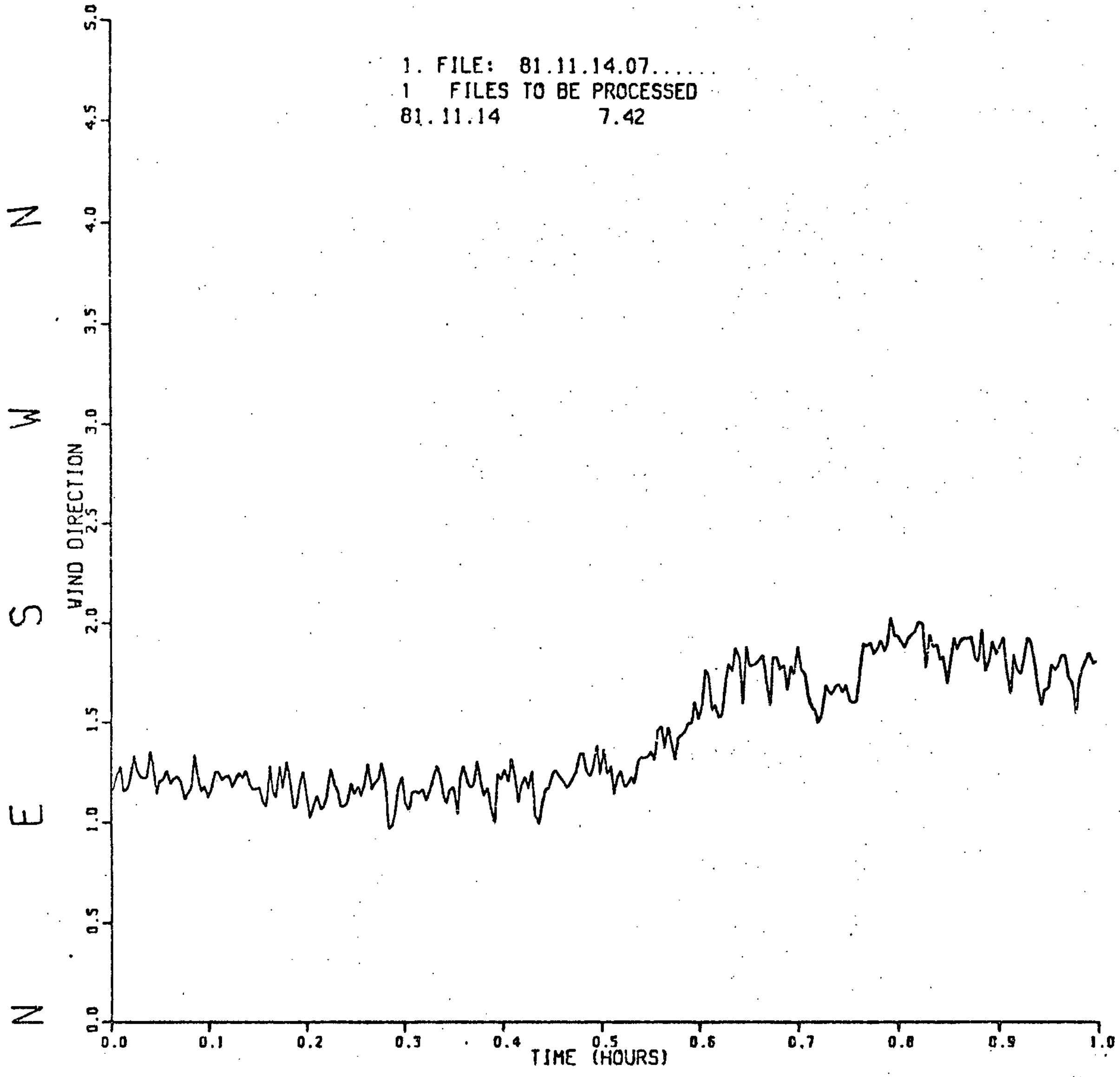

Fig. 6.9.2. Wind direction, 10 s avg. for 81.11.14.07.

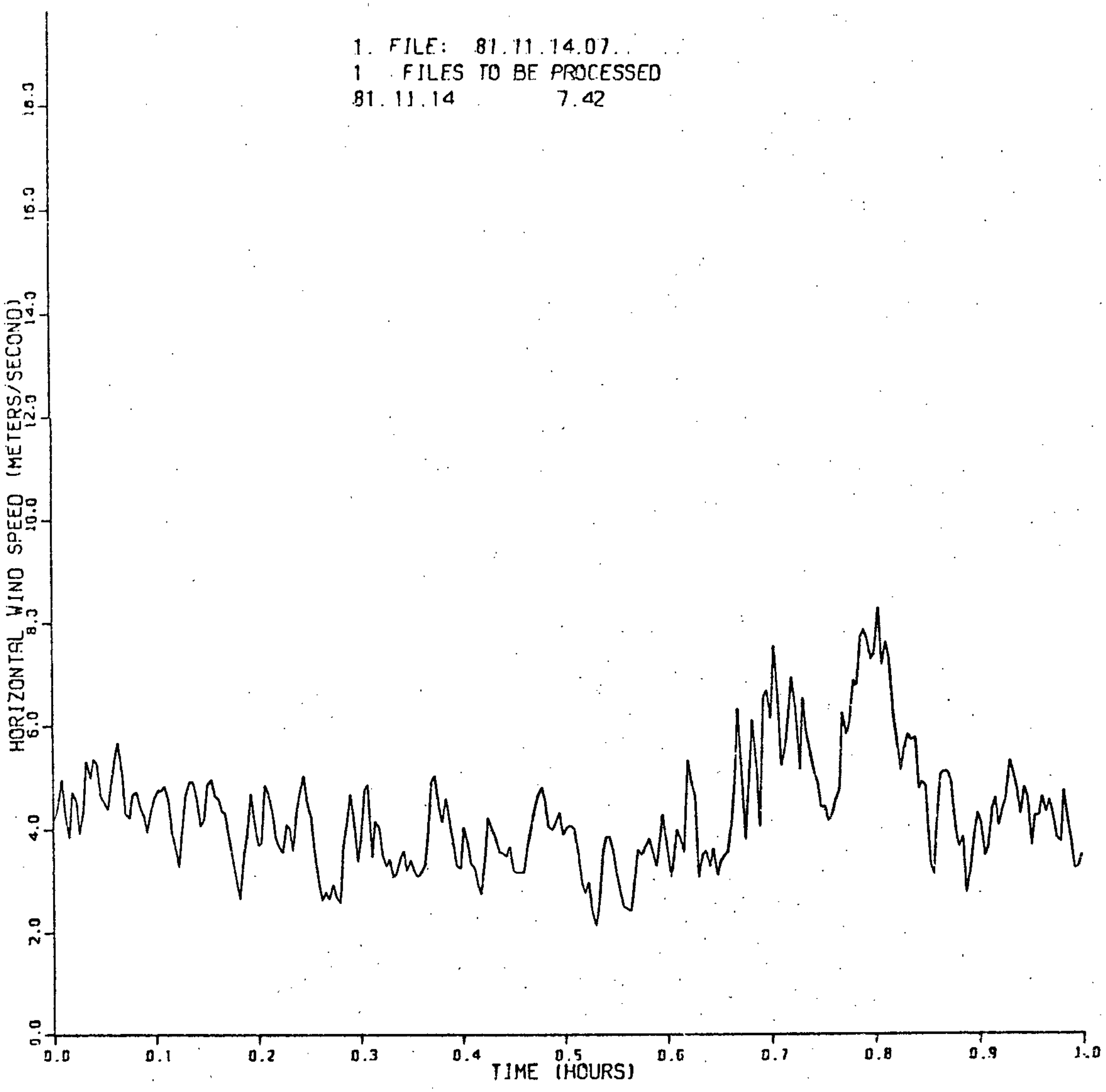

Fig. 6.9.3 Horizontal wind velocity, 10 s avg. for 81.11.14.07.

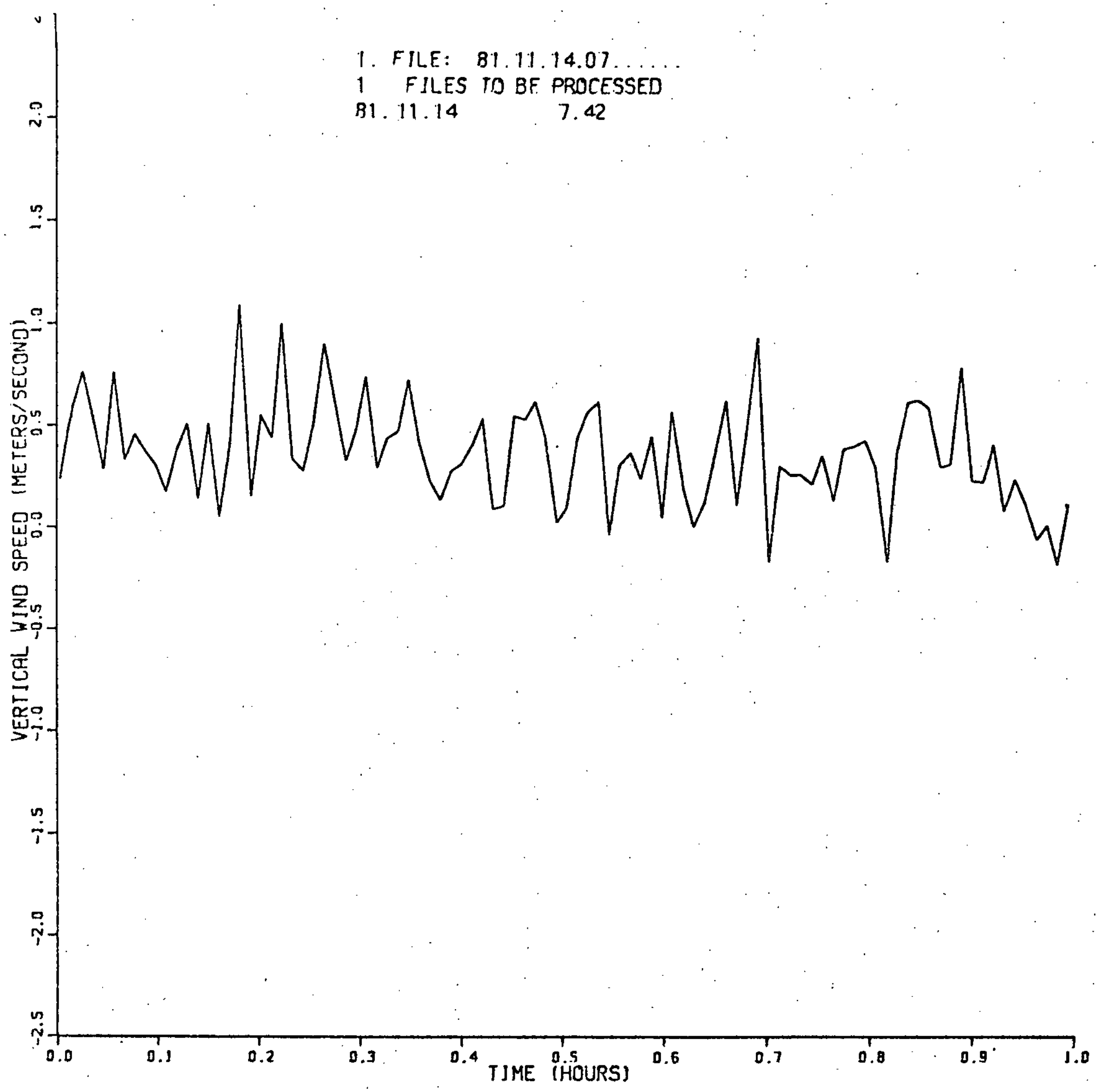

Fig. 6.9.4. Vertical wind velocity, 30 s avg. for 81.11.14.07.

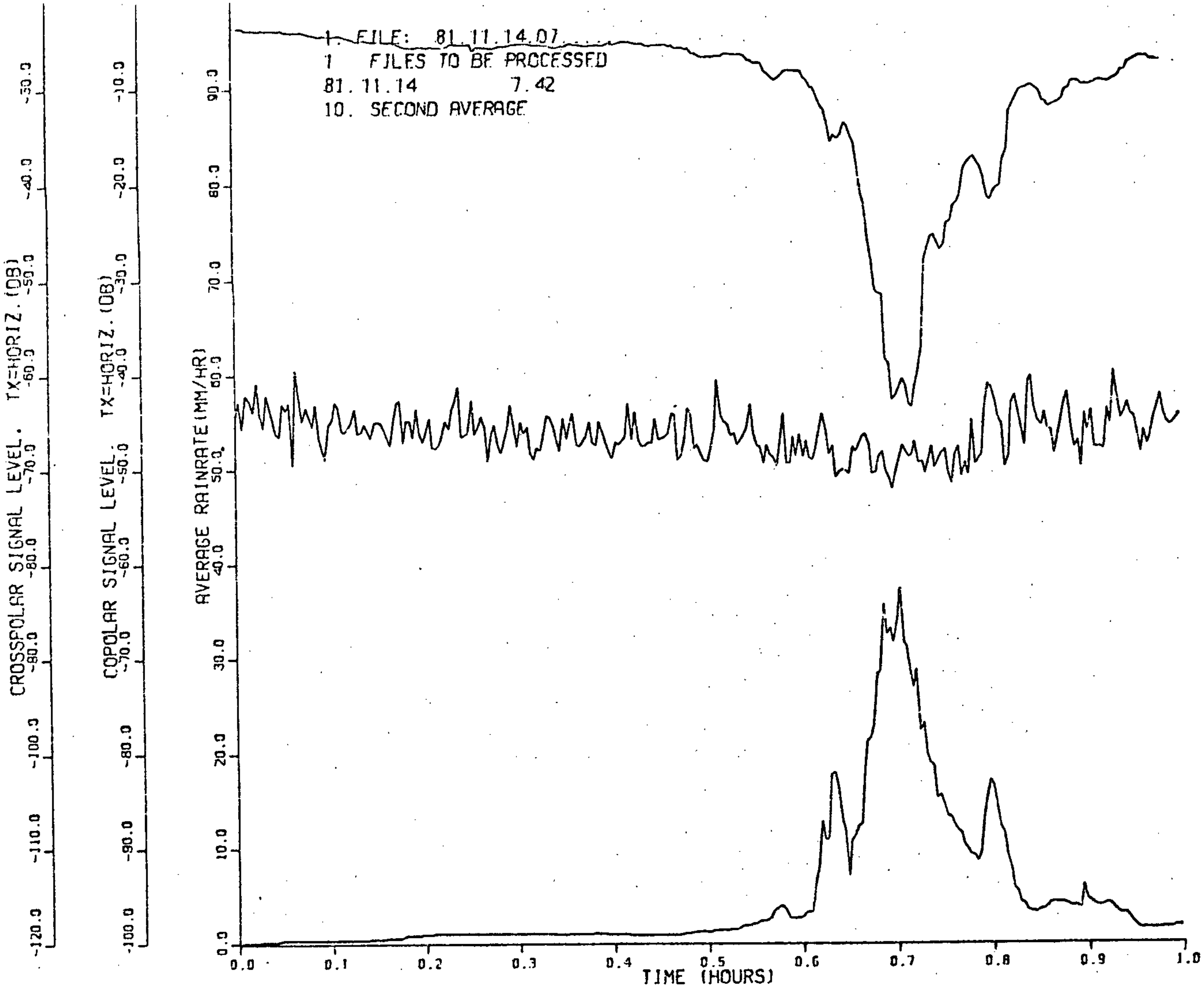

Fig. 6.9.5(a). Signal levels for horizontal polarization transmitted, 10 s avg. for 81.11.14.07.

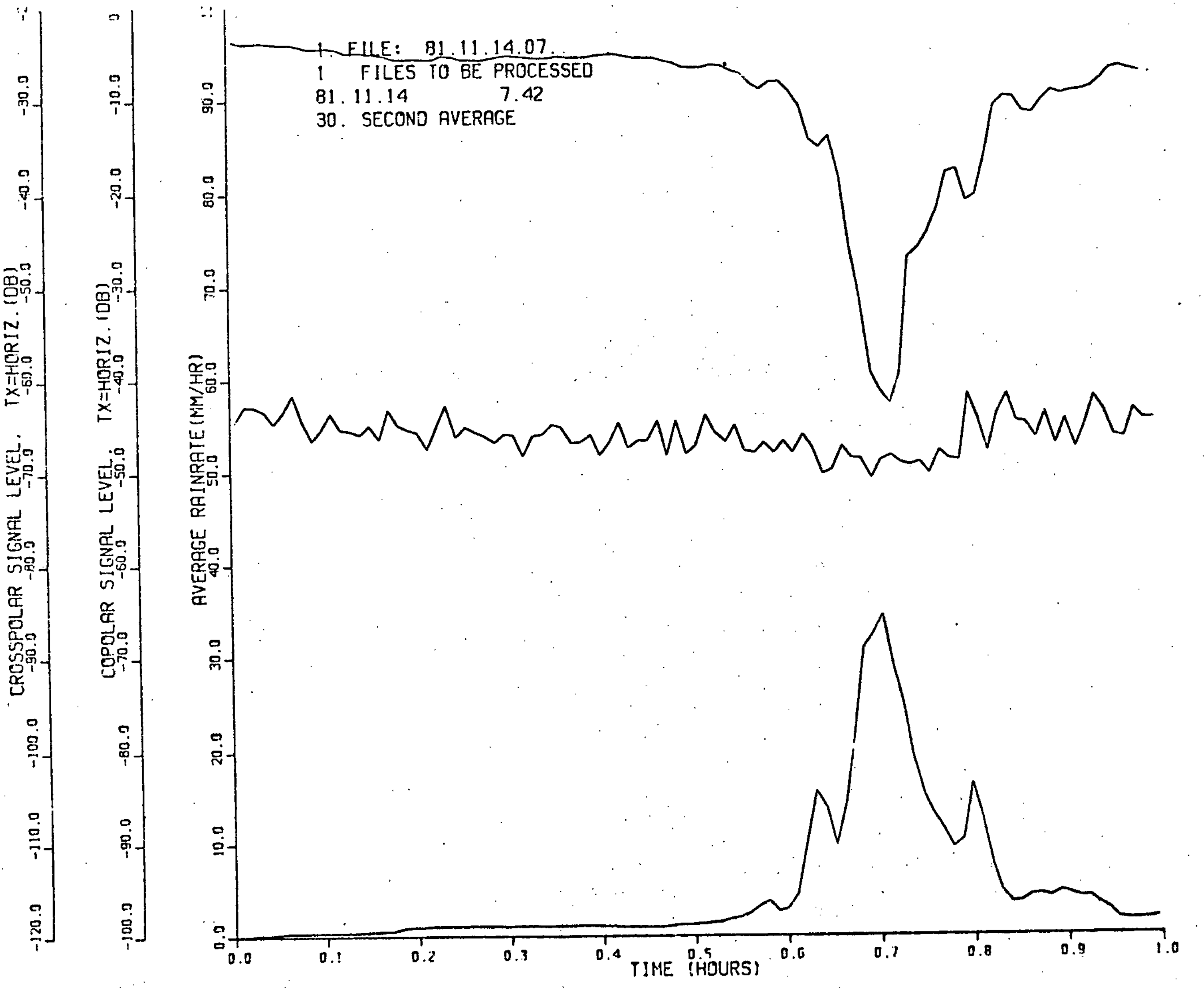

Fig. 6.9.5(b). Signal levels for horizontal polarization transmitted, 30 s avg. for 81.11.14.07.

Corresponding 10 s average levels for vertical polarization transmitted are shown in Fig. 6.9.6.

6.9.1 Attenuation Data for 81.11.14.07

Each of the intervals to be analyzed includes one of the three peaks in the measured rainrate. The peak path-average rainrates in intervals T_1 and T_3 are similar in magnitude but the individual rainrates show that the raincell structure during these two periods was very different. The peak rainrates were much higher and the cell area much smaller in the T_1 interval at the beginning of the storm. From Figs. 6.9.5 and 6.9.6 it can be seen that the attenuations for the same rainrates were very much lower during T_1 than during T_3.

A summary of the attenuation results for this storm are given in Table 6.9.1.

6.9.1.1 Attenuation During T_1, 0.56-0.65 h

During interval T_1, the attenuation at rainrates above 10 mm/h were similar to, or slightly lower than, those predicted for the JOT distribution. The vertical wind (Fig. 6.9.4(b)) went through an upward peak as the rainrate began to increase during T_1. This may account for the relatively higher attenuations at the lower rainrates. During the high rainrates in T_1, the 30 second vertical wind was close to zero and therefore could not have significantly affected the attenuation. In this case, the lower attenuations were probably due to a large number of large drops at the leading edge of this

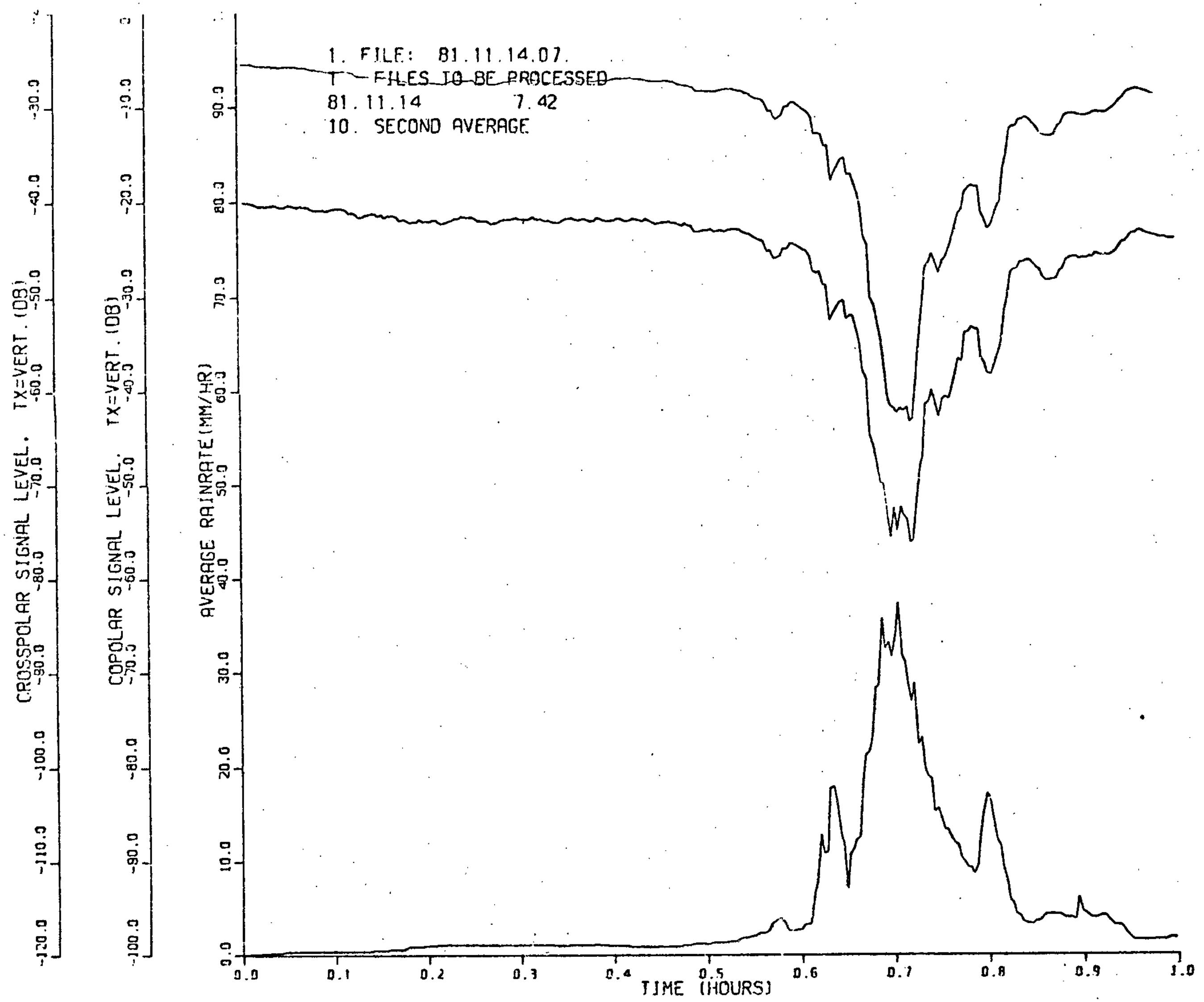

Fig. 6.9.6. Signal levels for vertical polarization transmitted, 10 s avg. for 81.11.14.07.

Period	Measured Attenuation Compared to Standard Predictions	Vertical Wind During Rain	Data is in Approximate Agreement with Predictions for:	Comments
T_1 0.56-0.65 h	Agreed with JOT above 10 mm/h. Higher at low rainrates. Fig. 6.9.7	$\cong$.5 m/s peak during increasing rainrate Approx. zero during higher rainrates. Fig. 6.9.4	JOT with zero vert. wind above 10 mm/hr. Fig. 6.9.7	Vertical wind peak probably accounts for higher atten. at low rainrates. Generally low at leading edge of storm.
T_2 0.65-0.77 h	Generally higher than T_1. Fig. 6.9.8	Generally upward (See also T_2(a) and T_2(b) Fig. 6.9.4	Varied between JOW to higher than JOD Fig. 6.9.8	Generally higher than T_1 because of change in drop distribution as storm progresses.
T_2(a) 0.68-0.70 h	Slightly higher than JOD, largest at higher rainrates. Fig. 6.9.9	Increased from $\cong$0.2 to 1.0 m/s as rainrate increased. Fig. 6.9.4	Higher than JOW and vert. wind = 1 m/s at high rainrates. Fig. 6.9.9	4

. . . continued

Period	Measured Attenuation Compared to Standard Predictions	Vertical Wind During Rain	Data is in Approximate Agreement with Predictions for:	Comments
T_2(b) 0.70-0.72 h	Higher than T_2(a) Generally increasing atten. during decreasing rainrate. Fig. 6.9.10	Decreased from $\cong$+1.0 to -0.2 m/s as rainrate began to decrease. Fig. 6.9.4	Refer to comments and Section 6.9.1.2	3
T_3 0.77-0.84 h	Between JOW and JOD Fig. 6.9.11	Relatively constant at +0.4 m/s during highest rainrates See also T_3(a) Fig. 6.9.4	Slightly higher than JOT and vert. wind = 1 m/s or close to JOW and zero vert. wind at higher rainrates. Fig. 6.9.11	2 if actual drop distribution was close to JOT
T_3(a) 0.80-0.84 h	Close to JOD Fig. 6.9.12	Decreased from +0.4 m/s to -0.2 m/s as rainrate decreased. Fig. 6.9.4	JOW and vert. wind $\cong$ +1 m/s. Fig. 6.9.12	3

Table 6.9.1 Summary of Attenuation Data for 81.11.14.07

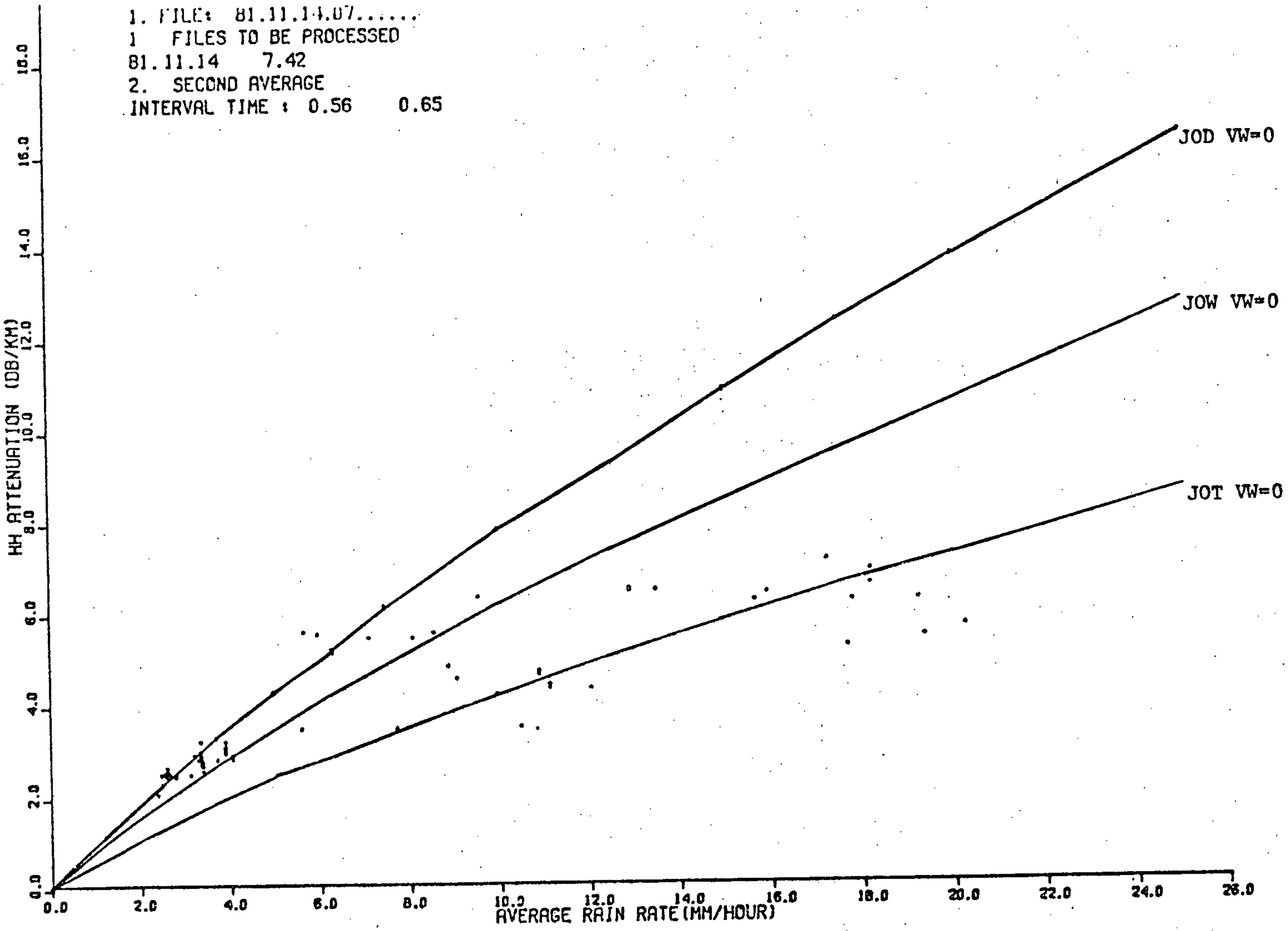

Fig. 6.9.7. CPA during T_1.

storm and may have been partially due to the small cell area causing some inaccuracy in the path rainrate measurement.

6.9.1.2 Attenuation During T_2, 0.65-0.72 h

During T_2, the CPA which is shown in Fig. 6.9.8, was generally much higher than during T_1 and at times was even higher than the standard predictions for the JOD distribution. The generally higher attenuations are thought to be due to a change in the drop distribution as this storm progressed.

The exceptionally high attenuations during T_2 were due to vertical wind effects. To illustratre this, two subperiods of T_2, i.e. T_2(a) and T_2(b), will be analyzed (Figs. 6.9.9 and 6.9.10). During T_2(a) the vertical wind increased from approximately +0.2 to +1.0 m/s as the rainrate increased, explaining the unusually high attenuations at higher rainrates in Fig. 6.9.9. At the start of T_2(b), the vertical wind changed direction and decreased from approximately 1.0 m/s to -0.2 m/s as the rainrate started to decrease. This decreasing vertical wind "released" the small drops stored above the path by the previous upward velocity resulting in very high attenuations and the generally increasing attenuation with decreasing rainrate as shown in Fig. 6.9.10.

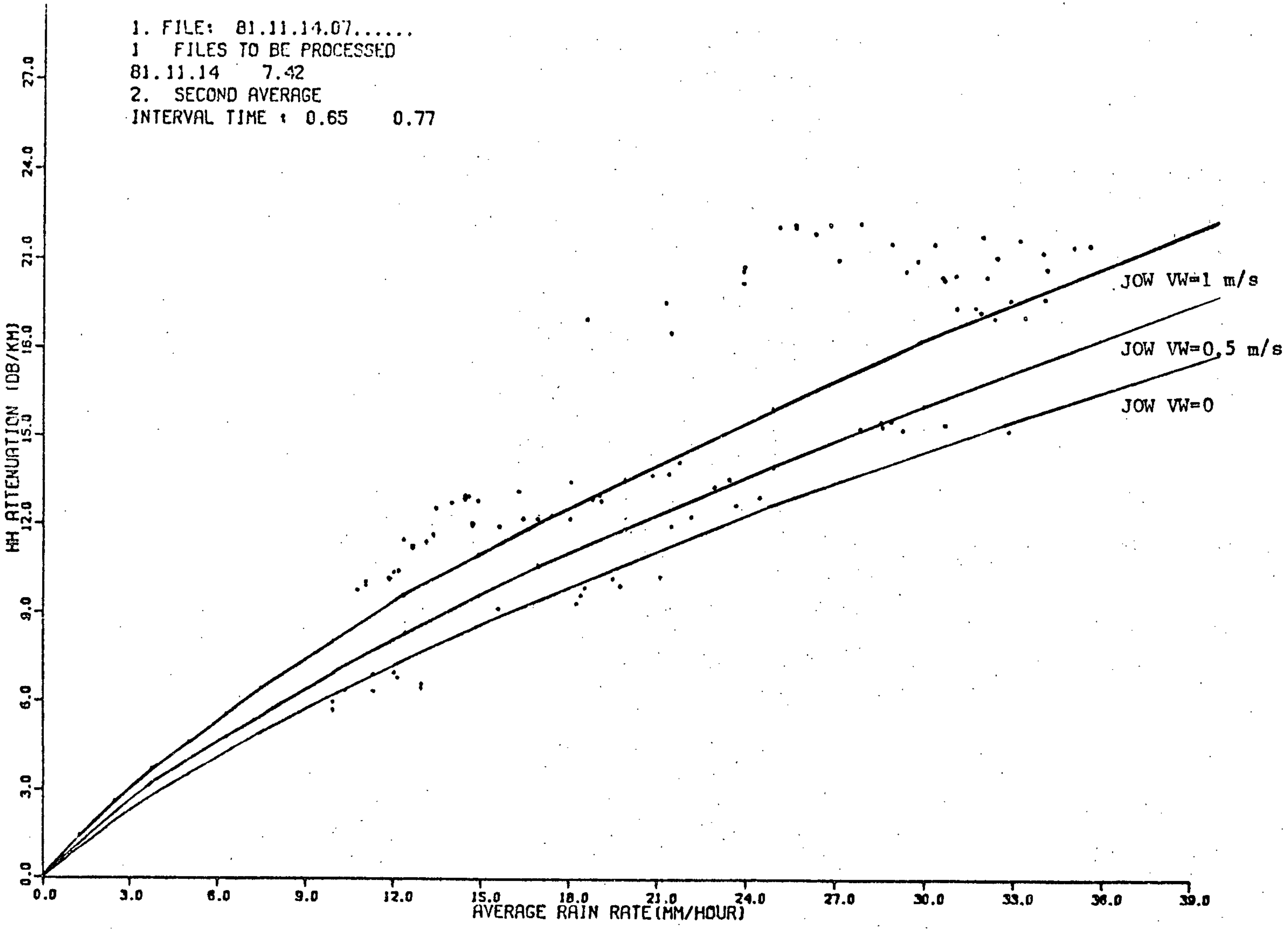

Fig. 6.9.8. CPA during T_2.

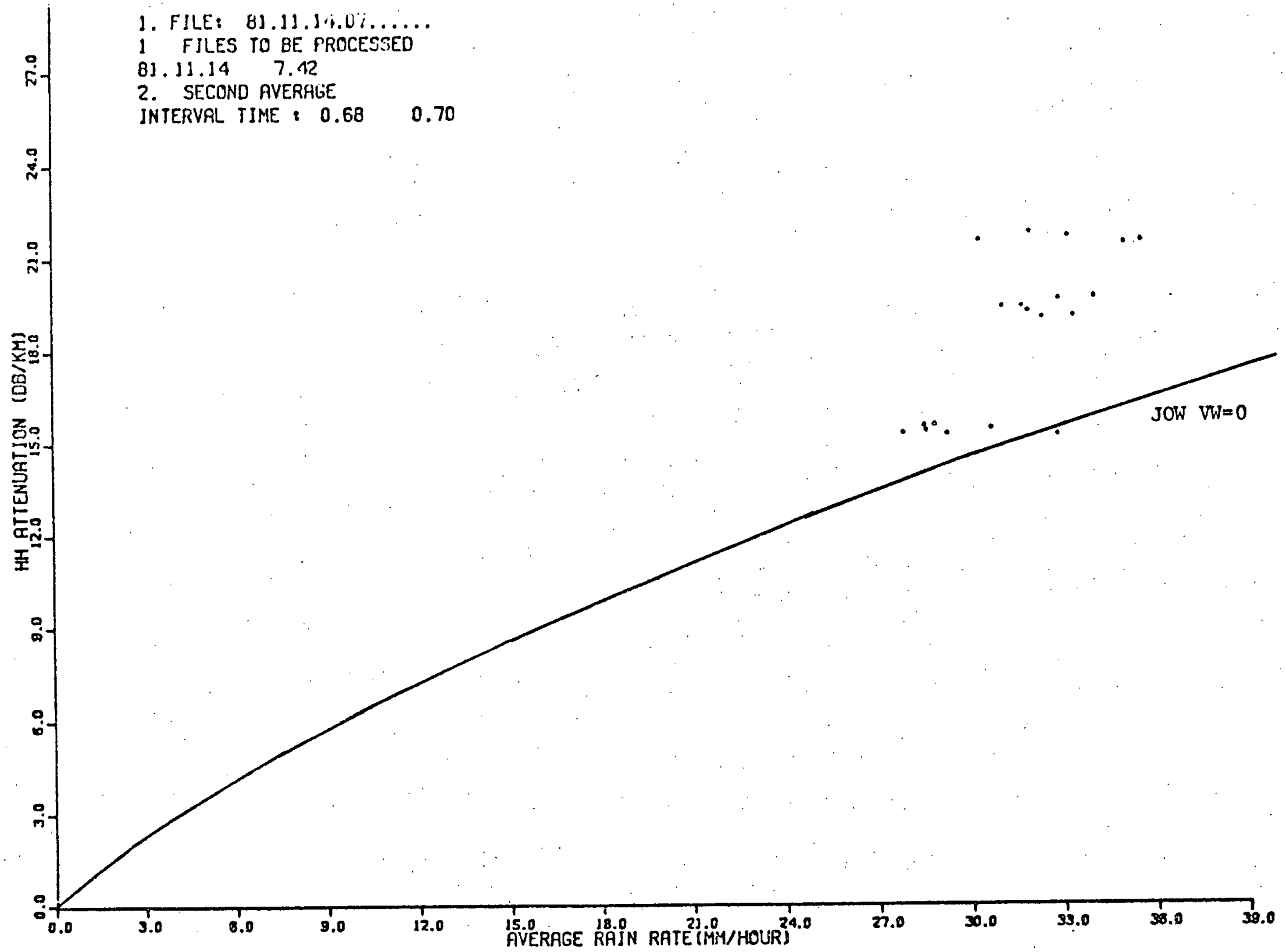

Fig. 6.9.9. CPA during T_2(a).

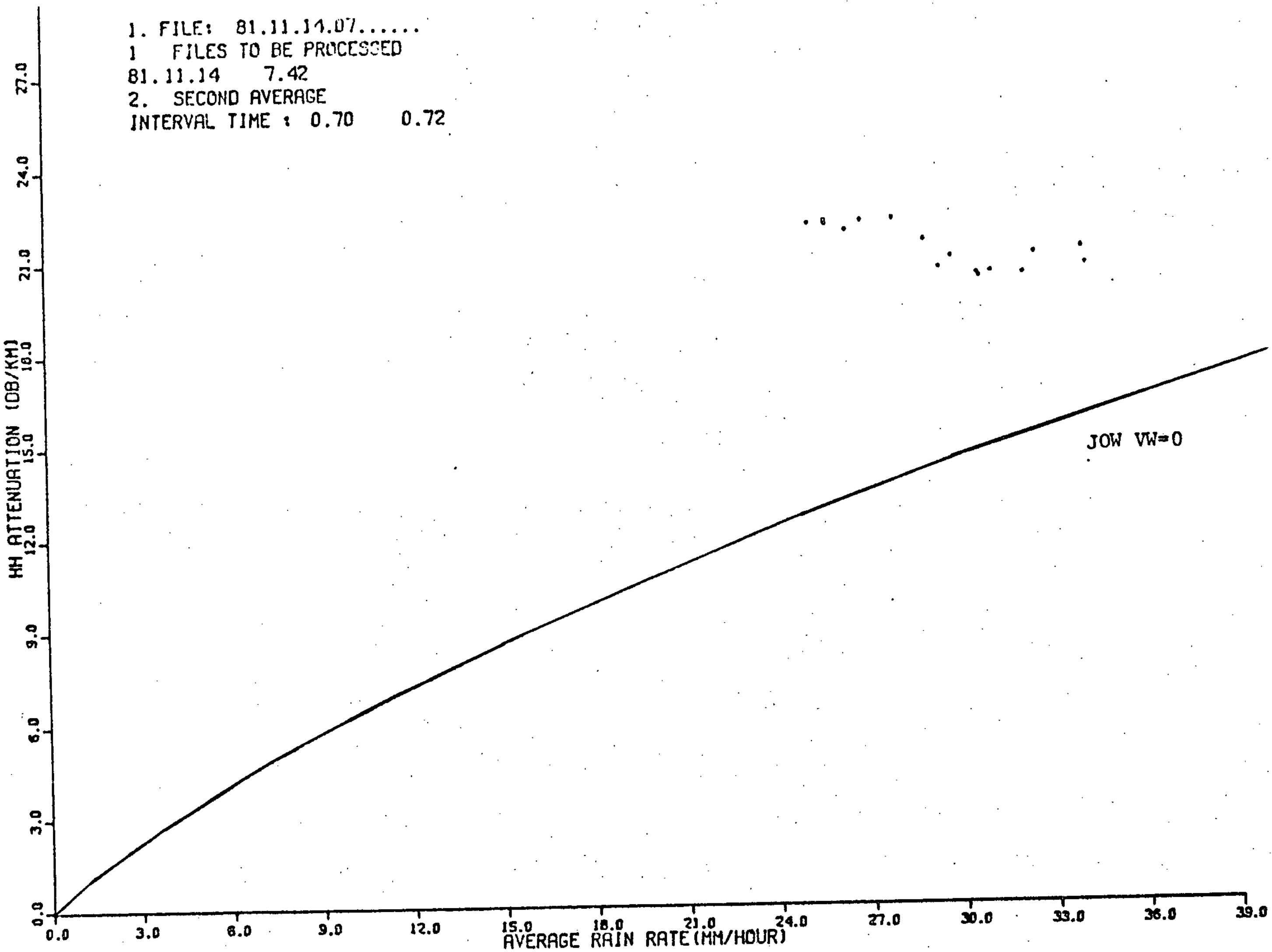

Fig. 6.9.10. CPA during T_2(b).

6.9.1.3 Attenuation During T_3, 0.77-0.84 h

Attenuation during T_3, Fig. 6.9.11, was slightly higher than expected for this type of rainstorm. This is thought to be due to the small but relatively constant upward wind velocity observed during the periods of relatively high rainrate (i.e. up to 0.81 h).

Most of the higher attenuations during this period occurred during T_3(a), 0.80-0.83 h, shown in Fig. 6.9.12. This higher attenuation was the result of the vertical wind decreasing from approximately +0.4 m/s to -0.2 m/s after a period of constant upward flow.

6.9.2 XPD and Differential Attenuation Data for 81.11.14.07

Figs. 6.9.13(a) and (b) are the 10 second and 30 second average time-series cancelled-system XPDs for horizontal transmitted polarization. From Fig. 6.9.5(b), it can be seen that during at least part of T_2, the system XPD measurement range was exceeded because the crosspolar signal level is at, or close to, the noise floor. For this crosspolar signal channel, the noise level was usually a few dB lower than the lowest levels in Fig. 6.9.5(b), suggesting that some depolarized signal may have been received. During parts of T_1, the measurement range may also have been exceeded, so the XPD data for this interval (Fig. 6.9.15) must be considered to be the XPD indicated or possibly some higher value. In other words, the actual system XPD could be higher but not lower than the 53 dB indicated during T_1. During T_3 the peak crosspolar signal levels are at least 10 dB above the noise level and can therefore be considered as reasonably accurate.

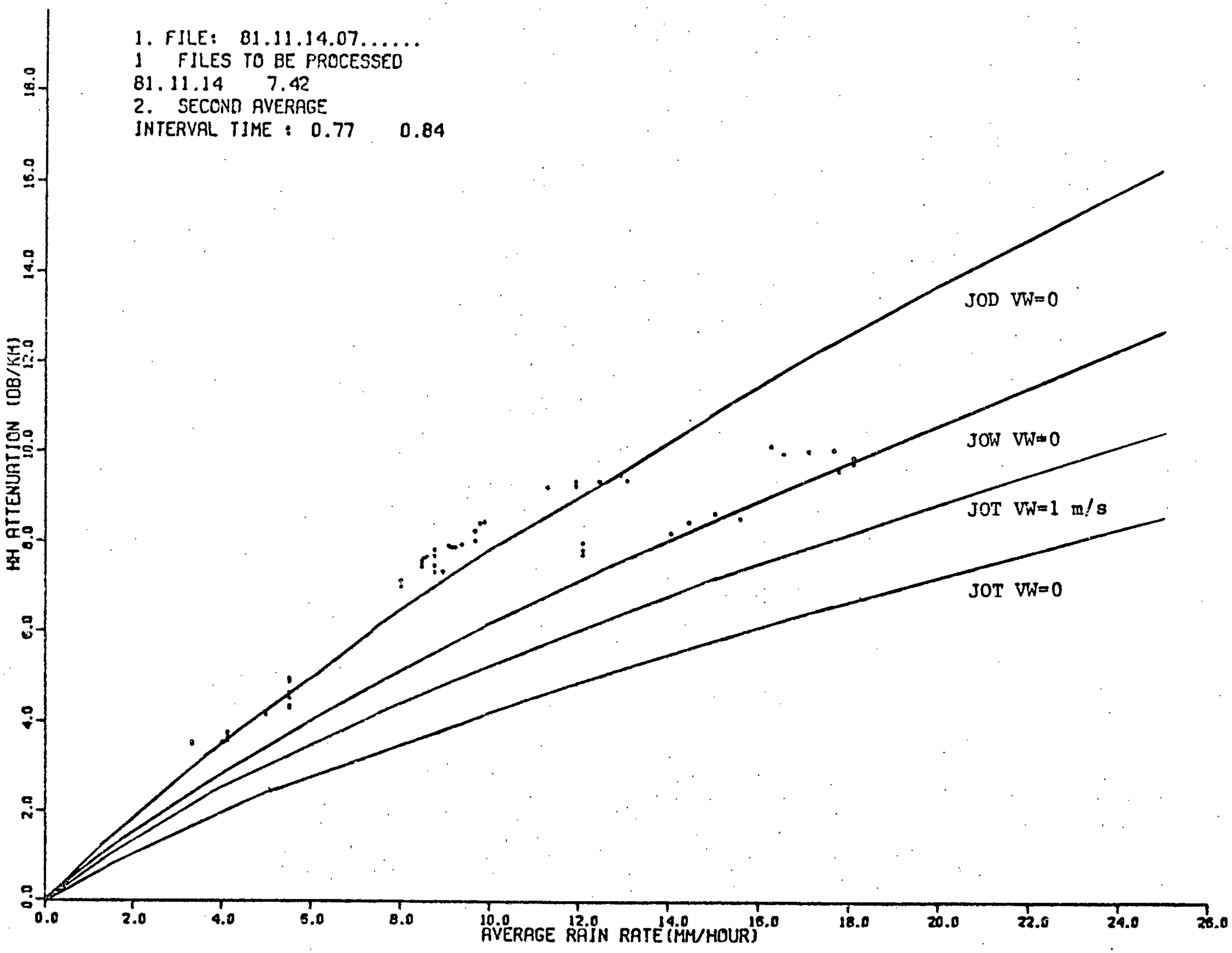

Fig. 6.9.11. CPA during T_3.

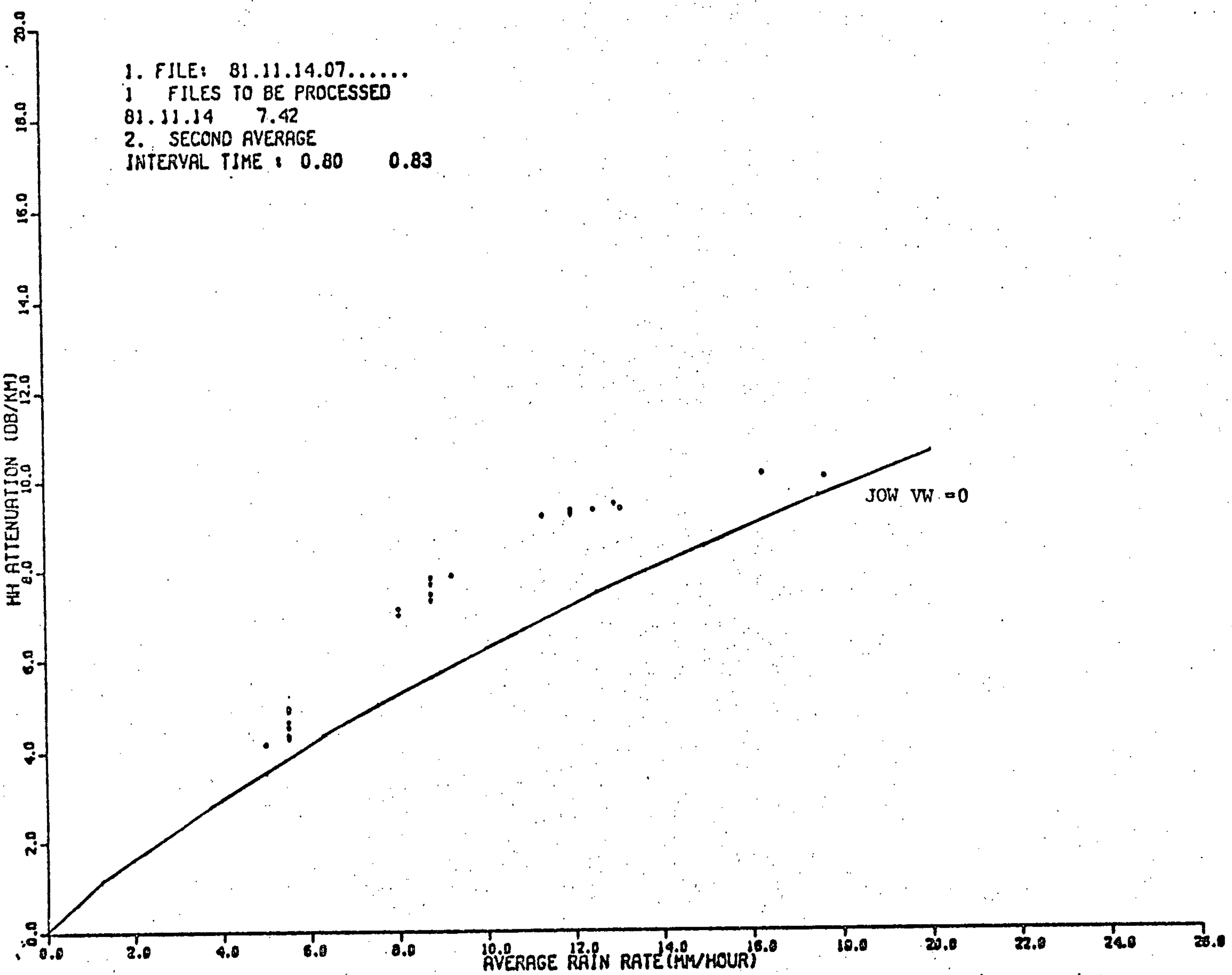

Fig. 6.9.12. CPA during T_3(a).

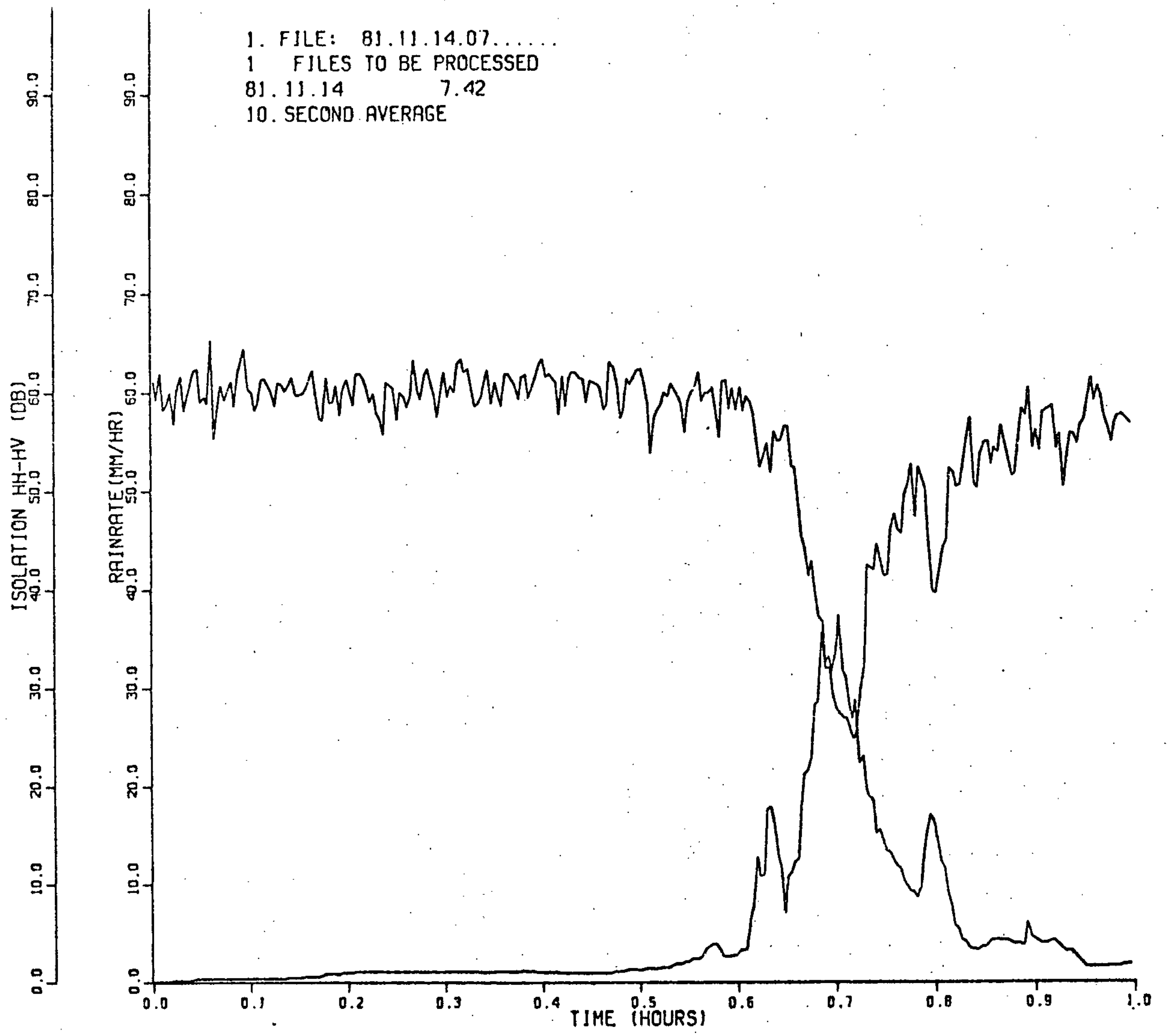

Fig. 6.9.13(a). XPD for horizontal transmitted polarization, 10 s avg. for 81.11.14.07.

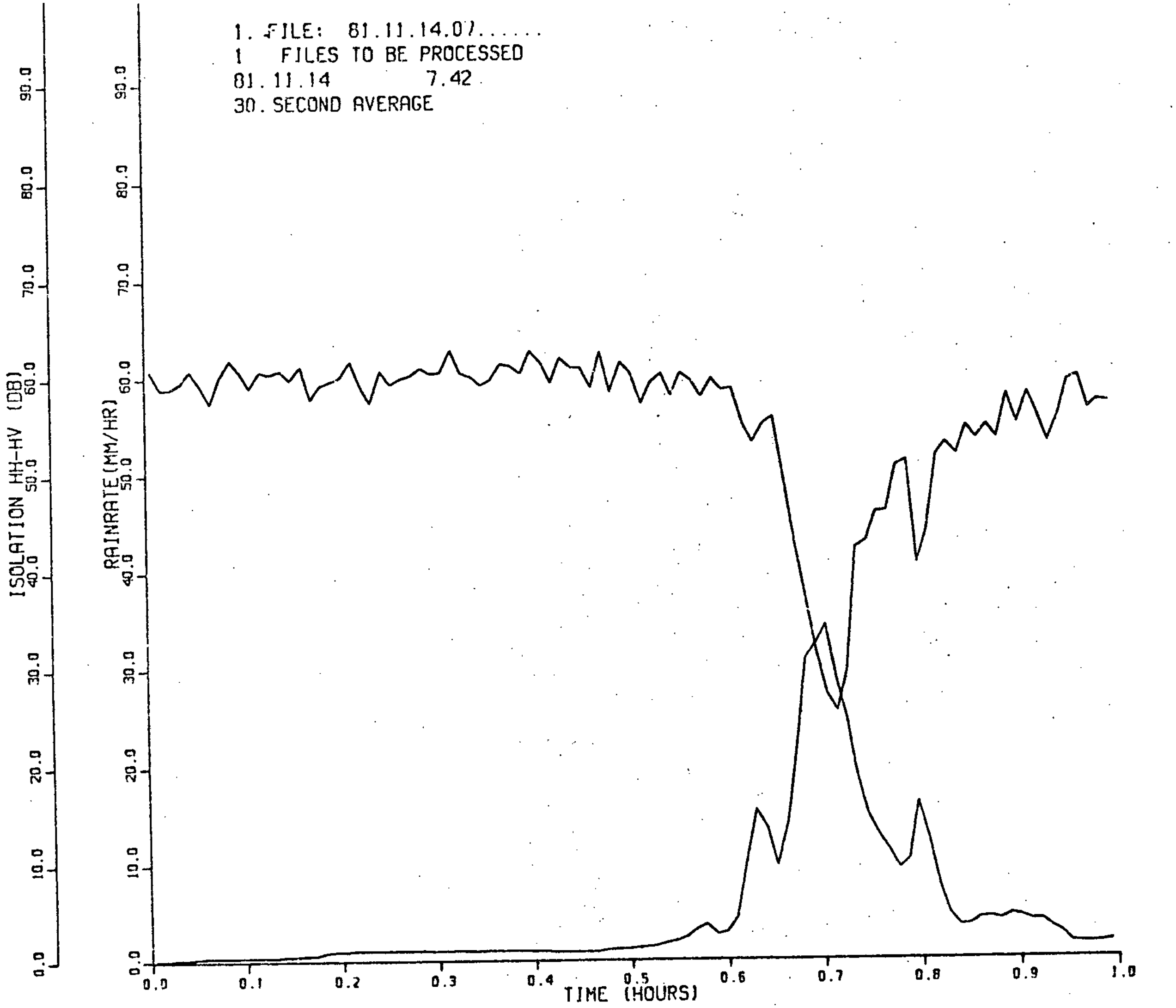

Fig. 6.9.13(b). XPD for horizontal polarization transmitted, 30 s avg. for 81.11.14.07.

At other times during this file, there are a few crosspolar signal level peaks of the same amplitude as the one during the rain peak at around 0.80 hours during T_3. However, these occurred during periods when the received copolar signal level was at least 12 dB higher. This means that the proportion of the signal depolarized by the path was actually much lower during these crosspolar signal level peaks because more signal was available to be depolarized or equivalently because the depolarized signal suffered less attenuation.

The uncancelled XPD for vertical transmitted polarization is shown in Fig. 6.9.14 (10 s average). In this file the path depolarized signal was generally increasing the total system XPD. The apparent decrease in XPD during T_2 was again because the XPD measurement range had been exceeded for part of this interval. Fig. 6.9.14 shows very little or no XPD variation during T_1 and a small XPD increase during T_3, which is basically similar to the uncancelled XPD for these periods.

The differential attenuation measured during this data file is shown in Fig. 6.9.15. During almost all of this period the differential attenuation was positive, again presumably because the wind velocities were relatively constant.

Table 6.9.2 is a summary of the XPD and differential attenuation data for this data file.

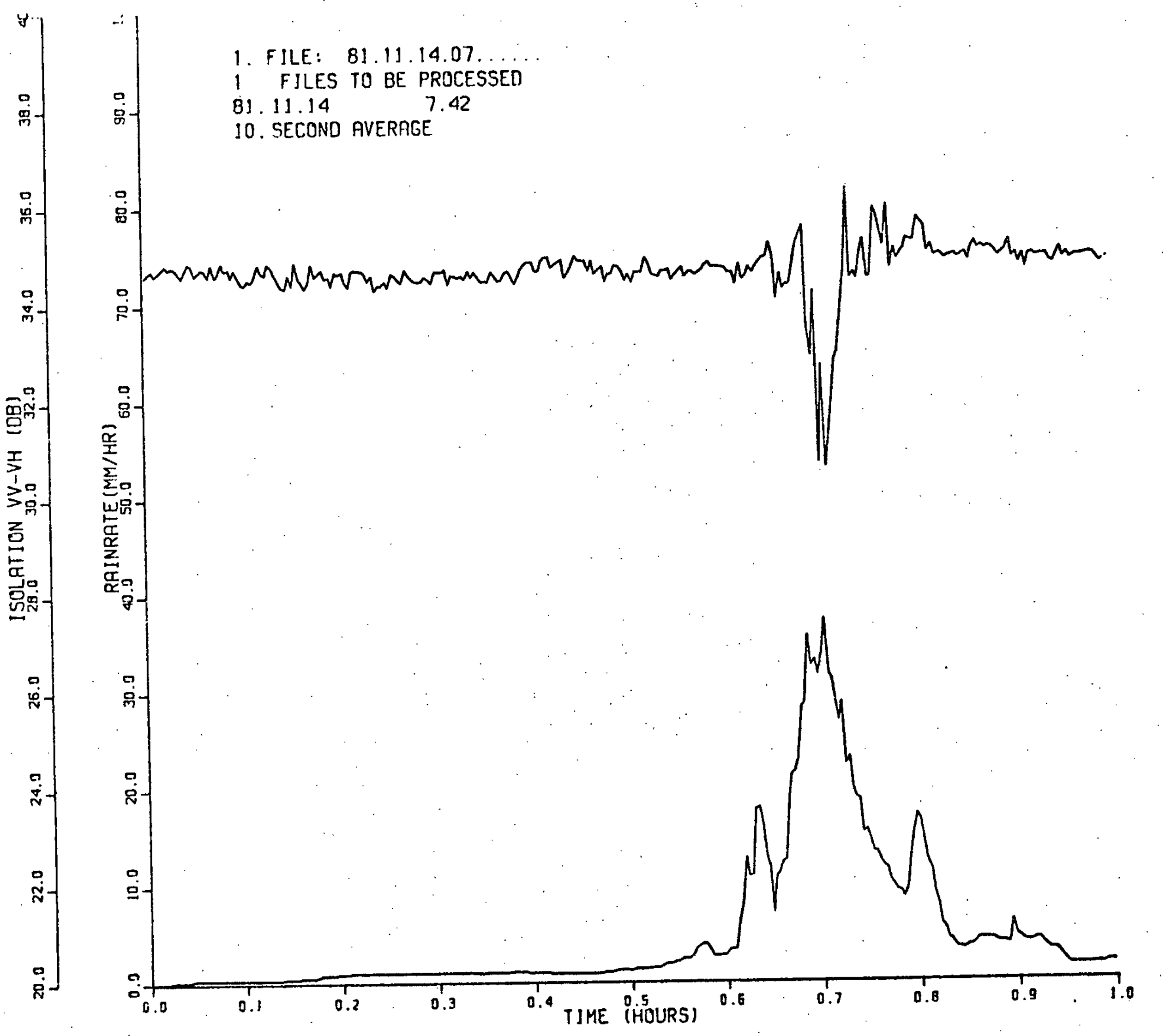

Fig. 6.9.14. XPD for vertical transmitt polarization, 10s avg. for 81.11.14.07.

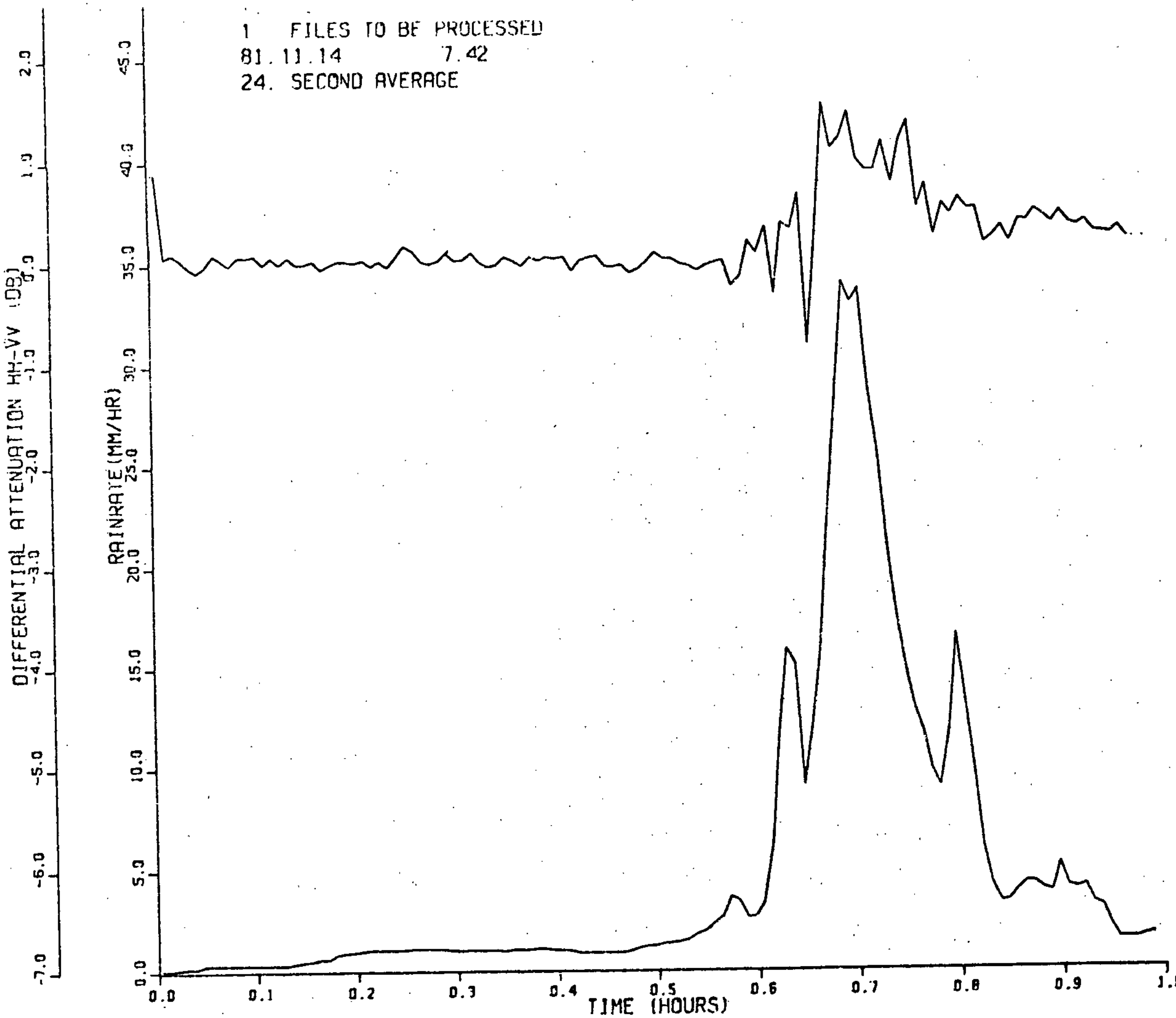

Fig. 6.9.15. Differential attenuation for 81.11.14.07.

Period	XPD	Differential Attenuation	Wind Velocities During Rain	XPD is in Approximate Agreement with Model Predictions for:	Comments
T_1 0.56-0.65 h	XPD_H: 53-62 dB. Fig. 6.9.16 XPD_V almost no change from clear weather XPD Fig. 6.9.17	$\cong$ +0.4 dB at highest rain-rates.	Horiz. wind $\cong$ 4.0 m/s avg. Fig. 6.9.3	XPD_H agrees with predictions for $\phi \cong 2°$ at low rainrates and $\phi \cong 1°$ at higher rainrates. XPD_V within range predicted for $\phi \cong 1°$ Figs. 6.9.16 and 6.9.17	
T_3 0.77-0.84 h	XPD_H: 42-57 dB Fig. 6.9.18 XPD_V slightly larger change from clear weather XPD than during T_1 Fig. 6.9.19	$\cong$+0.4 dB at highest rain-rates.	Horiz. wind $\cong$7.0 m/s avg. Fig. 6.9.3	XPD_H agrees with predictions for $\phi \cong$ 3-5° XPD_V within range of slightly larger than 1°	Uncancelled XPD change is small because of relative XPD angle.

Table 6.9.2 Summary of XPD and Differential Attenuation Data for 81.11.14.07

6.9.2.1 XPD and Differential Attenuation During T_1, 0.56-0.65 h

During T_1, the cancelled XPD agreed with model predictions for an approximate 2° canting angle at low rainrates and approximately 1° at higher rainrates. The uncancelled XPD shows little or no change from the clear weather value. This is probably due to the relative angle between the path and antenna XPDs for the uncancelled channel and/or the possibility that the cancelled channel results are inaccurate due to the low crosspolar signal levels. The horizontal wind velocity averaged approximately 4.0 m/s during this period.

The differential attenuation during T_1 was approximately +0.4 dB during the maximum rainrates in this period. This value is just slightly lower than the theoretical predictions for this rainrate.

During T_2, the differential attenuation reached values of approximately 1.3 dB which is in reasonable agreement with predictions for the maximum rainrates during T_2.

6.9.2.2 XPD and Differential Attenuation During T_3, 0.77-0.84 h

During this period, the average horizontal wind velocity was approximately 7.0 m/s, considerably higher than during T_1. The cancelled XPD now agrees with model predictions for canting angles between approximately 3° and 5°. The uncancelled XPD also shows a larger change from the clear weather value but it is assumed that the relative XPD angles resulted in relatively small changes preventing an accurate comparison to the theory.

During T_3, the differential attenuation was again approximately +0.4 dB at the higher rainrate, which was slightly lower than predicted.

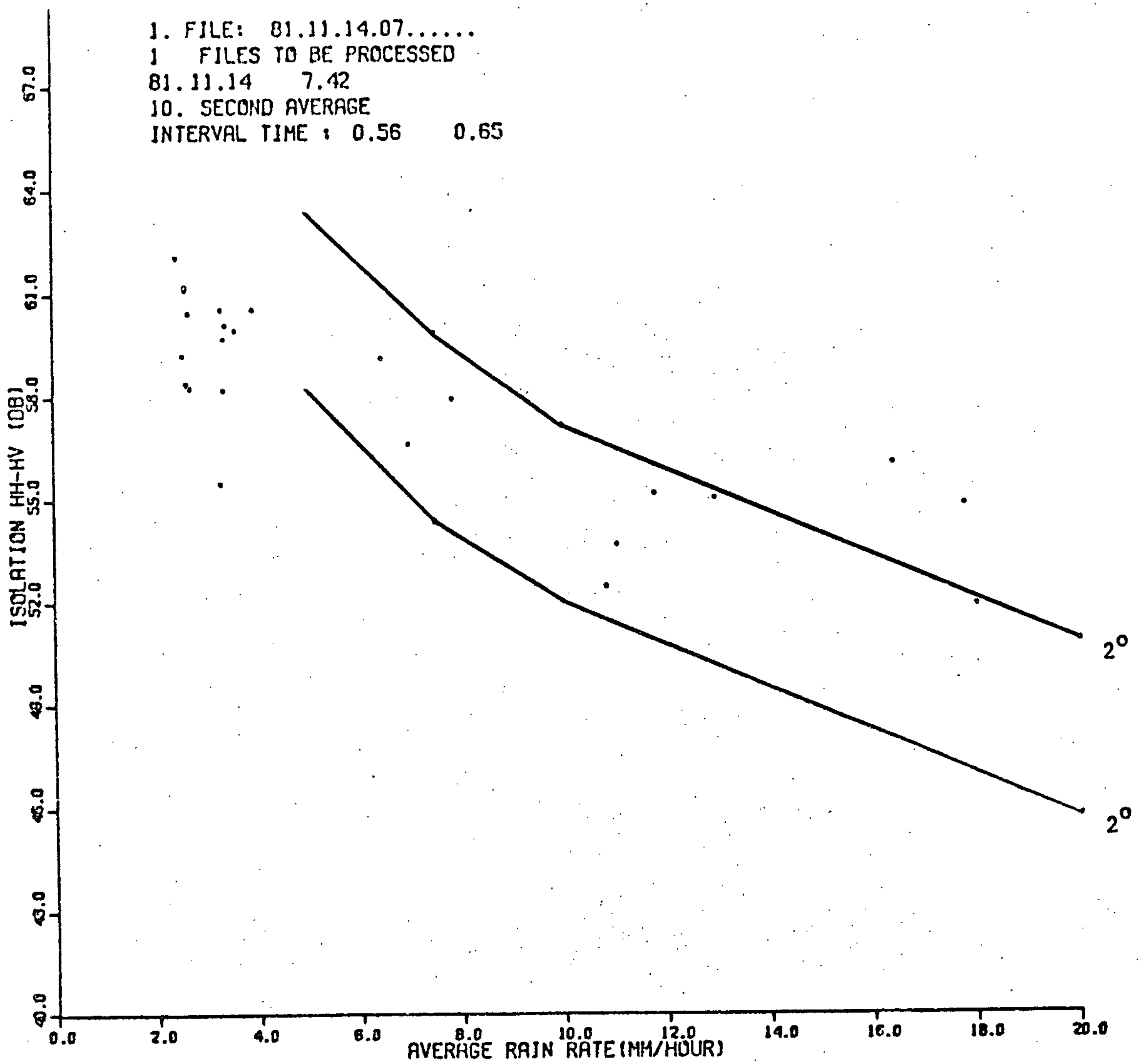

Fig. 6.9.16. XPD_H for T_1.

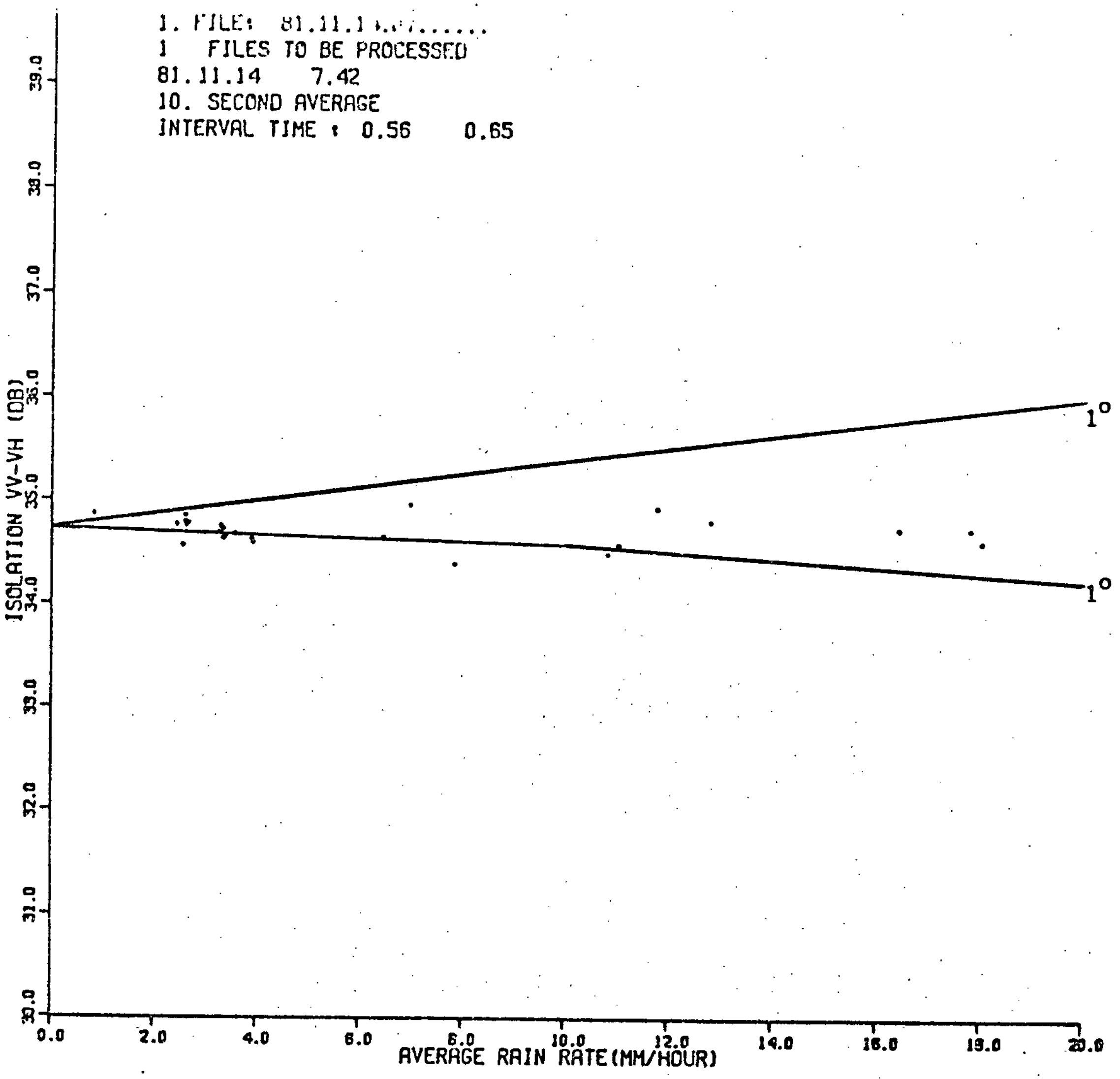

Fig. 6.9.17. XPD_V for T_1.

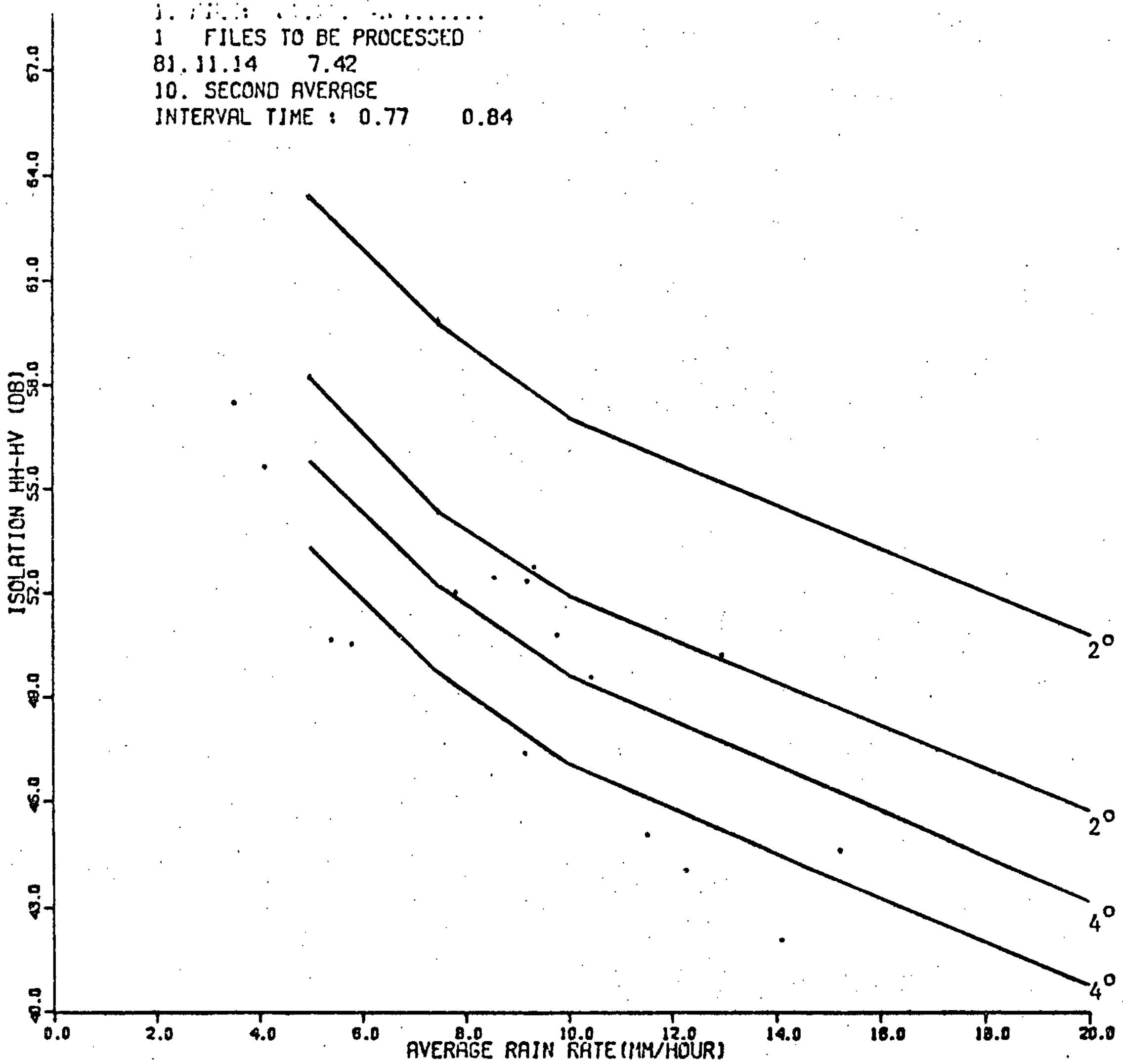

Fig. 6.9.18. XPD_H for T_3.

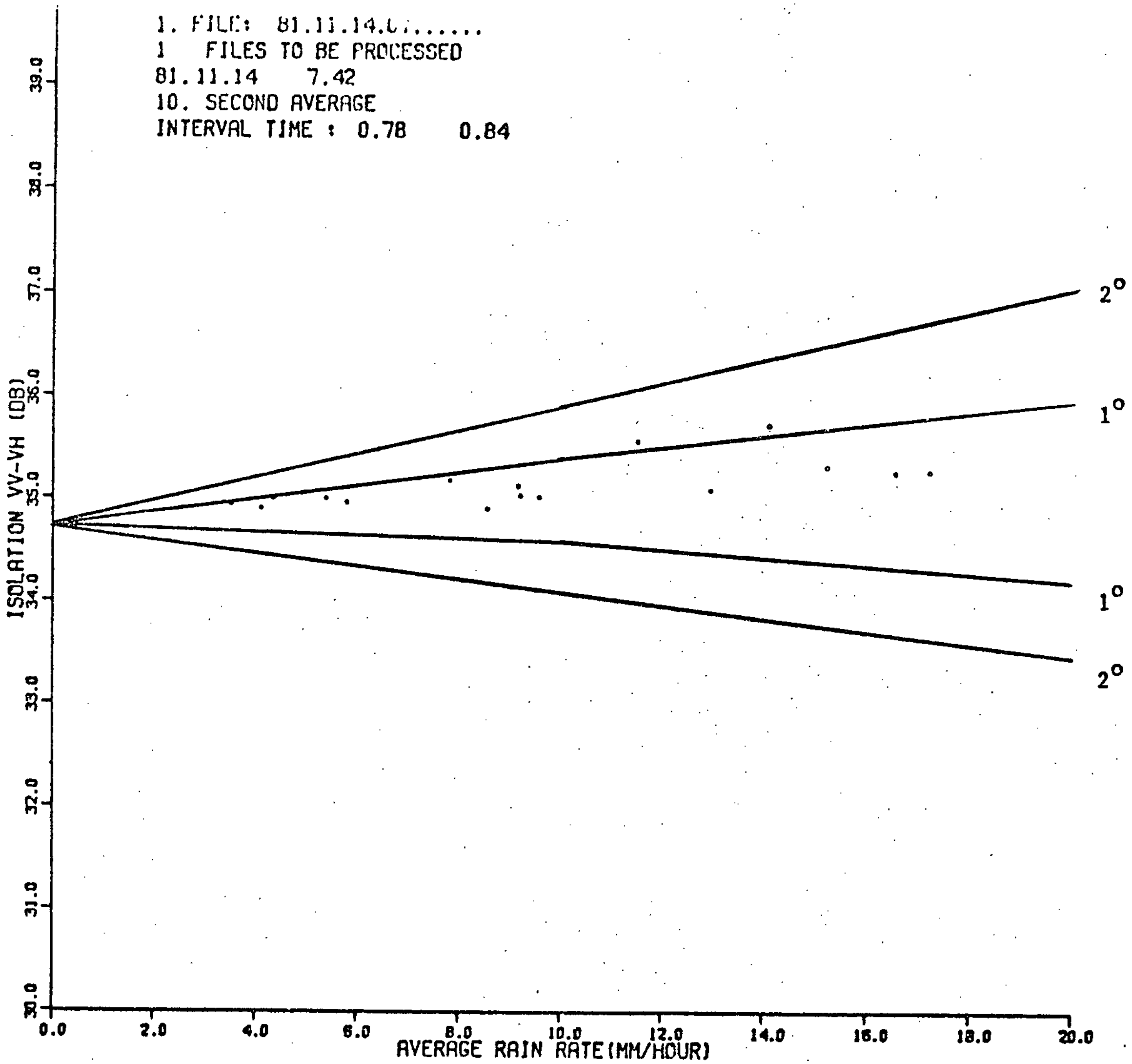

Fig. 6.9.19. XPD_V for T_3.

7. CONCLUSIONS

The objective of this thesis was to investigate dual-polarized millimetre-wave atmospheric propagation during rain, including crosspolar discrimination, differential attenuation and copolar attenuation. The fulfillment of this objective was described in the previous chapters. The major contributions resulting from this work are:

- what are believed to be the first dual-polarized propagation measurements in this frequency range.
- experimental observations leading to the conclusion that drops often did not have a consistent shape and canting angle.
- observations of copolar attenuation much higher than expected from the standard predictions and their explanation in terms of constant and transient vertical wind conditions.
- the proposal of a simple extension to the standard prediction methods to include the effects of constant vertical wind velocities.
- the development of a comprehensive experimental model to predict cancelled system XPD response including the effects of OMT mismatches and the crosspolar cancellation network.
- the phase compensation improvement to the basic crosspolar cancellation network.
- the improved electrostatic disdrometer, and
- a novel, high performance microstrip IF/LO diplexer.

7.1 Millimetre-Wave Equipment

The millimetre-wave portion of this experimental system basically consisted of a switched polarization transmitter, two-channel receiving system and radar propagation path. A two-channel receiver front-end was constructed which was very linear, had excellent channel-to-channel isolation and was as sensitive as economically possible. As part of this front-end, an IF/LO diplexer was developed which had low loss, very good impedance matching and was readily constructed in microstrip. This diplexer circuit topology has not, to our knowledge, been described previously.

The front-end noise power in the receiver prediction bandwidth (30 Hz) was calculated to be -129 dBm, measured to be approximately -122 dBm on the bench and -127 dBm when installed on the roof. The entire receiving system was accurate for 73 GHz input levels below -100 dBm. This resulted in a copolar fade margin of 65 dB, and up to 70 dB for longer averaging periods, over the 1.8 km total length radar path.

A crosspolar cancellation network included in the receiving system resulted in much more accurate measurements of path depolarization. The clear weather, uncancelled system XPD of this experimental system was 33-36 dB, which is considered to be very good for this frequency range. This was improved to over 60 dB, on one channel, by the addition of a crosspolar cancellation network. The cancelled isolation obtained was also high compared to other reported systems incorporating XPD improvement circuits.

7.2 Meteorological Instrumentation

Meteorological instrumentation for this experiment included an improved electrostatic disdrometer, a raingauge network with very high spatial and temporal resolution, and a three-vector anemometer. The electrostatic disdrometer which was developed is considered to be significantly better than the previously described devices of this type. It also appears to be more accurate than other basic disdrometer methods, when used in this type of experiment.

7.3 Experimental Model

A comprehensive experimental model was developed to predict the total system XPD response under a wide variety of conditions. This model included a crosspolar cancellation network and the important effects of impedance mismatches on OMTs. Using this experimental model, the following have been analyzed, for what is believed to be the first time: the effects of OMT port mismatches, the frequency response and error sensitivity of crosspolar cancellation systems and the possible range of cancelled system XPD responses during rain including all propagation and experimental effects. The results of this model also led to the development of a new phase compensation network which improves the frequency and temperature stability of cancelled systems. Where comparisons were possible, experimental results conformed well to the experimental model predictions.

7.4 Experimental Results

7.4.1 XPD Results

This experiment has provided what are believed to be the first, dual-polarized propagation results in this frequency range. The inclusion of the crosspolar cancellation network and the application of the experimental model allowed far more accurate determinations of path XPD than would have been otherwise possible . In general, the cancelled system XPDs were correlated with the horizontal wind velocity and rainrate as expected from the basic theoretical predictions (e.g. Sections 6.2.2.1, 6.2.2.2, 6.2.2.4, 6.4.2.1 and 6.7.2.2). One data file also suggests a greater reduction in path XPD for rain with large numbers of large drops (Section 6.4.2). Most of the accurate XPD results, observed during relatively constant wind conditions, agreed with the model predictions for a range of effective mean canting angles between 0 and 6°, depending on cross-path horizontal wind velocity. These values of canting angle are in range predicted by Brussaard's model [4.15], Fig. 4.1, but the variable height and unknown terrain roughness over this path make comparisons difficult. Good examples of uncancelled system XPD consistently increasing and decreasing from the clear weather value, due to path XPD angle changes, were also observed during this experiment (e.g. Section 6.7.2).

7.4.2 Conclusions Regarding Drop Shape and Canting Angle

Differential attenuation observed during this experiment was usually positive, but was also often negative, in contradiction with the basic theoretical predictions and drop shape and orientation assumptions. One example of negative differential attenuation had been reported previously, [1.74]. During this experiment, negative differential attenuations were usually observed during periods of rapidly increasing, but occasionally decreasing, horizontal wind velocity. The uncancelled XPD during these periods of extremely variable wind conditions usually increased and decreased erratically from the clear weather value. These results appear to indicate that the rain drops often did not have a consistent shape and canting angle. This had also been suspected by Warner [4.13] and Haworth and McEwan [4.14] although they used different types of evidence to support their beliefs, as discussed in Section 4.1.3.

This conclusion is reasonable if the effects of the extremely rapid wind variations observed during this experiment on drop shape and orientation are considered. The generally assumed drop shapes result from the balance of hydrostatic and aerodynamic forces on the drop falling at its terminal velocity in still air. However, changes in horizontal wind velocity, which had magnitudes greater than the drop terminal velocities were often observed over periods of only a few seconds. A drop experiencing a change in horizontal aerodynamic force equal to or greater than, the vertical force must obviously change shape and/or orientation. During several data periods, it is believed that the wind conditions were so variable that no consistent drop shape and canting angle existed.

7.4.3 Effects of Vertical Wind Velocities on CPA

This experiment has also demonstrated, for what is believed to be the first time, several important effects of vertical wind on copolar attenuation. Attenuations were frequently observed which were much higher and occasionally lower, than expected from the standard predictions. These results are attributed to vertical wind conditions.

During periods of relatively constant upward vertical wind velocities, attenuation was higher than expected because the drop terminal velocities had been reduced, causing an increase in N_D, especially for small drop sizes. A modification to the standard predictions based on a simple meterological model to include the effects of vertical wind has been proposed. The modified prediction results generally agree with the experimental observations after the application of a corrective factor ($\cong 2$) to the vertical wind velocity. This correction is believed to be necessary to compensate for a reduced anemometer response, due to boundary effects and a terminal velocity simplification in the meteorological model. Examples are shown in Sections 6.2.1.5, 6.4.1.1, 6.5.1.2, and 6.5.1.3.

Three significant, previously unreported, CPA results were observed during transient vertical wind conditions. During moderately increasing upward vertical wind velocities, attenuation was considerably higher than expected from the standard predictions due to an increasing number of smaller drops in the antenna beams (e.g. Sections 6.6.1.3 and 6.6.1.5). However, during large and rapidly increasing upward vertical winds, the path CPA was lower than expected because the number of smaller drops in the path was reduced and presumably increased at some height above the path (e.g. Sections 6.2.1.1, 6.2.1.8 and 6.4.1.5). The most important vertical wind induced CPA changes occurred when the vertical wind velocity decreased rapidly after a period of upward flow. This resulted in a large increase in the number of small drops in the path as the drops "stored" above the path during the period of upward flow are "released" by the decreasing vertical wind velocity. This condition frequently resulted in attenuations much higher than were previously thought to be possible for the measured rainrates on the ground (e.g. Sections 6.2.1.1, 6.2.1.3, 6.2.1.6, 6.4.1.2, and 6.4.1.4). These higher attenuations persisted for periods of up to a few minutes as the stored drops fell through the antenna beams. For the prediction of reliability on microwave links, where predicted outages are only a few minutes per year, this effect will be very important in geographic locations where this type of wind condition can occur.

7.4.4 Future Work

It is believed that this experimental investigation has added to what is known about atmospheric propagation of millimetre-waves during rain. To be able to further understand some of the effects observed, and explanations proposed, in this report, more complete meterological instrumentation would be required. It would be necessary to develop: a direct method of measuring drop shape and canting angle in the path and wind vectors and drop size distributions at points above the path. Theoretical models should also be developed to more completely explain the vertical wind effects on CPA and variable wind effects on drop shape and orientation.

8. REFERENCES

1.1 Fedi, F. "Prediction of Attenuation Due to Rainfall on Terrestrial Links - A Review," URSI Commission F Symposium, Effects of the Lower Atmosphere on Radio Propagation at Frequencies Above 1 GHz, Lennoxville Canada, 26-30, May 1980.

1.2 Holland, X.D., Hilsen, N.B., Gallagher, J.J. and Stevens, G., "System Analysis for Millimeter-Wave Communication Satellites," Microwave Journal, pp. 35-43, June 1980.

1.3 Falk, H., "Communications and Microwaves," IEEE Spectrum, pp. 32-33, Jan. 1974.

1.4 Decardi, L.J., "Research and Development Efforts Necessary to Evolving Satellite Communications Systems," IEEE Ant. and Prop. Soc. Newsletter, pp. 8-11, Aug. 1981.

1.5 Change, Y.W. and Yuan, L.T., "Millimeter-Wave Binocular Radio," Microwave Journal, pp. 31-36, March 1980.

1.6 Delange, O.E., Dietrich, A.F. and Hogg, D.C., "An Experiment on Propagation of 60 GHz Waves Through Rain," BSTJ, vol. 50, no. 1, pp. 165-176, Jan. 1975.

1.7 Roche, J.F. et al., "Radio Propagation at 27-40 GHz," IEEE Trans. Ant. and Prop., vol. AP-18, no. 4, pp. 452-462, July 1970.

1.8 Fedi, F., "Criteria and expected accuracy of the measurements envisaged in the research programme under way in Italy," Agard Conf. no 107, Telecommunications Aspects on Frequencies Between 10 and 100 GHz, Gausdal, Norway, pp. 8-1-8-23, 18-21, Sept. 1972.

1.9 Keizer, W.P.M.N, Snieder, J., de Haan, G.D., "Rain Attenuation Measurements at 94 GHz: Comparison of Theory and Experiment," Agard Conf. no. 245, Millimeter and Submillimeter Wave Propagation and Circuits, Munich, Germany, pp. 44-1-44-9, 4-8, Sept. 1978.

1.10 Hogg, D.C. and Chu, T.S., "The Role of Rain in Satellite Communications," Proc. IEEE, vol. 63, pp. 1308-1331, Sept. 1975.

1.11 Barsis, A.P. and Samson, C.A., "Performance Estimation for 15 GHz Microwave Links as a Function of Rain Attenuation," IEEE Trans. Comm., pp. 462-470, April 1976.

1.12 Ananasso, F., "Coping With Rain Above 11 GHz," MSN, pp. 58-72, Mar. 1980.

1.13 Dintelman, F. and Rucher, F. "Analysis of an XPD Event at 30 GHz Measured with ATS-6," Proc. IEEE, vol. 65, no. 3, pp. 477-479, Mar. 1977.

1.14 Lee, L.S., "The Feasibility of Two One-Parameter Polarization Control Methods in Satellite Communications," IEEE Trans. Comm. vol. COM-29, no. 5, pp. 735-743, May 1981.

1.15 Dilworth, I.J., "Depolarization at 11.6 GHz on a Terrestrial Radio Link," Ann. Telecommunic, 32, no. 11-12, pp. 469-477, 1977.

1.16 Segal, B., "High-intensity rainfall statistics for Canada," CRC report no. 1329-E, Communications Research Centre, Dept. of Communications, Ottawa, Canada, Nov. 1979.

1.17 Ciapura, D., "How to manage your way into earth terminals," Broadcast Communications, pp. 51-55, Nov. 1978.

1.18 Szojka, F.G., "Carriers develop interference calculation system for microwave," Canadian Electronics Engineering, pp. 24-27, Sept. 1978.

1.19 Ippolito, L.J., "Radio Propagation for Space Communications Systems," Proc. IEEE, vol. 69, no. 6, pp. 697-729, June 1981.

1.20 Katzenstein, W.E., Moore, R.P. and Kimball, H.G., "Spectrum Allocations Above 40 GHz," IEEE Trans. Comm., vol. Com-2, no. 8, pp. 1136-1141, Aug. 1981.

1.21 "International Radio Consultative Committee (CCIR)," XIVth Plenary Assembly, Kyoto 1978, vol. V.

1.22 "Implementation of the spectrum allocation decision of the 1979 world administrative radio conference," vol. I and II, Government of Canada, Department of Communications.

1.23 Wiltse, J.C., "Millimeter Wave Technology and Applications," Microwave Journal, pp. 39-42, Aug. 1979.

1.24 Taub, J.J., "Will Component Advances Finally Yield Millimeter Systems?," MSN, pp. 62-69, Jan. 1980.

1.25 Cuccia, C.L., and Spilker, J.J., "Wideband Spectrum Utilization Above 10 GHz for Communications and Monitoring the Ecology," Microwave Journal, pp. 24-30, Nov. 1971.

1.26 Kariotis, G.S., "Millimeters and Manana," Microwave Journal, pp. 15-16, Nov. 1976.

1.27 Dees, J.W. and Wiltse, J.C., "An Overview of Millimeter Wave Systems," Microwve Journal, pp. 42-49, Nov. 1969.

1.28 "Millimetre Waves - Semiconductors and Systems" published by the Hughes Aircraft Co., 1979.

1.29 McNabb, J., "Local Distribution - A Potential Millimeter-Wave Market," Microwave Journal, pp. 54-56, Nov. 1971.

1.30 Konishi, Y. and Uenakada, K., "Millimeter Wave FM Radio Equipment for Multi Channel Video Transmission," IEEE Int'l Conf. Comm., pp. 5C-1-5, 1974.

1.31 Volckman, P.A., Bibbs, S.E. and Denniso, P., "30 GHz High-Speed Portable Data Link," IEEE Int'l Conf. Comm., pp. 5F-1-5, 1974.

1.32 Mosckowitz, S., "Millimetre-wave radio evaluated for covert battlefield communications, Microwaves, pp. 23-24, Mar. 1980.

1.33 Steffes, P.G. and Meck, R.A., "Prototype Tests Secure Millimeter Communications," MSN, pp. 59-68, Oct. 1980.

1.34 Schuchardt, J.M., et al., "The Coming of mm-Wave Forward Looking Imaging Radiometers," Microwave Journal, pp. 45-55, June 1981.

1.35 Cuccia, C.L., "Digital Communications at Gigahertz Data Rates," Microwave Journal, pp. 89-93, Jan. 1970.

1.36 Arnaud, J.A. and Ruscio, J.T., "Guidance of 100 GHz Beams by Cylindrical Mirrors," IEEE Trans. MTT, vol. MTT-23, no. 4, pp. 377-379, April 1975.

1.37 Kuno, H.J., "Solid State Millimeter-Wave Power Sources and Combiners," Microwave Journal, pp. 21-34, June 1981.

1.38 MSN staff, "Millimetres Turn Practical," MSN, pp. 19-28, May 1980.

1.39 Yen, H.C. and Chang, K., "A 63 W-Band and Injection-Locked Pulsed Solid State Transmitter," 1981 IEEE MTT-S Int'l Microwave Symp., pp. 341-343, 15-19 June 1981.

1.40 Ma, Y., Sun, C. and Nakaji, "V-Band High-Power Impatt Amplifier," IEEE MTT-S Int'l Symp. pp. 73-74, 28-30 May 1980.

1.41 Cardiasmenos, A.C., "Planar Devices Make Production Practical," MSN, pp. 46-52, May 1979.

1.42 Cardiasmenos, A.G., "New Diodes Cut the Cost of Millimeter Wave Mixers," Microwaves, pp. 78-88, Sept. 1978.

1.43 Chang, Y.W. and Yuan, L.T., "IC's for 94 GHz Radar Applications, "Microwave Journal, pp. 81-ff, June 1981.

1.44 Itoh, T., "Open Guided Wave Structure for Millimeter-Wave Circuits, 1981 IEEE MTT-S Int'l Microwave Symp. pp. 3-4, 15-19 June 1981.

1.45 Skih, Y., Rivera, J. and Itoh, T., "Directive Planar Excitation of an Image-Guide," 1981 IEEE MTT-S Int'l Microwave Symp. pp. 5-7, 15-19 June 1981.

1.46 Solbach, K., and Wolff, I., "Slots As New Circuit Elements in Dielectric Image Line," 1981 IEEE MTT-S Int'l Microwave Symp. pp. 8-10, 15-19 June 1981.

1.47 Sharma, A.K. and Hoefer, J.R., "Empirical Analytical Expressions for FIN Line Design," 1981 IEEE MTT-S Int'l Microwave Symp. pp. 102-104, 15-19 June 1981.

1.48 Willing, H.A. and Spielman, B.E., "Experimental Assessment of Bilateral FIN-Line Impedance for Device Matching, 1981 IEEE MTT-S Int'l Microwave Symp. pp. 105-107, 15-19 June 1981.

1.49 Yatsuka, H. et al., "Millimeter-Wave IC Components Using Fine Grain Alumina Substrates," 1980 IEEE MTT-S Int'l Microwave Symp. pp. 276-278, 28-30 May 1980.

1.50 Dydyk, M., "Shielded Microstrip: Transmission Media for MM-Wave Integrated Circuits," 1981 IEEE MTT-S Int'l Microwave Symp., pp. 99-101, 15-19 June 1981.

1.51 Komizo, H. and Tokumitsu, Y., "Millimeter wave Integrated Circuits," 1981 IEEE MTT-S Int'l Microwave Symp., pp. 179-181, 15-19 June 1981.

1.52 Cardiasmenos, A.G., "Low-Noise Thin-Film Downconverters for Millimeter Systems Applications," 1978 IEEE MTT-S Int'l Microwave Symp., pp. 399-401, 29 June 1978.

1.53 Meier, P.J., "E-Plane Components For a 94 GHz Printed circuit Balanced Mixer," IEEE 1980 MTT-S Int'l Microwave Symp., pp. 267-269, 28-30 May 1980.

1.54 Segal, B., "High-Intensity Rainfall Statistics for Canada," CRC Report no. 1329-E, Communications Research Center, Department of Communications, Ottawa, Nov. 1979.

1.55 Crane, R.K., "Prediction of Attenuation by Rain," IEEE Trans. Comm., vol. COM-28, no. 9, pp. 1717-1733, Sept. 1980.

1.56 Crane, R.K., "A Global Model for Rain Attenuation Prediction," Eascon 78 conf., pp. 391-395, April 1978.

1.57 Neves, J. and Watson, P.A., "Cross-Polarization, Differential Attenuation and Differential Phase Shift Measured on a 36.5 GHz Terrestrial Link," URSI Commission F, Effects of the lower atmosphere on radio propagation above 1 GHz, Lennoxville, Quebec, pp. 5.1.1-6, 28-30 May 1980.

1.58 Watson, P.A., "Survey of measurements of attenuation by rain and other hydrometeors," Proc. IEE, vol. 123, no. 9, pp. 863-871, Sept. 1976.

1.59 Zavody, A.M. and Harden, B.N., "Attenuation/Rain-Rate Relationships at 36 and 110 GHz," Elect. Lett., vol. 12, no. 17, pp. 422-424, 19 Aug. 1976.

1.60 Llewellyn Jones, D.T., "Attenuation by Rainfall in the Submillimetre Wave Region," Proc. Nato, Adv. Study Inst. Modern Topics in Microwave Propagation and Air-Sea Interaction, Sorrento, Italy, pp. 285-290, 5-14 June 1973.

1.61 Butler, S., "Measurements of Cross-Polarization Discrimination at 11 and 17 GHz," URSI Commission F, Effects of the lower atmosphere on radio propagation above 1 GHz, Lennoxville, Quebec, pp. 5.3.1-.4, 28-30 May 1980.

1.62 Evans, B.G., Uzunoglu, N.K. and Holt, A.R., "Two New Approaches to the Calculation of Rain Induced Attenuation and Cross Polarization" Ann. Telecommunic., vol. 32, no. 11-12, pp. 1/6-6/6, 1977.

1.63 Johnston, S.L., "A Radar System Engineer Looks at Current Millimeter-Submillimeter Atmospheric Propagation Data," Eascon 79, Electronics and Aerospace Systems Conf., Arlinton, Va, pp. 27-35, 9-11 Oct. 1979.

1.64 Hogg, D.C. and Chu, T.S., "The Role of Rain in Satellite Communications," Proc. IEEE, vol. 63, pp. 1308-1331, Sept. 1975.

1.65 Barbaliscia, F., Fedi, F., Maggiore, D. and Migliorine, P., "Frequency scaling of Rain Induced Attenuation at 11, 18 and 30 GHz," URSI Commission F, Effects of the Lower Atmosphere on Radio Propagation at Frequencies Above 1 GHz, Lennoxville, Quebec, pp. 2.2.1-2.2.6, 26-30 May 1980.

1.66 Holt, A.R. and Evans, B.G., "The Scattering of Millimeter Waves by Precipitation Particles," URSI Commission F, The effects of the Lower Atmosphere on Radio Propagation at Frequencies Above 1 GHz, Lennoxville, Quebec, pp. 1.1.1-1.1.6, 28-30 May 1980.

1.67 Crane, R.K., "Propagation Phenomena Affecting Satellite Communication Systems in the Centimeter and Millimeter Wavelength Bands," Proc. IEEE, vol. 59, no. 2, pp. 173-188, Feb. 1971.

1.68 Crane, R.K., "Attenuation due to Rain - A Mini-Review," IEEE Trans. Ant. and Prop., pp. 750-752, Sept. 1975.

1.69 Fedi, F., Merlo, U., and Migliorini, P., "Effect of Rain Structure on Rain Induced Attenuation," Ann. Telecommunic., vol. 32, no. 11-12, pp. 1/5-6/6, 1977.

1.70 Fedi, F. and Mandarini, P., "Analysis of the Influence of the Various Parameters on the Attenuation-Rain Rate Relation," Nato Adv. Study Institute, Modern Topics in Microwave Propagation and Air-Sea Interaction, Sorrento, Italy, pp. 325-342, 5-14 June 1973.

1.71 Roche et al., "Radio Propagation at 27-40 GHz," IEEE Trans. Ant. and Prop. vol. AP-18, no. 4, pp. 453-462, July 1970.

1.72 Ugai, S. et al., "Fine Structure of Rainfall," Ann. Telecommunic., no. 32, no. 11-12, pp. 422-429, 1977.

1.73 Medhurst, R.C., "Rainfall Attenuation of Centimeter Waves: Comparison of Theory and Measurement," IEEE Trans. Ant. and Prop., vol. AP-13, pp. 550-564, July 1965.

1.74 DeLange, O.E., Dietrich, A.R., and Hogg, D.C., "An Experiment on Propagation of 60 GHz Waves Through Rain," B.S.T.J., vol. 54, No. 1, pp. 165-176, January 1975.

1.75 Hogg, D.C. and Chu, T.S., "The Role of Rain in Satellite Communications," Proc. IEEE, vol. 63, pp. 1308-1331, September 1975.

1.76 Thomas, D.T., "Cross-Polarization Distortion in Microwave Transmission Due to Rain," Radio Science, vol. 6, no. 10, pp. 833 - 837, October 1971.

1.77 Neves, J. and Watson, P.A. "Cross-Polarization, Differential Attenuation and Differential Phase Shift Measured on a 36.5 GHz Terrestrial Link," URSI Commission F Open Symposium, Lennoxville, Quebec, pp. 5.1.1-5.1.6, 26-30 May 1980.

1.78 Semplak, R.A. "Measurements of Rain-Induced Polarization Rotation at 30.9 GHz," Radio Science, vol. 9, no. 4, pp. 425-429, April 1974.

1.79 Semplak, R.A., "Effect of oblate raindrops on attenuation at 30.9 GHz," Radio Science, vol. 5, no. 3, pp. 559-563, Mar. 1970.

1.80 Turner, D.J.W., "Measurements of Cross Polar Discrimination at 22 GHz and 37 GHz," Conf. on Propagation of Radio Waves at Frequencies Above 10 GHz, London, pp. 256-263, 10-13 April 1973.

1.81 Shimba, M. and Morita, K, "Radio Propagation Characteristics Due to Rainfall at 19 GHz," Proc. IEEE/G-AP Int'l. Symp. 1972, pp. 246-249.

1.82 Morita, K., Hosoya, Y. and Akeyama, A. "Some Experimental Results on 20 GHz Band Rain Attenuation," Proc. IEEE/G-AP, Int'l. Symp. 1973, pp. 285-288.

1.83 Shimba, M., Morita, K. and Akeyama, A. "Radio Propagation Characteristics Due to Rain at 20 GHz Band," IEEE Trans. Ant. and Prop., vol. AP-22, pp. 507-509, May 1974.

1.84 Sander, J., "Rain Attenuation of Millimeter Waves at $\lambda = 5.77$, 3.3 and 2 mm," IEEE Trans. Ant. and Prop., vol. AP-23, no. 2, pp. 213-220, March 1975.

1.85 Humpleman, R.J. and Watson, P.A., "Investigation of Attenuation by Rainfall at 60 GHz," Proc. IEE, vol. 125, no. 2, pp. 85-91, Feb. 1978.

1.86 Keizer, W.P.M.N., Snieder, J. and de Haan, C.D., "Propagation Measurements at 94 GHz and Comparison with Theoretical Results Derived from Actually Measured Raindrop Size Distributions," IEE Conf. Proceedings, pp. 72-76, Nov. 1978.

1.87 Keizer, W.P.M.N, Sneider, J. and de Haan, C.D., "Rain Attenuation Measurements at 94 GHz: Comparison of Theory and Experiment," Agard Conf. 245, Millimeter and Submillimeter Wave Propagation and Circuits, Munich, Germany, pp. 44-1-44-8, 4-8 Sept. 1978.

1.88 Llewellyn-Jones, D.T. and Zavody, A.M., "Microwave Attenuation Due to Rain at 110 GHz In South-East England," Elec. Lett., vol. 3, no. 4, pp. 97-98, 3 Feb. 1972.

2.1 Kharadly, M.M. "Atmospheric Propagation Characteristics of Electromagnetic Waves in the Short Millimetre Range," C.R.C. Contract report 05076-00097, 1 July, 1976 - 31 March 1977.

2.2 Harris, D.J. "Waveguiding Difficult at Near-Millimetres," MSN, pp. 62-73, December 1980.

2.3 Tischer, F.J. "Experimental Attenuation of Rectangular Waveguides at Millimetre Wavelengths," IEEE Trans. Microwave Theory and Tech., vol. MTT-27, no. 1, pp. 31-88, January 1979.

2.4 Kharadly, M.M. "Atmospheric Propagation Characteristics of Electromagnetic Waves in the Short Millimetre Range," C.R.C. Contract Report OST 78-00012, 12 May 1978 - 31 March 1979.

2.5 Gupta, K.C., Garg, R. and Bahl, I.J. "Microstrip Lines and Slotlines," Dedham, Mass: Artech House, 1979.

2.6 Belohoubek, E. and Denlinger, E., "Loss Considerations for Microstrip Resonators," IEEE Trans. Microwave Theory and Tech., vol. MTT-23, pp. 522-526, June 1975.

2.7 Hammerstad, E.O., "Equations for Microstrip Circuit Design," Proc. of the European Microwave Conf., Hamburg, Germany, September 1975, pp. 268-272.

2.8 Wheeler H.A., "Transmission-Line Properties of Parallel Strips Separated by A Dielectric Sheet," IEEE Trans. Microwave Theory and Tech., vol. MTT-13, pp. 172-185, March 1965.

2.9 Getzinger, W.J., "Microstrip Dispersion Model," IEEE Trans. Microwave Theory and Tech., vol. MTT-21, pp. 34-39, January 1973.

2.10 James, D.S. and Tse, S.H., "Microstrip End Effects," Elect. Lett., vol. 8, no. 1, pp. 46-47, 6th January 1972.

2.11 Cohn, S.B., "Parallel-Coupled Transmission-Line-Resonator Filters," IRE Trans. Microwave Theory and Tech., vol MTT-6, pp. 223-230, April 1958.

2.12 Garg, R, and Bahl, I.J., "Characteristics of Coupled Microstriplines," IEEE Trans. Microwave Theory Tech., vol. MTT-27, pp. 700-705, July 1979, and correction MTT-28, no. 3, p. 272, March 1980.

2.13 Kajfez, D and Govind, J., "Effect of Difference in Odd-and Even-Mode Wavelengths on a Parallel-Coupled Bandpass Fitler," Elec. Lett., vol. 11, no. 5, pp. 117-118, 6th March 1975.

2.14 Essayaz, G. and Sauve, B., "Effects of Geometrical Parameters of a Microstrip on its Dispersive Properties," Elect. Lett., vol. 8, no. 21, p. 529, 19 October 1972.

2.15 Okean, H.C. and Lombardo, P.P., "Noise Performance of M/W and MM-Wave Receivers", Microwave Journal, pp. 41-50, January 1973.

2.16 Gewartawski, J.W., "Noise Figure for a Mixer Diode," IEEE Trans. Microwave Theory and Techniques, vol. MTT-19, p. 481, May 1971.

2.17 Neuf, D., "What to Look for in Mixer Specs", Microwaves, pp. 87-92, November 1974.

2.18 Weinreb, S. and Kerr, A.R., "Cryogenic Cooling of Mixers for Millimeter and Centimeter Wavelengths," IEEE Journal of Solid-State Circuits, vol. SC-8, no. 1, pp. 58-62, Feb. 1973.

2.19 Kerr, A.R., "Shot-Noise in Resistive-Diode Mixers and the Attenuator Noise Model," IEEE Trans. Microwave Theory and Techniques, vol. MTT-27, no. 2, Feb. 1979, pp. 135-140.

2.20 Held, D.N. and Kerr, A.R., "Conversion Loss and Noise of Microwave and Millimeter-Wave Mixers," IEEE Trans. Microwave Theory and Techniques, vol. MTT-26, no. 2, Feb. 1978, pp. 49-61.

2.21 Winderman, J.B., "Perform True DSB-to-SSB Noise Figure Conversions", Microwaves, P. 69, July 1980. See also Feedback, Microwaves, p. 11 and p. 105, September 1980.

2.22 Kraus, J.D., "Radio Astronomy," New York, N.Y., McGraw-Hill, 1966.

2.23 Hewlett-Packard Application note 150-4 "Spectrum Analysis - Noise Measurements," April 1974.

2.24 Pratt, T. and Browning, D.J., "An Economical Microwave Phase and Amplitude Measuring Receiver," IERE Conf. Proc. no. 40, Radio Receivers and Associated Systems, pp. 289-297, 11-14 July 1978.

2.25 Cahill, T.C., Gill, C. and Syrogos, H., "Modular Design of Millimeter Antennas," Microwave Journal, pp. 53-57, November 1973.

2.26 Dilworth, I.J., "Adaptive Orthogonality Restoration Techniques on Millimetric and Microwave Communication Links," Proc. Conf. Radio Receivers and Associated Systems, IERE Conf. Proc. No. 40, pp. 179-188, July 1978.

2.27 Kreutel, R.W., Di Ronzo, D.F., English, W.J., and Grunner, R.W., "Antenna Technology for Frequency Reuse Satellite Communications," Proc. IEEE, vol. 65, no. 3, March 1977, pp. 370-378.

2.28 Barton, S.K., "Methods of Adaptive Cancellation for Dual Polarization Satellite Systems, The Marconi Review, vol. 39, no. 200, First Quarter 1976, pp. 1-24.

2.29 Chu, T.S., "Restoring the Orthogonality of Two Polarizations in Radio Communications Systems, Part I," BSTJ, vol. 50, no. 9, pp. 3063-3069, Nov. 1971.

2.30 Chu, T.S., "Restoring the Orthogonality of Two Polarization in Radio Communication Systems, Part II," BSTJ, vol. 52, no. 3, pp. 319-327, Mar. 1973.

2.31 Di Fonzo, D.F., Trochtman, W.S. and Williams, A.E., "Adaptive Polarization Control for Satellite Frequency Reuse Systems," Comsat Technical Review, vol. 6, no. 2, pp. 253-283, Fall 1976.

2.32 Kannowade, Heinz, "An Automatic control System for Compensating Cross-Polarization Coupling in Frequency-Reuse Communication Systems," IEEE Trans. Comm., vol. COM-24, no. 9, pp. 986-999, Sept. 1976.

2.33 Williams, A.E., "A dual-polarized 4/6-GHz adaptive polarization control network," Comsat Technical Review, vol. 7, no. 1, pp. 247-262, Spring, 1977.

2.34 Williams, A.E. and Frey, F.L., "Adaptive Polarization Control on a Dual-Polarized 4/6 GHz Satcom Link in the Presence of Rain," Elect. Lett., vol. 12, no. 25, pp. 686-687, 9 Dec. 1976.

2.35 Evans, B.G., and Thompson, P.T., "Use of Cancellation Techniques in the Measurement of Atmospheric Crosspolarization," Elect. Lett., vol. 9, no. 19, pp. 447-448, 20 Sept. 1973.

2.36 Sobieski, P.W., "Depolarization Measurements at 12 GHz," 4th European Microwave Conf., Montreux, Switzerland, 10-13 Sept. 1974.

2.37 Dilworth, I.J., and Evans, B.C., "Linear and Circular Crosspolarization on an 11 GHz Terrestrial Radio Link," URSI Commission F Open Symposium, Lennoxville, Que., pp. 6.1.1-6.1.7, 26-30 May 1980.

2.38 O'Neill, M.J., "The Design of a Small Earth Station," Conf. on Radio Receivers and Associated Systems, IERE Conf. Proc. No. 40, pp. 59-72, 10-14 July 1978.

2.39 Dintelmann, F., "12 GHz Slant-Path Propagation Studies with OTS: Polarization Measurements," URSI Commission F, Open Symposium, Lennoxville, Que., pp. 6.1.1-6.1.7, 26-30 May 1980.

2.40 Murphy, P.J., "A Theoretical and Experimental Investigation of Microwave Propagation at 30 GHz," Ph.D. Thesis, University College, Cork, Ireland, Nov. 1978.

2.41 Watson, P.A., Goodall, F. and Arbabi, M. "Linear Cross-Polarization and Attenuation Measurements at 11 and 36 GHz," Conf. on Propagation of Radio Waves at Frequencies Above 10 GHz, London, pp. 155-161, 10-13 April 1973.

2.42 Hoffman, H. "Hydrophobic Coating for Antenna Weather Windows," Microwave Journal, pp. 43-46, October 1979.

2.43 Ghabrial, S.I., "Axial Cross Polarization in Reflector Antennas with Surface Imperfections," IEEE Trans. Ant and Prop., AP-28, no. 5, pp. 610-616, September 1980.

2.44 Fedi, F., "Criteria and Expected Accuracy of the Measurements Envisaged in the Research Programme Under Way in Italy," Agard Conf. Proc., Telecom. Aspects on Freq. between 10 and 100 GHz, Gausdal, Norway, pp. 8-1 -8-23, 18-21 September 1972.

2.45 Olsen, R., "Cross polarization on terrestrial links - a review," URSI Commission F Int'l Symp. "Effects of the lower atmosphere on radio propagation at frequencies above 1 GHz, Lennoxville, Que., May 1980.

2.46 Dintelmann, F. and Rucker, F., "Analysis of an XPD Event at 30 GHz measured with ATS-6," IEEE Proc., vol. 65, no. 3, pp. 477-479, Mar. 1977.

2.47 Gruner, R.W., "Intelsat V earth station technology," Rec. IEEE Int'l Telecomm. Exp., vol. 1, Oct. 9-15, 1977, pp. 242-248.

2.48 Ghabrial, S.I., "Cross-polarization in satellite and earth-station antennas," Proc. IEEE, vol. 65, no. 3, Mar. 1977, pp. 378-386.

2.49 Hansen, R.C., "Microwave Scanning Antennas," Academic Press, New York, 1964.

2.50 Jasik, H., "Antenna Engineering Handbook," McGraw Hill, New York, 1961.

2.51 Jordan, E.C. and Balmain, K.G., "Electromagnetic Waves and Radiating Systems," Prentice-Hall, Englewood Cliffs, New Jersey, 1968.

2.52 Raff, S.J., "Microwave System Engineering Principles," Permagon Press, Elmsford, N.Y., 1977.

2.53 Liebe, H.J., "Atmospheric Water Vapour: A Nemesis for Millimeter Wave Propagation," Proc. IFAORS Workshop on Atmospheric Water Vapour," Vail, Colo, 11-13 September 1979, published by Academic Press, New York, May 1980.

3.1 Crane, R.K., "Attenuation due to Rain - A Mini-Review," IEEE Trans. Antennas and Prop., pp. 750-752, September 1975.

3.2 Crane, R.K., "Propagation Phenomena Affecting Satellite Communication Systems Operating in the Centimeter and Millimeter Wavelength Bands," Proc. IEEE, vol. 59, no. 2, pp. 177-188, February 1971.

3.3 Fedi, F., "Criteria and Expected Accuracy of the Measurements Envisaged in the Research Programme Under Way in Italy," Agard Conf. Proc. Telecomm. Aspects on Freq. Between 10 and 100 GHz, Gausdel, Norway, pp. 8-1, 8-23, 18-21 September 1972.

3.4 Fedi, F. and Mandarini, P., "Analysis of the Influence of the Various Parameters on the Attenuation - Rain Rate Relation," Proc. Nato Adv. Study Inst. Modern Topics in Microwave Prop and Air-Sea Interaction, Sorrento, Italy, pp. 325-342, 5-14 June 1973.

3.5 Watson, P.A., "Survey of Measurements of Attenuation by Rain and other Hydrometeors," Proc. IEE, vol. 123, no. 9, pp. 863-871, September 1976.

3.6 Hogg, D.C., "Millimeter-Wave Communication Through the Atmosphere," Science, vol. 159, no. 3810, pp. 39-46, 5 January 1968.

3.7 Barsis, A.P. and Samson, C.A., "Performance Estimation for 15 GHz Microwve Links as a Function of Rain Attenuation," IEEE Trans. Comm., pp. 462-470, April 1976.

3.8 Bodtmann, W.F. and Ruthroff C.L., "Rain Attenuation on Short Radio Paths: Theory, Experiment and Design," BSTJ, vol. 53, no. 7, pp. 1329-1349, September 1974.

3.9 Segal, B., "High-intensity rainfall statistics for Canada," CRC Report no. 1329-E, Department of Communications, Communications Research Center, Ottawa, Nov. 1979.

3.10 Semplak, R.A. and Keller H.E., " Dense Network for Radio Meausrement of Rainfall Rate," BSTJ, pp. 1745-1756, July-August 1969.

3.11 Freeny, A.E. and Gabbe, J.D., "A Statistical Description of Intense Rainfall," BSTJ, pp. 1789-1850, July-August 1969.

3.12 Freeny, A.E., "Statistical Treatment of Rain Gauge Calibration Data," BSTJ, pp. 1757-1766, July-August 1969.

3.13 Fedi, F. and Merlo, U., "Statistical Data on Point Rainfall Intensity for Radio - Relay Systems Design," Ann. Telecommunic. 32, no. 11-12, pp. 1/5-5/5, 1977.

3.14 Goldhirsh, J., "Predictive Methods for Rain Attenuation Using Radar and In-Situ Measurements Tested Against the 28 GHz Comstar Beacon Signal," IEEE Trans. Antenna and Prop., vol. AP-27, no. 3, pp. 398-406, May 1979.

3.15 Blevis, B.C., Dohoo, R.M. and McCormick, K.S., "Measurements of Rainfall Attenuation at 8 and 15 GHz," IEEE Trans. Antenna and Prop., vol. AP-15, no. 3, pp. 294-407, May 1967.

3.16 Skerjanec, R.E., and Samson, C.A., "Rain Attenuation Measurements in Mississippi at 10 and 14.4 GHz," IEEE Trans. Antennas and Prop., vol. 19, pp. 575-578, July 1971.

3.17 Ippolito, L.J., "Effects of Precipitation on 15.3 and 31.65 GHz Earth-Space Transmission with the ATS-V Satellite," Proc. IEEE, vol. 59, no. 2, pp. 109-205, February 1971.

3.18 Medhurst, R.G., "Rainfall Attenuation of Centimeter Waves: Comparison of Theory and Measurements," IEEE Trans. Ant. and Prop., pp. 550-564, July 1965.

3.19 Roche, J.F., et.al., "Radio Propagation at 27-40 GHz," IEEE Trans. Ant. and Prop., vol. AP-18, no.4, pp. 452-462, July 1970.

3.20 Ugai, S. et.al., "Fine Structure of Rainfall," Annales Des Telecomm. tomme 32, no. 11-12, pp. 422-429, November-December 1977.

3.21 Keizer, W.P., Snieder, J, de Haan, C.D., "Rain Attenuation Measurements at 94 GHZ: Comparison of Theory and Experiment," Agard Conf. preprint 245. Millimeter and Submillimeter Wave Prop. and Circuits, Munich, Germany, pp. 44-1 - 44-9, 4-8 September 1978.

3.22 Goldhirsh, J., "Predictive Methods for Rain Attenuation Using Radar and In-Situ Measurements Tested Against the 28 GHz Comstar Beacon Signal," IEEE Trans. Ant. and Prop. vol. AP-27, no. 3, pp. 398-406, May 1979.

3.23 Emery, R.J. and Zavody, A.M., "Atmospheric Propagation in the Frequency Range 100-1000 GHz," The Radio and Electronic Engineer, vol. 49, no. 7/8, pp. 370-380, July/August 1979.

3.24 Llewellyn Jones, D.T., "Attenuation by Rainfall in the Submillimetre Wave Region," Proc. Nato Adv. Study and Inst. Modern Topics in Microwave Prop. and Air-Sea Interaction, Sorrento, Italy, pp. 285-291, 5-14 June 1973.

3.25 Godard, S.L., "Propagation of Centimeter and Millemeter Wavelengths through Precipitation," IEEE Trans. Ant. and Prop., vol. AP-18, no. 4, pp. 530-534, July 1970.

3.26 Joss, J. and Waldvogel, A., "Raindrop Size Distribution Sampling Size Errors," J. Atmos. Sci., vol. 26, pp. 566-568, May 1969.

3.27 Cunningham, A., "Analysis of Particle Spectral Data From Optical Array 1D and 2D Sensors," Preprints of Fourth Symposium on Meteorological Observations and Instrumentation," Denver, Colo., 10-14 April 1978.

3.28 Knollenburg, R.C., "The Optical Array: An Alternative to Scattering or Extinction for Airborne Particle Size Determination," J. Appl. Meteor, vol. 9, pp. 86-103, February 1970.

3.29 Wang, T and Dilford, S.F., "Use of Rainfall - Induced Optical Scintillation to Measure Path Averaged Rain Parameters," J. Optical Society of America, vol. 65, no. 8, pp. 927-937, August 1975.

3.30 Wang. T., Earnshaw, K.B. and Lawrence, R.J., "A Fast-Response Optical Sensor for Measuring Rainfall Rate and Raindrop Size Distribution," Proc. IEEE Int'l. Symp. Ant. and Prop. Japan, pp. 493-495, 1978.

3.31 Foote, G.B. and Du Toit, P.S., "Terminal Velocity of Raindrops Aloft," J. Appl. Metoer. vol. 8, pp. 294-469, April 1969.

3.32 Mason, B.J. and Ramanadham, R. "A Photoelectric Raindrop Spectometer," Quart. J.R. Meteor., Soc., vol. 79, pp. 490-495, 1953.

3.33 Dingle, A.N. and Schulte, H.F., "A Research Instrument for the Study of Raindrop-Size Spectra," J. Appl. Meteor., vol. 1, pp. 48-59, March 1962.

3.34 Klaus, V., "Un Spectropluviometre Photoelectrique Fournissant En temps Reel Des Parametres Integris," Ann. Telecommunic., 32, no. 11-12, pp. 1/7-7/7, 1977.

3.35 Joss, V.J. and Waldvogel, A., "Ein Spektrograph fur Niederschlagstrophen mit Automotischer Auswertung," Pure Appl. Geophys., vol. 68, pp. 240-246, 1967.

3.36 Georgii, H.W. and Jung, E., "An Electro-Dynamic Raindrop Spectometer," Proc. Int'l. Conf. Cloud Physics, Toronto, pp. 393-399, August 1968.

3.37 Rowland, J.R., "Comparison of Two Different Raindrop Disdrometers," 17th Conf. on Radar Meteorology, Seattle, Wash., pp. 398-405, 26-29 October 1976.

3.38 Waldvogel, A., "The N_0 Jump of Raindrop Spectra," J. Atmos. Sci., vol. 31, pp. 1067-1078, May 1974.

3.39 Joss, J., Thams, J.C. and Waldvogel, A., "The Variation of Raindrop Size Distributions at Locarno," Proc. Int. Conf. Cloud Phys., Toronto, pp. 369-373, August 1968.

3.40 Breuer, L.J. and Kreuels, R.K., "Rainfall Drop Spectra Intensities and Fine Structures on Different Time Bases," Ann. Telecommunic. 32, no. 11-12, pp. 1/7-7/7, 1977.

3.41 Keizer, W.P., Snieder, J. and de Haan, C.D., "Rain Attenuation Measurements at 94 GHz: Comparision of Theory and Experiment," Agard Conf. preprint 245, Millimeter and Submillimeter Wave Prop. and Circuits, Munich, Germany, pp. 44-1 - 44-9, 4-8 September 1978.

3.42 Flach, T.E., "An Automated System for the Measurement and Analysis of Raindrop Size Distribution," M.Sc. Thesis, Univ. of Illinois, Urbana, Illinois, 1972.

3.43 Goldhirsh, J., "A Demonstration of Methods for Predicting Attenation Due to Rain Using the 28 GHz Comstar Beacon Signal with Radar, Disdrometer and Raingauge Data," Proc. Int'l. Symp. Ant. and Prop., Japan, pp 405-468, 1978.

3.44 Rowland, J.R., Bennett, L.W. and Miller, R.E., "Description of the APL Disdrometer - Raingauge System, Johns Hopkins University, Applied Physics Lab. Laurel, Maryland, 26 September 1975.

3.45 Kinnell, P.I., "The Acoustic Measurement of Water-Drop Impacts," J. Appl. Meteor., vol. 11, pp. 691-694, June 1972.

3.46 Katz, I., "A Momentum Disdrometer for Measuring Raindrop Size from Aircraft," Bull. Amer. Meteor. Soc., vol. 33, no. 9, pp. 365-368, November 1952.

3.47 Cunningham, R.M., "Some Observations of Natural Precipitation Processes," Bull. Amer. Met. Soc., vol. 32, no. 9, pp. 334-343, November 1951.

3.48 Kinnell, P.I.A., "Some Observations on the Joss Waldvogel Rainfall Disdrometer," J. Appl. Meteor., vol. 15, pp. 499-502, May 1976.

3.49 Lammers, U.H.W., "Electrostatic Analysis of Raindrop Distributions," J. Appl. Meteor., vol. 8, pp. 330-334, June 1969.

3.50 Keiley, D.P., and Millen, S.G., "An Airborne Cloud-Drop-Size Distribution Meter," J. Meteor., vol. 17, pp. 349-356, June 1960.

3.51 Sander, J., "Experimental Results with a Rain Analyzer," J. Appl. Meteor, vol. 14, no. 1, pp. 128-131, Feb. 1975.

3.52 Kharadly, M.M., "Atmospheric Propagation Characteristics of Electromagnetic Waves in the Short Millimetre Range," CRC Contract Report OSU77-00261, 1 October 1977 - 31 March 1978.

3.53 Kharadly, M.M., McNicol, J.D., and Peters, J.B., "Measurement of Attenuation Due to Rain at 74 GHz," Agard Conf. Proc. No. 245, Millimeter and Submillimeter Wave Prop. and Circuits, Munich, Germany, pp. 46-1 - 46-16, 4-8 September 1978.

4.1 Chu, T.S., "Rain-Induced Cross-Polarization at Centimeter and Millimeter Wavelengths," B.S.T.J., vol. 53, no. 8, pp. 1557-1579, Oct. 1974.

4.2 Evans, B.G., "Millimetre-Wave Propagation," Military Microwaves Conf., London, England, pp. 231-237, 22-24 Oct. 1980.

4.3 Holt, A.R. and Evans, B.G., "The scattering of millimetre waves by precipitation particles," URSI Commission F Open Symposium, Lennoxville, Quebec, pp. 1.1.1-1.1.6, 26-30 May 1980.

4.4 Neves, J. and Watson, P.A., "Cross-polarization, differential attenuation and differential phase shift measured on a 36.5 GHz terrestrial link," URSI Commission F Open Symposium, pp. 5.1.1-5.1.6, 26-30 May 1980.

4.5 Oguchi, T., "Scattering properties of Pruppacher-Pitter form raindrops and cross polarization due to rain: Calculations at 11, 13, 19.3 and 34.8 GHz," Radio Science, vol. 12, no. 1, pp. 41-51, Jan. - Feb. 1977.

4.6 Joss, J., Thams, J.C. and Waldvogel, A., "The variation of raindrop size distributions at Locarno," Proc. Int'l Conf. Cloud. Phys., Toronto, Canada, pp. 369-372, Aug. 1978.

4.7 Marshall, J.S. and Palmer W.M., "The distribution of raindrops with size," J. Meteorology, vol. 5, pp. 165-166, Aug. 1948.

4.8 Laws, J.O. and Parson, D.A., "The relations of raindrop size to intensity," Trans. Am. Geophys., Union, vol. 24, pp. 452-459, Sept. 1943.

4.9 Harden, B.N., Norbury, J.R. and White W.J.K., "Use of a Lognormal Distribution of Raindrop Sizes in Millmetric Radio Attenuation Studies," IEE Conf. Proc. on Ant. and Prop., London, Nov. 1978.

4.10 Olsen, R.L., Rogers, D.V. and Hodge, D.B., "The aR^b relation in the calculation of rain attenuation," IEEE Trans. Ant. and Prop., vol. AP-26, pp. 318-329, Mar. 1978.

4.11 Shkarofsky, I.P., "Dependence of Rain Attenuation and Cross-Polarizaiton on Drop Size Distribution, "IEEE Trans. Ant. and Prop., vol. AP-27, no. 4, pp. 538-542, July 1979.

4.12 Pruppacher, J.R., and Pitter, R.L., "A semi-empirical determination of the shape of cloud and rain drops," J. Atmos. Sci., vol. 28, no. 1, 1971, pp. 86-94.

4.13 Warner, C., "Collision Frequency of Raindrops," IEEE Trans. Ant. and Prop., pp. 583-585, July 1977.

4.14 Haworth, P. and McEwan, N.J., "Spectral Analysis of the Received Signal on a 20 GHz Bistatic Scatter Link," URSI Commission F, The Effects of the Lower Atmosphere on Radio Propagation at Frequencies above 1 GHz, Lennoxville, Quebec, pp. 1.5.1-1.5.8, 26-30 May 1980.

4.15 Brussaard, G., "A Meteorological Model for Rain-Induced Cross Polarization," IEEE Trans. Ant. and Prop., vol. AP-24, no. 1, pp. 5-11, Jan. 1976.

4.16 Maher, B.O., Murphy, P.J. and Sexton, M.C., "A theoretical model of the effect of wind-gusting on rain-induced cross-polarization," Ann. Telecommunic., vol. 32, no. 11-12, 1977.

4.17 Watson, P.A., "Crosspolarization measurements at 11 GHz," Proc. IEE, vol. 123, no. 7, pp. 667-675, July 1976.

4.18 Kobayashi, T., "Degradation of cross-polarization isolation due to rain," J. Radio Research Labs Japan, vol. 24, no. 114, pp. 101-107, July 1977.

4.19 Watson, P.A. and Arabi, M., "Crosspolarization isolation and discrimination," Elect. Lett., vol. 9, no. 22, pp. 516-517, 1 Nov. 1973.

4.20 Olsen, R.L., "Cross polarization on terrestrial links - a review,"URSI Commission F Open Symposium, Lennoxville, Quebec, 28-30 May 1980.

4.21 Kinzer, G.D. and Gunn, R., "The evaporation, temperature, and thermal relaxation - time of freely falling waterdrops," J. Meteor., vol. 8, no. 2, pp. 71-83, April 1951.

4.22 Rogers, D.V. and Olsen, R.L., "Calculation of radiowave attenuation due to rain at frequencies up to 1000 GHz," CRC Report 1299, Ottawa, Canada, Nov. 1976.

4.23 Saunders, M.J., "Crosspolarization at 18 and 30 GHz due to Rain," IEEE Trans. Ant. and Prop., vol. AP-19, no. 2, pp. 273-277, Mar. 1971.

4.24 Crane, R.K., "Prediction of Attenuation by Rain," IEEE Trans. Comm., vol. COM-28, no. 9, pp. 1717-1733, Sept. 1980.

4.25 Dissanayake, A.W. and Watson, P.A., "Forward scatter and crosspolarization from sheroidal ice particles," Elect. Lett., vol. 13, no. 5, pp. 140-142, 3 Mar. 1977.

4.26 Van de Hulst, H.C., "Light Scattering by Small Particles," New York, John Wiley, 1957.

4.27 Hogg, D.C. and Chu, T.S., "The role of rain in satellite communications," IEEE Proc., vol. 63, pp. 1308-1331, Sept. 1975.

4.28 Crane, R.K., "Attenuation due to Rain - A Mini-Review," IEEE Trans. Ant. and Prop., pp. 750-752, Sept. 1975.

4.29 Semplak, R.A. and Turrin, R.H., "Some Measurements of Attenuation by Rainfall at 18.5 GHz," BSTJ, pp. 1767-1787, July-Aug. 1969.

4.30 Caton, P.G.F., "A study of raindrop-size distributions in the free atmosphere," Quart, J. Roy. Meteor. Soc., vol. 92, pp. 15-30, 1966.

4.31 Medhurst, R.G., "Rainfall Attenuation of Centimeter Waves: Comparison of Theory and Measurements," IEEE Trans. Ant. and Prop., vol. AP-13, pp. 550-564, July 1965.

4.32 Norbury, R., and White, J.K., "Correlation Between Measurements of Rainfall Rate and Microwave Attenuation at 36 GHz," Conf. on Propagation of Radio Waves at Frequencies Above 10 GHz, London, pp. 45-51, April 1973.

4.33 Shimabukuro, F.I., "Bistatic Scattering From Rain at Millimeter Wavelength," Eascon 79 Conf., vol. 2, pp. 369-371, 9-11 Oct. 1979.

4.34 Crane, R.K., "Fundamental Limitations Caused by RF Propagation," Proc. IEEE, vol. 69, no. 2, pp. 196-209, Feb. 1981.

4.35 Currie, N.C., Dyer, F.B. and Hayes, R.D., "Some Properties of Radar Returns From Rain at 9.375, 35, 70 and 95 GHz," IEEE 1975 Int'l Radar Conf., Arlington, Va, pp. 215-220, 21-23 April 1975.

4.36 Dyer, F.B. and Currie, N.C., "Environmental Effects on Millimeter Radar Performance," Agard Conf. 245, Millimeter and Submillimeter Wave Propagation and Circuits, Munich, pp. 2-1-2-9, 4-8 Sept. 1978.

4.37 Tsang, L., and Kong, J.A., "Radiative transfer theory for active remote sensing of half-space random media," Radio Science, vol. 13, no. 5, pp. 763-773, Sept-Oct. 1978.

4.38 Oguchi, T., "Effects of Incoherent Scattering on Attenuation and Cross Polarization of Millimeter Wave Due to Rain: Preliminary Calculations at 34.8 and 82 GHz for Spherical Drops," URSI Commission F, Effects of the Lower Atmosphere on Radio Propagation at Frequencies Above 1 GHz, Lennoxville, Quebec, pp. 1.4.1-.7, 26-30 May 1980.

4.39 Shupyatsky, A.B., "Echo Depolarization as Measured with Bistatic Radar," J. Rech. Atmos., vol. 8, no. 1/2, pp. 201-204, 1974.

5.1 Shkarofsky, I.P., "Depolarization Due to Precipitation in Satellite Communications," RCA Review, vol. 38, pp. 257-309, June 1977.

5.2 Shkarofsky, I.P. and Moody, H.J., "Performance Characteristics of Antennas for Direct Broadcasting Satellite Systems Including Effects of Rain Depolarization," RCA Review, vol. 37, pp. 279-319, Sept. 1976.

5.3 Nowland, W.L. and Olsen, R.L., "A Simplified Analysis of Depolarization Due to Combined Propagation and Antenna Effects," private communication.

5.4 Delogne, P and Sobieski, P., "Fine Structure of Microwave Cross-Polarization Due to Precipitation," Ann. Telecommunic., vol. 32, no. 11-12, pp. 1/9-9/9, 1977.

5.5 Tompkins, R.D., "A Broad-Band Dual-Mode Circular Waveguide Transducer," IRE Trans. MTT, pp. 181-183, July 1956.

5.6 Ohm, E.A., "A Broadband Microwave Circulator," IRE Trans. MTT, p. 210-217, Oct. 1956.

5.7 Johnson, R.C., et al., "Dual-Mode Coupler," IEEE Trans. MTT, pp. 651-652, Nov. 1967.

6.1 Mason, B.J. and Andrews, J.B., "Drop-size distributions from various types of rain," Quart. J. Roy. Met. Soc., 86, pp. 364-353, 1960.

6.2 Dingle, A.N. and Hardy, K.R., "Description of rain by means of sequential drop-size distributions," Quart. J. Roy. Met. Soc., 88, pp. 301-314, 1962.

6.3 Du Toit, P.S., "Doppler Radar Observation of Drop Sizes in Continuous Rain," J. Appl. Meteor., vol. 6, pp. 1082-1087, Dec. 1967.

6.4 Ugai, S., "Notes on the oil method and data concerned with raindrop size," Faculty of Science and Technology, Sophia University, Tokyo, Japan, Mar. 1977.

6.5 Harden, B.N., Norbury, J.R., Tracey, M.A., and White, W.J.K., "Attenuation Ratios and Path Diversity Gains Observed in Rain on a Network of Short Terrestrial Links at Frequencies Near 11, 20 and 36 GHz," IEE conf. on Ant. and Prop., London, Nov. 1978, pp. 68-71.